

Did a food supplement
sleuth cook up data? p. 484

Evaluating the importance of
methane ultra-emitters pp. 490 & 557

Can NFTs enhance patients' control
over their health data? p. 500

Science

\$15
4 FEBRUARY 2022
science.org

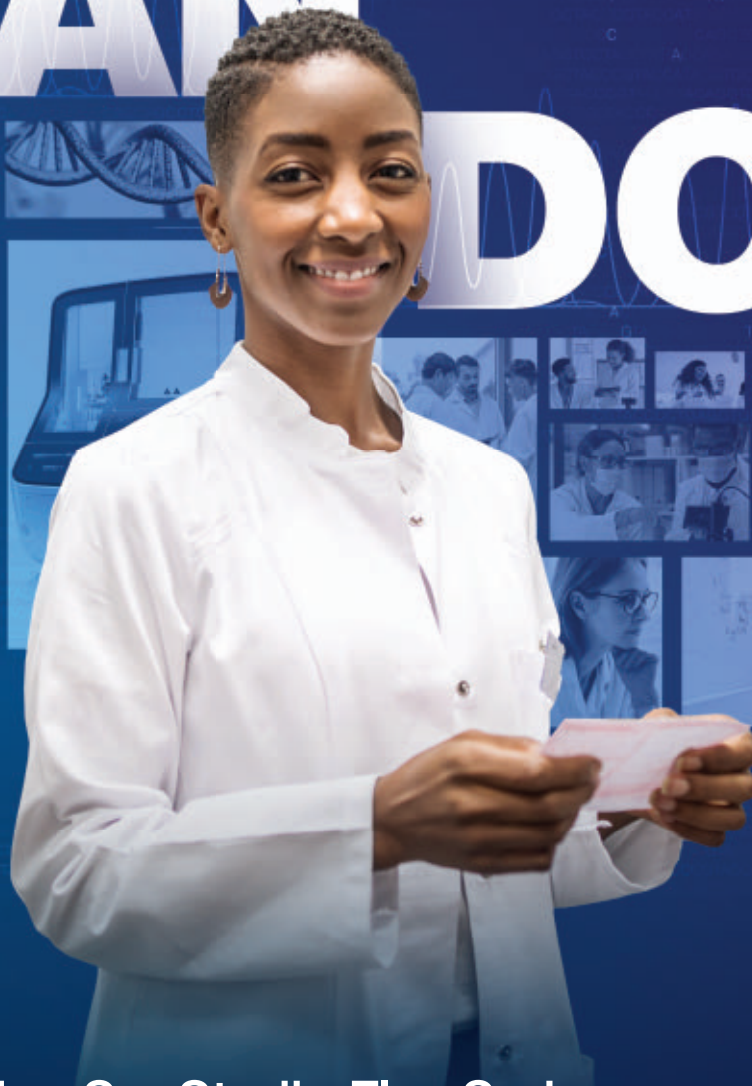
AAAS

A close-up photograph of a translucent green leafhopper perched on a green leaf. The insect's body is semi-transparent, revealing internal structures. It has long, thin legs and antennae. The leaf it is on is dark green with visible veins and some small, light-colored spots.

PLANT DEFENSE

Jasmonate signaling consequences
deter leafhopper pests p. 514

CAN DO



Introducing SeqStudio Flex Series Genetic Analyzers

Reliable performance plus the freedom to work how you want

Designed with users in mind, Applied Biosystems™ SeqStudio™ Flex Series Genetic Analyzers are the only mid-throughput Sanger sequencing and fragment analysis systems that deliver the high level of data quality you expect, while leveraging design improvements and technological advancements for increased flexibility, usability, connectivity, and serviceability for users of all skill levels.



 Learn more at thermofisher.com/seq-the-flex

applied biosystems

CONTENTS

4 FEBRUARY 2022

VOLUME 375 • ISSUE 6580

478

In this visualization, giant black holes are on the cusp of merging. A team of astronomers has predicted an imminent merger in a distant galaxy.

NEWS

IN BRIEF

474 News at a glance

IN DEPTH

478 Imminent merger of giant black holes predicted

Never-before-seen event could spark cosmic fireworks—if it is not a mirage *By D. Clery*

479 Indonesia's utopian new capital may not be as green as it looks

Moving the government to Borneo could speed deforestation *By D. Normile*

PODCAST

480 New Omicron begins to take over, despite late start

BA.2 strain may extend latest surge, but its overall impact remains unclear *By M. Wadman*

482 Massive wolf kill disrupts long-running Yellowstone park study

Hunters kill more than 500 wolves in surrounding states *By V. Morell*

483 Computer scan uncovers 100,000 new viruses

Clues to future outbreaks may be hidden in existing genomic databases *By E. Pennisi*

FEATURES

484 Failing the test

DNA barcoding brought botanist Steven Newmaster scientific fame and entrepreneurial success. Was it all based on fraud? *By C. Piller*

INSIGHTS

PERSPECTIVES

490 Chasing after methane's ultra-emitters

Leaks from oil and gas companies contribute substantially to global warming *By F. Vogel*
REPORT p. 557

491 Tethering gene regulation to chromatin organization

A two-tiered system of chromatin structure ensures robust gene expression *By M. Gaskill and M. Harrison*
REPORT p. 566

493 When viruses become more virulent

Natural selection favors virulence when it is coupled with increased viral transmission *By J. O. Wertheim*
RESEARCH ARTICLE p. 540

494 The adenine methylation debate

N⁶-methyl-2'-deoxyadenosine (6mA) is less prevalent in metazoan DNA than thought *By K. Boulias and E. L. Greer*
RESEARCH ARTICLE p. 515

495 An adaptive device for AI neural networks

The perovskite nickelate can transform among four different electronic components *By R. A. John*
RESEARCH ARTICLE p. 533

497 Lethal mutagenesis as an antiviral strategy

Lethal mutagenesis of RNA viruses is a viable antiviral strategy but has unknown risks *By R. Swanstrom and R. F. Schinazi*

499 Robert H. Grubbs (1942–2021)

Brilliant organic chemist and inspiring mentor *By M. Sanford*

POLICY FORUM

500 How NFTs could transform health information exchange

Can patients regain control over their health information? *By K. Kostick-Quenet et al.*

BOOKS ET AL.

503 From dualism to deism

A philosopher comes full circle *By J. Zerilli*

504 Imagining Rosalind Franklin

The crystallographer's story comes alive in a work of historical fiction *By K. Langin*

LETTERS

506 Particle toxicity's role in air pollution

By G. D. Thurston et al.

506 Response

By B. Gu et al.

507 The protein-folding problem: Not yet solved

By P. B. Moore et al.

RESEARCH

IN BRIEF

509 From *Science* and other journals

REVIEW

512 Chemical pollutionPer- and polyfluoroalkyl substances in the environment *M. G. Evich et al.*

REVIEW SUMMARY; FOR FULL TEXT: DOI.ORG/10.1126/SCIENCE.ABG9065

RESEARCH ARTICLES

513 Immunology

CRISPR activation and interference screens decode stimulation responses in primary human T cells

R. Schmidt et al.

RESEARCH ARTICLE SUMMARY; FOR FULL TEXT: DOI.ORG/10.1126/SCIENCE.ABJ4008

**514 Plant science**

Natural history-guided omics reveals plant defensive chemistry against leafhopper pests

Y. Bai et al.

RESEARCH ARTICLE SUMMARY; FOR FULL TEXT: DOI.ORG/10.1126/SCIENCE.ABM2948

515 Molecular biology

Critical assessment of DNA adenine methylation in eukaryotes using quantitative deconvolution

Y. Kong et al.

PERSPECTIVE p. 494

522 Neurogenomics

Discovery of genomic loci of the human cerebral cortex using genetically informed brain atlases

*C. Makowski et al.***528 Quantum gases**

Second sound attenuation near quantum criticality

*X. Li et al.***533 Emerging computing**

Reconfigurable perovskite nickelate electronics for artificial intelligence

H.-T. Zhang et al.

PERSPECTIVE p. 495

540 HIV

A highly virulent variant of HIV-1 circulating in the Netherlands

C. Wymant et al.

PERSPECTIVE p. 493

REPORTS

545 Organic chemistry

Diversification of aliphatic C–H bonds in small molecules and polyolefins through radical chain transfer

*T. J. Fazeekas et al.***551 Materials science**

Multiscale engineered artificial tooth enamel

*H. Zhao et al.***557 Greenhouse gases**

Global assessment of oil and gas methane ultra-emitters

T. Lauvaux et al.

PERSPECTIVE p. 490

562 Atmospheric chemistry

Nocturnal survival of isoprene linked to formation of upper tropospheric organic aerosol

*P. I. Palmer et al.***566 Gene regulation**

Genome organization controls transcriptional dynamics during development

P. J. Batut et al.

PERSPECTIVE p. 491

570 Neuroscience

Probing subthreshold dynamics of hippocampal neurons by pulsed optogenetics

*M. Valero et al.***574 Development**

Establishment of mouse stem cells that can recapitulate the developmental potential of primitive endoderm

Y. Ohinata et al.

DEPARTMENTS

473 Editorial

Science needs affirmative action

By H. Holden Thorp

582 Working LifeMore than an exam *By Gabriela Lopez*

ON THE COVER

An *Empoasca* leafhopper feeds on a wild tobacco plant (*Nicotiana attenuata*). Leafhopper pests select host plants by detecting consequences of jasmonate signaling, a hormonal signaling cascade elicited in response to physical disturbances. By studying recombinant inbred lines of tobacco plants



in their native habitat, researchers have identified chemistry created by the union of volatile and nonvolatile defenses in leaves that bolsters plants' resistance to leafhoppers. See page 514.

Photo: Danny Kessler

New Products.....	579
Science Careers	580

SCIENCE (ISSN 0036-8075) is published weekly on Friday, except last week in December, by the American Association for the Advancement of Science, 1200 New York Avenue, NW, Washington, DC 20005. Periodicals mail postage (publication No. 484460) paid at Washington, DC, and additional mailing offices. Copyright © 2022 by the American Association for the Advancement of Science. The title SCIENCE is a registered trademark of the AAAS. Domestic individual membership, including subscription (12 months): \$165 (\$74 allocated to subscription). Domestic institutional subscription (51 issues): \$2212; Foreign postage extra: Air assist delivery: \$98. First class, airmail, student, and emeritus rates on request. Canadian rates with GST available upon request. GST #125488122. Publications Mail Agreement Number 1069624. Printed in the U.S.A.

Change of address: Allow 4 weeks, giving old and new addresses and 8-digit account number. **Postmaster:** Send change of address to AAAS, P.O. Box 96178, Washington, DC 20090-6178. **Single-copy sales:** \$15 each plus shipping and handling available from backissues.science.org; bulk rate on request. **Authorization to reproduce** material for internal or personal use under circumstances not falling within the fair use provisions of the Copyright Act can be obtained through the Copyright Clearance Center (CCC), www.copyright.com. The identification code for Science is 0036-8075. Science is indexed in the Reader's Guide to Periodical Literature and in several specialized indexes.

Science needs affirmative action

As science struggles to correct systemic racism in the laboratory and throughout academia in the United States, external forces press on, making it even more difficult to achieve equity on all fronts—including among scientists. The latest example is the decision by the US Supreme Court to hear cases brought against Harvard University and the University of North Carolina (UNC) at Chapel Hill challenging their right to use race as a factor in undergraduate admissions. It is sometimes easy for scientists to let colleagues in other disciplines engage in a debate like this, but the dismantling of race-conscious admissions would deal another blow to equity in science. The Supreme Court has protected affirmative action in the past, but the Court's current majority of conservative justices could mean the end of the program. This is no time for the scientific community to stay silent. It is a crucial moment for science to mobilize against this latest assault on diversity.

For more than 50 years in the United States, colleges and universities have been using multiple criteria to select undergraduates, recognizing that a diverse student body is essential for the university to achieve its mission. I asked Peter Henry, the WR Berkley Professor of Economics and Finance at New York University, about the economic data on the matter. "Affirmative action corrects a market failure," he said. "Talent is broadly distributed across the US population, but opportunity is not." The process gives deserving students a chance that they might not otherwise have, adding excellence to the higher education system. It also acknowledges that not all students have an equal opportunity to excel at objective measures like standardized tests and grades, and it levels the playing field by giving students and universities the chance to spotlight other important attributes and factors in the admissions process.

I know something about this struggle because I was one of the chancellors of UNC who oversaw the admissions policies in question. When the Supreme Court took up the case of Abigail Fisher versus the University of Texas at Austin, I submitted an amicus brief prepared by UNC's law dean and general counsel. Fisher, a white student, challenged the university's consider-

ation of race in its undergraduate admission process. Denied admission in 2008, she argued that the use of race in this manner violated her constitutional right to equal protection. In the brief, it was shown convincingly that students chosen for admission based on a range of criteria, including race, ethnicity, and socioeconomic background, fared better than those chosen solely on the basis of standardized test scores and high school grades. This commitment to providing access to higher education has now landed UNC in the courts.

All of this is bad for science. Failure to enroll a diverse undergraduate population has already excluded outstanding people from science, and limiting affirmative action will only make matters worse. But much more insidious are the messages these fights continue to

send. It's bad enough that science faculty haven't continually updated their methods of teaching to ones known to be more inclusive. Likewise for universities and their processes for faculty hiring, promotion, and tenure that sustain inequity. Now, on top of all that, the highest court in the United States is going to engage in a highly public debate over whether many of the country's potential future students of science can enter the scientific community, continuing the perpetual message of exclusion.

The cases currently before the court involve claims that Asian Americans are penalized for their

race in admissions decisions at Harvard and UNC. As Jennifer Lee, Professor of Sociology at Columbia University, points out in the Editor's Blog this week, this misrepresents Asian American sentiment: 70% of Asian Americans support affirmative action, and fewer than 10% have reported being passed over for college admissions. As Lee notes, the cases before the court will not address real anti-Asian bias on college campuses.

What can scientists do to counteract all of this? Study the data showing that talent is broadly distributed and then use this evidence to help fight exclusive practices. It's also important to emphasize that grades and standardized test scores alone are insufficient selection criteria. But more importantly, show up this go-round. Students deserve to see science faculty rise up alongside colleagues in the humanities to support affirmative action. That will be a powerful message of welcome.

—H. Holden Thorp



H. Holden Thorp
Editor-in-Chief,
Science journals.
hthorp@aaas.org;
@hholdenthorp

**"...dismantling
of race-conscious
admissions
would deal another
blow to
equity in science."**

“Underserved communities ... have been waiting long enough, and they are counting on us to get this right.”

U.S. Environmental Protection Agency Administrator Michael Regan, about the agency's new plans to increase monitoring of industrial pollution implicated in high cancer rates.



IN BRIEF

Edited by Jeffrey Brainard

A miner in Madre de Dios in Peru pours a mixture of mercury and gold into a container.

ENVIRONMENT

Gold mines flood forests with mercury

A nearby gold rush has left protected jungles in the Peruvian Amazon polluted with toxic mercury at among the world's highest levels, comparable to those in forests near major industrial cities in China, a study has found. Small-scale, illicit gold miners around the world, often in impoverished regions such as Peru's Madre de Dios, use mercury to separate gold flakes from raw ore. The mercury is then burned off to extract the gold. In a protected forest near a Peruvian mining hot spot, researchers found mercury in tree leaves, runoff, and soil at levels up to 15 times higher than in nearby unforested areas, according to an article last week in *Nature Communications*. The results—the first tracking the toxic metal's pathway through forests near mine sites—suggest forests act as a mercury sponge, concentrating and storing it. But some mercury also finds its way into water bodies, where it is transformed to the more toxic methylmercury, the researchers discovered; that chemical showed up in the forest's songbirds at levels that would impair reproduction. Small-scale, “artisanal” gold mining recently outstripped coal burning as the world's single largest source of airborne mercury pollution, annually releasing as much as 1000 tons.

Watchdog chides health agency

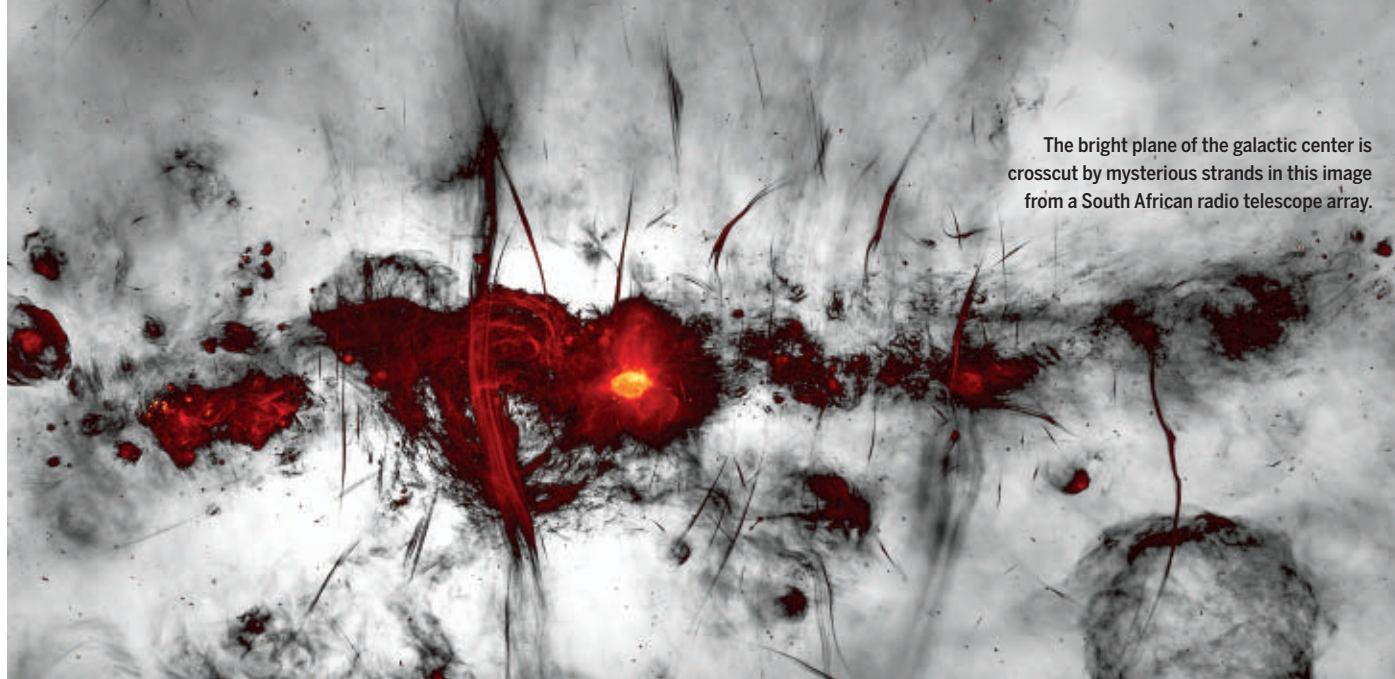
PUBLIC HEALTH | The auditing arm of the U.S. Congress last week slammed the Department of Health and Human Services (HHS) for “persistent deficiencies” in its response to the coronavirus pandemic and past public health emergencies. For example, HHS still has no comprehensive COVID-19 testing strategy, according to a 27 January report from the Government Accountability Office (GAO). The problems date back more than 10 years to other crises, including the H1N1 influenza pandemic, the Zika and Ebola virus outbreaks, and the public health threats posed by natural disasters such as hurricanes. The failures leave the nation vulnerable to future viruses and weather events, GAO says. In tandem with the release of the report, GAO announced it has added HHS leadership and public health emergency coordination to its list of “high-risk” issues that Congress and the executive branch should address. The list now highlights 37 problems at more than a dozen agencies, with some dating back to 1990.

Malaria bed nets protect long term

PUBLIC HEALTH | Bed nets can save young children from malaria, but some researchers have worried about a “rebound effect,” in which children succumb to the disease later in life because they lack natural immunity. A new, unusual follow-up study has dispelled those fears. Researchers tracked down nearly 6000 people who, as infants or toddlers, had been part of a study in Tanzania that measured the efficacy of insecticide-treated bed nets between 1998 and 2003. Among the participants—young adults today—they found no sign of a rebound effect: Those who, decades ago, slept under a bed net more than half the time still had a 40% survival advantage in 2019 over those who slept under nets less frequently, according to the study in this week's issue of *The New England Journal of Medicine*.

Breyer shaped law on experts

LAW | U.S. Supreme Court Justice Stephen Breyer, who last week announced he will



The bright plane of the galactic center is crosscut by mysterious strands in this image from a South African radio telescope array.

ASTRONOMY

Telescope reveals plethora of mysterious Milky Way filaments

One of the most detailed pictures yet of the center of the Milky Way has revealed nearly 1000 mysterious strands that slash across the plane of the galaxy, 10 times more than previously known. The image, released last week by South Africa's MeerKAT radio telescope array, shows a region 25,000 light-years from Earth. Colors denote the bright radio emissions from objects such as stellar nurseries and supernova remnants, the expanding shells of exploded stars. The brightest spot of all is the home of the Milky Way's giant

black hole, with a mass of 4 million Suns. But researchers were also intrigued to find so many radio-emitting filaments, up to 150 light-years long, cutting across the scene. They are thought to arise from electrons moving close to the speed of light as they gyrate around magnetic field lines. But researchers don't know what accelerates the electrons, why the filaments exist in regularly spaced clusters, or what creates the magnetic field lines in the first place. Some suspect outbursts of the black hole are responsible.

retire later this year, will leave a notable imprint on the use of science in U.S. courtrooms. During his 27 years on the bench, he wrote opinions that helped clarify how judges should decide what kinds of expert testimony to allow. In 1999, he authored a key opinion in *Kumho Tire Co. v. Carmichael*, which established that a judge's gatekeeping authority applies not only to testimony from witnesses who are scientists, but also those who are engineers or technical specialists. In a 1998 essay in *Science*, Breyer argued that judges increasingly needed education about technical issues. And in a separate, 2000 essay, he wrote that legal proceedings are not necessarily a "search for scientific precision. ... But the law must seek decisions that fall within the boundaries of scientifically sound knowledge."

Breeding the ideal, edible worm

GENETICS | A French company last week announced it is starting the first industrial breeding program to grow beetle larvae on a large scale as food for humans and animals. Ynsect already grows and processes

the yellow mealworm beetle (*Tenebrio molitor*) to turn into powders and oils for fishmeal and pig feed. In 2021, the company published the worm's genome. Now, it is working to identify strains of this species and other beetles with desirable traits, including faster growth and reproduction, more efficient food consumption, and pathogen resistance. Most traits involve a complicated tangle of genes, but large-scale screening could speed the selection, specialists say. Food specialists say mealworms could help alleviate food insecurity. They are high in protein, and raising them emits much



A French company is developing the larvae of the yellow mealworm beetle as a food source.

less greenhouse gas than other forms of animal protein. Last year, the European Food Safety Authority deemed the yellow mealworm safe for human consumption.

Awards bypass Asian researchers

DIVERSITY | Asian scientists are markedly underrepresented among recipients of U.S. biomedical research prizes, an analysis shows. Only 6.8% of 838 awardees who received 14 top U.S. prizes, such as the Albert Lasker Basic Medical Research Award, are of Asian descent, even though they make up more than 20% of U.S. biomedical faculty researchers, according to a commentary this week in *Cell*. For Black scientists, the picture is worse: They make up 2.6% of biological science faculty, but were shut out of the prizes. But there's some reason for hope: In the past decade, the percentage of female recipients of eight long-running prizes increased substantially, from 10% to almost 30%, a change that may reflect efforts to promote gender equality. To improve racial and ethnic diversity, award panels should encourage self-nominations, among other



Very old trees like “General Sherman,” a giant sequoia in California, can be a forest’s insurance policy for weathering environmental changes.

ECOLOGY

Elder trees promote forest health, diversity

Ancient trees are rare but play an outsize role in helping a forest survive, says a study that quantifies conditions under which a forest gains these old-timers. Charles Cannon of the Morton Arboretum and colleagues analyzed published annual death rates of forests—the percentage of trees that die each year. The team’s simulations indicated that if the rate does not exceed 1%, about 1% of a forest’s trees will eventually become long-lived behemoths—surviving for hundreds or thousands of years, up to 20 times longer than the trees around them, the scientists report this week in *Nature Plants*. Luck plays a large role in which trees survive lightning, fires, chain saws, drought, and disease. But the paper suggests genetics make the old-timers more resilient, particularly in dealing with long-term climate oscillations, which in turn helps make the entire forest more adaptable and sustainable. It’s yet another reason, the authors say, for protecting old-growth forests.

steps, says the commentary’s author, neuroscientist Yuh Nung Jan of the University of California, San Francisco.

Tighter soot limits offer benefits

EPIDEMIOLOGY | Tightening the air quality standard for particulate matter in the United States would prevent premature deaths in older people, a study has found. It offers stronger evidence than

previous analyses covering fewer people, which also found that low levels of the small particles, measuring no more than 2.5 micrometers wide, pose health risks. Researchers led by Francesca Dominici of Harvard University compared the health of 68.5 million Medicare recipients, all ages 65 or above, across the United States with their estimated exposure to air pollution between 2000 to 2016. More than 143,000 deaths in this group could have been

avoided if the U.S. standard for particulate matter had been 10 micrograms per cubic meter between 2006 and 2016, instead of the current 12 micrograms. The U.S. Environmental Protection Agency (EPA) had already planned to propose a new standard for the pollutant this spring, which is intended to protect people of all ages. The new study was released on 26 January by the Health Effects Institute, which is funded by EPA and industry groups.

COVID-19 vaccines make strides

PANDEMIC | Two makers of COVID-19 vaccines logged major milestones on 31 January. Moderna won full approval from the U.S. Food and Drug Administration (FDA) for its messenger RNA-based vaccine, 13 months after the agency granted the company an emergency use authorization (EUA). It is the country’s second fully authorized COVID-19 vaccine, after Pfizer’s, which won approval in August 2021. And after a monthslong delay caused by manufacturing issues, Novavax applied to FDA for an EUA for its protein-based vaccine. Last month, it won conditional marketing authorization in Europe, and the World Health Organization granted it an emergency use listing, opening up an avenue to buttress global vaccine supplies.

Prized dinosaur tracks damaged

PALEONTOLOGY | A backhoe operator last week reportedly damaged part of one of North America’s largest and most diverse sets of early Cretaceous dinosaur tracks near Moab, Utah. The Mill Canyon Dinosaur Tracksite contains more than 200 tracks left by at least 10 different species about 112 million years ago. Last week, work was underway to replace a boardwalk at the location, which is administered by the U.S. Bureau of Land Management (BLM). Paleontologists say the agency provided no notice of the work and had no fossil expert on site to monitor it; BLM’s Moab office has lacked a paleontologist on staff since 2018. In a statement this week, BLM did not explain the apparent damage or accept responsibility, saying only “heavy equipment is on location, but it is absolutely not used in the protected area,” and it “is committed to balancing resource protection and public access” to the site. The damage there was verified in person this week by Utah’s state paleontologist.

S **SCIENCE.ORG/NEWS**
Read more news from Science online.

science.org/journal/sciimmunol

READY TO PUT THE SPOTLIGHT ON YOUR RESEARCH?

Submit your research:
cts.ScienceMag.org

Science Immunology

AAAS

Twitter: @SciImmunology

Facebook: @ScienceImmunology

ASTRONOMY

Imminent merger of giant black holes predicted

Never-before-seen event could spark cosmic fireworks—if it is not a mirage

By **Daniel Clery**

Tick ... tick ... boom? In the center of a galaxy 1.2 billion light-years from Earth, astronomers say they have seen signs that two giant black holes, with a combined mass of hundreds of millions of Suns, are gearing up for a cataclysmic merger as soon as 100 days from now. The event, if it happens, would be momentous for astronomy, offering a glimpse of a long-predicted, but never witnessed mechanism for black hole growth. It might also unleash an explosion of light across the electromagnetic spectrum, as well as a surge of gravitational waves and ghostly particles called neutrinos that could reveal intimate details of the collision.

As soon as the paper appeared last week on the preprint server arXiv, other astronomers, eager to confirm the tantalizing signals, rushed to secure telescope observing time, says team member Huan Yang of the Perimeter Institute in Waterloo, Canada. “We’ve seen people acting pretty fast,” he says. Emma Kun of Konkoly Observatory in Budapest, Hungary, began to scour archives of radio observations for confirmation of the signal. “If the boom happens, it will confirm many things,” she says.

But the prediction may be a mirage. It’s not clear that the observed galaxy holds a pair of black holes, let alone a pair that’s about to merge, says Scott Ransom of the National

Radio Astronomy Observatory, who finds the presented evidence “pretty circumstantial.”

Supermassive black holes are thought to lurk at the heart of most, if not all, galaxies, but theorists don’t know how they grow so big. Some sporadically suck in surrounding material, fiercely heating it and causing the galaxy to shine brightly as a so-called active galactic nucleus (AGN). But the trickle of material may not be enough to account for the black holes’ bulk. They could gain weight more quickly through mergers: After galaxies collide, their central black holes could become gravitationally bound and gradually spiral together.

Such black hole pairs are not easy to detect. X-ray telescopes have discovered a handful of AGNs with two bright, separated central sources, but the putative black holes are hundreds of light-years apart and wouldn’t collide for billions of years. Once they get closer, it’s almost impossible to separate their light with a telescope. But some AGNs dim and brighten every few years—a sign, astronomers have argued recently, that they harbor pairs of black holes orbiting each other that regularly churn and heat the surrounding material. Some of these periodic oscillations have faded, however, calling into question the binary interpretation. “AGNs do all sorts of crazy things we don’t understand,” Ransom says.

In data from a survey telescope in California called the Zwicky Transient Facil-

In this visualization, a pair of giant black holes is about to merge—an event astronomers long to see.

ity (ZTF), a team led by Ning Jiang of the University of Science and Technology of China stumbled on a periodic AGN called SDSSJ1430+2303. “My first instinct was it must be related to a pair of supermassive black holes,” Jiang says.

Then, the researchers found something more: a trend they interpret as a binary pair closing in on a merger. The cycles were getting shorter, going from 1 year to 1 month in the space of 3 years. It is “the first official report of decaying periods which reduced over time,” says Youjun Lu, a theoretical astrophysicist at the National Astronomical Observatories of China, who was not part of the team.

The researchers confirmed the month-long oscillation in x-ray observations from NASA’s orbiting Neil Gehrels Swift Observatory. If this decreasing trend continues, the black holes, which Jiang says come as close to each other as the Sun is to Pluto, will merge in the next 100 to 300 days, they report in the paper, which has not been peer reviewed.

If the merger comes to pass, observers could have a field day. “There should be a huge burst across the electromagnetic spectrum, from gamma rays to radio,” Kun says. Some also expect a flood of neutrinos, which the IceCube detector at the South Pole—

1 cubic kilometer of polar ice outfitted with light sensors to detect neutrino impacts—could pick up. Neither kind of outburst is certain, however. Some predict a whimper rather than a bang. “We really don’t know what to expect,” Ransom says.

The only certain signal is gravitational waves, but the ponderous colliding masses would emit them at too low a frequency to be picked up by detectors such as the Laser Interferometer Gravitational-Wave Observatory, which is tuned to smaller mergers. They should, however, leave an imprint on spacetime itself, a sort of relaxation of distance and time dubbed gravitational wave memory, which could be detected over many years by monitoring the metronomic pulses of spinning stellar remnants known as pulsars. “It’s a very tricky signal to measure,” Ransom says, “but that would be definitive, a total smoking gun” of merging supermassive black holes.

But Ransom is braced for disappointment. He points out that the team is basing its prediction on just a handful of observed cycles. Theorist Daniel D’Orazio of the Niels Bohr Institute in Copenhagen, Denmark, says some aspects of the AGN’s light curve also raise doubts. For example, he says, the ZTF archives show SDSSJ1430+2303 lacked a periodic oscillation in the years before Jiang’s team discovered it; its dim, steady emission then looked more like a standard AGN with a single supermassive black hole. “Why has [the oscillation] just turned on now?” D’Orazio asks. “I’m not sure how that steady emission fits with binary emission models.”

Observations in the coming months should show whether the oscillation continues to shorten. The team had to halt its observing in August 2021 when Earth’s orbit put the distant galaxy too close to the Sun for telescopes to observe it safely. Observations restarted in November, but since then technical glitches have idled both ZTF and Swift.

Andrew Fabian of the University of Cambridge is among the astronomers who will be chasing the will o’ the wisp, having applied for time on NASA’s Neutron star Interior Composition Explorer, an x-ray telescope attached to the International Space Station. “If this is true, then it’s important to get as many observations as possible now to see what it’s doing,” he says. Fabian says the chance of such a merger taking place so close to Earth in any given year is one in 10,000. He’s skeptical that one is imminent, but says it’s worth monitoring for a few months to see whether the claim holds up. “Rare events do happen,” he says. ■

With additional reporting by Ling Xin in Beijing.

ENVIRONMENT

Indonesia’s utopian new capital may not be as green as it looks

Moving the government to Borneo could speed deforestation

By **Dennis Normile**

Indonesia has yet to start building its new capital, Nusantara, but a slick website shows what the country has in mind. A video shows people strolling on boardwalks through lush greenery, housing perched on the shores of an idyllic lake, stunningly modernistic buildings, elevated mass transit lines, and bicycles on tree-lined boulevards. Dominating the city is a cluster of monumental buildings, including a presidential palace in the shape of the mythical bird-like Garuda, Indonesia’s national emblem.

The new capital, whose construction on Borneo’s east coast was approved by Indonesia’s parliament on 18 January, will replace overcrowded and increasingly flood-prone Jakarta, on Java. Planners are envisioning an environmental utopia for Nusantara, which means “archipelago.” All residents will be within a 10-minute walk of green recreational spaces. Every high rise will utilize 100% eco-friendly construction and be energy efficient. Of trips taken within the city, 80% will be by public transport or on foot or bicycle. Nusantara presents an opportunity “to build a model city that is respectful of the environment,” says Sibarani Sofian, an urban designer with Urban+, the firm that won the competition for a basic design for the city’s governmental core. But others see shadows in this utopian vision.

“The big question, of course, is how and if they’ll achieve these ambitions,” says Kian

Goh, who studies urban planning at the University of California, Los Angeles. “Planning scholars are by and large skeptical of plans for smart or sustainable cities ‘from scratch,’” she says. And spillover effects across Borneo, including deforestation, “are likely to be far greater than the direct impacts within the city boundaries, unless carefully managed,” says ecologist Alex Lechner of Monash University, Indonesia.

Indonesian President Joko Widodo proposed the new capital in April 2019 and later that year picked the site in East Kalimantan province. He wanted to move the capital closer to the nation’s geographic center and spur economic growth in the archipelago’s east, while easing Jakarta’s burden. Sprawling over nearly 6300 square kilometers (km²), the Jakarta metropolitan area is Southeast Asia’s most populous conurbation, home to more than 31 million people. Haphazard growth has led to notorious traffic jams and pollution.

The old capital is also sinking. Many residents rely on wells that are pumping underground aquifers dry, leading to ground subsidence of more than 10 centimeters annually along the northern rim of the city, on the shores of Jakarta Bay—even as sea levels rise because of climate warming. The area, home to poor and working classes, floods annually. A 2020 flood killed more than 60 and displaced more than 60,000. Without heroic efforts to limit the sinking, 25% of the capital area will be

Starting from scratch

Indonesia will move its seat of government—and an estimated 4.8 million civil servants—from Jakarta to Nusantara, a brand new city on Borneo’s east coast that is closer to the country’s geographical center.





Plans for Nusantara include lots of green space and a palace in the shape of Garuda, a mythical birdlike creature.

submerged by 2050, says Edwin Aldrian, a climatologist at Indonesia's National Research and Innovation Agency.

Moving the seat of government and its estimated 4.8 million workers won't lighten Jakarta's burdens much, Aldrian says. "Jakarta will still be the economic center of Indonesia ... and still have to take on its social issues and environmental issues," Goh says.

Meanwhile, the \$32 billion new capital, whose construction can now get underway, will have an environmental impact on Borneo. Nusantara, to be built in stages through 2045, will cover 2560 km², about twice the area of New York City. (The government will occupy a 66-km² core.) Like the United States, Brazil, and other countries that built new capitals from scratch, Indonesia hopes to create a city that is modern, rationally planned, and—in Indonesia's case—green, with net-zero emissions. But critics are skeptical, because Indonesia's renewable energy sector currently provides just 11.5% of national energy. Environmental groups worry that as a stopgap Nusantara could rely on power from Kalimantan's numerous coal-fired power plants. And although well-designed public transport might keep cars off its roads, there will likely be extensive air travel between the new capital and Jakarta, about 1300 kilometers away.

The impact on Borneo's ecology could be substantial. An island the size of California, Borneo features coastal mangroves, forests, swamps, and mountains, hosting numerous endemic and rare species. Nusantara itself will be built on a previously cleared site and rely on existing highways, power lines, and other infrastructure. The city also lies inland, allowing for shoreline mangrove restoration. River valleys will be protected, creating what Lechner calls "green fingers" reaching through the city.

But the worry is that Nusantara will trigger sprawl beyond the city limits and development across Borneo. Spurring economic growth is, after all, one of the goals. By study-

ing the increase in nighttime lights associated with 12 previously relocated capitals, including Brasília and Naypyidaw, Myanmar, Lechner and his colleagues found that they burgeoned initially, then grew more slowly. "Our assessment suggests that it is likely that [Nusantara's] direct footprint could grow rapidly, expanding over 10 kilometers from its core in less than two decades and over 30 kilometers before mid-century," the team reported in 2020 in the journal *Land*.

The impacts are likely to go farther afield. The roads connecting Brasília to Brazil's coastal population centers "facilitated the destruction of the Amazon rainforest," Lechner says, opening undisturbed territory to wildlife poaching, illegal logging, and land clearing. There are fewer cities to connect to on Borneo, home to only 18 million people, but "clearly the new city will attract economic activity, including new roads, which are known to cause deforestation," says David Gaveau, a landscape ecologist who heads TheTreeMap, a company that studies tropical deforestation.

Kalimantan, the Indonesian part of Borneo, has already lost about 30% of its original forest cover to land clearing and fires since 1973, Gaveau says, leaving the Bornean orangutan and the proboscis monkey endangered and many other species threatened. A highway under construction called the Trans-Kalimantan Northern link "cuts right through remote pristine forests in the heart of Borneo," he says. Encouragingly, more effective law enforcement and a moratorium on new plantations helped drive 2020 deforestation to its lowest level in 17 years, Gaveau says, but new roads to and from Nusantara could reverse the trend.

The Indonesian government has not said much about Nusantara's environmental burden. Gaveau and others hope it will offset the city's impact with a similarly ambitious effort to turn the tide elsewhere in Kalimantan. "The solution lies in restoring all those degraded lands back to their original state: forest," Gaveau says. ■

COVID-19

New Omicron begins to take over, despite late start

BA.2 strain may extend latest surge, but its overall impact remains unclear

By **Meredith Wadman**

On 7 December 2021, as the Omicron variant of the pandemic coronavirus began to pummel the world, scientists officially identified a related strain. BA.2 differed by about 40 mutations from the original Omicron lineage, BA.1, but it was causing so few cases of COVID-19 that it seemed a sideshow to its rampaging counterpart.

"I was thinking: 'BA.1 has the upper hand. We'll never hear again from BA.2,'" recalls Mark Zeller, a genomic epidemiologist at the Scripps Research Institute. Eight weeks later, he says, "Clearly that's not the case. ... I'm pretty sure [BA.2] is going to be everywhere in the world, that it's going to sweep and will be the dominant variant soon in most countries if not all."

Zeller and other scientists are now trying to make sense of why BA.2 is exploding and what its emergence means for the Omicron surge and the pandemic overall. Already a U.K. report issued last week and a large household study from Denmark posted this week as a preprint make it clear BA.2 is inherently more transmissible than BA.1, leaving scientists to wonder which of its distinct mutations confer an advantage.

But so far, BA.2 does not appear to be making people sicker than BA.1, which itself poses less risk of severe disease than variants such as Delta and Beta. In Denmark, where by 21 January BA.2 accounted for 65% of new COVID-19 cases, "We see a continuous, steep decline in the number of intensive care unit patients and ... now a decrease in the number of hospital admissions related to SARS-CoV-2," says Tyra Grove Krause, an infectious disease epidemiologist at the country's public health agency. In fact, the Danish government is so confident the variant won't cause major upheaval that it lifted almost

all pandemic restrictions on 1 February.

Still, some scientists predict BA.2 will extend Omicron's impact. "I would guess we'll see [BA.2] create a substantially longer tail of circulation of Omicron than would have existed with just [BA.1], but that it won't drive the scale of epidemics we've experienced with Omicron in January," computational biologist Trevor Bedford of the Fred Hutchinson Cancer Research Center tweeted on 28 January. In South Africa, BA.2 already may be stalling the rapid decline in new infections seen after the country's Omicron wave peaked in December 2021.

Although BA.2 represented less than 4% of all Omicron sequences in the leading global virus database as of 30 January, it has been identified in 57 countries, with the earliest documented case dating to 17 November in South Africa. It likely now dominates in India, according to Bijaya Dhakal, a molecular biologist at the Sonic Reference Laboratory in Austin, Texas, who examined sequence data uploaded from eight large Indian states. In the United Kingdom, the proportion of likely BA.2 cases doubled from 2.2% to 4.4% in the 7 days that ended on 24 January.

In the United States, the Centers for Disease Control and Prevention is not yet tracking BA.2 separately. But Bedford estimates it accounted for 7% of new U.S. cases as of 30 January, up from 0.7% on 19 January. "In each country and across time, we see that the epidemic growth rate of Omicron BA.2 is greater than Omicron BA.1," he says.

The report last week from the UK Health Security Agency (UKHSA) backs up that assessment in England, finding BA.2 was spreading faster than BA.1 in all regions where enough data was available to make an assessment. UKHSA data also show that in late December 2021 and early January, transmission was higher among household contacts of BA.2 cases, at 13.4%, than in contacts of other Omicron cases (10.3%).

The study from Denmark, which sequences the virus from virtually every person who gets COVID-19, paints a more dramatic picture. In households where the first case was BA.1, on average 29% of other people in the household became infected. When the first case was BA.2, 39% of household members were infected.

Omicron was already known to have mutations that help it evade antibodies,

but the Danish researchers also found that BA.2 may be even better at dodging vaccine-induced immunity: Vaccinated and boosted people were three times as susceptible to being infected with BA.2 as with BA.1. Vaccinated but unboosted people were about 2.5 times as susceptible, and unvaccinated people 2.2 times as susceptible. Early U.K. data, however, showed vaccinated people, if boosted, had about the same level of protection against symptomatic infections with BA.1 or BA.2—63% and 70%, respectively.

In one hopeful and unexpected finding from Denmark, those who were vaccinated or vaccinated and boosted passed on BA.2 to household members less often, relative to BA.1. The same didn't hold for unvaccinated people, who passed BA.2 to their household contacts at 2.6 times the rate they passed BA.1.

lier variants of concern—Alpha, Beta, and Gamma—are from each other (see graphic, below). Some even think BA.2 shouldn't even be considered Omicron. "I hope in the near future that BA.2 gets its own variant of concern [label] because people assume it's very similar which it's not," Zeller says.

BA.2 doesn't have all of the mutations that help BA.1 avoid immune detection, but it has some its sibling doesn't. Thomas Peacock, a virologist at Imperial College London, notes that most of the differences are in an area of the spike protein, called the N-terminal domain (NTD), that houses antibody targets. "What we don't know is: Just because there are changes, are they changes that actually do something?" says Emma Hodcroft, a molecular epidemiologist at the University of Bern.

But one NTD difference—a deletion at amino acids 69 and 70 that is present in BA.1 and not in BA.2—could give researchers a tool for monitoring the spread of the up-and-coming Omicron strain. Certain SARS-CoV-2 polymerase chain reaction tests detect three genetic sequences of the virus, but the mutation in BA.1's NTD gene eliminates one of those targets. Polymerase chain reaction tests pick up all three targets in BA.2, providing a proxy for distinguishing the Omicron strains if there is no full virus sequence.

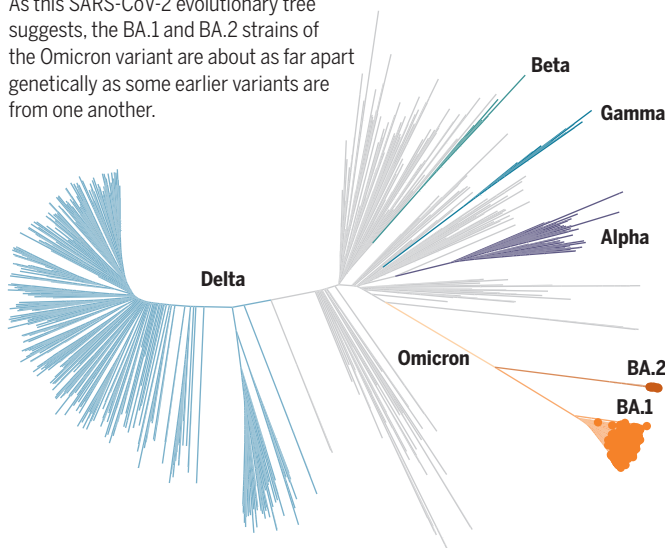
How the sibling strains were born is also preoccupying scientists. Viral evolution in a single immunocompromised patient is one theory, says Andrew Rambaut, an evolutionary biologist at the University of Edinburgh. "It's possible that long-term infection could produce quite a lot of diversity within a single individual. It could be compartmentalized. So different variants living in different parts of the body." Both Omicron strains could have also evolved in animals infected with human-adapted SARS-CoV-2, then spread back into people.

Why BA.2 is emerging only now is one more mystery, Hodcroft says. She speculates that a factor as simple as which Omicron caught an earlier flight out of South Africa, where both strains were first identified, may be the explanation. "BA.2 may have just been trapped for a little bit longer. But when it did finally get out and start spreading it started to show that it can edge out its big sister." ■

With reporting by Kai Kupferschmidt.

Not so similar

As this SARS-CoV-2 evolutionary tree suggests, the BA.1 and BA.2 strains of the Omicron variant are about as far apart genetically as some earlier variants are from one another.



Much as scientists a few weeks ago wondered whether a previous infection with Delta or another variant would protect people from Omicron overall, some are now looking for data on whether Omicron's first surge created a shield against BA.2. "To what extent does a BA.1 infection protect you against reinfection with BA.2?" Zeller asks. "From what I have seen in Denmark, it's not going to be 100%."

Scientists are also probing the variant's ability to dodge vaccine-induced antibodies in lab dish studies. And drugmaker GlaxoSmithKline is testing its monoclonal antibody, sotrovimab, made with Vir Biotechnology, against BA.2 in lab studies. It's the only widely authorized antibody that still thwarts BA.1.

Scientists note BA.1 and BA.2 are about as far apart on the evolutionary tree as ear-



Wolves feed on a bison carcass in Yellowstone National Park.

CONSERVATION BIOLOGY

Massive wolf kill disrupts long-running Yellowstone park study

Hunters kill more than 500 wolves in surrounding states

By Virginia Morell

Hunters are killing gray wolves in the northern Rocky Mountains in numbers not seen since the animals were nearly driven to extinction in the continental United States in the 20th century. The recent killing of some 500 wolves in Montana, Idaho, and Wyoming—including nearly 20% of the wolves that use Yellowstone National Park—threatens to undermine a decades-old effort to restore the predators to the landscape and disrupt a long-term Yellowstone research project that has produced influential findings on how wolves help shape ecosystems. Researchers and environmentalists are calling on officials to rethink the hunts, which have eliminated more than 15% of the wolves in the three states.

The loss of the Yellowstone wolves “is a huge setback,” says biologist Doug Smith of the National Park Service, who leads the park’s wolf study, which began in 1995. “We had in Yellowstone one of the best models for understanding the behaviors and dynamics of a wolf population unexploited by humans.” Now, he says, researchers will “do what we can to keep the science going—what we have left of it.”

For decades, wolves were strictly protected under the federal Endangered Species Act (ESA), but 10 years ago successful restoration efforts prompted federal officials to ease protections and give state governments a greater say in managing the species. With wolf numbers in the northern Rockies reaching about 3100 in late

2020, several states have legalized or expanded wolf hunts. Legislators in Montana, for example, last year set a goal of shrinking the state’s wolf population to “at least 15 breeding pairs,” the minimum required by the ESA; state rules allow a person to kill up to 20 wolves each season. Idaho also aims to shrink its wolf population and has no kill limits. Wyoming has nearly achieved its goal of maintaining just 100 wolves and 10 breeding pairs outside of Yellowstone (where hunting is not allowed).

Biologists say the killings won’t cause the regional extinction of wolves, although the U.S. Fish and Wildlife Service announced in fall of 2021 that it would review whether “potential increases in human-caused mortality” threaten the species. The losses will, however, alter the social structure of wolf packs—and reshape the Yellowstone study,

which has produced high-profile findings on how the return of wolves has affected willow, aspen, and cottonwood stands as well as elk, songbird, and scavenger populations. As of 31 January, hunters had killed 24 of the roughly 125 wolves that use the park, including five that carried tracking collars placed by scientists. Hunters killed 19 in Montana outside the park’s northern borders, where officials had recently lifted quotas, and five in Idaho and Wyoming.

Hunters have previously killed park wolves, up to seven each year from 2009 to 2020 in Montana. But the big new kill “complicates the research as we will now have to account for the confounding effects of hunting,” says ecologist Dan MacNulty of Utah State University, who studies how wolves affect food webs.

Smith believes it will take 4 or 5 years for the park’s packs to rebound from the losses, and is now planning to study how hunting affects the wolves. Last week, he placed tracking collars on wolves in the northern part of the park, hoping to “compare the persistence and reproductive rates” of packs that have lost members with those that haven’t. Studies have found packs with more than eight members “are more resilient” to diseases such as mange, Smith notes, and can “have greater prey kill rates and are better at territorial defense.”

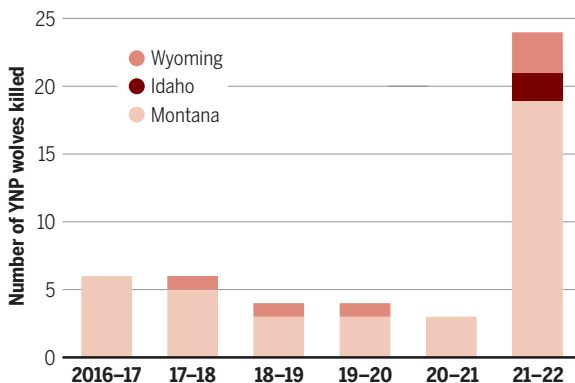
Smith expects the park’s wolves, which are a favorite attraction of visitors, to become warier and more difficult to see. Yellowstone superintendent Cam Sholly has said he wants “to make the case” to Montana officials “for reinstating quotas that would protect the [park’s] core wolf population.” But state leaders have shown little interest, and Montana’s wildlife commission recently declined to end hunting

in certain areas near the park. “We don’t manage for individual wolves or packs. We manage wolves across landscape and population scales,” says Greg Lemon, a spokesperson for Montana’s wildlife department.

Wolf advocates fear such stances will mean fewer wolves available to start new packs elsewhere. (Still, one nearby state, Colorado, is advancing a plan to restore the canids.) And they argue states are pursuing contradictory policies. Montana and Wyoming, for example, want to reduce elk populations that officials say have grown too large. But they’ve also embraced killing a predator that could help them reach that goal. “Their management objectives,” MacNulty says, “are at cross purposes.” ■

Nowhere to hide

Hunters have killed many more wolves that use Yellowstone National Park (YNP) during the 2021–22 hunting season than in past seasons.



MICROBIOLOGY

Computer scan uncovers 100,000 new viruses

Clues to future outbreaks may be hidden in existing genomic databases

By Elizabeth Pennisi

It took just one virus to cripple the world's economy and kill millions of people; yet virologists estimate that trillions of still-unknown viruses exist, many of which might be lethal or have the potential to spark the next pandemic. Now, they have a new—and very long—list of possible suspects to interrogate. By sifting through unprecedented amounts of existing genomic data, scientists have uncovered more than 100,000 novel viruses, including nine coronaviruses and more than 300 related to the hepatitis Delta virus, which can cause liver failure.

"It's a foundational piece of work," says J. Rodney Brister, a bioinformatician at the National Library of Medicine. The study, published last week in *Nature*, expands the number of known viruses that use RNA instead of DNA for their genes by an order of magnitude. It "demonstrates our outrageous lack of knowledge about this group of organisms," says disease ecologist Peter Daszak, president of the EcoHealth Alliance, a nonprofit research group in New York City that is raising money to launch a global survey of viruses.

Scientists predict the study will also help launch so-called petabyte genomics—the analyses of previously unfathomable quantities of DNA and RNA data. (One petabyte is 10^{15} bytes.) That wasn't exactly what computational biologist Artem Babaian had in mind when he came up with the project while in between jobs in early 2020. Instead, he was simply curious about how many coronaviruses—aside from the virus that had just launched the COVID-19 pandemic—could be found in sequences in existing genomic databases.

So, he and independent supercomputing expert Jeff Taylor scoured cloud-based genomic data that had been deposited to a global sequence database and uploaded by the U.S. National Institutes of Health. As of now, the database contains 16 petabytes of archived sequences, which come from genetic surveys of everything from fugu fish, the risky Japanese delicacy, to farm soils to human guts. (A database with a 5-megabyte digital photo of every person in the United States would take up about the same amount

of space.) The sequences also capture the genomes of viruses infecting different organisms in samples, but the viruses usually go undetected.

To sift through the reams of data, Babaian and Taylor devised a set of computer search tools specialized for cloud-based data. With the help of several bioinformaticians, some whom became collaborators on the project, they tweaked the new software to make their analysis "way faster than anyone thought possible," recalls Babaian, who is now at the University of Cambridge.

They soon expanded the viral hunt beyond coronaviruses and looked at all the

in many cases, there's just the gene for the core enzyme. But researchers can use even partial sequences to build family trees that reveal how different viruses are related. In some cases, they can also use the database to find out where around the world a particular virus was found—and what type of host it was in. And some of the discovered viruses could help researchers better understand how human pathogens arise, Brown says, or improve diagnostic tests for infections. Finally, when a new virus is isolated from a sick patient, a scan of the genomic database could show whether it was already present elsewhere. "We have turned this

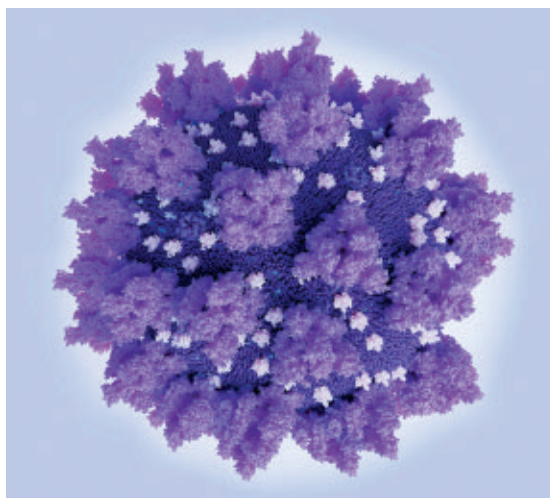
[database] into a giant virus surveillance network," Babaian says.

Some findings were unexpected, including new coronaviruses in the well-studied fugu fish and in the axolotl, an amphibian that is a common lab organism. In a few cases, researchers could piece together whole genomes for the viral finds. And in some aquatic animals, those sequences suggested their novel coronavirus genomes are spread across two separate RNA molecules, not the usual single strand, Babaian and his colleagues report.

Babaian's team also came across evidence of more than 250 giant bacteriophages—viruses that infect bacteria—that resemble ones already known in algae. These "huge phages" were detected in sequences from vastly different organisms. One

group of huge phages was found in a person in Bangladesh and also in cats and dogs in the United Kingdom, for example. These viruses are big enough to carry genes between different hosts species, suggesting they might provide a new source of genetic changes, Babaian notes. That's the way it is with viruses, Daszak says. "Every time we start digging, we get surprises."

To make sure others can take advantage of the work, Babaian's team has created a public repository of the tools it developed, along with the results. The amount of cloud-based, publicly available DNA sequences is expanding exponentially; if he did the same analysis next year, Babaian expects he would find hundreds of thousands more RNA viruses. "By the end of decade, I want to identify over 100 million." ■



In a vast repository of genetic sequences, scientists found nine unknown coronaviruses, relatives of SARS-CoV-2 (computer model).

data in the cloud. Babaian and his colleagues' programs hunted among the cloud's sequences for matches to the central core of the gene for RNA-dependent RNA polymerase, which is key to the replication of all RNA viruses. Such viruses include not only coronaviruses, but also those that cause flu, polio, measles, and hepatitis.

Babaian's approach was fast enough to work through 1 million data sets a day—at a computing cost of less than 1 cent per data set. "It's an impressive engineering feat," says C. Titus Brown, a bioinformatician at the University of California, Davis. When the researchers were finally finished, they had uncovered the partial genomes of almost 132,000 RNA viruses.

The group's new database doesn't have the complete sequence of each new virus—

FEATURES

FAILING THE TEST

DNA barcoding brought botanist Steven Newmaster scientific fame and entrepreneurial success. Was it all based on fraud?

By **Charles Piller**



Almost overnight, a 2013 paper made Steven Newmaster an expert on the verification of food and supplements.

PHOTO: ANDREW FRANCIS WALLACE/TORONTO STAR VIA GETTY IMAGES

In 2013, a team led by Steven Newmaster, a botanist at the University of Guelph (UG), took a hard look at popular herbal products such as echinacea, ginkgo biloba, and St. John's wort. The team published a study that used DNA barcoding—a system to identify species using small, unique snippets of genetic material—to test whether the bottles really contained what was printed on the label.

The results were troubling. Most of the tested products contained different plants, were larded with inert fillers, or were tainted with contaminants that could cause liver and colon damage, skin tumors, and other serious health problems. The paper, published in *BMC Medicine*, received prominent attention from *The New York Times*, CBC, and many other media outlets. The findings “pissed me off,” Newmaster told PBS's *Frontline*. “I go in to buy a product that I believe in, that I care about and I pay a lot of money for, and it's not even in the bottle? Are you kidding me?”

His work inspired then-New York Attorney General Eric Schneiderman to sponsor a similar study conducted by James Schulte, then at Clarkson University, who confirmed that consumers were often misled. At Schneiderman's request, major retailers such as GNC, Walgreens, and Walmart pledged to pull suspect products from the shelves or take other measures.

Almost overnight, Newmaster became an authority on the verification of food and supplement ingredients. He quickly went from industry adversary to ally, as major supplement-makers hired companies he created to certify their products as authentic. In 2017, Newmaster also founded the Natural Health Products Research Alliance (NHPRA), a venture within UG that aims to improve certification technologies for supplements. It raised millions of dollars from herbal suppliers, boosting UG's finances and prestige.

But in an ironic twist, eight experts in DNA barcoding and related fields now charge that the 2013 paper that indicted an entire industry and launched a new phase in Newmaster's career is itself a fraud. In a 43-page allegation letter, sent to UG in June 2021 and obtained by *Science*, the researchers—from UG, the University of Toronto, the University of British Columbia, and Stanford University—cited major problems in the study and two others by Newmaster and collaborators. “The data which underpin [the papers] are missing, fraudulent, or plagiarized,” the letter flatly stated. The group also charged that Newmaster “recurrently failed to disclose competing financial interests” in his papers.

The accusers include co-authors of two of the suspect papers, who now say they believe Newmaster misled them. “I felt that trust was betrayed,” says one of them, John Fryxell,

executive director of the Biodiversity Institute of Ontario. One paper, which compared the cost of DNA barcoding with traditional methods for cataloging forest biodiversity, was retracted last fall at the request of its junior author, Ken Thompson, now a Stanford postdoctoral fellow. The letter was also signed by evolutionary biologist Paul Hebert, sometimes called the “father of DNA barcoding,” who directs UG's Centre for Biodiversity Genomics (CBG).

Newmaster did not respond to interview requests or written questions. But in a defense he sent to UG—which *Science* has also obtained—he denied all charges. “I have never committed data fabrication, falsification, plagiarism, or inadequate acknowledgment in the publications as claimed,” Newmaster wrote. “I have never engaged in any unethical activity or academic misconduct.” He also said he had never made money from his network of businesses.

An investigation by *Science* found the problems in Newmaster's work go well beyond the three papers. They include apparent fabrication, data manipulation, and plagiarism in speeches, teaching, biographies, and schol-

“I have never engaged in any unethical activity or academic misconduct.”

Steven Newmaster, University of Guelph

arly writing. A review of thousands of pages of Newmaster's published papers, conference speeches, slide decks, and training and promotional videos, along with interviews with two dozen current and former colleagues or independent scientists and 16 regulatory or research agencies, revealed a charismatic and eloquent scientist who often exaggerated, fabulized his accomplishments, and presented other researchers' data as his own.

UG, which has been investigating the allegations since August 2021, declined to answer questions about its own investigation or *Science*'s findings, citing confidentiality rules. Other UG scientists say university administrators repeatedly pressured them to stop questioning Newmaster's research. UG also dismissed a detailed request for an investigation made by Thompson in 2020. Some now fear university administrators will quash the new accusations in a misguided attempt to protect UG's and their own reputations, and the university's share of funds raised by Newmaster. UG declined to comment on those concerns, as well.

“The 2013 herbal supplement paper reflects a pattern of deception and academic

misconduct. The university has chosen to stand back for reasons that I don't understand,” Hebert says. “I am disturbed to sit in a building where someone has been running a fabrication mill.”

ON SOCIAL MEDIA, Newmaster described himself as a scientific “explorer” and “adventurer.” His Instagram page showed him skiing double black diamond runs, riding dog sleds, and inspecting tea fields in China. (Newmaster's Instagram account became private after *Science* contacted him.)

According to his CV and LinkedIn page, Newmaster joined UG's faculty in 2001 or 2002, after earning a Ph.D. in environmental biology and ecology at the University of Alberta, and became curator of an herbarium housed at UG. His intrepid character, personal appeal, and ability to put people at ease charmed colleagues. Environmental physiologist Patricia Wright, retired from UG, describes him as “an upbeat, fun guy that students really liked.”

Not long after Newmaster arrived, seminal work by Hebert and others helped launch DNA barcoding as an important research tool with diverse applications such as cataloging biodiversity and monitoring water quality. Hebert raised funds to build a small barcoding empire at UG, with scores of researchers and two buildings, one of which became home to the herbarium and Newmaster's personal lab. Hebert also co-founded and serves as scientific director for the Barcode of Life Data System (BOLD), a repository with millions of barcodes for more than 300,000 named species.

Newmaster embraced the technology. He has used it not only to authenticate medicinal plants, but also to study plant diversity in Canada and India and catalog threatened tree species. Much of the DNA work was carried out by Subramanyam Ragupathy, a botanist in Newmaster's lab who did not respond to requests for an interview.

In the 2013 supplement paper, Newmaster, Ragupathy, and collaborators describe how they derived DNA barcodes for 44 popular herbal products and compared them with barcodes from validated sources. The explosive results—most of the products had DNA from herbs not on the label, and many contained plants with “known toxicity”—alarmed experts. “This suggests that the problems are widespread and that quality control for many companies, whether through ignorance, incompetence or dishonesty, is unacceptable,” nutritionist David Schardt, then with the Center for Science in the Public Interest, told *The New York Times*.

The paper drew criticism as well. A stinging 2013 analysis in *HerbalEgram*—a journal of the American Botanical Council, a

nonprofit research group—claimed many egregious errors and called for a retraction. The analysis accused Newmaster of not understanding that supplements use benign inactive substances such as rice powder as “carriers,” and that DNA can be destroyed during processing without altering a supplement’s effects.

Newmaster and his co-authors offered a solution to the problem they had identified. “We suggest that the herbal industry should voluntarily embrace DNA barcoding,” they wrote in the paper, to give companies “a competitive advantage as they could advertise that they produce an authentic, high quality product.” CBG scientist Masha Kuzmina, who cosigned the allegations against Newmaster, says the message was: “The paper is out. It’s [a] scandal. Now there is a problem and it needs to be solved. And who’s solving it? The same person” who exposed the problem.

Although the paper claimed “no competing interests,” Newmaster and UG geneticist Robert Hanner in 2012 had created Biological ID Technologies Inc., which conducted DNA barcoding for foods and herbal products and offered purity certifications for product labels. On 11 July 2013, about 1 week after the paper was submitted, Newmaster and Hanner incorporated a second company, named Tru-ID, which apparently assumed the business initiated by Biological ID Technologies. (Tru-ID folded in 2020, under “financial hardship during the pandemic,” Newmaster said in his response to the misconduct complaint. Hanner would not provide any comment for this article.)

When the New York attorney general’s probe triggered by Newmaster’s paper pressured companies to validate their ingredients, Tru-ID was ready to help, says Stefan Gafner, chief science officer at the American Botanical Council and co-author of the *HerbalEgram* critique. At least three major supplementmakers, Nature’s Way, Herbalife Nutrition, and Jamieson, hired Tru-ID and adopted its certifications. (The company also received more than \$369,000 in contributions and contracts from the Canadian government.) “The whole way [Newmaster] would talk about DNA was really a marketing pitch for the industry. And eventually, he got a lot of success,” Gafner says.

In the years after the paper was published, Newmaster acknowledged that critics had been partially correct. His methods could not accurately measure the components of herbal remedies, largely because DNA barcoding cannot distinguish varying amounts of different substances in a mixed sample, and because DNA degrades during processing.

NHPRA, the UG-based alliance Newmaster launched in 2017, aimed to improve practices in the nascent field, in part

by combining DNA barcoding with other approaches. The website of UG’s office of alumni affairs and development says the university is “raising \$20 million to create new verification standards and develop new technology” through NHPRA and offers sponsorship levels from \$25,000 to \$1 million. Several big industry players have joined; Tru-ID also committed \$500,000.

UG repeatedly touted Newmaster’s work in press releases and pushed back when that work was challenged. In 2017, Jonathan Newman, then-dean of the College of Biological Sciences, called UG scientists Evgeny Zakharov and Natalia Ivanova into his office for what Zakharov sarcastically calls a



“The university has chosen to stand back for reasons that I don’t understand.”

Paul Hebert, University of Guelph

“friendly discussion.” The two scientists had indirectly questioned Newmaster’s work at a conference, noting that DNA barcoding alone can’t always reliably identify ingredients in herbal products. Newman admonished them to avoid comments that might sour NHPRA contributors, says Zakharov, who is lab director for the Canadian Centre for DNA Barcoding. “I said to Newman, ‘Are you sure you are backing the right horse?’” Zakharov says. “Newman’s response was: ‘You’re not the one who brought me a \$1 million deal.’”

Ivanova, who’s now at a Guelph biomonitoring company, confirms the conversation and says Newman contacted her again later that year for a similar talk, also attended by Glen Van Der Kraak, who became interim dean in 2019. “I felt that I could not say no” to the requests, Ivanova says. The encounter gave her “the feeling that every step is being

watched for any critique towards technologies used by Newmaster’s lab.”

Newman, now vice president for research at Wilfrid Laurier University, says he connected Newmaster with Herbalife and supported his fundraising. He says he did not tell the duo what to say in public but asked them not to solicit companies Newmaster was courting. (Zakharov and Ivanova say they had never engaged in fundraising.) Van Der Kraak declined to comment.

More commercial ventures followed, in a network that is hard to disentangle. In 2019 or 2020, Newmaster became a science adviser to Purity-IQ, a startup that, like Tru-ID, aims to certify the ingredients of foods, herbs, wine, cannabis, and other comestibles. According to Purity-IQ’s website, NHPRA performs lab tests for the company, which pledged \$1 million to NHPRA in 2021.

After the COVID-19 pandemic broke out, Newmaster cofounded ParticleOne, which sells software to assess indoor air for SARS-CoV-2. He is an adviser to Songbird Life Science, which offers COVID-19 tests and shares technology and executives with ParticleOne and Purity-IQ. (All three companies declined to comment, except to say concerns about Newmaster did not involve their own work, and in Purity-IQ’s case, that it stands by its tests.)

Newmaster developed close ties with one sponsor, Herbalife, despite its checkered history. Herbalife paid a \$200 million fine in 2016 to settle allegations by the U.S. Federal Trade Commission that it was operating a sophisticated pyramid scheme, and another \$123 million in 2020 to settle federal charges that it engaged in bribery and other corrupt acts in China. Newmaster has touted Herbalife’s products in promotional materials, effusively praised its cultivation practices after a 2018 visit to a Chinese tea farm, and lauded its efforts “to achieve excellence.” He also came to the company’s defense in 2019, when Indian researchers published a paper in the *Journal of Clinical and Experimental Hepatology* about a woman who died from liver failure, which the researchers associated with her use of Herbalife dieting products. In a letter to the editor, Newmaster—who has no medical background—castigated the paper. (Elsevier, the publisher, removed the paper from its website in 2020 after legal threats from Herbalife.)

Web pages featuring Newmaster disappeared from Herbalife’s website last month, after *Science* contacted the company. Herbalife would not provide any comment for this story.

EVEN AS NEWMASER’S star was rising, some of his colleagues complained that he made exaggerated claims. Newmaster never

worked for CBG, but Thomas Braukmann, a former postdoc at the center who's now at Stanford, says he saw him host tours of CBG's handsome atrium and sequencing labs as if he ran the facility. "Those two buildings are my buildings," Newmaster said in a 2019 keynote speech at the CBD Expo, an industry conference on cannabis in Orlando, Florida, referencing the CBG complex. "I have 80 scientists working for me." That appears to be a reference to CBG's staff, who actually work under Hebert.

In his biography on UG's website, Newmaster noted a postdoctoral fellowship in "multidimensional matrix mathematics and multivariate analysis" at Australia's Commonwealth Scientific and Industrial Research Organisation, which says it has no record of Newmaster. (The claim was removed after *Science* asked Newmaster about it in January.) His CV listed a prestigious Discovery grant from the Natural Sciences and Engineering Research Council of Canada (NSERC) for \$198,000 over 5 years. NSERC says the grant was \$11,500 for 1 year. He claimed a separate NSERC award for \$240,000, but it was only worth \$40,000.

On its website, NHPRA listed many "strategic partners," including the U.S. Food and Drug Administration, U.S. Pharmacopeia, the Canadian Food Inspection Agency, the Canadian National Research Council, and the American Botanical Council. None has any defined relationship with NHPRA, they told *Science*. (In December 2021, after *Science* contacted the groups, NHPRA's website was replaced with a notice that it would be back in 2022.) In his 2019 cannabis speech, Newmaster also claimed links with U.S. regulators and standards boards that those groups say don't exist.

In one particularly odd boast during an October 2020 radio interview, Newmaster said he was working on SARS-CoV-2 tests, in part at the request of the U.S. Centers for Disease Control and Prevention (CDC), in the summer and fall of 2019, months before the COVID-19 pandemic erupted. "In the scientific community we were already sequencing samples, blood samples, saliva samples, and looking at this virus," he told an incredulous host. A CDC spokesperson could not locate information about working with Newmaster.

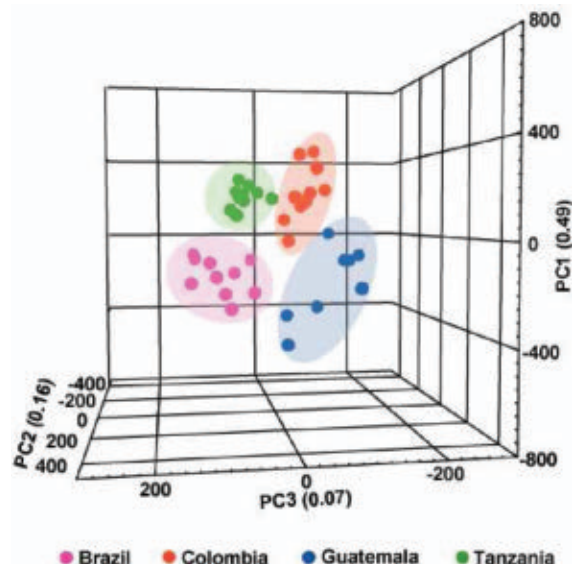
His colleagues complained of other kinds of dishonesty, too. In 2010, several UG scientists say, a student reported that Newmaster had taken large portions of his course materials from internet sites. "I was absolutely floored," says Wright, who co-taught that course with him. *Science* obtained a sample of the documents and verified substantial copying and pasting from Wikipedia and elsewhere. When Wright confronted him, Newmaster seemed unperturbed, she says: "I

Uncanny resemblance

During a 2020 online training for the Association of Food and Drug Officials about cannabis cultivar identification and purity verification, Steven Newmaster presented data from other researchers—and even from completely different fields—as his own.

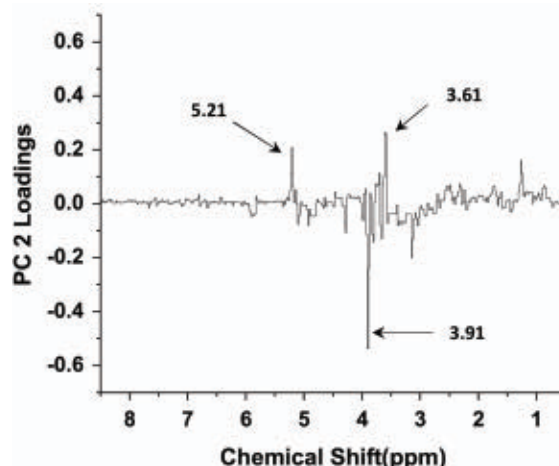
"Unique signatures"

In his talk, Newmaster described how "unique signatures" helped his team identify coffee cultivars from Guatemala, Colombia, Tanzania, and Brazil. But the image he showed was identical to one in a paper about coffee identification published in the *Journal of Agricultural and Food Chemistry* by a Japanese research group in 2012.



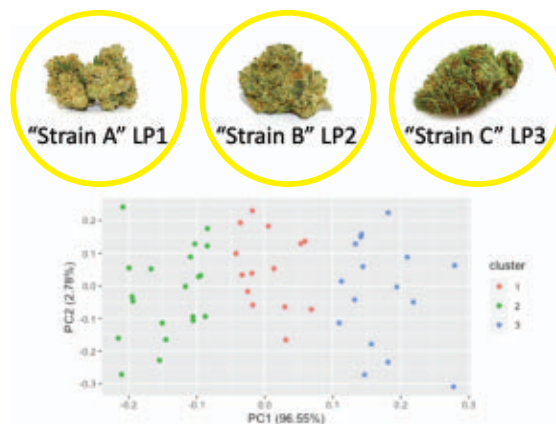
Bad chemistry

This graphic, which Newmaster said showed data from his work on cannabis identification, is identical—including the added numbers and text along the axes—to one in a paper about identifying ginseng types, published in *Analytical and Bioanalytical Chemistry* by a different research group in 2012.



Into the weeds

Newmaster said this slide showed nuclear magnetic resonance profiles for three cannabis strains; he added photos of each (circled here). But the graphic is identical to one showing arrest data for 50 U.S. states that appears on the Comprehensive R Archive Network, a support site for the programming language R.



lost hope in him as a scientist at that time.” UG quietly required Newmaster to fix the material, Wright and others say. *Science* also found plagiarized sections in several of his published papers, including one on millet identification in Southeast India (see graphic, p. 489). Jose Maloles, the paper’s first author, says it was based on his undergraduate thesis, but could not recall how it was drafted.

In a 2020 promotional video made by Purity-IQ, Newmaster warned about the risks of data manipulation. “We could have all the testing in the world,” he said, “and if that data could be counterfeited or could be changed in any way it doesn’t really matter how good the test is.” One month later, in a training video for the Association of Food and Drug Officials in which he promoted Purity-IQ testing, Newmaster displayed graphics from other sources without credit and described them as his own work, an analysis of his talk and PowerPoint slides shows (see graphic, p. 487).

“Here’s the little experiment that we ran,” Newmaster says in the video, calling it “a real life scenario” to guide industry quality control. But the image he showed, purportedly representing an analysis of cannabis strains, is identical to one assembled by other researchers that depicts U.S. arrest data.

Independent scientists identified more serious problems in Newmaster’s work, such as an analysis of sarsaparilla—a tropical plant used to treat joint pain—published in 2020 with other NHPRA researchers. Stanford’s Braukmann and Damon Little, a bioinformatics expert at the New York Botanical Garden, both examined the genetic sequences Newmaster provided, and found those labeled Indian sarsaparilla were actually near-exact matches for *Escherichia coli*, a common experimental bacterium. Prasad Kesanakurti, corresponding author for the paper, says the data merely reflected common *E. coli* contamination, and offered to provide the assembled plant sequences for review. Braukmann says only an examination of the raw data could clarify what went wrong. The paper is “an example of poorly done science,” he says. “It makes me not trust anything that comes out of [NHPRA].”

THE INQUIRY NOW UNDERWAY at UG was triggered by Thompson, who in 2012 was one of the first two students to enroll when Newmaster helped launch UG’s undergraduate biodiversity major. Newmaster asked Thompson to work on a paper comparing the cost of traditional taxonomic typing and DNA barcoding for identifying forest plants. Newmaster provided the summary data; Thompson had to analyze them and draft the paper. “We’re getting one-on-one time with this famous, supersuccess-

ful, important professor,” Thompson recalls thinking. The resulting 2014 paper in *Biodiversity and Conservation* was his first.

Years later, Thompson grew queasy. He realized the perfect species identification claimed in the paper was virtually impossible for some of the plants. And Newmaster had never shown him the raw data or uploaded it to BOLD or GenBank, the standard sequence repository. In early 2020, Thompson asked UG to investigate. “I wasn’t 100% confident that it was fraudulent,” he says. “I was 100% confident that it was worth asking the question.”

In September and October 2020, in response to Thompson’s inquiry, Newmaster’s



**“They thought that ...
I didn’t have a lot of power—
that they could squash me.”**

Ken Thompson, Stanford University

collaborator Ragupathy deposited thousands of sequence records, purportedly obtained for the forest paper, in GenBank. (Around the same time, he uploaded 126 records for the 2013 supplements paper.) Kuzmina, the CBG scientist, examined the sequences and found that 80% precisely matched others submitted earlier for another student’s thesis—collected at a different site hundreds of kilometers away.

Thompson—who later also detected some cases of Newmaster’s apparent image fabrication or plagiarism—says UG administrators slow-walked his request for an investigation, recast it as an informal query, and in early 2021 rejected his claims as insufficiently supported. “They thought that I was just one person, and I didn’t have a lot of power—that they could squash me,” he says. He then asked the editor of *Bio-*

diversity and Conservation to conduct his own review. But the editor deferred to UG.

In May 2021, Thompson self-published his concerns and posted a related commentary on a popular biodiversity blog, *Eco-Evo Eco*. “Doing this alone behind the scenes has been incredibly isolating,” he wrote. “I ... hope that by sharing an evidence-based critique of our paper some people will choose to support me.” Indeed, Hebert soon added a note of support.

Hebert says Thompson’s move revived his own long-running doubts about Newmaster’s work. He reached out to six other scholars who could offer authoritative assessments. They reexamined the forest paper and also scrutinized the supplements article and a third paper, published in 2013 in the *Canadian Journal of Forest Research*, which found that DNA barcoding of fecal matter from woodland caribou worked better than conventional methods to determine the animals’ diets. In June 2021, the eight requested the misconduct investigation by UG. More recently, some of them also asked the publishers to retract the supplement and caribou papers. Hebert says a request to retract a fourth paper is in preparation.

The allegation letter details the problems Thompson and Kuzmina detected and many others. It notes that the papers say barcoding for both the forest and supplement papers was carried out by the Canadian Centre for DNA Barcoding, also led by Hebert, but that the center has no record of that work. The letter adds that no sequences were deposited in BOLD or GenBank before publication of either paper, and that some of the data Ragupathy belatedly uploaded in 2020 contradicts the papers’ claims. For example, in the supplements paper, Newmaster’s group labeled a product as the laxative *Senna alexandrina*, but the sequence came from a legume. Moreover, some of the sequences contained errors that precisely matched those in sequences previously submitted by other researchers for several other studies.

In his response to the allegation letter, obtained by *Science*, Newmaster strenuously disputed the concerns. The close correspondence Kuzmina found with samples taken elsewhere reflected normal species similarity in the forest ecosystems, he said. Newmaster insisted his samples were correctly identified, and that innocent technical errors could account for matches between rare or unique mistakes in his sequences and ones published by other researchers.

Contradicting the papers, he said much of the barcoding was done not at the Canadian Centre for DNA Barcoding, but at another UG lab, the Advanced Analysis Centre (AAC) Genomics Facility, or in Newmaster’s personal “artisanal genomics lab.” Yet he

Borrowed words

Science found several instances of apparent plagiarism in Steven Newmaster's work. For example, a 2011 paper about millets on which he was the last author contained text from two earlier papers ([highlighted here](#)), including references (**bold**) that Newmaster and his co-authors failed to add to their own reference list.

Text in a 2011 paper by Steven Newmaster and colleagues

Malayali women prepare several dishes with millets for daily consumption and for festivals. Millets' use as a special food for women's prenatal care and the landrace quality are important factors in maintaining this traditional resource. Pregnant and lactating women in many households prefer a millet-based diet because it provides energy and prevents weight gain. They believe that during pregnancy, the consumption of millet helps to induce lactation and maintain body temperature and energy levels after delivery.

Maloles *et al.*, "The Fine Scale Ethnotaxa Classification of Millets in Southern India," *Journal of Ethnobiology*, 2011

Text in original papers

Malayali women prepare several dishes with millets for daily consumption and for festivals. Their use as a special food in prenatal care of women and their fodder quality are important factors in maintaining this traditional resource. Even nowadays pregnant and lactating women in many households prefer a millet-based diet. Millets provide energy and prevent weight gain. They believe that during pregnancy the consumption of millet helps to induce lactation and maintain body temperature after delivery.

R. Rengalakshmi, "Folk biological classification of minor millet species in Kolli Hills, India," *Journal of Ethnobiology*, 2005

Our research was conducted with the Malayali in the Kolli Hills, which lie in Tamil Nadu's Talaghat Plains (Bohle 1992), one of a series of hills of the Eastern Ghats (Figure 1). Covering approximately 282 square kilometers (Kumaran *et al.* 1998), the Hills rise between 1000 and 1400 meters above sea level (Kumar-Range 2001). Although surrounded by forest on the exterior, the interior has been extensively cleared for agricultural purposes. Presently, the area is approximately 51% agricultural land and 44% forest land (Kumar-Range 2001).

Maloles *et al.*, "The Fine Scale Ethnotaxa Classification of Millets in Southern India," *Journal of Ethnobiology*, 2011

The Kolli Hills lie in Tamil Nadu's Talaghat Plains (Bohle, 1992), one of a series of hills of the Eastern Ghats. Covering approximately 282 square kilometers (Kumaran *et al.*, 1998), the Hills rise between 1000 and 1400 meters above sea level (Kumar-Range, 2001). Although surrounded by forest on the exterior, the interior has been extensively cleared for agricultural purposes. Presently, the area is approximately 51% agricultural land, and 44% forest land (Kumar-Range, 2001).

Elizabeth Finnis, "The political ecology of dietary transitions: Changing production and consumption patterns in the Kolli Hills, India," *Agriculture and Human Values*, 2007

conceded he could not locate the sequencing records. As to why the sequences were not made public at the time, Newmaster says he submitted them to BOLD but blamed its staff for mishandling them. (Hebert, BOLD's scientific director, says records show Newmaster never submitted the data, and even if he had, BOLD's published policy requires a study's project manager to ensure the data go to GenBank as well.)

Newmaster also rejected allegations that he concealed business interests in his papers. "[T]he only income I have had during my tenure at the University of Guelph is my University salary," he wrote. *Science* filed a request with UG for Newmaster's outside income declarations, including from his own companies; UG Vice President for Research Malcolm Campbell responded that the records are exempt from disclosure. Purity-IQ, Songbird, and ParticleOne declined to comment about Newmaster's compensation.

Science asked Little, from the New York Botanical Garden, to review the allegation letter, Newmaster's response, and numerous related documents and provide an independent perspective on the case. Little calls the large number of precisely replicated errors in DNA sequences "bizarre" and suggestive of data manipulation. "People will get hit by cars," he says. "But will two of them be hit by cars while walking across the

same intersection on their hands at 4 a.m.?"

Newmaster's claim that forest ecology could explain the 80% match between the data in the forest paper and those in the graduate student thesis was "unbelievably wrong," Little adds. And the claim that Newmaster and AAC both lost the same sequencing records is implausible, he says, given how zealously scientists and service providers normally safeguard such data. Overall, Little calls the allegations against Newmaster credible. "The papers are at best inaccurate and at worst fraudulent," he says. "The end result is the same: They should be retracted and not trusted."

IN OCTOBER 2021—5 months after Thompson had gone public with his concerns—*Biodiversity and Conservation* reconsidered and agreed to retract the forest paper. GenBank has removed the DNA sequences purportedly associated with the paper. The UG inquiry into the three papers is ongoing. At UG's request, Canada's Secretariat on Responsible Conduct of Research extended the deadline for a decision until June. Newman, the former dean, says he hasn't seen the allegations, but "if Steve actually fabricated data for a publication ... I would just expect that's career death."

Yet, the composition of the investigative committee makes Hebert and other critics worry UG will again dismiss the allega-

tions against Newmaster. University rules require that such committees comprise the dean of the College of Biological Sciences, the associate vice president for research, and a representative from outside UG. But the final committee consists of a business professor, the dean of UG's veterinary college, and a psychologist from a nearby university—none with a background in the relevant science. (UG allows an accused scientist to challenge the panel's membership if they suspect bias; it's not clear whether Newmaster did so.) In an email to *Science*, a UG spokesperson wrote that the investigation is using "a fair and standard process" and the university will "take appropriate action based on the results."

Given Newmaster's high profile—and the way the university has handled the case so far—UG cannot be trusted to carry out an even-handed probe, Thompson says. He describes his treatment by UG after he tried to get his paper investigated as "gaslighting"—being provided with a false impression that his concerns were taken seriously. "We need an independent body [from outside UG] to review cases like this," Thompson says. "It's the only solution to stop history from repeating itself." ■

With reporting by Meagan Weiland and Jenny Carpenter. This story was supported by the *Science* Fund for Investigative Reporting.

INSIGHTS

PERSPECTIVES



POLLUTION

Chasing after methane's ultra-emitters

Leaks from oil and gas companies contribute substantially to global warming

By **Felix Vogel**

The latest emissions gap report from the United Nations Environment Programme highlighted that current and planned mitigation measures are insufficient to achieve the goal of the Paris Agreement of limiting global warming to 1.5°C above preindustrial temperatures (1). When national representatives gathered at the 26th UN Climate Change Conference of the Parties (COP26) in Glasgow last November, a plan to rapidly decrease methane emissions emerged, with over 100 countries joining the Global Methane Pledge aimed at reducing global methane emissions by at least 30% from 2020 amounts by 2030. While policy-makers try to enact climate-related legislation, scientists are trying to identify more cost-effective or quick ways

to curb greenhouse gas emissions. On page 557 of this issue, Lauvaux *et al.* (2) highlight how methane emissions can be effectively reduced by targeting ultra-emitter sites identified by the European Space Agency's satellite-based TROPospheric Monitoring Instrument (TROPOMI) (3).

Methane is a gas with a strong climate impact but short atmospheric lifetime of about 9 years. Mitigation of methane emissions can thus lead to faster reductions in atmospheric concentrations compared to the reduction of longer-lived greenhouse gases such as carbon dioxide (CO₂). Consequently, research on atmospheric methane and the importance of reducing its emissions for achieving the 1.5°C goal have been of increasing interest in recent years (4, 5).

As the second most harmful anthropogenic greenhouse gas—after CO₂—methane has long been the target for emission reduction in many countries. However, despite these efforts, over 350 million tonnes of anthropogenic methane are still being emitted

globally every year, with roughly one-third coming from the fossil fuel industry (6). In contrast to CO₂, which is produced when the fossil fuel is 100% burned, methane emissions are often the product of waste, such as from leaks or the incomplete combustion of fossil fuel, or as the unwanted by-product from agricultural activities. Those who favor methane regulations may argue that, unlike rules governing CO₂ emissions, methane regulations may incentivize more-efficient use of resources rather than causing a feared decrease in productivity—for example, by reducing methane losses in the oil and gas sector through leaks and unnecessary releases.

For methane emission, past data have indicated that a small number of super-emitters are responsible for a disproportionately large share of the emissions. These superemitters include thousands of oil and gas wells in Canada (7) and the natural gas distribution infrastructure in US cities (8). One study that monitored methane emis-

Climate Research Division, Environment and Climate Change Canada, Toronto, ON, Canada.
Email: felix.vogel@ec.gc.ca

PHOTO: VASILY FEDOSEENKO/REUTERS

Some oil and gas facilities, such as this refinery in Belarus, were identified as global methane emission hotspots by latest satellite data analysis.

sions across more than 250,000 facilities in California reported that 30 of those emitters were responsible for 20% of the total methane emission in the state (9).

Lauvaux *et al.* identified the leaders among these super-emitters—the so-called “ultra-emitters.” Using global data collected by the TROPOMI satellite over several years, the authors assembled a list of ultra-emitter sites responsible for a total of roughly 8 million tonnes of methane per year, with the warming potential equivalent to 250 million tonnes of CO₂ (10). To put this into perspective, 250 million tonnes of CO₂ is the carbon footprint of more than 40 million people. This finding is even more notable when one considers that the TROPOMI satellite was not designed to track emissions at the facility scale. However, the amount of emission from these ultra-emitters is so large that TROPOMI could track it with a spatial resolution in the 5-km range.

Researchers have quantified CO₂ emissions from super-emitters by comparing land-based measurements with satellite-based estimates, and combining those values with calculations of downwind plume concentrations using atmospheric modeling (11). However, in contrast to CO₂, the locations and emissions of major methane emitters are difficult to track, as methane emissions are an unwanted by-product of the oil and gas industry and often go unreported. The creation of a global inventory of methane ultra-emitters provides crucial information for targeting the strongest emitters. This should be a useful arsenal for policy-makers to enact effective regulations to combat climate change and alleviate climate-related economic calamity in the long run.

Given the 3 years left in the designed operational life span of TROPOMI, the project will continue to provide data for monitoring the known ultra-emitters and detecting new ones. Looking past TROPOMI, multi-satellite approaches are emerging. For example, by combining TROPOMI data with high-resolution satellites that are designed to track facility-scale emissions, scientists can now precisely determine the source locations and quantify emissions, such as during a recent blow-out event at the Ford Eagle Shale regions in Texas, where nearly 5000 tonnes of methane were emitted in only 20 days because of a control loss at a gas well (12). The global capacity for satellite-based monitoring of atmospheric methane should increase in the coming years, with a whole fleet of satellites waiting to join the hunt for methane sources.

The next generation of satellites is expected to have better spatial and temporal coverage, as well as improved resolutions and accuracies. However, many of the planned satellites may still struggle with measurements performed over water, through clouds, or at nighttime. They may also have shorter operational periods than ground-based networks. These satellites could struggle to track intermittent emitters with emissions under their detection threshold. Thus, it is important to integrate these satellite-based projects with drone-based and ground-based methods when tracking and quantifying emissions at the regional scale.

Any future global methane monitoring system, such as the International Methane Observatory (IMEO) of the UN Environment Programme and the European Commission (13), will have to combine observations across different scales and techniques to be truly comprehensive. As a first step, the different methods and algorithms will have to be standardized or at least be made compatible. For example, a measurement of kilograms of methane emission per hour at a specific site by satellite A should be reproducible using data collected by satellite B or by a drone at the same site. Such harmonization efforts and the collation of best practices for atmospheric monitoring are currently being advanced by the Integrated Global Greenhouse Gas Information System (IG³IS) of the World Meteorological Organization (14). These ongoing projects will continue to provide data to scientists, site operators, policy-makers, and citizens, to spur future research, help identify operational issues, develop cost-efficient mitigation strategies. They will also help to inform the public of where the planet is heading in the grand scheme of climate change and how successful the Paris Agreement and the increased ambitions announced at the COP26 in Glasgow are going to be. ■

REFERENCES AND NOTES

1. UN Environment Programme, Emissions Gap Report 2021, www.unep.org/resources/emissions-gap-report-2021.
2. T. Lauvaux *et al.*, *Science* **375**, 557 (2022).
3. J. Veefkind *et al.*, *Remote Sens. Environ.* **120**, 70 (2012).
4. A. L. Ganesan *et al.*, *Global Biogeochem. Cycles* **33**, 1475 (2019).
5. E. G. Nisbet *et al.*, *Rev. Geophys.* **58**, 1 (2020).
6. M. Saunio *et al.*, *Earth Syst. Sci. Data* **12**, 1561 (2020).
7. K. MacKay *et al.*, *Sci. Rep.* **11**, 8041 (2021).
8. Z. D. Weller, S. P. Hamburg, J. C. von Fischer, *Environ. Sci. Technol.* **54**, 8958 (2020).
9. R. M. Duren *et al.*, *Nature* **575**, 180 (2019).
10. M. Etminan, G. Myhre, E. J. Highwood, K. P. Shine, *Geophys. Res. Lett.* **43**, 12614 (2016).
11. R. Nassar *et al.*, *Geophys. Res. Lett.* **44**, 10045 (2017).
12. D. H. Cusworth *et al.*, *Geophys. Res. Lett.* **48**, 1 (2021).
13. UN Environment Programme, International Methane Emissions Observatory, www.unep.org/explore-topics/energy/what-we-do/methane.
14. Integrated Global Greenhouse Gas Information System, (IG³IS), <https://ig3is.wmo.int/>.

MOLECULAR BIOLOGY

Tethering gene regulation to chromatin organization

A two-tiered system of chromatin structure ensures robust gene expression

By Marissa Gaskill and Melissa Harrison

Precise regulation of gene expression is crucial to cellular identity, and changes to gene expression profiles drive developmental transitions. Distinct enhancer elements interact with promoters to control cell type-specific gene expression. These enhancers are often located at a considerable distance from the genes they regulate. Chromosome looping and three-dimensional (3D) genome organization have been suggested to bring the correct enhancers and promoters together to facilitate the exquisite spatiotemporal gene regulation required for successful development. Nonetheless, it remains unclear how genome organization is precisely regulated to ensure that distant enhancers locate the correct promoter to reliably drive gene expression. On page 566 of this issue, Batut *et al.* (1) define a distinct class of cis-regulatory elements called tethering elements that promote interactions between enhancers and promoters. They propose a two-tiered system of genome organization: tethering elements that connect distant enhancers to promoters and boundary elements that ensure the specificity of these enhancer-promoter interactions.

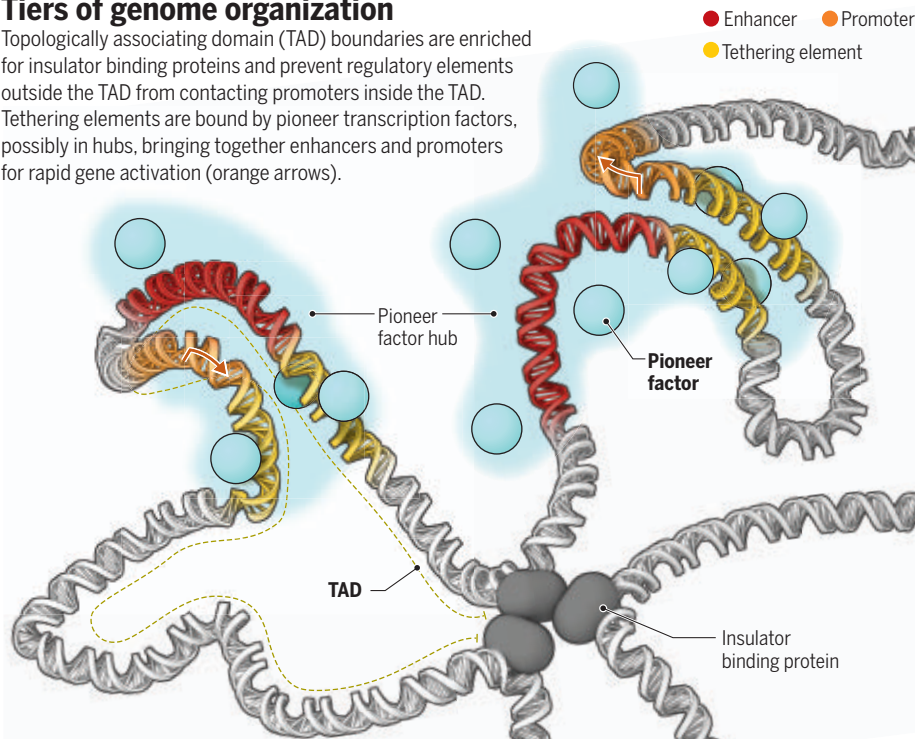
Within the nucleus, chromosomes are organized at multiple levels, including loops, topologically associating domains (TADs), and compartments. Investigations of the role of chromatin structure have largely focused on TADs, which are chromosomal regions enriched for self-interaction and delimited by insulator sequence elements. Despite TADs being a conserved feature of the eukaryotic genome, the importance of this 3D structure to gene regulation re-

Department of Biomolecular Chemistry, School of Medicine and Public Health, University of Wisconsin-Madison, Madison, WI, USA. Email: mharrison3@wisc.edu

10.1126/science.abm1676

Tiers of genome organization

Topologically associating domain (TAD) boundaries are enriched for insulator binding proteins and prevent regulatory elements outside the TAD from contacting promoters inside the TAD. Tethering elements are bound by pioneer transcription factors, possibly in hubs, bringing together enhancers and promoters for rapid gene activation (orange arrows).



mains controversial. Enhancers preferentially interact with promoters within the same TAD. Indeed, disruption of individual TAD boundaries results in defects in gene expression and disease (2, 3). By contrast, additional studies demonstrated that altering TAD boundaries at a genome level resulted in minimal effects on gene expression (4, 5). Furthermore, despite the pronounced changes in gene expression that drive development, TADs are notably stable over time and between cell types (6, 7). Because of these conflicting observations, there has been no overarching framework for how 3D chromatin structure affects enhancer-promoter contacts to promote gene expression.

Using Micro-C, a technique that enables single-nucleosome maps of 3D chromatin interactions, Batut *et al.* generated a detailed interaction map of the genome in *Drosophila melanogaster* embryos. The high degree of resolution provided by Micro-C allowed the authors to identify a new class of regulatory elements, tethering elements. Tethering elements do not activate transcription in transgenic reporter assays and therefore are distinct from enhancers. Instead, they facilitate interactions between enhancers and promoters. Similar enhancer-promoter interactions have been identified genome-wide in mammalian cells (8), suggesting that this is a conserved feature of genome structure. Focusing on the well-studied homeobox (*Hox*) locus, Batut *et al.* used live imaging of transcriptional dynamics to demonstrate that tethering

elements promote the rapid activation of gene expression and showed that disruption of these elements has phenotypic consequences in the adult. As suggested by prior studies (9), the authors show that TAD boundaries within the *Hox* locus prevent interactions between enhancers and promoters located in different TADs. Disruption of TAD boundaries affects gene expression, but this can vary depending on the regulatory elements that are in the neighboring TAD. Deletion of the genomic sequence of either tethering elements or TAD boundaries does not disrupt the formation of the other. Thus, tethering elements and TADs have independent contributions to chromatin organization and the regulation of gene expression (see the figure).

In addition to functional differences, tethering elements and TAD boundaries may be formed at discrete times. Chromatin structure is established in early development (10, 11). A recent imaging-based strategy to interrogate chromatin structure demonstrated that chromatin loops are evident before TAD formation, supporting the independent formation of loops and TADs (12). Batut *et al.* showed that tethering elements and TAD boundaries are defined by a distinct repertoire of binding factors. Whereas TAD boundaries are enriched for insulator binding proteins, tethering elements are bound by the pioneer transcription factors Zelda, GAGA factor (GAF), and Grainyhead. Pioneer factors are capable of binding closed chromatin, promoting chromatin

accessibility and thereby activating gene expression. Zelda and GAF are essential for defining chromatin accessibility and activating gene expression in the early *D. melanogaster* embryo (13, 14). Similarly, both factors have been implicated in the establishment of 3D chromatin structure (10, 11). A mechanistic connection between binding of Zelda and tethering element function is suggested by the finding that Zelda is essential for a subset of early formed loops between enhancers and promoters (12). The enrichment of multiple pioneer factor binding sites in tethering elements suggests that a shared property of these factors may be essential for tethering.

Although it remains for future studies to determine whether these pioneer factors are important for tethering element function and, if so, how they promote tethering, it is notable that GAF and Zelda are not uniformly distributed in the nucleus. Zelda forms hubs of high local concentration, which are important for its ability to recruit other transcription factors and potentiate gene expression (15). Thus, this property may be important for bringing enhancers and promoters in proximity. The recent identification of condensates or phase-separated domains of locally high concentrations of transcription factors has provided a framework to begin to understand these enhancer-promoter interactions. These transcription factor hubs may bring multiple enhancers and promoters together and, in this way, facilitate interaction between these cis-regulatory elements. It is not yet clear whether pioneer factors form condensates that recruit additional factors to facilitate chromatin accessibility and enhancer-promoter interaction or if pioneer factors mediate chromatin accessibility and this then drives subsequent hub formation. Defining these processes will be important for understanding how gene expression is precisely regulated to control development. ■

REFERENCES AND NOTES

1. P. J. Batut *et al.*, *Science* **375**, 566 (2022).
2. D. G. Lupiáñez *et al.*, *Cell* **161**, 1012 (2015).
3. M. Franke *et al.*, *Nature* **538**, 265 (2016).
4. Y. Ghavi-Helm *et al.*, *Nat. Genet.* **51**, 1272 (2019).
5. W. Schwarzer *et al.*, *Nature* **551**, 51 (2017).
6. J. R. Dixon *et al.*, *Nature* **485**, 376 (2012).
7. E. Ing-Simmons *et al.*, *Nat. Genet.* **53**, 487 (2021).
8. T. S. Hsieh *et al.*, *Mol. Cell* **78**, 539 (2020).
9. A. Deshpande *et al.*, *Nat. Genet.* **51**, 1263 (2019).
10. C. B. Hug, A. G. Grimaldi, K. Kruse, J. M. Vaquerizas, *Cell* **169**, 216 (2017).
11. Y. Ogiyama, B. Schuettengruber, G. L. Papadopoulos, J.-M. Chang, G. Cavalli, *Mol. Cell* **71**, 73 (2018).
12. S. M. Espinola *et al.*, *Nat. Genet.* **53**, 477 (2021).
13. M. M. Gaskill, T. J. Gibson, E. D. Larson, M. M. Harrison, *eLife* **10**, e66668 (2021).
14. H. L. Liang *et al.*, *Nature* **456**, 400 (2008).
15. M. Mir *et al.*, *eLife* **7**, e40497 (2018).

10.1126/science.abn6380

When viruses become more virulent

Natural selection favors virulence when it is coupled with increased viral transmission

By Joel O. Wertheim

The evolution of virulence—the degree to which a pathogen sickens, kills, or otherwise reduces its host's fitness—depends on the biology of infection and transmission (1). A more virulent virus may be less transmissible because in killing its host, it reduces the opportunity for transmission. But virulence and transmissibility can be intrinsically linked, so that to maintain or increase infectiousness, a virus must be virulent. On page 540 of this issue, Wymant *et al.* (2) describe the emergence of a more virulent and transmissible variant of HIV that has spread to 102 known cases, mostly in the Netherlands, over the past decade. This finding raises questions about the selective pressures and molecular mechanisms that drive increased virulence and transmission.

To appreciate the nuances in the evolution of virulence, it is worth revisiting the apocryphal tale of how a bioweapon—the extraordinarily lethal myxoma virus, which was released in Australia to exterminate the European rabbit infestation—quickly attenuated to become a benign infection. Myxoma virus is a vector-borne pathogen that, when introduced to Australia, had a >99% fatality rate. Less virulent myxoma virus evolved, but it continues to circulate and kill rabbits in Australia with a 50% mortality rate. Ample highly virulent myxoma virus strains persist, indicating that evolution toward attenuation did not drive the most virulent variants extinct (3). The key to maintaining virulence may lie in the inability of myxoma virus to replicate in its insect vectors; high titers of the virus must be maintained in rabbits to ensure transmissibility. Thus, virulence (which achieves high viral load) is critical to its evolutionary success.

In HIV, the biology is clear: There can be no decoupling of virulence and transmissibility (4). Upon initial HIV infection, the viral load peaks and then stabilizes to pro-

duce a prolonged, symptom-free chronic infection that can last a decade or more. This stabilized viral load is known as the set-point viral load and can be quite variable across infected people, differing by several orders of magnitude. This variability can partly be traced back to genetic variation in the virus itself. People with higher set-point viral load, left untreated, progress to AIDS more rapidly (5). Those same people will also be more infectious during this time period because higher viral load leads to more viral transmission.

By contrast, people with lower set-point viral load will live symptom-free longer and be less infectious over this period. Therein

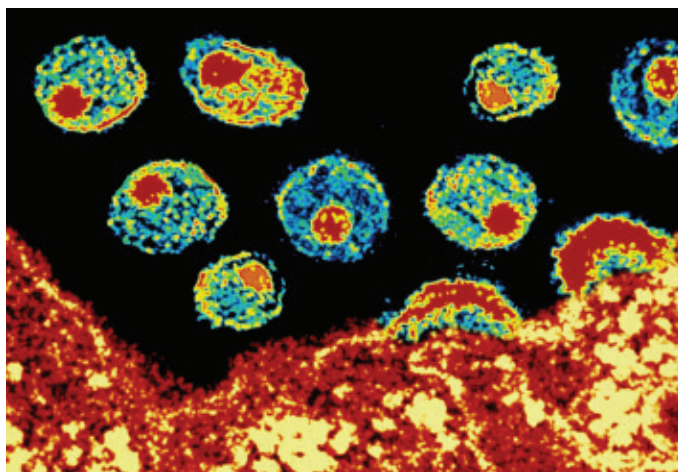
HIV in the United States is evolving in the opposite direction. Viral load at diagnosis has been increasing every decade since the pandemic was first identified in 1981 (7), and higher viral loads are found in people belonging to larger HIV transmission clusters (8). Notably, this trend toward more virulent HIV is not emanating from a single cluster of transmission. Like the myxoma virus, this adaptation appears to be found across the spectrum of HIV genetic diversity in the United States. By contrast, the virulent cluster described by Wymant *et al.* emanated from a single cluster on the phylogenetic tree, suggesting a single adaptive event in HIV evolution. However, the

specific mutations that are responsible for increased virulence were not identified. In both Europe and the United States, the genetic mechanisms underpinning viral adaptation remain unclear.

Antiretroviral therapy upon diagnosis reduces viral load to a point at which it is undetectable. Treatment not only improves survival among those infected with HIV but also largely prevents onward sexual transmission. Evolutionary modeling suggested that this intervention—which has been standard of care in the United States for a decade—would select for increasingly virulent HIV. By decoupling the opportunity for transmission from

disease progression, HIV with higher viral load would be favored. However, HIV in the United States apparently began increasing in virulence before the test-and-treat era. Why, after more than a century of human-to-human transmission, is HIV virulence still evolving, and how will this virus evolve in response to efforts to “end the epidemic” through substantial reduction of transmission over the next decade?

Observing the emergence of more virulent and transmissible HIV is not a public health crisis. Standard public health action—including molecular HIV surveillance (9), facilitating linkage to care, and partner notification—are still the best options when faced with a rapidly growing cluster of more virulent HIV. Let us not forget the overreac-



Colored transmission electron micrograph showing HIV-1 virions emerging from T cells (red), continuing the infection cycle. Virulence and transmission of HIV-1 are influenced by viral load.

lies the trade-off from the perspective of the virus. Burn bright and be brief, or smolder and persist? For HIV, natural selection favors a middle ground, but the trajectory depends on the host population and the initial starting conditions. In Uganda, where heterosexual HIV transmission predominates, there are two major subtypes of HIV: A and D. Subtype D was the most prevalent variant in the 1990s and is associated with higher viral load and more rapid progression to AIDS than that of subtype A. Over the past two decades, subtype D has been gradually outcompeted in Uganda by the comparatively less virulent subtype A, which itself may be becoming even less virulent (6). The selective driver behind this change remains unknown.

Department of Medicine, University of California, San Diego, La Jolla, CA, USA. Email: jwertheim@health.ucsd.edu

tion of the claim of “Super AIDS” in 2005, when alarm was raised over a rapidly progressing, multidrug-resistant HIV infection found in New York (10) that was ultimately restricted to a single individual.

These findings are relevant to the COVID-19 pandemic. Although it is certainly possible that severe acute respiratory syndrome coronavirus 2 (SARS-CoV-2) will evolve toward a more benign infection (11), like other “common cold” coronaviruses, this outcome is far from preordained. At the beginning of the COVID-19 pandemic, there was an underappreciation of the rapidity with which selection would lead to changes in transmissibility and virulence (12). But the ultimate outcome depends on whether and how SARS-CoV-2 transmission and virulence are linked. SARS-CoV-2 variants demonstrate that this virus is repeatedly evolving to be more transmissible, and not all of these adaptive variants are demonstrably more virulent. However, the Delta variant that dominated global cases in late 2021 shows how SARS-CoV-2 could evolve to be both more transmissible and more virulent (13). The Omicron variant is more transmissible, but whether it is more or less virulent in immunologically naïve individuals is unclear. Immune evasion, receptor binding efficiency, and tissue tropism may contribute to the evolution of virulence (14, 15). Deciphering the mechanisms of SARS-CoV-2 virulence and its relationship with transmission and immunity will be essential to understand how and why its virulence may evolve. But the HIV and SARS-CoV-2 pandemics show how viruses can and will evolve higher virulence when favored by natural selection. ■

REFERENCES AND NOTES

1. J. L. Geoghegan, E. C. Holmes, *Nat. Rev. Genet.* **19**, 756 (2018).
2. C. Wymant *et al.*, *Science* **375**, 540 (2022).
3. P. J. Kerr *et al.*, *Viruses* **7**, 1020 (2015).
4. C. Fraser *et al.*, *Science* **343**, 1243727 (2014).
5. C. Fraser, T. D. Hollingsworth, R. Chapman, F. de Wolf, W. P. Hanage, *Proc. Natl. Acad. Sci. U.S.A.* **104**, 17441 (2007).
6. F. Blanquart *et al.*, *eLife* **5**, e20492 (2016).
7. J. T. Herbeck *et al.*, *AIDS* **26**, 193 (2012).
8. J. O. Wertheim *et al.*, *Nat. Commun.* **10**, 5788 (2019).
9. A. M. Oster, A. M. France, J. Mermin, *JAMA* **319**, 1657 (2018).
10. L. M. Crawley, *JAMA* **7**, 790 (2005).
11. J. S. Lavine, O. N. Bjornstad, R. Antia, *Science* **371**, 741 (2021).
12. N. D. Grubaugh, M. E. Petrone, E. C. Holmes, *Nat. Microbiol.* **5**, 529 (2020).
13. A. Sheikh, J. McMenamin, B. Taylor, C. Robertson, *Lancet* **397**, 2461 (2021).
14. M. Diamond *et al.*, *Research Square* 10.21203/rs.3.rs-1211792/v1 (2021).
15. B. Meng *et al.*, *bioRxiv* 10.1101/2021.12.17.473248 (2021).

ACKNOWLEDGMENTS

J.O.W. is funded by the National Institutes of Health and US Centers for Disease Control and Prevention.

10.1126/science.abn4887

EPIGENETICS

The adenine methylation debate

N⁶-methyl-2'-deoxyadenosine (6mA) is less prevalent in metazoan DNA than thought

By Konstantinos Boulas^{1,2} and Eric Lieberman Greer^{1,2}

Adenine methylation, forming N⁶-methyl-2'-deoxyadenosine (6mA), is a prevalent DNA modification in prokaryotes and has recently been proposed to exist in multicellular eukaryotes (metazoans) to regulate diverse processes, including transcription, stress responses, and tumorigenesis. However, the existence of 6mA, and therefore its biological importance, in metazoan DNA has been debated by recent studies, which have either detected 6mA at much lower abundances than initially reported or failed to detect 6mA at all. On page 515 of this issue, Kong *et al.* (7) report the development of 6mASCOPE, a quantitative method that deconvolutes 6mA in samples of interest from contamination sources. They detected low amounts of 6mA in fruit flies (*Drosophila melanogaster*), plants (*Arabidopsis thaliana*), and humans, which suggests that 6mA is much less abundant in these organisms than previously thought. These data suggest that a reassessment of 6mA in eukaryotic DNA is warranted.

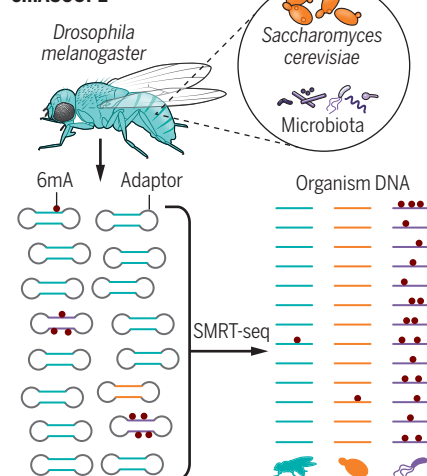
The discovery of 6mA in multicellular eukaryotic DNA (2–4) was facilitated by the

development of highly sensitive detection and mapping methodologies. These include ultrahigh-performance liquid chromatography coupled with tandem mass spectrometry (UHPLC-MS/MS), which has a detection limit of 0.1 to 1 parts per million (ppm) (5), and single-molecule real-time sequencing (SMRT-seq), a long-read DNA sequencing technique that maps methylated bases by quantifying rates of incorporation of complementary bases, which are altered when bases are modified (6). However, these methods have limitations: UHPLC-MS/MS cannot discriminate the source of 6mA, which becomes problematic when 6mA is of low abundance in the organism compared with the abundance in bacterial contaminants (7). Moreover, long-read sequencing methods, such as SMRT-seq, are error prone, and SMRT-seq requires high sequencing depth and loses accuracy when 6mA is lower than 10 ppm (7, 8). Because of these limitations, several laboratories have been unable to detect 6mA, or they have detected 6mA at substantially lower concentrations in metazoan genomes (7–10), which has led some to question whether 6mA is a directed DNA modification in metazoans. Kong *et al.* developed 6mASCOPE, a SMRT-seq analysis method that quantitatively de-

Organisms with adenine methylation

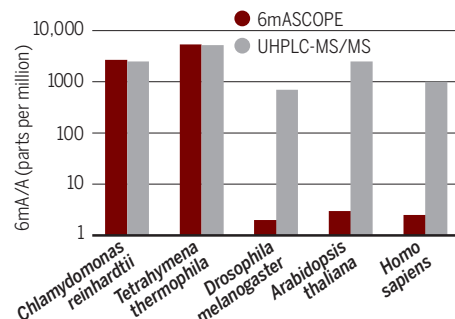
To quantify the amount of N⁶-methyl-2'-deoxyadenosine (6mA) present in genomic DNA, single-molecule real-time sequencing (SMRT-seq) data are analyzed with 6mASCOPE. In 6mASCOPE, small DNA fragments are produced, adaptors are added, and high-coverage SMRT-seq is performed. 6mASCOPE is a reference-free analysis method that deconvolutes SMRT-seq data to identify the source of 6mA.

6mASCOPE



The abundance of 6mA

Previously, ultrahigh-performance liquid chromatography coupled with tandem mass spectrometry (UHPLC-MS/MS) identified 6mA in prokaryotes and metazoans. However, analysis with 6mASCOPE found that 6mA was overestimated in metazoans owing to contamination with DNA from microbiota or food.



GRAPHIC: KELLIE HOLOSKY/SCIENCE

termines in which species 6mA is present, enabling discrimination between 6mA in the metazoan genome and that in contaminating microorganisms (see the figure).

Existing SMRT-seq methods compare the interpulse duration [(IPD) the time between successive base additions, which is altered by DNA modifications] of native template with the reference genome, ignoring contaminating DNA with abundant 6mA. Kong *et al.* overcome this limitation by devising a reference-free approach. By using the long-read sequencing to exclusively sequence short (200 to 400 base pairs) DNA sequences, each molecule is heavily resequenced, which leads to higher-confidence circular consensus sequence (CCS) base-calling accuracy. A metagenomic analysis allows for CCS reads to be mapped to both the genome of interest and to potential contamination sources by using a comprehensive set of genomes, including those from microbiota. The 6mA/A ratios were estimated using a machine learning model trained with a broad range of 6mA content. As a proof of principle, the authors performed 6mASCOPE on two unicellular eukaryotes with high amounts of 6mA, *Chlamydomonas reinhardtii* (11) and *Tetrahymena thermophila* (12). They confirmed high 6mA in these protists and further refined the methylation motif (VATB: V = A, C, or G; B = C, G, or T) and preference of 6mA to occur in specific locations in the linker regions between nucleosomes.

Kong *et al.* next applied 6mASCOPE to *D. melanogaster*, *A. thaliana*, and *Homo sapiens*—three multicellular eukaryotes with reported high 6mA abundances [~700 ppm for *D. melanogaster* embryos (2), 2500 ppm for *A. thaliana* seedlings (3), and 500 to 1000 ppm for *H. sapiens* lymphocytes (13) or primary glioblastomas (14)]. They found that bacteria in the gut of *D. melanogaster* or in the soil of *A. thaliana* samples, which made up a very small amount of the mapped reads, accounted for the majority of 6mA quantified by UHPLC-MS/MS. This led to 6mA abundance in *D. melanogaster* and *A. thaliana* genomes being quantified at ~2 or 3 ppm (near the limit of detection). These findings are bolstered by previous work that demonstrated that nematode worms (*Caenorhabditis elegans*) have substantially lower 6mA abundance (0.1 to 3 ppm) than previously estimated because of bacterial contamination in the gut and that zebrafish (*Danio rerio*) embryos have artificially increased 6mA quantifications because of bacteria adhering to the chorion membrane, which surrounds the

embryo, as assessed by UHPLC-MS/MS (7).

6mASCOPE performed on peripheral blood mononuclear cells and two glioblastoma brain tissue samples yielded 6mA abundances of 17 and 2 ppm, respectively. A recent study suggested that 6mA is increased in mammalian mitochondrial DNA (15), but 6mASCOPE also failed to detect increased amounts of 6mA in the mitochondrial DNA of human HEK293 cells. Kong *et al.* confirmed earlier results (7, 10) that exogenous premethylated DNA can be incorporated into eukaryotic DNA and increases 6mA content. Together, these findings challenge high 6mA abundances in multicellular eukaryotes. Instead, 6mA is likely much rarer than previously thought and is possibly variable between different tissue samples or cell lines. It is also possible that 6mA increases only under specific stress conditions (15).

6mASCOPE's limit of detection (~1 to 10 ppm) makes it hard to conclude whether estimated 6mA abundances of 2 to 3 ppm are real and above background. These limitations can be addressed through the development of sequencing methods that take advantage of the distinct chemistry of 6mA, similar to bisulfite sequencing for 5-methylcytosine. Additionally, future studies should combine this more-rigorous 6mASCOPE and optimized UHPLC-MS/MS methods (7) with a focus on stress conditions and mitochondrial DNA (15). Moreover, 6mASCOPE cannot discriminate potential misincorporation of either abundant messenger RNA containing 6mA or foreign methylated DNA that could be integrated into eukaryotic DNA through the nucleotide salvage pathway. Combining rigorous detection methods with the manipulations of putative 6mA-regulating enzymes and directed epigenomic editing of 6mA will help address whether rare 6mA in metazoans has a functional role in specific locations in the genome or is randomly localized as a potential by-product of misincorporation by the salvage pathway. ■

REFERENCES AND NOTES

1. Y. Kong *et al.*, *Science* **375**, 515 (2022).
2. G. Zhang *et al.*, *Cell* **161**, 893 (2015).
3. Z. Liang *et al.*, *Dev. Cell* **45**, 406 (2018).
4. E. L. Greer *et al.*, *Cell* **161**, 868 (2015).
5. W. Huang *et al.*, *RSC Adv.* **5**, 64046 (2015).
6. B. A. Flusberg *et al.*, *Nat. Methods* **7**, 461 (2010).
7. Z. K. O'Brien *et al.*, *BMC Genom.* **20**, 445 (2019).
8. K. Douvlataniotis *et al.*, *Sci. Adv.* **6**, eaay3335 (2020).
9. S. Schiffer *et al.*, *Angew. Chem. Int. Ed.* **56**, 11268 (2017).
10. B. Liu *et al.*, *Anal. Chem.* **89**, 6202 (2017).
11. Y. Fu *et al.*, *Cell* **161**, 879 (2015).
12. Y. Wang *et al.*, *Nucl. Acids Res.* **45**, 11594 (2017).
13. C.-L. Xiao *et al.*, *Mol. Cell* **71**, 306 (2018).
14. Q. Xie *et al.*, *Cell* **175**, 1228 (2018).
15. Z. Hao *et al.*, *Mol. Cell* **78**, 382 (2020).

ACKNOWLEDGMENTS

E.L.G. is supported by National Institutes of Health grants (DP2AG055947 and R01AI151215).

¹Department of Pediatrics, HMS Initiative for RNA Medicine, Harvard Medical School, Boston, MA, USA. ²Division of Newborn Medicine, Boston Children's Hospital, Boston, MA, USA. Email: eric.greer@childrens.harvard.edu

MATERIALS SCIENCE

An adaptive device for AI neural networks

The perovskite nickelate can transform among four different electronic components

By Rohit Abraham John

The human brain's ability to maneuver the avalanche of unstructured data, learn from experience, and process information with extreme energy efficiency inspires the next generation of computing technologies (1, 2). Neuronal plasticity is defined as the capability of the brain to change its structure and function in response to experience. This functional and structural plasticity is what researchers are trying to achieve in the so-called "neuromorphic" circuits and computer architectures (3–6). Specific learning rules observed in biology have been faithfully replicated recently in electrical components (7, 8). However, the ability for a logical device to learn and modify from experience, and to grow and shrink when required, have yet to be explicitly demonstrated. On page 533 of this issue, Zhang *et al.* (9) present highly plastic perovskite nickelate devices that can be electrically configured and reconfigured to become resistors, memory capacitors, artificial neurons, and artificial synapses.

The material design principle for creating reconfigurable devices is based on protonation-induced doping of nickelates such as NdNiO₃, or NNO. At room temperature, an ideal NNO is a correlated metal, which means that electrons would interact among themselves inside the material instead of behaving independently. Hydrogen, an electron donor, can be inserted into the NNO lattice by annealing the material in hydrogen gas while connected to a catalytic electrode. This process modifies the electrons'

Department of Chemistry and Applied Biosciences, Institute of Inorganic Chemistry, ETH Zürich, CH-8093 Zürich, Switzerland. Email: rohjohn@ethz.ch

orbital configuration in the nickel atoms to largely reduce the electrical conductivity. Upon applying single-shot electric pulses across the material, Zhang *et al.* could redistribute protons within the lattice. This generates a multitude of electronic states based on the final distribution and local concentration of the charges. These metastable states can then be configured on demand to perform the functionalities of resistors, memory capacitors, neurons, and synapses—a first for a single device (see the figure).

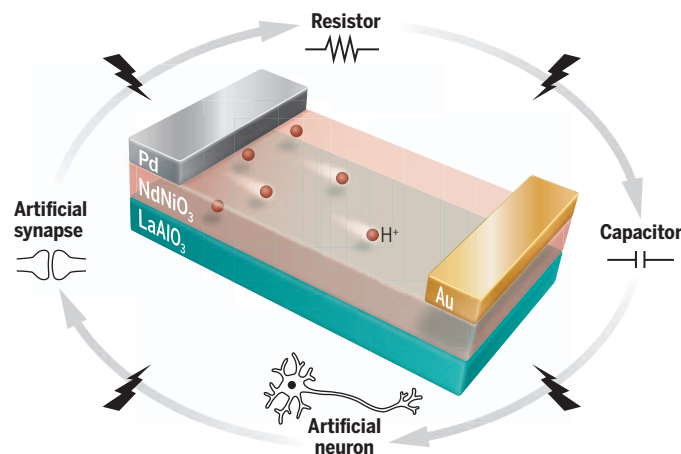
In comparison with oxide-based devices that rely on the migration of oxygen vacancies through the nickelate lattice, the proton-redistribution approach used by Zhang *et al.* enables a larger charge modulation at a faster time scale because of the much smaller ionic radius of protons as compared with those of oxygen atoms. Moreover, the devices are formed by using semiconductor foundry-compatible techniques and on substrates compatible with complementary metal-oxide semiconductor (CMOS) circuits, making this a promising “lab-to-fab” technology and immediately pertinent to the electronics industry.

All electronic materials have defects that can create a barrage of metastable conductivity states. As a result, the value of this research discipline lies in the ability to identify and engineer functional states for specific applications. Zhang *et al.* discovered in their device many metastable configurations, each having distinct electrical and chemical signatures. The authors first explore the possible configurations using theoretical calculations and subsequently confirm them using a combination of resistance and capacitance measurements, Raman spectroscopy, and scanning near-field optical microscopy.

The large pool of possible electronic states available within a single device would help to enable the implementation of reservoir computing frameworks in hardware. Reservoir computing is a computational framework inspired by a specific type of neural network theory that maps input signals into higher-dimensional computational spaces by using the dynamics of a fixed, nonlinear system known as a reservoir. The hydrogen-doped NNO of Zhang *et al.* is a strong candidate to be used as nodes for reservoir computing in hardware. Each node has two nonlinear components: the memristor—a device that combines functions of a memory

Hydrogen-doped perovskite nickelate as a versatile reconfigurable platform

By applying electric pulses, the hydrogen ions in the nickelate lattice can occupy metastable states and enable distinct functionalities. This allows the same device to be reconfigured on demand as a resistor, a memory capacitor, an artificial neuron, or an artificial synapse.



and a resistor—and the similarly named memcapacitor. Together, the two components represent an internal state and outperform theoretical reservoirs on several classification tasks in terms of improved accuracy and faster convergence.

A reconfigurable device may also help realize grow-when-required (GWR) networks, which is an artificial neural network in which the system can, as its name suggests, grow when required. In more technical terms, this means that when the input to the GWR network does not achieve a certain

“This can enable compact and energy-efficient neuromorphic system designs of reservoir computing frameworks and dynamic neural networks.”

threshold of activity, the system would automatically create a new node. Through the capacity to grow on demand, the network overcomes problems caused by resource depletion—a common problem for static computational networks. Similarly, the network can also shrink its size if inactive nodes are detected, saving operational costs. According to theoretical models created by Zhang *et al.*, their GWR network has supremacy over static networks by up to 250% accuracy for incremental learning scenarios. The reconfigurability offered by the device further ex-

pands the efficiency and reliability for a GWR system, at least in theory, and will help realize more dynamic architectures for continual learning.

The reconfigurable device by Zhang *et al.* represents a substantial advance by having multiple neuronal and synaptic functionalities embedded within a single device. This can enable compact and energy-efficient neuromorphic system designs of reservoir computing frameworks and dynamic neural networks. However, to bring this vision to practical hardware implementation, researchers still have to find answers to many questions, such as how to deal with the nonuniformity of the devices, how to make the device connect to or disconnect from the neural network, how to

rearrange the connections when the device is reconfigured from one function to another, and how to determine the role of each device and apply the correct voltage scheme on it.

The electrical circuits in use today are designed with multiple passive components such as resistors, capacitors, and inductors and active devices such as transistors. With the discovery of memristors, circuit designers now have an extra degree of freedom (10–12) when designing power-efficient, high-performance systems. However, from a material implementation perspective, the construction of these components still requires complex assembly of various conductive, semiconductive, and insulating materials. The ability to implement almost all of these elements with a single material platform can substantially change electronics. Hence, such reconfigurable electronic devices could have positive implications beyond neuromorphic computing and machine intelligence. ■

REFERENCES AND NOTES

1. P.A. Merolla *et al.*, *Science* **345**, 668 (2014).
2. M. Davies *et al.*, *IEEE Micro* **38**, 82 (2018).
3. R.A. John *et al.*, *Nat. Commun.* **11**, 1 (2020).
4. K. Janzakova *et al.*, *Nat. Commun.* **12**, 6898 (2021).
5. G. Milano *et al.*, *Nat. Mater.* 10.1038/s41563-021-01099-9 (2021).
6. J. Torrey *et al.*, *Nature* **547**, 428 (2017).
7. W. Yi *et al.*, *Nat. Commun.* **9**, 4661 (2018).
8. R.A. John *et al.*, *Adv. Mater.* **30**, 1800220 (2018).
9. H.-T. Zhang *et al.*, *Science* **375**, 533 (2022).
10. S. Kumar *et al.*, *Nature* **585**, 518 (2020).
11. S. Goswami *et al.*, *Nature* **597**, 51 (2021).
12. Z. Wang *et al.*, *Nat. Commun.* **9**, 2516 (2018).

ACKNOWLEDGMENTS

R.A.J. acknowledges the support from the ETH Zurich Postdoctoral Fellowship scheme.

10.1126/science.abn6196

Lethal mutagenesis as an antiviral strategy

Lethal mutagenesis of RNA viruses is a viable antiviral strategy but has unknown risks

By Ronald Swanstrom¹ and
Raymond F. Schinazi²

Viruses depend on the host cell to carry out much of their replication, with each offering only a few virus-specific targets for the development of antiviral therapies. This makes the development of broadly active antivirals difficult to conceptualize. Numerous RNA viruses—including severe acute respiratory syndrome coronavirus 2 (SARS-CoV-2), Zika virus, and Chikungunya virus—have led to recent epidemics, highlighting the need for effective antiviral drugs that can be enlisted quickly. Some years ago, a broadly applicable antiviral strategy was proposed in which a slight increase in the error rate of a rapidly replicating RNA virus would overwhelm the capacity to remove deleterious mutations, driving the viral population to extinction; this strategy is called lethal mutagenesis (*1*). Although the antivirals ribavirin and favipiravir were developed with this strategy in mind, the recent development of the much more potent molnupiravir to treat SARS-CoV-2 highlights the unknown risks to the host that this strategy entails.

The genome size of an organism is inversely related to the error rate during replication, and this holds true for small RNA viruses with genomes of 7 to 30 kb (*2*). For RNA viruses, this translates into one nucleotide substitution for every two to three genomes synthesized. Most mutations are deleterious, but a subset of mutations will give rise to potentially useful phenotypic diversity, which may undergo selection. Lethal mutagenesis is a universal antiviral strategy for RNA viruses (especially those that cause acute disease) because they all have the same vulnerabilities of small genomes and rapid replication, making them highly sensitive to an increased mutation rate.

The strategy for increasing the rate of new mutations in RNA viruses is to design ribonucleoside analogs that can be metabolized to ribonucleoside triphosphates in cells and then be incorporated into the viral genome during viral RNA synthesis. The design of the

analog allows the base portion of the ribonucleotide to base pair ambiguously during subsequent RNA synthesis. Thus, once incorporated into viral RNA, the analog will base pair with one of several natural nucleotides during RNA synthesis, leading to a mutation. RNA viruses synthesize complementary plus and minus strands of RNA during viral replication and do this multiple times. For example, it is estimated that the poliovirus RNA genome undergoes five consecutive rounds of replication within a cell before new virus particles are released (*3*). As the viral RNA genome is amplified in the cell, the effects of the mutagen are concentrated in the viral genome.

The first ribonucleoside analog that was identified as capable of inducing mutations in an RNA virus was the purine analog ribavirin, which forms base pairs as either adenosine or guanosine when used at high concentrations in human cells *in vitro* (*4*). Ribavirin has pleiotropic effects on the cell, and its limited antiviral effect *in vivo* is by an uncertain mechanism (*5*). Favipiravir is a base analog that is metabolized to a ribavirin-like molecule in the cell. It is approved for use against influenza virus infection in Japan, and it has been shown to be antiviral and mutagenic against SARS-CoV-2 when used at high doses in an animal model (*6, 7*). Favipiravir is now being evaluated in multiple human trials to treat COVID-19.

A significantly more potent antiviral drug that mediates lethal mutagenesis has recently come to the forefront as a potential antiviral in the current SARS-CoV-2 pandemic—molnupiravir (*8, 9*). This is an orally available 5'-isobutyl form of the cytidine analog β -D-*N*³-hydroxycytidine (NHC) (*10*). This molecule contains an additional oxygen atom in the extra-ring amino group at position four of the cytidine base. In this position, the oxygen destabilizes a hydrogen atom, also bound to this extra-ring nitrogen, leading to migration back and forth with the ring position three nitrogen; this changes the base-pairing properties back and forth between uridine and cytidine (*11, 12*) (see the figure). In uridine, position four in the ring of the base has an extra-ring oxygen as a carbonyl, suggesting that RNA synthesis is relatively insensitive to the chemical composition at this position (aside from its role in base pairing). This highlights why NHC should be readily metabolized by the cell. In a cell culture-

based assay, NHC was 100 times more potent as an inhibitor of SARS-CoV-2 than ribavirin or favipiravir (*13*). Molnupiravir was efficacious in mouse models of respiratory SARS-CoV and Middle East respiratory syndrome coronavirus (MERS-CoV) infection (*9*), consistent with NHC having broad antiviral activity (*10*).

A recently reported clinical trial of molnupiravir showed a 30% reduction in hospitalization when people with symptomatic SARS-CoV-2 infection (and at risk for more serious disease) were treated with molnupiravir within the first 5 days of symptoms (*14*). Based on these results, the US Food and Drug Administration (FDA) has approved an emergency use authorization (EUA) for molnupiravir to treat symptomatic SARS-CoV-2 infections. Molnupiravir has also been approved for the treatment of COVID-19 in the United Kingdom, and there are expectations that it will be made widely available around the world.

However, the antiviral strategy of lethal mutagenesis comes with a cautionary note. Ribonucleosides must be phosphorylated to the 5'-triphosphate form to be substrates for RNA synthesis (host or viral). Ribonucleosides synthesized by the host cell are formed as the 5'-monophosphate. Ribonucleoside analogs enter this biosynthetic pathway through phosphorylation by a salvage kinase to form the 5'-monophosphate (see the figure). The ribonucleoside 5'-monophosphate is phosphorylated to the ribonucleoside 5'-diphosphate and then to the 5'-triphosphate (now ready for RNA synthesis). The ribonucleoside 5'-diphosphate is the obligatory intermediate in this pathway, which creates a potential problem. Ribonucleoside 5'-diphosphate is also the obligatory intermediate in the synthesis of the 2'-deoxyribonucleoside 5'-diphosphate that is on the pathway to form 2'-deoxyribonucleoside 5'-triphosphates, which are used in DNA synthesis. The enzyme ribonucleotide reductase (RNR) is responsible for this reaction. Thus, there is a clear metabolic pathway for a mutagenic ribonucleoside analog to become a precursor for host DNA synthesis.

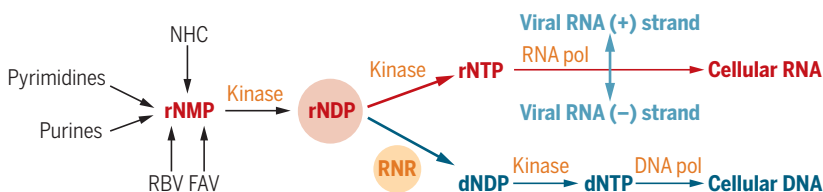
Molnupiravir was shown to be positive in the bacterial Ames test (an assay that measures mutagenic potential), where two animal model assays of mutagenic potential were largely negative, leading the FDA to state in the EUA fact sheet that "molnupiravir is low

¹Department of Biochemistry and Biophysics, University of North Carolina at Chapel Hill, Chapel Hill, NC, USA.

²Laboratory of Biochemical Pharmacology, Department of Pediatrics, Emory University School of Medicine and Children's Healthcare of Atlanta, Atlanta, GA, USA.
Email: risunc@med.unc.edu

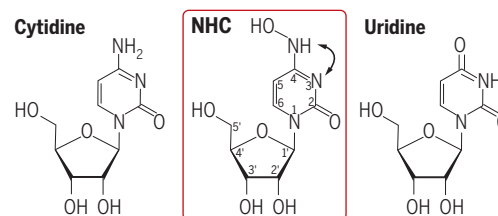
Mutagenesis with ribonucleoside analogs

Antiviral ribonucleoside analogs—such as NHC (molnupiravir), RBV, and FAV—transit the ribonucleotide biosynthetic pathway and become the substrate for host and viral RNA synthesis. They may also appear in the 2'-deoxyribonucleotide pathway owing to the activity of RNR.



Ribonucleoside analogs converge at the rNMP, which is metabolized to the rNDP and then to the rNTP to become the substrate for host and viral RNA synthesis. However, the rNDP is also the substrate for the synthesis of the DNA precursor dNDP.

dNDP, 2'-deoxyribonucleoside 5'-diphosphate; dNTP, 2'-deoxyribonucleoside 5'-triphosphate; FAV, favipiravir; NHC, β -D- N^4 -hydroxycytidine; pol, polymerase; RBV, ribavirin; rNDP, ribonucleoside 5'-diphosphate; rNMP, ribonucleoside 5'-monophosphate; RNR, ribonucleotide reductase; rNTP, ribonucleoside 5'-triphosphate.



Mutations are introduced during viral replication when the NHC-derived ribonucleotide in viral RNA is recognized as either cytosine or uridine owing to ambiguous base pairing.

risk for genotoxicity" (15). However, the ability of the molnupiravir metabolite NHC to transit the RNR pathway was demonstrated in a cell culture-based assay of mammalian cell mutagenesis (13), raising questions about which assays should be used for evaluating the risk of mutagenesis in humans.

There is a gap in our knowledge in scaling short-term lab-based assays (using bacteria, animal cells, and animal models) for mutagenic activity with long-term risk to human health. Mutagens that are incorporated during cellular DNA synthesis are problematic for a developing fetus (where cells are undergoing rapid division), male germline cells (which continue to divide throughout life), and cancer risk (where the small fraction of human cells that are dividing have the potential to incorporate a mutation that could contribute to cancer development). Humans are exposed to mutagens throughout life—for example, DNA mutations are induced by x-ray imaging or during air travel—so there are levels of DNA damage that are considered to be largely inconsequential. If the molnupiravir metabolite NHC really is a mutagen in dividing animal cells, how should negative data in an animal model be interpreted? Are such negative data sufficient to ensure long-term safety in humans, or does the lack of knowledge about the link between negative results in animal assays and long-term outcomes in human health need to be acknowledged? Molnupiravir use will come with some restrictions around short-term risks associated with reproductive health, but it may take years before potential long-term risks are understood. The best outcome, which is the assumption from the negative results in animals, is that molnupiravir treatment falls within the background level of exposure to mutagens that humans already experience and tolerate. The half-life of molnupiravir metabolites in human tissue is unknown.

By definition, lethal mutagenesis will cause increased sequence diversity within

the viral population. This has raised the issue of whether the intentional introduction of sequence diversity will speed up viral evolution, with the specific concern being antibody escape mutants that would undermine vaccine efforts. Adding random mutations at a density of 1 per 1000 bases of the viral genome is sufficient to reduce infectivity of the viral population in the range of 100-fold, as shown for poliovirus and SARS-CoV-2 (4, 13). Treatment with molnupiravir modestly reduces the shedding of viral RNA and significantly reduces the infectiousness of SARS-CoV-2 in patients with COVID-19 (8, 14). Thus, during successful treatment and clearance of the virus, the potential for evolution would appear minimal. However, for people who fail to clear the virus and maintain a persistent infection, whether treatment with molnupiravir will affect the course of viral evolution remains unknown. Similarly, attempts to treat patients with a combination of molnupiravir and the SARS-CoV-2 protease inhibitor nirmatrelvir should carefully follow any sequence changes within the viral 3CL protease coding domain to assess the potential evolution of resistance.

There is a desperate need to make efficacious SARS-CoV-2 treatments widely available, to develop new broadly active antiviral treatments to allow rapid response to new SARS-CoV-2 variants, and, more generally, to be able to respond to new RNA virus epidemics. Molnupiravir has the potential to lower the disease burden of SARS-CoV-2 infections and help contain future emerging RNA viruses. However, how can its potential long-term effects as a mutagen be assessed? The following steps are suggested: Treatment should be restricted to those who will benefit the most, such as those who cannot tolerate other available treatments, those who have a preexisting condition that enhances the risk of COVID-19, and those who are more than 50 years of age and would be less affected by a potential long-term risk of cancer or

reproductive risks. A registry of a cohort of people who received molnupiravir should be kept to longitudinally monitor the frequency of cancer and other potential outcomes so that the opportunity to understand the risk (or lack thereof) associated with the use of a mutagenic ribonucleoside as an antiviral is not missed. Strategies to limit metabolism of mutagenic analogs from the ribonucleotide pool into the 2'-deoxyribonucleotide pool should be explored to limit the potential DNA mutation load in the host. In addition, the viral population diversity should be evaluated after treatment with molnupiravir in those who fail to clear the virus to see whether the treatment accelerates viral evolution. Lethal mutagenesis has the potential to be an important antiviral strategy for RNA viruses, especially in emerging infections when there is an absence of virus-specific antivirals. The potential of this strategy should be exploited, but the possible risks should be acknowledged and addressed. ■

REFERENCES AND NOTES

1. S. S. Morse, E. Domingo, J. J. Holland, *The Evolutionary Biology of Viruses* (Raven Press, 1994).
2. E. C. Holmes, *J. Virol.* **85**, 5247 (2011).
3. M. B. Schulte et al., *eLife* **4**, e03753 (2015).
4. S. Crotty, C. E. Cameron, R. Andino, *Proc. Natl. Acad. Sci. U.S.A.* **98**, 6895 (2001).
5. J. D. Graci, C. E. Cameron, *Rev. Med. Virol.* **16**, 37 (2006).
6. S. J. F. Kaptein et al., *Proc. Natl. Acad. Sci. U.S.A.* **117**, 26955 (2020).
7. J.-S. Driouich et al., *Nat. Commun.* **12**, 1735 (2021).
8. W. A. Fischer II et al., *Sci. Transl. Med.* **14**, eab17430 (2021).
9. T. P. Sheahan et al., *Sci. Transl. Med.* **12**, eabb5883 (2020).
10. L. J. Stuyver et al., *Antimicrob. Agents Chemother.* **47**, 244 (2003).
11. D. M. Brown, M. J. Hewlins, P. Schell, *J. Chem. Soc. C* **1968**, 1925 (1968).
12. C. J. Gordon, E. P. Tchesnokov, R. F. Schinazi, M. Götte, *J. Biol. Chem.* **297**, 100770 (2021).
13. S. Zhou et al., *J. Infect. Dis.* **224**, 415 (2021).
14. A. Jayk Bernal et al., *N. Engl. J. Med.* **10.1056/NEJMoa2116044** (2021).
15. FDA, Fact sheet for healthcare providers: Emergency use authorization for molnupiravir (2021); www.fda.gov/media/155054/download.

ACKNOWLEDGMENTS

R.F.S. is a Merck & Co. shareholder.

10.1126/science.abn0048

Robert H. Grubbs (1942–2021)

Brilliant organic chemist and inspiring mentor

By **Melanie Sanford**

Robert Howard (Bob) Grubbs died on 19 December 2021. He was 79. Best known for developing catalysts that revolutionized the way organic and polymer chemists put molecules together, Bob was awarded the 2005 Nobel Prize in Chemistry for this work, along with Yves Chauvin and Richard Schrock. Grubbs was a rare example of a brilliant scientist who was also a true mensch. His most enduring legacy will be the generous friendship, support, and encouragement that he gave to colleagues, trainees, and others over the course of his distinguished career.

Born on 27 February 1942 in rural Kentucky, Grubbs was fascinated throughout his youth by tinkering, building, and trying to understand how things work. Grubbs initially planned to pursue agricultural chemistry, but after an early research experience, he changed his focus to organic chemistry. After completing his BS (1963) and MS (1965) degrees at the University of Florida, he earned a PhD in 1968 at Columbia University studying with chemist Ronald Breslow and completed a National Institutes of Health postdoctoral fellowship at Stanford University working with chemist James Collman. This training instilled a tremendous foundation in organic and inorganic reaction mechanisms and spurred his lifelong interest in organometallic chemistry. Grubbs started his independent career at Michigan State University in 1969. After 9 years, he moved to the California Institute of Technology (Caltech), where he maintained an active research group until his death.

Grubbs spent nearly his entire career studying a chemical reaction known as olefin metathesis. This reaction involves the breaking and forming of carbon-carbon double bonds ($C=C$), which are some of the strongest bonds present in organic molecules. Olefin metathesis was discovered in the 1950s, but the original catalysts were poorly defined, and their mechanisms were not well understood. In his early work, Grubbs focused on addressing these challenges by pursuing discrete catalysts for this transformation and interrogating the mechanism of the key $C=C$ bond cleavage and formation step.

His work in the early 1980s studying a titanium catalyst known as the Tebbe reagent was critical in shaping his research trajectory. It led him to recognize the power of well-defined catalysts for achieving controlled and predictable reactivity. However, the instability of this titanium catalyst toward common functional groups (Lewis bases, air, and water) inspired his pursuit of more practical and functional group tolerant catalysts. This laid the groundwork for his invention of the series of ruthenium catalysts that bear his name. These ruthenium carbene complexes are remarkable because they can be handled on the benchtop and are highly selective for $C=C$ bonds over more Lewis basic groups.

Grubbs was the central force both in developing the fundamental science behind ruthenium olefin metathesis catalysts and



in pioneering their translation to commercial applications. In 1998, he founded the company Materia, which scaled up the synthesis of these catalysts and made them widely available to the academic and industrial chemistry communities. Since then, the Grubbs catalysts have been used for the construction of hepatitis C drugs and in the development of biorefineries that convert plant oils into higher-value chemicals. They are also widely used for commercial production of polydicyclopentadiene, a moldable high-performance material with exceptional impact and corrosion resistance.

Grubbs delighted not only in field-changing scientific discoveries but also in the more mundane aspects of academic research. Whereas most faculty covet new

laboratory equipment, during my time in his research group from 1997 to 2001, Grubbs was proudest of his decades-old gloveboxes and gel permeation chromatographs. He regularly came through the lab to marvel at the spectacular red, orange, purple, and green colors of newly synthesized ruthenium complexes. He was passionate about demonstrations for his introductory organic chemistry course and loved to practice exploding hydrogen balloons (trying to get the biggest bang) and making polymers (trying to get the most dramatic polymerization).

A man of wide-ranging interests outside of the lab, Grubbs took frequent rock climbing excursions to Joshua Tree National Park and eagerly anticipated annual group camping trips in northern California. He was a passionate basketball player and fan. He could frequently be found on the sidelines of games at Caltech, at Yale (where his daughter, Katy, starred), and at the Staples Center, where he was famously photographed sitting court-side a few seats away from the late Kobe Bryant. His love of sports endeared him to his colleagues and also their children; indeed, my 14-year-old son has wonderful memories of a pickup basketball game that they played.

Beyond his scientific accomplishments, Grubbs's legacy is the people that he trained, mentored, and encouraged. He advised more than 300 graduate students and postdoctoral fellows, who have gone on to careers in academia, industry, law, and beyond. Grubbs was a fabulous mentor, offering trainees a balance of scientific vision and intellectual freedom that allowed us to discover and explore scientific directions that matched our passions. He encouraged his students to work hard and play hard, and he was a bemused spectator (and sometimes participant) in raucous St. Patrick's Day parties, Kit Kat tasting contests, and foosball competitions.

Grubbs was exceedingly generous in accepting seminar invitations, squeezing his six-foot-six frame into economy airplane seats to travel around the world. As such, thousands of scientists had the opportunity to interact with him throughout his career. Those visits were truly memorable for participants. Grubbs filled his talks with folksy words of wisdom, delivered in his characteristic mumble. After his talks, he was just as eager to interact with junior scientists as he was with established professors. Hundreds of these interactions have been shared over the past month in an outpouring of photos and memories on social media. Overall, Bob Grubbs will be remembered as a brilliant chemist who had an outsized impact on the people around him through his love of science, love of life, and generosity of spirit. ■

Department of Chemistry, University of Michigan, Ann Arbor, MI, USA. Email: mssanfor@umich.edu

10.1126/science.abo0193

POLICY FORUM

DATA

How NFTs could transform health information exchange

Can patients regain control over their health information?

By Kristin Kostick-Quenet¹, Kenneth D. Mandl^{2,3}, Timo Minssen⁴, I. Glenn Cohen⁵, Urs Gasser⁶, Isaac Kohane^{2,3}, Amy L. McGuire¹

Personal (sometimes called “protected”) health information (PHI) is highly valued (1) and will become centrally important as big data and machine learning move to the forefront of health care and translational research. The current health information exchange (HIE) market is dominated by commercial and (to a lesser extent) not-for-profit entities and typically excludes patients. This can serve to undermine trust and create incentives for sharing data (2). Patients have limited agency in deciding which of their data is shared, with whom, and under what conditions. Within this context, new forms of digital ownership can inspire a digital marketplace for patient-controlled health data. We argue that nonfungible tokens (NFTs) or NFT-like frameworks can help incentivize a more democratized, transparent, and efficient system for HIE in which patients participate in decisions about how and with whom their PHI is shared.

NFTs grew out of the concept of “tokens” in gaming, whereby a “fungible” token can be used to purchase a thing of value (e.g., a gold coin to spend on a superpower) but a NFT can only be traded, given its intrinsic value that is not directly comparable to that of another token (e.g., a specific sword versus a specific tapestry). NFTs have evolved into digital contracts composed of metadata to specify access rights and terms of exchange. Their nature as metadata means that NFTs point to digital content but are not the content itself. The use of NFTs as a tool for digital artists to prevent the unsanctioned circulation of artwork online has since bled into sports, entertainment, and even health care, commodifying digital information and creating a multi-billion-dollar market.

NFTs are made up of a unique 40-digit identification code (“hash”) and a uniform resource locator (URL) linking to the content online, forming a “smart contract” that can range from just a few lines of computer code to a more elaborate set of instructional code. These contracts designate a patient-controlled copy of the digital data and the terms under which they can be accessed and used, using pseudonyms that permit deidentification while ensuring transparency and accountability.

NFTs are created by “minting” digital content on a blockchain. Minting involves uploading and having other computers verify and time-stamp the content, location, and originator of digital information, and all subsequent transactions are recorded on a digital ledger that is distributed across a network of computers. Redundancy, along with the computational difficulty and processing energy required, makes it difficult to tamper with the transaction record. Blockchains, sometimes referred to as “trustless” systems, provide a verifiable infrastructure to manage digital assets.

There are many situations in which the distinctive features of NFTs could provide potential advantages over, and help address gaps in, the existing HIE system. For example, in 2020, the US Office of the National Coordinator of Health Information Technology (ONC) issued a rule as part of the 21st Century Cures Act that provided a technical basis for an individual to assert the right of access to a computable version of their medical record. By the end of 2022, all certified PHI technology will need to support Substitutable Medical Applications and Reusable Technologies (SMART) on the Fast Healthcare Interoperability Resources (FHIR) application programming interface (API), which allows third-party apps to connect with and request data from health care provider electronic health

records (EHRs) (3). To ease the cumbersome manual process of extracting data from EHRs, the SMART on FHIR API supports an ecosystem of patient-facing apps that could serve to enhance patient agency in directing sharing of their data. Although this represents a leap forward in engaging patients in HIE, the largely commercial nature of the marketplace may still serve to undermine trust and create disincentives for sharing PHI.

POTENTIAL BENEFITS

Automating data access and control

At least two scenarios could be realized under an NFT or NFT-like framework for personal control of health data. In the first, PHI would be uploaded (or “minted”) as a distinct, “original” version, with the generator or custodian (e.g., EHR company, hospital, biobank, etc.) required to register each new datum (e.g., diagnosis of illness, prescription) on a public blockchain. The encrypted PHI would only be accessible to those given explicit permission in a smart contract. Mann *et al.* (4) proposed such a scheme using blockchain and smart contracts to “prosent” (proactively consent) pseudonymously to data release or exchange for certain uses. In this way, patients could specify in advance with whom they agree to share data without needing to consent to every transaction, enabling greater patient control and more timely and efficient data exchanges. In cases where patients might present to the sale of their PHI or to participation in clinical trials offering compensation, the smart contract could allow for automated distribution of funds to the patient. If the patient ever wanted to modify the terms of the contract, each change of terms would be immutably stored as distinct, time-stamped events in the blockchain ledger.

In a second, but not mutually exclusive, scenario, a patient’s data could stay right where it is (for example, a hospital database or on a patient’s phone), and the smart contract could “push” an algorithm to summarize or analyze the data with automated permission from a smart contract. This approach is highly compatible with federated learning approaches that train machine-learning algorithms on multiple local datasets without explicitly exchanging data samples or compiling them into a centralized server. Smart contracts could help to realize data privacy and security goals of federated learning, recently credited as being the “future of digital health” (5).

¹Baylor College of Medicine, Houston, TX, USA. ²Computational Health Informatics Program, Boston Children’s Hospital, Boston, MA, USA. ³Department of Biomedical Informatics, Harvard Medical School, Boston, MA, USA. ⁴Centre for Advanced Studies in Biomedical Innovation Law (CeBIL), University of Copenhagen, Denmark. ⁵Harvard Law School, Boston, MA, USA. ⁶School of Social Sciences and Technology, Technical University of Munich, Munich, Germany. Email: kristin.kostick@bcm.edu

Transparency and efficiency

By automating data-sharing agreements, smart contracts can address long-standing inefficiencies and the lack of transparency in HIE (6) and may give rise to a marketplace of third-party user platforms that allow patients to consult an intuitive public ledger of transactions involving their PHI. With the right safeguards in place, patient-oriented industries might emerge for tracking and aggregating a patient's authenticated data and for providing proxy management of smart contracts on their behalf. Other types of new marketplaces might emerge as well. Advanced data-sharing agreements and contracts might enable the securitization of multiple NFTs into derivatives, which might lead to innovative markets. Experiences from the financial sector and the particular sensitivity of health applications point out the need for robust and proactive regulatory safeguards of such innovation.

Conversely, data requesters could benefit from easy verification of the authenticity and provenance of health data, as well as automated and streamlined data procurement. Each user, for instance, a prespecified set of research institutes, would be granted a particular access level according to the smart contract terms, and requests for data access could be made transparent. A PHI-specific blockchain (or set of interoperable blockchains) could ensure accountability by making available a patient-accessible index of requester identities while maintaining the pseudonymity of patients' IDs. This incorporation of "privacy by design" automation and pseudonyms lends NFT-type technologies their capacity to deidentify patient data and allows patients to participate in data-sharing decisions while making it easier for companies and institutions to access information about a subject without strongly increasing risk of reidentification. At least some of the information could be contained in metadata to flag certain PHI with substantial market value (e.g., genomic information from patients with rare diseases, patients on a newly approved medication, participants in particular clinical trials).

CHALLENGES

Data security and privacy

Blockchain technology upon which NFTs are built does not necessarily prevent data breaches because digital information itself

is not stored "on-chain." This leaves only the metadata (the NFTs) on-chain, protecting information integrity regarding data provenance, terms of data exchange, and transaction history. The underlying data pointed to by NFTs—the PHI—are only as secure as the practices and procedures of the myriad online platforms that provide health-data storage and access. Without proper digital security and data encryption infrastructure or technological advancements to counter the gradual accumulation of noncritical failures in data storage (i.e., "bit rot"), a NFT could eventually amount to nothing more than a defunct URL.

High-stakes NFTs are thus increasingly stored in decentralized and highly redundant networks like the InterPlanetary File System (IPFS). These systems reduce server resources and costs and provide multiple

curacies in personal data (7), which the immutable nature of blockchain technology and decentralized storage might render functionally difficult to exercise.

Another challenge is that the privacy-by-design feature of pseudonymity, which is so central to NFTs and blockchain, may be limited when pseudonyms are attached to health data. Many health data are becoming so granular as to constitute digital "fingerprints" for which only a few data elements could allow for patient reidentification (8). For NFTs to truly maintain pseudonymity, they must be supported with advancements in data encryption, for example, helping "hash" data before they reach human eyes (if they ever do).

In addition to technological advancements, NFT data security and protection concerns need to be addressed on a global stage and through regulatory means. The European Union (EU) General Data Protection Regulation (GDPR), for instance, imposes strict obligations for processing personal data and requires procedural safeguards to avoid and respond to data breaches and misuses (9). Although progress is being made in the United States (e.g., the California Consumer Privacy Act) and federal-level reforms are being debated (10), the US "patchwork" regulatory approach varies widely by state and circumstance and continues to lag behind the GDPR (11).

The EU-US Privacy Shield arrangement for cross-border flow of PHI was invalidated (12) in large part because of the fact that US regulation offers limited opportunities for legal redress for noncitizens. NFTs could help repair these agreements by helping to fill gaps in the capacity of individuals to seek legal redress in at least two ways. The first and most straightforward way is by concretizing a set of terms by which an individual (dis)agrees to contractually share PHI with certain other entities. Like other legally binding private contracts between individuals and entities, if those terms are clearly stated and thoroughly cover a wide range of possible data-sharing scenarios (including definitions of breach), and if the terms of NFT smart contracts are mutually recognized by governing bodies relevant to the jurisdictions in which PHI is being exchanged, then smart contracts should constitute a legally binding mechanism for seeking redress in cases where PHI exchanges break the terms of the contract.



sources of backup. Already, the NFT market has led to the emergence of third-party "pinning" platforms that afford digital content greater longevity, along with other data safekeeping solutions that are likely to affect digital security more broadly and to relieve high processing costs. Additionally, new blockchain protocols (notably Solana and Fantom at the time of writing) are rapidly evolving to accommodate scalable on-chain storage with high throughput while also keeping energy costs down. Likewise, Arweave has introduced "blockweaves" (as opposed to "chains") to incentivize nodes to ensure data replicability and permanent storage. These advancements improve data security, permanence, and scalability and potentially enable "a multichain future" where chains can specialize and interoperate to support high-performance smart contract platforms. However, they also carry other legal and ethical concerns related to the right to erase or to rectify inac-

A second and more indirect way to address the lack of legal redress is for NFT-type smart contract terms to stipulate in advance the approved entities with which an individual agrees to share (or prohibit access to) their PHI. By allowing patients to present in such a way, smart contracts provide a preemptive and automated mechanism for data exchange that is aligned with individuals' preferences. Unless PHI is accessed in a data breach (highly unlikely by virtue of no longer being stored in a centralized database and even less likely if stored "on-chain"), those data will be unavailable (i.e., "digitally locked") for access, purchase, or theft without the NFT owner's consent. A preemptive and automatically executed smart contract might, with the right legal design, minimize the need for individuals to seek legal redress.

Intellectual property rights

A major advantage of NFTs when discussed in the art world is their verification of authenticity and originality. Originality may be less of a concern for HIE. Many entities seeking to use PHI may not care about the originality of the data; they just care whether those data are accurate representations of a patient's PHI. Storing a patient's health data as an NFT could help to verify its provenance and accuracy. However, it also raises important questions about who legally controls PHI and has the right to share or sell it. The answer is not straightforward. Intellectual property rights (IPRs) over creative works usually lie with an artist or, in certain cases, with companies that curate digital information. By contrast, PHI is often thought of as collected or generated through the use of technology, rather than created, thus lacking the "originality" typically required for copyright protection. Once collected or generated and organized by hospitals, device manufacturers, or pharmaceutical companies, those data may become the property of the data collector, not the patient. Entities that eventually develop clinical follow-on innovations based on data stored as NFTs may also claim some form of IPR. Because rights over health data remain complex and contested (13), NFTs may be most useful for specifying collaboratively agreed-upon conditions for exchange and reciprocity, if not direct ownership.

Equity, sustainability, and trust

Given the complexity of NFTs and the legal structure, it is unclear whether average citizens will be able to take advantage of them in the health space. Most people will need

the aid of trusted intermediaries to mint their data and manage private keys. They will also need user-friendly interfaces to interpret requester and transaction ledgers. In addition, patients will need legal support to create smart contracts that serve their interests. Ironically, this need for intermediaries could be the slippery slope back to the centralization of PHI. If these intermediaries are costly, socioeconomic factors will act as gatekeepers for "digital ledger citizenship," exacerbating existing digital divides and participation gaps.

"By automating data-sharing agreements, smart contracts can address long-standing inefficiencies and the lack of transparency in HIE [health information exchange]..."

Another force winding back to centralization is that a widespread switch to PHI stored as NFTs on a blockchain would require more computer power to verify a growing amount of data and number of transactions, resulting in greater energy costs and necessitating more capital and physical investment. These dynamics may incentivize a return to powerful institutions and constitute critical challenges to the *raison d'être* of decentralized infrastructures. However, certain blockchain support innovations are emerging to address energy and climate burdens, with implications for the democratization of participation through reduced processing costs.

A PATH FORWARD

In addition to these challenges, attempts to democratize data-sharing decisions are likely to encounter resistance by key players who dominate the multi-billion-dollar medical-industrial complex and benefit from a status quo where the exchange of patients' digital health data remains unmonitored and largely unregulated (1). Their resistance against using NFTs to automate patient preferences may further strengthen if it is discovered that these preferences entail widespread reluctance to share personal data without express permission or compensation, as some evidence suggests (14). Any viable consideration of NFTs for health may require the gradual introduction of patient-focused control and dynamic consent clauses into existing data-sharing agreements, which currently

allow for large-scale exchanges of EHR data between health care organizations and third parties without express patient awareness or consent. Smart contracts have advantages over existing approaches to consent in that conditions for consent may be more granular and data exchanges can be tracked and verified by patients and do not require that exchanges occur through third-party custodians. As an immediate step, NFTs could be explored in experimental test cases that involve blockchains and smart contracts. Such flexible

frameworks may offer opportunities for simultaneous "symbiotic" development of technology and regulation to accommodate new digital ownership models like NFTs and test their impacts in real-world settings. Further, they could offer empirical insights into best practices for balancing innovation with individual rights and public interests (9). Accompanying qualitative research into patient preferences and attitudes toward NFT-like frameworks as

a means to exercise control over patients' PHI will be critical to understanding utility and acceptance, as well as to ensure the accessibility and interpretability of their PHI. ■

REFERENCES AND NOTES

1. K. D. Mandl, E. D. Perakslis, *N. Engl. J. Med.* **384**, 2171 (2021).
2. A. L. McGuire *et al.*, *J. Law Med. Ethics* **47**, 12 (2019).
3. K. D. Mandl, I. S. Kohane, *N. Engl. J. Med.* **382**, 1781 (2020).
4. S. Porsdam Mann, J. Savulescu, P. Ravaud, M. Benichoufi, *J. Med. Ethics* **47**, 244 (2021).
5. N. Rieke *et al.*, *NPJ Digit. Med.* **3**, 119 (2020).
6. K. D. Mandl, I. S. Kohane, *N. Engl. J. Med.* **374**, 205 (2016).
7. European Union, General Data Protection Regulation, Articles 16 to 19: Regulation (EU) 2016/679 of the European Parliament and of the Council of 27 April 2016 (2016).
8. L. Rocher, J. M. Hendrickx, Y.-A. de Montjoye, *Nat. Commun.* **10**, 3069 (2019).
9. W. N. Price 2nd, M. E. Kaminski, T. Minssen, K. Spector-Bagdady, *Science* **363**, 448 (2019).
10. M. Fazlioglu, in *Data Protection Around the World* (Springer, 2021), pp. 231–248.
11. Council on Foreign Relations, "Reforming the U.S. approach to data protection and privacy" (2018).
12. M. Corrales Compagnucci, T. Minssen, C. Seitz, M. Abouy, *EPLR* **4**, 153 (2020).
13. T. Minssen, J. Pierce, in *Big Data, Health Law, and Bioethics* (Cambridge Univ. Press, 2018), pp. 311–323.
14. F. Briscoe, I. Ajunwa, A. Gaddis, J. McCormick, *PLOS ONE* **15**, e0229044 (2020).

ACKNOWLEDGMENTS

T.M. and I.G.C. were supported by the Novo Nordisk Foundation (NNF17SA0027784). A.L.M. has received funding from Info Commons, Sulston, and BRAINshare through grants R01HG008918, R01CA237118, and R01MH126937, respectively, and is on the board of the Greenwall Foundation and on the science advisory board for DanaHER, the Morgridge Institute of Research, and Geisinger Research.

10.1126/science.abm2004



BOOKS *et al.*

PHILOSOPHY

From dualism to deism

A philosopher comes full circle

By John Zerilli

Among the various possibilities explored in David Chalmers's intriguing and entertaining romp through philosophy, *Reality+*, is a kind of deism—the view that the universe is the work of an intelligent being who sets its laws of operation in motion but then declines to intervene further. Deism was the theology de rigueur of elite opinion in the late 18th-century United States. But in Chalmers's hands, deism is not quite the view that a supernatural being created the universe. It is the view that there is “a serious possibility” that our universe is a computer simulation run by an advanced civilization.

There are a few strands to the argument, but the nub of it is that if an intelligent civilization lasts long enough, it will likely develop simulation technology and create many simulated universes inhabited by intelligent beings. Under minimal assumptions, it can be shown that these simulated universes will greatly outnumber nonsimulated ones. Thus, any extant intelligence has a considerably greater chance of being simulated than not.

As always, the soundness of the argument comes down to its premises. It is not clear that any civilization can survive long enough to develop simulation technology in the first place. Furthermore, consciousness may not be the sort of thing that can be simulated at all. Or ethical constraints in an advanced

civilization may forbid the running of simulations containing sentient creatures.

Chalmers considers all these objections and several more. He concludes that we can be highly confident that one of the following three scenarios holds true: (i) we are simulated entities, (ii) humanlike simulated entities are impossible, or (iii) humanlike simulated entities are possible, but few humanlike simulators will create them. He calculates the probability of the first scenario to be at least 25%. From this it follows that we cannot be sure we are not in a simulation. Furthermore, “If the simulation argument is even approximately as good as the design argument, it deserves to be in the pantheon of arguments for God's existence.”

Chalmers attained rock-star status in philosophy during the late 1990s as a defender of dualism, a metaphysical hypothesis that, at the time, was considered more or less defunct among naturalistically inclined philosophers. Dualists maintain that consciousness cannot be accounted for in purely physical, materialist terms (what Chalmers famously dubbed the “hard problem”). While dualism is certainly not a mainstream view, it is once again being taken seriously by a substantial minority of both scientists and philosophers, in no small part owing to Chalmers's distinctive arguments and thought experiments.

In this latest offering, Chalmers seems to have come full circle, articulating what he describes as an entirely naturalistic account of God—i.e., a god not exempt from natural

As virtual reality devices become more sophisticated, what we consider possible expands.

laws. That is why the book could mark a turning point in educated opinion. It may be that Chalmers will do for deism what he was able to do for consciousness: make the idea respectable again.

There are two reasons why the times may favor neo-deism. First, Chalmers is not alone or even the first high-profile secular or atheist voice to have mooted “simulation theology.” There are already enough heavyweights from the worlds of science, big business, and philosophy to make simulation theology respectable among an important section of the intelligentsia. Neil deGrasse Tyson, Elon Musk, and Nick Bostrom all spring to mind.

Second, computer science has expanded the horizons of what is considered possible. Consider that the Enlightenment forerunner of the simulation hypothesis was a thought experiment proposed by René Descartes. But Descartes's argument trafficked in evil spirits. Compelling though his meditations may once have been, their force was bound to wane in a secular age. Enter virtual reality, its inevitable improvement over the next few decades, and the possibility of a *Matrix*-style immersive experience, and suddenly Descartes's “evil demon” acquires a most contemporary garb.

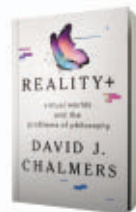
There is a lot more in this book than can be conveyed in the space of a short review. Chalmers has something to say on most of the “big questions” in philosophy:

on the immortality of the soul (simulations “may at least make an afterlife possible”); the freedom of the will (“the jury is still out”); the existence of an external world (even a simulated world would be real; it's just that at the most fundamental level it would be made up of bits in the simulator's computer, not quarks and electrons); and, of course, the existence of God. He also considers questions of value and politics in virtual worlds,

although these are not the most original parts of the book. While on all of these issues Chalmers cuts a Gordian knot in writing both accessibly and illuminatingly, it is the material in part 3 on the reality of virtual worlds, part 5 on the possibility of consciousness and mind-body interaction in digital worlds, and part 7 on language and structuralism in physics where Chalmers breaks new ground.

Chalmers's *Reality+* is sure to roil a good deal of philosophical banter—and not just in graduate seminar rooms. More seriously, it offers a lot for theists, atheists, and agnostics to ponder as they reassess their already “considered” views on a well-worn subject. ■

10.1126/science.abn2690



Reality+:
Virtual Worlds and the Problems of Philosophy
David J. Chalmers
Norton, 2022. 544 pp.

The reviewer is a philosopher at the Institute for Ethics in AI and the Faculty of Law, University of Oxford, Oxford OX1 3UL, UK. Email: john.zerilli@law.ox.ac.uk

SCIENCE LIVES

Imagining Rosalind Franklin

The crystallographer's story comes alive in a work of historical fiction

By **Katie Langin**

In *Her Hidden Genius*, author Marie Benedict transports readers to another time: Europe is rebuilding after World War II, the shock of the Holocaust reverberates, food rationing abounds. But the story's central struggles will feel all too familiar to anyone who has set foot in a modern scientific laboratory, as much of the action takes place in research environments beset with bullying, competition, and sexism.

The novel centers on a brilliant scientist who died far too young: Rosalind Franklin. Benedict has made a career out of writing novels about historically important women, profiling such figures as physicist Mileva Marić, novelist Agatha Christie, and librarian Belle da Costa Greene. She bases her fictionalized narratives on what is known about each woman, painting a picture of their lives with invented scenes and dialogue.

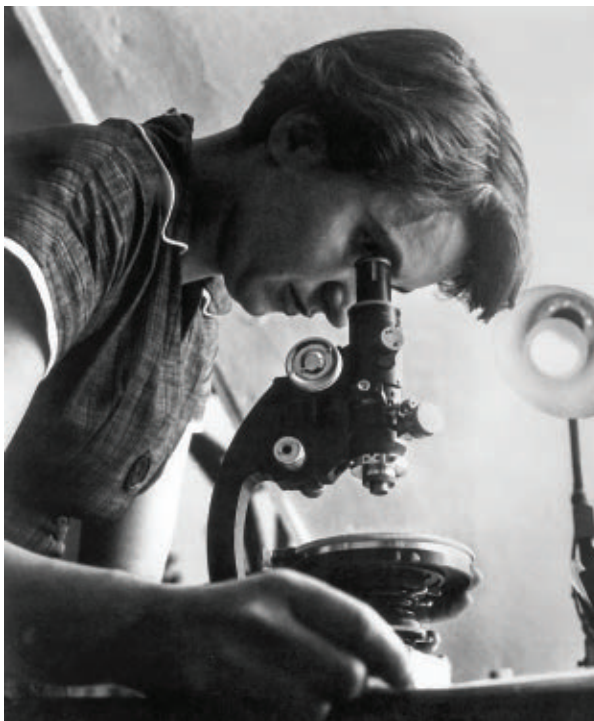
We meet Franklin on the streets of Paris as she walks to her first day of work at the Laboratoire Central des Services Chimiques. The 26-year-old, who received her PhD from the University of Cambridge 2 years earlier, is greeted warmly by lab members—a welcome change from her experience in England. In the months that follow, she learns x-ray crystallography, a technique that can be used to visualize the molecular structure of many substances, and becomes a star of the lab, known for her experimental prowess and technical skill, which she uses to study graphite.

Four years later, she leaves the Paris lab and accepts a position at King's College London. “I worry that I’ve made the wrong choice,” Benedict’s Franklin remarks. She loves Paris and the lab in which she works, but she is drawn back to England, in part to be closer to her family—an upper-class Jewish clan with deep roots in London. It is a career decision that proves pivotal.

On the first day in her new lab, Franklin learns that she is to use her x-ray crystallography skills to decipher the structure of

DNA. A physical scientist by training, she balks at first, responding, “Pardon?...Not crystalline substances?” But she quickly dives headfirst into the task, working long hours to generate images of DNA with unprecedented clarity. The helical structure of DNA begins to become apparent, but Franklin and her assistant, Raymond Gosling, keep the details of their discoveries largely secret while they work to amass an unimpeachable body of evidence.

Meanwhile, a pair of young scientists at the University of Cambridge—Francis



Franklin examines a sample with a microscope in 1955.

Crick and James Watson—enter the race to describe the structure of DNA and begin working on a theoretical model. Franklin rejects their first attempt, which featured phosphate groups on the inside of the DNA strand and bases on the outside, declaring it scientifically impossible. But they eventually get it right, aided by Franklin’s images and data, which were slipped to them without her knowledge or permission. (Maurice Wilkins, a King’s College colleague who had befriended Crick and Watson, is a prime suspect.)

Her Hidden Genius: A Novel

Marie Benedict
Sourcebooks
Landmark, 2022.
304 pp.



The book ends with Franklin, aged 37, on her deathbed. She was diagnosed with ovarian cancer a year and a half earlier while doing pioneering work on RNA viruses at Birkbeck College. She continued that work while undergoing treatment, at one point believing she had been cured. “Science has taken care of me. As it always has,” she declares. But the cancer comes back, and she dies in London on 16 April 1958.

Much of this tale will be familiar to scientific readers, but in Benedict’s telling, Franklin’s struggles come alive. She engages in fierce disputes with Wilkins, who eventually wins the Nobel Prize, along with Watson and Crick, for his work visualizing DNA. She misses important networking opportunities, in part because King’s College has a men-only dining area. She is repeatedly referred to as “Miss Franklin” instead of “Dr. Franklin”—an annoyance that will likely resonate with many women scientists today. And she bristles at the nickname “Rosy,” which Watson, Crick, and Wilkins use behind her back. (Watson was criticized for using this nickname in his 1968 book *The Double Helix*.)

Throughout the book, I found myself wondering whether certain conversations and events were based in fact or whether they were products of Benedict’s imagination, which led me to scour nonfiction sources for further information about Franklin. Readers who find themselves in a similar situation might choose to read as a companion Brenda Maddox’s biography *Rosalind Franklin: The Dark Lady of DNA*, which Benedict consulted during her research for this novel.

Overall, Benedict’s retelling of Franklin’s story offers a compelling look at the scientist’s impressive and all-too-short life. It also raises broader questions about the scientific enterprise: Are conditions much better for women scientists today? Does academia’s first-to-publish reward system pervert the process of science? Who deserves credit for a scientific discovery? There are no easy answers in *Her Hidden Genius*, but there is much food for thought. ■

The reviewer is an associate editor at *Science*, Washington, DC 20005, USA. Email: klangin@aaas.org

10.1126/science.abn2940



EMPOWER
WITH EVIDENCE

AAAS | ANNUAL MEETING

Important Meeting Update!

The 2022 AAAS Annual Meeting will gather online ONLY, February 17-20.
Deluxe Access registration and meeting program are now available!

BE A PART OF THE CONVERSATION



and more...

For more information, please visit:

aaas.org/meetings | [#AAASmtg](https://twitter.com/AAASmtg)



A man guides a car through the Great Smog of 1952 in London. The acidity of the particles in air pollution affects how harmful they are to humans.

Edited by Jennifer Sills

Particle toxicity's role in air pollution

In their Report "Abating ammonia is more cost-effective than nitrogen oxides for mitigating PM_{2.5} air pollution" (5 November 2021, p. 758), B. Gu and colleagues propose that reducing ammonia (NH₃) emissions could decrease air pollution caused by particles of less than 2.5 μm in diameter (PM_{2.5}), a change that they predict would benefit human health. However, not all particles affect health equally (1–4). Because ammoniated PM_{2.5} is less acidic than sulfuric particulate matter formed by, for example, burning coal (5), decreasing particles formed with NH₃ may make the remaining air pollution more lethal. Air pollution mitigation strategies should consider the risk to health posed by various components, not just the total particulate mass.

The role of acidity in enhancing particle toxicity has been recognized since the Great Smog of London in 1952. During the 5 days of extreme air pollution in the city, animals with higher NH₃ exposures were less adversely affected, and physicians placed vials of NH₃ in hospital wards to protect patients (6, 7). Subsequent research has confirmed that NH₃ in the air reduces the acidity of ambient particles (8) and that acidity mobilizes toxic transition metals, inducing oxidative

stress (9–11). Moreover, a recent epidemiological study has determined that the oxidative potential of outdoor PM_{2.5} is associated with acute cardiovascular events, and combined exposure to transition metals and acidic sulfate enhances those cardiovascular effects (12).

Because PM_{2.5} components' toxicities vary, estimates of the health impacts of each component should take into account its individual properties. Gu *et al.*'s suggested reduction in NH₃ emissions might well reduce PM_{2.5} mass but would also increase the acidity of the aerosol mixture. Rather than achieve the predicted health benefits, the change could regionally increase adverse health effects where acid-neutralizing NH₃ emissions are diminished. The health benefits that Gu *et al.* expect must be confirmed experimentally before the implementation of such a policy.

George D. Thurston^{1*}, Lung Chi Chen¹, Matthew Campen²

¹Department of Environmental Medicine, New York University Grossman School of Medicine, New York, NY 10010, USA. ²Department of Pharmaceutical Sciences, University of New Mexico College of Pharmacy, Albuquerque, NM 87131, USA.

*Corresponding author.

Email: george.thurston@nyu.edu

REFERENCES AND NOTES

1. H. Ozkaynak, G. D. Thurston, *Risk Anal.* **7**, 449 (1987).
2. B. Ostro, W. Y. Feng, R. Broadwin, S. Green, M. Lipsett, *Environ. Health Perspect.* **115**, 13 (2007).
3. S. Achilleos *et al.*, *Environ. Int.* **109**, 89 (2017).
4. M. Wang *et al.*, *Environ. Int.* **66**, 97 (2014).
5. J. J. Huntzicker, R. A. Cary, C. S. Ling, *Environ. Sci. Technol.* **14**, 819 (1980).

6. Ministry of Health of Great Britain, "Report on public health and medical subjects: Mortality and morbidity during the London Fog of December 1952" (Her Majesty's Stationary Office, London, 1954).
7. D. Bates, "The legacy of 'pea soupers': Impacts on health and research of London smogs and other pollution episodes," presented at the ISEA/ISEE Annual Conference (Vancouver, Canada, 2002).
8. H. H. Suh, P. Koutrakis, J. D. Spengler, *J. Expo. Anal. Environ. Epidemiol.* **4**, 1 (1994).
9. Committee on the Medical Effects of Air Pollutants, "Long-term exposure to air pollution: Effect on mortality" (Department of Health, London, 2009).
10. T. Fang *et al.*, *Environ. Sci. Technol.* **51**, 2611 (2017).
11. P. Maciejczyk, L. C. Chen, G. D. Thurston, *Atmosphere* **12**, 1086 (2021).
12. S. Weichenthal *et al.*, *Environ. Health Perspect.* **129**, 107005 (2021).

10.1126/science.abn4481

Response

Thurston *et al.* argue that ammonia (NH₃) abatement may not reduce the adverse health effects of particles with a diameter of less than 2.5 μm (PM_{2.5}) due to the dependence of toxicity on the acidity of PM_{2.5}. Although they have usefully highlighted the effect of acidity of PM_{2.5} on human health, there is no definitive evidence that quantification of the effects of PM_{2.5} components separately should be recommended in policy-making (1) or that emission controls of ammonia like those we suggest would substantially change the aerosol acidity. We are not arguing for NH₃ controls in isolation; rather, we contend that NH₃ abatement can play an important role in reducing exposure to PM_{2.5} and associated health impacts in the context of

continued mitigation of other pollutants, such as sulfur dioxide (SO₂) and nitrogen oxides (NO_x).

PM_{2.5} can vary across regions from highly acidic (pH of ~0.5) to mildly acidic (pH of ~6) (2). In the United States and Canada, large reductions in SO₂ and NO_x emissions over the past decade have not resulted in clear changes to acidity (3, 4). Global reduction of agricultural NH₃ emission alone by 50% (similar to the proposed mitigation in our study) would reduce PM_{2.5} pH (i.e., increase acidity) by about 0.6 units (5), and we would expect even weaker changes with joint controls of SO₂ and NO_x. Whether such changes in aerosol acidity are sufficient to affect the mobilization of harmful transition metals is still unknown.

Emissions of air pollutants have changed substantially since the 1952 Great Smog of London (6). At that time, SO₂ emissions from coal burning were indeed a dominant reason for adverse health effects (7), likely due in part to acute acidity. The use of NH₃ alleviated the acute acidity, but its effect could also be ascribed to a reduction in exposure to toxic concentrations of SO₂ (8).

Emission controls of SO₂ and NO_x have a long history, whereas NH₃ has too often been ignored (6, 9). It would thus be unrealistic to imagine effective control of NH₃ and unregulated emissions of SO₂ and NO_x. We argue for the need to start to control NH₃ emission given its large contribution to PM_{2.5} formation and its high cost-efficiency of abatement, thereby catching up to the progress already made in reducing SO₂ and NO_x emissions.

Baojing Gu^{1*}, Lin Zhang², Mike Holland³, Massimo Vieno⁴, Hans J. M. Van Grinsven⁵, Shaohui Zhang^{6,7}, Shilpa Rao⁸, Mark A. Sutton⁴

¹College of Environmental and Resource Sciences, Zhejiang University, Hangzhou 310058, China.

²Laboratory for Climate and Ocean-Atmosphere Sciences, Department of Atmospheric and Oceanic Sciences, School of Physics, Peking University, Beijing 100871, China. ³Ecometrics Research and Consulting, Reading RG8 7PW, UK. ⁴UK Centre for Ecology & Hydrology, Edinburgh Research Station, Bush Estate, Penicuik, Midlothian EH26 0QB, UK.

⁵PBL Netherlands Environmental Assessment Agency, 2500 GH The Hague, Netherlands.

⁶School of Economics and Management, Beihang University, Beijing 100091, China. ⁷International Institute for Applied Systems Analysis, A-2361 Laxenburg, Austria. ⁸Norwegian Institute of Public Health, Skøyen, N-0213 Oslo, Norway.

*Corresponding author.

Email: bjgu@zju.edu.cn

REFERENCES AND NOTES

1. World Health Organization (WHO), "WHO global air quality guidelines: Particulate matter (PM_{2.5} and PM₁₀), ozone, nitrogen dioxide, sulfur dioxide and carbon monoxide" (2021).
2. H. O. T. Pye *et al.*, *Atmos. Chem. Phys.* **20**, 4809 (2020).
3. Y. Tao *et al.*, *Atmos. Chem. Phys.* **18**, 7423 (2018).
4. R. J. Weber, H. Guo, A. G. Russell, A. Nenes, *Nat. Geosci.* **9**, 282 (2016).

5. A. Pozzer, A. P. Tsimpidi, V. A. Karydis, A. de Meij, J. Lelieveld, *Atmos. Chem. Phys.* **17**, 12813 (2017).
6. R. M. Hoesly *et al.*, *Geosci. Model Dev.* **11**, 369 (2018).
7. G. D. Thurston *et al.*, *Environ. Health Persp.* **79**, 73 (1989).
8. A. R. McLeod *et al.*, *Nature* **347**, 277 (1990).
9. X. Zhang *et al.*, *Nat. Commun.* **11**, 4357 (2020).

10.1126/science.abn7647

The protein-folding problem: Not yet solved

We agree with H. H. Thorp ("Proteins, proteins everywhere," Editorial, 17 December 2021, p. 1415) and numerous others (1) that the advance in protein structure prediction achieved by the computer programs AlphaFold (2) and RoseTTAfold (3) is worthy of special notice. The accuracies of the predictions afforded by these new approaches, which use machine-learning methods that exploit the information about the relationship between sequence and structure contained in the databases of experimental protein structures and sequences, are much superior to previous approaches. However, we do not agree with Thorp that the protein-folding problem has been solved.

AlphaFold achieves a mean C-alpha root mean square deviation (RMSD) accuracy of ~1 Å for the Critical Assessment of Structure Prediction 14 (CASP14) dataset (2). This accuracy corresponds to that of structures determined by x-ray crystallography or single-particle cryo-electron microscopy at very low resolution. The accuracy of these methods is several times better than machine learning methods; for example, at 3 Å resolution, the coordinate C-alpha RMSD accuracy for empirically determined structures is far better than 1 Å. At present, for the best cases, the C-alpha coordinate RMSD accuracy of AlphaFold-predicted structures roughly corresponds to the accuracy expected for structures determined at resolutions no better than ~4 Å. Thus, although structural predictions by AlphaFold and RoseTTAfold may be accurate enough to assist with experimental structure determination (3), they alone cannot provide the kind of detailed understanding of molecular and chemical interactions that is required for studies of molecular mechanisms and for structure-based drug design.

A further complication for structure prediction is the dynamic structural variation in a given sequence. Allosteric states, which can differ dramatically, may be in an intrinsic equilibrium or depend on a binding partner, which may be a ligand or cofactor (e.g., ATP or cobalamin), another macromolecule (e.g., DNA or a protein

partner), or aberrant self-association (e.g., pathogenic amyloids). Work is in progress to address protein complexes (4, 5), but structure prediction remains to be achieved for those in complicated molecular machines and for those with ligands that affect conformation, which may be as yet unidentified.

Recent advances should be taken as a call for further development. Moreover, lessons should be learned from history. In 1990, Alwyn Jones and Carl-Ivar Brändén published a commentary on errors in x-ray crystal structures (6) that stimulated the development of cross-validation and validation tools for structural biology (7–9) and that ultimately made the databases of experimental structures much more reliable. Thus, tools should be developed to assess coordinate accuracy of predictions and alleviate bias toward structural patterns observed in repositories.

Finally, it is necessary to reflect on what the word "solved" might mean in the context of the protein-folding problem. Some may feel that this problem will have been solved once any method has been found that enables one to obtain accurate predictions of the structures of proteins from their sequences. AlphaFold and RoseTTAfold represent a major step forward in that direction, but they are not the final answer. Others, including us, feel that solving the protein-folding problem means making accurate predictions of structures from amino acid sequences starting from first principles based on the underlying physics and chemistry. Despite these major advances in protein structure prediction, experimental structure determination remains essential.

Peter B. Moore¹, Wayne A. Hendrickson², Richard Henderson³, Axel T. Brunger^{4*}

¹Department of Chemistry, Yale University,

New Haven, CT 06520, USA. ²Department

of Biochemistry and Molecular Biophysics, Columbia University, New York, NY 10032,

USA. ³MRC Laboratory of Molecular Biology,

Cambridge CB2 0QH, UK. ⁴Department of

Molecular and Cellular Physiology, Howard

Hughes Medical Institute, Stanford University,

Stanford, CA 94305, USA.

*Corresponding author.

Email: brunger@stanford.edu

REFERENCES AND NOTES

1. P. Cramer, *Nat. Struct. Mol. Biol.* **28**, 704 (2021).
2. J. Jumper *et al.*, *Nature* **596**, 583 (2021).
3. M. Baek *et al.*, *Science* **373**, 871 (2021).
4. I. R. Humphreys *et al.*, *Science* **374**, eabm4805 (2021).
5. R. Evans *et al.*, *bioRxiv*, 10.1101/2021.10.04.463034 (2021).
6. C. Branden, T. Jones, *Nature* **343**, 687 (1990).
7. A. T. Brunger, *Nature* **355**, 472 (1992).
8. R. J. Read *et al.*, *Structure* **19**, 1395 (2011).
9. R. Henderson *et al.*, *Structure* **20**, 205 (2012).

10.1126/science.abn9422

ANNOUNCING THE 2021

Swanson & META award winners



The 2021 Lynwood W. Swanson Scientific Research Award was given to **Dr. Christopher Irwin Smith, Professor of Biology, Willamette University.** Dr. Smith's

research into the diversity of Yuccas has received global recognition, in addition to his scholarly work with undergraduates and his public-facing science communications.



The 2021 Lynwood W. Swanson Promise for Scientific Research Award was given to **Dr. Andrea Kunder, Assistant Professor of Physics, St. Martin's University.**

In addition to investing in hands-on research for her undergraduate students, Dr. Kunder has conducted significant research into the structure, composition, and dynamics of old stars in the Milky Way.



The 2021 Murdock Exemplary Teacher-Researcher Award was given to **Mr. Brian Wright, Science Teacher, Olympia High School.** Mr. Wright, a material science master

teacher, provides mentorship for his students to participate in authentic glass research and trains colleagues on how to incorporate rigorous content into the curriculum that is both experiential and engaging.



College Science Research
A MURDOCK TRUST PROGRAM



Partners in Science
A MURDOCK TRUST PROGRAM



M.J. Murdock
CHARITABLE TRUST

For more information on these awards and how scientific collaboration and partnership is helping to inspire the next generation of researchers and teachers, visit murdocktrust.org

Where Science Gets Social.

AAAS.ORG/COMMUNITY



**Member
COMMUNITY**
AAAS

AMERICAN ASSOCIATION FOR THE ADVANCEMENT OF SCIENCE

RESEARCH

IN SCIENCE JOURNALS

Edited by Michael Funk

MATERIALS SCIENCE

Artificial enamel analog

Tooth enamel is the thin outer layer of our teeth and is the hardest biological material in the human body. Zhao *et al.* engineered an enamel analog consisting of assembled hydroxyapatite nanowires with amorphous intergranular phase segments aligned using scalable, dual-directional freezing in the presence of polyvinyl alcohol. The artificial tooth enamel was designed to closely mimic the composition of the natural material by copying the shapes and sizes of the components found biologically and the organization of their interfaces. —MSL *Science*, abj3343, this issue p. 551

Self-assembly of hydroxyapatite nanowires can produce an artificial analog of enamel, the hard biomineral that covers the surface of the teeth.



NEUROSCIENCE

Unmasking place fields in hippocampal CA1

A basic transformation process in the brain is the conversion of a neuron's excitatory and inhibitory inputs to spikes. Experimentally examining the transformation process requires access to subthreshold membrane dynamics. To date, only intracellular recordings have met this requirement. Valero *et al.*, using a new technique based on optogenetic stimulation to probe the excitability of neurons, examined the subthreshold activity dynamics of CA1 pyramidal neurons during sharp-wave ripples, theta oscillations, and place fields. During sharp-wave ripples, overall excitability shifted toward synaptic inhibition. However, during theta waves and in the center of place fields, excitability moved in the direction of synaptic excitation. This stimulation unmasked the place fields of nonplace cells,

indicating that the proportion of place cells in CA1 is much higher than previously thought. —PRS

Science, abm1891, this issue p. 570

NEUROGENOMICS

Genes control cortical surface area

Humans exhibit heritable variation in brain structure and function. To identify how gene variants affect the cerebral cortex, Makowski *et al.* performed genome-wide association studies in almost 40,000 adults and 9000 children. They identified more than 400 loci associated with brain surface area and cortical thickness that could be observed through magnetic resonance imaging analyses. Examining the biological pathways linking gene variants to phenotypes identified region-specific enrichments of neurodevelopmental functions, some of which were associated with psychiatric disorders.

Partitioning genes with heritable variants relative to evolutionary conservation helped to identify a hierarchy of brain development. This analysis identified a human-specific gene-phenotype association related to speech and informs upon what genes can be studied in various model organisms. —LMZ

Science, abe8457, this issue p. 522

ORGANIC CHEMISTRY

A clean break for C–H bonds

Carbon–hydrogen (C–H) bonds are ubiquitous in pharmaceuticals and plastics but are difficult to transform. Fazekas *et al.* report a versatile reagent that strips hydrogen without immediately trapping the carbon. Heating or photolysis of the reagent produces a pair of radicals, one of which rapidly cleaves a C–H bond while the other remains comparatively inert. A wide variety of other radical sources can

then intercede to form carbon–halogen, carbon–carbon, and carbon–sulfur bonds. A two-step upcycling sequence that added imidazolium groups to postconsumer polyethylene foam produced a potentially valuable ionomer. —JSY

Science, abh4308, this issue p. 545

DEVELOPMENTAL BIOLOGY

Deriving primitive endoderm stem cells

The mammalian blastocyst forms early in development and consists of three distinct cell types: epiblasts, trophoblasts, and primitive endoderm (PrE). Although stem cell lines that retain the functional properties of epiblasts or trophoblasts have been established, we lack stem cell lines that retain the developmental potential of PrE, which gives rise to extra-embryonic lineages that nourish the embryo and promote its development. Ohinata *et al.* report derivation of PrE stem cells that are able to

give rise to all extra-embryonic primitive endoderm tissues and support fetal development of PrE-depleted blastocysts in mouse chimeras. —BAP

Science, aay3325, this issue p. 574

ATMOSPHERIC CHEMISTRY Nighttime surprise

Isoprene, which is emitted primarily by terrestrial vegetation, is the most abundant volatile organic compound in Earth's atmosphere and is central to controlling the oxidizing capacity of the troposphere and forming organic aerosols. Palmer *et al.* report that nighttime concentrations of tropospheric isoprene are unexpectedly high in much of the tropics. The authors link these anomalies to low concentrations of atmospheric nitrogen oxides and suggest that their findings will help to explain some observations of elevated levels of cloud condensation in the lower troposphere. —HJS

Science, abg4506, this issue p. 562

NEUROSCIENCE Feedback for breeding familiarity

Social memory enables the recognition of others and the formation and maintenance of relationships and is partially supported by the hormone oxytocin. Wang *et al.* found that an oxytocin-receptor-dependent

positive feedback loop contributes to long-term social memory in rodents. Reciprocal phosphorylation between the receptor and the kinase PKD1 promoted downstream oxytocin receptor signaling in cultured cells. Rodents in which this loop was disrupted in the medial amygdala of the brain showed behaviors and neuronal activity that indicated impaired recognition of familiar cage mates. —LKF

Sci. Signal. **15**, eabd0033 (2022).

BIOMATERIALS Sealing the deal

Tissue sealants and adhesives are potentially useful alternatives to sutures for tissue repair, but application to wet tissue can be complex or take too long to set during surgery. Wu *et al.* developed a flexible, transparent adhesive polymer hydrogel patch that seals gastric tissue defects. The patch could be applied to wet tissue and showed strong adhesion shortly after application and when fully swollen (6 hours after application). Patches sealed defects in rat colon, stomach, and small intestine, promoting tissue healing and maintaining adhesion over 4 weeks. The technology could be scaled to seal defects in pig colon. Results support further investigation of this easy-to-apply patch as an alternative to commercially available tissue adhesives. —CC

Sci. Transl. Med. **14**, eabh2857 (2022).



A molecular feedback loop in neurons mediates social bonding in rodents.

IN OTHER JOURNALS

Edited by Caroline Ash
and Jesse Smith

ECOLOGICAL ECONOMICS

Protecting wetlands pays off

The 47 million hectares of US wetlands provide an estimated \$1.2 to 2.9 trillion in flood damage mitigation, benefits that can reach far downstream. Taylor and Druckenmiller integrate data on flood insurance claims, hydrography, land cover, and property values to show that wetland loss to development increased insurance claims. Wetland increase showed no impact, suggesting that conservation should be prioritized over restoration. Wetlands that were 500 to 750 meters from the nearest stream or river were the most valuable, calling into question the 2020 removal of protections for “isolated” wetlands lacking a connection to surface water. —BW

Am. Econ. Rev. <https://www.aeaweb.org/articles?id=10.1257/aer.20210497> (2021).

PLANT SCIENCE

Global peanut improvement

Wild relatives of crop plants can supply genetic diversity useful for improving agricultural yields. In one such interaction six decades ago, the cultivated peanut was hybridized with a wild relative. The improved cultivar was resistant to certain diseases. Since then, those interested in crop improvement shared the peanuts through international networks. Bertoli *et al.* track where the hybrids have been shared globally. This genetic and pedigree analysis finds traces of the improved peanut cultivar in Africa, Asia, Oceania, and the Americas. Thus, food security and agricultural sustainability have been aided both by the scientific access to diverse gene plasmas and by the social network that shared the results. —PJH

Proc. Natl. Acad. Sci. U.S.A. **18**, e2104899118 (2021).

NEUROSCIENCE

Choosing simultaneously or sequentially

Economic decisions are linked to neuronal activity in the orbitofrontal cortex. Neurons in this brain region represent different decision variables in a categorical way. For example, when animals choose between different types of juice drinks, different groups of neurons encode individual offer values into the binary decision and the chosen value. In most studies, two types of juices were presented simultaneously. However, in real life, choices often appear sequentially. Therefore, Shi *et al.* alternated trials under simultaneous and sequential offers of drinks. The authors found that the same neural circuits supported both types of choice sequence. Ideas about how economic choices are made can now be generalized to a broader domain of decisions than previously recognized. —PRS

J. Neurosci. **42**, 33 (2022).



Wetland loss increases the cost of flooding and affects the resulting insurance claims.

to the recruitment and migration of neutrophils and T cells into the skin. These changes promoted fibroblast survival, migration, and damage repair. —SMH
eLife, **10**, e71052 (2021).

TEXTILES

Keeping the sweat off

Hot weather requires unique strategies for cooling the human body. Recent advances have included improving radiative heat transfer through fabrics. Alternatively, fabrics that wick sweat can lower skin temperature. Peng *et al.* developed an integrated cooling textile (i-Cool) designed to efficiently wick and evaporate sweat. The authors accomplished this by integrating channels into the fabric that quickly move sweat from the skin to the surface. The fabric also has enhanced heat transport compared with cotton. The strategy may lead to other textiles that are more comfortable to wear in hot weather. —BG

Nat. Commun. **12**, 6122 (2021).

MISINFORMATION

Identifying deepfake videos

Deepfake videos that have been digitally manipulated, from face swaps to filters, may look authentic to the untrained eye. As society debates the ethics of such technology, computer scientists are looking for ways to help humans and computer models better discern authentic videos from deepfakes. Groh *et al.* used data from more than 15,000 human participants to show that humans are on average as accurate as the leading detection model at detecting deepfakes, but they make different mistakes. The researchers are hoping that the differences they have identified can help in the design of future models that benefit from understanding the weaknesses and strengths of humans. —YY

Proc. Natl. Acad. Sci. U.S.A. **119**, e2110013119 (2022).

CELL BIOLOGY

Repairing UV-damaged skin

Sunburn and prematurely aged skin can be caused by exposure to high levels of ultraviolet (UV) radiation. Rognoni *et al.* examined UV damage repair processes in human and mouse skin. The

authors found that acute and chronic UV exposure selectively killed fibroblast cells in the papillary dermis layer of the skin. Live imaging and lineage tracing showed that acute damage was repaired by local papillary fibroblast proliferation with little need for fibroblast migration. Chronic UV exposure instead led



Ultraviolet radiation selectively kills fibroblast cells in the dermis of the skin.

DISEASE ECOLOGY

Surviving white-nose syndrome

White-nose syndrome, an emerging infectious disease caused by the fungus *Pseudogymnoascus destructans*, has been devastating bat populations since its introduction into North America in 2006. However, some bat populations have been able to rebound after the epidemic. Grimaudo *et al.* examined the roles of host traits and environmental conditions on white-nose syndrome severity and the persistence of remnant little brown bat (*Myotis lucifugus*) populations. Using a fully factorial translocation experiment, the authors found higher bat survival in established fungus-infected sites than occurred during initial epidemics, indicating that some level of resistance emerged in the bats. However, this effect was highly dependent on local temperature and humidity conditions. —BEL

Ecol. Lett. **10.1111/ele.13942** (2021).

ALSO IN *SCIENCE* JOURNALS

Edited by Michael Funk

CORONAVIRUS

The unknowns of an antiviral strategy

Broad antiviral drugs are needed to target RNA viruses, including severe acute respiratory syndrome coronavirus-2 (SARS-CoV-2), Zika virus, and Chikungunya virus, which have caused numerous epidemics. Lethal mutagenesis is an antiviral strategy whereby drugs form mutagenic ribonucleosides in host cells that are used in viral RNA genome replication, resulting in enough mutations to inactivate a replicating virus and thereby limit infection. The antiviral drug molnupiravir is designed to work in this manner and has recently been approved for the treatment of COVID-19. In a Perspective, Swanstrom and Schinazi discuss the potential risks of this antiviral approach, including the possibility of producing variants and the potential for host DNA mutagenesis. The potential for long-term effects suggests that safety assessments of mutagenic drugs should be examined more closely. —GKA

Science, abn0048, this issue p. 497

CHEMICAL POLLUTION

Living with forever chemicals

Per- and polyfluoroalkyl substances (PFAS) are products of the modern chemical industry that have been enthusiastically incorporated into both essential and convenience products. Such molecules, containing fully fluorine-substituted methyl or methylene groups, will persist on geologic time scales and can bioaccumulate to toxic levels. Evich *et al.* review the sources, transport, degradation, and toxicological implications of environmental PFAS. Despite their grouping together, these compounds are heterogeneous in chemical structure, properties, transformation pathways, and

biological effects. Remediation is possible but expensive and is complicated by dispersion in soil, water, and air. It is important that we thoroughly investigate the properties of potential replacements, many of which are merely different kinds of PFAS, and work to mitigate the harms of the most toxic forms already released. —MAF

Science, abg9065, this issue p. 512

IMMUNOLOGY

Probing human T cell function using CRISPR

CRISPR activation (CRISPRa) and CRISPR interference (CRISPRi) screens are powerful tools to test the gain and loss of gene function, but their use has largely been limited to immortalized cell lines. Schmidt *et al.* report an optimized method that allowed them to perform genome-wide CRISPRa and CRISPRi screens on primary human T cells. This approach was then used to scrutinize genes regulating the production of key therapeutically relevant cytokines. The combination of pooled CRISPRa perturbations with single-cell RNA sequencing (CRISPRa Perturb-seq) then allowed them to interrogate how the regulators of cytokine production can control T cell activation and programming into distinct postactivation states. —STS

Science, abj4008, this issue p. 513

PLANT SCIENCE

A volatile defense against leafhoppers

In established ecosystems, plants often fend off their insect attackers using chemical defenses that are elicited by herbivore wounding. Some of these same insects are pests in the agricultural setting as well, attacking plants that have not benefited from chemical defenses evolved over the ages.

Bai *et al.* leveraged genetic diversity in a population of *Nicotiana attenuata* plants that they grew in the plant's native habitat in Arizona to study how their chemical defenses provide resistance to the herbivorous leafhoppers. A multi-omics approach led to the identification of a volatile compound from leaves that confers resistance to those leafhoppers. —PJH

Science, abm2948, this issue p. 514

MOLECULAR BIOLOGY

Reassessment of DNA 6mA in eukaryotes

Certain forms of chemical modifications to DNA play important roles across the kingdoms of life; some forms have been widely studied and others are relatively new. DNA N⁶-methyldeoxyadenosine (6mA), which was recently reported to be prevalent across eukaryotes, has created excitement as a target to study in biology and diseases. However, some studies have highlighted confounding factors, and there is an active debate over 6mA in eukaryotes. Kong *et al.* describe a method for quantitative 6mA deconvolution and report that bacterial contamination explains the vast majority of 6mA in DNA samples from insects and plants. The method also found no evidence for high 6mA levels in humans (see the Perspective by Boulias and Greer). This work advocates for a reassessment of 6mA in eukaryotes and provides an actionable approach. —DJ

Science, abe7489, this issue p. 515;

see also abn6514, p. 494

QUANTUM GASES

Characterizing second sound

Heat usually propagates diffusively, but it can also under certain circumstances propagate like a wave, much as sound does. This phenomenon, called second

sound, has been observed in superfluids, including helium and ultracold atomic gases. However, measuring the attenuation of second sound remains tricky. Li *et al.* accomplished this feat by creating a uniform ultracold gas of strongly interacting fermionic lithium atoms with a very large Fermi energy. Placing the gas in an external periodic potential and measuring the response, the researchers extracted the coefficients characterizing second sound attenuation. —JS

Science, abi4480, this issue p. 528

EMERGING COMPUTING

Reconfigurable neuromorphic functions

Having all the core functionality required for neuromorphic computing in one type of a device could offer dramatic improvements to emerging computing architectures and brain-inspired hardware for artificial intelligence. Zhang *et al.* showed that proton-doped perovskite neodymium nickelate (NdNiO₃) could be reconfigured at room temperature by simple electrical pulses to generate the different functions of neuron, synapse, resistor, and capacitor (see the Perspective by John). The authors designed a prototype experimental network that not only demonstrated electrical reconfiguration of the device, but also showed that such dynamic networks enabled a better approximation of the dataset for incremental learning scenarios compared with static networks. —YS

Science, abj7943, this issue p. 533;

see also abn6196, p. 495

HIV

Evolving virulence in HIV

Changes in viral load and CD4⁺ T cell decline are expected signals of HIV evolution. By examining data from well-characterized European cohorts, Wymant *et al.* report an exceptionally virulent

subtype of HIV that has been circulating in the Netherlands for several years (see the Perspective by Wertheim). More than one hundred individuals infected with a characteristic subtype B lineage of HIV-1 experienced double the rate of CD4⁺ cell count declines than expected. By the time they were diagnosed, these individuals were vulnerable to developing AIDS within 2 to 3 years. This virus lineage, which has apparently arisen *de novo* since around the millennium, shows extensive change across the genome affecting almost 300 amino acids, which makes it difficult to discern the mechanism for elevated virulence. —CA

Science, abk1688, this issue p. 540;
see also abn4887, p. 493

GREENHOUSE GASES

Ultra smart

Methane emissions from oil and gas production and transmission make a significant contribution to climate change. Lauvaux *et al.* used observations from the satellite platform TROPOMI to quantify very large releases of atmospheric methane by oil and gas industry ultra-emitters (see the Perspective by Vogel). They calculate that these sources represent as much as 12% of global methane emissions from oil and gas production and transmission and note that mitigation of their emissions can be done at low cost. This would be an effective strategy to economically reduce the contribution of this industry to climate change. —HJS

Science, abj4351, this issue p. 557;
see also abm1676, p. 490

GENE REGULATION

Organization shapes expression

The role of genome organization in the regulation of gene activity during development has been the subject of considerable controversy. Batut *et al.* present evidence that dedicated “tethering elements” help to establish long-range enhancer-promoter interactions in the *Drosophila*

genome (see the Perspective by Gaskill and Harrison). Single-cell imaging of transcription in living embryos showed the importance of these elements in determining the timing of *Hox* gene activation during development. Tethers operate independently of boundary elements, which mediate the opposite function of blocking spurious regulatory interactions between neighboring loci. This work sheds light on how genome organization controls the dynamics of gene expression underlying complex developmental processes. —BAP

Science, abi7178, this issue p. 566;
see also abn6380, p. 491

T CELLS

Skin dwellers for the long haul

Transplantation with allogeneic hematopoietic stem cells after myeloablative conditioning enables near total replacement of host blood cells by donor cells. To ascertain whether skin-resident memory T cells are also replaced by donor T cells after therapeutic hematopoietic transplantation, de Almeida *et al.* used single-cell chimerism analysis of patient blood and skin T cells at multiple post-transplantation time points. Long-term chimerism of host T cells in skin was observed in 23% of patients. These patients retained a small number of host T cells in blood with features of tissue-resident lymphocytes, suggesting mobilization into the circulation after tissue residency. These studies open the door to learning more about tissue-resident human T cells through the analysis of patients with long-term chimerism of host skin T cells after hematopoietic transplantation. —IRW

Sci. Immunol. **7**, eabe2634 (2022).

REVIEW SUMMARY

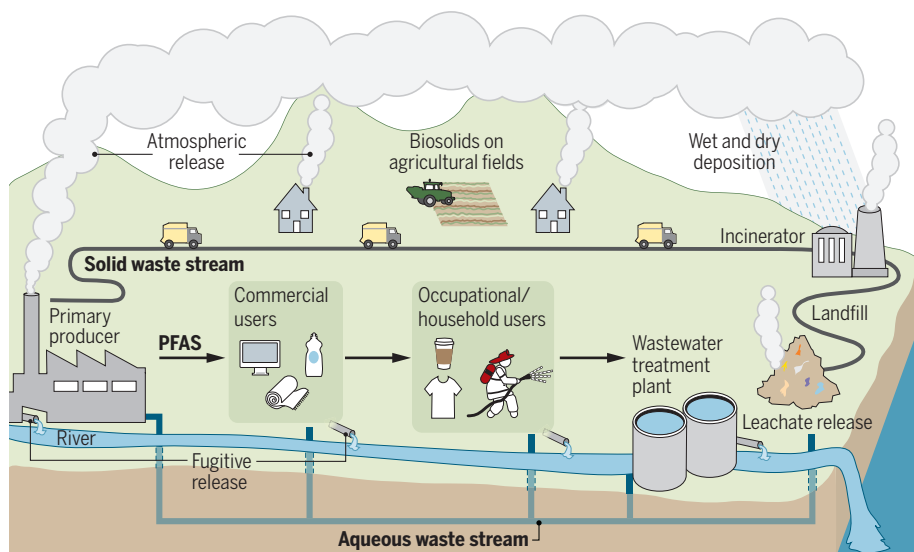
CHEMICAL POLLUTION

Per- and polyfluoroalkyl substances in the environment

Marina G. Evich[†], Mary J. B. Davis[†], James P. McCord[†], Brad Acrey, Jill A. Awkerman, Detlef R. U. Knappe, Andrew B. Lindstrom, Thomas F. Speth, Caroline Tebes-Stevens, Mark J. Strynar, Zhanyun Wang, Eric J. Weber, W. Matthew Henderson*, John W. Washington*

BACKGROUND: Dubbed “forever chemicals” because of their innate chemical stability, per- and polyfluoroalkyl substances (PFAS) have been found to be ubiquitous environmental contaminants, present from the far Arctic reaches of the planet to urban rainwater. Although public awareness of these compounds is still relatively new, PFAS have been manufactured for more than seven decades. Over that time, industrial uses of PFAS have extended to >200 diverse applications of >1400 individual PFAS, including fast-food containers, anti-staining fabrics, and fire-suppressing foams. These numerous applications are possible and continue to expand because the rapidly broadening development and manufacture of PFAS is creating a physiochemically diverse class of thousands of unique synthetic chemicals that are related by their use of highly stable perfluorinated carbon chains. As these products flow through their life cycle from production to disposal, PFAS can be released into the environment at each step

and potentially be taken up by biota, but largely migrating to the oceans and marine sediments in the long term. Bioaccumulation in both aquatic and terrestrial species has been widely observed, and while large-scale monitoring studies have been implemented, the adverse outcomes to ecological and human health, particularly of replacement PFAS, remain largely unknown. Critically, because of the sheer number of PFAS, environmental discovery and characterization studies struggle to keep pace with the development and release of next-generation compounds. The rapid expansion of PFAS, combined with their complex environmental interactions, results in a patchwork of data. Whereas the oldest legacy compounds such as perfluoroalkyl-carboxylic (PFCAs) and perfluoroalkanesulfonic (PFASAs) have known health impacts, more recently developed PFAS are poorly characterized, and many PFAS even lack defined chemical structures, much less known toxicological end points.



The PFAS life cycle. PFAS product flows from primary producer to commercial user to consumers to disposal. Each step is attended by atmospheric and aqueous fugitive releases. Soils constitute a long-term environmental sink, slowly releasing PFAS to the hydrosphere and allowing uptake in biota, but the ultimate reservoir is deep marine sediment.

ADVANCES: Continued measurement of legacy and next-generation PFAS is critical to assessing their behavior in environmental matrices and improving our understanding of their fate and transport. Studies of well-characterized legacy compounds, such as PFCAs and PFASAs, aid in the elucidation of interactions between PFAS chemistries and realistic environmental heterogeneities (e.g., pH, temperature, mineral assemblages, and co-contaminants). However, the reliability of resulting predictions depends on the degree of similarity between the legacy and new compounds. Atmospheric transport has been shown to play an important role in global PFAS distribution and, after deposition, mobility within terrestrial settings decreases with increasing molecular weight, whereas bioaccumulation increases. PFAS degradation rates within anaerobic settings and within marine sediments sharply contrast those within aerobic soils, resulting in considerable variation in biotransformation potential and major terminal products in settings such as landfills, oceans, or soils. However, regardless of the degradation pathway, natural transformation of labile PFAS includes PFAS reaction products, resulting in deposition sites such as landfills serving as time-delayed sources. Thus, PFAS require more drastic, destructive remediation processes for contaminated matrices, including treatment of residuals such as granular activated carbon from drinking water remediation. Destructive thermal and nonthermal processes for PFAS are being piloted, but there is always a risk of forming yet more PFAS products by incomplete destruction.

OUTLOOK: Although great strides have been taken in recent decades in understanding the fate, mobility, toxicity, and remediation of PFAS, there are still considerable management concerns across the life cycle of these persistent chemicals. The study of emerging compounds is complicated by the confidential nature of many PFAS chemistries, manufacturing processes, industrial by-products, and applications. Furthermore, the diversity and complexity of affected media are difficult to capture in laboratory studies. Unquestionably, it remains a priority for environmental scientists to understand behavior trends of PFAS and to work collaboratively with global regulatory agencies and industry toward effective environmental exposure mitigation strategies. ■

The list of author affiliations is available in the full article online.

*Corresponding author. Email: henderson.matt@epa.gov (W.M.H.); washington.john@epa.gov (J.W.W.)

[†]These authors contributed equally to this work.

Cite this article as M. G. Evich *et al.*, *Science* **375**, eabg9065 (2022). DOI: 10.1126/science.abg9065

S READ THE FULL ARTICLE AT
<https://doi.org/10.1126/science.abg9065>

REVIEW

CHEMICAL POLLUTION

Per- and polyfluoroalkyl substances in the environment

Marina G. Evich^{1†}, Mary J. B. Davis^{1†}, James P. McCord^{2†}, Brad Acrey¹, Jill A. Awkerman³, Detlef R. U. Knappe^{4,5}, Andrew B. Lindstrom⁶, Thomas F. Speth⁷, Caroline Tebes-Stevens¹, Mark J. Strynar², Zhanyun Wang⁸, Eric J. Weber¹, W. Matthew Henderson^{1*}, John W. Washington^{1,9*}

Over the past several years, the term PFAS (per- and polyfluoroalkyl substances) has grown to be emblematic of environmental contamination, garnering public, scientific, and regulatory concern. PFAS are synthesized by two processes, direct fluorination (e.g., electrochemical fluorination) and oligomerization (e.g., fluorotelomerization). More than a megatonne of PFAS is produced yearly, and thousands of PFAS wind up in end-use products. Atmospheric and aqueous fugitive releases during manufacturing, use, and disposal have resulted in the global distribution of these compounds. Volatile PFAS facilitate long-range transport, commonly followed by complex transformation schemes to recalcitrant terminal PFAS, which do not degrade under environmental conditions and thus migrate through the environment and accumulate in biota through multiple pathways. Efforts to remediate PFAS-contaminated matrices still are in their infancy, with much current research targeting drinking water.

The ubiquitous presence of per- and polyfluoroalkyl substances (PFAS) in the environment after decades of manufacturing and consumer use (Fig. 1) has garnered global interest, with an ever-expanding inventory of >1400 individual chemicals in the Toxic Substances Control Act Inventory and >8000 unique known structures (1). PFAS have been incorporated in >200 use areas ranging from industrial-mining applications to food production and fire-fighting foams because of the innate chemical and thermal stability of the carbon-fluorine bond and ability to repel oil and water (2). As PFAS flow through commerce from primary manufacturer to commercial user to final disposal, environmental release occurs through both controlled and fugitive waste streams. The stability of many PFAS degradants fosters their ubiquity in the environment. The growing number of PFAS susceptible to partial degradation (3) further complicates environmental fingerprinting and

remediation efforts. Whereas some PFAS transformation pathways have been well characterized, others degrade through as-yet unknown pathways, expanding the already immense PFAS inventory by untold numbers. Of the known PFAS, there is a paucity of data adequately describing potential impacts to ecosystems and their provisioning services, and few of these chemicals are well characterized by ecotoxicity studies, with the widely known perfluorooctanoic acid (PFOA) and perfluorooctane sulfonic acid (PFOS) alone covering 21 and 39% of the ECOTOX Knowledgebase (4), respectively. Furthermore, with their detection in sera across the human population, coupled with epidemiological evidence of the health impacts for legacy PFAS (5, 6), information on associations with human disease for emerging PFAS is needed. With global production volumes of fluoropolymers surpassing 230,000 tonnes/year (2) and estimated cumulative global emissions of perfluoroalkyl acids totaling >46,000 tonnes (7), scientists struggle to keep pace with manufacturing, use (Fig. 1), and subsequent release. Here, we summarize central concerns in PFAS production, persistence, environmental mobility, exposure, and remediation to inform the international community.

Major PFAS groups and uses

PFAS are a class of substances within a wide universe of organofluorine compounds (8), as first laid out by Buck *et al.* in 2011 (9). In 2021, the Organisation for Economic Cooperation and Development released a revised definition of PFAS, “PFAS are fluorinated substances that contain at least one fully fluorinated methyl or methylene carbon atom (without

any H/Cl/Br/I atom attached to it)” (10). This revised definition is more inclusive with unambiguous inclusion of PFAS such as side-chain fluorinated aromatics (Fig. 2) (11, 12). By contrast, most historical work within the research community has focused on a small set of perfluoroalkyl(ether) acids and their precursors, with an emphasis on environmental and biological occurrence investigations. Whereas the persistence associated with the perfluorinated-carbon chain is a fundamental underlying concern, PFAS also have a wide range of bioaccumulation and adverse-effect concerns, governed by their varied physicochemical properties.

Although industrial reviews include general synthetic routes and major applications of some PFAS groups (13), inadequate public information exists for many PFAS internationally, particularly those currently in use, because of confidential business information claims and insufficient regulatory structures (14–16). Critical data gaps include PFAS identities, locations and quantities of production and processing, and final uses of products, limiting the capability to identify where environmental and human exposure occur. Here, we summarize synthetic routes, structural traits, and uses of the major PFAS groups (Figs. 1 and 2) and describe implications and knowledge gaps for future research and action.

The fluorine in PFAS is mined from fluorite (CaF₂) mineral deposits, which is digested to form hydrofluoric acid (HF) (Fig. 1). HF and other non-PFAS-based chemicals are used in either of two general synthetic techniques to produce starting materials (e.g., perfluoroalkanoyle fluorides in Fig. 2) of individual PFAS groups, namely direct fluorination (i.e., turning nonfluorinated to fluorinated substances; e.g., electrochemical fluorination) and oligomerization (i.e., converting monomers to larger molecules; e.g., fluorotelomerization). Direct fluorination is aggressive and often results in uncontrolled chemical reactions such as carbon chain shortening and rearrangement (17–19), leading to a wide range of by-products including cyclic and branched isomers. Oligomerization is less aggressive and mainly results in a homologous series of target compounds (9), as have been observed near fluoropolymer (20) and perfluoropolyether (21) manufacturing and processing sites. Within individual PFAS groups, the functional moieties of starting materials may further react following conventional reaction pathways to yield different PFAS (9); thus, depending on the complexity of synthetic routes, final products may contain a number of unreacted intermediates and degradation products (22, 23). Whereas the summary below focuses on target and/or intentional PFAS, these unintentional PFAS can constitute an important part of human and environmental exposure and merit scrutiny.

¹U.S. Environmental Protection Agency (EPA), Office of Research and Development (ORD), Center for Environmental Measurement and Modeling, Athens, GA 30605, USA. ²EPA, ORD, Center for Environmental Measurement and Modeling, Durham, NC 27711, USA. ³EPA, ORD, Center for Environmental Measurement and Modeling, Gulf Breeze, FL 32561, USA. ⁴Department of Civil, Construction, and Environmental Engineering, North Carolina State University, Raleigh, NC 27695, USA. ⁵Center for Human Health and the Environment, North Carolina State University, Raleigh, NC 27695, USA. ⁶EPA, ORD, Center for Public Health and Environmental Assessment, Durham, NC 27711, USA. ⁷EPA, ORD, Center for Environmental Solutions and Emergency Response, Cincinnati, OH 45268, USA. ⁸Institute of Environmental Engineering, ETH Zürich, 8093 Zürich, Switzerland. ⁹Department of Geology, University of Georgia, Athens, GA 30602, USA.

*Corresponding author. Email: henderson.matt@epa.gov (W.M.H.); washington.john@epa.gov (J.W.W.)

†These authors contributed equally to this work.

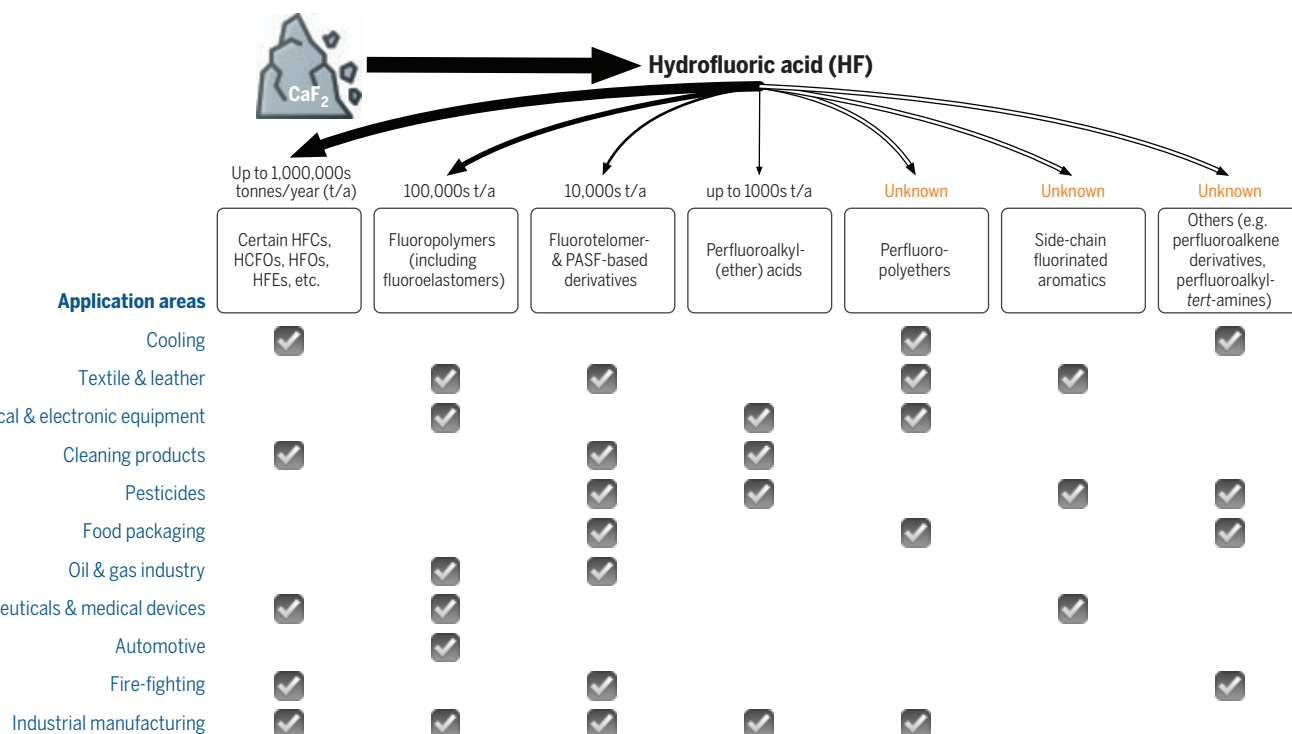


Fig. 1. Non-exhaustive summary of PFAS manufacturing, from production to consumer use. Numerous product fluxes are reasonably documented, but considerable lacunae remain. See text for details and citations. HFC, hydrofluorocarbon; HCFO, hydrochlorofluoroolefin; HFO, hydrofluoroolefin; HFE, hydrofluoroether; PASF, perfluoroalkanesulfonyl fluoride.

Major PFAS groups from direct fluorination include those hydrofluorocarbons, hydrofluoroethers, hydrochlorofluoroolefins, and hydrofluoroolefins that contain a $-\text{CF}_3$ moiety and have an overall global production of >1 megatonne/year (24). Including a range of low-molecular-weight and low-boiling-point compounds that are used as refrigerants, heat-transfer fluids, solvents, and foaming agents (2, 24), these compounds replaced ozone-depleting chlorofluorocarbons and hydrochlorofluorocarbons. Because of their high global-warming potential, the international community has agreed to phase down and eventually eliminate hydrofluorocarbons (25, 26). An ongoing industrial transition is taking place, including increasing large-scale replacement of hydrofluorocarbons with hydrofluoroethers and hydrofluoroolefins. Although they have low global-warming potentials, hydrofluoroethers and hydrofluoroolefins can ultimately degrade to highly persistent perfluoroalkylcarboxylic acids (PFCAs) such as trifluoroacetate, and a steep accumulation of trifluoroacetate in the environment is becoming increasingly evident (27).

Another important PFAS group resulting from direct fluorination is side-chain fluorinated aromatics (11, 12), with unknown but likely considerable amounts being produced and used annually. A common starting point

is the synthesis of benzotrifluorides from benzotrichlorides by reaction with HF (8). Addition of the $-\text{CF}_3$ moiety can reduce biological degradation, increase biological activity, and assist with membrane transport, making the parent compound longer lasting or more effective; therefore, many side-chain fluorinated aromatics are used in pharmaceutical (12) or agricultural (11) applications. These substances can also degrade to PFCAs such as trifluoroacetate.

Two other major PFAS groups produced from direct fluorination include perfluoroalkyl-tert-amines (28) and perfluoroalkanoyle/perfluoroalkanesulfonyl fluorides (PACF/PASFs), which are further reacted to produce PFCAs, perfluoroalkanesulfonates (PFSAs), and other derivatives (Fig. 2). Historically, hundreds of PACF/PASF-based derivatives with a wide range of perfluorocarbon-chain lengths were produced, on the order of kilotonnes/year (15, 29), and used for industrial and consumer applications (2). Since the early 2000s, numerous long-chain (fluoroalkyl carbon number ≥ 6) PACF/PASF-based derivatives have been—and are being—phased out because of widespread concern, whereas shorter-chain PACF/PASF-based derivatives still are being produced and widely used, although in unknown amounts (15, 29). In the environment and biota, PACF/PASF-based derivatives may

degrade and partially transform into different PFCAs and/or PFSAs.

On the oligomerization side, two major PFAS groups are fluoropolymers and perfluoropolyethers. These are high-production polymers having fluorinated backbones, with fluoropolymers being produced on the scale of 100 kilotonnes/year and unknown but likely considerable amounts for perfluoropolyethers. Despite often having simple names such as polytetrafluoroethylene, substances in these two groups can be highly diverse, including both nonfunctionalized (with $-\text{CF}_3$) and functionalized termini, with different structural combinations and molar ratios of monomers (for copolymers), and from low (< 1000 Da) to very high (> 100,000 Da) molecular weight (30–32); this complexity has not been clearly communicated with a comprehensive overview of different fluoropolymers and perfluoropolyethers on the market. Depending on structure, different fluoropolymers and perfluoropolyethers can be used in a range of industrial and consumer applications (2); in some applications, perfluoropolyethers are used as alternatives to PACF/PASF-based derivatives. Given their variety and complexity, their subsequent bioavailability and degradability are highly variable and complex, which is generally overlooked, understudied, and/or unknown.

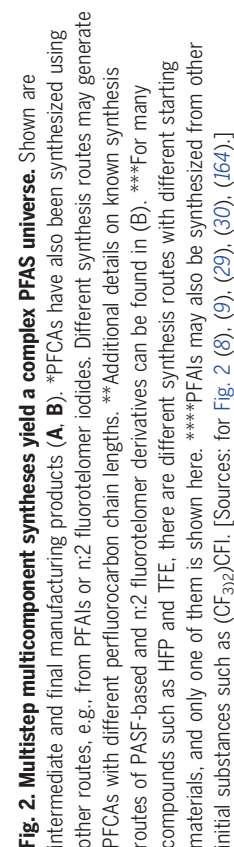


Fig. 2. Multistep multicomponent syntheses yield a complex PFAS universe. Shown are intermediate and final manufacturing products (**A, B**). *PFACs have also been synthesized using other routes, e.g., from PFALs or n:2 fluorotelomer iodides. Different synthesis routes may generate PFPCFs with different perfluorocarbon chain lengths. **Additional details on known synthesis routes of PASF-based and n:2 fluorotelomer derivatives can be found in (B). ***For many compounds such as HFP and TFE, there are different synthesis routes with different starting materials, and only one of them is shown here. ****PFALs may also be synthesized from other initial substances such as (C₃)₂OCFl. [Sources: for Fig. 2 (8), (9), (29), (30), (164).]

Three other major PFAS groups formed from oligomerization are fluorotelomers, perfluoroalkyl(ether) carboxylic and sulfonic acids, and perfluoroalkene derivatives. Fluorotelomers share many similarities to PACF/PASF-based derivatives other than perfluoroalkyl(ether) acids, including molecular structures, degradability (9, 23, 29), use applications (2), and manufacturing trends from a wide range of perfluorocarbon chain lengths to predominantly shorter chains. Fluorotelomers were historically produced on the order of 9 kilotonnes/year (33), with the current amounts produced unknown. Unknown amounts of perfluoroalkyl(ether) carboxylic and sulfonic acids are being used to replace long-chain PFCAs and PFSA (34) in industrial applications such as fluoropolymer production and metal plating, respectively. Perfluoroalkene derivatives such as *p*-perfluorooxynonene sulfonate have been produced since the 1980s; large-scale production (on the scale of kilotonnes/year) was recently initiated in China as an alternative to PFOS in firefighting and oil production (35). Despite having an unsaturated bond, *p*-perfluorooxynonene sulfonate is not readily biodegradable (36).

Environmental stability, degradation schemes, and transformation rates

Despite typically having high stability as a group, ~20% of PFAS may undergo transformation in the environment (3). These labile compounds are precursors to recalcitrant, terminal transformation products such as PFCAs and PFSA. For example, frequently detected precursors including perfluorooctane sulfonamides, fluorotelomer alcohols (FTOHs), and fluorotelomer sulfonates, have been found to contribute up to 86% of total PFAS identified in wastewater-treatment plant sludge (37).

Although PFAS can undergo complete degradation to inorganic components using high-energy remediation technologies, precursor transformations under environmental conditions, including processes such as hydrolysis (38), oxidation (39, 40), reduction, decarboxylation and hydroxylation (41), ultimately yield stable PFAS. Despite the low vapor pressure and high water solubilities of many PFAS, some conditions (e.g., within industrial stacks) can promote partitioning to air through particulate sorption, and volatile PFAS such as FTOHs can exist in the gas phase (42), making atmospheric and photochemical transformation possible. In the soil-water environment, microbe-facilitated functional group biotransformation can occur aerobically (43, 44) or anaerobically (45–47), and some microbes that carry out these reactions have been identified (46, 48, 49). Biotransformation of labile PFAS also can be mediated by plant-specific enzymes. For example, microbial transformation of 8:2 FTOH was substantially enhanced with

the addition of soybean root exudates in solution (50), and perfluorooctane sulfonamide was transformed in the presence of carrot and lettuce crops, but not in their absence, in amended soils (51). In both studies, enhanced degradation was attributed to the organic carbon content of the soil, because the addition of carbon sources can increase microbial degradation rates through co-metabolic processes (52).

Several PFAS can undergo transformation, resulting in the formation of FTOHs through processes such as oxidation, reduction (53), desulfonation (54), and hydrolysis (38, 55–58) (Fig. 3A). Although some fluorotelomers evidently transform without forming intermediate FTOHs (9, 22, 49, 59), one of the archetypal “legacy PFAS” transformation schemes involves FTOHs that are subject to (bio)transformation through numerous intermediates, leading to the formation of terminal PFCA through chain-shortening processes (Fig. 3A). The efficiency of these transformations decreases from aerobic to anoxic to anaerobic (60, 61) conditions, and PFCA yields and rates of formation depend on specific precursor and transformation conditions (9). On average, PFOA yields from 8:2 FTOH were reported to be 25% in aerobic soils compared with <1% in anaerobic sludge (62). This process is initiated by the oxidation of 8:2 FTOH to yield the inferred 8:2 fluorotelomer aldehyde and then the 8:2 fluorotelomer carboxylic acid, which is reduced through the loss of F to form 7:3 unsaturated fluorotelomer acid, which can form the terminal acid perfluorohexanoic acid (53, 63, 64) (Fig. 3A). A key step in the pathway is hydroxylation in the β position and subsequent oxidation to form the 7:3 3(keto) fluorotelomer carboxylic acid, which then undergoes β -oxidation to form PFOA, as well as α -decarboxylation to form the 7:2 ketone (53, 63, 64). The ketone then is reduced to form the secondary alcohol, 1-perfluoroheptyl ethanol [also known as 7:2 (sec) FTOH], which is oxidized to form PFOA (53, 63, 64).

In a second major transformation scheme, *N*-ethyl perfluorooctane sulfonamido ethanol is proposed to oxidize to form the aldehyde and subsequently to *N*-ethyl perfluorooctane sulfonamidoacetic (Fig. 3B) (65, 66). *N*-deacetylation of *N*-ethyl perfluorooctane sulfonamidoacetic acid then leads to the formation of *N*-ethyl perfluorooctane sulfonamide followed by C-hydroxylation to form perfluorooctane sulfonamido ethanol. Oxidation of perfluorooctane sulfonamido ethanol to perfluorooctane sulfonamido acetic acid is proposed to occur through the perfluorooctane sulfonamide aldehyde. *N*-deacetylation of perfluorooctane sulfonamido acetic acid to form perfluorooctane sulfonamide is then observed. Perfluorooctane sulfonamide may also form directly from the *N*-dealkylation of *N*-ethyl perfluorooctane sulfonamide (65, 66). Deami-

nation of perfluorooctane sulfonamide to form perfluorooctane sulfinic acid is commonly followed by oxidation to form the terminal product, PFOS.

PFAS transformation under environmental conditions can be approximated using first-order kinetics (67). Environmental degradation of labile precursors is observed to occur in a “tree structure,” with the formation of numerous intermediates along branching transformation pathways (53, 68). Along each branch, the formation and disappearance of intermediates can be modeled as a sequential decay chain (23), with each step characterized by a pseudo first-order rate constant (67).

In soils and sediment, sorption can slow the observed rate of microbial transformation (69). With long-chain PFAS preferentially adsorbing to soil phases, molecular weight can be used as an approximate indicator of relative stability among PFAS sharing common reaction centers (43). To address the effects of reversible sorption, some have proposed use of a double-first-order, in-parallel model (67), wherein rate-limited reversible sorption is included as a first-order process.

In addition to sorption, transformation rate is dependent on a number of other environmental factors including pH, temperature, and microbial population (70), and these factors contribute to a wide variation of reported precursor half-lives. For example, biodegradation studies of *N*-ethyl perfluorooctane sulfonamido ethanol in sludge reported a half-life of 0.7 to 4.2 days, yet the biodegradation in marine sediments was found to proceed at much slower rates ($t_{1/2}$, 4°C = 160 days and $t_{1/2}$, 25°C = 44 days), which could explain reports of elevated concentrations of *N*-ethyl perfluorooctane sulfonamido ethanol in marine environments (66). Similarly, the anaerobic biotransformations of 6:2 and 8:2 FTOHs slowed substantially (30 and 145 days, respectively) compared with aerobic conditions (<2 and 2 to 7 days, respectively) (62), which can foster enhanced levels of telomer acids [e.g., 5:3 fluorotelomer carboxylic acid by hydrogenation of the 5:3 fluorotelomer unsaturated carboxylic acid (53)] in landfills (71). Therefore, PFAS that typically are intermediates in oxidizing settings may exist as terminal products under reducing conditions. For example, variations in PFAS species detected in leachate from waste collection vehicles compared with landfill leachate suggest alternative biodegradation pathways in long-term anaerobic settings such as landfills (72). Consequently, degradation studies conducted under controlled conditions result in considerable variation in biotransformation potential and possibly different major stable perfluorinated degradation products when extrapolating half-lives and major products from laboratory to environmental conditions.

In addition to accounting for environmental conditions (67), another complicating factor is that contaminants commonly exist as components in complex mixtures. One common precursor source is aqueous-film-forming foam (AFFF), formulations of which contain mixtures of PFAS, and co-contaminants such as nonfluorinated surfactants. High concentra-

tions of organic solvents have been shown to inhibit PFOA degradation under in situ remedial chemical oxidation studies, suggesting that interactions of PFAS with other non-PFAS co-contaminants can alter PFAS transformation (40). Additionally, the presence of different PFAS has resulted in changing compositions of microbial communities

when comparing cultures spiked with PFOA or PFOS against microbial compositions without PFAS (46). Considering that PFAS environmental transformation is mediated primarily by microbes, data suggest that the presence of complex mixtures could indirectly alter biodegradation and that the presence of one PFAS may affect the transformation rate of another,

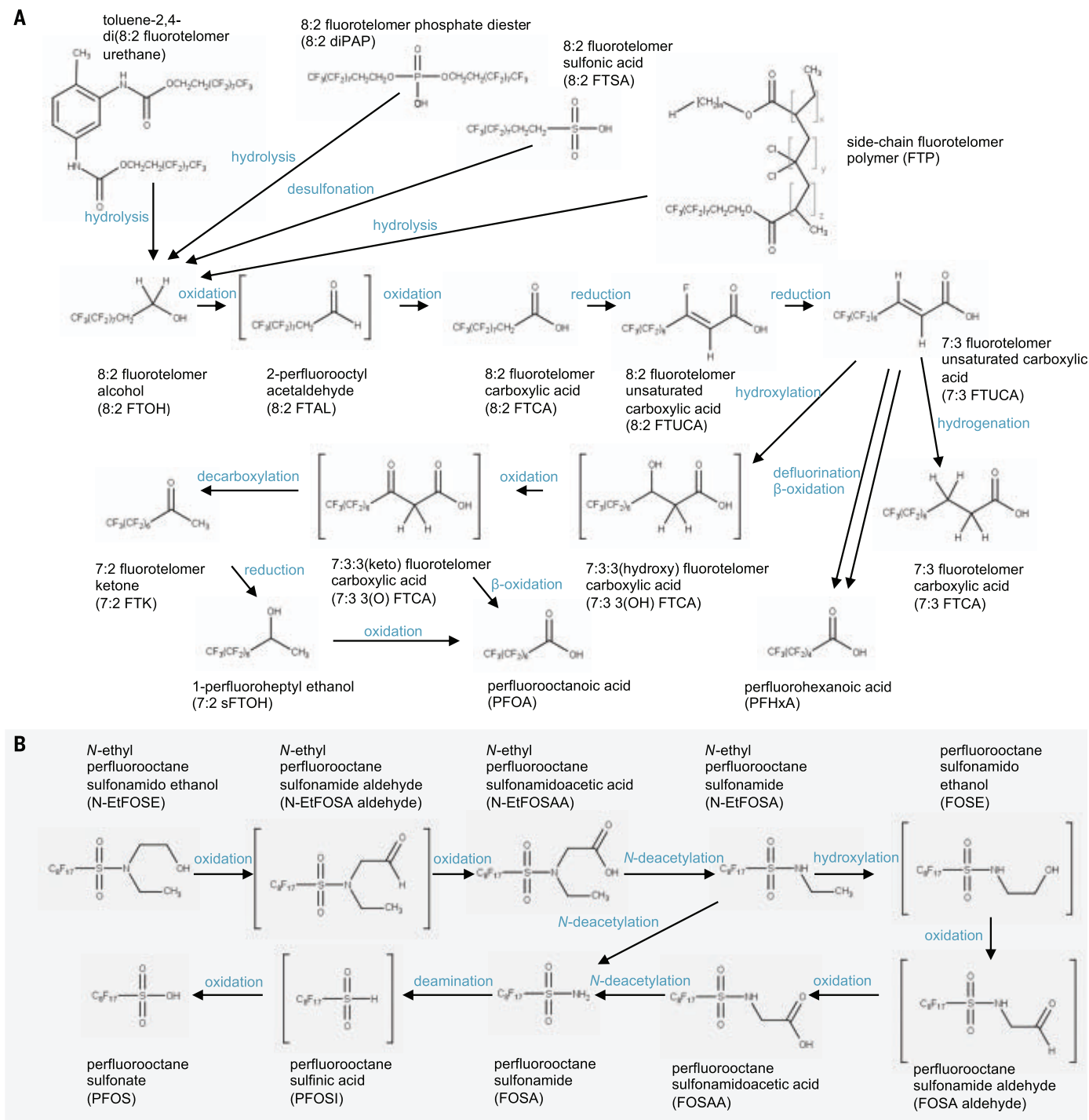


Fig. 3. Breakdown pathways of classes of PFAS. Shown are reaction schemes for 8:2 FTOH (47, 53, 63) (A) and N-EtFOSE (65, 66) (B). Transformation products proposed by the original investigators are shown with brackets.

although transformation kinetics of PFAS mixtures has not been reported. Furthermore, these complex mixtures could have downstream implications for PFAS mobility, because co-contaminants in AFFF mixtures affect microbial toxicity and PFAS solubility, partitioning (73), and remediation [PFAS can be transformed during treatment of organic contaminants (39)].

Taken together, the complexity of real-world environmental conditions acting on primary precursors, intermediates and terminal products can result in divergence from reaction schemes and degradation rates derived under laboratory conditions. These complexities are aggravated by the many experimental challenges associated with larger PFAS such as fluoropolymers and side-chain fluorinated polymers, the structure and monomeric compositions of which often are not completely characterized (23, 38, 74). In addition, there remain uncertainties regarding the levels of impurities or synthetic by-products and life cycle emissions of these polymers, which may affect degradation rates, further necessitating nontargeted analyses in conjunction with transformation prediction simulators such as *EnviPath* (75) and the Chemical Transformation Simulator (76) to identify new PFAS and transformation products in the environment.

Environmental mobility and distribution

The mobility of PFAS in the environment is dictated by properties of the mobile (usually air and water) and immobile phases [e.g., natural organic matter (NOM) and mineral assemblages] as well as the PFAS species. The transformation rates discussed above affect the time available for migration. When transformation rates of short-lived intermediates exceed environmental transport rates, these intermediates can remain proximate to their precursors, a phenomenon well established for the environmental distribution of short-lived radionuclides (77) because of secular (radio-decay) equilibrium with long-lived parents (78). Further, this secular equilibrium of short-lived intermediates might contribute to the undetectable status of some inferred compounds (e.g., 2-perfluorooctyl acetaldehyde; Fig. 3). For PFAS with intermediate transformation rates (e.g., FTOHs and fluorotelomer unsaturated carboxylic acids; Fig. 3) relative to environmental transport processes, these compounds can migrate considerable distances before transformation to recalcitrant PFAS, thereby dispersing widely in the environment (79).

Early precursor PFAS include volatile species (FTOHs and sulfonamido ethanol; Fig. 3), the presence of which has been established globally (80–82). Atmospheric residence time governs transport distance (83) and depends on a variety of PFAS properties, including

volatility, reactivity, molecular weight, and vapor-particulate partitioning (82, 84, 85). Atmospheric lifetimes have been reported for FTOHs of ~20 days (86). Consistent with these atmospheric lifetimes, air samples collected at remote oceanic locations are reported to contain several FTOH and/or perfluorosulfonamido ethanol species in both gas and particulate phases (80). On the basis of these and related observations, a large portion of PFAS global distribution, including that to remote regions, has been attributed to atmospheric transport (79, 87). For example, in a study of soils collected from remote sites globally, all samples contained PFAS, with homolog ratios [e.g., PFOA/perfluorononanoic acid (PFNA)] consistent with atmospheric transport (79). These soil concentrations have been used to define global-background PFAS ranges in surface soils (means ~10 to 60 pg/g), such that surface soils rarely contain lower PFAS, and higher concentrations suggest local or regional sources (88). Atmospherically transported ionic PFAS also have been shown to disperse widely, perhaps as far afield as >400 km (21, 89, 90), although the form of these species, e.g., free acid, dissolved in droplets or sorbed to particulates, has not been resolved.

In terrestrial settings, PFAS transport usually occurs through aqueous advection, with migration retarded by sorption on NOM, minerals, and at fluid-fluid interfaces (particularly air-water) (91). Most PFAS sorption studies have been conducted with surface soils in which NOM, which is typically present at relatively high concentrations (Fig. 4) (92), constitutes a major substrate. Exploring surface-soil sorption mechanisms of two PFAS having sulfonate termini revealed an easily extractable fraction, as well as less reversibly sorbed fractions composed of perfluoroalkyl groups hydrophobically associating with NOM, sulfonate moieties covalently binding to NOM–OH groups forming ester linkages, and physical entrapment in NOM or minerals (93). Comparing the sorption of cationic, zwitterionic, and anionic PFAS showed concentration-dependent sorption for cationic and zwitterionic PFAS, pronounced sorption hysteresis for zwitterions, and major electrostatic and NOM sorption for cationic and zwitterionic PFAS (94).

The high NOM concentrations of surface soils typically diminish precipitously in the first several centimeters below the ground surface, where mineral surfaces come to dominate the vertically more expansive subsurface realm (Fig. 4) (92). Authigenic minerals typically are abundant in the subsurface, and these minerals have surface charges for electrostatic sorption. Aluminosilicate clays bear permanent negative surface charges, presenting potential sorption sites for cationic and zwitterionic PFAS. Ferric and aluminum

(oxy)hydroxides bear pH-dependent, positive surface charges below their zero point of charge at a pH of ~8, so these minerals can electrostatically sorb anionic PFAS. In the vadose zone, recent studies have shown that the surfactant nature of PFAS also fosters sorption at the air-water interface, retarding PFAS migration (91).

To assess sorption across a wide breadth of PFAS species and complex sorption matrices, experiments have been performed on 29 PFAS in 10 soils (95). This study concluded that a simple distribution coefficient, K_d (soil/water concentration), effectively characterized relative distribution among PFAS. Recognizing that lower values of $\log K_d$ favor partitioning to water, thereby favoring higher environmental mobility, general patterns in these data (Fig. 4A) include the following: (i) the distribution coefficient increases logarithmically with fluoroalkyl carbon numbers >5, (ii) distribution coefficients converge to similar values among PFAS species and chain-lengths having fluorinated carbons ≤ 5 , and (iii) for equal fluoroalkyl carbon numbers, sorption generally decreases according to zwitterions > sulfonamides > telomers > PFASs > PFCAs > ethers. It also was observed that $\log K_d$ for anionic PFAS increased with decreasing pH, a pattern consistent with increasing positive electrostatic charge on pH-dependent surfaces of (oxy)hydroxide minerals and amorphous solids.

When precursor degradation does not complicate interpretation (96), relative values of $\log K_d$ are reflected in PFAS distribution patterns across the spectrum of environmental settings. Figure 4B depicts geometric mean ratios (subsoil/surface soil) of PFAS for three soil profiles after biosolids application at the ground surface (97); consistent with $\log K_d$ values, subsoil accumulation of PFCAs exceeds PFASs for the common fluoroalkyl number 8, shorter chains vary little from each other, and shorter chains exceed that of longer chains. It is noteworthy that subsoil accumulation for fluoroalkyl number >10 also varies little with chain length, perhaps reflecting facilitated transport of PFAS sorbed to colloids winnowing through the soil column (98).

Transport of PFAS into terrestrial plants occurs through a variety of pathways, with the most studied being uptake through roots. As with transport in soils, vegetative accumulation factors ($VAF = [PFAS]_{\text{vegetation}}/[PFAS]_{\text{soil}}$) are influenced by the propensity of specific PFAS to partition into water as they are transported through plants. These VAFs have revealed plant species- and tissue-specific trends (99–101). However, a recent review of VAFs across numerous species and tissues reported uniformly declining trends in total VAF with increasing fluoroalkyl number for PFCAs and PFASs (102) (Fig. 4C) (101). VAF trends with chain length and among terminal moieties

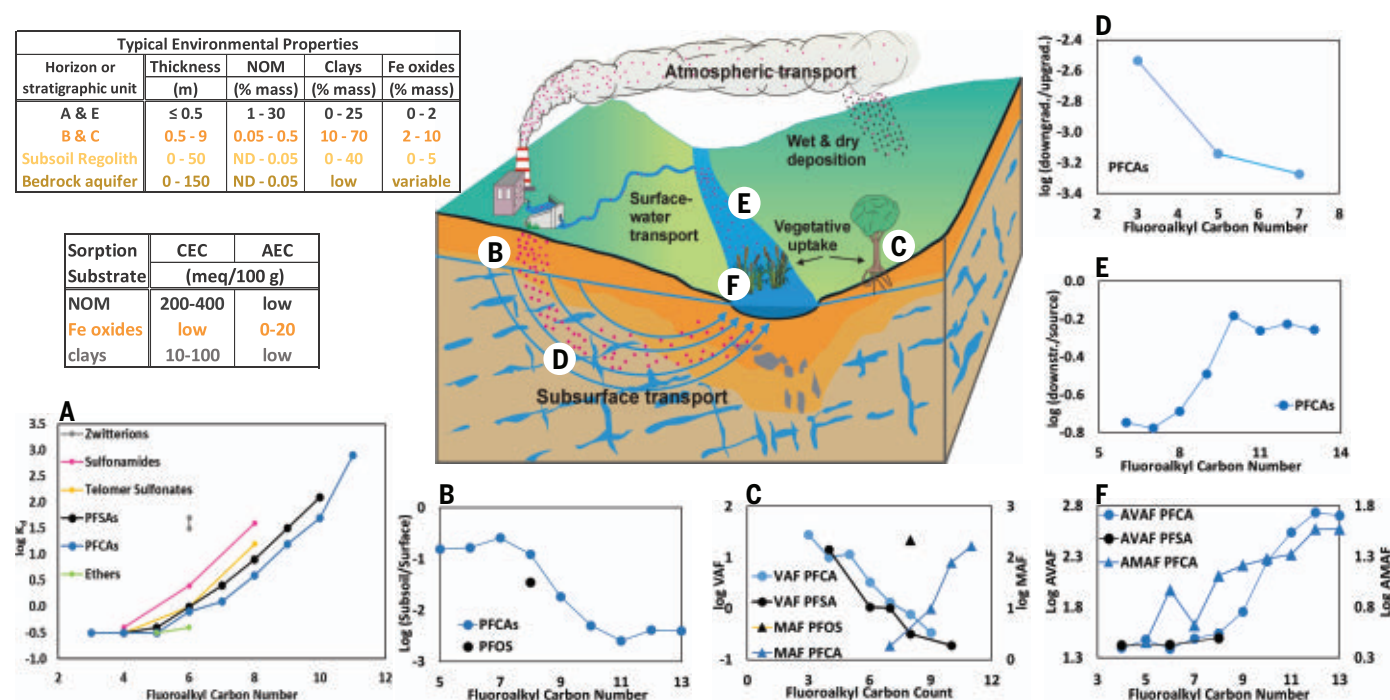


Fig. 4. PFAS partitioning in environmental media ($\log K_d$). The environmental sorption complex varies grossly with setting, with NOM concentrated in shallow soil horizons and ferric (oxy)hydroxides commonly dominating in subsurface media (Properties). Log K_d varies as a function of fluoroalkyl number and terminal moiety [(A) (95); pH = 5.2 values depicted]. Because of this partitioning behavior, when not complicated by precursor degradation, relative mobility

among PFAS commonly varies with fluoroalkyl carbon number [(B) (97), (D) (105), (E) (106)], and terrestrial vegetation accumulation diminishes with increasing fluoroalkyl number, but accumulation in terrestrial detrital feeders increases with fluoroalkyl number [(C) (101)]. In aquatic settings, vegetative and detrital-feeder accumulation both increase with fluoroalkyl number [(F) (107)]. CEC/AEC, cation-exchange capacity/anion-exchange capacity.

suggest that chemical properties of PFAS also exert a strong influence over plant uptake. Reports of plant uptake of emerging PFAS compounds are limited, but studies examining the concentration of chloroether sulfonic acids (F-53B, a replacement for PFOS in electroplating industry) suggest similar variation with chain length (103).

In contrast to the VAF patterns, which are largely governed by relative PFAS aqueous-sorbed partitioning, soil macroinvertebrates feeding directly on long-chain-rich vegetative detritus and NOM tend to express trends opposite to that for VAFs. For example, macroinvertebrate accumulation factors (MAF = $[\text{PFAS}]_{\text{macroinvertebrate}}/[\text{PFAS}]_{\text{soil}}$) reported for earthworms (*Eisenia andrei*) in biosolid-amended soil have trends of increasing MAF with fluoroalkyl number (Fig. 4C) (104).

After percolating through the vadose zone, relative PFAS mobility patterns have been reported in groundwater plumes. For example, PFAS concentrations were reported for wells in a groundwater plume flowing from a landfill, to an observation well, and then to water-supply well (105). Given travel times exceeding 24 years for flow from the landfill to the water-supply well, several PFCA homologs fell to undetectable levels, but perfluorobutanoic acid, perfluorohexanoic acid, and PFOA exhibited a

pattern of lower downgradient/upgradient ratios (specifically, downgradient well 1/upgradient well OW1f03) with increasing PFCA chain length (Fig. 4D).

In a riverine setting, sediments downstream of a carpet industry have been reported to retain higher ratios of long-chain homologs than short (downstream site 5/upstream source site 4; Fig. 4E) (106), consistent with preferential sorption of the longer homologs (perhaps affected by precursor transformation as well). In turn, this pattern also is expressed at the base aquatic autotrophic level; for example, aquatic vegetative-leaf accumulation (AVAF = $[\text{PFAS}]_{\text{vegetation}}/[\text{PFAS}]_{\text{water}}$; Fig. 4F) was relatively higher for long-chain compounds (107). Mirroring these AVAF trends, aquatic macroinvertebrate accumulation factors (AMAF = $[\text{PFAS}]_{\text{macroinvertebrate}}/[\text{PFAS}]_{\text{sediment}}$; Fig. 4F) for blackworms (*Lumbriculus variegatus*) increases with fluoroalkyl number as well (107).

Environmental exposure

Widespread global persistence of PFAS has resulted in detectable concentrations of the compounds in the blood of almost the entire human population (6). Human health effects from exposure to PFAS have been studied extensively, identifying possible carcinogenic, reproductive, endocrine, neurotoxic, dyslipide-

mic, and immunotoxic effects (6, 108, 109). However, with animal models reflecting similar postulated mechanisms of action, the potential toxicity of these compounds for wildlife cannot be dismissed (110). For humans, direct exposure through manufactured products can be managed more expediently than indirect exposure to accumulated sources in aquatic ecosystems. PFAS exposures through food chains are more difficult to resolve, and dietary exposure through drinking water and contaminated food sources (e.g., seafood and other animal products) are among the greatest exposure sources for ecosystems and human populations alike (109, 111). Here, we review the consequences of PFAS persistence in the environment and the resulting bioaccumulation in biota, present ecotoxicological details in the context of environmental distribution and exposure potential, and discuss the ecological effects of PFAS mixtures (112).

Estimation of environmental exposure to PFAS is hindered by the sheer number of functionally diverse PFAS and is further complicated by their presence as complex mixtures. A fundamental understanding of ecotoxicology requires comprehensive knowledge of all PFAS species to which target organisms have been exposed. Although pragmatic limitations have fostered studies reporting

summary characterizations such as Total Organic Fluorine and Total Oxidizable Precursor assays as proxies for more informative chemical-specific studies (113–116), more exhaustive approaches providing identification of individual compounds within PFAS mixtures remains the more informative strategy (117, 118). Ideally, such characterizations would include details regarding branched- versus linear-chain homologs, homolog ratios, isomer comparisons, and forensics with high-resolution mass spectrometry. In addition to pinpointing potential point sources, these methods can distinguish between receptor contact with precursor compounds and their terminal products.

An accurate assessment of PFAS risk must consider exposure to precursor compounds because these compounds transform and are thus important for characterizing environmental PFAS mixtures (119, 120). PFAS precursors are susceptible to *in vivo* metabolic conversion to terminal acids or sulfonamides after exposure, as well as transformation during (or subsequent to) atmospheric or oceanic transport (see previous sections). For example, whereas PFSAs were the most abundant PFAS in both sediment and water at sites contaminated with AFFF (114), aquatic invertebrates exposed to AFFF displayed elevated concentrations of PFCAs as well as the 6:2 fluorotelomer sulfonate (114, 115). Given the common detection of precursors, environmental-organismal uptake and distribution models should include both parent and degradant PFAS to best describe patterns of exposure and influence on biomagnification, especially considering the rapidly expanding incorporation of new, shorter-chain PFAS that tend to be detected less frequently in biota (121).

Key to understanding distribution of PFAS in biota are the specific interactions between PFAS and biological molecules. Although the bioaccumulation of some persistent organic pollutants is often related to lipid partition coefficients, PFAS are not exclusively associated with lipids (120). Bioaccumulation modeling suggests that both protein interactions and lipid partitioning are important parameters for accurately assessing PFAS (122, 123), although predicting biomacromolecule interactions has proven difficult because of their physiochemical properties. PFAS do not behave like neutral, hydrophobic organic contaminants and instead are hypothesized to involve both phospholipids and proteinaceous tissues due in part to their anionic nature (123). Cooperative binding models have further correlated (and predicted) protein associations, relying on traditional measures of hydrophobicity and its effect on biomacromolecule interactions (124). Therefore, both membrane-water partitioning and protein-water coefficients could be informative bioaccumulation indicators (i.e., bioconcentration

factors, bioaccumulation factors, and trophic magnification factors), and coupled with hepatic- and renal-clearance mechanisms across taxa are all vital in understanding PFAS persistence in organisms. Nevertheless, the specific physiochemical differences, such as chain length, result in different distribution of PFAS in biological tissues (125).

Ecotoxicological study of PFAS is further complicated by diversity of the PFAS class. Bioaccumulation factors for terrestrial vegetation are greater for PFCAs than for PFSAs, with shorter-chain perfluoroalkyl acids bioaccumulating to a greater degree than longer-chain ones, largely driven by variation in PFAS solubility (126), followed by uptake and translocation into tissues (Fig. 4C) (100, 101). Conversely, potential perfluoroalkyl acid bioaccumulation in other fauna is greatest in long-chain compounds (120), with clear trends of bioaccumulation increasing with chain length (Figs. 4, C and F, and 5) (121). Long-chain PFAS concentrations tend to increase with trophic level in aquatic food webs, consistent with biomagnification processes (127). However, transformation of precursors in exposure media and biota can confound interpretation of high concentrations of some PFAS (e.g., PFOS) as biomagnification without explicit identification of trophic magnification (128).

Biomagnification in predators is related to trophic level, food-chain length, and capacity to metabolize PFAS precursors (125). Seabirds, marine mammals, and terrestrial species show the greatest magnification factors compared with exclusively aquatic food webs, in which organisms with gills eliminate perfluoroalkyl acids more efficiently (120). Effects in predators, also frequently seen in humans, seem to be largely cytotoxic, immunological, reproductive, or carcinogenic (125). Exposure models for aquatic food webs at AFFF-contaminated sites found benthic invertebrate consumers to be the avian dietary guild at highest exposure risk (114). At higher trophic levels, PFSAs (e.g., PFOS) bioaccumulate at greater rates than PFCAs (e.g., PFOA) of the same chain length (Fig. 5) (114, 129) and tend to be more toxic (4).

Estuarine, marine, and freshwater environments have demonstrated trophic magnification of long-chain PFAS (Fig. 5) (130, 131). Discrepancies in the relative concentrations of PFAS in fish compared with benthic invertebrates appear largely dependent on the compounds' functional group and exposure routes, with elevated PFAS concentrations often linked to site-specific sources and/or benthic prey (131–133). Solubilized (i.e., water-borne) rather than dietary exposure was linked to reduced amphipod survival and reproduction (133), but higher trophic-level organisms are exposed primarily through ingestion (109). Counterintuitively, exposure to low concentrations of PFAS can exacerbate bioconcentra-

tion, motivating biologically based, physiological models exploring this phenomenon (127). Overall, evidence suggests that the ultimate global reservoirs of PFAS are oceans and marine sediments (134), emphasizing the importance of elucidating consequences of PFAS contamination in these ecosystems (135).

Ecological implications of PFAS exposure to aquatic and terrestrial organisms highlight the need to assess and incorporate new-approach methodologies that prioritize real-world hazard of organismal exposure and subsequent risk. Mechanism-based studies and *in silico* approaches are beginning to fill data gaps pinpointing the cellular and molecular pathways resulting in toxicity (136, 137). Elimination half-life has been identified as an end point relevant to bioaccumulation and effects (4). In addition to prioritizing chemical selection based on environmental fingerprinting, cross-taxa and sensitive-taxa toxicity testing research should focus on *in silico* model development that can determine tissue distribution, molecular perturbations, and trophic-level accumulation. As the scale of assessment expands, so does the need for the continued development of adverse-outcome-pathway models to facilitate translation of exposure concentration/dose to organismal-effect end points for the projection of population-level consequences, including multigenerational effects. For instance, unexposed progeny of fish exposed to PFOA and PFOS had lower survival rates, reduced growth, and thyroid-related effects as revealed by histology (138). Similarly, lipid metabolism (139) and behavioral end points (140) were affected in subsequent generations of other species.

Although data are available on potentially common mechanisms of action and toxicity between species (e.g., lipid metabolism, modification of cell membrane integrity, protein binding, and nuclear receptor activation), the large number of PFAS underscores the need to augment conventional *in vivo* testing with *in vitro* and *in silico* approaches (4). Using these approaches, a number of moderate- and long-chain PFAS have been shown to elicit varying degrees of oxidative stress and modify the antioxidant defense systems of invertebrates, induce neurotoxic and reprotoxic effects across species, and reside in organisms longer than or comparable to any known class of anthropogenic contaminants (120). PFAS toxicity, bioaccumulation, and persistence generally are increasingly problematic with increasing chain length.

Remediation

Treatment and remediation of PFAS-affected media is especially challenging because the chemistry of PFAS renders them unaffected by most traditional treatment technologies (141). Given the strength of the carbon-fluorine

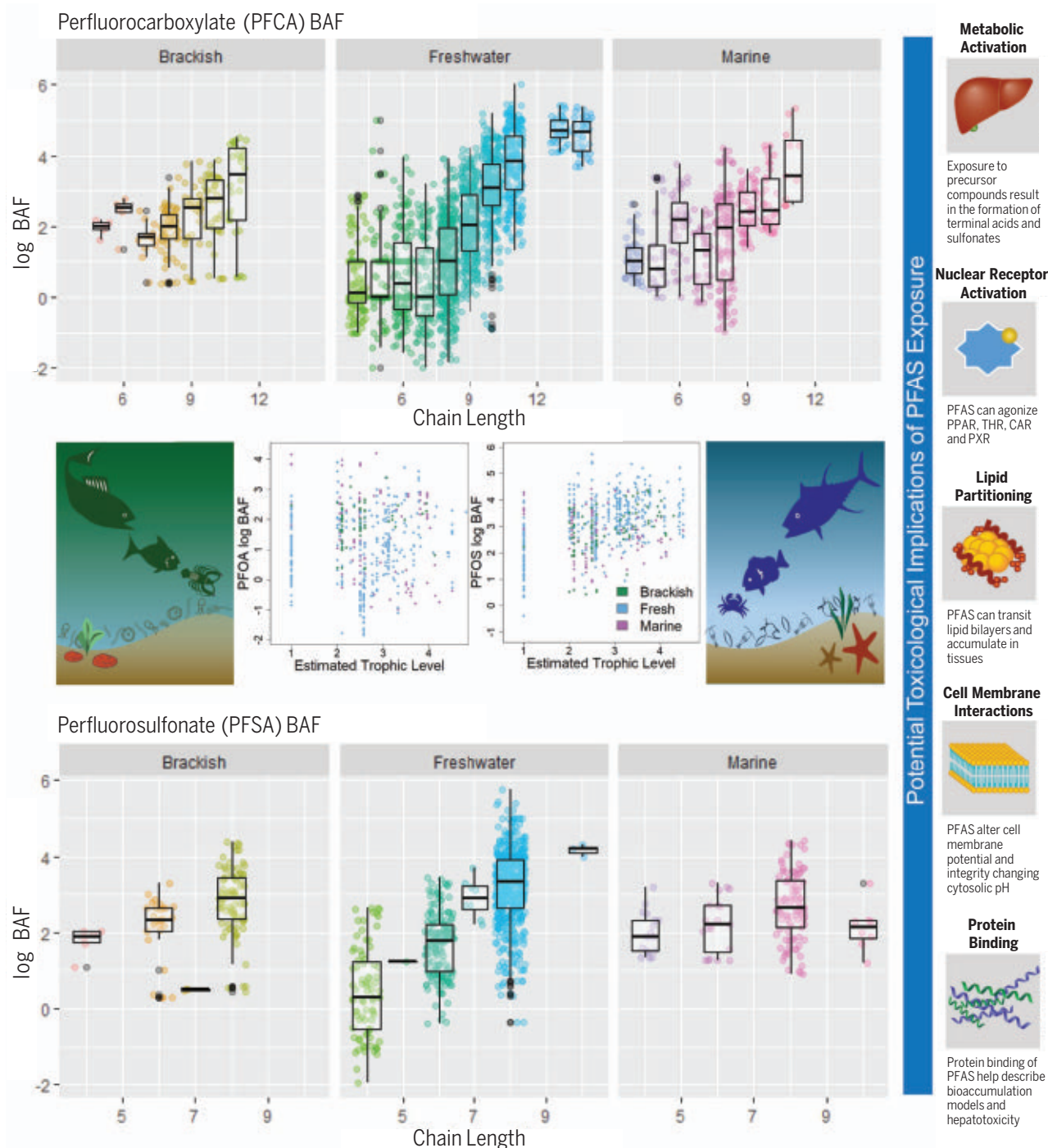


Fig. 5. Trophic transfer and environmental exposures. Bioaccumulation factors (BAFs) in aquatic food webs are greater for long-chain perfluorocarboxylates (top panel) and perfluorosulfonates (bottom panel) than for short-chain perfluoroalkylcarboxylates. Higher trophic-level organisms demonstrate greater bioaccumulation of PFOS than PFOA (center panel); trophic-level accumulation was

estimated for data with a single-prey classification method (FishBase) and standardized bioaccumulation factor by wet weight of organism. Multiple toxicological implications (right panel) reflect the diversity of PFAS physico-chemical properties and have been linked to both functional group and fluoroalkyl carbon chain length. Data were originally compiled by Burkhard (127).

bond, complete mineralization is difficult, with fluorinated products of incomplete destruction remaining a concern (142, 143). Many existing treatment technologies are only capable of concentrating PFAS (144), and concentrated treatment residuals can result in the

reintroduction of PFAS into the environment (Fig. 6). For example, treatment of drinking water can reduce human exposure at the site of treatment while also acting as a PFAS source where residuals are generated, reinforcing the need for a preventative and holistic approach

(145). Therefore, treatment and remediation approaches for contaminated media should be considered in terms of a total management approach influenced by the primary source(s), the affected media, and the ultimate method of destruction or long-term storage of PFAS.

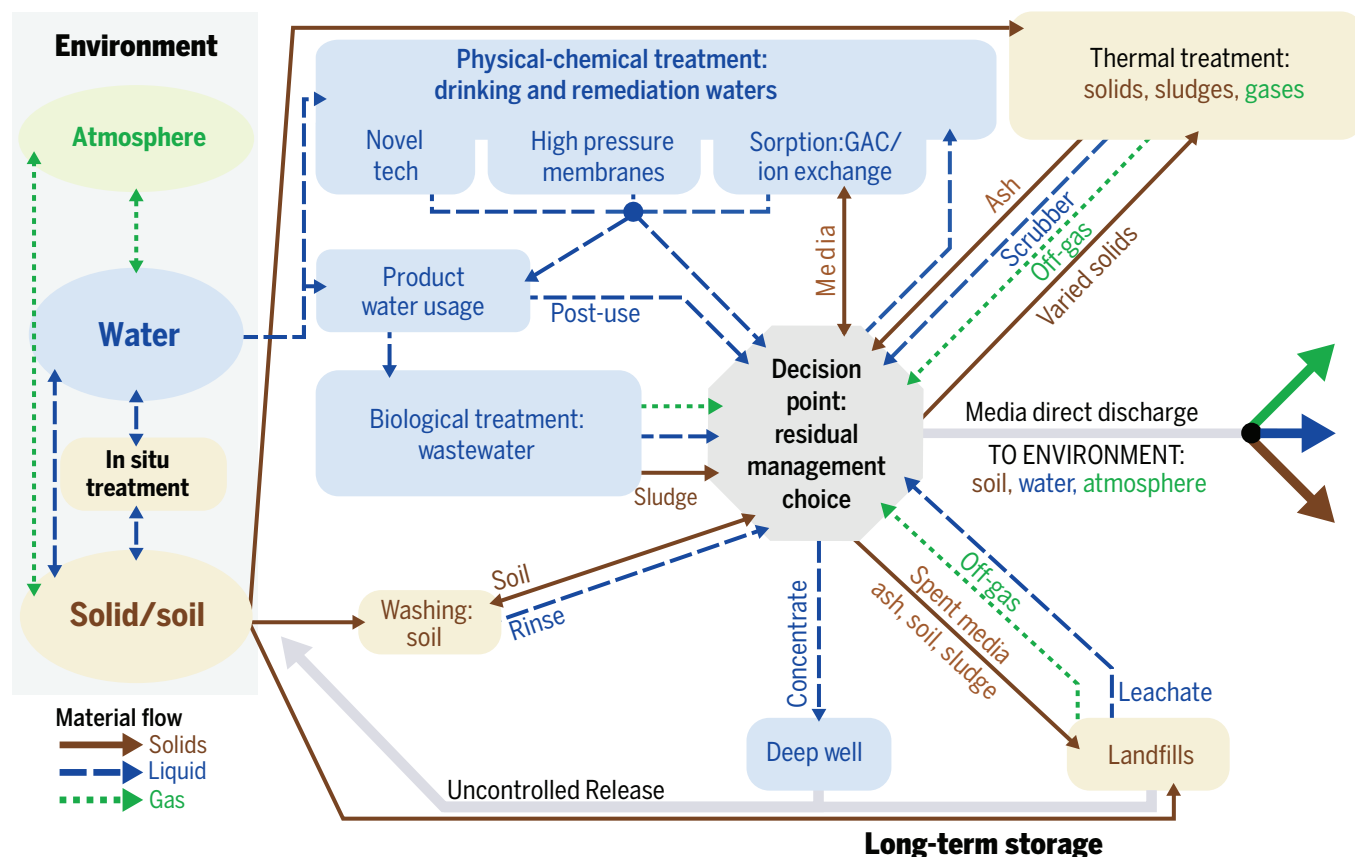


Fig. 6. Site management options for media streams containing PFAS. Brown, blue, and green indicate solid/semisolid, water/liquid, and air/gas phases, respectively. PFAS, including precursors and products of incomplete destruction, cycle through the management options based on treatment and operational choices. Without informed management choices, the persistence of PFAS results in rereleases into the environment. Only complete mineralization, with HF control, offers a permanent solution for breaking the treatment cycle.

PFAS-affected drinking water often is the primary route of human exposure (146), and treatment techniques for aqueous media are the most well established, although performance and cost for the removal of some short-chain PFAS can be particularly challenging. Management can occur at primary sources (i.e., treatment of industrial wastewater effluent), at the secondary concentration source (e.g., drinking water treatment plants or landfill leachate), or in diffuse environmental media (e.g., groundwater). Treatment of diffuse media can involve ex situ “pump-and-treat” approaches to adjoin groundwater to aqueous treatment technologies. The most established treatments for water are sorption to granular activated carbon (GAC) or ion-exchange stationary phases (141). Powdered sorbents can be used; however, particle-separation technology is needed to physically recover the spent sorbent (e.g., conventional treatment, microfiltration, or ultrafiltration).

Removal performance of sorbents differs among targeted PFAS, concentrations, background water quality, and sorbent properties among other parameters (141, 147, 148). Another concentrative approach is the use of high-

pressure membrane systems such as reverse osmosis or nanofiltration. The residual stream for sorbent technologies are the spent media or a regenerate stream for regenerable ion-exchange media, whereas high-pressure membranes yield an enriched retentate. Both residual streams need to be processed further (Fig. 6). GAC typically is reactivated and single-use resins typically are incinerated, but little is known regarding PFAS fate in full-scale facilities. Likewise, studies evaluating treatment options for PFAS-laden reverse-osmosis membrane concentrate or ion-exchange regenerant are in their infancy (149). Other, less-used techniques include membrane distillation, electrodialysis reversal, flotation, electrocoagulation, and evaporation. The niche applications of these technologies are because of their performance, cost, and lack of process familiarity.

Environmental media such as soils can be diffusely contaminated through wet/dry deposition; land application of PFAS-enriched materials such as biosolids, wastewater, or leachate; usage of PFAS-containing products such as AFFFs and pesticides or uncontrolled release through unlined landfills or spills. Soil

contamination is a threat to nearby water sources because of downward and lateral migration of PFAS into receiving water bodies (Fig. 4). In some cases, the large volume of soil that is affected makes ex situ removal and destruction a considerable logistics problem. Another approach to site management is in situ modification to enhance mobility of PFAS for pump-and-treat application or to stabilize PFAS migration using GAC or other sorbents (e.g., clays) to limit impacts (150). Although this can be an effective short-term site-management technique, it is not a permanent solution, and likely will not retain all PFAS species effectively (148, 150, 151). In situ treatment of PFAS in aquifers requires different techniques, such as permeable reactive barriers or addition of powdered activated carbon – of which, none have shown the ability to control PFAS plumes in the long term (150).

The terminal destination of PFAS wastes is of primary concern for the life cycle management of these compounds. Currently, two commercially viable long-term storage approaches are landfilling affected media or underground injection of contaminated water (145). Such sequestration is a temporary solution. Because

most PFAS do not naturally degrade to non-fluorinated chemical species, these long-term sinks are time-delayed sources. For example, landfills are recognized PFAS sources through PFAS-enriched landfill gas and liquid leachates (77). The only permanent solution to PFAS is the destructive remineralization of the underlying fluorine, whether directly acting on contaminated media or from treatment of residual streams of other treatment techniques, such as spent sorbents or regenerant solutions.

Thermal treatment is a destructive approach that can achieve PFAS mineralization. Incineration by itself has been shown to at least partially destroy even highly fluorinated wastes (143), and advanced thermal oxidation can be used on solid, liquid, and gas samples to convert PFAS to constituent gases with an acid-scrubber cleanup (152). Ideally, this process yields HF, NO_x, SO_x, and CO₂ gases that are handled by traditional air pollution control technologies. However, thermal treatment requires substantial temperatures (>700°C) for a sufficient period to convert PFAS into HF and nonfluorinated products, with more highly fluorinated species requiring more time and higher temperature (153, 154). Catalytic oxidation at lower temperatures (e.g., 400°C) has been demonstrated for some PFAS (155). Thermal processes, however, have not been demonstrated at scale, where inefficiencies can reduce performance. Atmospheric emission of products of incomplete destruction or the air pollution control technologies associated with thermal treatment processes, including the regeneration of spent GAC, can become additional PFAS sources. Capture or destruction of these products in the exhaust of thermal processes also is an area of active research, although forefront technologies are like those applied for other media, namely scrubbers, activated-carbon adsorption, and thermal oxidation.

Other destructive treatments for aqueous streams include electrochemical degradation, sonolysis, nonthermal plasma, advanced oxidation (e.g., sulfate radicals) and reduction (solvated electrons), biodegradation (Feammox), zero-valent iron, hydrothermal, and supercritical water oxidation (149, 156). Although many of these technologies have shown the ability to destroy select PFAS, none have demonstrated long-term performance approaching mineralization at full scale with natural and industrial water matrices for a wide assortment of PFAS. Also, the energy costs of many of these technologies limit their sustainability and desirability, and the formation of harmful by-products (e.g., bromate, perchlorate) remains a concern (144). The lack of widespread testing and limited field usage has led to a reluctance in using these technologies because additional management of the waste or residual streams will be needed. These unknowns, among others, fur-

ther demonstrate the need to minimize use of PFAS and find a total waste-management approach in which complete destruction of PFAS is ensured.

Conclusions

The pool of new PFAS, for which physical, chemical, and toxicological data remain undetermined, is expanding rapidly and now includes untold numbers of compounds having widely varying chemical structures, volatilities, and solubilities, as well as uncertain potential exposure consequences. Early studies on structurally similar PFAS suggest that behavioral trends gleaned from legacy PFAS studies can be useful as a basis to predict fate, toxicity, and remediation strategies for emerging compounds. Recently, an internationally authored paper called for PFAS to be managed as a class based upon widespread use in commerce, shared inclusion of strongly bonded perfluorocarbon moiety, and the resulting environmental persistence of common terminal products (157).

Current international reporting practices used to document PFAS synthesis, production volumes, and potential releases vary among countries and are not always tailored to provide the knowledge necessary to adequately track and understand the movement of these compounds in the environment. These efforts typically serve as a critical first step in developing knowledge to be used in future assessment and potential regulation of PFAS. In the United States, expansion of the Toxic Release Inventory will include ~172 long-chain PFAS starting in 2021, providing limited but valuable information in the form of sources, compositions, and quantities released for these compounds. However, under regulatory frameworks around the world, information on many PFAS is protected as confidential business information and will not be disclosed publicly (16), thereby necessitating substantial continued discovery and forensic identification efforts around the world. Other PFAS, such as many of those classified as chemical substances of unknown or variable composition, by-products, or biological materials and polymers, may be too complex to fully characterize and can challenge scientific investigation.

There is an ongoing need to advance responsive PFAS science, particularly regarding investigating environmental sources and sinks, toxicity, and remediation technologies, but evidence suggests that preventative upstream actions are critical to facilitating the transition to safer alternatives and minimizing the impact of PFAS on human health and the environment. Examples of these upstream actions include the EPA's Stewardship Program (158), the Amendment to the Polymer Exemption Rule removing side-chain fluorotelomer polymers from the Exemption Rule (159), the Significant New Use Rule removing an ex-

emption for a set of PFAS used as coatings (160), the recently announced Comprehensive National Strategy to confront PFAS pollution (161), and a ban on PFAS in food contact paper in Denmark (162). Regardless of the regulatory approach implemented, collaborative efforts among scientists, industrial producers, and policy makers will remain key in finding effective and timely solutions (163).

REFERENCES AND NOTES

1. US Environmental Protection Agency, "PFAS structures in DSSTox (update August 2020)" (EPA, 2020); https://comptox.epa.gov/dashboard/chemical_lists/PFASSTRUCTV3.
2. J. Glüge et al., An overview of the uses of per- and polyfluoroalkyl substances (PFAS). *Environ. Sci. Process. Impacts* **22**, 2345–2373 (2020). doi: [10.1039/D0EM00291G](https://doi.org/10.1039/D0EM00291G); pmid: 33125022
3. X. Jiao, Q. Shi, J. Gan, Uptake, accumulation and metabolism of PFASs in plants and health perspectives: A critical review. *Crit. Rev. Environ. Sci. Technol.* **51**, 1–32 (2020). doi: [10.1080/10643389.2020.1809219](https://doi.org/10.1080/10643389.2020.1809219)
4. G. T. Ankley et al., Assessing the ecological risks of per- and polyfluoroalkyl substances: Current state-of-the science and a proposed path forward. *Environ. Toxicol. Chem.* **40**, 564–605 (2021). doi: [10.1002/etc.4869](https://doi.org/10.1002/etc.4869); pmid: 32897586
5. S. M. Bartell, V. M. Vieira, Critical review on PFOA, kidney cancer, and testicular cancer. *J. Air Waste Manag. Assoc.* **71**, 663–679 (2021). doi: [10.1080/10962247.2021.1909668](https://doi.org/10.1080/10962247.2021.1909668); pmid: 33780327
6. S. E. Fenton et al., Per- and polyfluoroalkyl substance toxicity and human health review: current state of knowledge and strategies for informing future research. *Environ. Toxicol. Chem.* **40**, 606–630 (2021). doi: [10.1002/etc.4890](https://doi.org/10.1002/etc.4890); pmid: 33017053
7. J. H. Johansson et al., Global transport of perfluoroalkyl acids via sea spray aerosol. *Environ. Sci. Process. Impacts* **21**, 635–649 (2019). doi: [10.1039/C8EM00525G](https://doi.org/10.1039/C8EM00525G); pmid: 30888351
8. G. S. Siegemund, W. Schwertfeger, A. Feiring, B. Smart, F. Behr, H. Vogel, B. McKusick, P. Kirsch, *Fluorine Compounds*, Organic (Wiley, ed. 3, 2000), vol. 33.
9. R. C. Buck et al., Perfluoroalkyl and polyfluoroalkyl substances in the environment: Terminology, classification, and origins. *Integr. Environ. Assess. Manag.* **7**, 513–541 (2011). doi: [10.1002/ieam.258](https://doi.org/10.1002/ieam.258); pmid: 21793199
10. Organisation for Economic Co-operation and Development, "Reconciling terminology of the universe of per- and polyfluoroalkyl substances: recommendations and practical guidance." (OECD Series on Risk Management No. 61, 2021); [https://www.oecd.org/officialdocuments/publicdisplaydocumentpdf/?cote=ENV/CBC/MONO\(2021\)25&docLanguage=En](https://www.oecd.org/officialdocuments/publicdisplaydocumentpdf/?cote=ENV/CBC/MONO(2021)25&docLanguage=En).
11. Y. Ogawa, E. Tokunaga, O. Kobayashi, K. Hirai, N. Shibata, Current contributions of organofluorine compounds to the agrochemical industry. *iScience* **23**, 101467 (2020). doi: [10.1016/j.isci.2020.101467](https://doi.org/10.1016/j.isci.2020.101467); pmid: 32891056
12. M. Inoue, Y. Sumii, N. Shibata, Contribution of Organofluorine Compounds to Pharmaceuticals. *ACS Omega* **5**, 10633–10640 (2020). doi: [10.1021/acsomega.0c00830](https://doi.org/10.1021/acsomega.0c00830); pmid: 32455181
13. E. Kissa, *Fluorinated Surfactants and Repellents* (Marcel Dekker, 2001).
14. Organisation for Economic Co-operation and Development, "Toward a new comprehensive global database of per- and polyfluoroalkyl substances (PFASs): Summary report on updating the OECD 2007 list of per- and polyfluoroalkyl substances (PFASs)." (OECD Series on Risk Management No. 39, 2018); <https://www.oecd.org/officialdocuments/publicdisplaydocumentpdf/?cote=ENV-JM-MONO%282018%297&docLanguage=en>.
15. Z. Wang, I. T. Cousins, M. Scheringer, R. C. Buck, K. Hungerbühler, Global emission inventories for C4–C14 perfluoroalkyl carboxylic acid (PFCA) homologues from 1951 to 2030, part II: The remaining pieces of the puzzle. *Environ. Int.* **69**, 166–176 (2014). doi: [10.1016/j.envint.2014.04.006](https://doi.org/10.1016/j.envint.2014.04.006); pmid: 24861268
16. S. C. Gold, W. E. Wagner, Filling gaps in science exposes gaps in chemical regulation. *Science* **368**, 1066–1068 (2020). doi: [10.1126/science.abc1250](https://doi.org/10.1126/science.abc1250); pmid: 32499431
17. D. A. Jackson, S. A. Mabury, Polyfluorinated amides as a historical PFCA source by electrochemical fluorination

- of alkyl sulfonyl fluorides. *Environ. Sci. Technol.* **47**, 382–389 (2013). doi: [10.1021/es303152m](https://doi.org/10.1021/es303152m); pmid: 23205559
18. A. A. Rand, S. A. Mabury, Perfluorinated carboxylic acids in directly fluorinated high-density polyethylene material. *Environ. Sci. Technol.* **45**, 8053–8059 (2011). doi: [10.1021/es1043968](https://doi.org/10.1021/es1043968); pmid: 21688793
 19. T. Gramstad, R. N. Haszeldine, 512. Perfluoroalkyl derivatives of sulphur. Part VI. Perfluoroalkanesulphonic acids CF₃–[CF₂–SO₃H (n = 1–7). *J. Am. Chem. Soc. (Resumed)* **0**, 2640–2645 (1957).
 20. S. Newton *et al.*, Novel polyfluorinated compounds identified using high resolution mass spectrometry downstream of manufacturing facilities near Decatur, Alabama. *Environ. Sci. Technol.* **51**, 1544–1552 (2017). doi: [10.1021/acs.est.6b05330](https://doi.org/10.1021/acs.est.6b05330); pmid: 28084732
 21. J. W. Washington *et al.*, Nontargeted mass-spectral detection of chloroperfluoropolyether carboxylates in New Jersey soils. *Science* **368**, 1103–1107 (2020). doi: [10.1126/science.aba7127](https://doi.org/10.1126/science.aba7127); pmid: 32499438
 22. K. A. Barzen-Hanson *et al.*, Discovery of 40 classes of per- and polyfluoroalkyl substances in historical aqueous film-forming foams (AFFFs) and AFFF-impacted groundwater. *Environ. Sci. Technol.* **51**, 2047–2057 (2017). doi: [10.1021/acs.est.6b05843](https://doi.org/10.1021/acs.est.6b05843); pmid: 28098989
 23. J. W. Washington, T. M. Jenkins, K. Rankin, J. E. Naile, Decades-scale degradation of commercial, side-chain, fluorotelomer-based polymers in soils and water. *Environ. Sci. Technol.* **49**, 915–923 (2015). doi: [10.1021/es504347u](https://doi.org/10.1021/es504347u); pmid: 25426868
 24. C. Booten, S. Nicholson, M. Mann, O. Abdelaziz, “Refrigerants: Market trends and supply chain assessment,” (Tech. Rep. NREL/TP-5500-70207, Clean Energy Manufacturing Analysis Center, 2020); <https://www.nrel.gov/docs/fy20osti/70207.pdf>.
 25. US Environmental Protection Agency, “Proposed rule - phasedown of hydrofluorocarbons: Establishing the Allowance Allocation and Trading Program under the AIM Act” (EPA, 2021); <https://www.epa.gov/climate-hfcs-reduction/proposed-rule-phasedown-hydrofluorocarbons-establishing-allowance-allocation>.
 26. United Nations, “Chapter XXVII ENVIRONMENT: 2. f Amendment to the Montreal Protocol on Substances that Deplete the Ozone Layer” (UN, 2016); https://treaties.un.org/Pages/ViewDetails.aspx?src=TREATY&mtsd_no=XXVII-2-f&chapter=27&clang=en.
 27. Z. Zhai *et al.*, A 17-fold increase of trifluoroacetic acid in landscape waters of Beijing, China during the last decade. *Chemosphere* **129**, 110–117 (2015). doi: [10.1016/j.chemosphere.2014.09.033](https://doi.org/10.1016/j.chemosphere.2014.09.033); pmid: 25262947
 28. W. T. Tsai, Environmental implications of perfluorotributylamine—A potent greenhouse gas. *Mitig. Adapt. Strategies Glob. Change* **22**, 225–231 (2017). doi: [10.1007/s10227-015-9684-6](https://doi.org/10.1007/s10227-015-9684-6)
 29. Z. Wang, I. T. Cousins, M. Scheringer, R. C. Buck, K. Hungerbühler, Global emission inventories for C4–C14 perfluoroalkyl carboxylic acid (PFCA) homologues from 1951 to 2030, Part I: Production and emissions from quantifiable sources. *Environ. Int.* **70**, 62–75 (2014). doi: [10.1016/j.envint.2014.04.013](https://doi.org/10.1016/j.envint.2014.04.013); pmid: 24932785
 30. R. E. Banks, B. E. Smart, J. C. Tatlow, *Organofluorine Chemistry: Principles and Commercial Applications* (Plenum, 1994).
 31. S. Ebnesajjad, *Introduction to Fluoropolymers: Materials, Technology and Applications* (Elsevier, 2013).
 32. Z. Wang, G. Goldenman, T. Tugran, A. McNeil, M. Jones, “Per- and polyfluoroalkylether substances: identity, production and use” (Nordic Working Paper No. 901, Nordic Council of Ministers, 2020); <http://norden.diva-portal.org/smash/get/diva2:1392167/FULLTEXT02.pdf>.
 33. US Environmental Protection Agency, “Long-chain perfluorinated chemicals (PFCs) action plan” (EPA, 2009); <https://www.epa.gov/assessing-and-managing-chemicals-under-tasca/long-chain-perfluorinated-chemicals-pfcs-action-plan>.
 34. Z. Wang, I. T. Cousins, M. Scheringer, K. Hungerbühler, Fluorinated alternatives to long-chain perfluoroalkyl carboxylic acids (PFCA), perfluoroalkane sulfonic acids (PFSA) and their potential precursors. *Environ. Int.* **60**, 242–248 (2013). doi: [10.1016/j.envint.2013.08.021](https://doi.org/10.1016/j.envint.2013.08.021); pmid: 24660230
 35. L. Xu *et al.*, Discovery of a novel polyfluoroalkyl benzenesulfonic acid around oilfields in northern China. *Environ. Sci. Technol.* **51**, 14173–14181 (2017). doi: [10.1021/acs.est.7b04332](https://doi.org/10.1021/acs.est.7b04332); pmid: 29218982
 36. Y. Bao *et al.*, First assessment on degradability of sodium p-perfluorooctanoate (OBS), a high volume alternative to perfluorooctane sulfonate in fire-fighting foams and oil production agents in China. *RSC Advances* **7**, 46948–46957 (2017). doi: [10.1039/C7RA09728J](https://doi.org/10.1039/C7RA09728J)
 37. U. Eriksson, P. Haglund, A. Kärman, Contribution of precursor compounds to the release of per- and polyfluoroalkyl substances (PFASs) from waste water treatment plants (WWTPs). *J. Environ. Sci.* **61**, 80–90 (2017). doi: [10.1016/j.jes.2017.05.004](https://doi.org/10.1016/j.jes.2017.05.004); pmid: 29191318
 38. J. W. Washington, T. M. Jenkins, Abiotic hydrolysis of fluorotelomer polymers as a source of perfluorocarboxylates at the global scale. *Environ. Sci. Technol.* **49**, 14129–14135 (2015). doi: [10.1021/acs.est.5b03686](https://doi.org/10.1021/acs.est.5b03686); pmid: 26526296
 39. P. M. Dombrowski *et al.*, Technology review and evaluation of different chemical oxidation conditions on treatability of PFAS. *Rem. J.* **28**, 135–150 (2018). doi: [10.1002/rem.21555](https://doi.org/10.1002/rem.21555)
 40. T. A. Bruton, D. L. Sedlak, Treatment of aqueous film-forming foam by heat-activated persulfate under conditions representative of in situ chemical oxidation. *Environ. Sci. Technol.* **51**, 13878–13885 (2017). doi: [10.1021/acs.est.7b03969](https://doi.org/10.1021/acs.est.7b03969); pmid: 29164864
 41. J. Cui, P. Gao, Y. Deng, Destruction of per- and polyfluoroalkyl substances (PFAS) with advanced reduction processes (ARPs): A critical review. *Environ. Sci. Technol.* **54**, 3752–3766 (2020). doi: [10.1021/acs.est.9b05565](https://doi.org/10.1021/acs.est.9b05565); pmid: 32162904
 42. L. Ahrens, T. Harner, M. Shoeib, D. A. Lane, J. G. Murphy, Improved characterization of gas-particle partitioning for per- and polyfluoroalkyl substances in the atmosphere using annular diffusion denuder samplers. *Environ. Sci. Technol.* **46**, 7199–7206 (2012). doi: [10.1021/es300898s](https://doi.org/10.1021/es300898s); pmid: 22606993
 43. C. Liu, J. Liu, Aerobic biotransformation of polyfluoroalkyl phosphate esters (PAPs) in soil. *Environ. Pollut.* **212**, 230–237 (2016). doi: [10.1016/j.envpol.2016.01.069](https://doi.org/10.1016/j.envpol.2016.01.069); pmid: 26849529
 44. S. Mejía-Avendaño, J. Liu, Production of PFOS from aerobic soil biotransformation of two perfluoroalkyl sulfonamide derivatives. *Chemosphere* **119**, 1084–1090 (2015). doi: [10.1016/j.chemosphere.2014.09.059](https://doi.org/10.1016/j.chemosphere.2014.09.059); pmid: 25460746
 45. B. M. Allred, J. R. Lang, M. A. Barlaz, J. A. Field, Physical and biological release of poly- and perfluoroalkyl substances (PFASs) from municipal solid waste in anaerobic model landfill reactors. *Environ. Sci. Technol.* **49**, 7648–7656 (2015). doi: [10.1021/acs.est.5b01040](https://doi.org/10.1021/acs.est.5b01040); pmid: 26055930
 46. S. Huang, P. R. Jaffé, Defluorination of perfluorooctanoic acid (PFOA) and perfluorooctane sulfonate (PFOS) by *Acidimicrobium* sp. strain A6. *Environ. Sci. Technol.* **53**, 11410–11419 (2019). doi: [10.1021/acs.est.9b04047](https://doi.org/10.1021/acs.est.9b04047); pmid: 31529965
 47. H. Hamid, L. Y. Li, J. R. Grace, Review of the fate and transformation of per- and polyfluoroalkyl substances (PFASs) in landfills. *Environ. Pollut.* **235**, 74–84 (2018). doi: [10.1016/j.envpol.2017.12.030](https://doi.org/10.1016/j.envpol.2017.12.030); pmid: 29275271
 48. S. Yi *et al.*, Biotransformation of AFFF component 6:2 fluorotelomer thioether amide sulfonate generates 6:2 fluorotelomer thioether carboxylate under sulfate-reducing conditions. *Environ. Sci. Technol. Lett.* **5**, 283–288 (2018). doi: [10.1021/acs.estlett.8b00148](https://doi.org/10.1021/acs.estlett.8b00148); pmid: 30705920
 49. K. C. Harding-Marjanovic *et al.*, Aerobic biotransformation of fluorotelomer thioether amide sulfonate (Iodene) in AFFF-amended microcosms. *Environ. Sci. Technol.* **49**, 7666–7674 (2015). doi: [10.1021/acs.est.5b01219](https://doi.org/10.1021/acs.est.5b01219); pmid: 26042823
 50. H. Zhang *et al.*, Uptake, translocation, and metabolism of 8:2 fluorotelomer alcohol in soybean (*Glycine max* L. Merrill). *Environ. Sci. Technol.* **50**, 13309–13317 (2016). doi: [10.1021/acs.est.6b03734](https://doi.org/10.1021/acs.est.6b03734); pmid: 27993068
 51. E. Bizkarguenaga *et al.*, Uptake of perfluorooctanoic acid, perfluorooctane sulfonate and perfluorooctane sulfonamide by carrot and lettuce from compost amended soil. *Sci. Total Environ.* **571**, 444–451 (2016). doi: [10.1016/j.scitotenv.2016.07.010](https://doi.org/10.1016/j.scitotenv.2016.07.010); pmid: 27450950
 52. M. Lewis, M.-H. Kim, N. Wang, K.-H. Chu, Engineering artificial communities for enhanced FTOH degradation. *Sci. Total Environ.* **572**, 935–942 (2016). doi: [10.1016/j.scitotenv.2016.07.223](https://doi.org/10.1016/j.scitotenv.2016.07.223); pmid: 27519322
 53. J. W. Washington, T. M. Jenkins, E. J. Weber, Identification of unsaturated and 2H polyfluorocarboxylate homologous series, and their detection in environmental samples and as polymer degradation products. *Environ. Sci. Technol.* **49**, 13256–13263 (2015). doi: [10.1021/acs.est.5b03379](https://doi.org/10.1021/acs.est.5b03379); pmid: 26484632
 54. D. M. J. Shaw *et al.*, Degradation and defluorination of 6:2 fluorotelomer sulfonamidoalkyl betaine and 6:2 fluorotelomer sulfonate by *Gordonia* sp. strain NB4-1Y under sulfur-limiting conditions. *Sci. Total Environ.* **647**, 690–698 (2019). doi: [10.1016/j.scitotenv.2018.08.012](https://doi.org/10.1016/j.scitotenv.2018.08.012); pmid: 30092525
 55. U. M. L. Bratt, Hydrolysis of amides. Alkaline and general acid catalyzed alkaline hydrolysis of some substituted acetamides and benzamides. *Acta Chem. Scand.* **A 28**, 715–722 (1974).
 56. H. Lee, J. D’eon, S. A. Mabury, Biodegradation of polyfluoroalkyl phosphates as a source of perfluorinated acids to the environment. *Environ. Sci. Technol.* **44**, 3305–3310 (2010). doi: [10.1021/es9028183](https://doi.org/10.1021/es9028183); pmid: 20355697
 57. L. A. Royer, L. S. Lee, M. H. Russell, L. F. Nies, R. F. Turco, Microbial transformation of 8:2 fluorotelomer acrylate and methacrylate in aerobic soils. *Chemosphere* **129**, 54–61 (2015). doi: [10.1016/j.chemosphere.2014.09.077](https://doi.org/10.1016/j.chemosphere.2014.09.077); pmid: 25449186
 58. K. Dasu, L. S. Lee, Aerobic biodegradation of toluene-2,4-di (8:2 fluorotelomer urethane) and hexamethylene-1,6-di (8:2 fluorotelomer urethane) monomers in soils. *Chemosphere* **144**, 2482–2488 (2016). doi: [10.1016/j.chemosphere.2015.11.021](https://doi.org/10.1016/j.chemosphere.2015.11.021); pmid: 26624955
 59. N. Wang *et al.*, 6:2 fluorotelomer sulfonate aerobic biotransformation in activated sludge of waste water treatment plants. *Chemosphere* **82**, 853–858 (2011). doi: [10.1016/j.chemosphere.2010.11.003](https://doi.org/10.1016/j.chemosphere.2010.11.003); pmid: 2112609
 60. X. Yu, Y. Takabe, K. Yamamoto, C. Matsumura, F. Nishimura, Biodegradation property of 8:2 fluorotelomer alcohol (8:2 FTOH) under aerobic/anaerobic conditions. *J. Water Environ. Technol.* **14**, 177–190 (2016). doi: [10.2365/jwet.15-056](https://doi.org/10.2365/jwet.15-056)
 61. X. Yu, F. Nishimura, T. Hidaka, Effects of microbial activity on perfluorinated carboxylic acids (PFCA) generation during aerobic biotransformation of fluorotelomer alcohols in activated sludge. *Sci. Total Environ.* **610–611**, 776–785 (2018). doi: [10.1016/j.scitotenv.2017.08.075](https://doi.org/10.1016/j.scitotenv.2017.08.075); pmid: 28826115
 62. S. Zhang *et al.*, 6:2 and 8:2 fluorotelomer alcohol anaerobic biotransformation in digester sludge from a WWTP under methanogenic conditions. *Environ. Sci. Technol.* **47**, 4227–4235 (2013). doi: [10.1021/es4000824](https://doi.org/10.1021/es4000824); pmid: 23531206
 63. N. Wang *et al.*, 8:2 fluorotelomer alcohol aerobic soil biodegradation: Pathways, metabolites, and metabolite yields. *Chemosphere* **75**, 1089–1096 (2009). doi: [10.1016/j.chemosphere.2009.01.033](https://doi.org/10.1016/j.chemosphere.2009.01.033); pmid: 19217141
 64. H. Hamid, L. Y. Li, J. R. Grace, Aerobic biotransformation of fluorotelomer compounds in landfill leachate-sediment. *Sci. Total Environ.* **713**, 136547 (2020). doi: [10.1016/j.scitotenv.2020.136547](https://doi.org/10.1016/j.scitotenv.2020.136547); pmid: 31958722
 65. K. R. Rhoads, E. M. L. Janssen, R. G. Luthy, C. S. Criddle, Aerobic biotransformation and fate of N-ethyl perfluorooctane sulfonamidoethanol (N-EtFOSE) in activated sludge. *Environ. Sci. Technol.* **42**, 2873–2878 (2008). doi: [10.1021/es702866c](https://doi.org/10.1021/es702866c); pmid: 18497137
 66. J. P. Benskin *et al.*, Biodegradation of N-ethyl perfluorooctane sulfonamido ethanol (EtFOSE) and EtFOSE-based phosphate diester (SAmPAP diester) in marine sediments. *Environ. Sci. Technol.* **47**, 1381–1389 (2013). doi: [10.1021/es304336r](https://doi.org/10.1021/es304336r); pmid: 23305554
 67. M. W. Sima, P. R. Jaffé, A critical review of modeling poly- and perfluoroalkyl substances (PFAS) in the soil-water environment. *Sci. Total Environ.* **757**, 143793 (2021). doi: [10.1016/j.scitotenv.2020.143793](https://doi.org/10.1016/j.scitotenv.2020.143793); pmid: 33303199
 68. N. Wang *et al.*, Fluorotelomer alcohol biodegradation-direct evidence that perfluorinated carbon chains breakdown. *Environ. Sci. Technol.* **39**, 7516–7528 (2005). doi: [10.1021/es0506760](https://doi.org/10.1021/es0506760); pmid: 16245823
 69. S. Mejía-Avendaño, S. Vo Duy, S. Sauvé, J. Liu, Generation of perfluoroalkyl acids from aerobic biotransformation of quaternary ammonium polyfluoroalkyl surfactants. *Environ. Sci. Technol.* **50**, 9923–9932 (2016). doi: [10.1021/acs.est.6b00140](https://doi.org/10.1021/acs.est.6b00140); pmid: 27477739
 70. J. Liu, S. Mejía-Avendaño, Microbial degradation of polyfluoroalkyl chemicals in the environment: A review. *Environ. Int.* **61**, 98–114 (2013). doi: [10.1016/j.envint.2013.08.022](https://doi.org/10.1016/j.envint.2013.08.022); pmid: 24126208
 71. J. R. Lang, B. M. Allred, J. A. Field, J. W. Lewis, M. A. Barlaz, National estimate of per- and polyfluoroalkyl substance (PFAS) release to U.S. municipal landfill leachate. *Environ. Sci. Technol.* **51**, 2197–2205 (2017). doi: [10.1021/acs.est.6b05005](https://doi.org/10.1021/acs.est.6b05005); pmid: 28103667
 72. Y. Liu *et al.*, From waste collection vehicles to landfills: Indication of per- and polyfluoroalkyl substance (PFAS) transformation. *Environ. Sci. Technol. Lett.* **8**, 66–72 (2021). doi: [10.1021/acs.estlett.0c00819](https://doi.org/10.1021/acs.estlett.0c00819)
 73. N. J. M. Fitzgerald, H. R. Temme, M. F. Simcik, P. J. Novak, Aqueous film forming foam and associated perfluoroalkyl substances inhibit methane production and Co-contaminant

- degradation in an anaerobic microbial community. *Environ. Sci. Process. Impacts* **21**, 1915–1925 (2019). doi: [10.1039/C9EM00241C](https://doi.org/10.1039/C9EM00241C); pmid: 31454014
74. J. W. Washington, J. E. Naile, T. M. Jenkins, D. G. Lynch, Characterizing fluorotelomer and polyfluoroalkyl substances in new and aged fluorotelomer-based polymers for degradation studies with GC/MS and LC/MS/MS. *Environ. Sci. Technol.* **48**, 5762–5769 (2014). doi: [10.1021/es500373b](https://doi.org/10.1021/es500373b); pmid: 24749955
 75. L. P. Wackett, S. L. Robinson, The ever-expanding limits of enzyme catalysis and biodegradation: Polyaromatic, polychlorinated, polyfluorinated, and polymeric compounds. *Biochem. J.* **477**, 2875–2891 (2020). doi: [10.1042/BCJ20190720](https://doi.org/10.1042/BCJ20190720); pmid: 32797216
 76. C. Tebes-Stevens, J. M. Patel, W. J. Jones, E. J. Weber, Prediction of Hydrolysis Products of Organic Chemicals under Environmental pH Conditions. *Environ. Sci. Technol.* **51**, 5008–5016 (2017). doi: [10.1021/acs.est.6b05412](https://doi.org/10.1021/acs.est.6b05412); pmid: 28430419
 77. A. W. Rose, H. E. Hawkes, J. S. Webb, *Geochemistry in Mineral Exploration*. (Academic, ed. 2, 1979).
 78. G. Friedlander, J. W. Kennedy, E. S. Macias, J. M. Miller, *Nuclear and Radiochemistry* (Wiley Interscience, ed. 3, 1981).
 79. K. Rankin, S. A. Mabury, T. M. Jenkins, J. W. Washington, A North American and global survey of perfluoroalkyl substances in surface soils: Distribution patterns and mode of occurrence. *Chemosphere* **161**, 333–341 (2016). doi: [10.1016/j.chemosphere.2016.06.109](https://doi.org/10.1016/j.chemosphere.2016.06.109); pmid: 27441993
 80. M. Shoenib, T. Harner, P. Vlahos, Perfluorinated chemicals in the arctic atmosphere. *Environ. Sci. Technol.* **40**, 7577–7583 (2006). doi: [10.1021/es0618999](https://doi.org/10.1021/es0618999); pmid: 17256497
 81. A. Gawor et al., Neutral polyfluoroalkyl substances in the global atmosphere. *Environ. Sci. Process. Impacts* **16**, 404–413 (2014). doi: [10.1039/C3EM00499F](https://doi.org/10.1039/C3EM00499F); pmid: 24232015
 82. M. Shoenib et al., Survey of polyfluorinated chemicals (PFCs) in the atmosphere over the northeast Atlantic Ocean. *Atmos. Environ.* **44**, 2887–2893 (2010). doi: [10.1016/j.jatmosenv.2010.04.056](https://doi.org/10.1016/j.jatmosenv.2010.04.056)
 83. A. Dreyer, I. Weinberg, C. Temme, R. Ebinghaus, Polyfluorinated compounds in the atmosphere of the Atlantic and Southern Oceans: Evidence for a global distribution. *Environ. Sci. Technol.* **43**, 6507–6514 (2009). doi: [10.1021/es9010465](https://doi.org/10.1021/es9010465); pmid: 19764209
 84. E. L. D'Ambro et al., Characterizing the air emissions, transport, and deposition of per- and polyfluoroalkyl substances from a fluoropolymer manufacturing facility. *Environ. Sci. Technol.* **55**, 862–870 (2021). doi: [10.1021/acs.est.0c06580](https://doi.org/10.1021/acs.est.0c06580); pmid: 33395278
 85. A. Dreyer, T. Kirchgeorg, I. Weinberg, V. Matthias, Particle-size distribution of airborne poly- and perfluorinated alkyl substances. *Chemosphere* **129**, 142–149 (2015). doi: [10.1016/j.chemosphere.2014.06.069](https://doi.org/10.1016/j.chemosphere.2014.06.069); pmid: 25027782
 86. D. A. Ellis et al., Atmospheric lifetime of fluorotelomer alcohols. *Environ. Sci. Technol.* **37**, 3816–3820 (2003). doi: [10.1021/es034136j](https://doi.org/10.1021/es034136j); pmid: 12967100
 87. J. J. MacInnis et al., Fate and transport of perfluoroalkyl substances from snowpacks into a lake in the High Arctic of Canada. *Environ. Sci. Technol.* **53**, 10753–10762 (2019). doi: [10.1021/acs.est.9b03372](https://doi.org/10.1021/acs.est.9b03372); pmid: 31412696
 88. J. W. Washington, K. Rankin, E. L. Libelo, D. G. Lynch, M. Cyterski, Determining global background soil PFAS loads and the fluorotelomer-based polymer degradation rates that can account for these loads. *Sci. Total Environ.* **651**, 2444–2449 (2019). doi: [10.1016/j.scitotenv.2018.10.071](https://doi.org/10.1016/j.scitotenv.2018.10.071); pmid: 30336434
 89. E. L. D'Ambro et al., Characterizing the air emissions, transport, and deposition of per- and polyfluoroalkyl substances from a fluoropolymer manufacturing facility. *Environ. Sci. Technol.* **55**, 862–870 (2021). doi: [10.1021/acs.est.0c06580](https://doi.org/10.1021/acs.est.0c06580); pmid: 33395278
 90. J. E. Galloway et al., Evidence of air dispersion: HFPO-DA and PFOA in Ohio and West Virginia surface water and soil near a fluoropolymer production facility. *Environ. Sci. Technol.* **54**, 7175–7184 (2020). doi: [10.1021/acs.est.9b07384](https://doi.org/10.1021/acs.est.9b07384); pmid: 32458687
 91. M. L. Brusseau, The influence of molecular structure on the adsorption of PFAS to fluid-fluid interfaces: Using QSPR to predict interfacial adsorption coefficients. *Water Res.* **152**, 148–158 (2019). doi: [10.1016/j.watres.2018.12.057](https://doi.org/10.1016/j.watres.2018.12.057); pmid: 30665161
 92. US Department of Agriculture, "Soil taxonomy: A basic system of soil classification for making and interpreting soil surveys (Agricultural Handbook No. 436, USDA, Soil Conservation Service, 1975); <https://www.nrcs.usda.gov/wps/portal/nrcs/main/soils/survey/class/taxonomy/>.
 93. X. Zhu, X. Song, J. Schwarzbauer, First insights into the formation and long-term dynamic behaviors of nonextractable perfluorooctanesulfonate and its alternative 6:2 chlorinated polyfluorinated ether sulfonate residues in a silty clay soil. *Sci. Total Environ.* **761**, 143230 (2021). doi: [10.1016/j.scitotenv.2020.143230](https://doi.org/10.1016/j.scitotenv.2020.143230); pmid: 33158517
 94. F. Xiao, B. Jin, S. A. Golovko, M. Y. Golovko, B. Xing, Sorption and desorption mechanisms of cationic and zwitterionic per- and polyfluoroalkyl substances in natural soils: Thermodynamics and hysteresis. *Environ. Sci. Technol.* **53**, 11818–11827 (2019). doi: [10.1021/acs.est.9b05379](https://doi.org/10.1021/acs.est.9b05379); pmid: 31553179
 95. T. M. H. Nguyen et al., Influences of chemical properties, soil properties, and solution pH on soil-water partitioning coefficients of per- and polyfluoroalkyl substances (PFASs). *Environ. Sci. Technol.* **54**, 15883–15892 (2020). doi: [10.1021/acs.est.0c05705](https://doi.org/10.1021/acs.est.0c05705); pmid: 33249833
 96. M. E. McGuire et al., Evidence of remediation-induced alteration of subsurface poly- and perfluoroalkyl substance distribution at a former firefighter training area. *Environ. Sci. Technol.* **48**, 6644–6652 (2014). doi: [10.1021/es5006187](https://doi.org/10.1021/es5006187); pmid: 24866261
 97. J. W. Washington, H. Yoo, J. J. Ellington, T. M. Jenkins, E. L. Libelo, Concentrations, distribution, and persistence of perfluoroalkylates in sludge-applied soils near Decatur, Alabama, USA. *Environ. Sci. Technol.* **44**, 8390–8396 (2010). doi: [10.1021/es1003846](https://doi.org/10.1021/es1003846); pmid: 20949951
 98. A. Borthakur et al., Release of soil colloids during flow interruption increases the pore-water PFAS concentration in saturated soil. *Environ. Pollut.* **286**, 117297 (2021). doi: [10.1016/j.envpol.2021.117297](https://doi.org/10.1016/j.envpol.2021.117297); pmid: 33971474
 99. A. C. Blaine et al., Perfluoroalkyl acid distribution in various plant compartments of edible crops grown in biosolids-amended soils. *Environ. Sci. Technol.* **48**, 7858–7865 (2014). doi: [10.1021/es500016s](https://doi.org/10.1021/es500016s); pmid: 24918303
 100. A. C. Blaine et al., Perfluoroalkyl acid uptake in lettuce (*Lactuca sativa*) and strawberry (*Fragaria ananassa*) irrigated with reclaimed water. *Environ. Sci. Technol.* **48**, 14361–14368 (2014). doi: [10.1021/es504150h](https://doi.org/10.1021/es504150h); pmid: 25386873
 101. A. C. Blaine et al., Uptake of perfluoroalkyl acids into edible crops via land applied biosolids: Field and greenhouse studies. *Environ. Sci. Technol.* **47**, 14062–14069 (2013). doi: [10.1021/es403094q](https://doi.org/10.1021/es403094q); pmid: 24206563
 102. L. Lesmeister et al., Extending the knowledge about PFAS bioaccumulation factors for agricultural plants - A review. *Sci. Total Environ.* **766**, 142640 (2021). doi: [10.1016/j.scitotenv.2020.142640](https://doi.org/10.1016/j.scitotenv.2020.142640); pmid: 33077210
 103. C. Xu et al., Occurrence, source apportionment, plant bioaccumulation and human exposure of legacy and emerging per- and polyfluoroalkyl substances in soil and plant leaves near a landfill in China. *Sci. Total Environ.* **776**, 145731 (2021). doi: [10.1016/j.scitotenv.2021.145731](https://doi.org/10.1016/j.scitotenv.2021.145731); pmid: 33647664
 104. I. Navarro et al., Bioaccumulation of emerging organic compounds (perfluoroalkyl substances and halogenated flame retardants) by earthworm in biosolid amended soils. *Environ. Res.* **149**, 32–39 (2016). doi: [10.1016/j.envres.2016.05.004](https://doi.org/10.1016/j.envres.2016.05.004); pmid: 27174781
 105. C. Eschazuer, K. J. Raat, P. J. Stuyfzand, P. De Voegt, Perfluorinated alkylated acids in groundwater and drinking water: Identification, origin and mobility. *Sci. Total Environ.* **458–460**, 477–485 (2013). doi: [10.1016/j.scitotenv.2013.04.066](https://doi.org/10.1016/j.scitotenv.2013.04.066); pmid: 23692852
 106. P. J. Lasier, J. W. Washington, S. M. Hassan, T. M. Jenkins, Perfluorinated chemicals in surface waters and sediments from northwest Georgia, USA, and their bioaccumulation in *Lumbriculus variegatus*. *Environ. Toxicol. Chem.* **30**, 2194–2201 (2011). doi: [10.1002/etc.622](https://doi.org/10.1002/etc.622); pmid: 21766321
 107. N. Pi, J. Z. Ng, B. C. Kelly, Uptake and elimination kinetics of perfluoroalkyl substances in submerged and free-floating aquatic macrophytes: Results of mesocosm experiments with *Echinodorus horemanii* and *Eichhornia crassipes*. *Water Res.* **117**, 167–174 (2017). doi: [10.1016/j.watres.2017.04.003](https://doi.org/10.1016/j.watres.2017.04.003); pmid: 28391121
 108. M. Bonato et al., PFAS environmental pollution and antioxidant responses: An overview of the impact on human field. *Int. J. Res. Public Health* **17**, 8020 (2020). pmid: 33143342
 109. E. M. Sunderland et al., A review of the pathways of human exposure to poly- and perfluoroalkyl substances (PFASs) and present understanding of health effects. *J. Expo. Sci. Environ. Epidemiol.* **29**, 131–147 (2019). doi: [10.1038/s41370-018-0094-1](https://doi.org/10.1038/s41370-018-0094-1); pmid: 30470793
 110. J. C. DeWitt, M. M. Peden-Adams, J. M. Keller, D. R. Germolec, Immunotoxicity of perfluorinated compounds: Recent developments. *Toxicol. Pathol.* **40**, 300–311 (2012). doi: [10.1177/019262311428473](https://doi.org/10.1177/019262311428473); pmid: 22109712
 111. H. K. Knutsen et al., Risk to human health related to the presence of perfluorooctane sulfonic acid and perfluorooctanoic acid in food. *EFSA J.* **16**, e05194 (2018). pmid: 32625773
 112. P. E. Goodrum, J. K. Anderson, A. L. Luz, G. K. Ansell, Application of a framework for grouping and mixtures toxicity assessment of PFAS: A closer examination of dose-additivity approaches. *Toxicol. Sci.* **179**, 262–278 (2021). doi: [10.1093/toxsci/kfaa123](https://doi.org/10.1093/toxsci/kfaa123); pmid: 32735321
 113. C. Dassuncao et al., Temporal shifts in poly- and perfluoroalkyl substances (PFASs) in North Atlantic pilot whales indicate large contribution of atmospheric precursors. *Environ. Sci. Technol.* **51**, 4512–4521 (2017). doi: [10.1021/acs.est.7b00293](https://doi.org/10.1021/acs.est.7b00293); pmid: 28350446
 114. E. S. Larson, J. M. Conder, J. A. Arblaster, Modeling avian exposures to perfluoroalkyl substances in aquatic habitats impacted by historical aqueous film forming foam releases. *Chemosphere* **201**, 335–341 (2018). doi: [10.1016/j.chemosphere.2018.03.004](https://doi.org/10.1016/j.chemosphere.2018.03.004); pmid: 29525662
 115. A. Koch et al., Characterization of an AFFF impacted freshwater environment using total fluorine, extractable organofluorine and suspect per- and polyfluoroalkyl substance screening analysis. *Chemosphere* **276**, 130179 (2021). doi: [10.1016/j.chemosphere.2021.130179](https://doi.org/10.1016/j.chemosphere.2021.130179); pmid: 33735649
 116. D. A. Miranda et al., Bioaccumulation of per- and polyfluoroalkyl substances (PFASs) in a tropical estuarine food web. *Sci. Total Environ.* **754**, 142146 (2021). doi: [10.1016/j.scitotenv.2020.142146](https://doi.org/10.1016/j.scitotenv.2020.142146); pmid: 33254889
 117. R. M. Janousek, J. Mayer, T. P. Knepper, Is the phase-out of long-chain PFASs measurable as fingerprint in a defined area? Comparison of global PFAS concentrations and a monitoring study performed in Hesse, Germany from 2014 to 2018. *Trends Analyt. Chem.* **120**, 115393 (2019). doi: [10.1016/j.trac.2019.01.017](https://doi.org/10.1016/j.trac.2019.01.017)
 118. M. J. Benotti et al., A forensic approach for distinguishing PFAS materials. *Environ. Forensics* **21**, 319–333 (2020). doi: [10.1080/15275922.2020.1771631](https://doi.org/10.1080/15275922.2020.1771631)
 119. D. Glaser et al., The impact of precursors on aquatic exposure assessment for PFAS: Insights from bioaccumulation modeling. *Integr. Environ. Assess. Manag.* **17**, 705–715 (2021). doi: [10.1002/ieam.4414](https://doi.org/10.1002/ieam.4414); pmid: 33739579
 120. A. O. De Silva et al., PFAS exposure pathways for humans and wildlife: A synthesis of current knowledge and key gaps in understanding. *Environ. Toxicol. Chem.* **40**, 631–657 (2021). doi: [10.1002/etc.4935](https://doi.org/10.1002/etc.4935); pmid: 33201517
 121. D. Muir et al., Levels and trends of poly- and perfluoroalkyl substances in the Arctic environment – An update. *Emerg. Contam.* **5**, 240–271 (2019). doi: [10.1016/j.jemcon.2019.06.002](https://doi.org/10.1016/j.jemcon.2019.06.002)
 122. C. A. Ng, K. Hungerbühler, Bioaccumulation of perfluorinated alkyl acids: Observations and models. *Environ. Sci. Technol.* **48**, 4637–4648 (2014). doi: [10.1021/es404008g](https://doi.org/10.1021/es404008g); pmid: 24762048
 123. C. Dassuncao et al., Shifting global exposures to poly- and perfluoroalkyl substances (PFASs) evident in longitudinal birth cohorts from a seafood-consuming population. *Environ. Sci. Technol.* **52**, 3738–3747 (2018). doi: [10.1021/acs.est.7b06044](https://doi.org/10.1021/acs.est.7b06044); pmid: 29516726
 124. J. L. Alesio, A. Slitt, G. D. Bothun, Critical new insights into the binding of poly- and perfluoroalkyl substances (PFAS) to albumin protein. *Chemosphere* **287**, 131979 (2022). doi: [10.1016/j.chemosphere.2021.131979](https://doi.org/10.1016/j.chemosphere.2021.131979); pmid: 34450368
 125. Y. Chen et al., Occurrence, profiles, and ecotoxicity of poly- and perfluoroalkyl substances and their alternatives in global apex predators: A critical review. *J. Environ. Sci. (China)* **109**, 219–236 (2021). doi: [10.1016/j.jes.2021.03.036](https://doi.org/10.1016/j.jes.2021.03.036); pmid: 34607670
 126. H. Yoo, J. W. Washington, T. M. Jenkins, J. J. Ellington, Quantitative determination of perfluorochemicals and fluorotelomer alcohols in plants from biosolid-amended fields using LC/MS/MS and GC/MS. *Environ. Sci. Technol.* **45**, 7985–7990 (2011). doi: [10.1021/es102972m](https://doi.org/10.1021/es102972m); pmid: 21247105
 127. L. P. Burkhard, Evaluation of published bioconcentration factor (BCF) and bioaccumulation factor (BAF) data for per- and

- polyfluoroalkyl substances across aquatic species. *Environ. Toxicol. Chem.* **40**, 1530–1543 (2021). doi: [10.1002/etc.5010](https://doi.org/10.1002/etc.5010); pmid: 33605484
128. K. Borgå et al., Trophic magnification factors: Considerations of ecology, ecosystems, and study design. *Integr. Environ. Assess. Manag.* **8**, 64–84 (2012). doi: [10.1002/ieam.244](https://doi.org/10.1002/ieam.244); pmid: 21674770
 129. J. M. Conder, R. A. Hoke, W. De Wolf, M. H. Russell, R. C. Buck, Are PFAs bioaccumulative? A critical review and comparison with regulatory criteria and persistent lipophilic compounds. *Environ. Sci. Technol.* **42**, 995–1003 (2008). doi: [10.1021/es070895g](https://doi.org/10.1021/es070895g); pmid: 18351063
 130. E. I. H. Loi et al., Trophic magnification of poly- and perfluorinated compounds in a subtropical food web. *Environ. Sci. Technol.* **45**, 5506–5513 (2011). doi: [10.1021/es200432n](https://doi.org/10.1021/es200432n); pmid: 21644538
 131. G. L. Lescord et al., Perfluorinated and polyfluorinated compounds in lake food webs from the Canadian high Arctic. *Environ. Sci. Technol.* **49**, 2694–2702 (2015). doi: [10.1021/es5048649](https://doi.org/10.1021/es5048649); pmid: 25604756
 132. J. W. Martin, D. M. Whittle, D. C. G. Muir, S. A. Mabury, Perfluoroalkyl contaminants in a food web from Lake Ontario. *Environ. Sci. Technol.* **38**, 5379–5385 (2004). doi: [10.1021/es049331s](https://doi.org/10.1021/es049331s); pmid: 15543740
 133. S. L. Simpson et al., Chronic effects and thresholds for estuarine and marine benthic organism exposure to perfluorooctane sulfonic acid (PFOS)-contaminated sediments: Influence of organic carbon and exposure routes. *Sci. Total Environ.* **776**, 146008 (2021). doi: [10.1016/j.scitotenv.2021.146008](https://doi.org/10.1016/j.scitotenv.2021.146008)
 134. B. González-Gaya, P. Casal, E. Jurado, J. Dachs, B. Jiménez, Vertical transport and sinks of perfluoroalkyl substances in the global open ocean. *Environ. Sci. Process. Impacts* **21**, 1957–1969 (2019). doi: [10.1039/C9EM00266A](https://doi.org/10.1039/C9EM00266A); pmid: 31393489
 135. L. Ahrens, M. Bundschuh, Fate and effects of poly- and perfluoroalkyl substances in the aquatic environment: A review. *Environ. Toxicol. Chem.* **33**, 1921–1929 (2014). doi: [10.1002/etc.2663](https://doi.org/10.1002/etc.2663); pmid: 24924660
 136. G. Hoover, S. Kar, S. Guffey, J. Leszczynski, M. S. Sepúlveda, In vitro and in silico modeling of perfluoroalkyl substances mixture toxicity in an amphibian fibroblast cell line. *Chemosphere* **233**, 25–33 (2019). doi: [10.1016/j.chemosphere.2019.05.065](https://doi.org/10.1016/j.chemosphere.2019.05.065); pmid: 31163305
 137. C. J. McCarthy, S. A. Roark, E. T. Middleton, Considerations for toxicity experiments and risk assessments with PFAS mixtures. *Integr. Environ. Assess. Manag.* **17**, 697–704 (2021). doi: [10.1002/ieam.4415](https://doi.org/10.1002/ieam.4415); pmid: 33749053
 138. K. Ji et al., Toxicity of perfluorooctane sulfonic acid and perfluorooctanoic acid on freshwater macroinvertebrates (*Daphnia magna* and *Moina macrocopia*) and fish (*Oryzias latipes*). *Environ. Toxicol. Chem.* **27**, 2159–2168 (2008). doi: [10.1897/07-523.1](https://doi.org/10.1897/07-523.1); pmid: 18593212
 139. Z. Li, Z. Yu, P. Gao, D. Yin, Multigenerational effects of perfluorooctanoic acid on lipid metabolism of *Caenorhabditis elegans* and its potential mechanism. *Sci. Total Environ.* **703**, 134762 (2020). doi: [10.1016/j.scitotenv.2019.134762](https://doi.org/10.1016/j.scitotenv.2019.134762); pmid: 31761367
 140. M. I. Chowdhury, T. Sana, L. Panneerselvam, R. Dharmarajan, M. Megharaj, Acute toxicity and trans-generational effects of perfluorobutane sulfonate in *Caenorhabditis elegans*. *Environ. Toxicol. Chem.* **40**, 1973–1982 (2021). doi: [10.1002/etc.5055](https://doi.org/10.1002/etc.5055); pmid: 33792982
 141. B. C. Crone et al., Occurrence of per- and polyfluoroalkyl substances (PFAS) in source water and their treatment in drinking water. *Crit. Rev. Environ. Sci. Technol.* **49**, 2359–2396 (2019). doi: [10.1080/10643389.2019.1614848](https://doi.org/10.1080/10643389.2019.1614848); pmid: 32831535
 142. US Environmental Protection Agency, “Per- and polyfluoroalkyl substances (PFAS): Incineration to manage PFAS waste streams” (EPA, 2019); https://www.epa.gov/sites/production/files/2019-09/documents/technical_brief_pfases_incineration_ioaa_approved_final_july_2019.pdf.
 143. L. J. Winchell et al., Per- and polyfluoroalkyl substances thermal destruction at water resource recovery facilities: A state of the science review. *Water Environ. Res.* **93**, 826–843 (2021). doi: [10.1002/wer.1483](https://doi.org/10.1002/wer.1483); pmid: 33190313
 144. I. Ross et al., A review of emerging technologies for remediation of PFASs. *Rem. J.* **28**, 101–126 (2018). doi: [10.1002/rem.21553](https://doi.org/10.1002/rem.21553)
 145. US Environmental Protection Agency, “Interim guidance on PFAS destruction and disposal (Report EO 12866 - 12-17-20 - 508, EPA, 2020); <https://www.regulations.gov/document/EPA-HQ-OLEM-2020-0527-0002>).
 146. G. B. Post, J. A. Gleason, K. R. Cooper, Key scientific issues in developing drinking water guidelines for perfluoroalkyl acids: Contaminants of emerging concern. *PLOS Biol.* **15**, e2002855 (2017). doi: [10.1371/journal.pbio.2002855](https://doi.org/10.1371/journal.pbio.2002855); pmid: 29261653
 147. US Environmental Protection Agency, “Drinking water treatability database” (EPA, 2021); <https://tdb.epa.gov/tdb/home>.
 148. X. Xiao, B. A. Ulrich, B. Chen, C. P. Higgins, Sorption of poly- and perfluoroalkyl substances (PFASs) relevant to aqueous film-forming foam (AFFF)-impacted groundwater by biochars and activated carbon. *Environ. Sci. Technol.* **51**, 6342–6351 (2017). doi: [10.1021/acs.est.7b00970](https://doi.org/10.1021/acs.est.7b00970); pmid: 28582977
 149. E. W. Tow et al., Managing and treating per- and polyfluoroalkyl substances (PFAS) in membrane concentrates. *AWWA Water Sci.* **3**, 1–23 (2021). doi: [10.1002/aws2.1233](https://doi.org/10.1002/aws2.1233); pmid: 34938982
 150. N. Bolan et al., Remediation of poly- and perfluoroalkyl substances (PFAS) contaminated soils - To mobilize or to immobilize or to degrade? *J. Hazard. Mater.* **401**, 123892 (2021). doi: [10.1016/j.jhazmat.2020.123892](https://doi.org/10.1016/j.jhazmat.2020.123892); pmid: 33113753
 151. E. Barth, J. McKernan, D. Bless, K. Dasu, Investigation of an immobilization process for PFAS contaminated soils. *J. Environ. Manage.* **296**, 113069 (2021). doi: [10.1016/j.jenvman.2021.113069](https://doi.org/10.1016/j.jenvman.2021.113069); pmid: 34225046
 152. The Chemours Company, Fayetteville Works Plant, “Thermal oxidizer performance test report: Chemours Company Fayetteville Works” (Focus Project No. P-001393, Chemours, 2020); <https://www.chemours.com/en/-/media/files/corporate/fayetteville-works/2020-03-thermal-oxidizer-test-report.pdf>.
 153. M. Y. Khan, S. So, G. da Silva, Decomposition kinetics of perfluorinated sulfonic acids. *Chemosphere* **238**, 124615 (2020). doi: [10.1016/j.chemosphere.2019.124615](https://doi.org/10.1016/j.chemosphere.2019.124615); pmid: 31454742
 154. S. Rayne, K. Forest, Perfluoroalkyl sulfonic and carboxylic acids: A critical review of physicochemical properties, levels and patterns in waters and wastewaters, and treatment methods. *J. Environ. Sci. Health A Tox. Hazard. Subst. Environ. Eng.* **44**, 1145–1199 (2009). doi: [10.1080/10934520903139811](https://doi.org/10.1080/10934520903139811); pmid: 19847705
 155. T. P. Riedel et al., Low temperature thermal treatment of gas-phase fluorotelomer alcohols by calcium oxide. *Chemosphere* **272**, 129859 (2021). doi: [10.1016/j.chemosphere.2021.129859](https://doi.org/10.1016/j.chemosphere.2021.129859); pmid: 34675448
 156. B. N. Nzeribe, M. Crimi, S. Mededovic Thagard, T. M. Holsen, Physico-Chemical Processes for the Treatment of Per-And Polyfluoroalkyl Substances (PFAS): A review. *Crit. Rev. Environ. Sci. Technol.* **49**, 866–915 (2019). doi: [10.1080/10643389.2018.1542916](https://doi.org/10.1080/10643389.2018.1542916)
 157. C. F. Kwiakowski et al., Scientific basis for managing PFAS as a chemical class. *Environ. Sci. Technol. Lett.* **7**, 532–543 (2020). doi: [10.1021/acs.estlett.0c00255](https://doi.org/10.1021/acs.estlett.0c00255); pmid: 34307722
 158. US Environmental Protection Agency, “Fact sheet: 2010/2015 PFOA Stewardship Program” (EPA, 2010); <https://www.epa.gov/assessing-and-managing-chemicals-under-tsca/fact-sheet-20102015-pfoa-stewardship-program>.
 159. US Environmental Protection Agency, “Premanufacture notification exemption for polymers; amendment of polymer exemption rule to exclude certain perfluorinated polymers” (EPA, 2010); <https://www.regulations.gov/document/EPA-HQ-OPPT-2002-0051-0080>.
 160. US Environmental Protection Agency, “Long-chain perfluoroalkyl carboxylate and perfluoroalkyl sulfonate chemical substances; significant new use rule” (EPA, 2020); <https://www.federalregister.gov/documents/2020/07/27/2020-13738/long-chain-perfluoroalkyl-carboxylate-and-perfluoroalkyl-sulfonate-chemical-substances-significant>.
 161. US Environmental Protection Agency, “EPA administrator Regan announces comprehensive national strategy to confront PFAS pollution” (EPA, 2021); <https://www.epa.gov/newsreleases/epa-administrator-regan-announces-comprehensive-national-strategy-confront-pfas>.
 162. SGS, “Denmark bans PFAS chemicals in food contact paper and board” (SGS, 2019); <https://www.sgs.com/en/news/2020/05/safeguards-07320-denmark-bans-pfas-chemicals-in-food-contact-paper-and-board>.
 163. Z. Wang et al., We need a global science-policy body on chemicals and waste. *Science* **371**, 774–776 (2021). doi: [10.1126/science.abe9090](https://doi.org/10.1126/science.abe9090); pmid: 33602839
 164. W. Zhang et al., Manufacture of hydrofluorocarbons and hydrofluoroolefins as the CFCs-alternatives: From fundamental of catalytic reaction to commercialisation. *Scientia Sin. Chim.* **47**, 1312–1325 (2017). doi: [10.1360/NO32017-00105](https://doi.org/10.1360/NO32017-00105)

ACKNOWLEDGMENTS

We thank T. Collette, C. Lau, K. Godineaux, J. Johnston, B. Schumacher, B. Fisher, G. Hagler, T. Watkins, B. Rodan, and S. Burden and the anonymous referees for helpful comments and suggestions. **Funding:** This research was supported by the EPA Office of Research and Development; North Carolina State University (NCSU), the National Institute of Environmental Health Sciences of the National Institutes of Health (P42ES031009); and ETH Zürich, Institute of Environmental Engineering. It has been subjected to the EPA’s administrative review and approved for publication. Mention of trade names or commercial products does not constitute endorsement or recommendation for use. The views expressed in this article are those of the authors and do not necessarily represent the views or policies of the EPA. **Author contributions:** M.J.B.D., M.G.E., and J.P.M. wrote the print summary; A.B.L., M.J.S., and Z.W. wrote the products section; M.G.E., C.T.S., and E.J.W. wrote the degradation section; M.J.B.D. and J.W.W. wrote the mobility section; B.A., J.A.A., and W.M.H. wrote the exposure section; D.R.U.K., J.P.M., and T.F.S. wrote the remediation section. **Competing interests:** Z.W. has received compensation from the Organisation of Economic Co-operation and Development (OECD) to develop a synthesis report on side-chain fluorinated polymers. D.R.U.K. serves on the North Carolina Secretaries’ Science Advisory Board. The remaining authors declare no competing interests.

10.1126/science.abg9065

RESEARCH ARTICLE SUMMARY

IMMUNOLOGY

CRISPR activation and interference screens decode stimulation responses in primary human T cells

Ralf Schmidt†, Zachary Steinhart†, Madeline Layeghi, Jacob W. Freimer, Raymund Bueno, Vinh Q. Nguyen, Franziska Blaesche, Chun Jimmie Ye, Alexander Marson*

INTRODUCTION: Human T cell responses to antigen stimulation, including the production of cytokines, are critical for healthy immune function and can be dysregulated in autoimmunity, immunodeficiencies, and cancer. A systematic understanding of the regulators that orchestrate T cell activation with gain-of-function and loss-of-function gene perturbations would offer additional insights into disease pathways and further opportunities to engineer next-generation immunotherapies.

RATIONALE: Although CRISPR activation (CRISPRa) and CRISPR interference (CRISPRi) screens are powerful tools for gain-of-function and loss-of-function studies in immortalized cell lines, deploying them at scale in primary cell types has been challenging. Here, we developed a CRISPRa and CRISPRi discovery

platform in primary human T cells and performed genome-wide screens for functional regulators of cytokine production in response to stimulation.

RESULTS: We optimized lentiviral methods to enable efficient and scalable delivery of the CRISPRa machinery into primary human T cells. This platform allowed us to perform genome-wide pooled CRISPRa screens to discover regulators of cytokine production. Pools of CRISPRa-perturbed cells were isolated by fluorescence-activated cell sorting into high and low bins based on levels of endogenous Interleukin-2 (IL-2) production in CD4⁺ T cells or interferon- γ (IFN- γ) production in CD8⁺ T cells. Hits included proximal T cell receptor (TCR) signaling pathway genes, indicating that overexpression of these components

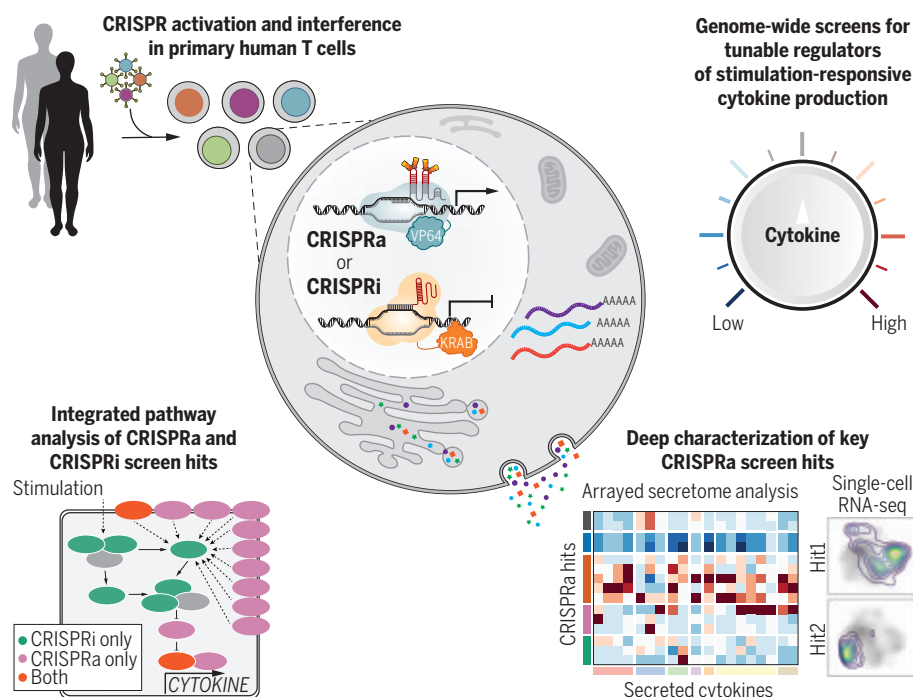
could overcome signaling “bottlenecks” and tune stimulation and cytokine production.

Reciprocal genome-wide loss-of-function screens with CRISPRi detected hits with critical regulatory functions, including some missed by CRISPRa. By contrast, CRISPRa also identified hits that may not be required and in some cases were expressed at only low levels under the conditions of the screen. This was strongly exemplified by regulation of IFN- γ production by the nuclear factor κ B (NF- κ B) signaling pathway, in which CRISPRi identified a required TCR–NF- κ B signaling circuit (including *MALT1* and *BCL10*). CRISPRa selectively detected a set of tumor necrosis factor superfamily receptors that also signal through NF- κ B, including 4-1BB, CD27, CD40, and OX40. These receptors were not individually required for signaling in our experimental conditions but could promote IFN- γ when overexpressed. Thus, CRISPRa and CRISPRi complement each other for the comprehensive discovery of functional cytokine regulators.

Arrayed CRISPRa perturbation validated the effects of key hits in CD4⁺ and CD8⁺ T cells. We also assessed how individual CRISPRa perturbations more broadly reprogram cytokine production beyond IL-2 and IFN- γ by measuring a panel of secreted cytokines and chemokines.

Finally, we developed a platform for pooled CRISPRa perturbations coupled with single-cell RNA-sequencing (scRNA-seq) readout (CRISPRa Perturb-seq) in primary human T cells. We used CRISPRa Perturb-seq for deep molecular characterization of single-cell states caused by 70 genome-wide screen hits and controls to reveal how regulators of cytokine production both tune T cell activation and program cells into different stimulation-responsive states.

CONCLUSIONS: Our study demonstrates a robust platform for large-scale pooled CRISPRa and CRISPRi in primary human T cells. Paired CRISPRa and CRISPRi screens enabled comprehensive functional mapping of gene networks that can modulate cytokine production. Follow-up of CRISPRa hits with arrayed phenotypic analyses and with pooled scRNA-seq approaches enabled precise functional characterization of key screen hits, revealing how key perturbations may tune T cells to therapeutically relevant states. Future CRISPRa and CRISPRi screens in primary cells could identify targets for improved next-generation cellular therapies. ■



Genome-wide CRISPRa/i screens discover tunable regulators of stimulation-responsive cytokine production in primary human T cells. Genome-wide CRISPRa/i gain-of-function and loss-of-function screens in human T cells allowed for systematic identification of regulators of cytokine production. Follow-up on key CRISPRa screen hits with secretome and scRNA-seq analysis helped to decode how these regulators tune T cell activation and program cells into different stimulation-responsive states.

The list of author affiliations is available in the full article online.

*Corresponding author. Email: alexander.marson@ucsf.edu

†These authors contributed equally to this work and are co-first authors.

Cite this article as R. Schmidt et al., *Science* 375, eabj4008 (2022). DOI: 10.1126/science.abj4008

S READ THE FULL ARTICLE AT
<https://doi.org/10.1126/science.abj4008>

RESEARCH ARTICLE

IMMUNOLOGY

CRISPR activation and interference screens decode stimulation responses in primary human T cells

Ralf Schmidt^{1,2,†}, Zachary Steinhart^{1,2,†}, Madeline Layeghi¹, Jacob W. Freimer^{1,2,3},
Raymund Bueno², Vinh Q. Nguyen⁴, Franziska Blaesche^{1,2},
Chun Jimmie Ye^{1,2,5,10,11,12,13,14}, Alexander Marson^{1,2,5,6,7,8,9,10,11,*}

Regulation of cytokine production in stimulated T cells can be disrupted in autoimmunity, immunodeficiencies, and cancer. Systematic discovery of stimulation-dependent cytokine regulators requires both loss-of-function and gain-of-function studies, which have been challenging in primary human cells. We now report genome-wide CRISPR activation (CRISPRa) and interference (CRISPRi) screens in primary human T cells to identify gene networks controlling interleukin-2 (IL-2) and interferon- γ (IFN- γ) production. Arrayed CRISPRa confirmed key hits and enabled multiplexed secretome characterization, revealing reshaped cytokine responses. Coupling CRISPRa screening with single-cell RNA sequencing enabled deep molecular characterization of screen hits, revealing how perturbations tuned T cell activation and promoted cell states characterized by distinct cytokine expression profiles. These screens reveal genes that reprogram critical immune cell functions, which could inform the design of immunotherapies.

Regulated T cell cytokine production in response to stimulation is critical for balanced immune responses. Cytokine dysregulation can lead to autoimmunity, immunodeficiency, and immune evasion in cancer (1–4). Interleukin-2 (IL-2), which is secreted predominantly by CD4⁺ T cells, drives T cell expansion (5) and is therapeutically applied in autoimmunity and cancer at different doses (6). Interferon- γ (IFN- γ) is a cytokine secreted by both CD4⁺ and CD8⁺ T cells that promotes a type I immune response against intracellular pathogens, including viruses (4), and is correlated with positive cancer immunotherapy responses (7–9). Much of our current

understanding of the pathways leading to cytokine production in humans originates from studies in transformed T cell lines, which often are not representative of primary human cell biology (10–12). Comprehensive understanding of pathways that control cytokine production in primary human T cells would facilitate the development of next-generation immunotherapies.

Unbiased forward genetic approaches can uncover the components of regulatory networks systematically, but challenges with efficient Cas9 delivery have limited their application in primary cells. Genome-wide CRISPR knockout screens have been completed using primary mouse immune cells from Cas9-expressing transgenic mice (13–15), including a screen for regulators of innate cytokine production in dendritic cells (13). Genome-scale CRISPR studies in human primary cells have recently been accomplished using transient Cas9 electroporation to introduce gene knockouts (16, 17). However, comprehensive discovery of regulators requires both gain-of-function and loss-of-function studies. For example, CRISPR activation (CRISPRa) gain-of-function screens can discover genes that may not normally be active in the tested conditions but can promote phenotypes of interest (18, 19). In contrast to a CRISPR knockout, CRISPRa or CRISPR interference (CRISPRi) require the sustained expression of an endonuclease-dead Cas9 (dCas9) and, because of poor lentiviral delivery, has been limited to small-scale experiments in primary cells (20, 21). Here, we developed a CRISPRa and CRISPRi screening platform in primary human T cells, which allowed for the systematic discovery of genes

and pathways that can be perturbed to tune stimulation-dependent cytokine responses.

Genome-wide CRISPRa screens identify regulators of IL-2 and IFN- γ production in T cells

To enable scalable CRISPRa in primary human T cells, we developed an optimized high-titer lentiviral production protocol with a minimal dCas9-VP64 vector (pZR112), allowing for transduction efficiencies up to 80% (fig. S1). A second-generation CRISPRa synergistic activation mediator (SAM) system (22, 23) induced robust increases in target expression of established surface markers (fig. S2). Next, we scaled up our platform to perform pooled genome-wide CRISPRa screens targeting >18,800 protein-coding genes with >112,000 single-guide RNAs (sgRNAs) (22). We used fluorescence-activated cell sorting (FACS) to separate IL-2-producing CD4⁺ T cells and IFN- γ -producing CD8⁺ T cells into high and low bins (Fig. 1A and fig. S3A to D). Subsequent sgRNA quantification confirmed that sgRNAs targeting IL-2 (*IL2*) and IFN- γ (*IFNG*) were strongly enriched in the respective cytokine high populations, and nontargeting control sgRNAs were not enriched in either bin (Fig. 1B). Both CRISPRa screens were highly reproducible in two different human blood donors (Fig. 1, C and D, and fig. S3, E and F). Gene-level statistical analysis of the IL-2 and IFN- γ CRISPRa screens revealed 444 and 471 hits, respectively, including 171 shared hits (Fig. 1E; fig. S3, G and H; and tables S1 and S2). Thus, CRISPRa screens provide a robust platform to discover gain-of-function regulators of stimulation-dependent responses in primary cells.

CRISPRa hits included components of the T cell receptor (TCR) signaling pathway and T cell transcription factors. Activation of *TBX21* (encoding T-bet), which promotes both memory CD8⁺ T cell and CD4⁺ T helper cell 1 (T_H1) differentiation (24–26), selectively enhanced the signature type I cytokine IFN- γ (Fig. 1E). By contrast, sgRNAs activating *GATA3*, which promotes type II differentiation by antagonizing T-bet (25, 27), had the opposite effects (Fig. 1E). Overexpression of members of the proximal TCR signaling complex, such as *VAV1*, *CD28*, *LCP2* (encoding SLP-76), and *LAT* (28, 29) reinforced T cell activation and were enriched in both cytokine-high bins. Conversely, the negative TCR signaling regulators *MAP4K1* and *SLA2* were depleted in these bins (Fig. 1, B and E) (30, 31). Thus, CRISPRa identifies critical “bottlenecks” in signals leading to cytokine production.

Complementary CRISPRa and CRISPRi screens comprehensively reveal circuits of cytokine production in T cells

CRISPRa screens were effective in identifying limiting factors in cytokine production but

¹Gladstone-UCSF Institute of Genomic Immunology, San Francisco, CA 94158, USA. ²Department of Medicine, University of California San Francisco, San Francisco, CA 94143, USA. ³Department of Genetics, Stanford University, Stanford, CA 94305, USA. ⁴Department of Surgery, University of California San Francisco, San Francisco, CA 94143, USA. ⁵Chan Zuckerberg Biohub, San Francisco, CA 94158, USA. ⁶Department of Microbiology and Immunology, University of California San Francisco, San Francisco, CA 94143, USA. ⁷Diabetes Center, University of California San Francisco, San Francisco, CA 94143, USA. ⁸Innovative Genomics Institute, University of California Berkeley, Berkeley, CA 94720, USA. ⁹UCSF Helen Diller Family Comprehensive Cancer Center, University of California San Francisco, San Francisco, CA 94158, USA. ¹⁰Parker Institute for Cancer Immunotherapy, University of California San Francisco, San Francisco, CA 94129, USA. ¹¹Institute for Human Genetics, University of California San Francisco, San Francisco, CA 94143, USA. ¹²Department of Epidemiology and Biostatistics, University of California, San Francisco, San Francisco, CA 94158, USA. ¹³Department of Bioengineering and Therapeutic Sciences, University of California, San Francisco, San Francisco, CA 94158, USA. ¹⁴Baker Computational Health Sciences Institute, University of California, San Francisco, San Francisco, CA 94143, USA.

*Corresponding author. Email: alexander.marson@ucsf.edu
†These authors contributed equally to this work and are co-first authors.

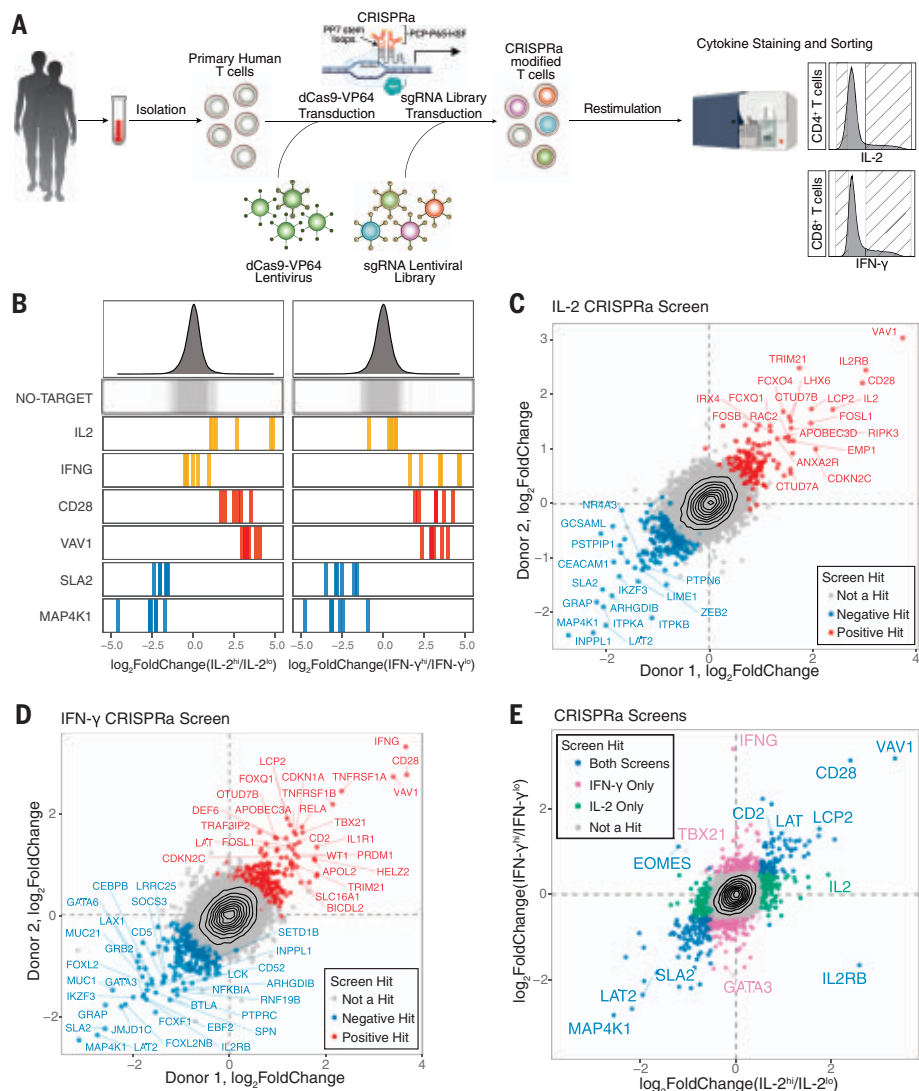


Fig. 1. Genome-wide CRISPRa screens for cytokine production in stimulated primary human T cells. (A) Schematic of CRISPRa screens. (B) sgRNA \log_2 -fold changes for genes of interest in IL-2 (left) and IFN- γ (right) screens. Bars represent the mean \log_2 -fold change for each sgRNA across two human blood donors. Density plots above represent the distribution of all sgRNAs. (C and D) Scatter plots of median sgRNA \log_2 -fold change (high/low sorting bins) for each gene, comparing screens in two donors, for IL-2 (C) and IFN- γ (D) screens. (E) Comparison of gene \log_2 -fold change (median sgRNA, mean of two donors) in IL-2 and IFN- γ screens.

they could miss necessary components that would only be identified through loss-of-function studies. We therefore performed reciprocal genome-wide CRISPRi screens, adapting our optimized lentiviral protocols (Fig. 2, A and B; fig. S4; and tables S1 and 2). Dropout of gold standard essential genes (32) and reproducibility across two human donors confirmed the screen quality (fig. S5). The CRISPRi IL-2 and IFN- γ screens identified 226 and 203 gene hits, respectively, including 92 shared hits (Fig. 2, A and B). As expected, the CRISPRi hits were biased toward genes with high mRNA expression, including members of the CD3 complex, whereas CRISPRa additionally identified

regulators that were expressed either at low levels or not at all in T cells under the screened conditions (Fig. 2, C and D, and fig. S6). For example, *PIK3AP1* and *IL1R1* were expressed at low levels under the screened conditions (fig. S7A). They are potentially inducible in some T cell contexts (fig. S7, B to D); however, they were detected as hits by CRISPRa but not CRISPRi.

The power of coupling activation and interference screening was exemplified further by the identification of two IFN- γ -regulating circuits. CRISPRi screens identified key components of the nuclear factor κ B (NF- κ B) pathway that are required for IFN- γ production (and,

to a lesser extent, IL-2 production). CRISPRi detected a circuit of T cell stimulation signaling through MAL1, BCL10, TRAF6, and TAK1 (encoded by *MAP3K7*) to the inhibitor of the NF- κ B complex (I κ B complex, encoded by *CHUK*, *IKBKB*, and *IKBK*) that promotes IFN- γ production (Fig. 2, E and F, and fig. S8A). By contrast, CRISPRa revealed a set of positive IFN- γ regulators that included members of the tumor necrosis factor receptor superfamily (TNFRSF) and *IL1R1*. These regulators also signal through NF- κ B even though they are not individually required and therefore not detected by CRISPRi (Fig. 2, E and F). Thus, CRISPRa and CRISPRi complement each other for the comprehensive discovery of functional cytokine regulators.

To gain insights into functional pathways enriched across CRISPRi and CRISPRa screens, we completed gene set enrichment analysis (GSEA) of Kyoto Encyclopedia of Genes and Genomes (KEGG) pathways, identifying multiple immune-related pathways as being enriched across screens (fig. S8B). Furthermore, we analyzed data from numerous genome-wide association studies (GWAS) to determine whether the heritability of complex immune traits was enriched in genomic regions harboring our screen hits by stratified linkage disequilibrium score regression (s-LDSC). Both CRISPRi and CRISPRa regulators of IFN- γ and CRISPRa regulators of IL-2 were in regions enriched for immune trait heritability compared with nonimmune traits or an expression-matched background set (fig. S8C). Thus, these forward genetic screens may serve as a resource to help prioritize candidate functional genes in genomic regions associated with complex immune diseases.

We next completed integrative analyses of gene hits across CRISPRa and CRISPRi screens for both cytokines. We found that a few genes were identified across all screens (e.g., *ZAP70* as a positive regulator and *CBLB* as a negative regulator), representing core regulators of stimulation-responsive cytokine production in T cells. Most hits, however, were either cytokine-specific (IL-2 in CD4⁺ T cells or IFN- γ in CD8⁺ T cells) or perturbation-specific (activation or interference) (fig. S8D). For a few target genes, including *PTPRC* (CD45), CRISPRa and CRISPRi both influenced cytokine production in the same direction, suggesting that for some genes, activation and interference both impair optimal levels (fig. S8E). The marked overlap in regulators between IL-2 in CD4⁺ T cells and IFN- γ in CD8⁺ T cells led us to perform additional genome-wide CRISPRa screens for IL-2, IFN- γ , and TNF- α in CD4⁺ T cells, allowing for direct comparisons of type 1 cytokine regulators in CD4⁺ T cells (fig. S9). Many of the strongest positive (e.g., *VAV1*, *CD28*, and *LCP2*) and negative hits (e.g., *MAP4K1*, *LAT2*, and *GRAP*)

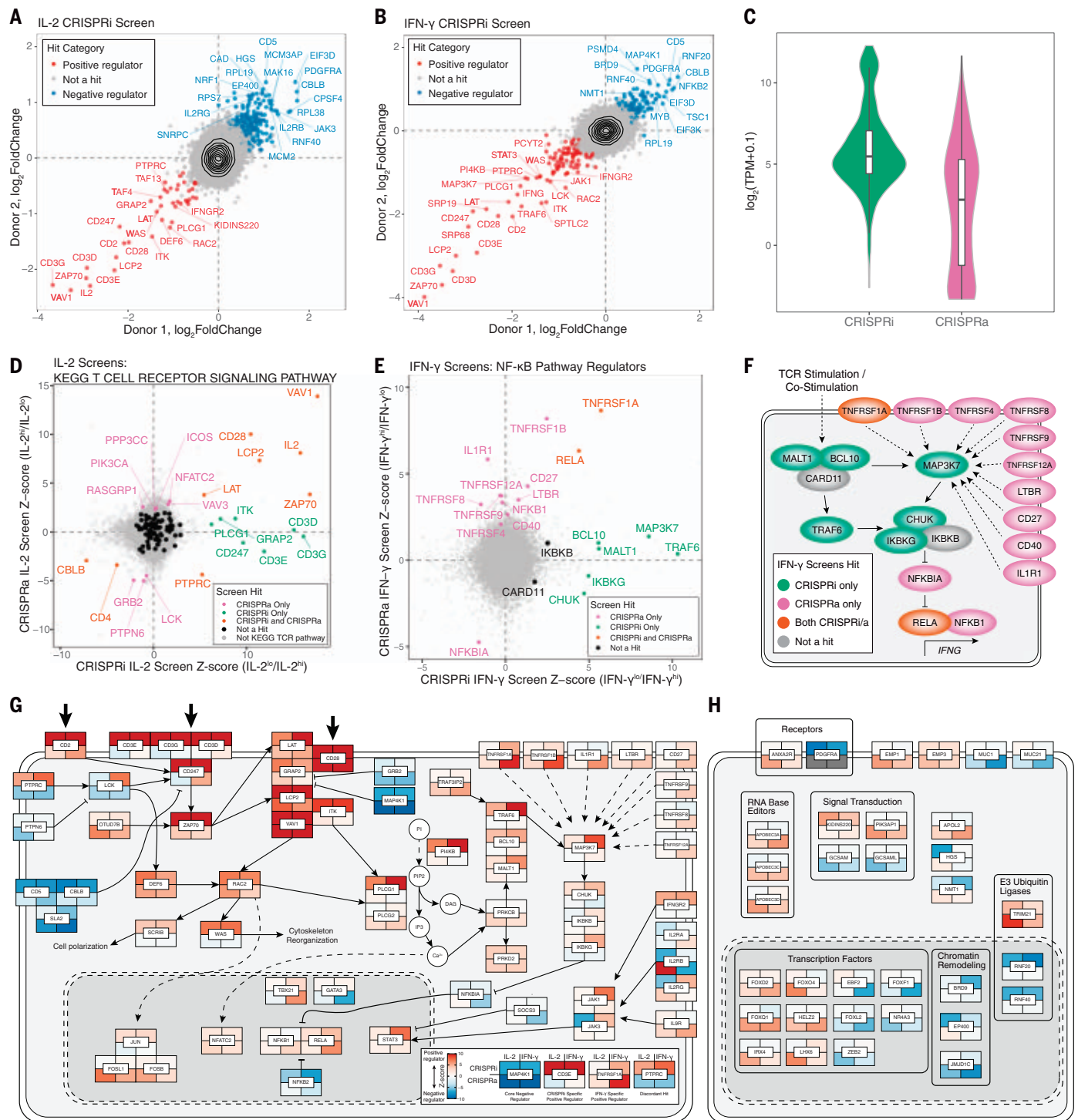


Fig. 2. Integrated CRISPRa and CRISPRi screens mapping the genetic circuits underlying T cell cytokine response in high resolution. (A and B) Median sgRNA log₂-fold change (high/low sorting bins) for each gene, comparing CRISPRi screens in two donors, for IL-2 (A) and IFN-γ (B) screens. (C) Distributions of gene mRNA expression for CRISPRa and CRISPRi cytokine screen hits in resting CD4⁺ T cells (this study). (D) Comparison of IL-2 CRISPRi and CRISPRa screens with genes belonging to the TCR signaling pathway (KEGG pathways) indicated in colors other than gray. (E) Comparison of IFN-γ CRISPRi and CRISPRa screens with manually selected NF-κB pathway regulators labeled. All other genes are shown in gray. (F) Map of NF-κB pathway regulators labeled in (D). (G) Map of screen hits with previous evidence of defined function in T cell stimulation and costimulation

signal transduction pathways. Genes shown are significant hits in at least one screen and were selected based on review of the literature and pathway databases (e.g., KEGG and Reactome). Tiles represent proteins encoded by indicated genes with the caveat that, because of space constraints, subcellular localization is inaccurate because many of the components shown in the cytoplasm occur at the plasma membrane. Tiles are colored according to log₂-fold change Z score, as shown in the subpanel, with examples of different hits. Large arrows at the top represent stimulation/costimulation sources. (H) Select screen hits with less well-described functions in T cells in the same format as (G). For (H), only significant hits from the top 20 positive and negative ranked genes by log₂-fold change for each screen were candidates for inclusion.

overlapped across all CRISPRa screens, likely representing core regulators of type 1 cytokine production in response to stimulation and costimulation. Additionally, these screens identified hits that could potentially increase or decrease individual cytokines selectively. Thus, CRISPRi and CRISPRa hits reveal both core and context-specific regulators of cytokine production.

We used our integrated dataset combined with literature review to build a high-resolution map of tunable regulators of signal transduction pathways leading to cytokine production (Fig. 2G). This included calcium pathway signaling genes (e.g., *PLCG1*, *PLCG2*, *PRKCB*, *PRKD2*, and *NFATC2*), and cytokine signaling genes (e.g., *STAT3*, *JAK1*, *JAK3*, and *SOC3*), the latter suggesting feedback circuits among cytokine signals. In particular, CRISPRa identified regulators absent from previous literature (e.g., *APOBEC3A/D/C*, *FOXQ1*, and *EMPI*) (Fig. 2H), underscoring the need for gain-of-function screens for comprehensive discovery. Thus, CRISPRa and CRISPRi screens complement one another to map the tunable genetic circuits controlling T cell stimulation-responsive cytokine production.

Arrayed characterization of selected CRISPRa screen hits

We next performed arrayed CRISPRa experiments for deeper phenotypic characterization of screen hits (Fig. 3A). We selected 14 screen hits (from different screen categories) (Fig. 3B) including the established regulators *VAV1* and *MAP4K1* and the positive controls *IL2* and *IFNG*. Notably, we included genes with relatively low expression in T cells under our experimental conditions, *FOXQ1*, *ILIR1*, *LHX6*, and *PIK3API* (fig. S7). First, we validated that selected sgRNAs increased the expression of target gene mRNA (fig. S10). Next, we assessed IL-2, IFN- γ , and TNF- α by intracellular staining in both CD4⁺ and CD8⁺ T cells. Thirteen of 14 target genes caused significant ($q < 0.05$) changes in the proportion of cells positive for the relevant cytokine(s), with at least one sgRNA (Fig. 3, C and D, and fig. S11). Furthermore, we observed effects on both IL-2 and IFN- γ double- and single-positive populations (fig. S12, A to C). With the exception of *TNFRSF1A* (and *IL2* or *IFNG*), positive regulators did not cause spontaneous cytokine production without stimulation (Fig. 3D and fig. S11B). Although IL-2 was screened in CD4⁺ T cells and IFN- γ in CD8⁺ T cells, CRISPRa sgRNA effects were highly correlated across both lineages (Fig. 3E). We also assessed T cell differentiation and observed that *FOXQ1* and *TNFRSF1A* significantly decreased the percentage of CD62L⁺ cells, indicating a shift toward effector T cell states as a potential mechanism (fig. S12D). Thus, these studies validate the pooled CRISPRa screens and begin to characterize

cytokine production and cell differentiation states promoted by activation of key target genes.

We next tested whether genes identified by CRISPRa could also regulate cytokines when overexpressed as cDNA transgenes, because continuous expression of CRISPRa would present challenges in cell therapies caused by Cas9 immunogenicity (33) (fig. S13A). cDNA transgene overexpression of CRISPRa hits affected cytokine production in T cells stimulated with antibodies or antigen-positive cancer cells (fig. S13, B to D). Thus, this strategy could potentially be used to implement CRISPRa discoveries in engineered T cell therapies.

We next assessed how individual CRISPRa perturbations reprogram cytokine production by measuring a broad panel of 48 secreted cytokines and chemokines, 32 of which were detected in control samples (fig. S14A and table S6). After confirming that the effects on IL-2, IFN- γ , and TNF- α measurements were generally consistent with intracellular staining (Fig. 3F and fig. S14B), we performed principal component analysis and hierarchical clustering on all cytokines. We observed sgRNA categorical grouping consistent with that observed in the screens, with sgRNAs targeting genes identified as regulators of both cytokines, causing broad increases or decreases in cytokine concentration (Fig. 3G and fig. S14C). There were distinct patterns in the classes of cytokines increased by different regulators (Fig. 3H). *VAV1* and *FOXQ1* (a transcription factor that has not been well characterized in T cells) led to preferential increases in type 1 signature cytokines and dampened type 2 cytokines. Unexpectedly, *OTUD7B*, a positive regulator of proximal TCR signaling (34), had a distinct effect and increased type 2 cytokines (fig. S14D). We next investigated whether modulations in the secretome correlated with transcriptional control of the corresponding genes. Taking *FOXQ1* as an example, we performed bulk RNA sequencing (RNA-seq) on *FOXQ1* and control sgRNA CD4⁺ T cells and found that it correlated strongly with the secretome effects (fig. S15). Thus, the identified regulators may not only modulate TCR stimulation and signaling but also tune the T cell secretome toward specific signatures.

CRISPRa Perturb-seq characterizes the molecular phenotypes of cytokine regulators

To assess the global molecular signatures resulting from each CRISPRa gene induction, we developed a platform to couple pooled CRISPRa perturbations with barcoded single-cell RNA-seq (scRNA-seq) readouts (CRISPRa Perturb-seq) (Fig. 4A). Because similar CRISPRa Perturb-seq approaches have been powerful in cell lines and animal models (35–37), we incorporated a direct-capture sequence into the CRISPRa-SAM modified sgRNA scaffold to

enable compatibility with droplet-based scRNA-seq methods (fig. S16).

We performed CRISPRa Perturb-seq characterization of regulators of stimulation responses in ~56,000 primary human T cells, targeting 70 hits and controls from our genome-wide CRISPRa cytokine screens (Fig. 4, A and B, and fig. S17, A to C). First, we confirmed that sgRNAs led to significant increases in the expression of their target genes (fig. S17D). Next, uniform manifold approximation and projection (UMAP) dimensionality reduction revealed discrete separation of the resting and restimulated cells (fig. S17E) and showed relatively even distribution of cells from two donors (Fig. 4C and fig. S17F). Gene signatures allowed us to resolve most T cells as either CD4⁺ or CD8⁺ (Fig. 4D and fig. S17, G and H). Thus, we generated a high-quality CRISPRa Perturb-seq dataset.

Cytokine production can be tuned by reinforced TCR signaling. To identify CRISPRa gene perturbations that tune the general strength of stimulation-responsive genes, we calculated a scRNA-seq “activation” score based on a gene signature that we derived by comparing resting and restimulated cells within the nontargeting control sgRNA group (fig. S18). Projecting activation scores on the stimulated cell UMAP revealed discrete regions of higher and lower activation scores among the restimulated cells (Fig. 4E). We next examined activation scores across CRISPRa perturbations (Fig. 4F). Negative regulators except *IKZF3* (encoding the transcription factor Aiolos) decreased activation scores, suggesting that they act to broadly dampen stimulation strength. By contrast, *IKZF3* reduced *IFNG* expression without reducing the overall activation score (Fig. 4F and fig. S19A), indicative of a possible distinct mechanism of cytokine gene regulation. Many of the positive regulators significantly increased activation score, with *VAV1* causing the strongest activation potentiation (Fig. 4F). Thus, many, but not all, hits act by tuning overall T cell activation to varying degrees.

We next investigated how different perturbations affected the expression of cytokine and other effector genes in stimulated cells. We analyzed pseudobulk differential gene expression under restimulated conditions for each sgRNA target cell group compared with no-target control cells (fig. S19, A and B). *IFNG* was differentially expressed in 29 different sgRNA targets, with only sgRNAs targeting negative regulators causing decreased expression. *IL2*, however, was barely detectable by scRNA-seq (fig. S19C). Only *IL2* and *VAV1* sgRNAs caused its increased expression, consistent with our observations that *VAV1* activation caused the greatest level of IL-2 release (Fig. 3H). Many of the negative regulators drove a stereotyped pattern of differential

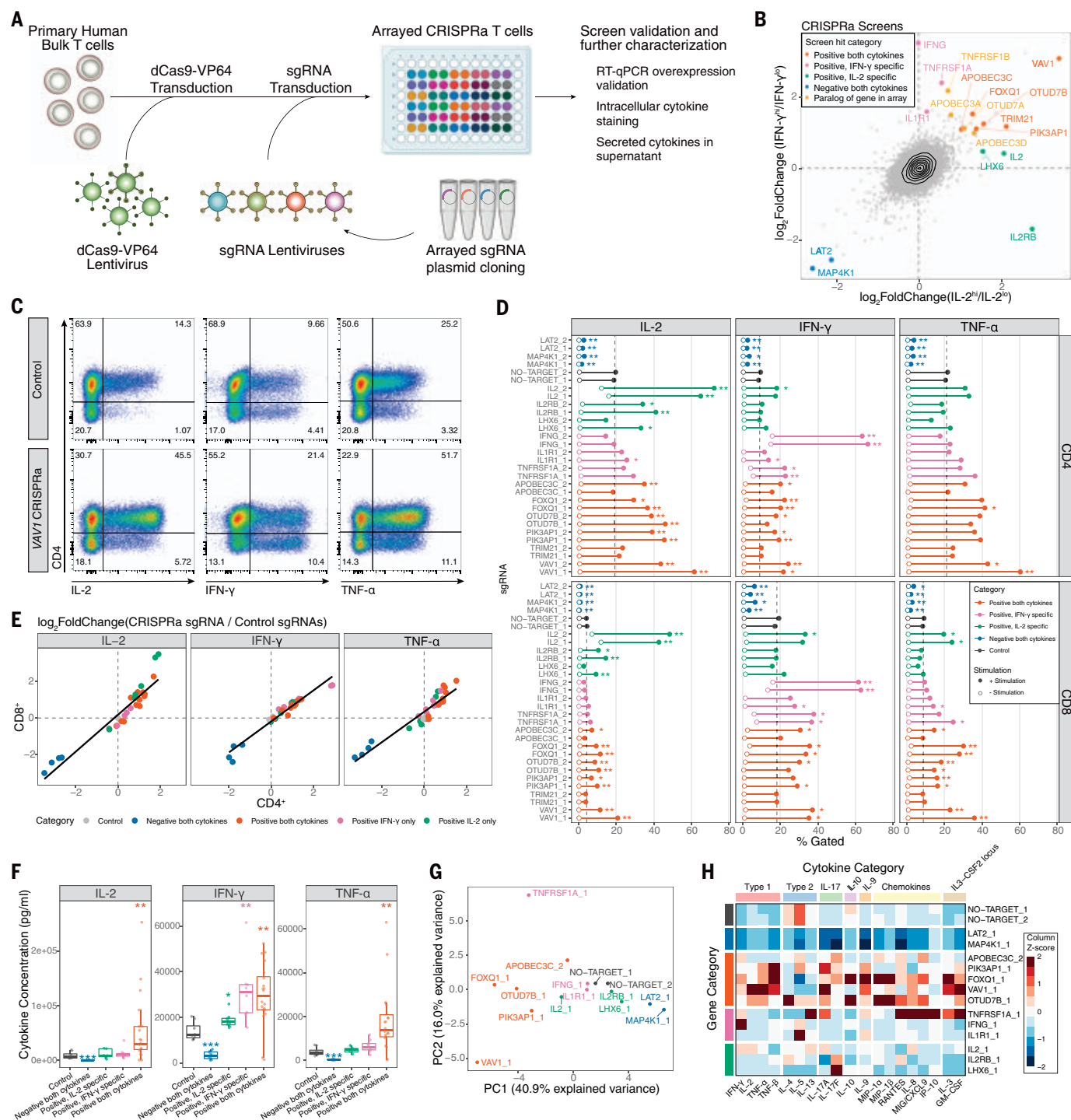


Fig. 3. Characterization of CRISPRa screen hits by arrayed profiling.

(A) Schematic of arrayed experiments. (B) Comparison of IL-2 (in CD4 $^+$ T cells) and IFN- γ (in CD8 $^+$ T cells) CRISPRa screens, with genes targeted by the arrayed sgRNA panel indicated, as well as their screen hit categorization. Paralogs of arrayed panel genes that were also highly ranked hits are additionally indicated. (C) Representative intracellular cytokine staining flow cytometry for indicated cytokines in control (NO-TARGET_1 sgRNA) or VAV1 (VAV1_1 sgRNA) CRISPRa T cells after 10 hours of stimulation. (D) Intracellular cytokine staining of full arrayed sgRNA panel, showing the percentage of cells that gated positive for the indicated cytokines in CD4 $^+$ or CD8 $^+$ T cells. Points represent the mean value of four donors, with and without stimulation. Dashed vertical lines represent the mean no-target control sgRNA control value with stimulation. * $q < 0.05$, ** $q < 0.01$, Mann-Whitney U test, followed by q value

multiple-comparisons correction. Full data are provided in fig. S11B. The medium stimulation dose is shown for IL-2 and IFN- γ , and low-dose stimulation is shown for TNF- α . (E) Scatter plot comparison of \log_2 -fold changes in the percentage of cytokine-positive cells for arrayed panel sgRNAs versus the mean of no-target control sgRNAs in stimulated CD4 $^+$ and CD8 $^+$ cells using the same data from (D). (F) Secreted cytokine staining arrayed panel grouped by indicated gene categories, with sgRNAs targeting the *IL2* and *IFNG* genes removed. Points represent a single gene and donor measurement. * $P < 0.05$, ** $P < 0.01$, *** $P < 0.001$, Mann-Whitney U test. (G) Principal component analysis of secreted cytokine measurements resulting from the indicated CRISPRa sgRNAs. (H) Heatmap of selected secreted cytokine measurements grouped by indicated biological category. Values represent the median of four donors, followed by Z-score scaling for each cytokine.

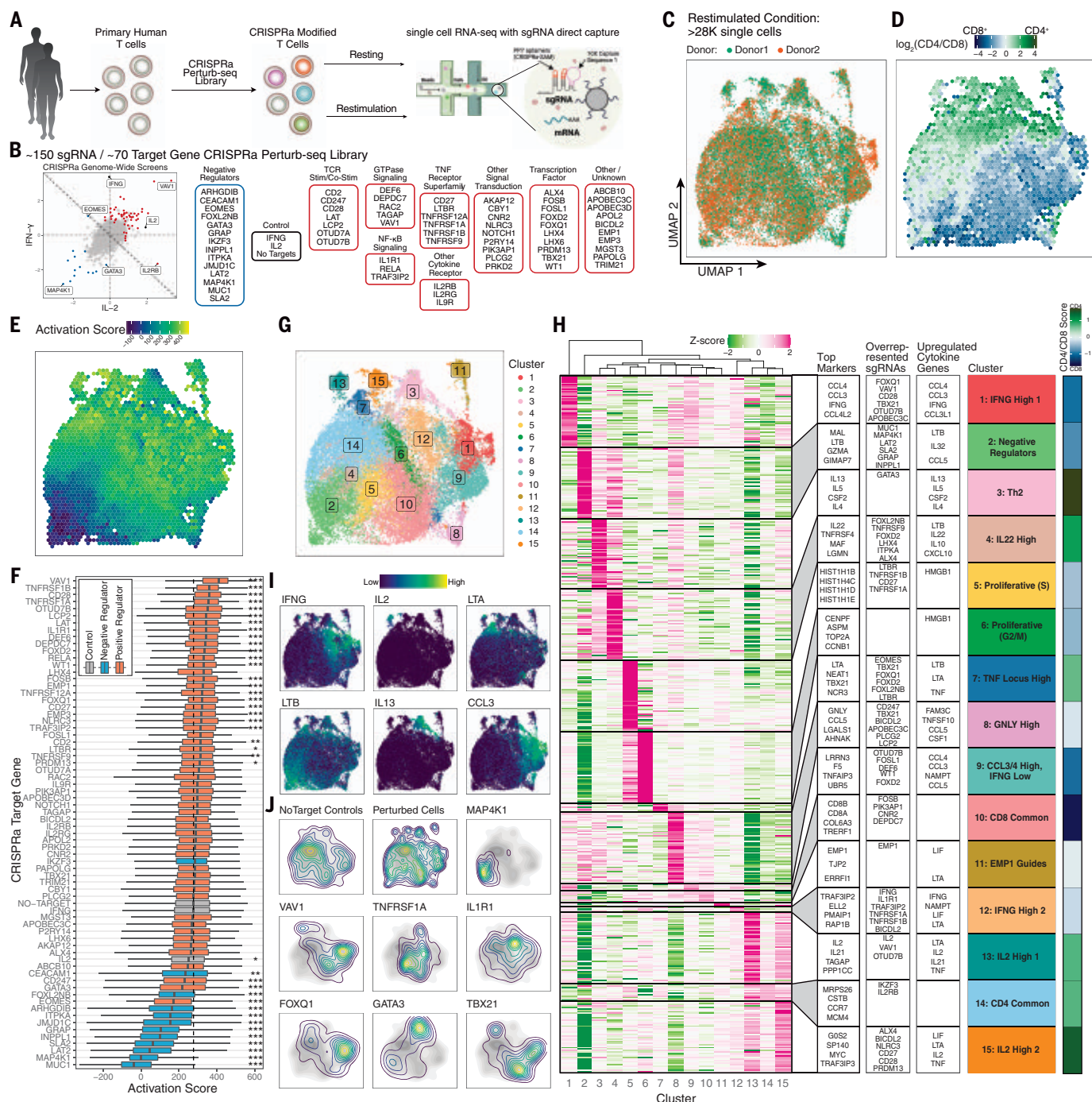


Fig. 4. CRISPRa Perturb-seq captures diverse T cell states driven by genome-wide cytokine screen hits. (A) Schematic of CRISPRa Perturb-seq experiment. (B) Categorical breakdown of genes targeted by the sgRNA library comprising hits from our primary genome-wide CRISPRa cytokine screens as indicated. Genes with a summed log₂-fold change less than zero across both screens (diagonal line) are categorized as negative regulators. (C) UMAP projection of post-quality control filtered restimulated T cells, colored by blood donor. (D) Distribution of CD4⁺ and CD8⁺ T cells across restimulated T cell UMAP projection. Each bin is colored by the average log₂(CD4/CD8) transcript levels of cells in that bin. (E) Restimulated T cell UMAP colored by average cell activation score in each bin. (F) Boxplots of restimulated T cells' activation scores grouped by sgRNA target genes. Dashed line represents the median activation score of no-target control cells. *P < 0.05, **P < 0.01, ***P < 0.001, Mann-Whitney U test with Bonferroni correction. (G) Restimulated T cell

UMAP with cells colored by cluster. (H) Heatmap of differentially expressed marker genes in each cluster. The top 50 statistically significant (FDR < 0.05) differentially up-regulated genes for each cluster are shown, with genes that are up-regulated in multiple clusters being given priority to the cluster with the higher log₂-fold change for the given gene. To the right of the heatmap are (left to right), the top marker genes by log₂-fold change in each clusters' section, the top overrepresented sgRNAs in each cluster by odds ratio (full data are provided in fig. S20G), and the top differentially up-regulated cytokine genes in each cluster. Mean cell log₂(CD4/CD8) cell transcript values in each cluster are shown on the far right. (I) Restimulated T cell UMAP with the expression of indicated genes shown. (J) Contour density plots of restimulated cells assigned to indicated sgRNA targets in UMAP space. The no-target control contour is shown in grayscale underneath. "Perturbed cells" represents all cells assigned a single sgRNA other than no-target control sgRNAs.

cytokine gene expression, whereas positive regulators generally promoted more diverse cytokine expression patterns than negative regulators (fig. S19A). *TBX21* (T-bet) modulated the expression of most detectable cytokine genes. Furthermore, unlike most perturbations, it altered cytokine expression independently of stimulation (fig. S19D).

We next used clustering analysis to characterize CRISPRa-driven cell states in restimulated and resting T cells (Fig. 4G and fig. S20). For each cluster, we identified the top up-regulated gene expression markers and cytokine genes, contributions of CD4⁺/CD8⁺ T cells, and overrepresented sgRNAs revealing a diverse landscape of T cell states promoted by CRISPRa (Fig. 4, H to J, and fig. S20, D to G). Negative cytokine regulators (e.g., MAP4K1) were highly enriched in cluster 2, marked by *LTB* expression and low activation score. Only *GATA3* promoted a T helper 2 (Th2) phenotype (cluster 3), suggesting that altered Th differentiation was not a common mechanism among negative *IFNG* regulators. Thus, Perturb-seq reveals cell states promoted by the overexpression of different key regulators.

We identified two *IL2*-expressing clusters, despite poor capture of the transcript, with both clusters consisting primarily of CD4⁺ T cells. Cluster 13 had the higher *IL2* expression of the two and was promoted by *VAV1* and *OTUD7B* sgRNAs. *VAV1* sgRNAs were strongly enriched in both *IFNG*- and *IL2*-expressing clusters, suggesting that *VAV1*-mediated potentiation of T cell stimulation may drive differentiation toward multiple distinct cytokine-producing populations.

We also identified two distinct clusters of cells expressing *IFNG* (clusters 1 and 12) and containing both CD4⁺ and CD8⁺ T cells. Cluster 1 was marked by high expression of *CCL3* and *CCL4* and was enriched for sgRNAs with strong activation score potentiation such as *VAV1*, *CD28*, and *FOXQ1*. By contrast, cluster 12 was enriched for sgRNAs known to activate the NF- κ B pathway, such as *IL1R1*, *TRAF3IP2*, *TNFRSF1A*, and *TNFRSF1B*. These observations suggest that potentiated stimulation/costimulation may drive T cells to an activated *IFNG*-expressing state distinct from more specific signaling through the NF- κ B pathway. Activation of a subset of TNFRSF receptor genes (*TNFRSF1A*, *TNFRSF1B*, *LTBR*, and *CD27*) also promoted cell states (clusters 5 and 6) marked by the high expression of cell cycle genes. *LTBR* and *CD27* sgRNAs were almost exclusively found in cells of this cluster, whereas *TNFRSF1A/B* sgRNAs appeared to push cells to both proliferative and *IFNG*-expressing states. Thus, CRISPRa Perturb-seq reveals how regulators of cytokine production both tune T cell activation and program cells into different stimulation-responsive states.

Discussion

Paired CRISPRa and CRISPRi screens complement one another to decode the genetic programs regulating stimulation-responsive cytokine production in primary human T cells. CRISPRi identified required cytokine regulators, whereas CRISPRa uncovered key signaling bottlenecks in pathway function as well as regulators that are not necessarily active in ex vivo-cultured T cells. Future screens performed in various other experimental conditions will have the potential to identify additional regulators of T cell states and functions.

The technologies developed in this study will enable screening approaches in primary human T cells and potentially other primary cell types, such as screens for functional non-coding regions of the human genome (18, 38, 39). Furthermore, this screening framework should be adaptable to other nonheritable editing applications of the CRISPR toolkit (40), continuing to expand opportunities to investigate complex biological questions in primary cells, especially when CRISPR perturbations are coupled with single-cell analyses.

Major efforts are underway to discover gene modifications that enhance the efficacy of adoptive T cell therapies. Although we do not expect all perturbations that lead to increased cytokine production to translate to enhanced in vivo antitumor efficacy, we are encouraged by the identification of genes in various stages of therapeutic development, including *CD5* (41), *TNFRSF9* (encoding 4-1BB), *CD27*, *CD40*, and *TNFRSF4* (encoding OX40). Recent preclinical work (42) highlights c-JUN overexpression to limit T cell exhaustion and further enhance cell therapies. Thus, loss- and gain-of-function discovery platforms can guide efforts to engineer T cells for different clinical indications. Future CRISPRa and CRISPRi screens in human T cells will continue to nominate targets for improved next-generation cellular therapies.

Materials and Methods

Isolation and culture of human T cells

Human T cells were sourced from PBMC-enriched leukapheresis products (Leukopaks, STEMCELL Technologies, catalog no. 70500.2) from healthy donors, after institutional review board-approved informed written consent (STEMCELL Technologies). Bulk T cells were isolated from Leukopaks using EasySep magnetic selection following the manufacturers' recommended protocol (STEMCELL Technologies, catalog no. 17951). Unless stated otherwise, bulk T cells were frozen in Bmbanker Cell Freezing Medium at 5×10^7 cells/ml (Bulldog Bio, catalog no. BB01) and kept at -80°C for short-term storage or in liquid nitrogen for long-term storage immediately after isolation. Unless otherwise noted, thawed T cells were cultured in X-VIVO 15 (Lonza Bioscience, catalog no. 04-418Q) sup-

plemented with 5% fetal calf serum (FCS), 55 mM 2-mercaptoethanol, 4 mM N-acetyl L-cysteine, and 500 IU/ml of recombinant human IL-2 (Amerisource Bergen, catalog no. 10101641). Primary T cells were activated using anti-human CD3/CD28 CTS Dynabeads (Fisher Scientific, catalog no. 40203D) at a 1:1 cell:bead ratio at 10^6 cells/ml.

Cell line maintenance

Lenti-X HEK293T cells (Takara Bio, catalog no. 632180) were maintained in high-glucose Dulbecco's modified Eagle's medium with GlutaMAX (Fisher Scientific, catalog no. 10566024), supplemented with 10% FCS, 100 U/ml of penicillin/streptomycin (PenStrep; Fisher Scientific, catalog no. 15140122), 1 mM sodium pyruvate (Fisher Scientific, catalog no. 11360070), $1\times$ minimal essential medium (MEM) nonessential amino acids (Fisher Scientific, catalog no. 11140050), and 10 mM HEPES solution (Sigma-Aldrich, catalog no. H0887-100ML). Cells were passaged every 2 days using Tryple Express (Fisher Scientific, catalog no. 12604013) for dissociation and maintained at <60% confluency.

NALM6 cells were engineered to express NY-ESO-1 peptide in an HLA-A0201 background, recognizable with the 1G4 TCR by the Eyquem laboratory at University of California San Francisco (UCSF) and provided for TCR stimulation coculture experiments. For simplicity, these cells are referred to as NALM6. NALM6 cells were cultured in RPMI (Invitrogen, catalog no. 21870092) supplemented with 10% FCS, 100 U/ml PenStrep (Fisher Scientific, catalog no. 15140122), 1 mM sodium pyruvate (Fisher Scientific, catalog no. 11360070), and $1\times$ MEM nonessential amino acids (Fisher Scientific, catalog no. 11140050), 10 mM HEPES solution (Sigma-Aldrich, catalog no. H0887-100ML), and 2 mM L-glutamine (Lonza Bioscience, catalog no. 17-605E).

Plasmids

dCas9-VP64 originated from lentiSAMv2 (Addgene, catalog no. 75112) and cloned into the lentiCRISPRv2-dCas9 backbone (Addgene, catalog no. 112233) with Gibson Assembly. The promoter was switched to SFFV and mCherry was introduced upstream of dCas9-VP64, separated by a P2A sequence resulting in the pZR112 plasmid. The LTR-LTR range was minimized to enhance lentiviral titer. For CRISPRi, BFP in pHR-SFFV-dCas9-BFP-KRAB (Addgene, catalog no. 46911) was switched to mCherry with Gibson Assembly, resulting in pZR071.

Single sgRNAs for arrayed experiments have been introduced by Golden Gate Cloning as described previously (22). Briefly, DNA oligomers with Golden Gate overhangs were annealed and subsequently cloned into the nondigested target plasmid using the Golden Gate Assembly Kit (BsmBI-v2, New England

Biolabs, catalog no. E1602L). sgRNAs have been cloned into pXPR_502 (Addgene, catalog no. 96923) for CRISPRa and into CROPseq-Guide-Puro (43) (Addgene, catalog no. 86708) for CRISPRi. All single sgRNAs used in this study can be found in table S3.

The genome-wide CRISPRa (Calabrese A, catalog no. 92379 and Calabrese B, catalog no. 92380) and CRISPRi libraries (Dolcetto A, catalog no. 92385 and Dolcetto B, catalog no. 92386) (22) were obtained from Addgene. Forty nanograms of each library were transformed into Endura ElectroCompetent Cells (Lucigen, catalog no. 60242-2) following the manufacturer's instructions. After transformation, Endura cells were grown in a shaking incubator for 16 hours at 30°C in the presence of ampicillin. Library plasmid has been isolated using the Plasmid Plus MaxiKit (Qiagen, catalog no. 12963) and sequenced for sgRNA representation as described under the section titled "Genome-wide CRISPRa and CRISPRi screens."

For cDNA-mediated target overexpression, the lentiCRISPRv2 (Addgene, catalog no. 75112) backbone was rebuilt to a lentiviral cDNA cloning plasmid with an SFFV promoter followed by BsmBI restriction sites and P2A-Puro. Transgene cDNAs were purchased from Genscript, choosing the canonical (longest) isoform for each gene, and BsmBI restriction sites were introduced by polymerase chain reaction (PCR). The final lentiviral transfer plasmids were assembled using the Golden Gate Assembly Kit (BsmBI-v2, New England Biolabs, catalog no. E1602L).

To clone direct-capture compatible CRISPRa-SAM plasmids for Perturb-seq, different sgRNA designs were synthesized as G-Blocks (Integrated DNA Technologies) and cloned into pXPR_502 (Addgene, catalog no. 96923) by Gibson assembly, replacing its sgRNA cassette.

Lentivirus production

Unless otherwise stated, human embryonic kidney (HEK) 293T cells were seeded in OPTI-MEM I Reduced Serum Medium (OPTI-MEM) with GlutaMAX Supplement (Invitrogen, catalog no. 31985088) supplemented with 5% FCS, 1 mM sodium pyruvate (Fisher Scientific), and 1× MEM nonessential amino acids (Fisher Scientific) (cOPTI-MEM) at 3.6×10^7 cells per T225 flask in 45 ml of medium overnight to achieve confluency between 85 and 95% at the time point of transfection. The following morning, HEK293Ts cells were transfected with second-generation lentiviral packaging plasmids and transfer plasmid using Lipofectamine 3000 transfection reagent (Fisher Scientific, catalog no. L3000075). Briefly, 165 µl of Lipofectamine 3000 reagent was added to 5 ml of room-temperature OPTI-MEM without supplements. Forty-two micrograms of Cas9 transfer plasmid, 30 µg of psPAX2 (Addgene 12260), 13 µg of pMD2.G

(Addgene 12259), and 145 µl of p3000 reagent were added to 5 ml of room-temperature OPTI-MEM without supplements and mixed by gentle inversion. The plasmid and Lipofectamine 3000 mixtures were combined, mixed by gentle inversion, and incubated for 15 min at room temperature. After incubation, 20 ml of medium was removed from the T225 flask and the 10-ml transfection mixture was carefully added without detaching HEK293T cells. After 6 hours, the transfection medium was replaced with 45 ml of cOPTI-MEM supplemented with 1× ViralBoost (Alstem Bio, catalog no. VB100). Lentiviral supernatant was harvested 24 hours after transfection (first harvest) and replaced with 45 ml of fresh cOPTI-MEM. A second harvest was performed 48 hours after transfection. Immediately after collection, the medium was centrifuged at 500g for 5 min at 4°C to clear cellular debris. Unless otherwise noted, Lenti-X-Concentrator (Takara Bio, catalog no. 631232) was added to the collected supernatant, and lentivirus was concentrated following the manufacturer's instructions and resuspended in OPTI-MEM in 1% of the original culture volume without supplements. Lentiviral particles were subsequently aliquoted and frozen at -80°C.

Flow cytometry

Aria 2, Aria 3, and Aria Fusion cell sorters (BD Biosciences) at the UCSF Parnassus Flow Core and the Gladstone Institute Flow Core were used for sorting. The Attune NxT (Thermo Fisher Scientific) and LSRFortessa X-20 (BD Biosciences) flow cytometers were used for flow cytometry. Antibodies used for flow cytometric analyses and sorting are summarized in table S4.

Intracellular cytokine staining

Unless indicated otherwise, T cells were stimulated with ImmunoCult Human CD3/CD28/CD2 T Cell Activator (STEMCELL Technologies, catalog no. 10990) with 6.25 µl/ml of culture medium at 2×10^6 cells/ml. One hour after restimulation, Golgi Plug protein transport inhibitor (BD Biosciences, catalog no. 555029) was added at a 1/1000 dilution. Nine hours after the addition of Golgi Plug, T cells were stained for surface antigens before fixation and subsequently processed for intracellular cytokine staining using the BD Cytofix/Cytoperm kit instructions (BD Biosciences, catalog no. 554714).

Genome-wide CRISPRa and CRISPRi screens

One day after activation, T cells from two human blood donors were infected with 2% v/v concentrated dCas9-VP64 lentivirus. Two days after activation, T cells were split into two populations and infected with 1% v/v [multiplicity of infection (MOI) ~ 0.5] Calabrese Set A (Addgene, catalog no. 92379) or 0.8% v/v

(MOI ~0.5) Calabrese Set B (Addgene, catalog no. 92380) lentivirus. These two sets were independently cultured and processed in parallel until analysis. Three days after activation, fresh medium with IL-2 (final concentration 500 IU/ml) and puromycin (final concentration 2 µg/ml) was added to bring cells to 3×10^5 cells/ml. Cells were split 2 days later and fresh medium with IL-2 was added to bring cells to 3×10^5 cells/ml. Two days later, fresh medium without IL-2 was added to bring the concentration to 10^6 /ml. Eight days after initial activation, cells were harvested, centrifuged at 500g for 5 min, and resuspended at 2×10^6 cells/ml X-VIVO 15 without supplements. The following day, cells were restimulated and stained for FACS as described under the "Intracellular cytokine staining" section. Over the subsequent 2 days, cells were sorted at the Parnassus Flow Cytometry Core (PFCC) facility into IL-2^{lo} and IL-2^{hi} CD4⁺ and IFN-γ^{lo} and IFN-γ^{hi} CD4⁺ T cell populations (see fig. S3C for gating strategy). Sorted cells were stored in EasySep Buffer (phosphate-buffered saline with 2% FCS and 1 mM EDTA) overnight until genomic DNA isolation.

The same experimental procedure using T cells from the same donors was followed for the CRISPRi screens. T cells were infected with dCas9-mCherry-KRAB at 2% v/v and Dolcetto A (Addgene, catalog no. 92385) and B (Addgene, catalog no. 92386) sgRNA libraries at 10% v/v or 25% v/v unconcentrated virus, respectively (~0.5 MOI).

Genomic DNA was extracted from fixed cells as described previously (44). Integrated sgRNA sequences were amplified as described previously (22), and sequencing libraries were subsequently agarose gel purified using NucleoSpin Gel and PCR Clean-up Mini kit (Machery-Nagel, catalog no. 740609.50). Libraries were sequenced on a NextSeq500 instrument to a targeted depth of 100-fold coverage.

For the supplementary CD4⁺ T cell set of genome-wide CRISPRa screens, CD4⁺ T cells were isolated from Leukopaks using magnetic negative selection (STEMCELL Technologies, catalog no. 17952) and subsequently stimulated as described in the section entitled "Isolation and culture of human T cells." T cells were then cultured and infected with lentivirus as described for the primary CRISPRa screens above. For library lentivirus production, Calabrese Set A and Set B plasmid were mixed at equimolar ratios before transfection, and the pooled lentiviral particles from both sets was used for transduction. CD4 flow cytometry staining on day 7 after T cell activation confirmed >98% purity. T cells were further processed and restimulated as described above. T cells were separately stained for IL-2, IFN-γ, or TNF-α for FACS. After our initial analysis, it appeared that the IFN-γ screen was potentially undersampled because of lower hit resolution

than the other screens. To address this, additional fixed cells from the same experiment were stained and sorted as an additional technical replicate and then computationally merged (described below).

CRISPR screen analysis

Reads were aligned to the appropriate reference library using MAGECK version 0.5.9.2 (45) using the *-trim-5 22,23,24,25,26,28,29,30* argument to remove the staggered 5' adapter. Next, raw read counts across both library sets were normalized to the total read count in each sample, and each of the matching samples across two sets were merged to generate a single normalized read count table. Normalized read counts in high versus low bins were compared using *mageck test* with *-norm-method none*, *-paired*, and *-control-sgrna* options, pairing samples by donor and using non-targeting sgRNAs as controls, respectively. Gene hits were classified as having a median absolute log₂-fold change >0.5 and a false discovery rate (FDR) <0.05. For supplemental CD4⁺ screens (fig. S9), reads were aligned to the full Calabrese A and B library in a single reference file. For the supplemental CD4⁺ IFN-γ screen, which was sorted and sequenced as two technical replicates, normalized counts were averaged across technical replicates before analysis with *mageck test*.

Gene-set enrichment analysis

Gene-set enrichment analysis (GSEA) was completed with the fgsea Bioconductor R package using the default settings (46). KEGG pathways version 7.4 were obtained from GSEA mSigDB <http://www.gsea-msigdb.org/gsea/downloads.jsp>. The KEGG NF-κB signaling pathway (entry hsa04064) was missing from this dataset and added manually from <https://www.genome.jp/entry/pathway+hsa04064>.

Stratified linkage disequilibrium score analysis

GWAS summary statistics were downloaded from the Price laboratory website (https://alkesgroup.broadinstitute.org/sumstats_formatted/ and <https://alkesgroup.broadinstitute.org/UKBB/>). Linkage disequilibrium (LD) scores were created for each screen [corresponding to a set of single-nucleotide polymorphisms (SNPs) within 100 kb of genes identified as significant hits in each screen or their corresponding matched background sets] using the 1000G Phase 3 population reference. Each annotation's heritability enrichment for a given trait was computed by adding the annotation to the baselineLD model and regressing against trait chi-squared statistics using HapMap3 SNPs with the stratified LD score regression package (47). Heritability enrichments were then meta-analyzed across immune or nonimmune traits using inverse variance weighting. The sets of background

genes were sampled from the set of all genes that were expressed in the control sgRNA, stimulated bulk RNA-Seq data. For each screen, the background genes were sampled to match the significant screen hits in number and based on deciles of gene expression. Immune traits used for analysis were: "Eosinophil Count," "Lymphocyte Count," "Monocyte Count," "White Count," "Autoimmune Disease All," "Allergy Eczema Diagnosed," "Asthma Diagnosed," "Celiac," "Crohn's Disease," "Inflammatory Bowel Disease," "Lupus," "Multiple Sclerosis," "Primary Biliary Cirrhosis," "Rheumatoid Arthritis," "Type 1 Diabetes," "Ulcerative Colitis." Nonimmune traits used were: "Heel Tscore," "Balding1," "Balding4," "Bmi," "Height," "Type 2 Diabetes," "Neuroticism," "Anorexia," "Autism," "Bipolar Disorder," "Depressive Symptoms," "Fasting Glucose," "Hdl," "Ldl," "Triglycerides," and "Fasting Glucose."

Arrayed CRISPRa experiments

For each gene chosen to target in follow-up experiments, one sgRNA was chosen from the Calabrese library used in screens. The first sgRNAs ("1") were manually chosen for consistent log₂-fold change observed in both donors. The second sgRNA ("2") was picked from the hCRISPRa-v2 genome-wide library (48), choosing the top-ranked sgRNA not present in Calabrese libraries for each gene. sgRNAs were cloned into the pXPR_502 vector as described in the plasmid section.

Primary human T cells were transduced with 2% v/v mCherry-2A-dCas9-VP64 lentivirus (pZR112) 1 day after activation. The following day (day 2), the dCas9-VP64-transduced cells were split into 96-well flat-bottom plates, avoiding edge wells, and transduced with a different sgRNA lentivirus in each well (5% v/v). One day after sgRNA transduction, fresh medium was added with IL-2 (500 IU/ml) and 2 μg/ml puromycin (final culture concentrations). Cells were passaged 2 days later, adding fresh medium with 500 IU/ml of IL-2 and maintaining a concentration of 3 × 10⁵ to 1 × 10⁶ cells/ml, with 96-well plates copied as needed to maintain this concentration. On day 8, cells from copied plates were pooled and samples were counted. Cells were pelleted and resuspended at a concentration of 2 × 10⁶ cells/ml in fresh X-VIVO-15 without additives. On day 9, cells were restimulated with anti-CD3/CD28/CD2 ImmunoCult T Cell Activator (as described in the "Intracellular cytokine staining" section) or left resting.

RT-qPCR

T cells were prepared as described under the "Arrayed CRISPRa experiments" section. Seven days after sgRNA transduction, 100,000 T cells per well were pelleted at 500g for 5 min at 4°C. Cells were lysed and RNA was extracted using the Quick-RNA 96 kit (Zymo Research)

following the manufacturer's protocol but skipping the option of in-well DNase treatment. DNase treatment and cDNA synthesis were subsequently completed with Maxima First Strand cDNA Synthesis Kit for reverse transcription quantitative PCR (RT-qPCR) with double-stranded DNase (Thermo Fisher Scientific). qPCR was performed with the PrimeTime PCR Master Mix (Integrated DNA Technologies) and PrimeTime qPCR probe assays (Integrated DNA Technologies; a list of probes used is provided in table S5) on an Applied Biosystems Quantstudio 5 real-time PCR system. Data were analyzed using the ΔΔCt method. The mean Ct values of two housekeeping genes, *PPIA* and *GUSB*, to calculate the ΔCt, and the mean ΔCt of nontargeting controls to calculate ΔΔCt.

cDNA experiments

See fig. S13A for an experimental overview. One day after activation, T cells were transduced with the IG4 TCR lentivirus recognizing the NY-ESO-1 antigen or nontransduced for immunocult assay. One day later, cells were transduced with the transgenes in cDNA format. Three days after initial activation, puromycin was added to obtain a final concentration of 2 μg/ml, along with fresh X-VIVO 15 medium with 500 IU/ml of IL-2, and further cultured and expanded analogous to the genome-wide CRISPR screens. Nine days after initial activation, T cells were centrifuged and resuspended at 2 × 10⁶ cells/ml in X-Vivo 15 without supplements. On the same day, IG4 TCR expression was assessed by flow cytometry after dextramer staining (Immudex, catalog no. WB3247-PE) to ensure even expression across different cDNA constructs. The following day, T cells were restimulated with either 6.25 μl/ml of Immunocult or NALM6 cells at an effector: target ratio of 1:2 for IG4 TCR-transduced cells. Cells were further processed as described under the "Intracellular cytokine staining" section. CD22 was used as a marker for NALM6 cells to discriminate them from T cells in the coculture. Overexpression of *OTUD7B* cDNA together with the IG4 TCR (but not alone) caused toxicity and was therefore excluded from analyses. Two donors were excluded from the IG4 TCR assay because of poor TCR transduction.

Cytokine Luminex assay

T cells were prepared as explained under the "Arrayed CRISPRa experiments" section. On day 9 after activation, T cells at a concentration of 2 × 10⁶ cells/ml were restimulated with ImmunoCult Human CD3/CD28/CD2 (STEMCELL Technologies, catalog no. 10970) at 6.25 μl/ml. Twenty-four hours after restimulation, supernatant was collected and frozen at -20°C. After a serial pilot titration, cytokine analyses were performed at a 1/200 dilution by Eve Technologies with the Luminex xMAP technology on the Luminex 200 system

(Luminex). To remove very lowly expressed cytokines for downstream analysis, any group in which three of four donors had undetectable cytokines, the cytokine was removed. Additionally, the sgIL1R1-1 donor 4 measurement for IL-1 α was removed manually because this was an extremely high outlier.

Bulk RNA-seq sample preparation

FOXQ1 and nontargeting sgRNA control primary human T cells from four donors were transduced and expanded as described in the “Arrayed CRISPRa experiments” section. On day 8, mCherry⁺CD4⁺ populations were sorted and resuspended in X-VIVO-15 without additives at 2×10^6 cells/ml. On day 9, cells were restimulated with 6.25 μ l/ml of anti-CD3/CD28/CD2 ImmunoCult or left unperturbed for resting (nonstimulated) condition. Twenty-four hours later, cells were lysed for RNA.

RNA was purified using the Quick-RNA Microprep kit (Zymo Research) without the optional in-well DNase treatment step. Purified RNA was treated with TURBO DNase (Thermo Fisher Scientific) to remove potential contaminating DNA. RNA was subsequently purified using the RNA Clean & Concentrator-5 kit (Zymo Research). RNA quality control was performed using an RNA ScreenTape assay (Agilent Technologies), with all samples having an RNA integrity number >7. RNA-seq libraries were prepared using the Illumina Stranded mRNA Prep kit with 100 ng of input RNA. Libraries were sequenced using paired-end 72-bp reads on a NextSeq500 instrument to an average depth of 3.2×10^7 clusters per sample.

Bulk RNA-seq data analysis

Adapters were trimmed from fastq files using cutadapt version 2.10 (49) with default settings keeping a minimum read length of 20 bp. Reads were mapped to the human genome GRCh38 keeping only uniquely mapping reads using STAR version 2.7.5b (50) with the setting “-outFilterMultimapNmax 1.” Reads overlapping genes were then counted using featureCounts version 2.0.1 (51) with the setting “-s 2” and using the Gencode version 35 basic transcriptome annotation.

The count matrix was imported into R. Only genes with at least 1 count per million across at least four samples were kept. TMM normalized counts were used for heatmaps. Differentially expressed genes between FOXQ1 overexpression and control samples were then identified using limma version 3.44.3 (52) while controlling for any differences between donors. Significant differentially expressed genes were defined as having an FDR-adjusted *P* value <0.05.

Perturb-seq library design and cloning

The CRISPRa Perturb-seq target genes were selected from the primary IL-2 and IFN- γ

CRISPRa screen results. First, genes that had a significant fitness defect were removed from the gene list (fig. S5). Next, genes were ranked by median sgRNA log₂-fold change and the top ranked, not previously selected gene, was picked in the following order: (1) IL-2-positive hit, (2) IFN- γ -positive hit, (3) IL-2-positive hit, (4) IFN- γ -positive hit, and (5) IL-2- or IFN- γ -negative hit (alternating each round), such that positive hits outnumbered negative hits at a 4:1 ratio. Only hits that were significant (FDR < 0.05) were selected in each round. The one exception was *TCF7*, which was added manually because we considered it worthwhile to analyze due to its known effects on T cell function. To select sgRNAs, the top two enriched sgRNAs by log₂-fold change in the screen for which the gene was selected were used. The library was ordered as pooled single-stranded oligos, PCR amplified, and cloned into the CRISPRa-SAM direct-capture design I cloning vector (pZR158).

Perturb-seq sample preparation and sequencing

Bulk CD3⁺ primary human T cells from two donors were transduced and cultured as described in the “Genome-wide CRISPRa and CRISPRi screens” section, except library transduction was completed at lower MOI of 0.3. Cells in the stimulated condition were stimulated with 6.25 μ l/ml of anti-CD3/CD28/CD2 immunocult. Twenty-four hours later, cells from both the stimulated and nonstimulated condition were sorted for mCherry⁺ (marking dCas9-VP64). Sorted cells were processed to single-cell RNA-seq and sgRNA sequencing libraries by the Institute for Human Genetics (IHG) Genomics Core using Chromium Next GEM Single Cell 3' Reagent Kit version 3.1 with feature barcoding technology for CRISPR screening, following the manufacturer's protocol. Before loading the Chromium chip, sorted cells from two blood donors were normalized to 1000 cells/ μ l and mixed at a 1:1 ratio for each condition. Twenty microliters of cell suspension was loaded into four replicate wells per condition, for a total 80,000 cells loaded per condition. Final sgRNA sequencing libraries were further purified for the correct size fragment by 4% agarose E-Gel EX Gels (Thermo Fisher Scientific) and gel extracted. Libraries were sequenced over two NovaSeq S4 lanes (two stimulated wells and two nonstimulated wells per lane) at a 2:1 molar ratio of the gene expression libraries to sgRNA libraries.

Perturb-seq analysis

Alignments and count aggregation of gene expression and sgRNA reads were completed with Cell Ranger version 6.1.1. Gene expression and sgRNA reads were aligned using *cellranger count*, with default settings. Gene expression reads were aligned to the “refdata-gex-GRCh38-2020-A” human transcriptome reference down-

loaded from 10x Genomics. sgRNA reads were aligned to the Perturb-seq library using the pattern (BC)GTTTAAGAGCTATG. Counts were aggregated with *cellranger aggr* with default arguments. To assign sgRNAs to cells, *cellranger count* output files “protospacer_calls_per_cell.csv” were used, filtering out droplets with >1 sgRNA called, returning a median of 133 sgRNA UMIs in sgRNA singlets. For increased stringency, only droplets with ≥ 5 sgRNA UMIs were used in further analysis.

Cell donors were genetically demultiplexed using Souporecell (53) (<https://github.com/wheaton5/souporecell>). The input for each run was the bam file and barcodes.tsv file from the cellranger count output and the reference fasta. Donor calls across wells were harmonized using the vcf file outputs from Souporecell using a publicly available python script (<https://github.com/hyunminkang/apigenome/blob/master/scripts/vcf-match-sample-ids>).

Gene expression data were imported and analyzed in R with the Seurat version 4.0.3 *Read10X* function (54). Cells were initially quality filtered for percentage of mitochondrial reads <25% and number of detected RNA features >400 and <6000, removing 4% of cells. After filtering, a median of 401 cells per sgRNA target gene per condition (median of 127 sgRNA unique molecular indices (UMIs) per singlet) were recovered, along with ~2000 cells with no-target control guides per condition. Four sgRNA targets, *HELZ2*, *TCF7*, *PRDM1*, and *IRX4*, were removed from downstream analysis because of low cell counts (<100).

Gene-expression counts were normalized and transformed using the Seurat SCTransform function (55), with the following variables regressed: percentage mitochondrial reads, S-phase score, and G₂/M-phase score, performing the regression as described on the Satija laboratory website (https://satijalab.org/seurat/articles/cell_cycle_vignette.html). Normalized and transformed counts were used for all downstream analysis. To call CD4⁺ and CD8⁺ T cells, a CD4/CD8 score for each cell using following formula was used: log₂[CD4/mean(CD8A, CD8B)], with a score <-0.9 called as a CD8⁺ cell and a score >1.4 called as a CD4⁺ cell (fig. S17G).

For both restimulated and resting conditions, UMAP reduction was performed with dimensions 1 to 20, and otherwise default settings of the *RunUMAP* Seurat function. For clustering, *FindClusters* was run using algorithm 3, resolution 0.4 for the restimulated condition and resolution 0.5 for the resting condition. Two clusters in the restimulated condition were manually merged to form “Cluster 2: Negative Regulators.” The merged clusters showed highly similar gene expression patterns, with one cluster containing the bulk of cells containing negative regulator sgRNAs and the other containing sgRNAs targeting the negative regulator *MUC1*. Cluster

trees shown were generated using the Seurat *BuildClusterTree* function with default arguments. For pseudobulk differential expression analyses, the Seurat *FindMarkers* function was used with the default method, Wilcoxon rank sum test.

To generate the T cell activation score, pseudobulk differential expression analysis was first performed on restimulated versus resting no-target control sgRNAs, and \log_2 -fold change outputs were used as gene weights. Only genes that had an absolute \log_2 -fold change >0.25 and were detected in 10% of restimulated or resting cells were used for gene weights. For a given cell, the activation score was calculated as $\text{sum}(G_E \times G_W/G_M)$, where G_E is a gene's normalized/transformed expression count, G_W is the gene's weight, and G_M is the gene's mean expression in no-target control cells (to correct for differential levels of baseline expression).

Statistical analysis

All statistical analyses were performed in R version 4.0.2 unless otherwise noted. To address ties in nonparametric tests, Mann-Whitney *U* tests were performed using the `wilcox_test` function of the `Coin` R package (version 1.4-1), with default arguments. For *q*-value-based multiple-comparisons correction, the `Rqvalue` package (version 2.20.0) was used, with default arguments.

REFERENCES AND NOTES

1. A. K. Abbas, E. Trotta, D. R. Simeonov, A. Marson, J. A. Bluestone, Revisiting IL-2: Biology and therapeutic prospects. *Sci. Immunol.* **3**, eaat1482 (2018). doi: [10.1126/sciimmunol.aat1482](https://doi.org/10.1126/sciimmunol.aat1482); pmid: 29980618
2. L. Ni, J. Lu, Interferon gamma in cancer immunotherapy. *Cancer Med.* **7**, 4509–4516 (2018). doi: [10.1002/cam4.1700](https://doi.org/10.1002/cam4.1700); pmid: 30039553
3. F. Castro, A. P. Cardoso, R. M. Gonçalves, K. Serre, M. J. Oliveira, Interferon-gamma at the crossroads of tumor immune surveillance or evasion. *Front. Immunol.* **9**, 847 (2018). doi: [10.3389/fimmu.2018.00847](https://doi.org/10.3389/fimmu.2018.00847); pmid: 29780381
4. L. B. Ivashkiv, IFN γ : Signalling, epigenetics and roles in immunity, metabolism, disease and cancer immunotherapy. *Nat. Rev. Immunol.* **18**, 545–558 (2018). doi: [10.1038/s41577-018-0029-z](https://doi.org/10.1038/s41577-018-0029-z); pmid: 29921905
5. T. R. Malek, The biology of interleukin-2. *Annu. Rev. Immunol.* **26**, 453–479 (2008). doi: [10.1146/annurev.immunol.26.021607.090357](https://doi.org/10.1146/annurev.immunol.26.021607.090357); pmid: 18062768
6. D. A. Boardman, M. K. Levings, Cancer immunotherapies repurposed for use in autoimmunity. *Nat. Biomed. Eng.* **3**, 259–263 (2019). doi: [10.1038/s41551-019-0359-6](https://doi.org/10.1038/s41551-019-0359-6); pmid: 30952977
7. J. Gao et al., Loss of IFN- γ pathway genes in tumor cells as a mechanism of resistance to anti-CTLA-4 therapy. *Cell* **167**, 397–404.e9 (2016). doi: [10.1016/j.cell.2016.08.069](https://doi.org/10.1016/j.cell.2016.08.069); pmid: 27667683
8. J. M. Zaretsky et al., Mutations associated with acquired resistance to PD-1 blockade in melanoma. *N. Engl. J. Med.* **375**, 819–829 (2016). doi: [10.1056/NEJMoa1604958](https://doi.org/10.1056/NEJMoa1604958); pmid: 27433843
9. M. Ayers et al., IFN- γ -related mRNA profile predicts clinical response to PD-1 blockade. *J. Clin. Invest.* **127**, 2930–2940 (2017). doi: [10.1172/JCI91190](https://doi.org/10.1172/JCI91190); pmid: 28650338
10. R. Bartelt, N. Cruz-Orcutt, M. Collins, J. C. D. Houtman, Comparison of T cell receptor-induced proximal signaling and downstream functions in immortalized and primary T cells. *PLOS ONE* **4**, e5430 (2009). doi: [10.1371/journal.pone.0005430](https://doi.org/10.1371/journal.pone.0005430); pmid: 19412549
11. H. Colin-York, S. Kumari, L. Barbieri, L. Cords, M. Fritzsche, Distinct actin cytoskeleton behaviour in primary and immortalised T-cells. *J. Cell Sci.* **133**, jcs.232322 (2019). doi: [10.1242/jcs.232322](https://doi.org/10.1242/jcs.232322); pmid: 31413071
12. E. Astoul, C. Edmunds, D. A. Cantrell, S. G. Ward, PI 3-K and T-cell activation: Limitations of T-leukemic cell lines as signaling models. *Trends Immunol.* **22**, 490–496 (2001). doi: [10.1016/S1471-4906\(01\)01973-1](https://doi.org/10.1016/S1471-4906(01)01973-1); pmid: 11525939
13. O. Parnas et al., A genome-wide CRISPR screen in primary immune cells to dissect regulatory networks. *Cell* **162**, 675–686 (2015). doi: [10.1016/j.cell.2015.06.059](https://doi.org/10.1016/j.cell.2015.06.059); pmid: 26189680
14. M. B. Dong et al., Systematic immunotherapy target discovery using genome-scale in vivo CRISPR screens in CD8 T cells. *Cell* **178**, 1189–1204.e23 (2019). doi: [10.1016/j.cell.2019.07.044](https://doi.org/10.1016/j.cell.2019.07.044); pmid: 31442407
15. J. Henriksson et al., Genome-wide CRISPR screens in T helper cells reveal pervasive crosstalk between activation and differentiation. *Cell* **176**, 882–896.e18 (2019). doi: [10.1016/j.cell.2018.11.044](https://doi.org/10.1016/j.cell.2018.11.044); pmid: 30639098
16. E. Shifrut et al., Genome-wide CRISPR screens in primary human T cells reveal key regulators of immune function. *Cell* **175**, 1958–1971.e15 (2018). doi: [10.1016/j.cell.2018.10.024](https://doi.org/10.1016/j.cell.2018.10.024); pmid: 30449619
17. P. Y. Ting et al., Guide Swap enables genome-scale pooled CRISPR-Cas9 screening in human primary cells. *Nat. Methods* **15**, 941–946 (2018). doi: [10.1038/s41592-018-0149-1](https://doi.org/10.1038/s41592-018-0149-1); pmid: 30297964
18. D. R. Simeonov et al., Discovery of stimulation-responsive immune enhancers with CRISPR activation. *Nature* **549**, 111–115 (2017). doi: [10.1038/nature23875](https://doi.org/10.1038/nature23875); pmid: 28854172
19. Y. Liu et al., CRISPR activation screens systematically identify factors that drive neuronal fate and reprogramming. *Cell Stem Cell* **23**, 758–771.e8 (2018). doi: [10.1016/j.stem.2018.09.003](https://doi.org/10.1016/j.stem.2018.09.003); pmid: 30318302
20. X. Chen et al., Functional interrogation of primary human T cells via CRISPR genetic editing. *J. Immunol.* **201**, 1586–1598 (2018). doi: [10.4049/jimmunol.1701616](https://doi.org/10.4049/jimmunol.1701616); pmid: 30021769
21. R. Nasrallah et al., A distal enhancer at risk locus 11q13.5 promotes suppression of colitis by T_{reg} cells. *Nature* **583**, 447–452 (2020). doi: [10.1038/s41586-020-2296-7](https://doi.org/10.1038/s41586-020-2296-7); pmid: 32499651
22. K. R. Sanson et al., Optimized libraries for CRISPR-Cas9 genetic screens with multiple modalities. *Nat. Commun.* **9**, 5416 (2018). doi: [10.1038/s41467-018-07901-8](https://doi.org/10.1038/s41467-018-07901-8); pmid: 30575746
23. S. Konermann et al., Genome-scale transcriptional activation by an engineered CRISPR-Cas9 complex. *Nature* **517**, 583–588 (2015). doi: [10.1038/nature14136](https://doi.org/10.1038/nature14136); pmid: 25494202
24. S. M. Kaech, W. Cui, Transcriptional control of effector and memory CD8+ T cell differentiation. *Nat. Rev. Immunol.* **12**, 749–761 (2012). doi: [10.1038/nri3307](https://doi.org/10.1038/nri3307); pmid: 23080391
25. J. Zhu, H. Yamane, W. E. Paul, Differentiation of effector CD4 T cell populations (*). *Annu. Rev. Immunol.* **28**, 445–489 (2010). doi: [10.1146/annurev-immunol-030409-101212](https://doi.org/10.1146/annurev-immunol-030409-101212); pmid: 20192806
26. V. Lazarevic, L. H. Glimcher, G. M. Lord, T-bet: A bridge between innate and adaptive immunity. *Nat. Rev. Immunol.* **13**, 777–789 (2013). doi: [10.1038/nri3536](https://doi.org/10.1038/nri3536); pmid: 24113868
27. C. M. Evans, R. G. Jenner, Transcription factor interplay in T helper cell differentiation. *Brief. Funct. Genomics* **12**, 499–511 (2013). doi: [10.1093/bfpg/elt025](https://doi.org/10.1093/bfpg/elt025); pmid: 23878131
28. A. H. Courtney, W.-L. Lo, A. Weiss, TCR signaling: Mechanisms of initiation and propagation. *Trends Biochem. Sci.* **43**, 108–123 (2018). doi: [10.1016/j.tibs.2017.11.008](https://doi.org/10.1016/j.tibs.2017.11.008); pmid: 29269020
29. G. Gaud, R. Lesourne, P. E. Love, Regulatory mechanisms in T cell receptor signalling. *Nat. Rev. Immunol.* **18**, 485–497 (2018). doi: [10.1038/s41577-018-0020-8](https://doi.org/10.1038/s41577-018-0020-8); pmid: 29789755
30. S. J. Holland et al., Functional cloning of Src-like adapter protein-2 (SLAP-2), a novel inhibitor of antigen receptor signaling. *J. Exp. Med.* **194**, 1263–1276 (2001). doi: [10.1084/jem.194.9.1263](https://doi.org/10.1084/jem.194.9.1263); pmid: 11696592
31. J.-W. Shui et al., Hematopoietic progenitor kinase 1 negatively regulates T cell receptor signaling and T cell-mediated immune responses. *Nat. Immunol.* **8**, 84–91 (2007). doi: [10.1038/ni1416](https://doi.org/10.1038/ni1416); pmid: 17115060
32. T. Hart et al., Evaluation and design of genome-wide CRISPR/SpCas9 knockout screens. *G3* **7**, 2719–2727 (2017). doi: [10.1534/g3.117.041277](https://doi.org/10.1534/g3.117.041277); pmid: 28655737
33. S. R. Ferdosi et al., Multifunctional CRISPR-Cas9 with engineered immunosilenced human T cell epitopes. *Nat. Commun.* **10**, 1842 (2019). doi: [10.1038/s41467-019-09693-x](https://doi.org/10.1038/s41467-019-09693-x); pmid: 31015529
34. H. Hu et al., Otd7b facilitates T cell activation and inflammatory responses by regulating Zap70 ubiquitination. *J. Exp. Med.* **213**, 399–414 (2016). doi: [10.1084/jem.20151426](https://doi.org/10.1084/jem.20151426); pmid: 26903241
35. E. P. Mimitou et al., Multiplexed detection of proteins, transcriptomes, clonotypes and CRISPR perturbations in single cells. *Nat. Methods* **16**, 409–412 (2019). doi: [10.1038/s41592-019-0392-0](https://doi.org/10.1038/s41592-019-0392-0); pmid: 31011886
36. C. Alda-Catalinas et al., A single-cell transcriptomics CRISPR-activation screen identifies epigenetic regulators of the zygotic genome activation program. *Cell Syst.* **11**, 25–41.e9 (2020). doi: [10.1016/j.cels.2020.06.004](https://doi.org/10.1016/j.cels.2020.06.004); pmid: 32634384
37. J. M. Replogle et al., Combinatorial single-cell CRISPR screens by direct guide RNA capture and targeted sequencing. *Nat. Biotechnol.* **38**, 954–961 (2020). doi: [10.1038/s41587-020-0470-y](https://doi.org/10.1038/s41587-020-0470-y); pmid: 32231336
38. P. I. Thakore et al., Highly specific epigenome editing by CRISPR-Cas9 repressors for silencing of distal regulatory elements. *Nat. Methods* **12**, 1143–1149 (2015). doi: [10.1038/nmeth.3630](https://doi.org/10.1038/nmeth.3630); pmid: 26501517
39. C. P. Fulco et al., Systematic mapping of functional enhancer-promoter connections with CRISPR interference. *Science* **354**, 769–773 (2016). doi: [10.1126/science.aag2445](https://doi.org/10.1126/science.aag2445); pmid: 27708057
40. X. Xu, L. S. Qi, A CRISPR-dCas toolbox for genetic engineering and synthetic biology. *J. Mol. Biol.* **431**, 34–47 (2019). doi: [10.1016/j.jmb.2018.06.037](https://doi.org/10.1016/j.jmb.2018.06.037); pmid: 29958882
41. I. Chun et al., CRISPR-Cas9 knock out of CD5 enhances the anti-tumor activity of chimeric Antigen Receptor T cells. *Blood* **136** (Supplement 1), 51–52 (2020). doi: [10.1182/blood-2020-136860](https://doi.org/10.1182/blood-2020-136860)
42. R. C. Lynn et al., c-Jun overexpression in CAR T cells induces exhaustion resistance. *Nature* **576**, 293–300 (2019). doi: [10.1038/s41586-019-1805-z](https://doi.org/10.1038/s41586-019-1805-z); pmid: 31802004
43. P. Datlinger et al., Pooled CRISPR screening with single-cell transcriptome readout. *Nat. Methods* **14**, 297–301 (2017). doi: [10.1038/nmeth.4177](https://doi.org/10.1038/nmeth.4177); pmid: 28099430
44. J. W. Freimer et al., Systematic discovery and perturbation of regulatory genes in human T cells reveals the architecture of immune networks. *bioRxiv* 2021.04.18.440363 (2021); <https://www.biorxiv.org/content/10.1101/2021.04.18.440363v1>
45. W. Li et al., MAGeCK enables robust identification of essential genes from genome-scale CRISPR/Cas9 knockout screens. *Genome Biol.* **15**, 554 (2014). doi: [10.1186/s13059-014-0554-4](https://doi.org/10.1186/s13059-014-0554-4); pmid: 25476604
46. G. Korotkevich, V. Sukhov, N. Budin, B. Shpak, M. N. Artyomov, A. Sergushichev, Fast gene set enrichment analysis. *bioRxiv* 060012 (2016); <https://www.biorxiv.org/content/10.1101/060012v3>; doi: [10.1101/060012](https://doi.org/10.1101/060012)
47. H. K. Finucane et al., Partitioning heritability by functional annotation using genome-wide association summary statistics. *Nat. Genet.* **47**, 1228–1235 (2015). doi: [10.1038/ng.3404](https://doi.org/10.1038/ng.3404); pmid: 26414678
48. M. A. Horlbeck et al., Compact and highly active next-generation libraries for CRISPR-mediated gene repression and activation. *eLife* **5**, e19760 (2016). doi: [10.7554/eLife.19760](https://doi.org/10.7554/eLife.19760); pmid: 27661255
49. M. Martin, Cutadapt removes adapter sequences from high-throughput sequencing reads. *EMBnet* **J.** **17**, 10–12 (2011). doi: [10.14806/ej.17.1.200](https://doi.org/10.14806/ej.17.1.200)
50. A. Dobin et al., STAR: Ultrafast universal RNA-seq aligner. *Bioinformatics* **29**, 15–21 (2013). doi: [10.1093/bioinformatics/bts635](https://doi.org/10.1093/bioinformatics/bts635); pmid: 23104886
51. Y. Liao, G. K. Smyth, W. Shi, featureCounts: An efficient general purpose program for assigning sequence reads to genomic features. *Bioinformatics* **30**, 923–930 (2014). doi: [10.1093/bioinformatics/btt656](https://doi.org/10.1093/bioinformatics/btt656); pmid: 24227677
52. M. E. Ritchie et al., limma powers differential expression analyses for RNA-sequencing and microarray studies. *Nucleic Acids Res.* **43**, e47 (2015). doi: [10.1093/nar/gkv007](https://doi.org/10.1093/nar/gkv007); pmid: 25605792
53. H. Heaton et al., Souporell: Robust clustering of single-cell RNA-seq data by genotype without reference genotypes. *Nat. Methods* **17**, 615–620 (2020). doi: [10.1038/s41592-020-0820-1](https://doi.org/10.1038/s41592-020-0820-1); pmid: 32366989
54. R. Satija, J. A. Farrell, D. Gennert, A. F. Schier, A. Regev, Spatial reconstruction of single-cell gene expression data. *Nat. Biotechnol.* **33**, 495–502 (2015). doi: [10.1038/nbt.3192](https://doi.org/10.1038/nbt.3192); pmid: 25867923

55. C. Hafemeister, R. Satija, Normalization and variance stabilization of single-cell RNA-seq data using regularized negative binomial regression. *Genome Biol.* **20**, 296 (2019). doi: [10.1186/s13059-019-1874-1](https://doi.org/10.1186/s13059-019-1874-1); pmid: [31870423](https://pubmed.ncbi.nlm.nih.gov/31870423/)
56. Z. Steinhart, Code repository for: "CRISPR activation and interference screens decode stimulation responses in primary human T cells," Zenodo (2022); doi: [10.5281/zenodo.578465](https://doi.org/10.5281/zenodo.578465)

ACKNOWLEDGMENTS

We thank E. Shifrut, J. Carnevale, and V. Tobin for help related to the development of CRISPRa technologies in T cells; J. Eyquem for providing NY-ESO-1-expressing NALM6 cells; D. Goodman, D. Lee, and B. Hwang for advice related to development of the Perturb-seq platform and analysis; all members of the Marson laboratory for critical insight and discussion over the course of this study; and the staff of the PFCC for support with sorting. Some of the figures were generated using BioRender (<https://biorender.com/>). **Funding:** This work was supported by the National Institute of Diabetes and Digestive and Kidney Diseases (grant DP3DK111914-01 to A.M.); Simons Foundation (A.M.); Burroughs Wellcome Fund, Career Award for Medical Scientists (A.M.); The Cancer Research Institute Lloyd J. Old STAR grant (A.M.); Parker Institute for Cancer Immunotherapy (A.M.); Innovative Genomics Institute (A.M.); National Institutes of Health grant P30 DK063720 to the Parnassus Flow Cytometry Core and A.M.; National Institutes of Health grant S10 1S10D0021822-01 to the PFCC and A.M.; gifts from B. Byers, B. Bakar, K. Jordan, and E. Radutzky (A.M.); Parker Institute for Cancer Immunology scholarship (Z.S.); Austrian Exchange Service and Austrian Society

of Laboratory Medicine Fellowships (R.S.); Max Kade Foundation (R.S.); Care-for-Rare Foundation and German Research Foundation Fellowships (F.B.); National Institutes of Health grant R01HG008140 (J.W.F.); and National Institutes of Health grant S10 RR028962 and James B. Pendleton Charitable Trust to the Gladstone Institutes Flow Cytometry Core Facility. A.M. and C.J.Y. are Chan Zuckerberg Biohub investigators. **Author contributions:** Conceptualization: R.S., Z.S., A.M.; Funding acquisition: R.S., Z.S., A.M.; Investigation: R.S., Z.S., J.W.F., A.M.; Methodology: R.S., Z.S., M.L., R.B., F.B., V.Q.N.; Project administration: R.S., Z.S., A.M.; Supervision: C.J.Y., A.M.; Visualization: R.S., Z.S.; Writing – original draft: R.S., Z.S., A.M.; Writing – review and editing: R.S., Z.S., M.L., J.W.F., R.B., V.Q.N., F.B., C.J.Y., A.M.; **Competing interests:** A.M. is a compensated cofounder, member of the boards of directors, and member of the scientific advisory boards of Spotlight Therapeutics and Arsenal Biosciences. A.M. and C.J.Y. are cofounders, members of the boards of directors, and members of the scientific advisory board of Survey Genomics. A.M. is a compensated member of the scientific advisory board of NewLimit. A.M. was a compensated member of the scientific advisory board at PACT Pharma and was a compensated adviser to Juno Therapeutics. A.M. owns stock in Arsenal Biosciences, Spotlight Therapeutics, NewLimit, Survey Genomics, PACT Pharma, and Merck. A.M. has received fees from Vertex, Merck, Amgen, Trizell, Genentech, AlphaSights, Rupert Case Management and Bernstein and is an investor in and informal adviser to Offline Ventures and a client of EPIQ. The Marson laboratory has received research support from Juno Therapeutics, Epinomics, Sanofi, GlaxoSmithKline,

Gilead, and Anthem. C.J.Y. is a Scientific Advisory Board member for and holds equity in Related Sciences and ImmunAI, a consultant for and holds equity in Maze Therapeutics, and a consultant for TReX Bio. C.J.Y. has received research support from Chan Zuckerberg Initiative and Genentech. J.W.F. is a consultant for NewLimit. R.S., Z.S., and A.M. are listed as inventors on a patent application related to this work. The remaining authors declare no competing interests. **Data and materials availability:** All raw sequencing data critical to the findings of this study, including pooled CRISPR screens and RNA-seq, are deposited at the National Center for Biotechnology Information (NCBI) Gene Expression Omnibus under accession numbers GSE174292, GSE190604, and GSE190846. Custom code critical to reproducing the findings of this study, in addition to analyzed Perturb-seq data, are archived at Zenodo (56). All other data are available in the main text or the supplementary materials.

SUPPLEMENTARY MATERIALS

science.org/doi/10.1126/science.abj4008

Figs. S1 to S20

Tables S1 to S6

References (57–59)

MDAR Reproducibility Checklist

10 May 2021; resubmitted 7 October 2021

Accepted 23 December 2021

[10.1126/science.abj4008](https://doi.org/10.1126/science.abj4008)

RESEARCH ARTICLE SUMMARY

PLANT SCIENCE

Natural history-guided omics reveals plant defensive chemistry against leafhopper pests

Yuechen Bai*, Caiqiong Yang, Rayko Halitschke, Christian Paetz, Danny Kessler, Konrad Burkard, Emmanuel Gaquerel, Ian T. Baldwin*, Dapeng Li*

INTRODUCTION: Although much is known about plant traits that function in nonhost resistance against pathogens, little is known about nonhost resistance against herbivores, despite its agricultural importance, because of the lack of fieldwork. *Empoasca* leafhoppers, serious agricultural pests, identify host plants by eavesdropping on unknown outputs of jasmonate (JA)-mediated signaling in a native tobacco plant that is naturally variable in its JA signaling. The known sectors of this tobacco plant's specialized defense metabolism are not effective against this insect, which calls for an unbiased approach.

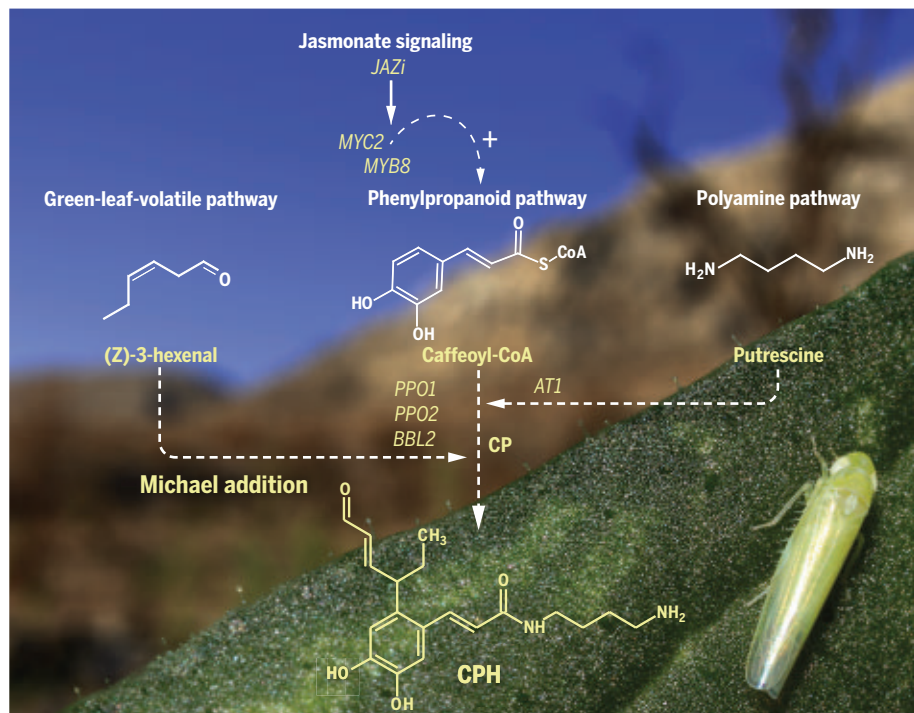
RATIONALE: An unbiased forward-genetics approach based on the screening of a 26-parent recombinant inbred line population in a

natural habitat with native herbivores was wedded with unbiased transcriptomic and mass spectrometry-based metabolomic analyses of reverse-genetics lines to identify defense chemistries produced by this native tobacco when probed by leafhoppers. Synthetic biology approaches were used to reconstitute these chemistries in crop plants.

RESULTS: The analysis revealed an *Empoasca*-elicited JA-JAZi module that pointed to the phenolamide master transcription factor, *MYB8*, as a central genetic hub clustering with putrescine-derived phenolamides. Using tobacco plants silenced for components of JA signaling (*JAZ* and *MYC2* genes) and phenolamide biosynthesis, the central role of a *MYC2*-*MYB8*-*JAZi* branch of JA signaling was confirmed;

however, infiltration of *MYC2*-silenced plants with known putrescine-derived phenolamides did not alter *Empoasca* preference. Subsequent detailed structural analysis revealed an unknown metabolite whose abundance was regulated by the *MYC2*-*MYB8*-*JAZi* branch of JA signaling and was negatively correlated with *Empoasca* damage. Previous work on this unknown metabolite suggested a conjugate of caffeoylputrescine with a C-6 aldehyde produced during wound-induced lipid peroxidation—a process that leads to the formation of green leaf volatiles. Metabolite quantitative trait locus (mQTL) analysis and coexpression analysis pointed to two polyphenol oxidases (PPOs) and one berberine bridge enzyme-like 2 (*BBL2*) gene associated with the metabolite's biosynthesis. The function of the proteins encoded by these genes was tested in both in vitro [*Escherichia coli* expression and enzymatic assays with (Z)-3-hexenal and caffeoylputrescine] and in vivo (transient expression in *Solanum chilense* and *Vicia faba*) systems. The structure of the unknown metabolite was identified by nuclear magnetic resonance (NMR) to be a caffeoylputrescine–green leaf volatile compound (CPH), catalyzed by a PPO in a Michael addition reaction and requiring *BBL2* in planta. Synthetic biology approaches confirmed the function of CPH in nonhost resistance against *Empoasca* leafhoppers in *Nicotiana attenuata* lines silenced to be defective in CPH production; in *V. faba*, a bean crop host plant of the leafhoppers unable to produce caffeoylputrescine; and in *S. chilense*.

CONCLUSION: The natural history-driven multi-omics framework used for the discovery of CPH and its marriage with synthetic biology approaches highlight how readily the results of millions of years of innovation by natural selection can be amortized and transferred to crop plants to catalyze a greener and ecologically more nuanced revolution in plant protection. Crop plants face challenges not substantially different from those faced by native plants; they are constantly tested by hidden herbivore communities that challenge the host-nonhost distinction. In a world of climate change and globally homogenized herbivore communities, opportunistic associations will dominate natural and man-made ecosystems. CPH represents a chemical innovation that allows a native plant to cope with these opportunistic associations and is readily engineered in crop plants. ■



Opportunistic leafhopper attack elicits caffeoylputrescine–green leaf volatile defenses. Attack elicits a JAZi-mediated sector of JA signaling to condense the products of three branches of specialized metabolism (green leaf volatile, phenylpropanoid, and polyamine pathways) in a native tobacco plant through a PPO-catalyzed and *BBL2*-mediated Michael addition reaction to produce previously unobserved defense chemistry (CPH) that was reconstituted in crop plants for durable nonhost resistance. CP, caffeoylputrescine; AT1, acyltransferase 1.

The list of author affiliations is available in the full article online.

*Corresponding author. Email: ybai@ice.mpg.de (Y.B.); baldwin@ice.mpg.de (I.T.B.); dpli@cemps.ac.cn (D.L.)
Cite this article as Y. Bai et al., *Science* 375, eabm2948 (2022). DOI: 10.1126/science.abm2948

READ THE FULL ARTICLE AT
<https://doi.org/10.1126/science.abm2948>

RESEARCH ARTICLE

PLANT SCIENCE

Natural history-guided omics reveals plant defensive chemistry against leafhopper pests

Yuechen Bai^{1*}, Caiqiong Yang¹, Rayko Halitschke¹, Christian Paetz², Danny Kessler¹, Konrad Burkard¹, Emmanuel Gaquerel³, Ian T. Baldwin^{1*}, Dapeng Li^{4,5*}

Although much is known about plant traits that function in nonhost resistance against pathogens, little is known about nonhost resistance against herbivores, despite its agricultural importance. *Empoasca* leafhoppers, serious agricultural pests, identify host plants by eavesdropping on unknown outputs of jasmonate (JA)-mediated signaling. Forward- and reverse-genetics lines of a native tobacco plant were screened in native habitats with native herbivores using high-throughput genomic, transcriptomic, and metabolomic tools to reveal an *Empoasca*-elicited JA-JAZi module. This module induces an uncharacterized caffeoylputrescine–green leaf volatile compound, catalyzed by a polyphenol oxidase in a Michael addition reaction, which we reconstitute in vitro; engineer in crop plants, where it requires a berberine bridge enzyme-like 2 (BBL2) for its synthesis; and show that it confers resistance to leafhoppers. Natural history-guided forward genetics reveals a conserved nonhost resistance mechanism useful for crop protection.

Being at the bottom of most terrestrial food chains, plants are continuously attacked by herbivores and pathogens (1, 2). Research into plant traits that provide resistance against these biotic agents has primarily focused on nonhost resistance to pathogens (3–5) and host resistance to herbivores (6, 7). This difference in emphasis likely reflects the greater physiological autonomy of herbivores, which are selective in choosing plants to attack, coupled with the challenge of discovering resistance traits of hosts that herbivores refuse to attack. Plants rendered defenseless by the abrogation of defense pathways can be attacked by nonhost herbivores in nonchoice assays in the laboratory (8, 9). However, these assays do not capture the selective procedures by which insects choose their host plants in nature, which limits the inferences that can be drawn from these laboratory studies about nonhost resistance. Because of the paucity of field studies, the mechanisms and metabolic traits underlying nonhost resistance against herbivores remain largely unknown.

We found that *Nicotiana attenuata* plants—transformed to silence the signaling that me-

diates inducible expression of host resistance traits—when released into the wild, are continuously assessed and attacked by nonhost insect herbivores when rendered defenseless (10). Among these opportunistic herbivores is the *Empoasca* leafhopper—a major pest common to many crops. These leafhoppers probe nonhost plants to eavesdrop on a plant's jasmonate (JA) signaling, which is elicited upon probing (11). However, *N. attenuata*'s portfolio of JA-elicited specialized metabolites, such as alkaloids, protease inhibitors, diterpene glycosides (17-HGL-DTGs), and elicited volatiles, which are effective against host herbivores, were excluded as nonhost resistance traits (11). Because many agricultural pests may be opportunistic herbivores, understanding mechanisms of nonhost resistance against insects could accelerate the breeding of durable resistance in crops. To date, the most commonly used strategies to control agricultural pests are insecticidal sprays and ectopic expression of insecticidal proteins, both of which have ecological drawbacks (12, 13).

To uncover the JA-elicited nonhost resistance traits of *N. attenuata*, we adopted a forward-genetics strategy. We planted a replicated population of 650 recombinant inbred lines (RILs) from a 26-parent multiparent advanced generation intercross (MAGIC) population into a native habitat in Arizona, USA (Fig. 1A and fig. S1). In this setting, *Empoasca* leafhoppers are abundant and damage their native host cucumbers (*Cucurbita foetidissima*). JA-deficient *N. attenuata* lines were attacked by the leafhoppers (11) at rates that varied within the MAGIC populations (Fig. 1A). We quantified *Empoasca* attack levels in 1907 indi-

vidual plants of 674 RILs and parental lines of the field-grown MAGIC population and constructed a multi-omics dataset based on high-throughput analyses of phytohormones, transcriptomes, and metabolomes. This multi-omics dataset was produced from leaves elicited by a simulated herbivory treatment. We mimicked herbivore attack by treating standardized puncture wounds (W) with oral secretions (OS) of *Manduca sexta* larvae (W + OS) to remove confounding factors caused by the stochastic nature of insect attack in nature and to capture transiently expressed genes and metabolites in these samples from field-grown plants (Fig. 1B and fig. S2).

To analyze associations among the genetic and metabolic responses of this multi-omics dataset, we first focused on JA signaling-related genes and used previously acquired knowledge of *N. attenuata* leaf chemistry (14, 15) to construct a coassociation network of the JA-dependent module. This network considered not only the correlations among metabolites, phytohormones, and gene expressions but also the shared single-nucleotide polymorphisms (SNPs) inferred from metabolic quantitative trait locus (mQTL) or expression QTL (eQTL) analyses for each of these components (Fig. 1C, fig. S3, and data S1). This coassociation network revealed that JAs and JA-related genes nucleated by the JA-regulated phenolamide master transcription factor (TF) regulator NaMYB8 (16) formed a genetic hub that clustered with induced phenolamides, such as *N*-coumaroylputrescine (CoP), *N*-caffeoylputrescine (CP), *N*-feruloylputrescine (FP), and malonylated 17-HGL-DTGs (Fig. 1C). More peripheral to this hub were glycosylated 17-HGL-DTG precursors, such as lyciumoside I, lyciumoside IV, attenoside, and nicotianoside III, and other specialized metabolites, such as nicotine, acylsugars, and flavonoids (fig. S3). A *NaJAZi* gene clustered centrally to JAs but was distant from *NaJAR4* and *NaCOI1*, which suggests the engagement of JA signaling.

To further resolve the components in the coassociation network responsible for *Empoasca* susceptibility, we conducted a pairwise correlational analysis among the omics datasets and *Empoasca* abundance and leaf area damaged in the RILs of the MAGIC populations (Fig. 1D). The putrescine-derived phenolamides and malonylated 17-HGL-DTGs were negatively correlated with the *Empoasca* numbers and damage, whereas glycosylated 17-HGL-DTG precursors were positively correlated. JA-related genes *NaMYB8*, *NaLOX3*, *NaAOC*, *NaOPR3*, *NaJAR6*, and *NaWIPK* exhibited the highest negative correlation scores with the *Empoasca* numbers and damage. There was considerable heterogeneity in the expression of the JA-related family of JAZ genes, with the expression of *NaJAZa*, *NaJAZd*, *NaJAZf*,

¹Department of Molecular Ecology, Max Planck Institute for Chemical Ecology, D-07745 Jena, Germany. ²Department of Biosynthesis/NMR, Max Planck Institute for Chemical Ecology, D-07745 Jena, Germany. ³Institut de Biologie Moléculaire des Plantes du CNRS, Université de Strasbourg, Strasbourg, France. ⁴National Key Laboratory of Plant Molecular Genetics, CAS Center for Excellence in Molecular Plant Sciences, Institute of Plant Physiology and Ecology, Chinese Academy of Sciences, Shanghai, China. ⁵CAS-JIC Center of Excellence for Plant and Microbial Sciences (CEPAMS), Institute of Plant Physiology and Ecology, Chinese Academy of Sciences, Shanghai, China.

*Corresponding author. Email: ybai@ice.mpg.de (Y.B.); baldwin@ice.mpg.de (I.T.B.); dpli@ceps.ac.cn (D.L.)

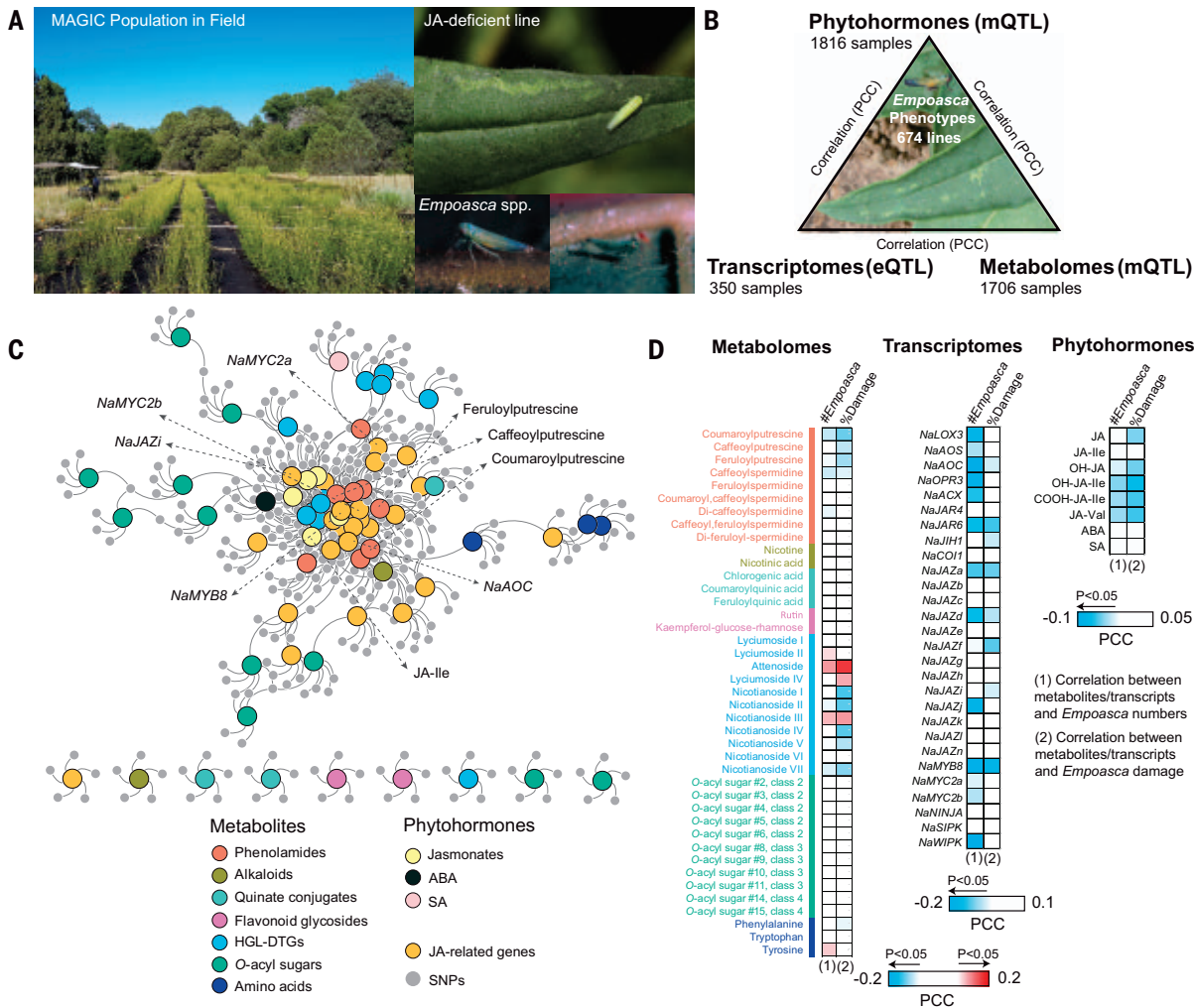


Fig. 1. A native insect-guided multi-omics atlas of forward-genetics lines of a field-grown *N. attenuata* MAGIC population highlights deviations from canonical JA signaling for *Empoasca* leafhopper nonhost resistance. (A) Field plantation of the MAGIC RIL population of native *N. attenuata* tobacco plants in their native habitat at the WCCER field station in Arizona, USA. Native opportunistic *Empoasca* leafhopper communities and their feeding damage on leaves are illustrated. Leafhoppers attack these plants in a JA-dependent manner and preferentially select JA-deficient plants as hosts (images: R. Halitschke, D. Kessler, A. Kessler). (B) Schematic of high-throughput phenotyping of phytohormones (1816 samples), transcriptomes (350 samples), and metabolomes (1706 samples) and *Empoasca* phenotypes (1907 observations of *Empoasca* abundance and leaf damage) of 674 MAGIC RILs and parental lines in the field. To remove confounding factors caused by the stochastic nature of insect attack in nature, we mimicked herbivore feeding by immediately applying freshly collected oral secretions of *M. sexta* larvae to standardized puncture wounds in leaves at standardized leaf positions. This procedure, referred to as W + OS treatment,

standardizes the elicitation by precisely timing the initiation of herbivory-elicited responses. The phytohormone and transcriptome datasets were collected 1 hour after W + OS treatment and the metabolome dataset after 72 hours. PCC, Pearson correlation coefficient. (C) Coassociation network built from correlations among metabolomes, transcriptomes, phytohormones, and SNPs (PCC cutoff, $P < 0.05$), and the top five most significant SNPs for each gene (small gray circles), metabolites, or phytohormones from eQTL or mQTL imputations were retained. Phytohormones and metabolites of different compound classes and JA-related genes are labeled with different colors. JA-Ile, JA signaling genes (*NaAOC*, *NaMYC2a*, *NaMYC2b*, and *NaJAZi*), *NaMYB8*, and phenolamides (*N*-coumaroylputrescine, *N*-caffeoylputrescine, and *N*-feruloylputrescine) form a central cluster and are labeled. See fig. S3 for identities of the more peripheral nodes. ABA, abscisic acid; SA, salicylic acid. (D) Heatmap of coexpressions among metabolites, JA-related genes, and phytohormones with *Empoasca* phenotypes (numbers and area damaged) calculated as pairwise PCC (only significant correlations with $P < 0.05$ are shown with colors).

NaJAZi, and *NaJAZj* negatively correlated with the *Empoasca* numbers and damage. The expression of JAZ genes known to mediate *M. sexta* defense responses, such as *NaJAZh* (17), showed no significant correlations. JA, but not the canonical mediator of JA signaling, JA-Ile, was negatively correlated with the *Empoasca* numbers and damage, and

negative correlations were also observed for the hydroxylated and carboxylated JAs (OH-JA, OH-JA-Ile, and COOH-JA-Ile) and JA-valine conjugates (JA-Val). These results provided forward-genetics confirmation of the central role of JA signaling and pointed to downstream components likely involved in the *Empoasca* leafhopper resistance response.

An elicited JA-JAZi module regulates *Empoasca* resistance
To further disentangle the intricacies of the *Empoasca*-elicited JA signaling sector and its regulated downstream metabolic signatures responsible for *Empoasca* resistance, we adopted a reverse-genetics approach to examine the involvement of phenolamides. Isogenic

lines of *N. attenuata* plants individually RNA interference (RNAi)-silenced [inverted repeat (ir)] or overexpressed (ov) in different JAZ genes and *NaMYC2* to evaluate JA signaling-deficiency; in *NaMYB8*, the phenolamide master TF regulator; and in *DH29* and *CV86*, which catalyze spermidine conjugation steps in phenolamide biosynthesis, were screened in a glasshouse open-choice screening experiment using laboratory colonies of *Empoasca decipiens* (Fig. 2A and figs. S4 and S5). Nymphs and adult *E. decipiens* preferentially selected irMYC2, irMYB8, and ovJAZi plants for feeding and reproduction in contrast to the other transgenic lines, which were only slightly damaged by a few probing events (Fig. 2A). Diverse JAZ proteins allow the JA signaling cascade to regulate an array of metabolic and developmental traits in different tissues at different times (18, 19), thereby contextualizing responses and optimizing fitness. The modularity of the JA-JAZi sector may provide specific responses relevant to *Empoasca* leafhoppers. A tissue-wide transcriptomics analysis of all JAZ genes in the *N. attenuata* genome revealed that *NaJAZi* is highly expressed in flower tissues and is not responsive to *M. sexta* attack in leaves (20), whereas *NaJAZh* showed the opposite pattern (Fig. 2B and fig. S6). These patterns were confirmed by exposing leaves to *E. decipiens* and *M. sexta* attack and monitoring the kinetics of the JAZ transcript accumulations: *M. sexta* feeding elicited *NaJAZh* transcripts in leaves, whereas *Empoasca* feeding elicited *NaJAZi* transcript in leaves (Fig. 2B). Yeast two-hybrid (Y2H) assays revealed that *NaJAZi* interacts with *NaMYC2a*, whereas *NaMYB8* interacts with *NaMYC2b* (fig. S7). These data reveal that a sector of JA signaling involving MYC2, MYB8, and JAZi is engaged in *Empoasca* resistance in leaves.

To identify the metabolites elicited by this JA sector, we reared either *E. decipiens* adults and nymphs or *M. sexta* larvae on leaves of rosette-stage plants of JA signaling-deficient transgenic lines (Fig. 2A) as well as on irAOC and irCOII plants; on irGGPPS, which are deficient in 17-HGL-DTGs accumulations; and on irPMT plants, which are impaired in nicotine accumulations (fig. S8). We used an analytical and computational workflow (14, 15, 21) to collect high-resolution indiscriminant (data-independent) tandem mass spectrometry (MS/MS) spectra (termed idMS/MS) from extracts of *Empoasca*- and *Manduca*-damaged leaves. We quantified metabolome specialization (δj index), metabolome diversity (Hj index), and metabolic specificity of individual metabolites (Si index) using an information theory framework (21, 22). In the dimensions of information theory-processed metabolome specialization and diversity, *M. sexta* attack elicited overall higher metabolome plasticity, resulting in higher δj scores than those elicited by attack

by *E. decipiens*. The different transgenic lines showed distinct trajectories of metabolome plasticity reprogrammed by the attack of the two insect species (Fig. 2C and fig. S9).

Focusing on transgenic lines preferred by *Empoasca*, we noticed that the distinct signatures of metabolome specialization elicited by herbivore attack were weaker in irMYC2 and irMYB8 plants (Fig. 2C and fig. S9). This suggested that MYC2 is a master regulator of metabolome plasticity in response to insect attack and that MYB8-dependent herbivory-induced phenolamides make up the metabolic sector responsible for the increases in metabolome specialization. The separation of the trajectories of metabolome changes elicited by *Empoasca* and *Manduca* attack in the ovJAZi lines, rather than their abolishment, further pointed to a small set of metabolites elicited by *Empoasca* attack, regulated by *NaJAZi*, and potentially involved in *Empoasca* resistance.

To identify these metabolites, we ranked Si scores for metabolite specificity calculated for each MS/MS spectrum from the *E. decipiens*-elicited metabolomes from the four transgenic lines and linked the Si scores with coexpression heatmaps derived from correlations calculated among individual metabolites and *Empoasca* numbers and damage using the global variance generated from all reverse-genetics lines used in the feeding experiment (Fig. 2D and fig. S9). Phenolamides ranked at the top of the metabolic specificity Si scores, with the putrescine-derived metabolites among the highest, and these were negatively correlated with *Empoasca* numbers and damage, in contrast to particular 17-HGL-DTGs, quinate conjugates, and nicotinic acid, which showed positive correlations (Fig. 2D).

The putrescine-derived phenolamides, CoP, CP, and FP, were reduced in irAOC, irCOII, irMYC2, and irMYB8 lines and selectively decreased in ovJAZi plants damaged by *Empoasca* feeding but not in those damaged by *Manduca* feeding, whereas other spermidine-derived phenolamides showed similar responses to the attacks of the two herbivore species in ovJAZi plants (fig. S10). The spermidine-derived metabolites could be excluded as mediators of *Empoasca* nonhost resistance on the basis of the lack of responses of leafhoppers to the irDH29 and irCV86 lines (Fig. 2A). To further explore the involvement of CoP, CP, and FP, we conducted in vivo *Empoasca* choice assays by individually infiltrating physiologically relevant concentrations of synthetic CoP (7 μ M), CP (100 μ M), and FP (10 μ M) into leaves of irMYC2 plants that are devoid of elicited phenolamides (Fig. 2E and fig. S11). However, these infiltrations did not alter the preference of *Empoasca* for irMYC2 plants. In vitro *Empoasca* direct feeding assays conducted with individual compounds at physiologically relevant concentrations in glucose solutions revealed no

significant changes in mortality rates of *E. decipiens* compared with those fed on glucose controls (Fig. 2E). These data suggest that CoP, CP, and FP were not directly responsible for *Empoasca* resistance and that other yet-unknown putrescine-derived phenolamide metabolites were responsible.

Multi-omics reveals the defense and its three-pronged pathway

Leaves of herbivore-attacked *N. attenuata* plants grown in the glasshouse accumulate a variety of putrescine- and spermidine-derived phenolamides (14, 16). We selected 15 RILs from the field-based multi-omics dataset of the MAGIC population (Fig. 1) that accumulated high levels of structurally diverse OS-induced phenolamides to construct idMS/MS and identify the structures of putrescine-derived phenolamides. This effort resulted in 518 nonredundant idMS/MS spectra (Fig. 3A). We performed a biclustering analysis to cluster spectra according to fragment [normalized dot product (NDP)] and neutral loss (NL)-based similarities, which resulted in seven modules (Fig. 3A). Module 5, particularly enriched in phenolamide-related compounds containing caffeoyl or putrescine moieties, was further mapped onto a molecular network (Fig. 3A). An unknown compound at mass/charge ratio (m/z) 347.196 ($[M+H]^+$, $C_{19}H_{27}N_2O_4^+$) occupied the first layer of directly linked network neighbors for the two isomers of CP (m/z 251.14) because of their shared neutral losses of putrescine of $\Delta 88.10$ Da and fragment peak at m/z 163.04 ($C_9H_7O_3^+$) corresponding to the caffeoyl moiety (Fig. 3A and fig. S12). The idMS/MS for a fragment peak at m/z 259.09 ($C_{15}H_{15}O_4^+$), which resulted from the loss of putrescine of the molecular ion, further fragmented to m/z 163.04 with a neutral loss of 96.055 Da (C_6H_8O). This implied that the unknown m/z 347.19 is a CP derivative decorated with a C_6H_8O residue on the aromatic ring of the caffeoyl moiety (fig. S12), which had previously been associated with JA signaling in natural accessions of *N. attenuata* (14).

To test whether the unknown m/z 347.19 metabolite is regulated by the specific JA-JAZi module, we explored the coassociation network and conducted coexpression analyses for induced m/z 347.19 against *Empoasca* numbers and damage and JAs in the field-planted MAGIC population (Fig. 1). The m/z 347.19 was negatively correlated with *Empoasca* damage but positively correlated with JA, JA-Ile, and JA-Val (fig. S13). We then mined the *Empoasca*-induced metabolomes of JA-deficient transgenic lines (Fig. 2). However, with similar computational workflows, we were unable to identify this compound in the dataset described earlier (Fig. 2). Extensive experimentation revealed that field-planted RILs elicited more of this unknown compound than glasshouse-grown

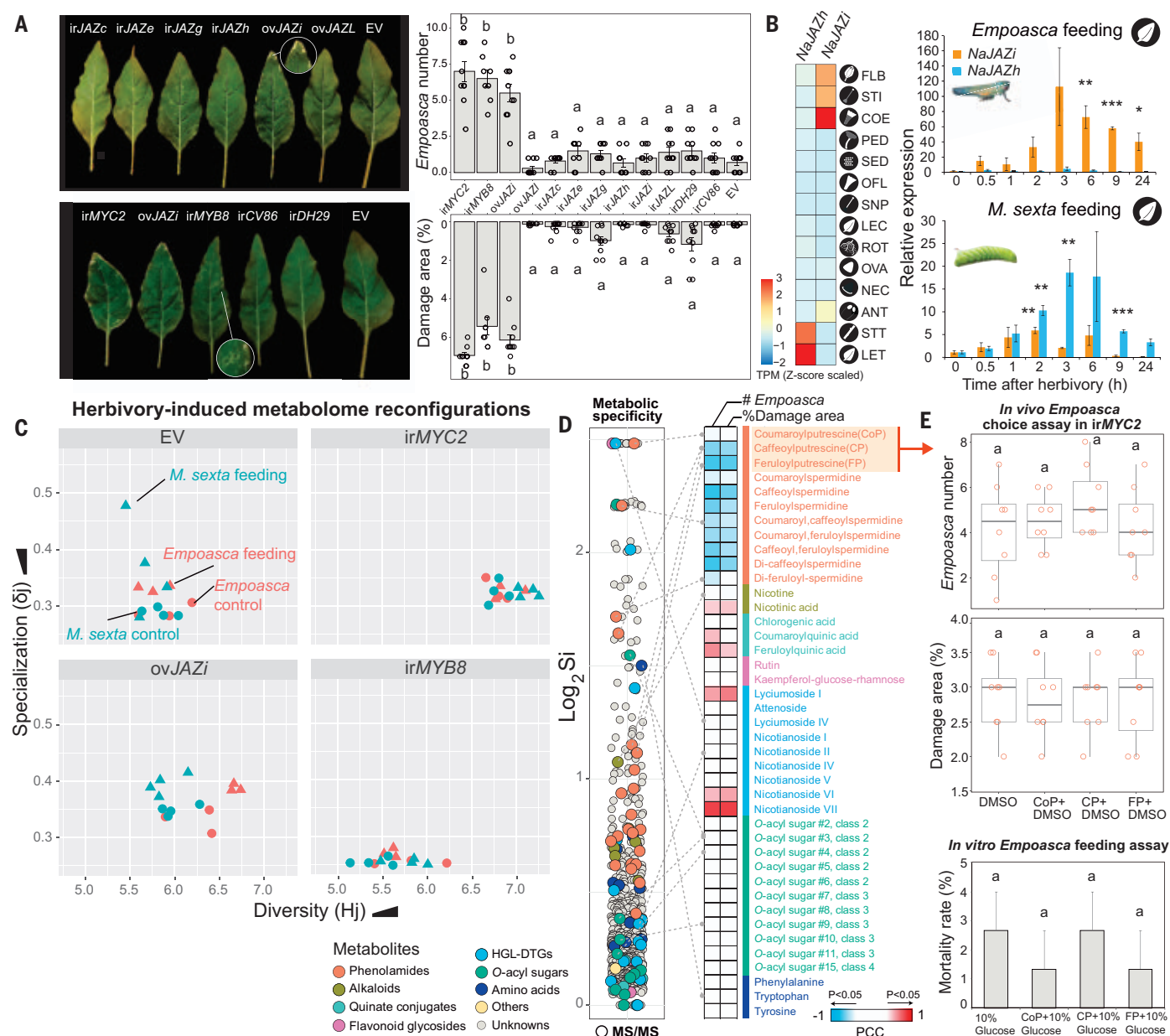


Fig. 2. Reverse genetics coupled with information theory-based unbiased metabolomics reveal an *Empoasca*-elicited JA-JAZi module regulating induced unknown putrescine-containing phenolamides correlated with *Empoasca* nonhost resistance. (A) Phenotypes of *Empoasca*-damaged leaves on transgenic *N. attenuata* lines. Plants ($n = 10$) were randomly placed in an open-choice glasshouse environment containing *Empoasca* leafhoppers (fig. S4). Representative leaves are shown for each genotype, with insets highlighting the damage of *ovJAZi* and *irMYB8* lines. Different letters indicate significant differences [$P < 0.001$, one-way analysis of variance (ANOVA) followed by Tukey's post hoc multiple comparisons]. (B) Tissue-specific expression profiles of *NaJAZh* and *NaJAZi* in *N. attenuata* WT (left); heatmap coloring depicts the Z-score-scaled transcripts per million (TPM). Kinetics of relative transcript accumulations of *NaJAZh* and *NaJAZi* in leaves of *N. attenuata* ($n = 3$) in response to continuous *E. decipiens* and *M. sexta* feeding with samples harvested at 0 to 24 hours after the start of feeding. FLB, flower bud; STI, stigma; COE, corolla early; PED, pedicel; SED, seed; OFL, opening flower; SNP, style; LEC, leaf control; ROT, roots from OS-treated plants; OVA, ovary; NEC, nectary; ANT, anther; STT, stem treated; LET, leaf treated. (C) Scatterplots of specialization (δ_j) versus diversity (H_j) indices for specialized metabolomes of leaves ($n = 4$) after 72 hours of feeding by *E. decipiens* and *M. sexta* on four transgenic lines selected from a set of

16 transgenic lines (see fig. S9 for the complete dataset). An increase in metabolome specialization (δ_j) indicates that, on average, more herbivory or genotype-specific metabolites are produced, whereas an increase in metabolome diversity (H_j) indicates that either qualitatively more metabolites are produced or that quantitatively the global metabolic frequency profile is more uniformly distributed. Colors denote different insects, and symbols denote different treatments—triangles indicate insect feeding, and circles indicate untreated controls. (D) A ranked metabolite specificity (S_i) index distribution plot was calculated for each metabolite on the basis of *E. decipiens* specifically elicited metabolomes from the four transgenic lines shown in (C) (left) and further linked with a PCC coexpression heatmap among metabolites and *E. decipiens* number and damage phenotypes (right) for which the data from all reverse-genetics lines shown in (A) were used to enhance the statistical power of the PCC calculations. Dots are colored on the basis of compound class annotations. Only significant correlations with $P < 0.05$ are shown with colors. (E) In vivo *Empoasca* choice assays ($n = 8$) conducted by infiltrating synthetic CoP, CP, or FP diluted in 0.1% dimethyl sulfoxide (DMSO) solutions into *irMYC2* leaves (top) and in vitro *Empoasca* nonchoice assays ($n = 3$, 25 *Empoasca* leafhoppers per replicate) by feeding *Empoasca* with synthetic CoP, CP, or FP diluted in 10% glucose solutions (bottom) revealed that these phenolamides were not affecting leafhopper behavior or performance.

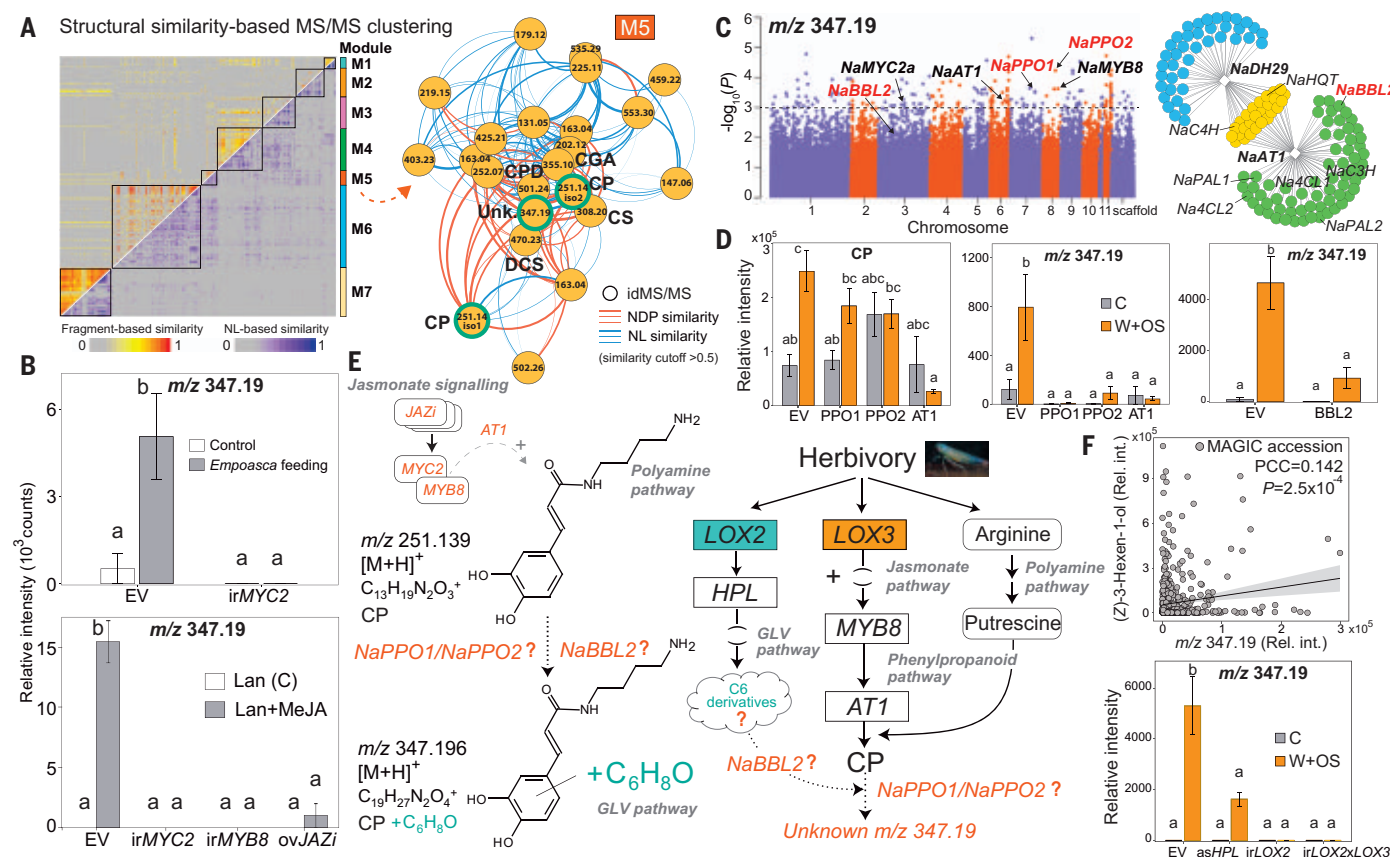


Fig. 3. Elucidating an herbivory-elicited GLV-caffeoylputrescine metabolite and its three-pronged biosynthetic pathways by combining MS/MS structural metabolomics with forward and reverse genetics. (A) (Left) Biclustering of 518 idMS/MS spectra constructed from 15 RILs of the field-planted MAGIC population based on shared fragments (NDP-based similarity) and shared neutral losses (NL-based similarity) reveals seven distinct modules (M1 to M7) in the molecular network. (Right) Close-up of module 5 in which putrescine- or caffeoyl-derived phenolamides are enriched harboring an unknown metabolite m/z 347.19 that is directly linked to two isomers of CP (circled in green). CS, *N*-caffeoylspermidine; CoCS, *N*,*N'*-coumaroyl, caffeoylspermidine; CFS, *N*,*N'*-caffeoyl, feruloylspermidine; DCS, *N*,*N'*-dicaffeoylspermidine; CPD, caffeoylputrescine dimer; CGA, chlorogenic acid; Unk., unknown. (B) Accumulations of m/z 347.19 in *Empoasca*-elicited EV and *irMYC2* lines (top) and MeJA-induced EV, *irMYC2*, *irMYB8*, and *ovJAZi* lines (bottom). (C) (Left) Manhattan plot for herbivory-induced unknown m/z 347.19 from an mQTL analysis of W + OS-elicited leaves from the MAGIC RIL population grown in the glasshouse and extracted with procedures that minimize losses of the phenolamide sector. Core JA signaling gene, *NaMYC2a*; phenolamide regulator, *NaMYB8*; CP biosynthetic gene, *NaAT1*; and two unknown biosynthetic candidate genes, *NaPPO1* and *NaPPO2*, were

imputed in the mQTL analysis (P value cutoffs = 10^{-3}) as well as an uncharacterized candidate gene, *NaBBL2* (P = 0.0013). (Right) Gene coexpression network constructed using a previously published microarray dataset of *irMYB8* plants harvested 1 and 5 hours after W + OS elicitation. The phenolamide biosynthetic genes, *NaAT1* and *NaDH29*, were used as baits (diamonds). Yellow dots depict genes coexpressed with both baits, whereas the green (*NaAT1*) and blue (*NaDH29*) dots depict genes coexpressed with a single bait. (D) VIGS of biosynthetic gene candidates involved in m/z 347.19 production. Silencing *NaPPO1*, *NaPPO2*, *NaAT1*, and *NaBBL2* expression abolished the elicitation of m/z 347.19 by W + OS treatment observed in EV control plants (C indicates untreated controls). (E) Proposed three-pronged biosynthetic pathway for the *Empoasca*-elicited m/z 347.19 production, which requires the LOX2-HPL-dependent C6 GLV metabolism, LOX3-dependent and JA-regulated phenylpropanoid metabolism, and polyamine metabolism, the outputs of which are putatively conjugated in *NaBBL2*- and *NaPPO1/2*-dependent reactions. (F) Scatterplots of metabolite abundance of m/z 347.19 against (Z)-3-hexen-1-ol volatile emissions in MAGIC accessions from the glasshouse (top) and m/z 347.19 accumulation after W + OS treatment in leaves of stably transformed EV, *asHPL*, *irLOX2*, and *irLOX3* lines (bottom).

RILs (data S2) and that seemingly minor differences in leaf sampling and extraction technique—potentially the simultaneous exposure of leaves to aluminum foil and liquid N_2 and unfavorable pH conditions (table S1)—resulted in the loss of this unstable phenolamide in plants grown and sampled under glasshouse conditions.

We reared *Empoasca* on *irMYC2* plants again and, by optimizing extraction conditions, found that *Empoasca* feeding strongly elicited m/z

347.19 accumulations in empty vector (EV)-transformed plants; these accumulations were abolished in *irMYC2* lines (Fig. 3B). During this extraction optimization effort, we realized that the *Empoasca* leafhopper elicitation procedure could be replaced by the experimentally more tractable elicitations by larval oral secretions or methyl jasmonate (MeJA). Consistently, MeJA-induced production of m/z 347.19 was hampered in *irMYC2*, but also in *irMYB8* and *ovJAZi* lines (Fig. 3B). These re-

sults revealed that the unknown m/z 347.19 is regulated by the JA-JAZi-MYC2-MYB8 signaling sector, which is likely responsible for *Empoasca* resistance.

To investigate the biosynthetic origins of m/z 347.19, we extracted OS-elicited leaves of the entire MAGIC RIL population grown under glasshouse conditions and phenolamide-permissive conditions and conducted an mQTL analysis (Fig. 3C). The analysis imputed a series of genes (with P values $<10^{-3}$) known to be

involved in the regulation and biosynthesis of CP and m/z 347.19, including *NaMYC2a*, *NaMYB8*, and *NaAT1*, which encodes a hydroxycinnamoyl-coenzyme A:putrescine acyltransferase responsible for CP biosynthesis (16), as well as two polyphenol oxidases (PPOs), *NaPPO1* and *NaPPO2*, which are located on chromosomes 7 and 8, respectively (Fig. 3C). Coexpression analyses of a microarray dataset of *irMYB8* lines (23) using *NaAT1* and *NaDH29* as baits revealed a cluster of genes in the *NaAT1* groupings known to be involved in the biosynthesis of CP, including *NaPAL1*, *NaPAL2*, *Na4CL1*, and *NaC3H*. A berberine bridge enzyme-like (BBL) gene, *NaBBL2*, was highly coexpressed with *NaAT1* and decreased in its induced expressions in *irMYB8* lines (Fig. 3C and fig. S14A). We revisited the mQTL dataset and found that *NaBBL2*, located on chromosome 3, was associated with m/z 347.19 (Fig. 3C), albeit at reduced statistical significance ($P = 0.0013$). Time-resolved microarray data (24) of herbivory-elicited expression of *NaAT1*, *NaPPO2*, and *NaBBL2* revealed that *NaAT1* and *NaPPO2* showed similar induction patterns in *N. attenuata* wild type (WT), whereas *NaBBL2* was highly induced at 1 hour and retained its induction at later time points, albeit at reduced levels (fig. S14B). Moreover, the herbivory-elicited inductions of *NaAT1*, *NaPPO1*, *NaPPO2*, and *NaBBL2* were reduced in an RNA sequencing (RNA-seq) transcriptome dataset of *irMYC2* lines (fig. S14C).

Although the number and order of the biosynthetic steps for m/z 347.19 accumulations remained elusive, we hypothesized that possible oxidation and acylation reactions were likely required. We therefore focused on oxidases and acyltransferases collectively imputed from the multi-omics analysis. Candidate genes included three acyltransferases, *NaAT1*, *NaAT2*, and *NaAT3*; three polyphenol oxidases, *NaPPO1*, *NaPPO2*, and *NaPPO3*; and a BBL gene, *NaBBL2*. We evaluated the *in vivo* functions of the candidate genes as well as *NaAT1* as a positive control by silencing their expression in *N. attenuata* using virus-induced gene silencing (VIGS). Consistent with a previous analysis, VIGS of *NaAT1* abolished m/z 347.19 accumulation (14). Similarly, silencing *NaPPO1*, *NaPPO2*, and *NaBBL2* expression also truncated the elicitation of m/z 347.19 (Fig. 3D and fig. S15). Untargeted metabolomics analysis of the VIGS-silenced plants revealed that silencing *NaPPO1* and *NaPPO2* truncated m/z 347.19 accumulations without changes in other phenolamides (Fig. 3D and fig. S16). These results suggest that *NaPPO1*, *NaPPO2*, and *NaBBL2* are required for the *in vivo* production of m/z 347.19.

Previous analysis has suggested that the additional C_6H_8O residue of m/z 347.19 is produced from the fatty acid oxylipin cascade, which converts $C18$ polyunsaturated fatty acids

released from biological membranes during stresses, wounding, and herbivory (25) to produce green leaf volatiles (GLVs) enriched in reactive C_6 derivatives (14). We measured herbivory-elicited GLVs in the same glasshouse-grown MAGIC RIL population used for the imputation (Fig. 3) and conducted correlational analysis with herbivory-elicited m/z 347.19 accumulations. (*Z*)-3-hexenal-derived volatiles, such as (*Z*)-3-hexenyl-propanoate and (*Z*)-3-hexenol, were the most significantly positively correlated metabolites with m/z 347.19, whereas 1-hexanol, linalool, and other elicited volatiles were not (Fig. 3F and fig. S17).

The C_6 aldehydes, with their molecular formula of C_6H_8O , are the most reactive aldehydes produced from the GLV pathway and have been hypothesized (14) to be the missing substrates for the biosynthesis of m/z 347.19. Consistent with previous analyses (26), stably silencing *LIPOXYGENASE2* (*irLOX2*) in *N. attenuata*, which controls the first committed step in the GLV pathway, abolishes C_6 aldehydes production and total GLV emissions (14), and stably silenced crosses of *irLOX2* and *irLOX3* (*irLOX2* × *irLOX3*) completely eliminated m/z 347.19 production (Fig. 3F). Additionally, silencing *NaHPL* (with an antisense construct, as *HPL*)—which catalyzes the formation of the initial C_6 GLV product, (*Z*)-3-hexenal, and its isomer, (*E*)-2-hexenal—results in considerable time-dependent reductions of GLVs in *N. attenuata* (27) and reduced m/z 347.19 accumulations to $\sim 1/3$ of the WT levels (Fig. 3F). From these results, we surmised that in response to *Empoasca* probing, m/z 347.19 is produced by a three-pronged metabolic pathway composed of the *LOX2*–*HPL*–GLV pathway, the *LOX3*–*JA*–regulated phenylpropanoid pathway, and the polyamine pathway, which are condensed by *NaPPO1*, *NaPPO2*, and *NaBBL2* using CP and (*Z*)-3-hexenal or (*E*)-2-hexenal to produce m/z 347.19 (Fig. 3E).

To test this hypothesis, we isolated purified *NaPPO1*, *NaPPO2*, and *NaBBL2* proteins with N-terminal hexahistidine tags after expression in *Escherichia coli* (fig. S18). Incubation of either *NaPPO1* or *NaPPO2* (*NaPPO1/2*) with CP and (*Z*)-3-hexenal yielded a m/z 347.19 peak with a MS/MS spectrum and retention time identical to that of the m/z 347.19 induced in *N. attenuata* leaves (fig. S19). Additionally, by-products of doubly charged CP dimers at m/z 250.13 ($[M+2H]^{2+}$, $C_{26}H_{36}N_4O_6^{2+}$), which are not detected in OS-induced leaves of *N. attenuata* WT (data S2), were also produced *in vitro* (Fig. 4A and fig. S20). These doubly charged CP dimers were only produced when the quantities of the (*Z*)-3-hexenal substrate were lower than those of the CP substrate *in vitro*. *NaPPO1/2* showed little-to-no activity when incubated with CP and (*E*)-2-hexenal (Fig. 4A). *NaBBL2* alone could not use CP and (*Z*)-3-hexenal as the substrates to pro-

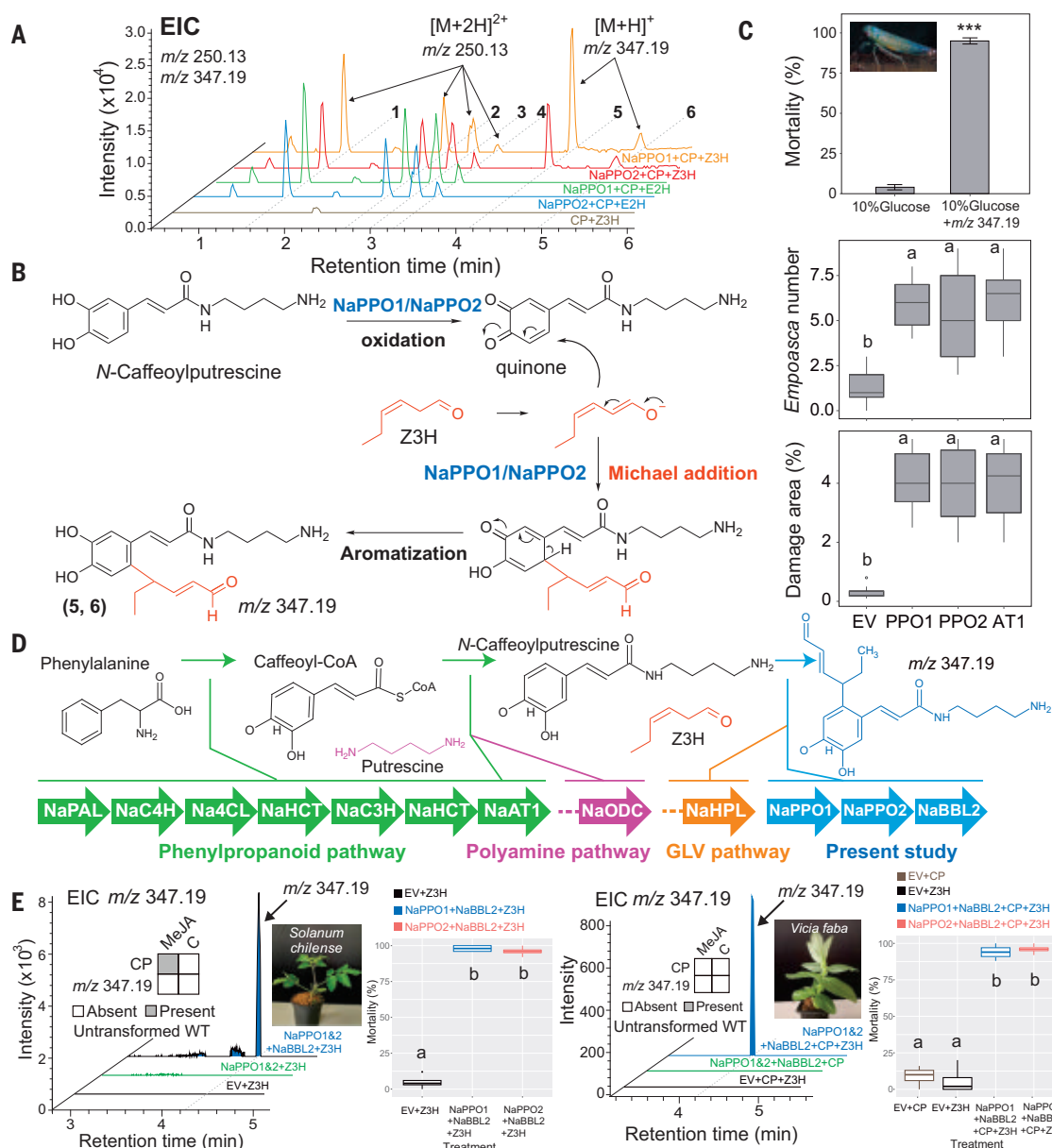
duce m/z 347.19, and under *in vitro* conditions, the addition of *NaBBL2* in the presence of *NaPPO1/2*, CP, and (*Z*)-3-hexenal did not significantly increase the production of m/z 347.19 (figs. S21 and S22 and table. S2). As PPOs have broad substrate specificities that can accept both hydroxy benzenes and/or ortho-dihydroxylated benzenes as substrates (28), we further explored the substrate specificities of *NaPPO1* and *NaPPO2* by incubating *NaPPO1/2* and (*Z*)-3-hexenal with CoP or with chlorogenic acid (CGA), which contains the same aromatic dihydroxylation pattern as CP. However, no new products were found, which indicates that CoP and CGA are not accepted as substrates by *NaPPO1/2* (fig. S23). Together, these data reveal that *NaPPO1/2* accepts CP and (*Z*)-3-hexenal as substrates to produce m/z 347.19 *in vitro*.

Biosynthetic logic of the reactive m/z 347.19 chemistry

To elucidate the chemical structure of m/z 347.19, we attempted to isolate and purify the m/z 347.19 using induced *N. attenuata* leaf material and enzyme assay-derived products. However, several attempts failed because of the instability of m/z 347.19. Although relatively stable in ammonium-acetate buffer (pH 4.8), when concentrated either by rotatory evaporation or freeze drying, m/z 347.19 rapidly decomposed (table S1). These observations indicate that m/z 347.19 is reactive and unstable at high pH. We modified the purification procedures for m/z 347.19 to produce large quantities from enzymatic assays under weak acidic conditions and purified m/z 347.19 using solid-phase extraction under argon atmospheres. The purified m/z 347.19 was then subjected to nuclear magnetic resonance (NMR) analysis, which elucidated its structure as a CP-5-(*Z*)-3-hexenal compound (hereafter referred to as CPH) (fig. S24 and data S3). CPH's half-life is only ~ 22 hours in acidified methanol- d_3 (0.1% formic acid) at room temperature in darkness (fig. S25 and data S3). CPH contains both the reactive moiety of an α,β -unsaturated aldehyde derived from (*Z*)-3-hexenal, which is electrophilic, and an amine feature of CP, which is nucleophilic.

CPH results from the biochemical union of so-called direct (CP) and indirect [(*Z*)-3-hexenal] defense metabolism, and we hypothesized that CPH was the metabolic trait underlying *Empoasca* nonhost resistance. We suggest two possible mechanisms of action: The rapid polymerization of the electrophilic and nucleophilic groups could occlude the mouthparts of probing *Empoasca* leafhoppers, or the α,β -unsaturated aldehyde may function as a protein cross-linker that disables *Empoasca* proteins (29). We propose a three-step biosynthetic mechanism for the production of CPH—*NaPPO1/2* oxidizes CP to the corresponding caffeoyl quinone derivative and activates (*Z*)-3-

Fig. 4. Structural elucidation, biosynthesis, function, and engineering of *m/z* 347.19 in vitro and in planta. (A) In vitro enzymatic assays for *m/z* 347.19 production revealed that either NaPPO1 or NaPPO2 can catalyze the condensation of CP and (Z)-3-hexenal (Z3H) to form *m/z* 347.19. Extracted ion chromatograms (EICs) for doubly charged CP dimer (*m/z* 250.13) and *m/z* 347.19 in *E. coli*-expressing NaPPO1 and NaPPO2 with CP and Z3H or (E)-2-hexenal (E2H). Compounds 1, 2, 3, and 4 denote isomers of CP dimer; compounds 5 and 6 denote isomers of *m/z* 347.19. (B) Proposed enzymatic reactions mediated by NaPPO1 or NaPPO2 for *m/z* 347.19 synthesis: NaPPO1/2 oxidize CP to caffeoyl quinone putrescine and activate Z3H for the Michael addition reaction, followed by aromatization to yield *m/z* 347.19. (C) Mortality rates of in vitro *Empoasca* nonchoice assays ($n = 4$, 25 *Empoasca* leafhoppers per replicate) in which *Empoasca* were fed for 6 hours either with 1 μM *m/z* 347.19 synthesized by using NaPPO1/2, CP, and Z3H and diluted in 10% glucose solution or with 10% glucose as control (top). *Empoasca* in planta choice assays ($n = 8$) conducted with VIGS plants of EV, PPO1, PPO2, and AT1 (bottom). (D) Genes involved in the biosynthesis of *m/z* 347.19. (E) Engineering of biosynthetic pathways for the production of *m/z* 347.19 in plants. Neither *V. faba* nor the wild tomato *S. chilense* accumulate *m/z* 347.19 in response to elicitation. *S. chilense* accumulates CP after MeJA elicitation, whereas *V. faba* does not (inserted heatmaps). *S. chilense* can be engineered to produce *m/z* 347.19 by expressing NaPPO1, NaPPO2, and NaBBL2 with Z3H infiltrations in MeJA-elicited *S. chilense* leaves. *m/z* 347.19 accumulates only in *S. chilense* expressing NaPPO1/2 together with NaBBL2, but not NaPPO1/2 alone. *V. faba* can be engineered to produce *m/z* 347.19 by expressing NaPPO1, NaPPO2, and NaBBL2 with Z3H and CP infiltrations in leaves. Also shown are mortality rates of in vivo *Empoasca* feeding assays ($n = 4$, 25 *Empoasca* leafhoppers per replicate) in which *Empoasca* were fed for 10 hours on leaves of reconstituted *S. chilense* and *V. faba*, respectively.



hexenal for a Michael addition reaction, the product of which is aromatized to form CPH (Fig. 4B).

CPH is responsible for *Empoasca* resistance

To test whether CPH is responsible for *Empoasca* resistance, we fed *E. decipiens* with physiologically relevant concentrations of 1 μM (estimated from field-collected elicited leaves) of NMR-confirmed CPH in diets containing 10%

glucose in vitro. After 6 hours of feeding, the CPH treatment caused almost 100% mortality of *E. decipiens*, in contrast to leafhopper growth on control diets ($P = 3 \times 10^{-8}$; Student's *t* test) (Fig. 4C). We further silenced *NaAT1* expression in *N. attenuata* plants using VIGS, which disrupted the production of both CP and CPH (14) (Fig. 3D). In vivo choice assays revealed that *NaAT1*-silenced plants received significantly more *Empoasca* damage and

higher *Empoasca* numbers than EV plants (Fig. 4C). Similarly, silencing either *NaPPO1* or *NaPPO2* in plants abolished only the accumulation of CPH in plants, without significant alterations in other phenolamide pools (Fig. 3D and fig. S16), and resulted in a clear *Empoasca* feeding preference ($P = 0.013$ and $P = 0.022$, respectively) and greater *Empoasca* damage ($P = 0.008$ and $P = 0.008$, respectively) compared with that observed in EV plants (Fig. 4C).

Together, these in vitro and in vivo results suggest that CPH in *N. attenuata* is responsible for the plant's *Empoasca* nonhost resistance.

NaBBL2 is required to engineer CPH biosynthesis in crop species

The discovery of CPH and its biosynthetic pathways underlying nonhost resistance offers a framework for the engineering of CPH biosynthesis in crop plants as a means of optimizing a plant's endogenous metabolism for defense against the attack of devastating leafhopper pests, the diseases they vector, and other nonhost pests. We investigated whether CPH is widely found in *Solanaceae* and other plant taxa. Metabolic profiling of *N. attenuata*'s close relatives revealed that six of seven *Nicotiana* species induced CPH in a coordinated fashion with CP when elicited by MeJA (fig. S26A). We selected 13 different taxa from different plant families, including several crop species, and compared amino acid identities of NaAT1, NaPPO1, NaPPO2, and NaBBL2 with their closest homologs using Basic Local Alignment Search Tool (BLAST) searches of the National Center for Biotechnology Information (NCBI) sequence database (fig. S26B). Five *Solanaceae* taxa of the 13 species examined contain all orthologs of the four protein sequences. Moreover, we detected MeJA-induced CP in eight species, including seven *Solanaceae* species and wheat, whereas only two species other than *N. attenuata*, *Capsicum annuum* and *Nicotiana benthamiana*, produced CPH (fig. S26B). These results suggest that CPH production may be restricted to the *Solanaceae*.

Synthetic biology has enabled the transfer of metabolic pathways among taxa because of shared cofactors and metabolism (30–33). We attempted to reconstitute the CPH pathway in vivo (Fig. 4D). We selected *Vicia faba* and *Solanum chilense* for *Agrobacterium*-mediated transient expression of the CPH pathway for several reasons. Neither species accumulated CPH in untreated and MeJA-treated tissues. *V. faba* is an ideal host plant for *Empoasca* rearing. CoP, CP, and FP do not accumulate in *V. faba*, whereas CP levels are induced by MeJA treatment of *S. chilense*, which provides an internal precursor for CPH production (Fig. 4E). Moreover, both are readily transformed and likely to produce correctly folded active proteins with which to test biochemical activities of CPH biosynthetic genes in planta.

We transiently coexpressed NaPPO1 or NaPPO2 together with (Z)-3-hexenal and CP leaf infiltrations in *V. faba* or without CP infiltrations in *S. chilense*. However, we failed to detect any CPH in either species (Fig. 4E). PPOs are generally localized to plastids, physically separating them from their phenolic substrates, which are known to be localized in vacuoles (34). In *N. attenuata*, a thylakoid

transfer domain was identified in both NaPPO1 and NaPPO2 N-terminal sequences (fig. S27A). Transient expression of green fluorescent protein (GFP)-tagged NaPPO1 and NaPPO2 in *N. attenuata* leaves confirmed that both NaPPO1 and NaPPO2 are plastid localized (fig. S27B).

Our three-pronged pathway proposal for CPH biosynthesis is therefore challenged by the separate enzymatic localizations of the different components—CP (likely vacuolar or cytosolic) (34, 35), GLVs, JAs, and PPOs (plastidial) (34, 36). This challenge was reminiscent of nicotine biosynthesis, which requires a BBL gene to join the mitochondria-localized pyridine ring, derived from nicotinic acid, with the pyrrolidine ring, derived from the peroxisome-localized *N*-methylpyrrolinium cation, to produce nicotine (37). We hypothesized that NaBBL2 is required for the production of CPH in vivo, and to test this hypothesis, we expressed NaBBL2 along with NaPPO1 or NaPPO2 in *S. chilense* plants. One day after *Agrobacterium* infiltration, *S. chilense* plants were treated with MeJA to induce CP production, and 3 days later, we infiltrated leaves with (Z)-3-hexenal. After 6 hours, we harvested leaves for liquid chromatography–mass spectrometry (LC-MS) analysis and found that the leaves had accumulated substantial quantities of CPH (Fig. 4E). For *V. faba* plants, we expressed NaBBL2 along with NaPPO1 or NaPPO2; 3 days after *Agrobacterium* infiltration, we infiltrated leaves with both CP and (Z)-3-hexenal and harvested leaves for LC-MS analysis after 6 hours. Again, CPH accumulated (Fig. 4E). From these results, we infer that NaBBL2, although not required for in vitro synthesis, is required for in vivo CPH biosynthesis. Additional work is required to evaluate whether NaBBL2 plays a role in solving the localization challenge, which could have other possible solutions (figs. S28 and S29 and supplementary materials). Finally, we conducted *Empoasca* feeding trials on the CPH-engineered *V. faba* and *S. chilense* plants and observed that these *Empoasca* host crop plants become lethal host plants for *Empoasca* (Fig. 4E).

This mechanistic analysis of *Empoasca* nonhost resistance provides another example of the innovative chemical solutions that native plants have evolved to solve their ecological challenges (38). The natural history–driven multi-omics framework that we used for the discovery of CPH and its marriage with synthetic biology approaches highlights how readily the results of millions of years of innovation by natural selection can be transferred to our crop plants to catalyze the next, greener, and ecologically more nuanced revolution in plant protection (39) and domestication (40–42). Crop plants face challenges not substantially different from those of native plants, being constantly tested by an herbivore community that challenges the host–nonhost distinction.

In a world of climate change and globally homogenized herbivore communities, opportunistic associations will dominate natural and man-made ecosystems. Insight into how native plants cope with opportunistic associations will help us to design crops that are more resilient in the face of unknown stresses as the world's climate changes (43).

Materials and methods summary

Two replicates of the 650 RILs from a 26-parent MAGIC population and their 26 parental lines were planted at the WCCER field station in Prescott, Arizona, USA. To elicit a standardized herbivory response, leaves of all RILs, which were in the early flowering stage, were wounded and immediately treated with diluted *M. sexta* oral secretions (W + OS) or were left untreated (control). Leaves were then harvested on dry ice at 1 and 72 hours. One week after metabolite sampling, all plants of the field population were screened for natural *Empoasca* leafhopper numbers and damage. These leafhoppers had opportunistically sampled the *N. attenuata* plants from neighboring native cucumber host plants. The mQTL and eQTL mapping between SNPs and the relative abundance of each compound or transcript using a set of 646 RILs of the MAGIC population was done with the R package software GAPIT using general linear models (GLMs). The multi-omics coassociation network was built from correlations among metabolomes, transcriptomes, phytohormones, and SNPs. For *Empoasca* choice assays, transgenic lines of *N. attenuata* at the early rosette growth stage were randomly placed in an open-choice glasshouse environment containing *Empoasca* leafhoppers reared on bean plants in the MPI-CE glasshouse in Isserstedt, Germany. Y2H assays and quantitative reverse transcription polymerase chain reaction (qRT-PCR) were used for characterizing *Empoasca*-induced JA signaling genes. Compound-specific idMS/MS was constructed using ultrahigh-performance liquid chromatography–electrospray ionization (UHPLC-ESI)–quadrupole time-of-flight mass spectrometry (qTOF-MS) for idMS/MS acquisition and rule-based computational approaches for idMS/MS assembly. Metabolome diversity and specialization and metabolic specificity were calculated using information theory by considering the Shannon entropy of the idMS/MS frequency distributions. In vivo *Empoasca* choice and in vitro *Empoasca* feeding assays were conducted by infiltrating synthetic CP, CoP, or FP into irMYC2 leaves or by feeding *Empoasca* with the compounds diluted in 10% glucose solutions. Fifteen RILs, which induced putrescine-containing phenolamides after OS elicitation and accumulated a diverse set of known and unknown phenolamides, were used to construct idMS/MS for MS/MS structural metabolomics analysis.

MS/MS similarity scoring, biclustering, and molecular networking were used to identify the unknown *m/z* 347.19 metabolite. OS-induced volatile emissions were collected using polydimethylsiloxane (PDMS) tubing from 650 MAGIC RILs planted in the main MPI-CE glasshouse and analyzed by thermal desorption–gas chromatography–mass spectrometry (TD-GC-MS). *NaPPO1/2* and *NaBBL2* genes were elucidated by combining mQTL analysis for herbivory-induced unknown *m/z* 347.19 and transcriptomics analysis of the microarray and RNA-seq datasets of OS-induced kinetics of WT and *irMYC2* and *irMYB8* lines. The candidate genes were functionally validated by VIGS and in vitro enzymatic assays using *E. coli*-expressed *NaPPO1*, *NaPPO2*, and *NaBBL2* with CP and (*Z*)-3-hexenal. The CPH [CP-5-(*Z*)-3-hexenal] chemical structure was characterized by NMR. CPH's resistance function against *Empoasca* was tested by in vitro nonchoice assays with synthesized CPH or by in planta choice assays conducted with VIGS plants of EV, *NaPPO1*, *NaPPO2*, and *NaATI*. The biosynthetic pathway of CPH was reconstituted in *V. faba* and *S. chilense* by transiently coexpressing *NaPPO1*, *NaPPO2*, and *NaBBL2* with CP and (*Z*)-3-hexenal leaf infiltrations. The nonhost resistance function of CPH against *Empoasca* was further evaluated with the CPH-engineered *V. faba* and *S. chilense* plants.

REFERENCES AND NOTES

1. A. Kessler, A. Kalske, Plant Secondary Metabolite Diversity and Species Interactions. *Annu. Rev. Ecol. Syst.* **49**, 115–138 (2018). doi: [10.1146/annurev-ecolsys-110617-062406](https://doi.org/10.1146/annurev-ecolsys-110617-062406)
2. P. Bednarek, A. Osbourn, Plant-microbe interactions: Chemical diversity in plant defense. *Science* **324**, 746–748 (2009). doi: [10.1126/science.1171661](https://doi.org/10.1126/science.1171661); pmid: 19423814
3. J. Fan *et al.*, *Pseudomonas* sav genes overcome aliphatic isothiocyanate-mediated non-host resistance in *Arabidopsis*. *Science* **331**, 1185–1188 (2011). doi: [10.1126/science.1199707](https://doi.org/10.1126/science.1199707); pmid: 21385714
4. J. R. Peart *et al.*, Ubiquitin ligase-associated protein SGT1 is required for host and nonhost disease resistance in plants. *Proc. Natl. Acad. Sci. U.S.A.* **99**, 10865–10869 (2002). doi: [10.1073/pnas.152330599](https://doi.org/10.1073/pnas.152330599); pmid: 12119413
5. K. H. Sohn *et al.*, HopAS1 recognition significantly contributes to *Arabidopsis* nonhost resistance to *Pseudomonas syringae* pathogens. *New Phytol.* **193**, 58–66 (2012). doi: [10.1111/j.1469-8137.2011.03950.x](https://doi.org/10.1111/j.1469-8137.2011.03950.x); pmid: 22053875
6. A. A. Agrawal, Induced responses to herbivory and increased plant performance. *Science* **279**, 1201–1202 (1998). doi: [10.1126/science.279.5354.1201](https://doi.org/10.1126/science.279.5354.1201); pmid: 9469809
7. R. Karban, I. T. Baldwin, *Induced Responses to Herbivory* (Univ. Chicago Press, 2007).
8. R. Müller *et al.*, Differential effects of indole and aliphatic glucosinolates on lepidopteran herbivores. *J. Chem. Ecol.* **36**, 905–913 (2010). doi: [10.1007/s10886-010-9825-z](https://doi.org/10.1007/s10886-010-9825-z); pmid: 20617455
9. C. Barth, G. Jander, *Arabidopsis* myrosinases TGG1 and TGG2 have redundant function in glucosinolate breakdown and insect defense. *Plant J.* **46**, 549–562 (2006). doi: [10.1111/j.1365-3113.2006.02716.x](https://doi.org/10.1111/j.1365-3113.2006.02716.x); pmid: 16640593
10. A. Kessler, R. Halitschke, I. T. Baldwin, Silencing the jasmonate cascade: Induced plant defenses and insect populations. *Science* **305**, 665–668 (2004). doi: [10.1126/science.1096931](https://doi.org/10.1126/science.1096931); pmid: 15232071
11. M. Kallenbach, G. Bonaventure, P. A. Gilardoni, A. Wissgott, I. T. Baldwin, *Empoasca* leafhoppers attack wild tobacco plants in a jasmonate-dependent manner and identify jasmonate mutants in natural populations. *Proc. Natl. Acad. Sci. U.S.A.* **109**, E1548–E1557 (2012). doi: [10.1073/pnas.1200363109](https://doi.org/10.1073/pnas.1200363109); pmid: 22615404
12. A. Hayward *et al.*, The leafcutter bee, *Megachile rotundata*, is more sensitive to *N*-cyanamide neonicotinoid and butenolide insecticides than other managed bees. *Nat. Ecol. Evol.* **3**, 1521–1524 (2019). doi: [10.1038/s41559-019-1011-2](https://doi.org/10.1038/s41559-019-1011-2); pmid: 31666734
13. S. Alseikh *et al.*, Domestication of Crop Metabolomes: Desired and Unintended Consequences. *Trends Plant Sci.* **26**, 650–661 (2021). doi: [10.1016/j.tplants.2021.02.005](https://doi.org/10.1016/j.tplants.2021.02.005); pmid: 33653662
14. D. Li, I. T. Baldwin, E. Gaquerel, Navigating natural variation in herbivory-induced secondary metabolism in coyote tobacco populations using MS/MS structural analysis. *Proc. Natl. Acad. Sci. U.S.A.* **112**, E4147–E4155 (2015). doi: [10.1073/pnas.1503106112](https://doi.org/10.1073/pnas.1503106112); pmid: 26170304
15. D. Li, S. Heiling, I. T. Baldwin, E. Gaquerel, Illuminating a plant's tissue-specific metabolic diversity using computational metabolomics and information theory. *Proc. Natl. Acad. Sci. U.S.A.* **113**, E7610–E7618 (2016). doi: [10.1073/pnas.1610218113](https://doi.org/10.1073/pnas.1610218113); pmid: 27821729
16. N. Onkokesung *et al.*, MYB8 controls inducible phenolamide levels by activating three novel hydroxycinnamoyl-coenzyme A: polyamine transferases in *Nicotiana attenuata*. *Plant Physiol.* **158**, 389–407 (2012). doi: [10.1104/pp.111.187229](https://doi.org/10.1104/pp.111.187229); pmid: 22082505
17. Y. Oh, I. T. Baldwin, I. Gális, NaJAZh regulates a subset of defense responses against herbivores and spontaneous leaf necrosis in *Nicotiana attenuata* plants. *Plant Physiol.* **159**, 769–788 (2012). doi: [10.1104/pp.112.193771](https://doi.org/10.1104/pp.112.193771); pmid: 22496510
18. A. Chini, S. Gimenez-Ibanez, A. Goossens, R. Solano, Redundancy and specificity in jasmonate signalling. *Curr. Opin. Plant Biol.* **33**, 147–156 (2016). doi: [10.1016/j.pbi.2016.07.005](https://doi.org/10.1016/j.pbi.2016.07.005); pmid: 27490895
19. I. T. Major *et al.*, Regulation of growth–defense balance by the JASMONATE ZIM-DOMAIN (JAZ)-MYC transcriptional module. *New Phytol.* **215**, 1533–1547 (2017). doi: [10.1111/nph.14638](https://doi.org/10.1111/nph.14638); pmid: 28649719
20. R. Li *et al.*, Flower-specific jasmonate signaling regulates constitutive floral defenses in wild tobacco. *Proc. Natl. Acad. Sci. U.S.A.* **114**, E7205–E7214 (2017). doi: [10.1073/pnas.1703463114](https://doi.org/10.1073/pnas.1703463114); pmid: 28784761
21. D. Li, R. Halitschke, I. T. Baldwin, E. Gaquerel, Information theory tests critical predictions of plant defense theory for specialized metabolism. *Sci. Adv.* **6**, eaaz0381 (2020). doi: [10.1126/sciadv.aaz0381](https://doi.org/10.1126/sciadv.aaz0381); pmid: 32577508
22. D. Li, E. Gaquerel, Next-Generation Mass Spectrometry Metabolomics Revives the Functional Analysis of Plant Metabolic Diversity. *Annu. Rev. Plant Biol.* **72**, 867–891 (2021). doi: [10.1146/annurev-arplant-071720-114836](https://doi.org/10.1146/annurev-arplant-071720-114836); pmid: 33781077
23. M. Schäfer *et al.*, NaMYB8 regulates distinct, optimally distributed herbivore defense traits. *J. Integr. Plant Biol.* **59**, 844–850 (2017). doi: [10.1111/jipb.12593](https://doi.org/10.1111/jipb.12593); pmid: 28843024
24. S. G. Kim, F. Yon, E. Gaquerel, J. Gulati, I. T. Baldwin, Tissue specific diurnal rhythms of metabolites and their regulation during herbivore attack in a native tobacco, *Nicotiana attenuata*. *PLOS ONE* **6**, e26214 (2011). doi: [10.1371/journal.pone.0026214](https://doi.org/10.1371/journal.pone.0026214); pmid: 22028833
25. K. Matsui, Green leaf volatiles: Hydroperoxide lyase pathway of oxylipin metabolism. *Curr. Opin. Plant Biol.* **9**, 274–280 (2006). doi: [10.1016/j.pbi.2006.03.002](https://doi.org/10.1016/j.pbi.2006.03.002); pmid: 16595187
26. S. Allmann, R. Halitschke, R. C. Schuurink, I. T. Baldwin, Oxylipin channelling in *Nicotiana attenuata*: Lipoxygenase 2 supplies substrates for green leaf volatile production. *Plant Cell Environ.* **33**, 2028–2040 (2010). doi: [10.1111/j.1365-3040.2010.02203.x](https://doi.org/10.1111/j.1365-3040.2010.02203.x); pmid: 20584148
27. Y. Joo *et al.*, Herbivory elicits changes in green leaf volatile production via jasmonate signaling and the circadian clock. *Plant Cell Environ.* **42**, 972–982 (2019). doi: [10.1111/pce.13474](https://doi.org/10.1111/pce.13474); pmid: 30378135
28. M.-A. McLarin, I. K. H. Leung, Substrate specificity of polyphenol oxidase. *Crit. Rev. Biochem. Mol. Biol.* **55**, 274–308 (2020). doi: [10.1080/10409238.2020.1768209](https://doi.org/10.1080/10409238.2020.1768209); pmid: 32441137
29. K. Konno, C. Hirayama, H. Yasui, M. Nakamura, Enzymatic activation of oleuropein: A protein crosslinker used as a chemical defense in the privet tree. *Proc. Natl. Acad. Sci. U.S.A.* **96**, 9159–9164 (1999). doi: [10.1073/pnas.96.16.9159](https://doi.org/10.1073/pnas.96.16.9159); pmid: 10430912
30. P. D. Sonawane *et al.*, Plant cholesterol biosynthetic pathway overlaps with phytosterol metabolism. *Nat. Plants* **3**, 16205 (2016). doi: [10.1038/nplants.2016.205](https://doi.org/10.1038/nplants.2016.205); pmid: 28005066
31. C. Y. Kim *et al.*, The chloroalkaloid (–)-acutamine is biosynthesized via a Fe(II)- and 2-oxoglutarate-dependent halogenase in Menispermaceae plants. *Nat. Commun.* **11**, 1867 (2020). doi: [10.1038/s41467-020-15777-w](https://doi.org/10.1038/s41467-020-15777-w); pmid: 32313070
32. J. Reed *et al.*, A translational synthetic biology platform for rapid access to gram-scale quantities of novel drug-like molecules. *Metab. Eng.* **42**, 185–193 (2017). doi: [10.1016/j.ymben.2017.06.012](https://doi.org/10.1016/j.ymben.2017.06.012); pmid: 28687337
33. W. Lau, E. S. Sattely, Six enzymes from mayapple that complete the biosynthetic pathway to the etoposide aglycone. *Science* **349**, 1224–1228 (2015). doi: [10.1126/science.aac7202](https://doi.org/10.1126/science.aac7202); pmid: 26359402
34. T. Boeckx, A. L. Winters, K. J. Webb, A. H. Kingston-Smith, Polyphenol oxidase in leaves: Is there any significance to the chloroplastic localization? *J. Exp. Bot.* **66**, 3571–3579 (2015). doi: [10.1093/jxb/erv141](https://doi.org/10.1093/jxb/erv141); pmid: 25873687
35. R. Marchiosi *et al.*, Biosynthesis and metabolic actions of simple phenolic acids in plants. *Phytochem. Rev.* **19**, 865–906 (2020). doi: [10.1007/s11101-020-09689-2](https://doi.org/10.1007/s11101-020-09689-2)
36. T. Savchenko *et al.*, Functional convergence of oxylipin and abscisic acid pathways controls stomatal closure in response to drought. *Plant Physiol.* **164**, 1151–1160 (2014). doi: [10.1104/pp.113.234310](https://doi.org/10.1104/pp.113.234310); pmid: 24429214
37. F. F. Zenkner, M. Margis-Pinheiro, A. Cagliari, Nicotine Biosynthesis in *Nicotiana*: A Metabolic Overview. *Tob. Sci.* **56**, 1–9 (2019). doi: [10.3381/18-063](https://doi.org/10.3381/18-063)
38. J. Rajniak, B. Barco, N. K. Clay, E. S. Sattely, A new cyanogenic metabolite in *Arabidopsis* required for inducible pathogen defence. *Nature* **525**, 376–379 (2015). doi: [10.1038/nature14907](https://doi.org/10.1038/nature14907); pmid: 26352477
39. S. M. Cook, Z. R. Khan, J. A. Pickett, The use of push-pull strategies in integrated pest management. *Annu. Rev. Entomol.* **52**, 375–400 (2007). doi: [10.1146/annurev.ento.52.110405.091407](https://doi.org/10.1146/annurev.ento.52.110405.091407); pmid: 16968206
40. G. Zhu *et al.*, Rewiring of the Fruit Metabolome in Tomato Breeding. *Cell* **172**, 249–261.e12 (2018). doi: [10.1016/j.cell.2017.12.019](https://doi.org/10.1016/j.cell.2017.12.019); pmid: 29328914
41. R. Sánchez-Pérez *et al.*, Mutation of a bHLH transcription factor allowed almond domestication. *Science* **364**, 1095–1098 (2019). doi: [10.1126/science.aav8197](https://doi.org/10.1126/science.aav8197); pmid: 31197015
42. J. Szymański *et al.*, Analysis of wild tomato introgression lines elucidates the genetic basis of transcriptome and metabolome variation underlying fruit traits and pathogen response. *Nat. Genet.* **52**, 1111–1121 (2020). doi: [10.1038/s41588-020-0690-6](https://doi.org/10.1038/s41588-020-0690-6); pmid: 32989321
43. S. Y. Xu, J.-K. Weng, Climate change shapes the future evolution of plant metabolism. *Adv. Genet.* **1**, e10022 (2020). doi: [10.1002/ggn2.10022](https://doi.org/10.1002/ggn2.10022)

ACKNOWLEDGMENTS

We thank B. Hong for technical support and fruitful discussions regarding CPH's chemistry; J. Li for insightful discussions regarding insect treatments; V. Grabe and X. Jiang for microscopic support; Prescott College, Northern Arizona University, the Arboretum at Flagstaff, Prescott National Forest, and the Southwest Experimental Garden Array for the use of a field plot at the Walnut Creek Center for Education and Research; Brigham Young University for the use of its Lytle Ranch Preserve, where this work started; R. Carlson and N. Carlson for logistics support of the 2019 field team; G. Baldwin for support in sowing the MAGIC population and plant transformations; K. Gase for preparations of transformation constructs; the 2019 MPI-CE field team (E. McGale, H. Valim, R. Ray, J. Li, P. Harary, C. Mahadevan, and M. Smith) for planting, screening, and oral secretion-eliciting the MAGIC population; R. Ray for help in preparing the eQTL dataset; C. Rocha for help with metabolite extractions and analyses; and J. Gershenzon and S. O'Connor for comments on an early draft of the manuscript. **Funding:** This work was supported by the Max Planck Society, advanced grant no. 293926 of the European Research Council to I.T.B., and the Deutsche Forschungsgemeinschaft - SFB 1127/2 ChemBioSys – 239748522 to I.T.B. **Author contributions:** Y.B., R.H., I.T.B., and D.L. conceived and designed the project. Y.B., C.Y., R.H., C.P., D.K., K.B., I.T.B., and D.L. performed experiments. Y.B., C.Y., C.P., E.G., I.T.B., and D.L. analyzed data. Y.B., I.T.B., and D.L. wrote the manuscript, with contributions from all authors. **Competing interests:** The authors have filed a patent (EP 21 217 268.8 and US 63/293,193) on CPH production and function. They declare no other competing interests. **Data and materials availability:** All data are available in the manuscript or the supplementary materials. Transformed lines are available from I.T.B.

SUPPLEMENTARY MATERIALS

science.org/doi/10.1126/science.abm2948

Materials and Methods

Figs. S1 to S29

Tables S1 to S3

References (44–73)

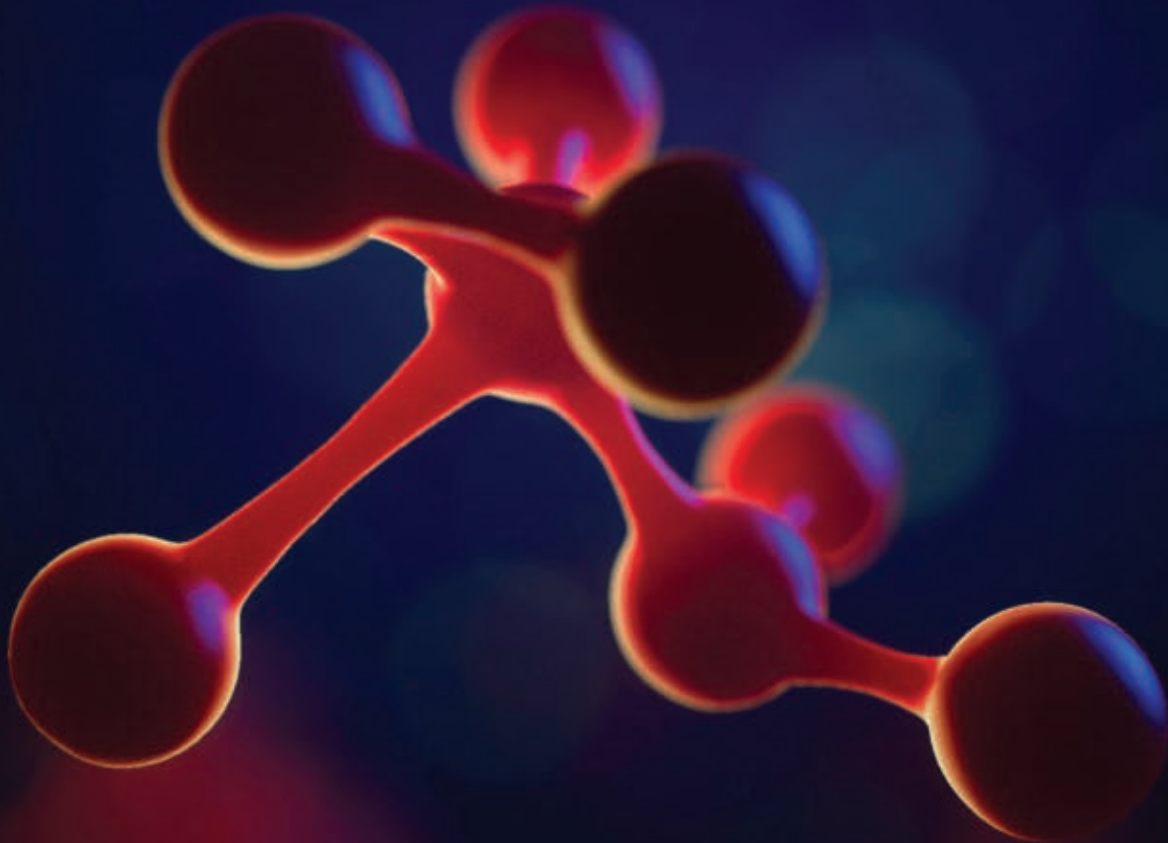
MDAR Reproducibility Checklist

Data S1 to S3

7 September 2021; accepted 22 December 2021
10.1126/science.abm2948

Science

J O U R N A L S 



Publish your research in the Science family of journals

The Science family of journals (*Science*, *Science Advances*, *Science Immunology*, *Science Robotics*, *Science Signaling*, and *Science Translational Medicine*) are among the most highly-regarded journals in the world for quality and selectivity. Our peer-reviewed journals are committed to publishing cutting-edge research, incisive scientific commentary, and insights on what's important to the scientific world at the highest standards.

Submit your research today!

Learn more at **[Science.org/journals](https://www.science.org/journals)**

RESEARCH ARTICLES

MOLECULAR BIOLOGY

Critical assessment of DNA adenine methylation in eukaryotes using quantitative deconvolution

Yimeng Kong¹, Lei Cao^{1†}, Gintaras Deikus^{1†}, Yu Fan^{1†}, Edward A. Mead^{1†}, Weiyei Lai², Yizhou Zhang³, Raymund Yong³, Robert Sebra^{1,4,5}, Hailin Wang², Xue-Song Zhang⁶, Gang Fang^{1*}

The discovery of N⁶-methyldeoxyadenine (6mA) across eukaryotes led to a search for additional epigenetic mechanisms. However, some studies have highlighted confounding factors that challenge the prevalence of 6mA in eukaryotes. We developed a metagenomic method to quantitatively deconvolve 6mA events from a genomic DNA sample into species of interest, genomic regions, and sources of contamination. Applying this method, we observed high-resolution 6mA deposition in two protozoa. We found that commensal or soil bacteria explained the vast majority of 6mA in insect and plant samples. We found no evidence of high abundance of 6mA in *Drosophila*, *Arabidopsis*, or humans. Plasmids used for genetic manipulation, even those from Dam methyltransferase mutant *Escherichia coli*, could carry abundant 6mA, confounding the evaluation of candidate 6mA methyltransferases and demethylases. On the basis of this work, we advocate for a reassessment of 6mA in eukaryotes.

For decades, N⁶-methyldeoxyadenine (6mA) has been known to be widespread in prokaryotes as a regulator of DNA replication, repair, and transcription (1–3). Recently, 6mA has also been reported to be prevalent in eukaryotes. Unlike the generally high abundance of 6mA in bacteria, 6mA/A levels (6mA events relative to all adenines) in eukaryotic organisms vary over several orders of magnitude (4–13). A few unicellular organisms have very high 6mA/A levels: 0.4% in *Chlamydomonas reinhardtii* (4), 0.66% in *Tetrahymena thermophila* (5), and as much as 2.8% in early-diverging fungi (6). In contrast, 6mA/A levels reported in multicellular eukaryotes are much lower: ~0.1% to ~0.0001%, or undetectable (8, 10–12, 14, 15). Nonetheless, important functions have been assigned to 6mA in eukaryotes, suggesting additional epigenetic mechanisms in basic biology and human diseases (11). However, other studies have cast doubt on the existence and levels of 6mA in eukaryotic DNA (15–19). For example, liquid chromatography coupled with tandem mass spectrometry (LC-MS/MS) can reliably quantify 6mA with high sensitivity, but it cannot dis-

criminate eukaryotic 6mA from bacterial 6mA contamination (16, 20). Unique metabolically generated stable isotope labeling can address this limitation of LC-MS/MS (17, 18); however, it can only be used in cultured cells. Anti-6mA antibody-based dot blotting is commonly used to estimate 6mA levels (4, 5, 7, 9–12), but it cannot rule out bacterial contamination. In addition, anti-6mA antibody-based DNA immunoprecipitation sequencing (DIP-seq) is often used for 6mA mapping (7, 8, 10, 13, 21), but it can be confounded by 6mA-independent factors such as DNA secondary structures (20) and RNA contamination (15). Restriction enzyme-based 6mA analyses are constrained by their limited recognition motifs (4, 22). Single-molecule real-time (SMRT) sequencing (23) and nanopore sequencing (24) provide opportunities for directly mapping 6mA events (3, 25, 26), but the existing methods are mainly for mapping 6mA in prokaryotes and protozoa with high 6mA abundance (3, 14, 26–29). For eukaryotes with low 6mA abundance, these methods are prone to yield many false positive calls due to low sensitivity (14–16).

The lack of a reliable technology that accurately quantifies 6mA/A levels in eukaryotic genomes motivated us to develop a method, named 6mASCOPE, for quantitative 6mA deconvolution (Fig. 1). The method, based on a short-insert SMRT library design (Fig. 1A), examines all DNA molecules sequenced in a genomic DNA (gDNA) sample, separates the total sequences into different sources, and quantitatively deconvolves the total 6mA events into each of the sources (Fig. 1B). We first validated our method over a wide range of 6mA/A levels, from 10^{−6} to 10^{−1}, and then examined a number of eukaryotes.

A method for quantitative 6mA deconvolution

Existing SMRT sequencing-based methods for modification detection require a reference genome, as they compare the interpulse duration (IPD) associated with a base of interest in the native DNA to the expected IPD value estimated according to the base and its flanking DNA sequence in the provided reference genome (25, 29, 30). Within this design, only those sequencing reads that map to the provided reference genome are analyzed for 6mA, ignoring potential bacterial contamination, which is known to have abundant 6mA events.

To help solve this problem, we took a metagenomic approach. First, in contrast to existing methods that depend on a reference genome for IPD analysis, we took a reference-free approach by using the circular consensus sequence (CCS), a feature of SMRT sequencing for error correction) of an individual DNA molecule as its molecule-specific reference for IPD analysis (23, 25, 31) (Fig. 1A), thus examining all the sequenced genetic contents for 6mA analysis. We designed relatively short SMRT insert libraries of 200 to 400 base pairs (fig. S1A) (31) so that each DNA molecule could be sequenced for a large number of passes (mean, 272×; median, 181×; Fig. 1A and fig. S1B), which facilitated a CCS base calling accuracy of >99.84% (Phred score 28; fig. S2) (31) and enabled reliable IPD analysis on single molecules (Fig. 2, A and B). We then used a metagenomic approach to map the CCS reads to a comprehensive collection of genomes (31) and performed 6mA quantification (described below) separately for each subgroup of genetic contents in a gDNA sample: species of interest, genomic regions of interest, and sources of contamination.

The current standard method to detect 6mA from SMRT sequencing is based on a defined cutoff on a modification quality value (QV; essentially a transformed *P* value) (3, 28, 31, 32). Because QV varies markedly over sequencing depth or number of CCS passes on individual molecules (Fig. 2C) (28, 30), a fixed cutoff can create false positive 6mA calls, especially from genomic regions with high sequencing depth (e.g., mitochondrial genomes). We built on a critical observation of linear increase (slope ~1.7 for 6mA events) of QV over CCS passes (better separation from nonmethylated adenines at higher coverages; Fig. 2, C and D) and developed a machine learning model for 6mA quantification from QV values calculated in the reference-free single-molecule IPD analysis. The core idea was to train the machine learning model across a wide range of 6mA/A levels (training datasets described below) and to use the model to predict 6mA/A levels of newly sequenced gDNA samples based on the collective QV distribution instead of an arbitrary QV cutoff (Fig. 2D) (31).

¹Department of Genetics and Genomic Sciences and Icahn Institute for Genomics and Multiscale Biology, Icahn School of Medicine at Mount Sinai, New York, NY 10029, USA. ²State Key Laboratory of Environmental Chemistry and Ecotoxicology, Research Center for Eco-Environmental Sciences, Chinese Academy of Sciences, Beijing 100085, China. ³Department of Neurosurgery and Oncological Sciences, Icahn School of Medicine at Mount Sinai, New York, NY 10029, USA. ⁴Black Family Stem Cell Institute, Icahn School of Medicine at Mount Sinai, New York, NY 10029, USA. ⁵Sema4, a Mount Sinai Venture, Stamford, CT 06902, USA. ⁶Center for Advanced Biotechnology and Medicine, Rutgers University, New Brunswick, NJ 08854, USA.

*Corresponding author. Email: gang.fang@mssm.edu

†These authors contributed equally to this work.

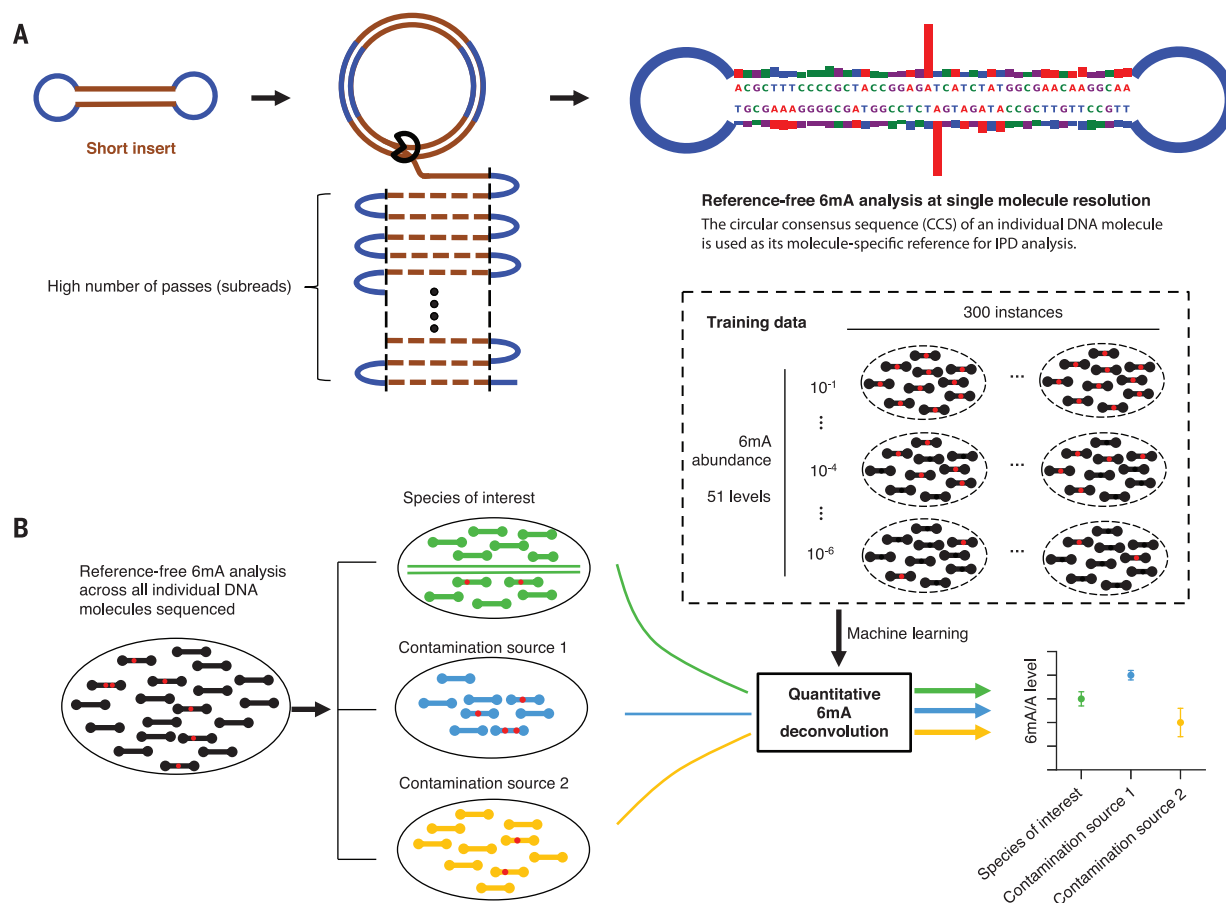


Fig. 1. Overview of 6mASCOPE for quantitative 6mA deconvolution.

(A) Reference-free 6mA analysis of single molecules. Each molecule (short insert) is sequenced for a large number of passes (subreads). The subreads are combined to a circular consensus sequence (CCS), serving as the molecule-specific reference for in silico IPD estimation, and they provide repeated measures of IPD values for 6mA analysis (31). Blue segment denotes SMRT

adapter. **(B)** After single-molecule 6mA analysis (a red dot indicates a 6mA event), CCSs (black rods) from a sequenced gDNA sample are separated into the eukaryotic genome (green) and contamination sources (blue and yellow). The 6mA/A levels of each species (or genomic region) are estimated using a machine learning model trained across a wide range of 6mA abundance, with defined confidence intervals.

We constructed high-quality benchmark datasets for the machine learning model training. For 6mA negative controls, we used HEK-WGA [whole-genome amplification of human embryonic kidney (HEK)-293 cell gDNA, 6mA/A level $< 10^{-6}$ by ultrahigh-performance liquid chromatography–tandem mass spectrometry (UHPLC-MS/MS)], HEK293 (native gDNA, 6mA/A level $< 10^{-6}$ by UHPLC-MS/MS), and HEK-WGA-MssII (CpG sites in vitro methylated using a 5mC methyltransferase, MssII), with the latter two representing the influence of 5mC events on IPD (16, 25, 31). These samples were each methylated in vitro using three bacterial 6mA methyltransferases (Dam, GATC; TaqI, TCGA; and EcoRI, GAATTC) to create three positive controls: HEK-WGA-3M, HEK293-3M, HEK-WGA-MssII-3M (fig. S3). By mixing negative and positive controls in silico at different ratios, we created a wide range of 6mA/A levels (10^{-1} to 10^{-6}) for the model training (Fig. 2E) (31). Using leave-one-

out cross-validation, we compared several models (fig. S4) and selected Random Forest. Our model showed reliable quantification of 6mA/A levels with defined 95% confidence intervals (CIs; Fig. 2F and fig. S5) (31). CI depends on both 6mA/A level and number of CCS reads (Fig. 2F and fig. S5B) (31), which facilitated dataset-specific CI estimation along with 6mA quantification.

In contrast to existing methods (table S1), 6mASCOPE takes a metagenomic approach and specifically quantifies 6mA events in eukaryotic genomes over contamination, because CCS reads, grouped by species (or specific genomic regions), are separately quantified for 6mA/A levels. For validation, we applied 6mASCOPE on a series of in vitro mixed *E. coli*, *Helicobacter pylori*, and *Saccharomyces cerevisiae* samples with a wide range of 6mA/A levels (10^{-2} to 10^{-6} by UHPLC-MS/MS) and found that 6mASCOPE reliably deconvolved different sources into expected

ratios along with stable 6mA quantification (fig. S6).

High-resolution insights of 6mA deposition in two protozoans

Although previous studies reported enrichment of 6mA events in the linkers near transcription start sites (TSSs) in two protozoans, *C. reinhardtii* and *T. thermophila* (4, 5), it remains unclear which specific regions within the linkers are enriched for 6mA events. We sequenced both organisms using the SMRT method and obtained 862,205 and 975,050 CCS reads, respectively, for single-molecule 6mA analysis (table S2) (31). We first verified that 6mA has a periodic pattern inversely correlated with nucleosomes near TSSs (fig. S7) (31). Next, by dividing genomic regions between the nucleosome dyad and the middle of each nucleosome linker into 10 bins (31) and quantifying 6mA/A levels in each bin using 6mASCOPE, we found that

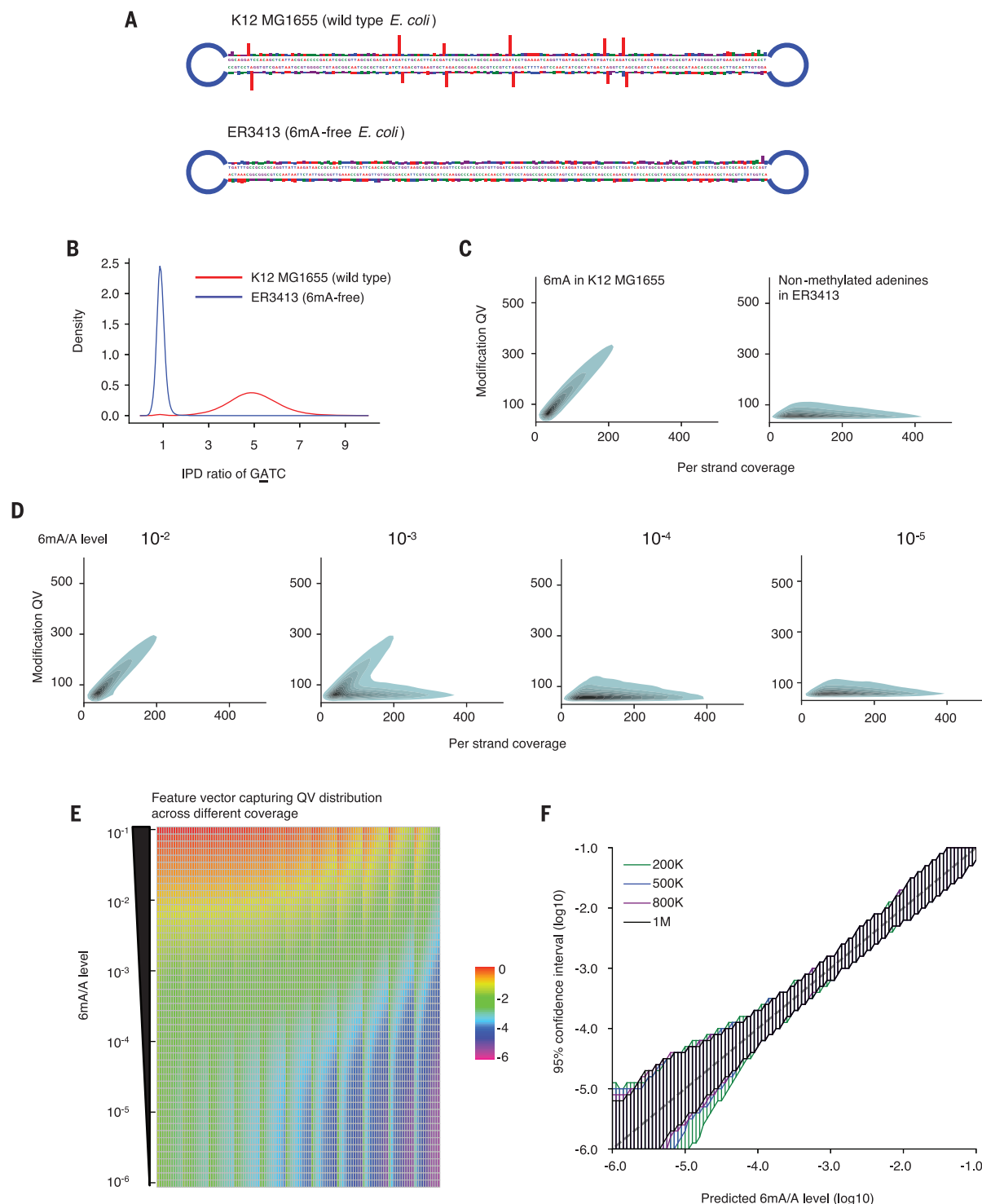


Fig. 2. 6mASCOPE method evaluation. (A) IPD ratios (the mean IPD in the native sample divided by the IPD expected from the in silico model) on illustrative molecules from *E. coli* wild-type strain K12 MG1655 and 6mA-free strain ER3413. Blue segment denotes SMRT adapter. (B) IPD ratio of adenines on GATC motif in *E. coli* K12 MG1655 and ER3413. 6mA events have IPD ratios of ~5; nonmethylated adenines have IPD ratios of ~1. (C) Modification quality values (QVs) of 6mA linearly deviate from the nonmethylated adenines (slope ~1.7), with better separation at high numbers of CCS passes. For illustration, kernel density estimation of adenines with QC > 50 is shown. Left: 6mA in GATC, GCACNNNNNGTT, and AACNNNNNTGC

from *E. coli* K12 MG1655. Right: Nonmethylated adenines in *E. coli* ER3413. (D) QV distribution varies across different 6mA/A levels. (E) Feature vectors used for machine learning model training. In each row, one of 51 6mA/A levels (10^{-1} to 10^{-6}) is constructed by mixing negative and positive controls in silico at different ratios. Each column represents the percentage (averaged across 300 replicates, \log_{10} -transformed) of adenines over a number of slopes across CCS pass numbers 20 to 240, divided into 11 bins (31). (F) For each 6mA quantification (x axis), 6mASCOPE also provides the 95% confidence interval (y axis) (31). Colors represent the number of CCS reads used for 6mA quantification.

6mA was enriched at the nucleosome-linker boundaries in *C. reinhardtii* (Fig. 3, A and D) instead of at the middle of the linkers, as previously reported. In contrast, 6mA/A levels of *T. thermophila* increased from the nucleosome boundaries to the middle of linkers (Fig. 3, A and E, and fig. S8). We further used 6mASCOPE to examine the enrichment of 6mA across different motifs. For *C. reinhardtii*,

we confirmed that 6mA is enriched in the VATB motif (Fig. 3B; V = A, C, or G; B = C, G, or T) and is essentially absent in non-VATB motifs; for *T. thermophila*, although 6mA was reported to be enriched across the NATN motif (5), our 6mASCOPE analysis revealed that VATB sites have a higher 6mA/A level than TATN and NATN sites by a factor of 2 to 3 (Fig. 3C).

6mA from commensal bacteria contribute to most 6mA events in insect and plant samples
A previous study quantified 6mA in *D. melanogaster* using UHPLC-MS/MS and reported that 6mA/A reaches the peak level of ~700 ppm (parts per million) in ~0.75-hour embryos and falls to ~10 ppm at later stages such as adult tissues (8). We first collected the fly embryo sample at ~0.75 hours and got

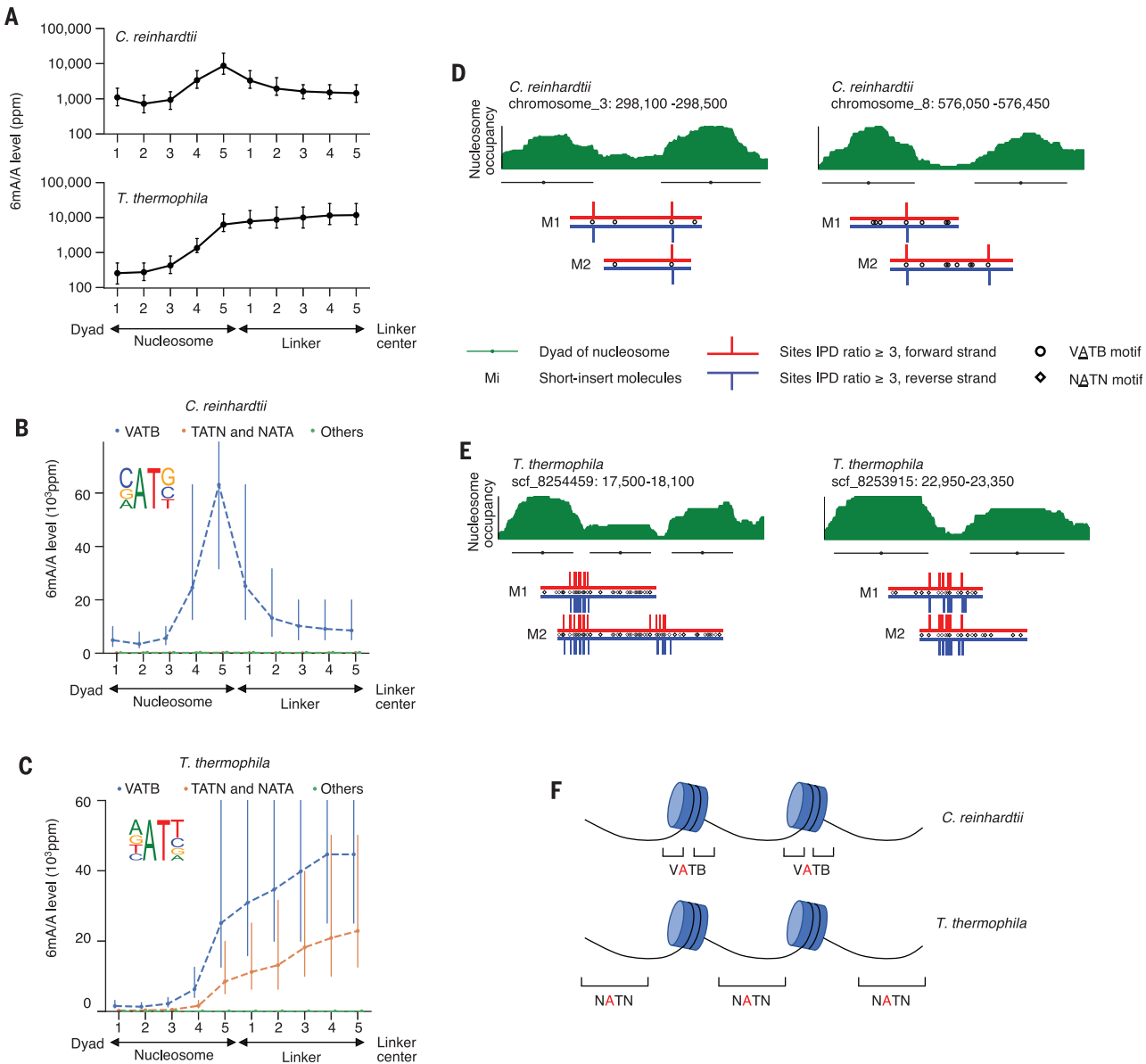


Fig. 3. 6mASCOPE reveals high-resolution 6mA deposition in *C. reinhardtii* and *T. thermophila*. (A) 6mA deposition relative to nucleosomes and linkers in *C. reinhardtii* and *T. thermophila*. Genomic regions between the nucleosome dyad and the linker center are divided into 10 bins (x axis) across the genome. The 6mA/A level (y axis) was quantified with 6mASCOPE. Error bars are 95% CIs. (B) 6mA is enriched in the VATB motif at nucleosome-linker boundaries in *C. reinhardtii*. Adenines in each bin are divided into three groups: VATB, TATN/NATN, and others. The dashed line indicates the trend of 6mA/A levels from nucleosome dyad to linker center; x and y axes are the same as in (A). Error

bars are 95% CIs. (C) 6mA is enriched across the NATN motif at linkers in *T. thermophila*. (D and E) Illustrative examples of 6mA enrichment in *C. reinhardtii* (D) and *T. thermophila* (E). Nucleosome occupancy (green stack) is based on MNase-seq data (31). Nucleosomes (green lines) and dyads (green dots) are determined by iNPS (v1.2.2). SMRT CCS reads (Mi) are shown with red (forward strand) and blue (reverse strand) lines. IPD ratios of 3 or higher are shown. (F) Schematic of 6mA enrichment at the nucleosome-linker boundaries in *C. reinhardtii* and the gradual 6mA increase from nucleosome boundaries to linker centers in *T. thermophila*.

674,650 SMRT CCS reads for single-molecule 6mA analysis (table S2). Despite strict measures to avoid contamination (31), we found that 96.12% of the CCS reads mapped to the *D. melanogaster* genome reference, whereas 3.88% of the CCS reads mapped to a few microbes (Fig. 4A). Specifically, the contamination reads came from *S. cerevisiae* (1.65%), the major food source of *Drosophila* (33), and two genera of bacteria, *Acetobacter* (0.86%) and *Lactobacillus* (0.23%), the main gut commensal bacteria of *D. melanogaster* (34). We separately quantified 6mA/A levels in the *D. melanogaster* genome and in each contamination source and found that the level of 6mA/A in total gDNA was 100 ppm (CI, 50 to 200 ppm, consistent with the ~121 ppm UHPLC-MS/MS estimate), 2 ppm in *D. melanogaster* (CI, 1 to 10 ppm), 2 ppm in *Saccharomyces* (CI, 1 to 10 ppm), 5495 ppm in *Acetobacter* (CI, 3162 to 10,000 ppm), 977 ppm in *Lactobacillus* (CI, 501 to 1995 ppm), and 7413 ppm in Others (including additional bacterial genera and unannotated sequences; CI, 3981 to 12,589 ppm) (Fig. 4B and fig. S9) (31). Despite their relatively low abundance (3.88%), bacteria contributed to most of the 6mA events in the total gDNA (Fig. 4C). In *Acetobacter*, we observed a high-confidence bacterial 6mA motif (GANTC) (Fig. 4B), consistent with the REBASE database (35). The 6mA/A level of 2 ppm (CI, 1 to 10 ppm) estimated for *D. melanogaster*, in contrast to the ~700 ppm previously reported, only explains 1.44% of the total 6mA events in the gDNA sample (considering taxonomy abundances; Fig. 4C).

We next applied 6mASCOPE to examine a *D. melanogaster* adult sample (whole animal), which showed very different microbiome composition with extremely low bacteria contamination, yet still no evidence of a high 6mA/A level in *Drosophila* (fig. S10). We also reanalyzed the 6mA DIP-seq data from a previous *D. melanogaster* study (8) and found reads that mapped to multiple bacterial genomes. It is also worth noting that N⁴-methylcytosine (4mC), another form of DNA methylation prevalent in bacteria, was also detected in CCS reads from *Acetobacter* enriched at GTAC sites (fig. S11), a motif previously reported in *Acetobacter* (35). This observation shows that 4mC analysis for eukaryotic organisms also should be cautiously examined for possible bacterial contamination.

In addition to insects, we hypothesized that soil bacteria can confound 6mA analysis in plants. We applied 6mASCOPE to *A. thaliana* 21-day-old seedlings (31), which were reported as having ~2500 ppm 6mA/A by LC-MS/MS (9). Among the total 535,030 SMRT CCS reads for single-molecule 6mA analysis, 98.52% could be mapped to the *A. thaliana* genome (Fig. 4D). Among the other 1.48% (subgroup Others), 24.12% were annotated and classified (using Kraken2) into several phyla: Proteobacteria

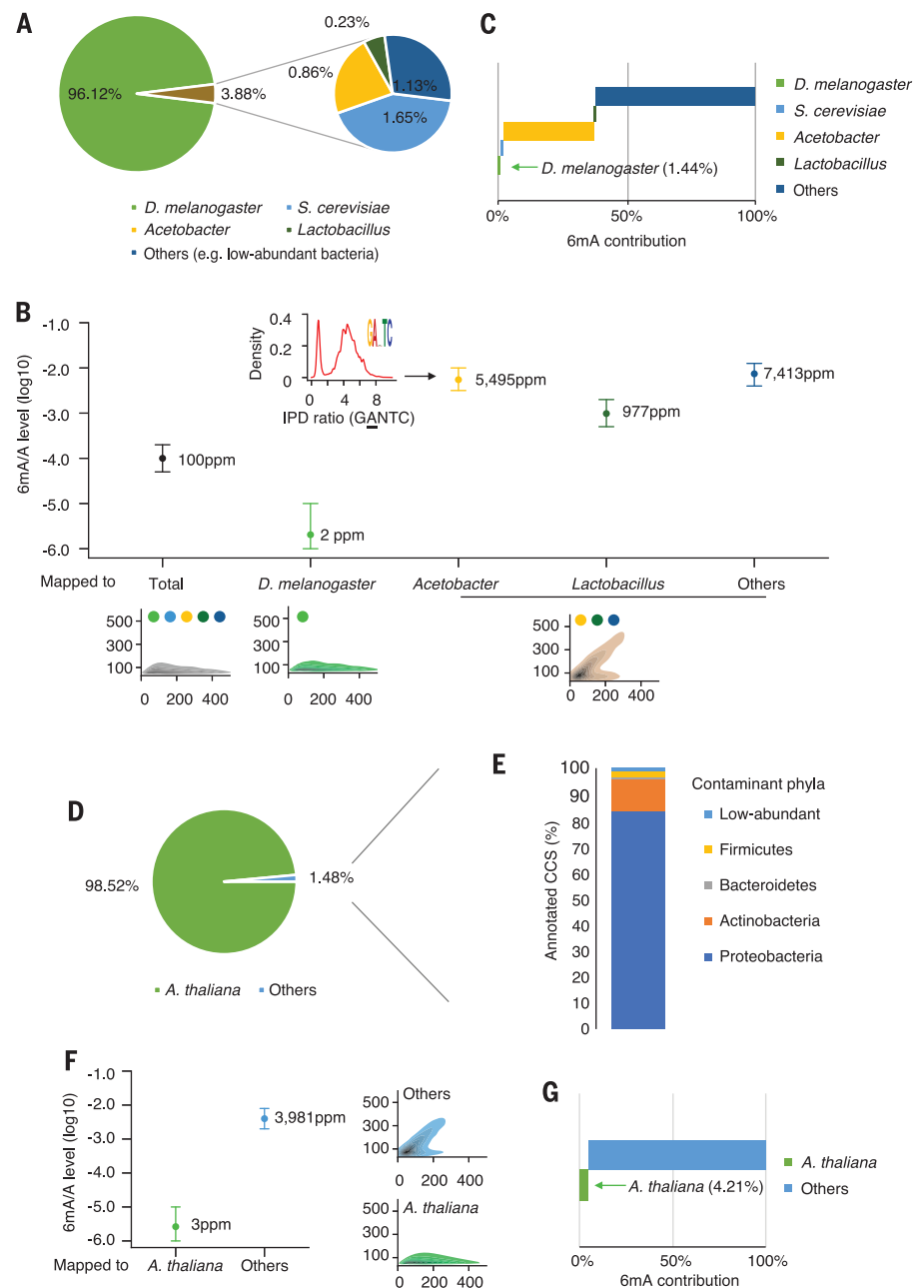


Fig. 4. 6mASCOPE analyses show that commensal bacteria contribute to the vast majority of 6mA events in insect and plant samples. (A) Taxonomic compositions (percent) in the *D. melanogaster* embryo ~0.75-hour gDNA sample. CCS reads mapped to *Acetobacter* or *Lactobacillus* are summarized by genus. **(B)** 6mA quantification of the *D. melanogaster* genome and contaminations. For each subgroup, 6mA/A levels are quantified by 6mASCOPE (error bars are 95% CIs). QV distributions are shown at bottom (colored dots refer to species/genus colors in main panel). 6mA/A level of *S. cerevisiae* is further examined with additional sequencing (fig. S9). CCS reads from *Acetobacter*, *Lactobacillus*, and Others (e.g., low-abundant bacteria) are grouped together because CCS read counts within each subgroup are low; CIs are defined on the basis of 8000 CCS reads. Arrow denotes the density of IPD ratios in the GANTC motif in *Acetobacter*. **(C)** 6mA contribution (percent) from each subgroup in the *D. melanogaster* embryo sample. **(D and E)** Taxonomic compositions (percent) in the *A. thaliana* 21-day seedling gDNA sample. The CCS reads in subgroup "Others" (D) are classified with Kraken2. Main classes of Proteobacteria are shown in fig. S12. **(F)** 6mA quantification of the *A. thaliana* genome and the contamination (Others). **(G)** 6mA contribution (percent) from each subgroup in the *A. thaliana* seedling sample.

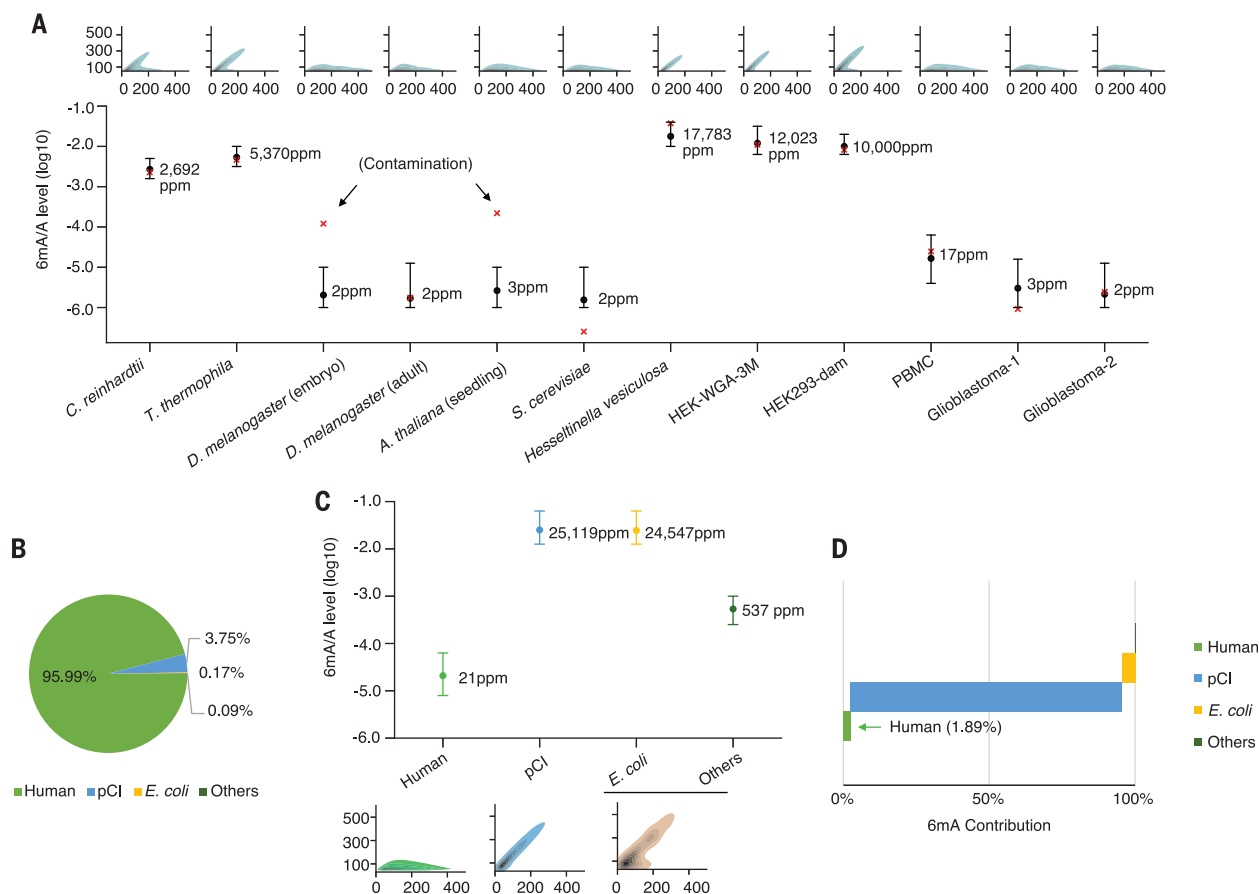


Fig. 5. 6mASCOPE-based quantitative deconvolution across multiple human gDNA samples. (A) 6mA/A levels on the genome of interest quantified by 6mASCOPE (error bars are 95% CIs). The 6mA/A level in *S. cerevisiae* is consistent with independent UHPLC-MS/MS measurement (0.3 ppm, lower than the minimum 6mA/A level used in the 6mASCOPE training dataset). Except for *D. melanogaster* embryo and *A. thaliana* gDNA samples (both are contaminated by bacteria), 6mA/A levels by 6mASCOPE are consistent with UHPLC-MS/MS (red cross). For all samples except HEK-WGA-3M and HEK293-dam, the UHPLC-MS/MS is performed indepen-

dently using the same batch of gDNA samples. For HEK-WGA-3M and HEK293-dam, the UHPLC-MS/MS estimates are mimicked: Nearly all the expected motif(s) are methylated in vitro by the methyltransferase(s). The QV distribution for each gDNA sample is shown at the top. (B) Sources (percent) of CCS reads in the HEK-pCI sample (transfection of an empty pCI plasmid into HEK 293 cells). (C) 6mA quantification (percent) of different sources in HEK-pCI. CCS reads from *E. coli* and Others are grouped together, and their CIs are determined on the basis of 8000 CCS reads. (D) 6mA contribution (percent) from the subgroups in the HEK-pCI sample.

(fig. S12), Actinobacteria, Bacteroidetes, and Firmicutes. These phyla and classes (Fig. 4E and fig. S12) are consistent with *A. thaliana* root microbiome (36). Using 6mASCOPE, we separately quantified 6mA/A levels for *A. thaliana* (3 ppm; CI, 1 to 10 ppm) and Others (3981 ppm; CI, 1995 to 7943 ppm) and found that CCS reads mapped to *A. thaliana* contributed to only 4.21% of the total 6mA events in the total gDNA sample (Fig. 4, F and G). Consistently, 6mASCOPE analysis of the *A. thaliana* 21-day-old root sample also demonstrated remarkable microbiome contamination (greater than the seedlings), with a smaller contribution from *A. thaliana* to the total 6mA events (fig. S13).

6mASCOPE finds no evidence of high abundance of 6mA in the human cells examined

We next examined the abundance of 6mA in human cells and tissues. We chose to investigate

peripheral blood mononuclear cells (PBMCs), which are composed of 70 to 90% lymphocytes (37), because lymphocytes have been shown to have a high 6mA/A level of ~0.051% (510 ppm) (12). We also collected and examined two glioblastoma brain tissue samples because glioblastoma stem cells and primary glioblastoma were reported to have a 6mA/A level of ~1000 ppm by dot blotting and mass spectrometry (11).

We obtained 570,283, 247,700, and 280,763 SMRT CCS reads from the PBMC sample and the two glioblastoma brain tissues, respectively, for single-molecule 6mA analysis. Of these, 99.53%, 99.88%, and 99.86% of CCS reads were mapped to the human reference genome, indicating highly pure samples. The 6mA/A levels estimated by 6mASCOPE in glioblastoma samples were $\sim 10^{-6}$, with 3 ppm for glioblastoma-1 (CI, 1 to 16 ppm) and 2 ppm for glioblastoma-2 (CI, 1 to 13 ppm) (Fig. 5A) (37).

This level is comparable to the negative controls with extremely low 6mA/A levels: HEK-WGA (1 ppm; CI, 1 to 6 ppm) and native HEK293 (1 ppm; CI, 1 to 6 ppm), when the confidence intervals are taken into consideration. In the PBMC sample, the 6mA/A level estimation of 17 ppm (CI, 4 to 63 ppm) by 6mASCOPE is consistent with the measurements of UHPLC-MS/MS (Fig. 5A). These data suggested either that the abundance of 6mA, if present in glioblastoma and PBMCs, was much lower than the reported levels in the recent studies (glioblastoma, ~1000 ppm; lymphocytes, ~510 ppm) or that 6mA/A levels may be highly heterogeneous or variable between different samples of the same cell type, the same tissue, or a specific disease. Motif enrichment analysis did not support a reliable motif in these samples (fig. S14).

Across all the samples examined in this study, we observed largely consistent 6mA/A

level estimates between 6mASCOPE and UHPLC-MS/MS (Fig. 5A) except the *D. melanogaster* embryo and *A. thaliana* samples, for which the much higher 6mA/A estimates by UHPLC-MS/MS were due to bacterial contamination (Fig. 4), highlighting the capability and reliability of 6mASCOPE. In addition to 6mA quantification of individual species, our method was also able to quantify 6mA/A levels in specific genomic regions of interest. Previous studies have reported enrichment of 6mA in mitochondrial DNA (mtDNA) (12, 13, 21, 38) and in young full-length LINE-1 elements (L1s) (10, 11, 21). For mtDNA, 6mASCOPE did not find 6mA enrichment in the 7205 CCS reads from the HEK293 sample that mapped to mtDNA, in comparison to a negative control (targeted mitochondrial genome amplification, $10^{-5.72}$; CI, $10^{-6.00}$ to $10^{-4.90}$; fig. S15). For L1 elements, although 6mASCOPE appeared to suggest a higher 6mA/A level in the young full-length L1s than in older L1s, a further comparison with a WGA negative control did not support 6mA enrichment in young L1 elements (fig. S16), highlighting the importance of using negative controls to capture possible uncharacterized biases (14, 39). This result was consistent with our previous study of human lymphoblastoid cells, in which increased IPD patterns exist not only in adenines but also in cytosines, guanines, and thymines of young L1 elements, which suggested confounding factors such as secondary structure (14).

Plasmids used for genetic manipulation can carry confounding bacterial-origin 6mA

Genetic manipulation is commonly used in epigenetic research to characterize putative methyltransferases and demethylases. *E. coli* is often used as a host for plasmid selection and expansion. As a result, the plasmids can contain 6mA events written by bacterial methyltransferase(s) and can confound 6mA study in eukaryotic cells.

To illustrate this, we transfected an empty pCI plasmid vector from *E. coli* into HEK293 cells, following the standard lipofection-based protocol (31). Total gDNA harvested at 72 hours after transfection was sequenced using SMRT technology and analyzed using 6mASCOPE. Among the 741,558 CCS reads, 95.99% were mapped to the human genome and 3.75% came from the pCI vector (Fig. 5B), and the remaining 0.26% of CCS reads (Fig. 5B) included reads that mapped to the *E. coli* genome (31), implying possible carryover of gDNA from *E. coli* to the HEK293 cells during transfection. By separately quantifying the 6mA/A level in each subgroup, pCI showed a high 6mA/A level of $10^{-1.60}$ (25,119 ppm), about the same as *E. coli* (Fig. 5C). Considering its abundance, pCI contributed to 93.91% of the total 6mA events in this post-transfection HEK293 total gDNA (Fig. 5, C and D). Hence, genetic manipulation

experiments involving plasmids may confound the characterization of putative 6mA methyltransferases and demethylases. Although the use of methylation-free bacteria as the host for plasmid preparation can avoid this type of contamination, it is worth noting that the Dam methyltransferase mutant *E. coli*, previously used in a few studies (7, 38), still has substantial 6mA events because of the remaining 6mA methyltransferase hsdM (2, 28) (fig. S17, based on 6mASCOPE analysis). We therefore suggest the use of *E. coli* strains with both Dam and hsdM deleted as the plasmid host.

Discussion

Our study cannot exclude the potential presence of authentically high levels of 6mA/A in multicellular eukaryotes in certain samples that we did not examine here. However, our results suggest that a reassessment of 6mA across eukaryotic genomes, using 6mASCOPE to quantitatively estimate the confounding impact of bacterial contamination, is warranted. To facilitate the broad use of 6mASCOPE, we have released a detailed experimental protocol and an automated software package on Zenodo (40) and GitHub.

We caution that plasmid 6mA contamination, even from Dam methyltransferase mutant *E. coli*, is possible during genetic manipulation and may have confounded previous characterizations of 6mA enzymes. Lipofection or electroporation, which is used to transfect plasmid DNA directly into the target cells, is more likely to introduce contamination, whereas lentiviral transduction would be less affected if the original plasmids are completely removed during viral packaging.

Our 4mC result suggests that similar caution should be exercised when studying 4mC in eukaryotes by means of SMRT sequencing, which has found 4mC in several eukaryotes [see (41)], despite SMRT sequencing being prone to making false positive calls (16), especially given the lack of evidence for 4mC in mice even when ultrasensitive UHPLC-MS/MS is used (19). More broadly, this study will also help to guide rigorous technological development for the detection of other forms of rare DNA and RNA modifications.

Our study has a few limitations: (i) The focus of 6mASCOPE is more about quantitatively deconvolving the global 6mA/A level into different species and genomic regions of interests, rather than mapping specific 6mA events in a particular genome. We prioritized this focus because the most controversial 6mA findings to date were those reporting high 6mA/A levels in multicellular eukaryotes. The precise mapping of specific 6mA events in a particular genome would require deeper SMRT sequencing and can be pursued in future work. (ii) For reliable data interpretation, it is important to combine the 6mA/A levels estimated

by 6mASCOPE with their confidence intervals, which depend on sequencing depth. However, even with a large number of CCS reads, 6mASCOPE does not precisely differentiate 6mA/A levels below 10 ppm because the confidence interval includes 1 ppm, which is the lowest 6mA/A level in our training dataset (Fig. 2F) (31). (iii) Two recent studies reported that ribo-m6A on mRNA can be a source of 6mA on DNA via the nucleotide-salvage pathway (17, 18). 6mA events that are misincorporated via this pathway cannot be distinguished from other 6mA events by SMRT sequencing or 6mASCOPE, and isotope labeling coupled with LC/MS-MS is needed instead (17). (iv) For each gDNA sample, the CCS reads analyzed by 6mASCOPE only represent the DNA molecules that were sequenced by SMRT sequencing. Although SMRT DNA polymerases can effectively sequence through diverse genomic regions with very complex secondary structures (42), it might miss some DNA molecules with certain unknown properties. (v) Although 6mASCOPE enables quantitative 6mA deconvolution, it could be confounded by other DNA modifications that indirectly influence SMRT DNA polymerase kinetics of adenines or flanking bases (3, 25, 30), so we suggest combining LC/MS-MS and 6mASCOPE for 6mA quantification and deconvolution of eukaryotic gDNA samples.

REFERENCES AND NOTES

- M. A. Sánchez-Romero, J. Casadesús, *Nat. Rev. Microbiol.* **18**, 7–20 (2020).
- G. Fang et al., *Nat. Biotechnol.* **30**, 1232–1239 (2012).
- J. Beaulaurier, E. E. Schadt, G. Fang, *Nat. Rev. Genet.* **20**, 157–172 (2019).
- Y. Fu et al., *Cell* **161**, 879–892 (2015).
- Y. Wang, X. Chen, Y. Sheng, Y. Liu, S. Gao, *Nucleic Acids Res.* **45**, 11594–11606 (2017).
- S. J. Mondo et al., *Nat. Genet.* **49**, 964–968 (2017).
- E. L. Greer et al., *Cell* **161**, 868–878 (2015).
- G. Zhang et al., *Cell* **161**, 893–906 (2015).
- Z. Liang et al., *Dev. Cell* **45**, 406–416.e3 (2018).
- T. P. Wu et al., *Nature* **532**, 329–333 (2016).
- Q. Xie et al., *Cell* **175**, 1228–1243.e20 (2018).
- C. L. Xiao et al., *Mol. Cell* **71**, 306–318.e7 (2018).
- Z. Hao et al., *Mol. Cell* **78**, 382–395.e8 (2020).
- S. Zhu et al., *Genome Res.* **28**, 1067–1078 (2018).
- K. Doulatianotis, M. Bensberg, A. Lentini, B. Gylemo, C. E. Nestor, *Sci. Adv.* **6**, eaay3335 (2020).
- Z. K. O'Brien et al., *BMC Genomics* **20**, 445 (2019).
- M. U. Musheev, A. Baumgärtner, L. Krebs, C. Niehrs, *Nat. Chem. Biol.* **16**, 630–634 (2020).
- X. Liu et al., *Cell Res.* **31**, 94–97 (2021).
- S. Schiffrers et al., *Angew. Chem. Int. Ed.* **56**, 11268–11271 (2017).
- A. Lentini et al., *Nat. Methods* **15**, 499–504 (2018).
- C. W. Q. Koh et al., *Nucleic Acids Res.* **46**, 11659–11670 (2018).
- G. Z. Luo et al., *Nat. Commun.* **7**, 11301 (2016).
- A. M. Wenger et al., *Nat. Biotechnol.* **37**, 1155–1162 (2019).
- D. Deamer, M. Akeson, D. Branton, *Nat. Biotechnol.* **34**, 518–524 (2016).
- B. A. Flusberg et al., *Nat. Methods* **7**, 461–465 (2010).
- A. Tourancheau, E. A. Mead, X. S. Zhang, G. Fang, *Nat. Methods* **18**, 491–498 (2021).
- J. Beaulaurier et al., *Nat. Biotechnol.* **36**, 61–69 (2018).
- M. J. Blow et al., *PLoS Genet.* **12**, e1005854 (2016).
- J. Beaulaurier et al., *Nat. Commun.* **6**, 7438 (2015).
- E. E. Schadt et al., *Genome Res.* **23**, 129–141 (2013).
- See supplementary materials.
- P. H. Oliveira et al., *Nat. Microbiol.* **5**, 166–180 (2020).
- J. Murgier, C. Everaerts, J. P. Farine, J. F. Ferveur, *Sci. Rep.* **9**, 8873 (2019).
- W. J. Lee, P. T. Brey, *Annu. Rev. Cell Dev. Biol.* **29**, 571–592 (2013).

35. R. J. Roberts, T. Vincze, J. Posfai, D. Macelis, *Nucleic Acids Res.* **43**, D298–D299 (2015).
36. D. S. Lundberg et al., *Nature* **488**, 86–90 (2012).
37. C. P. Corkum et al., *BMC Immunol.* **16**, 48 (2015).
38. C. Ma et al., *Nat. Cell Biol.* **21**, 319–327 (2019).
39. W. M. Guiblet et al., *Genome Res.* **28**, 1767–1778 (2018).
40. Y. Kong, L. Cao, G. Deikus, Y. Fan, E. Mead, W. Lai, Y. Zhang, R. Yong, R. Sebra, H. Wang, X.-S. Zhang, G. Fang, Code and processed data for “Critical assessment of DNA adenine methylation in eukaryotes using quantitative deconvolution” (2022). doi:10.5281/zenodo.5838427
41. P. Ye et al., *Nucleic Acids Res.* **45**, D85–D89 (2017).
42. E. W. Loomis et al., *Genome Res.* **23**, 121–128 (2013).

ACKNOWLEDGMENTS

We thank P. Hegemann (Humboldt University of Berlin) for the *C. reinhardtii* strains, H. D. Madhani (University of California, San Francisco) for the *S. cerevisiae* strain, F. Wang and B. Yao (Emory University) for the *D. melanogaster* embryos and adults, J. Dong (Rutgers University) for the *A. thaliana* strains, J. Mo (Chinese Academy of Sciences) for help with UHPLC-MS/MS analysis,

members of the Fang lab for helpful discussions, and the Department of Scientific Computing at the Icahn School of Medicine at Mount Sinai for computational resources and staff expertise. **Funding:** Supported by the Icahn Institute for Genomics and Multiscale Biology, NIH grants R35 GM139655, R01 HG011095, and R56 AG071291, the Irma T. Hirsch/Monique Weill-Caulier Trust, and the Nash Family Foundation (G.F.). UHPLC-MS/MS analyses of 6mA were supported by Strategic Priority Research Program of the Chinese Academy of Sciences grant XDPB2004 and National Natural Science Foundation of China grant 22021003 (H.W.). **Author contributions:** G.F. conceived the study and supervised the research; Y.K. and G.F. developed the 6mASCOPE method; Y.K. performed all the computational analyses; Y.K., L.C., E.A.M., X.-S.Z., and G.F. designed the experiments; L.C., E.A.M., and X.-S.Z. performed most of the experiments; G.D. and R.S. optimized short-insert PacBio library preparation and performed all PacBio sequencing; Y.F. performed raw PacBio sequencing data processing and quality control; W.L. and H.W. performed the UHPLC-MS/MS analysis; Y.Z. and R.Y. performed glioblastoma sample preparation; X.-S.Z. assisted the characterization of bacterial strains and collected *A. thaliana* samples; Y.K., L.C., Y.F., E.A.M., X.-S.Z., and G.F. analyzed the

data; and Y.K. and G.F. wrote the manuscript with additional information inputs from other co-authors. **Competing interests:** Y.K. and G.F. are the co-inventors of a pending patent application based on the method described in this work. **Data and materials availability:** All sequencing data generated in this study have been submitted to NCBI with accession number PRJNA667898. The software supporting all proposed methods is available along with a tutorial at Zenodo (40) and at GitHub, www.github.com/fanglab/6mASCOPE.

SUPPLEMENTARY MATERIALS

science.org/doi/10.1126/science.abe7489

Materials and Methods

Supplementary Text

Figs. S1 to S17

Tables S1 and S2

References (43–56)

MDAR Reproducibility Checklist

29 September 2020; resubmitted 8 September 2021

Accepted 7 December 2021

10.1126/science.abe7489

NEUROGENOMICS

Discovery of genomic loci of the human cerebral cortex using genetically informed brain atlases

Carolina Makowski¹, Dennis van der Meer^{2,3}, Weixiu Dong⁴, Hao Wang¹, Yan Wu^{4†}, Jingjing Zou⁵, Cin Liu¹, Sara B. Rosenthal⁶, Donald J. Hagler Jr.¹, Chun Chieh Fan¹, William S. Kremen⁷, Ole A. Andreassen², Terry L. Jernigan⁸, Anders M. Dale^{1,2}, Kun Zhang⁴, Peter M. Visscher⁹, Jian Yang^{9,10}, Chi-Hua Chen^{1*}

To determine the impact of genetic variants on the brain, we used genetically informed brain atlases in genome-wide association studies of regional cortical surface area and thickness in 39,898 adults and 9136 children. We uncovered 440 genome-wide significant loci in the discovery cohort and 800 from a post hoc combined meta-analysis. Loci in adulthood were largely captured in childhood, showing signatures of negative selection, and were linked to early neurodevelopment and pathways associated with neuropsychiatric risk. Opposing gradations of decreased surface area and increased thickness were associated with common inversion polymorphisms. Inferior frontal regions, encompassing Broca's area, which is important for speech, were enriched for human-specific genomic elements. Thus, a mixed genetic landscape of conserved and human-specific features is concordant with brain hierarchy and morphogenetic gradients.

Large-scale magnetic resonance imaging and genetics datasets have afforded the opportunity to discover common genetic variants contributing to the morphology of the human cortex. Studies in model organisms have revealed intricate genetic mechanisms underlying cortical area and thickness (i.e., laminar) patterning, although it has been challenging to define aspects of cortical development that are shared across mammals as opposed to those that are human-specific (1). Nevertheless, many studies have shown support for the radial unit hypothesis, which posits differential neurodevelopment programs shaping and regulating these two cortical measures (2).

Consistent with this, the ENIGMA (Enhancing Neuroimaging Genetics through Meta-Analysis) Consortium's genome-wide association study (GWAS) of the human cortex found many variants associated with surface area and thickness linked to neurodevelopmental processes during fetal development (3). Such evidence for neurodevelopmental programming

indicates the need to investigate these questions at earlier ages, as previous cortical GWASs have almost exclusively been conducted in older adults.

Cortical expansion and regional patterning are largely genetically determined (2); therefore, we used data-driven genetically informed atlases in this study (4, 5), rather than atlases primarily determined by sulcal-gyral patterns. These genetically determined atlases capture patterns of hierarchical genetic similarity following known developmental gradients that shape the cortex along their anterior-posterior (A-P) and dorsal-ventral (D-V) axes, including 12 surface area and 12 thickness regions (2, 4, 5), and increase discoverability of genetic variants underlying the cortex (6).

Results

Genetic variants underlying cortical thickness and area

In our discovery UK Biobank (UKB) sample of 32,488 individuals (table S1), we found 440

genome-wide significant [mixed linear model association tests (7), $P < 5 \times 10^{-8}$] variants after clumping each phenotype separately in PLINK (8) [linkage disequilibrium (LD) $R^2 = 0.1$, 250 kb], where 305 and 88 regional genetic variants were associated with the 12 surface area phenotypes and the 12 cortical thickness phenotypes, respectively (Fig. 1 and tables S2 and S3). Twenty-seven genetic variants were significantly associated with total surface area and 20 variants with mean cortical thickness (table S2). After correction for multiple comparisons, 234 genetic variants remained significant ($P < 2.27 \times 10^{-9}$, $5 \times 10^{-8}/t_e$, with $t_e = 22$ being the effective number of independent traits). We performed subsequent functional analyses for the 393 regional variants. Single-nucleotide polymorphisms (SNPs) were mapped to genes on the basis of their genomic position with FUMA (9). Across all phenotypes, SNPs were significantly enriched for noncoding regions (44.0% enriched for intronic variants, 33.4% for intergenic, and 17.7% for noncoding intronic RNA; Fisher's exact test, $P < 0.05$) (Fig. 1 and table S4).

¹Center for Multimodal Imaging and Genetics, University of California, San Diego, CA, USA. ²Norwegian Centre for Mental Disorders Research (NORMENT), Division of Mental Health and Addiction, Oslo University Hospital and Institute of Clinical Medicine, University of Oslo, Oslo, Norway.

³School of Mental Health and Neuroscience, Faculty of Health, Medicine and Life Sciences, Maastricht University, Maastricht, Netherlands. ⁴Department of Bioengineering, University of California, San Diego, CA, USA. ⁵Division of Biostatistics, Herbert Wertheim School of Public Health and Human Longevity Science, University of California, San Diego, CA, USA. ⁶Center for Computational Biology and Bioinformatics, University of California, San Diego, CA, USA. ⁷Department of Psychiatry and Center for Behavior Genetics of Aging, University of California, San Diego, CA, USA.

⁸Center for Human Development, University of California, San Diego, CA, USA. ⁹Institute for Molecular Bioscience, The University of Queensland, Brisbane, Queensland, Australia. ¹⁰School of Life Sciences, Westlake University, Hangzhou, Zhejiang, China.

*Corresponding author. Email: chc101@ucsd.edu (C.-H.C.)

†Present address: Cellarity, Somerville, MA, USA.

Replication and generalization

Replication was performed on an admixed sample of 7410 individuals from UKB, including 2232 of European descent, using mixed linear model association (MLMA) analysis in GCTA (genome-wide complex trait analysis) (10). We modeled population structure using GENESIS (11) to estimate principal components and kinship. Estimated genetic effects in the discovery dataset were correlated with those in the replication dataset, as indexed by significant beta correlations (ranging from a correlation coefficient, r , of 0.66 to 0.95 after correcting for errors in the estimated SNP effects) (fig. S1), sign concordance rate (binomial test, $P < 0.05$), and proportion of variants replicated after multiple comparison correction (12).

MLMA and GENESIS were also used for generalization to data from 9136 individuals from the Adolescent Brain Cognitive Development (ABCD) Study (table S1), given the high degree of admixture and relatedness in this sample. Generalization to ABCD was quite high, as can be observed through significant beta correlations (r range: 0.46 to 0.92) (fig. S2), sign concordance rate, and proportion of variants replicated after correction for multiple comparisons (12). This suggests that the genetic architecture of the cortex found in adulthood is largely generalizable to earlier life stages of neurodevelopment, particularly for surface area. We also examined correspondence between the two datasets by calculating genetic correlations with LD score regression (LDSC) for each region. Eighteen of 24 phenotypes

were significantly genetically similar between ABCD and UKB (genetic correlation, r_g , range: 0.38 to 1.21) (fig. S3).

Given the evidence of comparable results, we ran a joint meta-analysis of the three samples using METAL (12). After clumping each phenotype separately to obtain independent loci, the meta-analysis revealed 800 genome-wide significant regional loci, with 467 passing correction for multiple comparisons (table S5). Of 800 loci, 526 were found to be independent by merging hits from these 26 phenotypes into one file and clumping with PLINK (8) ($R^2 = 0.1$, 250 kb). With the exception of one SNP, all had a nonsignificant heterogeneity P value ($P > 1 \times 10^{-6}$) associated with Cochran's Q statistic, suggesting comparability among samples. SNPs from the meta-analysis with

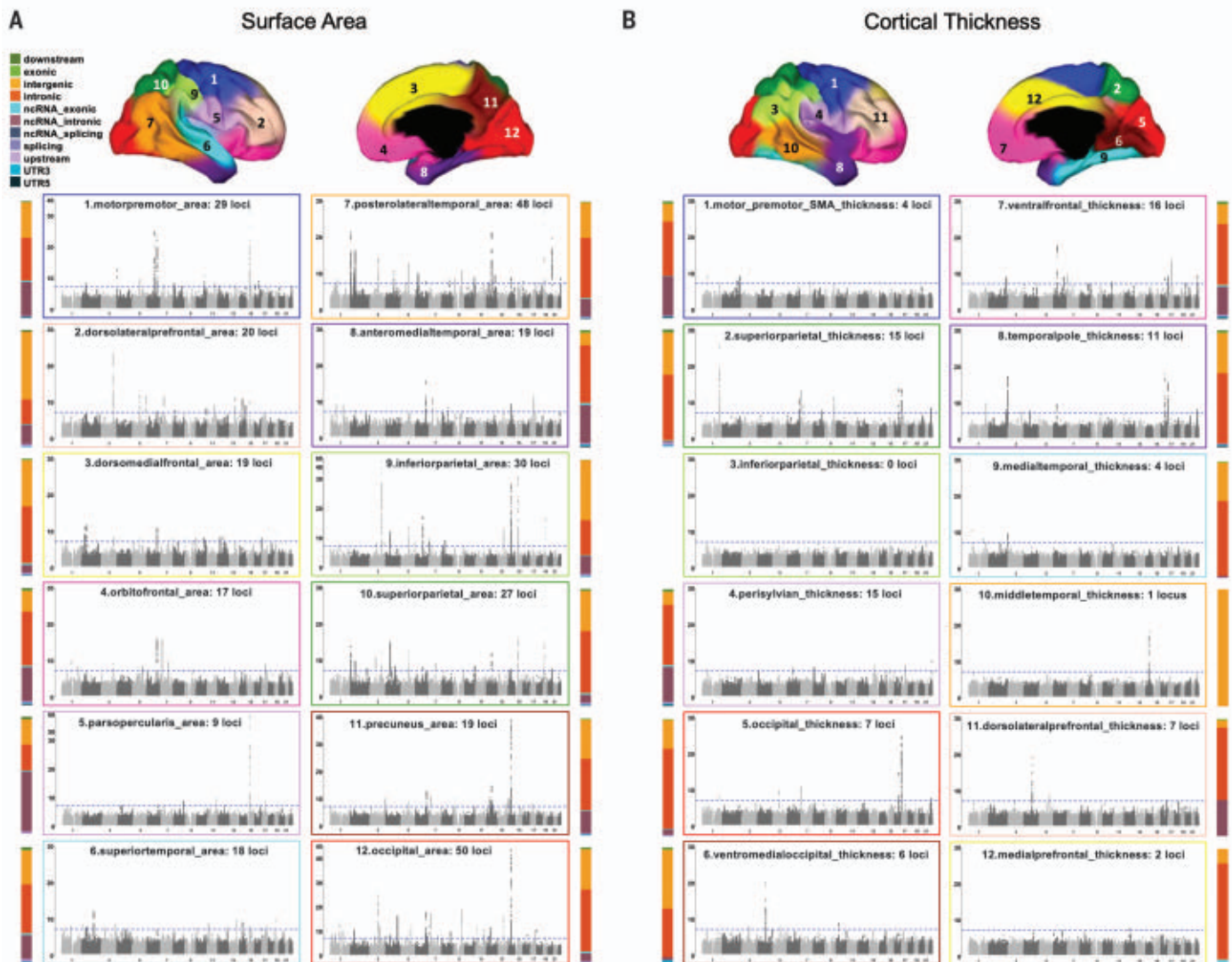


Fig. 1. Manhattan plots of genetic variants underlying surface area and cortical thickness. Results are shown separately for surface area (A) and cortical thickness (B). Numbers on brain atlases represent each brain region. Plots are color coded by brain atlas region. Number of significant genetic loci are listed

in Manhattan subplot titles, with the horizontal dashed line denoting genome-wide significance. Vertical bar charts show breakdown of genomic position of SNPs, with corresponding legend at the top of (A). ncRNA, noncoding RNA; UTR3, 3' untranslated region; UTR5, 5' untranslated region.

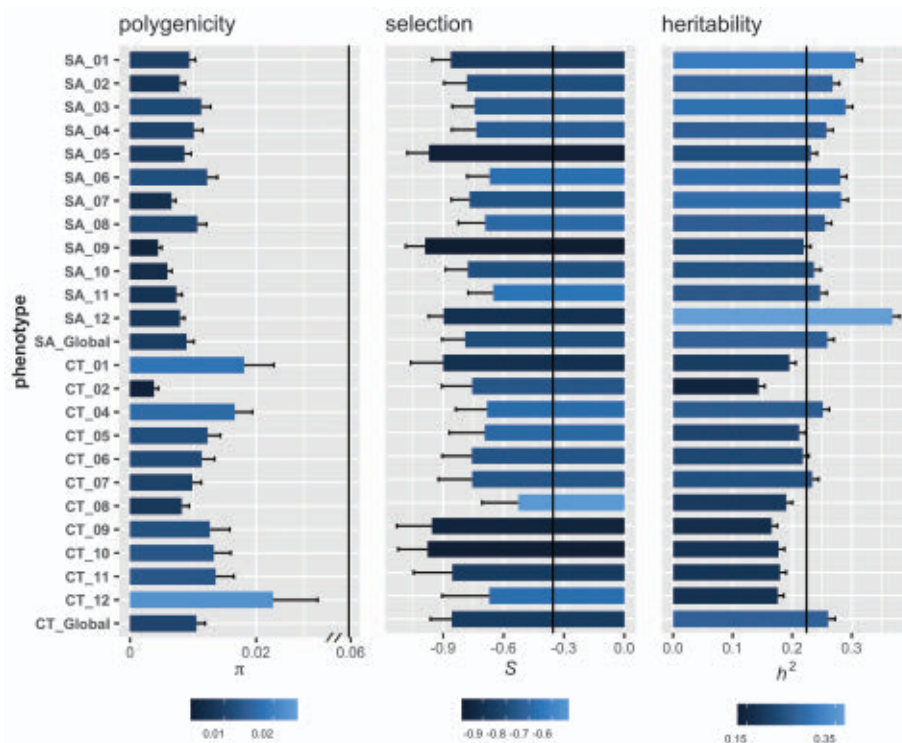


Fig. 2. Genetic architecture of the cortex. Cortical phenotypes generally have low polygenicity, medium to high heritability, and are under strong negative selection. Vertical black lines on each plot are average reference lines for relevant estimates of commonly studied traits taken from (16). Numbering of regions follows labels in Fig. 1. SA, surface area; CT, cortical thickness; π , polygenicity; S , selection; h^2 , heritability.

a significant heterogeneity $P < 1 \times 10^{-6}$ are listed in table S6.

Comparison to previous cortical GWAS

We used conditional and joint analysis (COJO) (13) to identify novel loci compared with the most recent GWAS of cortical architecture which identified 369 loci (3). Of these loci, 206 were found to be independent by clumping all 70 phenotypes together ($R^2 = 0.1$, 250 kb). COJO revealed that 63.6% of our 393 regional variants remained genome-wide significant and thus are considered novel associated variants (12) (table S7).

Assigning SNPs to genes and neuropsychiatric implications

All SNPs in LD ($R^2 > 0.6$) with the 393 regional variants were mapped to genes using positional, gene expression [expression quantitative trait locus (eQTL)], and chromatin interaction information in FUMA SNP2GENE (9). This mapped our genetic variants to 915 genes (tables S8 and S9). MAGMA gene-based analyses yielded 575 significant genes (mean χ^2 statistics, $P < 2.6 \times 10^{-6}$) (table S10). According to the National Institutes of Health Genetics Home Reference, many significant genes are related to neurodevelopmental disorders (autism, epilepsy, microcephaly) or dementia (table S11).

Further support for this conclusion was determined by investigating the shared genetic effects between our brain phenotypes and disorders by estimating genetic correlations through LDSC (fig. S4 and table S12). We found a significant association between global surface area and attention-deficit/hyperactivity disorder (ADHD) after multiple comparison correction, as well as nominal significant associations [e.g., temporal area with schizophrenia and autism spectrum disorder (ASD)]. To examine putative causal association, we performed Mendelian randomization (14) on global area and ADHD that showed the most significant r_g , and we did not find evidence of causality. We also examined ASD, a neurodevelopmental disorder with early onset, and its relationship with anteromedial temporal area indexed by a significant r_g . We found a significant unidirectional causation ($b_{xy} = -0.36$, $P = 9.5 \times 10^{-5}$), indicating that decreased anteromedial temporal area may cause ASD. These SNPs could be missed in classical GWAS of ASD, but nevertheless are important genetic factors in the pathogenesis of this disorder through their contributions to anteromedial temporal morphology.

Genetic architecture of the cortex

Compared with other common complex traits, cortical phenotypes tend to have low polygenic-

ity (proportion of genome-wide SNPs with non-null effects; range: 0.0038 to 0.040; area: $\pi = 0.0085 \pm 0.0011$; thickness: $\pi = 0.015 \pm 0.0039$) and average-to-high SNP-based heritability (range: 0.14 to 0.37; area: $h^2 = 0.27 \pm 0.012$; thickness: $h^2 = 0.20 \pm 0.011$) (Fig. 2). Pedigree-based heritability for the UKB discovery sample (range: 0.31 to 0.95), calculated with multiple genetic relatedness matrices (15), and twin-based heritability approximated by Falconer's formula from the ABCD sample (range: 0.39 to 0.96) can be found in table S13. Negative selection signatures can be inferred from the relationship between minor allele frequency and effect size, quantified by the S parameter implemented in SBayesS (16) (fig. S5). We found that loci associated with our cortical phenotypes may be under strong negative selection pressures (16) compared with phenotypes with similar levels of heritability and polygenicity (range: -0.99 to 0.045 ; area: $S = -0.79 \pm 0.11$; thickness: $S = -0.72 \pm 0.18$). It should be noted that π is slightly dependent on sample size and thus should be interpreted with caution. However, others have shown similar estimates of polygenicity for brain phenotypes (17).

Partitioned heritability

Different functional regions of the genome can contribute disproportionately to complex human traits. Thus, we applied stratified LDSC regression to partition heritability estimates of our 24 cortical phenotypes for 97 annotations from the baseline model (18, 19) (table S14), from which we focused on enriched annotations where regression coefficients are significantly positive ($z > 1.96$, two-tailed $P < 0.05$). We classified the annotations into three categories determined from conserved, developmental, and regulatory genomic partitions. We found seven conserved annotations (found in primates and other mammals) to be significantly enriched after multiple comparison correction ($P < 0.0025$, where $P < 0.05/t_c$) (Fig. 3A and table S15) across 16 cortical phenotypes, with notable enrichment for seven phylogenetically conserved cortical regions (e.g., medial temporal lobe, motor and orbitofrontal regions) for the annotation "ancient sequence age human promoter." This conserved promoter annotation reflects a genomic region that is evidenced to have existed before the evolutionary split of marsupial and placental mammals (18).

Seven regions, mostly indexing surface area, were significantly enriched for developmental annotations of fetal deoxyribonuclease I (DNase I) hypersensitive sites (DHSs), a marker of accessible chromatin (20), along with enrichment of 15 cortical phenotypes for 13 regulatory annotations (table S15). We performed an additional partitioned heritability analysis using differential methylation regions (DMRs) that

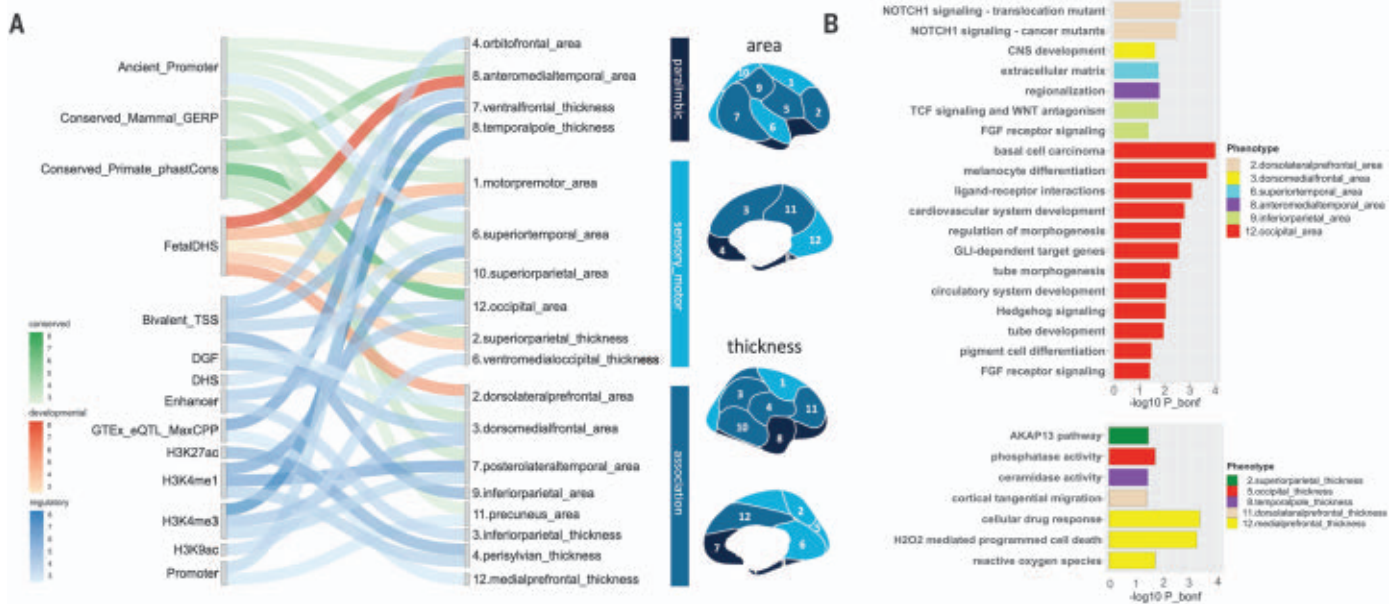


Fig. 3. Partitioned heritability and Gene Ontology (GO) enrichment.

(A) Heritability of cortical phenotypes is significantly enriched for conserved, developmental, and regulatory annotations. The river plot depicts mapping between significant annotations (18) and cortical phenotypes. Color coding of the river plot is based on $-\log_{10}$ enrichment P values. (B) Significantly

enriched GO terms from MAGMA gene set analysis for surface area (top) and cortical thickness (bottom). GERP, genomic evolutionary rate profiling; TSS, transcription start site; DGF, digital genomic footprint; GTE_{ex}, genotype-tissue expression; CNS, central nervous system; TCF, T cell factor; FGF, fibroblast growth factor; bonf, Bonferroni.

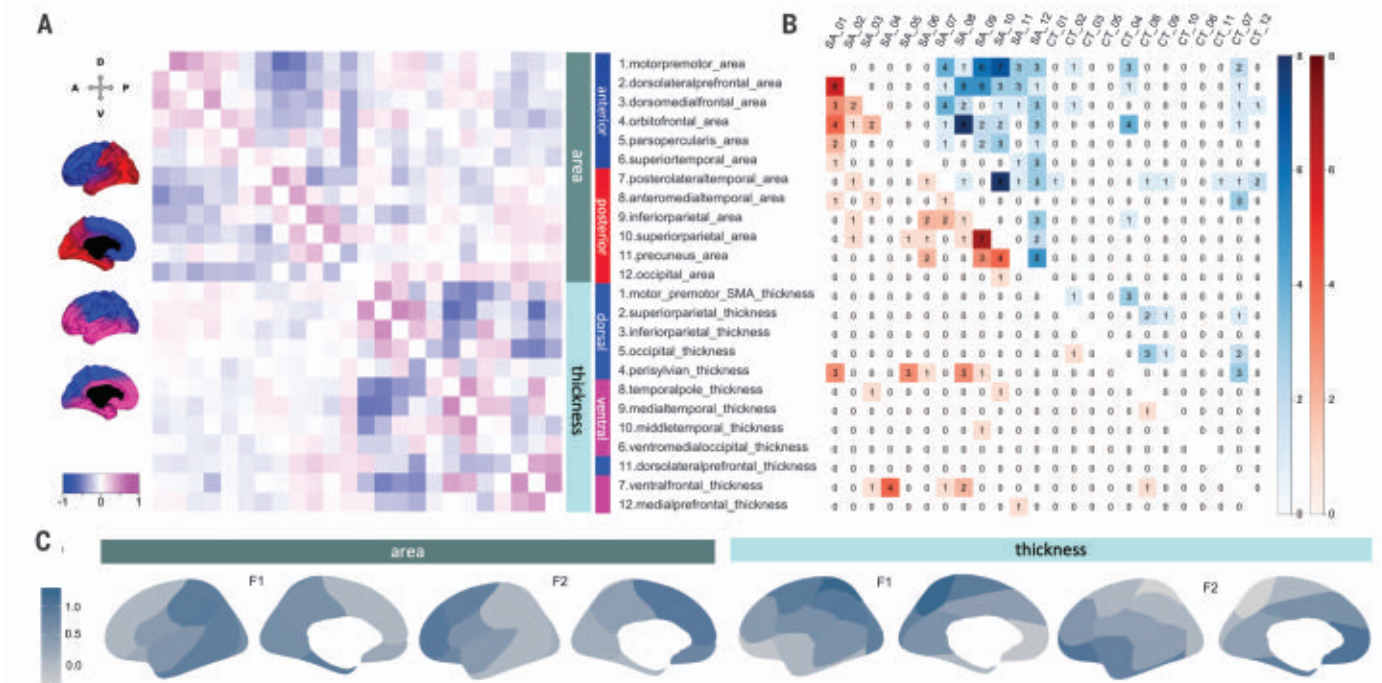


Fig. 4. Three-dimensional genetic characterization of the cortex.

(A) Phenotypic and genotypic correlations between 24 regions, ordered by hierarchical clustering that shows A-P divisions for area and D-V divisions for thickness. Phenotypic correlations are in bottom left triangle, and genetic correlations are in the upper right. SMA, supplementary motor area.

(B) Pleiotropic SNP counts for each pair of regions, using the same ordering as in (A). Agonistic or same direction of effects are in the lower red triangle, antagonistic or opposing effects are in upper blue triangle. (C) Brain maps of standardized effects of each latent factor (F1 and F2) derived from genomic SEM on each brain region. See fig. S7 for detailed statistics.

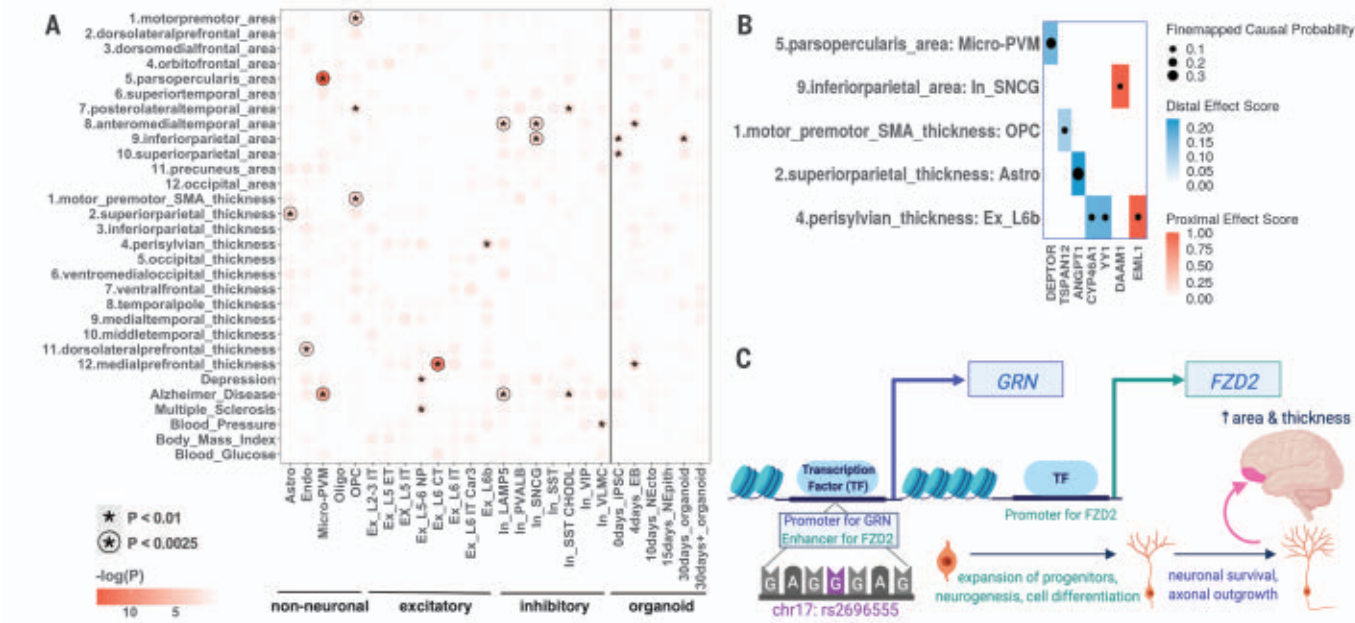


Fig. 5. Enrichment of cell type-specific accessible chromatin sites and fine-mapping to regulatory regions of genes. (A) Heatmap of enrichment for cortical phenotypes and cell type-specific accessible chromatin peaks. Phenotypes also include three metabolic (blood glucose, body mass index, and blood pressure) and three cortical-related (multiple sclerosis, Alzheimer’s disease, and depression) controls. Vertical black line differentiates M1 cell types (left) from organoid developmental stages (right). Significant values are based on the bias-corrected enrichment statistic from g-chromVAR (12). (B) Mapped

genes and the regulatory region (blue, enhancer; red, promoter) of the causal SNPs carried forward by positively enriched M1 cell type–cortical phenotype pairs ($z > 2.36$, $P < 0.01$). Size of dot reflects probability of SNP being causal. Colors represent peak to gene coaccessibilities, where a score of 1 reflects a peak being in the gene’s promoter region. (C) A selected pleiotropic SNP (rs2696555) influencing both orbitofrontal area and ventral frontal thickness, mapped to target genes on the basis of coaccessibility with M1. Cell types are outlined in table S23.

were previously found to be associated with present-day humans compared to Neanderthal and Denisovan genomes (21). Perisylvian thickness was nominally enriched for present-day human DMRs (LDSC Jackknife test, $P = 0.03$). By partitioning the genome into meaningful functional categories, we capture patterns of hierarchical brain organization with evolutionarily conserved (paralimbic, sensory motor) regions enriched for conserved and developmental annotations and association areas more strongly associated with regulatory annotations.

Gene Ontology enrichment

To elucidate the biological pathways associated with our discovered genetic variants, MAGMA-mapped genes were input into the Molecular Signatures Database to obtain Gene Ontology (GO) terms. Twenty-six GO terms, predominantly related to neurodevelopment, were significantly associated with our brain phenotypes after Bonferroni correction (Fig. 3B and table S16). Notable biological pathways included *WNT*/beta-catenin, *TCF*, *FGF*, and hedgehog signaling, which are important for axis specification and areal identity (1). For higher-order association regions, the dorsolateral prefrontal cortex was linked to cortical tangential migration.

Three-dimensional genetic characterization of the cortex

To better understand the relationship between our cortical phenotypes, we computed phenotypic and genetic correlation matrices using LDSC (Fig. 4A). Significant correspondence was observed between matrices (Mantel test: $r = 0.85$, $P = 0.001$), suggesting substantial genetic influences on cortical patterning. Hierarchical clustering was applied to genetic correlations of area and thickness separately, revealing a clear separation in genetic architecture between A-P divisions in area and between D-V divisions in thickness (Fig. 4, A and B, and fig. S6). Regions anatomically closer to each other tended to be more correlated with each other. However, homologous regions in contralateral hemispheres had high genetic correlations despite their physical distance (4) (table S18).

Given the observed correlations, we sought to estimate the shared genetic effects across phenotypes with genomic structural equation modeling (SEM) (Fig. 4C and figs. S7 and S8) (12, 22). We found that two-factor models fit our data well (comparative fit index of >0.98). The two latent factors recapitulated the A-P and D-V gradations of cortical patterning for area and thickness, respectively. The strongest association signals between the latent factors

and variants reside in the 17q21.31 inversion region for area ($P < 1.48 \times 10^{-56}$), and more widespread effects across the genome with notable peaks on chromosomes 3 and 17 for thickness ($P < 3.39 \times 10^{-15}$) (fig. S8). We further performed association testing of inversion polymorphisms on 17q21.31 with our cortical phenotypes (table S19). We found the inverted allele to be highly associated with overall surface area reductions, with stronger effects in posterior regions along the A-P gradient and a modest positive correlation with increasing thickness in ventral regions. The opposing effects on area and thickness may in part account for the observation of a modest negative association between area and thickness (“cortical stretching”) after accounting for total brain size (23).

After extracting salient latent factors underlying multiple brain regions, we searched for pleiotropic loci between pairs of regions. We used COJO to map SNPs with potential pleiotropic effects (i.e., that influence two regions), defined by the loci of region i that were no longer genome-wide significant when conditioned on the loci of region k (13). Using this approach, we found that 107 of our 393 loci had pleiotropic effects on two phenotypes (Fig. 4B and table S20). Surface area of parietal and posterolateral temporal regions shared eight SNPs

with antagonistic effects (i.e., increasing area of one region while decreasing area of the other); these regions show good correspondence between ABCD and UKB and are both enriched for fetal DNase hypersensitive sites (Fig. 3A). Two of these antagonistic SNPs, rs10878269 and rs142166430, are intronic variants of methionine sulfoxide reductase B3 (*MSRB3*), a gene that is important for protein repair and metabolism (24).

We also noted antagonistic pleiotropic effects of two SNPs, rs12676193 and rs6986885, in the 8p23.1 inversion polymorphism linked to motor-premotor area and perisylvian thickness (table S20). These SNPs were mapped to methionine sulfoxide reductase A (*MSRA*), a gene that is important for repair of oxidatively damaged proteins (25). Further, the 8p23.1 region is considered to be a potential hub for neurodevelopmental and psychiatric disorders (26). Another notable SNP with pleiotropic effects was rs888812, with antagonistic effects on precuneus and prefrontal area. This and other variants were mapped to *NR2F1/COUP-TF1*, a transcription factor influencing A-P patterning of the cortex in development (1).

Enrichment of cell type–specific accessible chromatin sites and fine-mapping to regulatory regions of genes

To map putative causal genes for our genetic variants—motivated by observed enrichment of our phenotypes for regulatory genomic regions—we computed cell type–specific enrichment for our fine-mapped GWAS SNPs on the basis of high-resolution accessible chromatin sites drawn from human primary motor cortex (M1) (27) and cerebral organoid data (28) using g-chromVAR (fig. S9). To quantify enrichment, we computed the accessibility deviations as the expected number of feature counts per peak per cell type, weighted by the fine-mapped variant posterior probabilities. This revealed 11 significantly positively enriched cell type–phenotype pairs after Bonferroni correction ($z > 2.8$, $P < 0.0025$) (Fig. 5A), including enrichment of the motor-premotor region for accessible chromatin sites in oligodendrocyte precursor cells (OPCs). This result is particularly compelling given that OPCs give rise to mature oligodendrocytes which in turn myelinate axons in the central nervous system, and the motor cortex is known to be a region rich in intracortical myelin content (29). In control analyses, no significant enrichment was found for metabolic traits, suggesting that this approach is specific to cortical phenotypes. This approach is further supported by the consistent finding of the significant Alzheimer's-microglia pair (30).

For each significant M1 cell type–phenotype pair from Fig. 5A, we identified putative causal genes from a locus's genomic position relative to its gene targets and chromatin coaccessi-

bility relationships (i.e., both the genomic locus and its gene target were simultaneously accessible). From the initial 25 target genes, five distal and two proximal genes remained (Fig. 5B) after filtering out genes with weak evidence of gene expression in the corresponding cell type (fig. S10 and table S21).

We applied the same mapping approach to pleiotropic SNPs and found three SNPs that overlapped with the M1 accessible chromatin peaks (Fig. 5 and table S22). Notably, rs2696555, a SNP in the 17q21.31 inversion region, was associated with increases in orbitofrontal area and ventral frontal thickness and mapped to the promoter region of *GRN*, a granulin precursor that helps preserve neuronal survival, axonal outgrowth, and neuronal integrity through its impact on inflammatory processes in the brain (31). This SNP was also mapped at a distal putative enhancer site of *FZD2*, which encodes a Frizzled receptor within the *WNT*/beta-catenin pathway and is expressed in cortical progenitor cells of the dorsal and ventral telencephalon of the developing brain (32). A schematic of how this single variant could influence area and thickness is depicted in Fig. 5C.

Discussion

This study advances understanding of the genetic architecture underlying the organization of the cerebral cortex and uniquely human traits. Our genetically informed atlases enhanced discovery of significant loci compared with previous cortical GWAS with traditional nongenetic atlases (3, 6). The improved discovery is likely aided by the fact that our atlases conform to genetic cortical patterning (4, 5), thereby increasing discoverability and heritability, while also having lower polygenicity.

Making use of two large cohorts of adults and children, we found that many genetic variants in our findings pinpoint genetic mechanisms influencing cortical patterning of the human brain in early development. Our data, particularly findings with *COUP-TF1*, support the protomap hypothesis whereby genes hold spatial and temporal instructions to initiate a cortical map by graded signaling from patterning centers in early development (1, 2). Our results are consistent with reports of loss of *COUP-TF1* function leading to expansion of frontal motor areas at the expense of posterior sensory areas in the rodent brain (1), which is intriguing given the challenges in defining rodent-specific versus human-specific developmental mechanisms. These variants are promising candidates for future functional experiments.

We also uncovered latent factors describing our area phenotypes, suggesting genetic effects related to inversion polymorphisms. Recurrent inversions of genomic regions, such as 17q21.31 identified here along with 8p23, have occurred through primate evolution and show that the

inverted orientation is the ancestral state. Specifically, both 17q21.31 and 8p23 inversions appear to have occurred independently within the *Homo* and *Pan* lineages (33, 34). 17q21.31 inversion contains microtubule associated protein tau (*MAPT*), a risk gene for neurodegeneration (35). The inverted (minor) allele has been associated with lower susceptibility for Parkinson's dementia but higher predisposition to developmental disorders (33).

We linked several of our findings to the *WNT*/beta-catenin pathway, which regulates cortical size by controlling whether progenitors continue to proliferate or exit the cell cycle to differentiate (36). Cell proliferation is thought to exponentially enlarge the progenitor pool and the number of cortical columns, which results in expansion of cortical surface area and gyrification. On the other hand, cortical thickness is largely determined by cell differentiation and a linear production of neurons within each cortical column (2, 36). In addition to 17q21.31, our results revealed loci linked to various cortical regions in this pathway (e.g., *WNT3*, *GSK3B*), and their combined interactive effects may be differentially involved in shaping area and thickness.

The brain is particularly vulnerable to insults (genetic and environmental) during sensitive periods of neurodevelopment, and changes during this time can have lasting impacts on the brain over the life span. This perspective helps situate our findings of predominantly negative selection acting on our cortical phenotypes (Fig. 2), which may be linked to conserved genomic loci and those enriched for neuropsychiatric diseases (18, 19). Here we uncovered a putative causal relationship of reduced anteromedial temporal area potentially giving rise to ASD. The medial temporal lobe has been linked to abnormal connectivity in some types of ASD and houses structures (e.g., amygdala, hippocampus) important in regulating emotion and social behaviors (37). We also found this region to be enriched for accessible chromatin sites in inhibitory neurons; thus, these findings may provide clues to the long-standing theory of excitatory-inhibitory imbalance in ASD (38).

Intriguingly, most of our phenotypes, especially paralimbic and sensory motor regions, exhibited enriched heritability for conserved genomic partitions (Fig. 3A) including promoter regions, rather than enhancers, consistent with the idea that the former are more evolutionarily conserved (18). However, we also identified brain regions that have evolved to support human-specific behaviors, such as language and communication. Differential methylation and human-specific SNPs in association with perisylvian thickness lead us to speculate that altered morphology of the perisylvian region, and potentially also motor-premotor regions, were important in the evolution of speech articulation (39).

Our results with genetically informed atlases demonstrate that human brain arealization and regionalization largely arise from phylogenetically conserved regions and multiple neurodevelopmental programs, but that a select few regulatory features, some of which may be specific to modern-day humans, have had widespread downstream effects on brain morphology and may have given rise to human-specific traits and diseases.

REFERENCES AND NOTES

1. Z. Molnár *et al.*, *J. Anat.* **235**, 432–451 (2019).
2. P. Rakic, *Nat. Rev. Neurosci.* **10**, 724–735 (2009).
3. K. L. Grasby *et al.*, *Science* **367**, eaay6690 (2020).
4. C.-H. Chen *et al.*, *Science* **335**, 1634–1636 (2012).
5. C.-H. Chen *et al.*, *Proc. Natl. Acad. Sci. U.S.A.* **110**, 17089–17094 (2013).
6. D. van der Meer *et al.*, *Cereb. Cortex* **30**, 5597–5603 (2020).
7. L. Jiang *et al.*, *Nat. Genet.* **51**, 1749–1755 (2019).
8. S. Purcell *et al.*, *Am. J. Hum. Genet.* **81**, 559–575 (2007).
9. K. Watanabe, E. Taskesen, A. van Bochoven, D. Posthuma, *Nat. Commun.* **8**, 1826 (2017).
10. J. Yang, S. H. Lee, M. E. Goddard, P. M. Visscher, *Am. J. Hum. Genet.* **88**, 76–82 (2011).
11. S. M. Gogarten *et al.*, *Bioinformatics* **35**, 5346–5348 (2019).
12. See supplementary materials.
13. J. Yang *et al.*, *Nat. Genet.* **44**, 369–375, S1–S3 (2012).
14. Z. Zhu *et al.*, *Nat. Commun.* **9**, 224 (2018).
15. N. Zaitlen *et al.*, *PLOS Genet.* **9**, e1003520 (2013).
16. J. Zeng *et al.*, *Nat. Genet.* **50**, 746–753 (2018).
17. N. Matoba, M. I. Love, J. L. Stein, *Hum. Brain Mapp.* **43**, 329–340 (2022).
18. M. L. A. Huijoe, S. Gazal, F. Hormozdiari, B. van de Geijn, A. L. Price, *Am. J. Hum. Genet.* **104**, 611–624 (2019).
19. S. Gazal *et al.*, *Nat. Genet.* **50**, 1600–1607 (2018).
20. G. Trynka, S. Raychaudhuri, *Curr. Opin. Genet. Dev.* **23**, 635–641 (2013).
21. D. Gokhman *et al.*, *Science* **344**, 523–527 (2014).
22. A. D. Grotzinger *et al.*, *Nat. Hum. Behav.* **3**, 513–525 (2019).
23. L. J. Hogstrom, L. T. Westlye, K. B. Walhovd, A. M. Fjell, *Cereb. Cortex* **23**, 2521–2530 (2013).
24. T.-J. Kwon *et al.*, *Hum. Mol. Genet.* **23**, 1591–1601 (2014).
25. A. N. Minniti *et al.*, *Antioxid. Redox Signal.* **22**, 48–62 (2015).
26. M.-T. Lo *et al.*, *Nat. Genet.* **49**, 152–156 (2017).
27. T. E. Bakken *et al.*, *Nature* **598**, 111–119 (2021).
28. S. Kanton *et al.*, *Nature* **574**, 418–422 (2019).
29. M. F. Glasser, D. C. Van Essen, *J. Neurosci.* **31**, 11597–11616 (2011).
30. B. B. Lake *et al.*, *Nat. Biotechnol.* **36**, 70–80 (2018).
31. X. Gao *et al.*, *Protein Cell* **1**, 552–562 (2010).
32. S. J. Harrison-Uy, S. J. Pleasure, *Cold Spring Harb. Perspect. Biol.* **4**, a008094 (2012).
33. M. C. Zody *et al.*, *Nat. Genet.* **40**, 1076–1083 (2008).
34. M. P. A. Salm *et al.*, *Genome Res.* **22**, 1144–1153 (2012).
35. K. H. Strang, T. E. Golde, B. I. Giasson, *Lab. Invest.* **99**, 912–928 (2019).
36. A. Chenn, C. A. Walsh, *Science* **297**, 365–369 (2002).
37. P. Rane *et al.*, *Harv. Rev. Psychiatry* **23**, 223–244 (2015).
38. G. Cellot, E. Cherubini, *Front. Pediatr.* **2**, 70 (2014).
39. D. Gokhman *et al.*, *Nat. Commun.* **11**, 1189 (2020).
40. Adolescent Brain Cognitive Development Study (ABCD) 2.0.1 release #721, NIMH Data Archive (2021); <https://doi.org/10.15154/1504041.10.15154/1504041>.
41. Derived data from Discovery of genomic loci of the human cerebral cortex using genetically informed brain atlases release #1303, NIMH Data Archive (2022); <https://doi.org/10.15154/1523026>.

ACKNOWLEDGMENTS

The authors thank the research participants and staff involved in data collection of the UK Biobank and Adolescent Brain Cognitive Development (ABCD) Study. The ABCD Study is a multisite, longitudinal study designed to recruit more than 10,000 children ages 9 and 10 and follow them over 10 years into early adulthood. The ABCD Study is supported by the National Institutes of Health (NIH) and additional federal partners under award numbers

U01DA041048, U01DA050989, U01DA051016, U01DA041022, U01DA051018, U01DA051037, U01DA050987, U01DA041174, U01DA041106, U01DA041117, U01DA041028, U01DA041134, U01DA050988, U01DA051039, U01DA041156, U01DA041025, U01DA041120, U01DA051038, U01DA041148, U01DA041093, U01DA041089, U24DA041123, and U24DA041147. A full list of supporters is available at <https://abcdstudy.org/federal-partners.html>. A listing of participating sites and a complete listing of the study investigators can be found at <https://abcdstudy.org/study-sites/>. ABCD consortium investigators designed and implemented the study and/or provided data but did not necessarily all participate in analysis or writing of this report. This manuscript reflects the views of the authors and may not reflect the opinions or views of the NIH or ABCD consortium investigators. **Funding:** This research was supported by the NIH under grants R01MH118281, R56AG061163, R01MH122688, R01AG050595, and R01AG022381. C.M. is supported by the Canadian Institutes of Health Research (CIHR), Fonds de Recherche du Québec-Santé (FRQS), and the Kavli Institute for Brain and Mind (KIBM). P.M.V. and J.Y. acknowledge funding from the National Health and Medical Research Council (1113400) and the Australian Research Council (FT180100186 and FL180100072). J.Y. is supported by the Westlake Education Foundation. D.v.d.M. is supported by the Research Council of Norway (project 276082). O.A.A. is funded by the Research Council of Norway (283798, 273291, 248778, and 223273) and KG Jebsen Stiftelsen. **Author contributions:** Study design: C.M., D.v.d.M., W.D., H.W., Y.W., K.Z., P.M.V., J.Y., and C.-H.C. Data analysis: C.M., D.v.d.M., W.D., Y.W., J.Z., H.W., S.B.R., and C.-H.C. Manuscript writing: C.M., D.v.d.M., W.D., and C.-H.C. UKB data processing: D.v.d.M. and O.A.A. ABCD data collection and processing: C.M., D.J.H., C.C.F., T.L.J., and A.M.D. Single-cell data processing: W.D., Y.W., and K.Z. Data visualization: C.M., D.v.d.M., W.D., Y.W., C.L., and C.-H.C. Manuscript preparation and revisions: All authors. **Competing interests:** O.A.A. has received speaker's honoraria from Lundbeck and Sunovion and is a consultant to HealthLytix. A.M.D. is a

founder of and holds equity in CorTechs Labs, Inc., and serves on its scientific advisory board. A.M.D. is also a member of the scientific advisory board of Human Longevity, Inc., and receives funding through research agreements with General Electric Healthcare and Medtronic, Inc. The terms of these arrangements have been reviewed and approved by the University of California, San Diego, in accordance with its conflict of interest policies. The other authors declare no competing interests. **Data and materials availability:** The individual-level raw data used in this study can be obtained from two accessible data resources, UK Biobank (www.ukbiobank.ac.uk/) and ABCD Study (<https://abcdstudy.org>). ABCD Study data were processed from the raw structural imaging data held in the National Institute of Mental Health (NIMH) Data Archive (NDA). The ABCD data repository grows and changes over time. The ABCD data used in this report came from ABCD Collection Release 2.0.1 (40). Data access details can be found on the NDA website (<https://nda.nih.gov/abcd/request-access>). GWAS summary statistics are accessible in an NDA study (41). We made use of publicly available software and tools. The analysis code is available in the Bio-protocol.

SUPPLEMENTARY MATERIALS

science.org/doi/10.1126/science.abe8457
Materials and Methods
Supplementary Text
Figs. S1 to S11
Tables S1 to S24
References (42–119)
MDAR Reproducibility Checklist

17 September 2020; resubmitted 12 March 2021
Accepted 28 December 2021
10.1126/science.abe8457

QUANTUM GASES

Second sound attenuation near quantum criticality

Xi Li^{1,2,3†}, Xiang Luo^{1,2,3†}, Shuai Wang^{1,2,3}, Ke Xie^{1,2,3}, Xiang-Pei Liu^{1,2,3}, Hui Hu^{4,1}, Yu-Ao Chen^{1,2,3*}, Xing-Can Yao^{1,2,3*}, Jian-Wei Pan^{1,2,3*}

Second sound attenuation, a distinctive dissipative hydrodynamic phenomenon in a superfluid, is crucial for understanding superfluidity and elucidating critical phenomena. Here, we report the observation of second sound attenuation in a homogeneous Fermi gas of lithium-6 atoms at unitarity by performing Bragg spectroscopy with high energy resolution in the long-wavelength limit. We successfully obtained the temperature dependence of second sound diffusivity D_2 and thermal conductivity κ . Furthermore, we observed a sudden rise—a precursor of critical divergence—in both D_2 and κ at a temperature of about 0.95 superfluid transition temperature T_c . This suggests that the unitary Fermi gas has a much larger critical region than does liquid helium. Our results pave the way for determining the universal critical scaling functions near quantum criticality.

Second sound, an entropy wave predicted by the seminal two-fluid hydrodynamic theory (1, 2), directly couples to the superfluid order parameter (3–5). In contrast to first sound, which is a density wave existing both below and above the superfluid transition, second sound propagates only in the superfluid phase. As a macroscopic manifestation of heat and momentum diffusion,

second sound attenuation is characterized by several important transport coefficients (6–8), such as the shear viscosity η and the thermal conductivity κ . In liquid helium, the measurement of second sound attenuation and the related thermal transport led to the establishment of dynamic scaling theory (3, 5, 9–11). However, owing to the narrow critical region and limited controllability of liquid helium, a deeper

¹Hefei National Laboratory for Physical Sciences at the Microscale and Department of Modern Physics, University of Science and Technology of China, Hefei 230026, China. ²Shanghai Branch, CAS Center for Excellence in Quantum Information and Quantum Physics, University of Science and Technology of China, Shanghai 201315, China. ³Shanghai Research Center for Quantum Sciences, Shanghai 201315, China. ⁴Centre for Quantum Technology Theory, Swinburne University of Technology, Melbourne, VIC 3122, Australia.

*Corresponding author. Email: yaochen@ustc.edu.cn (Y.-A.C.); yaoxing@ustc.edu.cn (X.-C.Y.); pan@ustc.edu.cn (J.-W.P.)

†These authors contributed equally to this work.

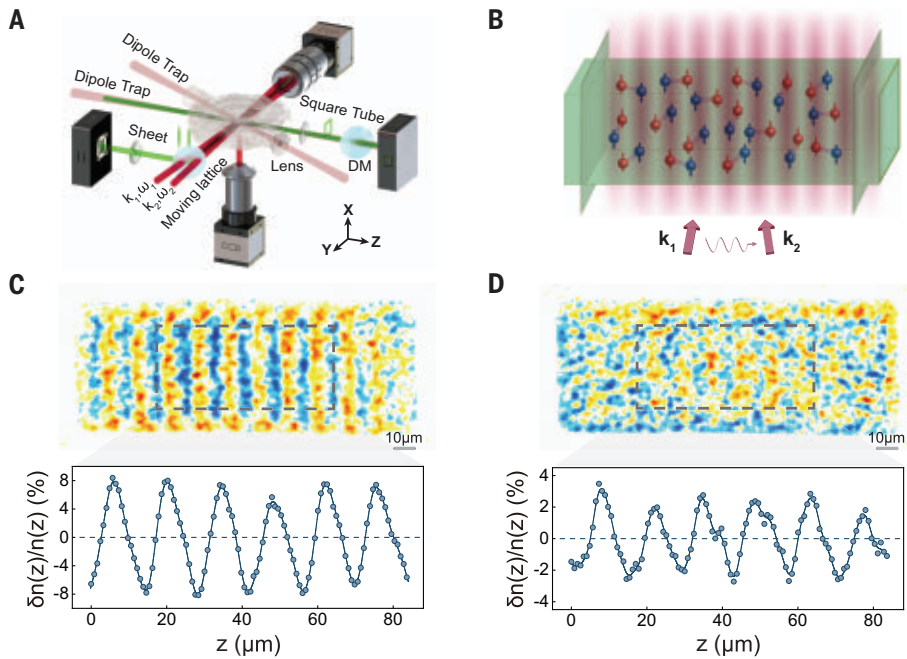


Fig. 1. Creation of sound waves. (A) Sketch of the experimental setup. The rectangular-box trap consists of a square tube and two sheets of 532-nm laser beams, generated by two spatial light modulators. DM, dichroic mirror; CCD, charge-coupled device. (B) A pair of 741-nm laser beams with wave vectors (\mathbf{k}_1 , \mathbf{k}_2) and frequencies (ω_1 , ω_2) exactly intersect on the homogeneous unitary Fermi gas with a small angle, producing a one-dimensional moving-lattice potential. The wave number $k = |\mathbf{k}_1 - \mathbf{k}_2|$ of the Bragg lattice can be accurately determined by the horizontal CCD camera in (A), whereas another vertical CCD camera is used to probe the in situ density profile of the cloud. (C and D) First and second sound waves in a unitary Fermi superfluid at $0.84(2)T/T_c$. The top panels show typical single-shot difference images of density response δn , with the lattice frequency $\omega = \omega_1 - \omega_2$ of $2\pi \times 2.1$ kHz for first sound (C) and $2\pi \times 0.3$ kHz for second sound (D) (see text). $n(z)$ and $\delta n(z)$ are obtained, respectively, by further integrating the reference and difference images along the transverse direction in the dashed box (i.e., region of interest $84.40 \mu\text{m}$ by $41.39 \mu\text{m}$). The bottom panels show the normalized density waves $\delta n(z)/n(z)$ along the longitudinal z axis. The solid line is a guide to the eye.

understanding and quantitative account of critical scaling functions remain elusive. Related issues arise in a wide range of strongly correlated materials such as high-temperature superconductors, where the anomalous charge and energy transport near quantum criticality is not well understood (12, 13).

Ultracold fermionic atoms in the strongly interacting limit, that is, the unitary Fermi gas (14), offer great promise for studying the second sound attenuation and elucidating the critical phenomena. First, as a consequence of scale invariance, the thermodynamic and dynamic properties of the unitary Fermi gas are universal functions of the reduced temperature T/T_F (15–20). Here, the Fermi temperature $T_F \equiv \hbar^2 k_F^2 / (2mk_B)$ is determined by the atomic mass m , the density n , and the Fermi wave number $k_F = (3\pi^2 n)^{1/3}$; k_B and \hbar denote the Boltzmann and reduced Planck constants, respectively. Thus, the second sound diffusivity D_2 and the thermal conductivity κ at temperature T are similarly universal functions of T/T_F . Second, thanks to the unprecedented controllability (14), the critical region of the unitary Fermi gas can be precisely probed to

investigate the critical transport behaviors. Over the past decades, great efforts have been devoted to probing the sound propagation and attenuation in the unitary Fermi gas. The second sound propagation has been observed in a highly elongated harmonic trap (21), but the attenuation remains undetermined because of the density inhomogeneity. The first sound attenuation has been recently measured by confining the unitary Fermi gas into a box potential, eliminating the inhomogeneity problem (22). However, observing the second sound attenuation is challenging because the signal is too weak to be resolved from noise.

Here, we measured second sound attenuation in a homogeneous unitary Fermi gas of ^6Li atoms (23, 24) with extremely large Fermi energy by developing a Bragg spectroscopy technique with small wave number k and high energy resolution. We successfully determined the second sound diffusivity and the thermal conductivity of the unitary Fermi gas; the superfluid fraction and the shear viscosity are also obtained with improved accuracy. In the superfluid phase, D_2 and κ attain the universal quantum values of \hbar/m and nhk_B/m , respec-

tively. Near the superfluid transition, a sudden rise in D_2 and κ is observed, consistent with the critical divergence phenomena predicted by the dynamic scaling theory (3–5). We find a surprisingly large quantum critical region characterized by $|t| \lesssim 0.05$, where the dimensionless temperature $t \equiv 1 - T/T_c$ measures the proximity to the superfluid transition temperature T_c . Our measurements accomplish a quantitative experimental examination of the dissipative two-fluid hydrodynamic theory for the strongly interacting Fermi gas. Furthermore, the observed universal transport coefficients can provide insight into the anomalous transport of strongly correlated materials such as the cuprates (13) and provide a benchmark for many-body theories (25).

Experimental scheme and setup

The measurement of first and second sound rests on the dissipative two-fluid hydrodynamic theory for the density response function at wave number k and frequency ω (6–8, 26):

$$\chi_{nn}(k, \omega) = \frac{nk^2}{m} \frac{1}{\omega^2 - v^2 k^2 + iD_s k^2 \omega} \frac{1}{(\omega^2 - c_1^2 k^2 + iD_1 k^2 \omega)(\omega^2 - c_2^2 k^2 + iD_2 k^2 \omega)} \quad (1)$$

which is deduced from the conservation laws for momentum and energy. Here, c_1 (c_2) and D_1 (D_2) are, respectively, the speed and diffusivity of first (second) sound, whereas v and D_s are, respectively, the speed and diffusivity associated with thermodynamic and transport properties of the system (6–8, 26). In the superfluid phase, two propagating sound waves with attenuation or damping rate $\Gamma_i \equiv D_i k^2$ ($i = 1, 2$) can be clearly identified near the two poles $\omega_i = c_i k$ in the response function, which can be expressed as $\chi_{nn}^{(i)} \sim Z_i / (\omega^2 - c_i^2 k^2 + i\Gamma_i \omega)$ with weight Z_i ; above the superfluid transition, the critical second sound becomes a thermally diffusive mode $\chi_{nn}^{(2)} \sim 1/(\omega + iD_2 k^2)$, and the diffusivity $D_2 = \kappa/(mnc_p)$ is fully characterized by the thermal conductivity κ and the specific heat at constant pressure c_p .

It is notable that the simple form of Eq. 1 is applicable for quantum liquids with strong correlations (6), provided that k and ω are small in comparison with the inverse correlation length ξ^{-1} and inverse collision time τ^{-1} . However, a careful experimental validation of this theory is difficult in liquid helium for two reasons: (i) The narrow critical region is difficult to reach by Brillouin scattering (9), and (ii) the second sound weight Z_2 determined by the Landau-Placzek ratio ϵ_{LP} is very small; here, $\epsilon_{LP} \equiv c_p/c_v - 1$, with c_v being the specific heat at constant volume. In this work, we accomplish this by developing a high-resolution Bragg spectroscopy technique with small k to probe the density response of a homogeneous unitary

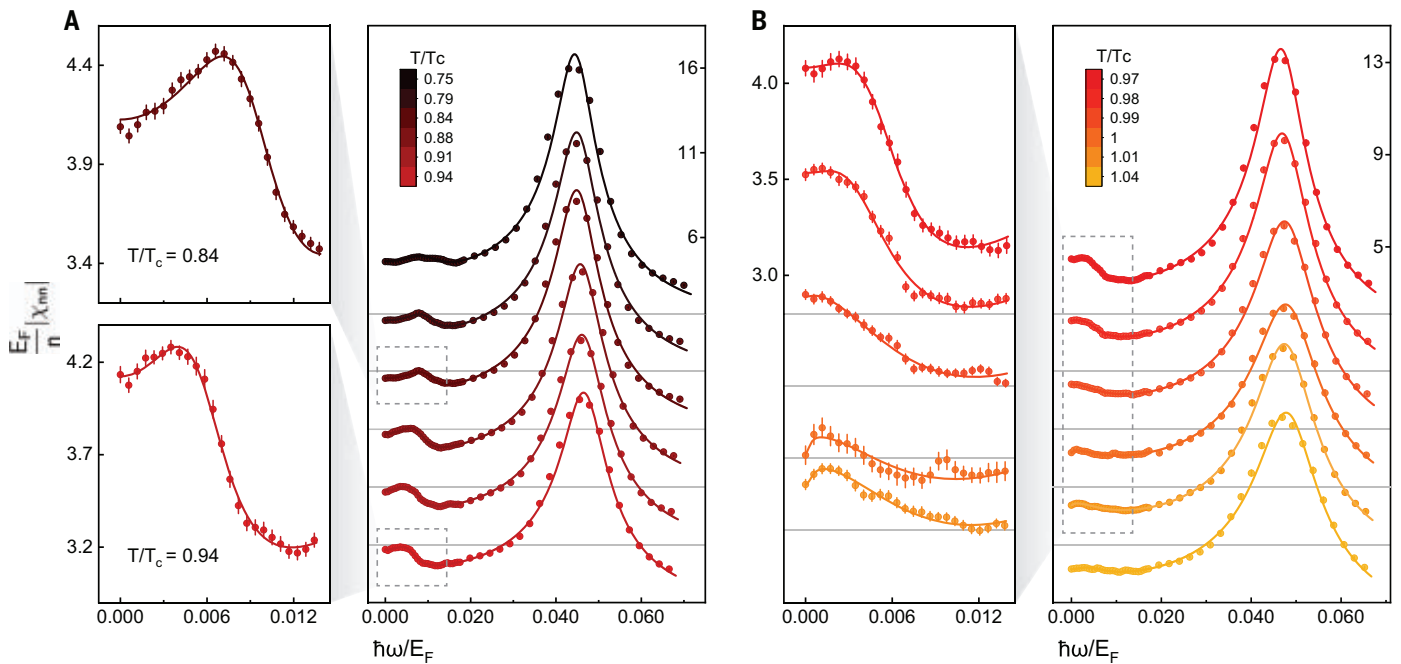


Fig. 2. Cascade plots of density response spectra at various temperatures. (A) The spectra from $0.75(2)T_c$ to $0.94(2)T_c$ (top to bottom) are shown on the right. The two subplots on the left give a zoomed-in view of the low-frequency second sound response at $0.84(2)T_c$ and $0.94(2)T_c$, respectively. (B) The spectra from $0.97(2)T_c$ to $1.04(2)T_c$ (top to bottom), with the second sound response highlighted on the left. Every data point corresponds to an average value of about 30 to 50 independent results, each obtained from a measured single-shot density wave similar to the one shown in Fig. 1, C or D (32). The error bars represent one standard deviation. The solid lines are the fitting curves, obtained by using Eq. 1.

Fermi gas, in which Z_2 and ϵ_{1P} turn out to be sizable near the superfluid transition (26).

In Bragg spectroscopy (27–29), the density response function links the density fluctuation $\delta n(k, \omega)$ (i.e., the response of the system) to an applied weak potential perturbation $\delta V(k, \omega)$ via $\delta n(k, \omega) = \chi_{nm}(k, \omega) \delta V(k, \omega)$. To achieve a good signal δn , we create a high-density spin mixture of ^6Li atoms, which are equally populated in the lowest two hyperfine states at 832.18 G [i.e., the unitarity, where s-wave scattering length diverges (30)]. After using forced evaporative cooling in a crossed dipole trap, about 1×10^7 atoms close to T_c are adiabatically loaded into a $151 \mu\text{m}$ -by- $55 \mu\text{m}$ -by $55 \mu\text{m}$ rectangular-box trap (23, 24, 31). The box trap consists of a square tube and two sheets of 532-nm laser beams, as depicted in Fig. 1A, and has a maximal potential depth of about $2\pi\hbar \times 160 \text{ kHz}$. To prepare homogeneous Fermi superfluids at various T/T_c , where $T_c \approx 0.17T_F$, we adiabatically lower the potential depth to different final values and hold the trap for an additional 500 ms to reach thermal equilibrium. We find that the density n and the reduced temperature T/T_c decrease monotonically with the decreasing potential depth of the box trap. For a typical cloud at $T/T_c \approx 0.84$, the realized density is $n \approx 1.56 \times 10^{13} \text{ cm}^{-3}$, the Fermi number is $k_F \approx 2\pi \times 1.23 \mu\text{m}^{-1}$, and the Fermi energy is $E_F \approx 2\pi\hbar \times 50.1 \text{ kHz}$. Two important features of our system are worth mentioning: (i) The density n decreases by only about

8%, from $1.64 \times 10^{13} \text{ cm}^{-3}$ close to T_c to $1.50 \times 10^{13} \text{ cm}^{-3}$ at $0.75(2)T_c$. (ii) The $1/e$ lifetime, where e is Euler's number, of the unitary Fermi superfluid is quite long, that is, more than 20 s, and the heating of the system is very weak. This preparation of a homogeneous unitary Fermi gas with well-controlled temperature and extremely large Fermi energy makes the probe of the extremely weak second sound response possible (32).

The Bragg lattice potential $\delta V(z, t_B) = V_0 \sin(kz - \omega t_B) \Theta(t_B)$ is engineered by applying a pair of coherent 741-nm laser beams with a frequency difference ω that intersect at the location of the gas (see Fig. 1B). Here, $2V_0$ is the potential depth, z is the longitudinal axis of the cloud, and $\Theta(t_B)$ is the Heaviside step function. The laser beams are carefully chosen to be far-off-resonant and to have a large beam diameter, which is pivotal for minimizing unwanted heating during the perturbation and ensuring the uniformity of the Bragg lattice potential. It is known that the correlation length diverges as $\xi \sim k_F^{-1}|t|^{-\nu}$ near the superfluid transition with the critical exponent $\nu \approx 2/3$ given by the F model (5). Experimentally, a small wave number $k = 2\pi \times 0.071 \mu\text{m}^{-1} \approx 0.058 k_F$ is applied by adjusting the intersection angle between two lattice lasers. If we use the criterion $k\xi \sim 0.058|t|^{-2/3} < 1$, the hydrodynamic regime could be reached over a wide range of temperatures unless it is very close to T_c , that is, $|t| < 0.014$. Arising from

the Bragg lattice potential, the steady-state density response takes the form of $\delta n(z, t_B) = |\chi_{nm}(k, \omega)| V_0 \sin[kz - \omega t_B + \phi(k, \omega)]$, where $|\chi_{nm}(k, \omega)|$ and $\phi(k, \omega)$ are the modulus and argument of $\chi_{nm}(k, \omega)$, respectively. Experimentally, a carefully chosen V_0 of about 0.5% E_F ($1.51 \times 10^{-31} \text{ J}$) and perturbation duration of 3 ms are implemented to satisfy the criteria of linear steady-state response. With these optimized parameters, the density response δn at ω can be acquired by subtracting two high-resolution in situ images, which are taken at the given ω and $\omega_{\text{ref}} = 2\pi \times 1 \text{ MHz}$, respectively, with the latter being the reference. Figure 1, C and D, shows two distinct density waves $\delta n(z)/n(z)$ of the superfluid at $T \approx 0.84T_c$, that is, first sound at $\omega = 2\pi \times 2.1 \text{ kHz}$ and second sound at $\omega = 2\pi \times 0.3 \text{ kHz}$, respectively (32).

Two key technical advantages of our Bragg spectroscopy are worth noting (32): (i) The modulus $|\chi_{nm}(k, \omega)|$ can be directly obtained from the integration of $|\delta n(z)/n(z)|$ as a function of ω so that we avoid potential errors owing to the imperfect phase synchronization for acquiring $\text{Im}[\chi_{nm}(k, \omega)]$ from out-of-phase density response. (ii) A steady-state density response is taken, and thus the finite perturbation duration does not lead to a spectrum broadening nor does it set a frequency resolution in our experiment. These two advantages, combined with the ability to prepare a homogeneous Fermi gas with extremely large

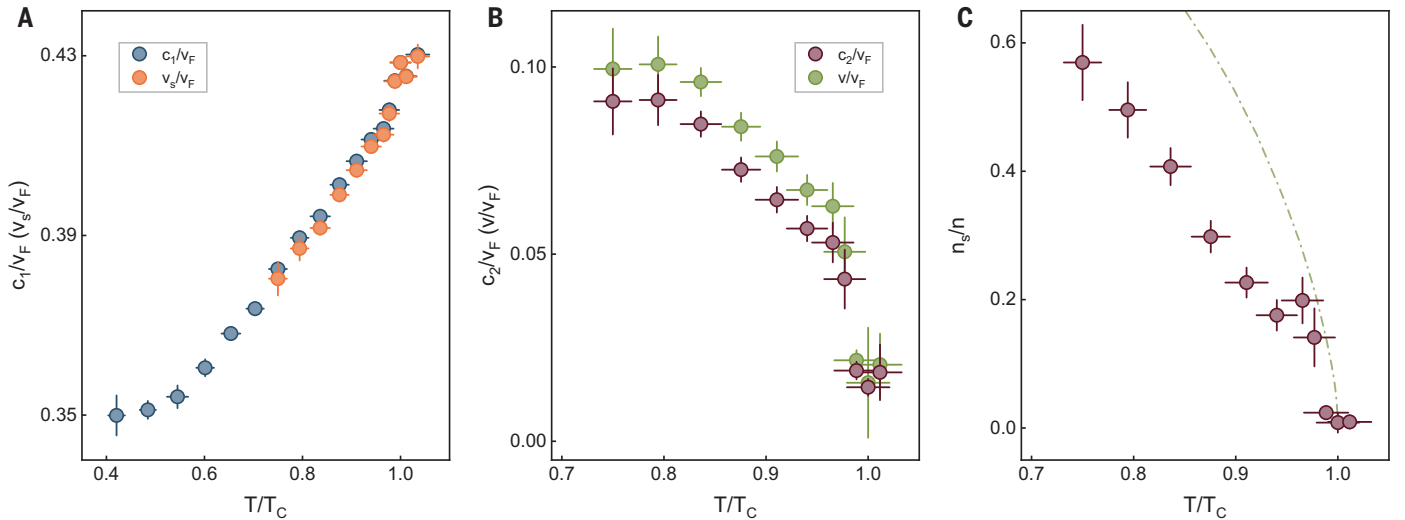


Fig. 3. Sound speeds and superfluid fraction. (A) Temperature dependence of the normalized first sound speed c_1/v_F (blue circles) and adiabatic sound speed v_s/v_F (orange circles). (B) Temperature dependence of the normalized second sound speed c_2/v_F (purple circles) and associated sound speed v/v_F (green circles), where $v = \sqrt{c_1^2 + c_2^2} - v_F$. Here, $v_F = \hbar k_F/m$ is the Fermi speed, and all the sound speeds are obtained from fitting the density response spectra (see Fig. 2). (C) Temperature dependence of the superfluid fraction n_s/n , compared with that of superfluid helium (green dash-dotted line). Vertical error bars represent one standard uncertainty obtained from the curve fitting and the measured universal thermodynamic functions; the horizontal error bars show the statistical uncertainty of the temperature determination.

E_F as mentioned earlier, enable us to measure the density response function χ_{nn} with high signal-to-noise ratio.

Density response spectra

The density response spectra $|\chi_{nn}(k, \omega)|$ over a wide temperature range of $0.42 \leq T/T_c \leq 1.04$ were systematically measured. The spectra from $0.75(2)T_c$ to $1.04(2)T_c$ are presented in Fig. 2, accompanied by the fittings to Eq. 1 (solid lines). A high-frequency first sound peak at $\hbar\omega \sim 0.046E_F$ is clearly visible over the whole temperature range, varying smoothly across the superfluid transition. More importantly, a second sound peak can be unambiguously identified at low frequency $\hbar\omega < 0.01E_F$. This is particularly evident in the temperature range of $0.79 \leq T/T_c \leq 0.94$, as highlighted in the left panel of Fig. 2A. There is a notable change in the second sound peak from $0.98(2)T_c$ to $1.01(2)T_c$: The line shape becomes diffusive and shoulder-like with much reduced height (see the left panel of Fig. 2B), indicating that second sound is the critical mode characterizing the superfluid transition. Two intriguing features of the spectra are worth mentioning: (i) $|\chi_{nn}(k, \omega)|$ is nonzero at $\omega = 0$, which is contributed by the real part of $\chi_{nn}(k, \omega)$ and agrees with the compressibility sum rule (6), $\chi_{nn}(k, \omega = 0) = -n/(mv_T^2)$. Here, $v_{T(S)} = \sqrt{(\partial P/\partial n)_{T(S)}/m}$ is the isothermal (adiabatic) sound speed. (ii) The coupling between first and second sound is appreciable, and thus the sound peaks do not show the symmetric Lorentzian line shape expected for propagating sound. To recognize the respective contributions of the first and second sound

responses, the imaginary parts of $\chi_{nn}(k, \omega)$ and $\chi_{nn}^{(i)}(k, \omega)$ are reconstructed using the fitting results of sound speed and diffusivity. A well-defined propagating second sound with a Lorentzian line shape is then observed for temperatures up to a threshold value of $0.98(2)T_c$ (see fig. S10).

The threshold temperature $0.98(2)T_c$ is consistent with $T < 0.986T_c$, an estimate based on the hydrodynamic criterion $k\xi < 1$. The confirmation of two-fluid hydrodynamics is also supported by the excellent curve fittings in the temperature range of $0.75 \leq T/T_c \leq 0.98$, as reported in Fig. 2, allowing us to accurately determine the sound speed c_i and diffusivity D_i . Moreover, to independently validate the reach of the hydrodynamic regime, a series of wave numbers k around $0.058k_F$ are implemented to measure $|\chi_{nn}(k, \omega)|$, and $\Gamma_i = D_i k^2$ is achieved with nearly the same sound speed and diffusivity (32).

However, for temperatures from $0.99(2)T_c$ to $1.01(2)T_c$, the two-fluid hydrodynamic model becomes inadequate. Although the sound speeds and diffusivities can be still acquired from the curve fitting to Eq. 1, a more accurate determination requires a nonperturbative dynamic scaling analysis (3–5), in which the critical second sound response is a universal function (33) of $\omega/(a_\infty k^{3/2})$ at fixed values of $k\xi$. Here, the constant a_∞ sets the energy scale in the critical regime. Finally, we mention that the second sound cannot be resolved in the spectra for $T < 0.75T_c$ (see fig. S6 for an example) for two possible reasons. First, the Landau-Placzek ratio ϵ_{LP} becomes smaller (7, 26), leading to a negligible second sound weight Z_2 in the density response spectrum

$|\chi_{nn}(k, \omega)|$. Second, there is a transition from the hydrodynamic to collisionless regime toward low temperatures (7), which occurs at a typical temperature of about $0.4T_c$ for superfluid helium (34). Nevertheless, the high-frequency sound peak is consistently well-resolved in the spectra down to the lowest achieved temperature of $0.42(2)T_c$.

Sound speeds and superfluid fraction

The normalized sound speeds c_1/v_F and v_s/v_F as a function of T/T_c are reported in Fig. 3A. Our high-resolution spectra yield very accurate first sound speeds c_1 and adiabatic sound speeds v_s , with a typical relative error of just $\sim 1\%$, allowing us to determine the universal state functions (16–19) of the unitary Fermi gas through standard thermodynamic relations (32). Specifically, from the saturated first sound speed $c_1/v_F = 0.350(4)$ at the lowest achieved temperature $0.42(2)T_c$, we deduce the Bertsch parameter $\xi = 0.367(9)$ by using the relation $c_1/v_F = \sqrt{\xi/3}$. This value is in excellent agreement with the previous thermodynamic measurement value (18) corrected in (30) of $\xi = 0.370(5)(8)$ and the latest quantum Monte Carlo result (35) of $\xi = 0.367(7)$.

For the second sound speed c_2 , an intriguing feature is the sensitive temperature dependence: c_2/v_F decreases rapidly with increasing temperature up to $0.98(2)T_c$ (Fig. 3B). Notably, c_2/v_F suddenly jumps to a saturated value of ~ 0.02 at $0.99(2)T_c$, implying the breakdown of hydrodynamics near the superfluid transition. From the measured sound speed c_2 or v , we determine a fundamental quantity for the macroscopic description of superfluidity—the superfluid fraction n_s/n —by applying the

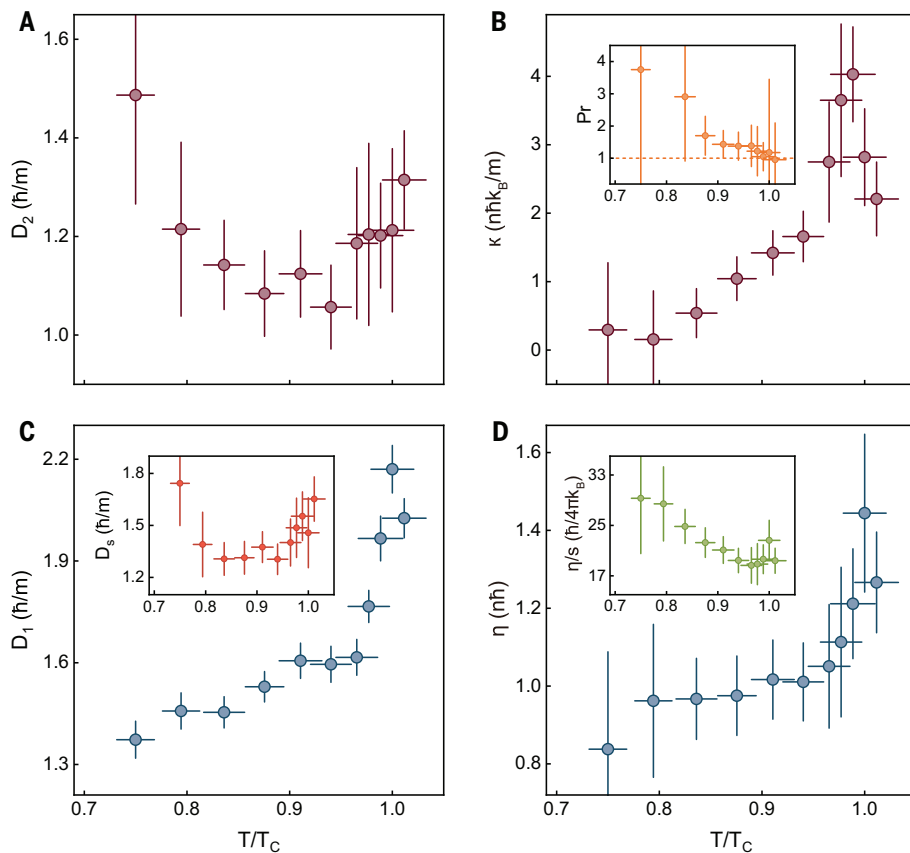


Fig. 4. Temperature dependence of sound diffusivities and transport coefficients. (A) The second sound diffusivity D_2 . (B) The thermal conductivity κ . The inset shows the Prandtl number, with the line marking $Pr = 1$. (C) The first sound diffusivity D_1 , together with the associated sound diffusivity D_s in the inset, where $D_s = D_1 + D_2 - \frac{4\eta}{3nm}$. (D) The shear viscosity η . The inset shows the viscosity-to-entropy ratio, in the units of $\hbar/(4\pi k_B)$. Away from the superfluid transition, the temperature dependence in D_1 and D_2 can be understood from the relations $D_1 \sim \eta/(nm)$ and $D_2 \sim \eta n_s/(nmn_n)$, which are valid at low temperatures. The saturated D_1 is consistent with a nearly constant shear viscosity, whereas the rapid increase of D_2 may be caused by the loss of the normal fluid component, that is, $n_s/n_n \rightarrow \infty$ as $T \rightarrow 0$. A similar temperature dependence of the second sound diffusivity D_2 has been observed in the superfluid helium (10). Vertical error bars represent one standard error.

well-known relation $c_2^2 = (T^2 n_s)/(c_P n_n)$ or $v^2 = (T^2 n_s)/(m c_V n_n)$, where s is the entropy density and $n_n \equiv n - n_s$ is the normal fluid density (32). As shown in Fig. 3C, the superfluid fraction of a unitary Fermi superfluid is close to that of superfluid helium (36) in the vicinity of the superfluid transition; for example, the system contains about 20% superfluid component at $0.97(2)T/T_c$. However, as the temperature decreases further, n_s/n of the unitary Fermi superfluid notably deviates from that of superfluid helium, indicating the distinctive nature of superfluidity in the system. n_s/n of the unitary Fermi superfluid has been indirectly extracted from the one-dimensional second sound speed measured in a highly elongated harmonic trap (21). Our direct measurements improve the accuracy on n_s/n , thereby providing a benchmark for theoretical calculations, which so far remain a notoriously difficult task in quantum many-body physics.

Sound diffusivity and transport coefficients

To address the main focus of this work—the first and second sound attenuation—we present the temperature dependence of sound diffusivities and transport coefficients in Fig. 4. For the sound diffusivity D_i , two important features are evident, as shown in Fig. 4, A and C. One is that all the D_i are in the vicinity of the quantum Heisenberg limit, that is, $D_i \sim \hbar/m$, which is anticipated for strongly correlated quantum liquids owing to the absence of well-defined quasiparticles (7). For instance, motivated by holographic duality (13, 37), the diffusivity D of any diffusive mode should obey $D \gtrsim \hbar c^2/(k_B T)$, where c is a typical speed scale of the system. By taking $T \sim T_c \approx 0.17T_F$ and $c \sim v_S \approx 0.43v_F$ at T_c (see Fig. 3) for the unitary Fermi gas, we find the bound $D \sim \hbar/m$. The other one is that each diffusivity shows a sudden rise very close to T_c (i.e., at $T \sim 0.95T_c$), with an increment $\Delta D_i \sim 0.3\hbar/m$. We interpret

the sudden rise as a precursor of quantum criticality near the superfluid transition, where the sound attenuation and thermal conductivity start to exhibit critical divergence (3, 5).

In liquid helium, the critical divergence has been observed both in the first and second sound attenuation in the temperature interval of $|T - T_c| < 1$ mK or $|t| < 5 \times 10^{-4}$ (9, 10). The quantum critical region of the unitary Fermi gas (i.e., $|t| < 0.05$) is thus about 100 times larger than that of the liquid helium. This extremely large critical region makes the unitary Fermi gas an ideal platform to determine the universal critical ratios [e.g., $R_2 = D_2/(2c_2\xi)$] that remain elusive (5). We note that the first sound diffusivity D_1 of the unitary Fermi gas has been measured recently (22), and the obtained results agree with ours. However, the sudden rise in D_1 near T_c has not been resolved because of the relatively large uncertainty of the measurement (22).

Two general damping mechanisms account for the sound attenuation: (i) The first is the viscous damping stemming from the diffusion of momentum, characterized by the shear viscosity η and four bulk viscosities ζ_i ($i = 1, 2, 3, 4$). For the unitary Fermi gas, most of the bulk viscosities vanish thanks to the scale invariance, and the only remaining ζ_3 turns out to be negligible (38). (ii) The second is the thermal damping caused by the diffusion of heat, characterized by the thermal conductivity κ . The relative contribution of these mechanisms can be quantified by the dimensionless Prandtl number $Pr \equiv \eta c_P/\kappa$. From the sound diffusivity, we determine $\kappa = c_V[(D_1 + D_2)mn - 4\eta n/(3n_n)]$ and $\eta = 3nm(D_1 + D_2 - D_s)/4$ (32) and present the results in Fig. 4, B and D, respectively.

The shear viscosity in Fig. 4D exhibits a weak temperature dependence below about $0.95T_c$, settling at a nearly constant value—the quantum limit $\eta \sim n\hbar$. However, a smooth, but pronounced, increase is observed in the vicinity of the superfluid transition. The trap-averaged shear viscosity of a unitary Fermi gas in a harmonic trap has been previously measured through anisotropic expansion (20), and the local shear viscosity has also been indirectly extracted (39). The η obtained from our direct measurement is about two times larger than the previous result (39) in the superfluid phase. Moreover, as a quantitative measure, the inset of Fig. 4D shows the ratio of shear viscosity to entropy density η/s , which is expressed in the unit of $\hbar/(4\pi k_B)$, the lower bound conjectured by Kovtun, Son, and Starinets (KSS) for a perfect fluid (40). Around the superfluid transition, η/s is about 18 times larger than the KSS bound, suggesting that the unitary superfluid is not a “perfect fluid.”

The thermal conductivity κ similarly attains the universal quantum limit $\sim n\hbar k_B/m$ below about $0.95T_c$, as shown in Fig. 4B. Notably, a

weak but distinct divergence is revealed on both sides of the superfluid transition, leading to a pronounced λ peak around T_c with a considerable increment $\delta\kappa \sim 3\pi\hbar k_B/m$. This weak divergence is consistent with the dynamic critical scaling theory of the superfluid transition (3–5), in which $\kappa \sim |t|^{-\nu/2} \simeq |t|^{-1/3}$. The observed sudden rise in the sound diffusivity, as shown in Fig. 4, A and C, can be also attributed to such a divergence. Finally, the Prandtl number Pr (inset of Fig. 4B) is about unity near the superfluid transition, suggesting that the viscous damping and thermal damping are equally important to the sound attenuation. The obtained $Pr \approx 1$ implies that the unitary Fermi gas can be treated as a holographic conformal nonrelativistic fluid (47). In liquid helium, the investigations of critical divergence in the thermal conductivity above the λ -transition and in the second sound attenuation below the λ -transition play a vital role in setting up the effective theory for the critical mode across the superfluid transition (3–5). For the unitary Fermi gas, our measurements not only complete the macroscopic description of its superfluidity but also provide a means to understand the microscopic details of the superfluid transition in the strongly interacting regime.

Outlook

Our system offers great promise for studying many fundamental problems in quantum many-body systems with strong interactions. For example, by investigating the temperature and wave number dependence of the density response, the transition from collisionless to hydrodynamic behavior of the unitary Fermi gas can be fully characterized and thus illuminate the establishment of hydrodynamics in the strongly interacting regime. Moreover, by adjusting the box-trap geometry (e.g., a longer longitudinal length) and further optimizing the system, Bragg spectroscopy with a smaller wave number and a higher energy resolution can be implemented. Therefore, a systematic exploration of the quantum critical region with improved temperature controllability can be achieved, paving the way to map out several long-sought universal critical dynamic scaling functions. Our setup can also be readily modified to realize a two-dimensional homogeneous Fermi superfluid and thus provides an ideal platform for investigating the second sound attenuation and related quantum transport across the Berezinskii-Kosterlitz-Thouless transition.

REFERENCES AND NOTES

1. L. Tisza, *Nature* **141**, 913 (1938).
2. L. Landau, *Phys. Rev.* **60**, 356–358 (1941).
3. R. A. Ferrell, N. Menyhard, H. Schmidt, F. Schwabl, P. Szépfalusy, *Phys. Rev. Lett.* **18**, 891–894 (1967).
4. P. C. Hohenberg, A. Aharony, B. I. Halperin, E. D. Siggia, *Phys. Rev. B* **13**, 2986–2996 (1976).
5. P. C. Hohenberg, B. I. Halperin, *Rev. Mod. Phys.* **49**, 435–479 (1977).
6. P. C. Hohenberg, P. C. Martin, *Ann. Phys.* **34**, 291–359 (1965).
7. H. Hu, P. Zou, X.-J. Liu, *Phys. Rev. A* **97**, 023615 (2018).
8. P. Zhang, Z. Yu, *Phys. Rev. A* **97**, 041601 (2018).
9. J. A. Tarvin, F. Vidal, T. J. Greytak, *Phys. Rev. B* **15**, 4193–4210 (1977).
10. G. Ahlers, *Phys. Rev. Lett.* **43**, 1417–1420 (1979).
11. R. A. Ferrell, J. K. Bhattacharjee, *Phys. Rev. Lett.* **51**, 487–489 (1983).
12. P. A. Lee, N. Nagaosa, X.-G. Wen, *Rev. Mod. Phys.* **78**, 17–85 (2006).
13. S. A. Hartnoll, *Nat. Phys.* **11**, 54–61 (2014).
14. S. Giorgini, L. P. Pitaevskii, S. Stringari, *Rev. Mod. Phys.* **80**, 1215–1274 (2008).
15. H. Hu, P. D. Drummond, X.-J. Liu, *Nat. Phys.* **3**, 469–472 (2007).
16. T.-L. Ho, Q. Zhou, *Nat. Phys.* **6**, 131–134 (2009).
17. S. Nascimbène, N. Navon, K. J. Jiang, F. Chevy, C. Salomon, *Nature* **463**, 1057–1060 (2010).
18. M. J. H. Ku, A. T. Sommer, L. W. Cheuk, M. W. Zwierlein, *Science* **335**, 563–567 (2012).
19. M. Horikoshi, S. Nakajima, M. Ueda, T. Mukaiyama, *Science* **327**, 442–445 (2010).
20. C. Cao et al., *Science* **331**, 58–61 (2011).
21. L. A. Sidorenkov et al., *Nature* **498**, 78–81 (2013).
22. P. B. Patel et al., *Science* **370**, 1222–1226 (2020).
23. B. Mukherjee et al., *Phys. Rev. Lett.* **118**, 123401 (2017).
24. L. Baird, X. Wang, S. Roof, J. E. Thomas, *Phys. Rev. Lett.* **123**, 160402 (2019).
25. B. Frank, W. Zwerger, T. Enss, *Phys. Rev. Res.* **2**, 023301 (2020).
26. H. Hu, E. Taylor, X.-J. Liu, S. Stringari, A. Griffin, *New J. Phys.* **12**, 043040 (2010).
27. J. Stenger et al., *Phys. Rev. Lett.* **82**, 4569–4573 (1999).
28. S. Hoinka et al., *Nat. Phys.* **13**, 943–946 (2017).
29. T. L. Yang et al., *Phys. Rev. Lett.* **121**, 103001 (2018).
30. G. Zürn et al., *Phys. Rev. Lett.* **110**, 135301 (2013).
31. A. L. Gaunt, T. F. Schmidutz, I. Gotlibovych, R. P. Smith, Z. Hadzibabic, *Phys. Rev. Lett.* **110**, 200406 (2013).
32. See supplementary materials.
33. P. C. Hohenberg, E. D. Siggia, B. I. Halperin, *Phys. Rev. B* **14**, 2865–2874 (1976).
34. A. D. B. Woods, R. A. Cowley, *Rep. Prog. Phys.* **36**, 1135–1231 (1973).
35. S. Jensen, C. N. Gilbreth, Y. Alhassid, *Phys. Rev. Lett.* **125**, 043402 (2020).
36. R. J. Donnelly, C. F. Barenghi, *J. Phys. Chem. Ref. Data* **27**, 1217–1274 (1998).
37. M. Blake, *Phys. Rev. Lett.* **117**, 091601 (2016).
38. D. T. Son, *Phys. Rev. Lett.* **98**, 020604 (2007).
39. J. A. Joseph, E. Elliott, J. E. Thomas, *Phys. Rev. Lett.* **115**, 020401 (2015).
40. P. K. Kovtun, D. T. Son, A. O. Starinets, *Phys. Rev. Lett.* **94**, 111601 (2005).
41. M. Rangamani, S. F. Ross, D. T. Son, E. G. Thompson, *J. High Energy Phys.* **2009**, 075 (2009).
42. X. Li, X. Luo, S. Wang, K. Xie, X.-P. Liu, H. Hu, Y.-A. Chen, X.-C. Yao, J.-W. Pan, Data for “Second sound attenuation near quantum criticality,” Zenodo (2021); <https://doi.org/10.5281/zenodo.5767197>.

ACKNOWLEDGMENTS

We thank X.-J. Liu, H. Zhai, M. K. Tey, H.-N. Dai, and Q.-J. Chen for their critical reading of the manuscript; J. E. Thomas, M. K. Tey, and M. W. Zwierlein for sharing their experimental data; and J. E. Drut, G. Wlazłowski, S. Jensen, and Y. Alhassid for sharing their quantum Monte Carlo (QMC) data. **Funding:** This work is supported by the National Key R&D Program of China (grant no. 2018YFA0306501), National Natural Science Foundation of China (grant no. 11874340), the Chinese Academy of Sciences (CAS), the Anhui Initiative in Quantum Information Technologies, the Shanghai Municipal Science and Technology Major Project (grant no. 2019SHZDZX01), and the Fundamental Research Funds for the Central Universities (under grant no. WK2340000081). **Author contributions:** Y.-A.C., X.-C.Y., and J.-W.P. conceived the research. X.Li, X.Luo, S.W., K.X., X.-P.L., and X.-C.Y. performed the experiment and collected the data. X.Li, X.Luo, S.W., H.H., Y.-A.C., X.-C.Y., and J.-W.P. contributed to the data analysis and writing of the manuscript. **Competing interests:** The authors declare no competing interests. **Data and materials:** The data are archived at Zenodo (42).

SUPPLEMENTARY MATERIALS

science.org/doi/10.1126/science.abi4480
Supplementary Text
Figs. S1 to S10
References (43–62)

31 March 2021; accepted 21 December 2021
10.1126/science.abi4480

EMERGING COMPUTING

Reconfigurable perovskite nickelate electronics for artificial intelligence

Hai-Tian Zhang^{1*}†, Tae Joon Park^{1*}†, A. N. M. Nafiul Islam²†, Dat S. J. Tran³†, Sukriti Manna^{4,5}†, Qi Wang¹†, Sandip Mondal¹§, Haoming Yu¹, Suvo Banik^{4,5}, Shaobo Cheng⁶¶, Hua Zhou⁷, Sampath Gamage⁸, Sayantan Mahapatra⁹, Yimei Zhu⁶, Yohannes Abate⁸, Nan Jiang⁹, Subramanian K. R. S. Sankaranarayanan^{4,5}, Abhronil Sengupta², Christof Teuscher¹⁰, Shriram Ramanathan^{1*}

Reconfigurable devices offer the ability to program electronic circuits on demand. In this work, we demonstrated on-demand creation of artificial neurons, synapses, and memory capacitors in post-fabricated perovskite NdNiO_3 devices that can be simply reconfigured for a specific purpose by single-shot electric pulses. The sensitivity of electronic properties of perovskite nickelates to the local distribution of hydrogen ions enabled these results. With experimental data from our memory capacitors, simulation results of a reservoir computing framework showed excellent performance for tasks such as digit recognition and classification of electrocardiogram heartbeat activity. Using our reconfigurable artificial neurons and synapses, simulated dynamic networks outperformed static networks for incremental learning scenarios. The ability to fashion the building blocks of brain-inspired computers on demand opens up new directions in adaptive networks.

Continual learning in artificial intelligence (AI) presents a formidable challenge. Models are generally trained on stationary data distributions, and thus when new data are presented incrementally to a neural network, this interferes with the previously learned knowledge, resulting in

poor performance, which is known as catastrophic forgetting and remains an active field of research (1, 2). One of the major approaches to tackle this issue is to actively adapt the structure of the network itself when new data becomes available. Not only does modulating the architecture of the network in response to

the input distribution allow the network to manage its resources efficiently, recent discoveries also suggest that a dynamic network can show better performance as compared with that of a static network when provided with equal resources (3, 4). Moreover, as smart edge devices become more integrated into society, they will require the implementation of sophisticated networks in hardware constrained by both chip area and power. Having the ability to reallocate network resources dynamically to perform various tasks in an ever-changing environment will be of fundamental importance (3). Having programmable capabilities

in hardware can be game changing for future computers whose designs are inspired by the intelligence of animal brains.

In this work, we showed that perovskite nickelates, a class of quantum materials that undergo room-temperature electronic phase transitions upon hydrogen doping, enable a versatile, reconfigurable hardware platform for adaptive computing. A single device made from H-doped NdNiO₃ (NNO), for example, could be electrically reconfigured on demand to take on the functionalities of either neurons, synapses, or memory capacitors (Fig. 1A). Such versatile tunability was distinctively en-

abled by the synergistic combination of a vast array of metastable configurations for protons in the perovskite lattice that can also be voltage controlled. Although a variety of ionic-electronic switches are being explored for neuromorphic computing (5–10), complete reconfiguration of neuromorphic functions has remained elusive. To demonstrate example applications in AI, we used the experimental data from our memory capacitors in a reservoir computing (RC) framework (Fig. 1B), a brain-inspired machine learning architecture, and simulation results demonstrated excellent performance comparable with those of

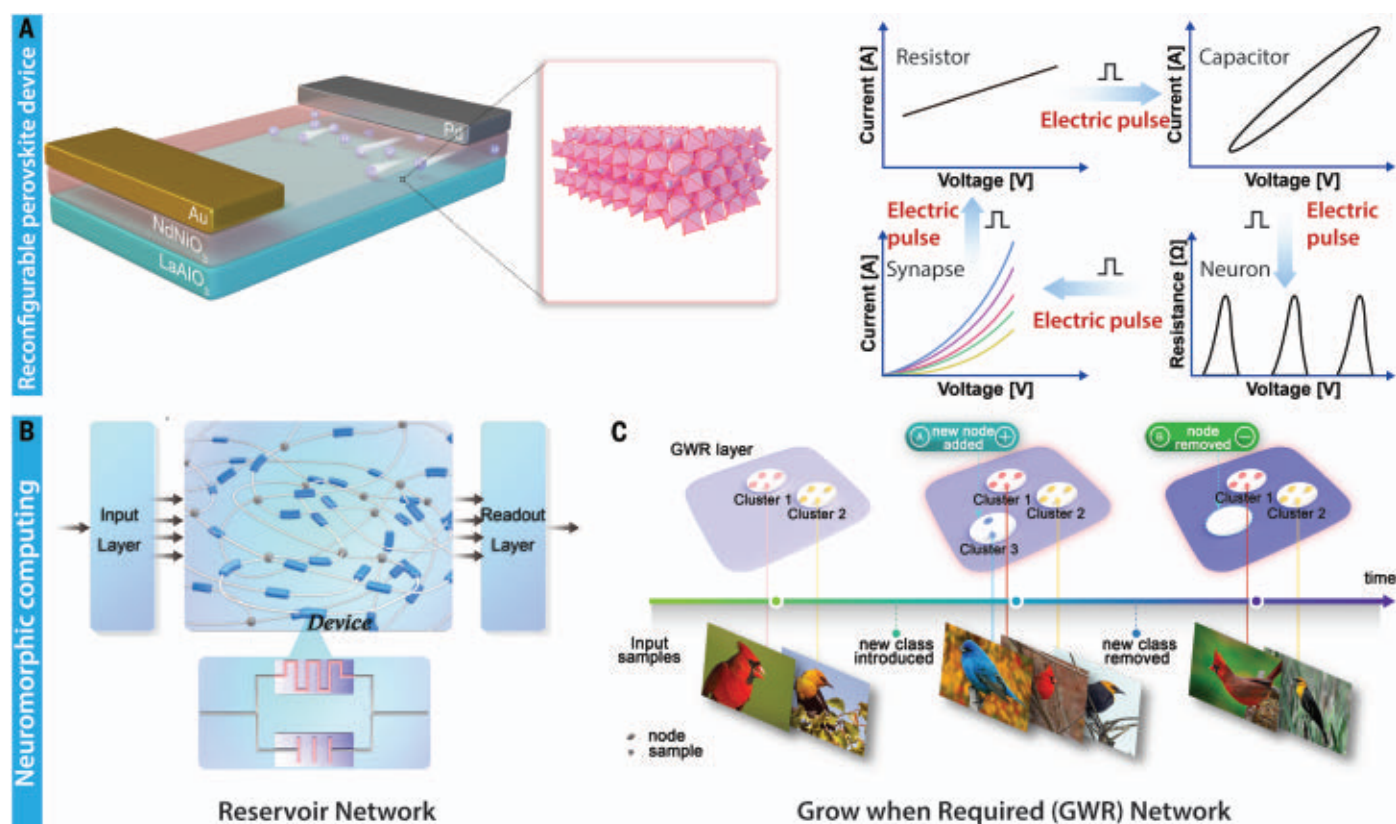


Fig. 1. Reconfigurable perovskite devices. (A) Schematic of hydrogen-doped perovskite nickelate as a versatile reconfigurable platform that can be electrically transformed between neurons, synapses, and memory capacitors to enable adaptive neuromorphic computing. By applying electric pulses, the hydrogen ions in the nickelate lattice can occupy metastable states and enable distinct functionalities. (B) Schematic of a generic RC framework. An input layer distributes the signals into the reservoir, which projects the inputs into a high-dimensional space. Here, the reservoir is built randomly from programmable devices with memory. No training happens in the reservoir; only the linear

readout layer is trained by a simple gradient descent algorithm. The role of the readout layer is to map the high-dimensional dynamics of the reservoir to the output states. (C) Schematic of GWR networks. As the network is shown various classes of data, it maps high-dimensional data to a low-dimensional map field to perform clustering on the classes. When a new class is added to the input stream, the network can detect the new input and grow in size by adding network nodes to accommodate it. Additionally, if any of the classes do not appear in the input stream for a long time, the corresponding nodes become inactive, saving resources.

¹School of Materials Engineering, Purdue University, West Lafayette, IN 47907, USA. ²Department of Electrical Engineering, Pennsylvania State University, University Park, PA, 16802, USA. ³Department of Electrical and Computer Engineering, Santa Clara University, Santa Clara, CA 95053, USA. ⁴Center for Nanoscale Materials, Argonne National Laboratory, Argonne, IL 60439, USA. ⁵Department of Mechanical and Industrial Engineering, University of Illinois Chicago, Chicago, IL 60607, USA. ⁶Department of Condensed Matter Physics and Materials Science, Brookhaven National Laboratory, Upton, NY 11973, USA. ⁷X-ray Science Division, Advanced Photon Source, Argonne National Laboratory, Lemont, IL 60439, USA. ⁸Department of Physics and Astronomy, University of Georgia, Athens, GA 30602, USA. ⁹Department of Chemistry, University of Illinois Chicago, Chicago, IL 60607, USA. ¹⁰Department of Electrical and Computer Engineering, Portland State University, Portland, OR 97201, USA.

*Corresponding author. Email: htzhang@uuaa.edu.cn (H.-T.Z.); park1080@purdue.edu (T.J.P.); shriram@purdue.edu (S.R.)

†These authors contributed equally to this work.

‡Present address: School of Materials Science and Engineering, Beihang University, Beijing 100191, China.

§Present address: Department of Electrical Engineering, Indian Institute of Technology Bombay, Mumbai 400076, India.

¶Present address: Key Laboratory of Material Physics, School of Physics and Microelectronics, Zhengzhou University, Zhengzhou 450052, China.

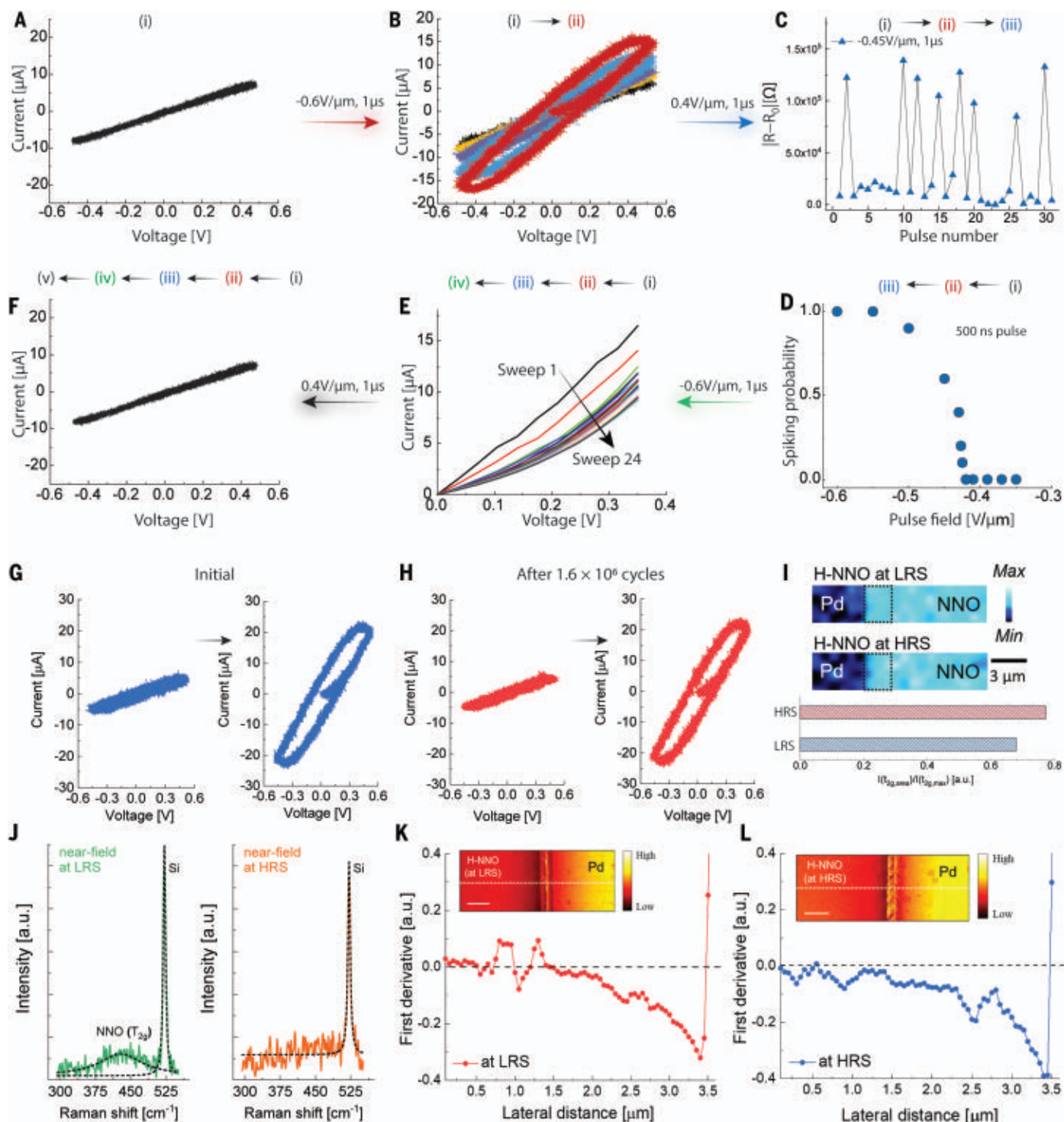


Fig. 2. A single perovskite device can be electrically reconfigured to perform essential functions in a neuromorphic computer. (A) Nickelate device as a linear resistor under cyclic voltage sweep. (B) Nickelate device as a capacitor under cyclic voltage sweep. The appearance of an I - V loop indicates stored energy in the device. I - V loops of different sizes can be generated by applying pulse fields (ii). Complete details can be found in supplementary text 2. (C) Nickelate device as a spiking neuron (iii). Resistance changes of the nickelate device were monitored in response to consecutive electric pulses ($-0.45\text{ V}/\mu\text{m}$ for $1\mu\text{s}$). After the spike fires, the resistance of the device was restored to the original state by applying reset voltage pulse ($+0.45\text{ V}/\mu\text{m}$ for

$1\mu\text{s}$). (D) Spiking probability of nickelate device as a function of pulse field, showing stochastic behavior. (E) Nickelate device as a synapse. I - V curves of nickelate devices were measured under continuous voltage sweeps. The resistance of the device increases continuously, showing analog synaptic updates. (F) Resetting the nickelate device back to initial linear resistor state. (G and H) Representative electrical reconfiguration between linear resistor and capacitor of the scaled nickelate device at initial and after 1.6×10^6 cycles of endurance measurement. Reconfiguration of all modes are presented in fig. S11. Details of endurance measurement are provided in fig. S22. (I) Spatial mapping of Raman (signal to baseline of Raman shift ranging from 320 to

470 cm^{-1}) of a 15 by 3 μm^2 rectangular area near the Pd electrode for the H-NNO device at both HRS and LRS. Scale bar, 3 μm . The bright areas correspond to NNO regions in the nickelate device, which showed strong peak intensity of T_{2g} mode at $\sim 439 \text{ cm}^{-1}$. The normalized T_{2g} peak intensity $[(t_{2g,\text{area}})/(t_{2g,\text{max}})]$ near the Pd electrode were obtained from the dashed rectangular area. The relative peak intensity of the H-NNO device at LRS was 0.77, whereas that of H-NNO at HRS dropped to 0.68. (J) Near-field spectrum (TERS) of H-NNO device at LRS (green) and at HRS (orange), when

the Ag tip was engaged near the Pd electrode. The dashed line indicates the fitting of the Raman peak. At LRS of H-NNO, T_{2g} mode was found near the electrode and was suppressed from H-NNO at HRS. (K and L) Zoom-in of first derivative of the normalized second-harmonic IR near-field amplitude of the H-NNO device at LRS and at HRS near the boundary between the Pd and H-NNO. (Insets) Second-harmonic IR ($\omega = 952 \text{ cm}^{-1}$) near-field amplitude images of H-NNO devices at LRS and HRS, respectively. Scale bar, 1 μm .

theoretical and experimental reservoirs. The experimental characteristics of neurons and synapses obtained from the perovskite nickelate devices and their run-time reconfigurability were leveraged to design self-adaptive dynamic grow-when-required (GWR) networks (Fig. 1C). Motivated by the cortical data processing in the brain, GWR networks present an unsupervised approach to lifelong learning in real-world scenarios with limited availability of training samples, which in turn may have missing or noisy labels. We demonstrated that such networks can exploit the creation and deletion of network nodes on the fly to offer greater representation power and efficiency in comparison with those of static counterparts.

Results and discussion

Perovskite nickelates (chemical formula ReNiO_3 , where Re is a rare-earth ion such as Nd) are a class of quantum materials whose electronic properties are mediated by strong electron interactions. Pristine NNO is a correlated metal at room temperature. Hydrogen dopants as electron donors can lead to a reduction in electrical conductivity by several orders of magnitude through modifying the Ni orbital configuration (11). Gently redistributing the hydrogen ions (protons) already doped in the lattice by electric fields can modify the electrical conductivity systematically to generate a multitude of electronic states. For example, by annealing NNO devices in hydrogen gas (with catalytic electrodes such as Pd or Pt), hydrogen can be doped interstitially into the NNO lattice proximal to the electrode. The hydrogen atoms then donate electrons to the Ni d orbitals, which changes the filling state in the NNO d band and results in a phase transition with a change in resistivity several orders of magnitude. (From here on, the hydrogen-doped NNO will be referred as H-NNO for simplicity.) A vast array of metastable energy states are available to the protons in the lattice, and thus, their distribution and local concentration (and therefore function) can be subsequently modulated with electric fields applied to the electrode. The switching mechanism of the H-NNO device is compared with traditional nonfilamentary resistive memory devices in table S1.

To demonstrate reproducible electrical reconfiguration in H-NNO, 50-nm-thick NNO films were deposited through different meth-

ods, sputtering and atomic layer deposition (ALD), as well as on different substrates, LaAlO_3 and SiO_2 on Si (structural characterizations of representative pristine NNO films are provided in fig. S3, and device details are provided in fig. S4). First, we described the capacitive behavior (charge storage) in our devices. Capacitors not only are useful for storing charge in the conventional sense but are also central for numerous brain-inspired computing architectures. Evolution of memcapacitive loop states in the perovskite nickelate device as a function of hydrogen doping is shown in fig. S5. With increasing hydrogen doping, the H-NNO film resistance increased and then eventually saturated at $\sim 10^8$ ohms (fig. S5A). Without any hydrogen recharging process to the device for 6 months, hydrogen remained in the NNO lattice, and the resistance of the H-NNO device was stable. To explore the capacitive behaviors of the H-NNO device at different hydrogen doping states, we performed cyclic voltage sweeps (figs. S5, B to H). Pristine and weakly doped perovskite NNO showed linear resistor behavior. At the intermediate doping state, capacitive behavior appears. Electrical reconfiguration of the H-NNO device is summarized in Fig. 2, A to F. By applying positive and negative electric pulses, the resistance state of the device could be modulated carefully, and the programmed resistance states are nonvolatile (fig. S6). At the electronic state i, cyclic voltage sweep measurements of the nickelate device were performed, and linear resistor behavior was observed (Fig. 2A). The electronic state i was then switched to electronic state ii by applying a single voltage pulse, where a current-voltage (I - V) loop appeared, indicating stored energy in the device (Fig. 2B). Memristive and memcapacitive behaviors were also demonstrated at state ii (supplementary text 2).

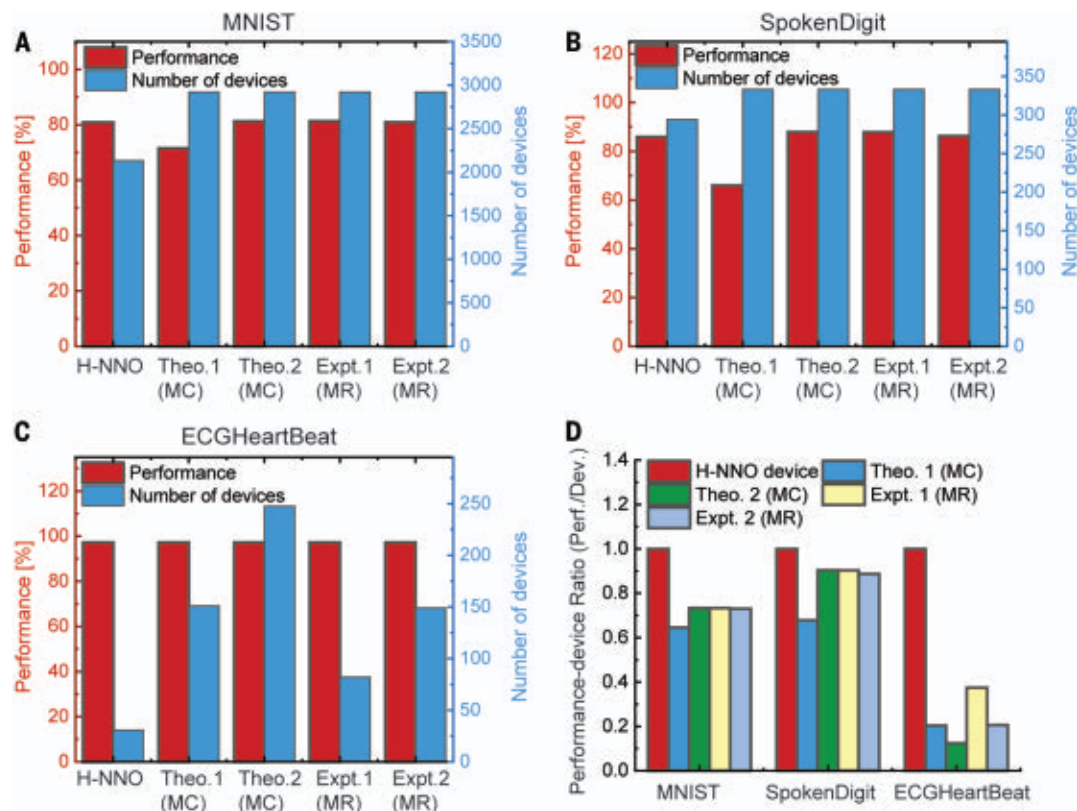
Next, we showed the creation of artificial neurons and synapses (that are responsible for information transfer and memory in the brain) from the same device. Spiking neuronal behavior in the H-NNO device was studied at the electronic state iii (Fig. 2C). Consecutive electric stimuli were applied to the device, and once a critical level was reached, abrupt changes in the device resistance were observed. The nonvolatile neuronal response of the nickelate device to electric stimulus depended on both pulse voltage and pulse width

(figs. S7 and S8). A typical spiking probability plot is shown in Fig. 2D, which could be directly implemented in neural networks. We then demonstrated synaptic behavior at electronic state iv in the nickelate device by means of continuous voltage sweeps (Fig. 2E). As shown in fig. S9, threshold pulse fields were investigated for both high-resistance state (HRS; state iii) and low-resistance state (LRS; state iv). At LRS, a smaller threshold pulse field (V_{th}) was sufficient to modulate the device resistance, which was suitable for analog behavior with gradual resistance changes. However, this analog update of device resistance prohibited the sudden jump in resistance necessary for spiking. At HRS, a much higher V_{th} was required to change the resistance and was beneficial for spiking neuronal behavior. Last, the linear resistor state v in Fig. 2F could be restored by applying a single electric pulse. Electrical reconfiguration at various resistance states of the H-NNO device is shown in fig. S10, demonstrating versatility of the device platform. After 1.6×10^6 cycles of endurance measurement of a scaled nickelate device, we performed electrical reconfiguration of the device, and the results showed that all functional modes were reproducible (fig. S11). For example, configuration between linear resistor and capacitor states at initial and after 1.6×10^6 cycles of endurance measurement are presented in Fig. 2, G and H, respectively. A single device could be reconfigured as resistor, memcapacitor, neuron, or synapse with electric pulses.

To understand the nanoscale mechanisms that enable electrical reconfiguration, we performed in-depth characterization on representative H-NNO devices at LRS and HRS (Fig. 2, I to L) that correspond to synapse and neuronal states, respectively. Confocal Raman spectra ranging from 300 to 550 cm^{-1} were first collected from two control samples: a pristine NNO film near the Pd electrode and a heavily doped NNO film near the Pd electrode (fig. S12). The T_{2g} mode of NNO was present at $\sim 439 \text{ cm}^{-1}$ for pristine NNO, whereas it disappeared for heavily doped NNO, indicating dense proton concentration near the Pd electrode. We performed two-dimensional (2D) Raman mapping (signal to baseline mode, scan range from 320 to 470 cm^{-1}) over a rectangular region (15 by 3 μm^2) at this boundary for the H-NNO device at LRS and at HRS in Fig. 2I.

Fig. 3. Reservoir computing simulations with data measured from nickelate devices. (A to D)

The simulation results of reservoirs with H-NNO devices, compared with theoretical and experimental memristive models of reservoirs, demonstrated that a large and random network of H-NNO devices could function as a hardware platform for neuromorphic computing in solving complex tasks. The simulation results were based on the average results of simulating a sample size of 100 reservoirs with similar hyperparameters for each reservoir type to reduce uncertainty owing to the stochastic nature of reservoir networks. As shown in (A) to (C), the H-NNO reservoirs could achieve comparable performances on three tasks with fewer devices. The performance/device ratios in (D) indicate that the H-NNO reservoirs, on average, outperformed the theoretical and memristive reservoirs by a factor of 1.4 \times , 1.2 \times , and 5.1 \times for MNIST, isolated spoken digits, and ECG heartbeats, respectively.



The relative peak intensity of T_{2g} mode of the H-NNO device at LRS was 0.77, whereas for HRS this dropped to 0.68, indicating higher local proton distribution of H-NNO at HRS near the Pd electrode. Near-field tip-enhanced Raman scattering (TERS) was carried on the H-NNO device at LRS and at HRS near the Pd electrode (Fig. 2J). Details of control experiments for near-field TERS are provided in fig. S13. A broad T_{2g} peak of NNO could be seen near the Pd electrode at LRS; however, no such weak peak was detected on NNO near the Pd electrode for H-NNO at HRS, indicating relatively higher proton concentration near the Pd electrode. We used scattering-type scanning near-field optical microscopy (s-SNOM) at a laser frequency of $\omega = 952 \text{ cm}^{-1}$ to image the local distribution of doping of H-NNO devices at LRS and HRS. Details of control experiments for s-SNOM on reference devices are included in fig. S14. Second harmonic infrared (IR) ($\omega = 952 \text{ cm}^{-1}$) near-field amplitude images of the H-NNO device at LRS and HRS near the Pd electrode are shown in Fig. 2, K and L, insets, respectively. Normalized amplitude line profiles of the NNO devices at LRS and HRS are provided in fig. S15. The first derivative of the normalized amplitude indicates proton concentration changes near the boundary between the Pd electrode and H-NNO channel shown in Fig. 2, K and L. At

HRS, the proton concentration changed over a longer lateral distance compared with that of at LRS. The s-SNOM amplitude signal differences revealed local chemical composition differences in H-NNO at different functional states, which was consistent with Raman results. Further, the carrier localization length scale of H-NNO device at HRS was smaller than that at LRS, as determined from temperature-dependent electrical transport measurements (fig. S16). The nanoscale characterization of devices showed consistent results that the local proton distribution of H-NNO device at LRS and HRS near the Pd electrode were different. Density functional theory (DFT) calculations further indicated that differences in the location of protons could lead to modulation of energy band gap of NNO (figs. S17 to S20), which is of relevance to different functional states. Nudged elastic band (NEB) calculations showed that the proton migration barrier could vary from 0.2 to 0.6 eV, depending on the migration path (supplementary text 1). Therefore, different local proton distributions at LRS and at HRS of the H-NNO device could lead to different functional states.

We also fabricated nickelate devices with 100 nm gap size to demonstrate scalability, endurance, reproducibility, and ultralow energy consumption (figs. S21 to S24). In scaled devices, electrical reconfiguration could be

realized with <10-ns electric pulses. The energy cost for a single synaptic update was $\sim 2 \text{ fJ}$, which is comparable with that in the brain (1 to $\sim 100 \text{ fJ}$) (12). To demonstrate compatibility with CMOS (complementary metal-oxide semiconductor) technology, nickelate devices were fabricated on SiO_2 on Si substrates through both sputtering and ALD (an industrial technique used to grow high-quality metal-oxide films for state-of-the-art electronics), and data are shown in figs. S25 and S26.

To showcase applications of the adaptive nickelate hardware, we applied the experimental memristive and memcapacitive behaviors in RC, a brain-inspired machine-learning architecture that addresses the issue of training complexity and parameter explosion, commonly observed in traditional recurrent neural networks (RNNs), by only adapting a simple output layer. RC explains higher-order cognitive functions and the interaction of short-term memory with other cognitive processes (13). Details can be found in supplementary text 2. To have a baseline comparison, we evaluated the performance of our H-NNO device in comparison with theoretical models (14, 15) and experimental reports (16, 17) for three different tasks: MNIST (Modified National Institute of Standards and Technology database) digit recognition, isolated spoken digit recognition,

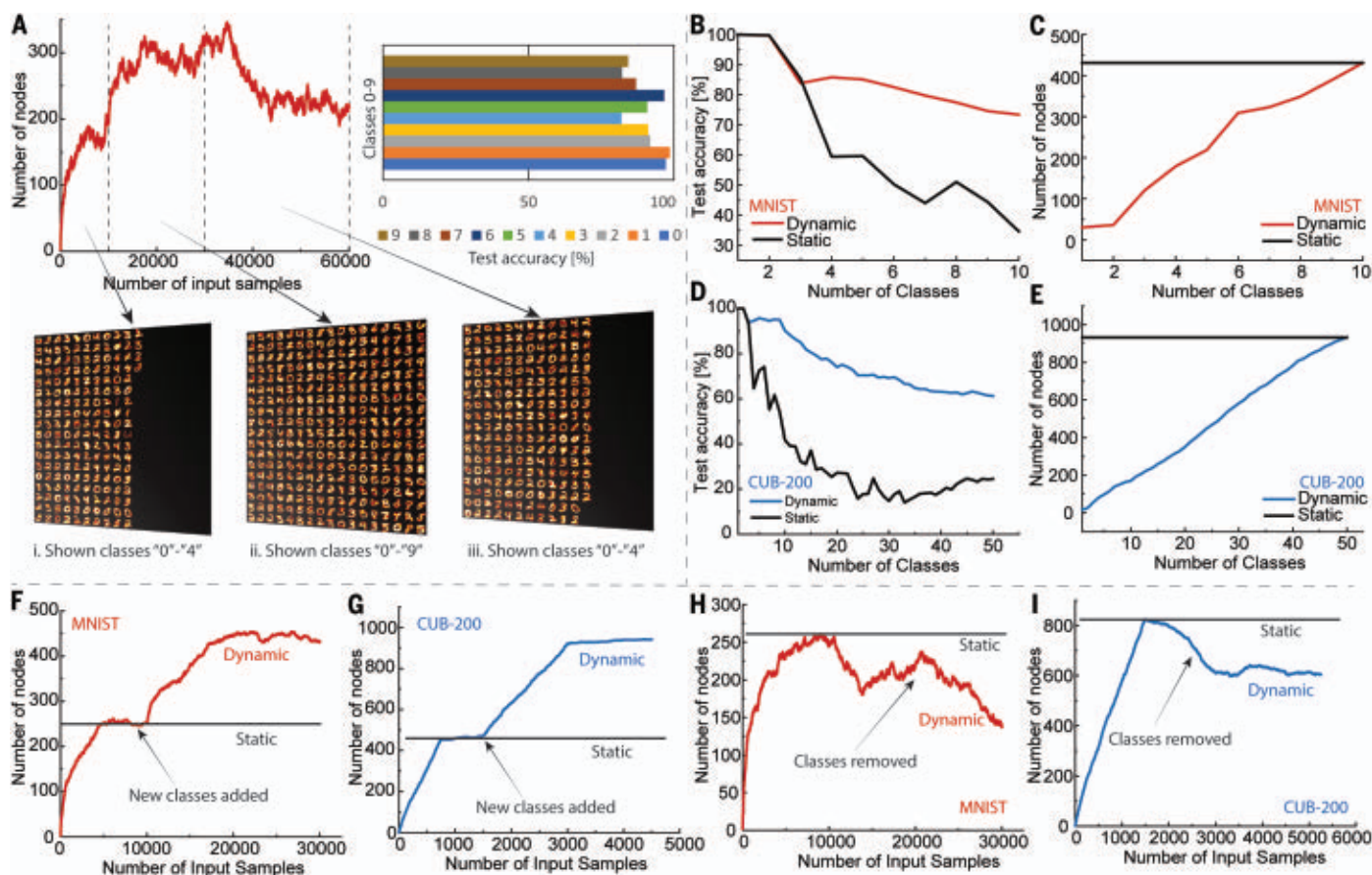


Fig. 4. Dynamic grow-when-required computing with experimental characteristics measured from nickelate devices. (A) Visualization of the GWR network's ability to dynamically respond to changes in the input distribution over time for the MNIST dataset. First, we showed the network 10,000 input samples from the first five classes ("0" to "4") of the MNIST dataset. The network could grow and learn the representation as seen in i. Next, the network was trained on 20,000 samples from all the 10 classes of the MNIST. Because of the addition of new classes, the network grew in size and accommodated them, as seen in ii. The accuracy over all the classes is shown in the bar chart (top right). Last, we again changed the input class distribution by only showing the network the classes "0" to "4". We observed that the network could gradually shrink its size as nodes associated with the last five classes slowly became inactive and were removed from the network, as seen in iii. Here, the digits are the learned representations of the nodes, whereas each unit of the black region indicates an unused and inactive node in the

network. (B to E) Network performance for incremental learning of classes. (B) Test accuracy for MNIST as the number of classes is incrementally increased from 1 to 10. (C) Number of nodes as the number of classes is increased for MNIST. (D) Test accuracy for the 50 classes of CUB-200 as the number of classes is incrementally increased from 1 to 50. (E) Number of nodes as the number of classes is increased for CUB-200. (F to I) Assessing the effect of dynamically changing size of GWR compared with static network with fixed number of nodes. [(F) and (G)] The GWRs achieved 51.6% better accuracy on MNIST and 41.3% better accuracy on CUB-200 as compared with static networks that were not allowed to grow beyond the size of the dynamic network before learning the new classes. [(H) and (I)] We observed similar performance on the classes that are available in both the networks; however, the dynamic network achieves these results with almost half (~47.3%) the number of resources and nodes for MNIST and ~27% fewer nodes for the 50 classes of CUB-200 compared with the static networks.

and ventricular heartbeat classification on an electrocardiogram (ECG) dataset. The simulation results in Fig. 3, A to C, demonstrate that our H-NNO reservoirs could achieve comparable performances on the three tasks with fewer devices compared with the theoretical and experimental reservoirs. The results of performance-device ratios in Fig. 3D show that our H-NNO reservoirs, on average, outperformed the theoretical and experimental reservoirs by a factor of 1.4×, 1.2×, and 5.1× for MNIST, isolated spoken digits, and ECG heartbeat, respectively. Detailed explanations of the performance are in supplementary text 2.

Having the neuronal and synaptic functionality in a single type of device could enable compact and energy-efficient neuromorphic system designs. Discussion on deep neural networks that use such perovskite networks is given in supplementary text 3. Furthermore, the ability to reconfigure devices for multiple neuromorphic functions opens up their innovative use in next-generation AI—namely, in the emerging domain of dynamic neural networks. The GWR network is one such example that creates new nodes and their interconnections according to competitive Hebbian learning. The GWR networks expand on the

concept of self-organizing neural networks by adding or removing network nodes in an unsupervised manner to approximate the input space accurately and at times more parsimoniously as compared with a static self-organizing map (18). We can compare the dynamic GWR with a static self-organizing network that uses the same Hebbian learning scheme but has a fixed number of nodes, initialized randomly in the beginning. We trained our network on two archetypal datasets used to evaluate performance in literature, MNIST (19) and a subset of CUB-200 (20), to simulate how such a network will perform on the fly.

Discussion on the datasets and details of the simulation are available in the supplementary materials, materials and methods, and supplementary text 4. The GWR network's ability to dynamically respond to changes in the input distribution is visualized in Fig. 4A for MNIST.

For both the datasets and networks, we conducted two sets of simulations using the experimental data from our H-NNO devices: (i) incremental learning, in which the network is shown newer classes of data over time, and (ii) assessing the effect of growing or shrinking compared with static networks—how efficiently the GWR can represent the input space. The network's test accuracy and the number of nodes as each new class was trained for both the datasets in the incremental learning scenario are shown in Fig. 4, B to E. We observed that the dynamic network was able to retain its learned representations much better than could the static network, with the final test of accuracy resulting in MNIST being 212% more accurate and CUB-200 being 250% more accurate. By growing its size, the network avoided suffering from catastrophic forgetting and showed only a smooth degradation in performance as the number of classes was increased. The size of the static network was chosen to be equal to the maximum number of nodes that the GWR network required. This arrangement ensured that the difference we observed was not due to the size difference of the two networks but rather because of the dynamic network's ability to grow and learn.

We then studied the ability of the GWR network to dynamically change its size to adapt to the input space. First, we assessed the networks' ability to grow as the number of classes in the network was increased abruptly (Fig. 4, F and G). Initially, we presented the networks with the first half of the total number of classes in the datasets, and the GWR grew and saturated in size. Afterward, when the networks were presented with the entire dataset, the GWR rapidly grew its size to accommodate the change. The static network was not able to do so and thus failed to learn the new data, also suffering degradation in performance in the initial classes (detailed accuracy results are provided in supplementary text 4 and figs. S27 and S28). Overall, the dynamic networks achieved better accuracy on the test set in comparison with that of the static network: 210% for MNIST and 170% for CUB-200. Next, we demonstrated that the GWR was able to efficiently allocate its resources compared with a large static network. We presented the network with all the classes of the dataset at the beginning. After learning occurred, we removed half the categories and let the GWR network reduce its size and reach an equilibrium number of nodes (Fig. 4, H and I). We found that the GWR was able to retain a similar level of the performance

to that of the large static network (accuracy difference, 2 to 3%) on the subset of interest and demonstrated higher efficiency through shrinking its size by ~47% for MNIST and ~27% for CUB-200 (detailed accuracy results are provided in supplementary text 4 and figs. S29 and S30). In addition to simulation studies, we conducted proof-of-concept experiments to demonstrate the reconfiguration ability of the H-NNO devices in hardware for an incremental learning scenario, in comparison with a static network. Detailed discussions on the results are included in supplementary text 5.

Conclusions

We have demonstrated artificial neurogenesis in perovskite electronic devices: the ability to reconfigure hardware building blocks for brain-inspired computers on demand within a single device platform. Dynamic deep learning networks simulated with the experimentally measured characteristics of the nickelate devices consistently outperformed static counterparts. The results showcase the potential of reconfigurable perovskite quantum electronic devices for emerging computing paradigms and AI machines. Additionally, semiconductor technology-compatible ALD on Si platforms and room-temperature operation of test chips can further enable widespread adoption of perovskite quantum materials into mainstream integrated circuit manufacturing.

REFERENCES AND NOTES

1. J. Kirkpatrick *et al.*, *Proc. Natl. Acad. Sci. U.S.A.* **114**, 3521–3526 (2017).
2. G. I. Parisi, R. Kemker, J. L. Part, C. Kanan, S. Wermter, *Neural Netw.* **113**, 54–71 (2019).
3. G. I. Parisi, X. Ji, S. Wermter, On the role of neurogenesis in overcoming catastrophic forgetting, from NIPS'18 Workshop on Continual Learning, Montreal, Canada, 7 December 2018.
4. K. O. Stanley, J. Clune, J. Lehman, R. Miikkulainen, *Nat. Mach. Intell.* **1**, 24–35 (2019).
5. N. K. Upadhyay *et al.*, *Adv. Mater. Technol.* **4**, 1800589 (2019).
6. T. Ohno *et al.*, *Nat. Mater.* **10**, 591–595 (2011).
7. R. A. John *et al.*, *Adv. Mater.* **30**, e1800220 (2018).
8. R. A. John *et al.*, *Nat. Commun.* **11**, 3211 (2020).
9. W. Yi *et al.*, *Nat. Commun.* **9**, 4661 (2018).
10. J. H. Yoon *et al.*, *Nat. Commun.* **9**, 417 (2018).
11. J. Shi, Y. Zhou, S. Ramanathan, *Nat. Commun.* **5**, 4860 (2014).
12. Y. van de Burgt *et al.*, *Nat. Mater.* **16**, 414–418 (2017).
13. M. Rigotti, D. Ben Dayan Rubin, X.-J. Wang, S. Fusi, *Front. Comput. Neurosci.* **4**, 24 (2010).
14. M. G. A. Mohamed, H. Kim, T. W. Cho, *ScientificWorldJournal* **2015**, 910126 (2015).
15. D. Bialek, M. Di Ventra, Y. V. Pershin, *Wuxiandian Gongcheng* **22**, 945–968 (2013).
16. S. H. Jo *et al.*, *Nano Lett.* **10**, 1297–1301 (2010).
17. A. S. Obblea, A. Timilsina, D. Moore, K. A. Campbell, Silver chalcogenide based memristor devices, in *The 2010 International Joint Conference on Neural Networks (IJCNN)* (IEEE, 2010), pp. 1–3.
18. S. Marsland, J. Shapiro, U. Nehmzow, *Neural Netw.* **15**, 1041–1058 (2002).
19. Y. LeCun, L. Bottou, Y. Bengio, P. Haffner, *Proc. IEEE* **86**, 2278–2324 (1998).
20. C. Wah, S. Branson, P. Welinder, P. Perona, S. Belongie, The Caltech-UCSD Birds-200-2011 Dataset, *Comput. Neural Syst.*

Tech. Rep. CNS-TR-2011-001 (California Institute of Technology, 2011).

21. H.-T. Zhang *et al.*, Data from reconfigurable perovskite nickelate electronics for artificial intelligence, *Zenodo* (2021).

ACKNOWLEDGMENTS

We sincerely thank A. Chubykin at the Purdue Institute for Integrative Neuroscience for valuable discussions on neurogenesis, synaptogenesis, and repair of neural circuits. We sincerely thank K. Rabe (Rutgers University), S. Mandal (Rutgers University), and M. Kotiuga (EPFL) for valuable discussions on mechanisms leading to capacitive behavior in hydrogen-doped nickelates. We thank A. Hexemer for providing us computational time on NERSC and useful discussions on the workflow development for predicting the metastable phases of materials. **Funding:** The analysis of the synaptic properties and related measurements were supported by Quantum Materials for Energy Efficient Neuromorphic Computing (Q-MEEN-C), an Energy Frontier Research Center (EFRC) funded by the US Department of Energy (DOE), Office of Science, Basic Energy Sciences (BES), under award DE-SC0019273. The fabrication and pulsed field measurements were supported by the Air Force Office of Scientific Research (AFOSR) FA9550-19-1-0351 and ARO W911NF-19-2-0237, respectively. A.N.M.N.I. and A.S.'s research was funded in part by the National Science Foundation (NSF) under grants BCS-2031632 and CCF-1955815. Use of the Center for Nanoscale Materials and Advanced Photon Source, both Office of Science user facilities, was supported by the DOE, Office of Science, BES, under contract DE-AC02-06CH11357. This research used resources of the National Energy Research Scientific Computing Center (NERSC), a DOE Office of Science User Facility located at Lawrence Berkeley National Laboratory, operated under contract DE-AC02-05CH11231. This material is based on work supported by the DOE, Office of Science, BES Data, Artificial Intelligence and Machine Learning at DOE Scientific User Facilities program. This work at BNL was supported by DOE-BES, Materials Sciences and Engineering Division under contract DE-SC0012704. This research used resources of the Advanced Photon Source, a DOE Office of Science User Facility, operated for the DOE Office of Science by Argonne National Laboratory under contract DE-AC02-06CH11357. Extraordinary facility operations were supported in part by the DOE Office of Science through the National Virtual Biotechnology Laboratory, a consortium of DOE national laboratories focused on the response to COVID-19, with funding provided by the Coronavirus CARES Act. S.G. and Y.A. acknowledge support from the AFOSR, grant FA9559-16-1-0172, and NSF under grant DMR-1904097. S.M. and N.J. acknowledge support from NSF grant CHE-1944796. **Author contributions:** H.-T.Z., T.J.P., and S.R. conceived the study. T.J.P. and H.-T.Z. grew the nickelate films. Q.W. fabricated the devices. H.-T.Z., T.J.P., and S. Mo. conducted electrical measurements. H.Y. and T.J.P. performed XRD characterization. H.Z. performed synchrotron x-ray characterization. S.C. and Y.Z. performed transmission electron microscopy (TEM) characterization. S.G. and Y.A. carried out scattering-type scanning near-field optical microscopy. S. Mah. and N.J. performed near-field tip-enhanced Raman measurements. A.N.M.N.I. and A.S. performed the all-perovskite deep network and the GWR neural network simulations and analysis. D.S.J.T. performed the RC simulation, and C.T. co-led the discussions of these results. S. Man., S.B., and S.K.R.S.S. carried out all the reinforcement learning-based search and the ab initio calculations. H.-T.Z., T.J.P., and S.R. organized the manuscript. All authors participated in discussing the results and providing various sections and comments for the paper. **Competing interests:** The authors declare no competing interests. **Data and materials availability:** All data needed to evaluate the conclusions in the paper are present in the paper or the supplementary materials. Data can be found at the Zenodo repository (21).

SUPPLEMENTARY MATERIALS

science.org/doi/10.1126/science.abj7943
Materials and Methods
Supplementary Text
Figs. S1 to S55
Tables S1 to S4
References (22–58)

2 June 2021; resubmitted 19 November 2021
Accepted 13 December 2021
10.1126/science.abj7943

HIV

A highly virulent variant of HIV-1 circulating in the Netherlands

Chris Wymant^{1*}, Daniela Bezemer², François Blanquart^{3,4}, Luca Ferretti¹, Astrid Galli⁵, Matthew Hall¹, Tanya Golubchik¹, Margreet Bakker⁶, Swee Hoe Ong⁷, Lele Zhao¹, David Bonsall^{1,8}, Mariateresa de Cesare⁸, George MacIntyre-Cockett^{1,8}, Lucie Abeler-Dörner¹, Jan Albert^{9,10}, Norbert Bannert¹¹, Jacques Fellay^{12,13,14}, M. Kate Grabowski¹⁵, Barbara Günsenheimer-Bartmeyer¹⁶, Huldrych F. Günthard^{17,18}, Pia Kivela¹⁹, Roger D. Kouyos^{17,18}, Oliver Laeyendecker²⁰, Laurence Meyer²¹, Kholoud Porter²², Matti Ristola¹⁹, Ard van Sighem², Ben Berkhout⁶, Paul Kellam^{23,24}, Marion Cornelissen^{6,25}, Peter Reiss^{2,26}, Christophe Fraser^{1,8*}, the Netherlands ATHENA HIV Observational Cohort[†], the BEEHIVE Collaboration[†]

We discovered a highly virulent variant of subtype-B HIV-1 in the Netherlands. One hundred nine individuals with this variant had a 0.54 to 0.74 log₁₀ increase (i.e., a ~3.5-fold to 5.5-fold increase) in viral load compared with, and exhibited CD4 cell decline twice as fast as, 6604 individuals with other subtype-B strains. Without treatment, advanced HIV–CD4 cell counts below 350 cells per cubic millimeter, with long-term clinical consequences—is expected to be reached, on average, 9 months after diagnosis for individuals in their thirties with this variant. Age, sex, suspected mode of transmission, and place of birth for the aforementioned 109 individuals were typical for HIV-positive people in the Netherlands, which suggests that the increased virulence is attributable to the viral strain. Genetic sequence analysis suggests that this variant arose in the 1990s from de novo mutation, not recombination, with increased transmissibility and an unfamiliar molecular mechanism of virulence.

The risk posed by viruses evolving to greater virulence—i.e., causing greater damage to their hosts—has been extensively studied in theoretical work despite few population-level examples (1–3). The most notable recent example is the B.1.617.2 lineage (Delta variant) of severe acute respiratory syndrome coronavirus 2 (SARS-CoV-2), for which an increased probability of death has been reported (4–6), as well as increased transmissibility (7, 8). RNA viruses have long been a particular concern, as their error-prone replication results in the greatest known rate of mutation—and thus high potential for adaptation. Greater virulence could benefit a virus if it is not outweighed by reduced opportunity for transmission. These antagonistic selection pressures may result in an intermediate level of virulence being optimal for viral fitness, as observed for HIV (9). Concrete examples of such evolution in action, however, have been elusive. Continued monitoring of HIV virulence is important for global health: 38 million people currently live

with the virus, and it has caused an estimated 33 million deaths (www.unaids.org).

The main (M) group of HIV-1, responsible for the global pandemic, first emerged around 1920 in the area of what is now Kinshasa, Democratic Republic of the Congo (10), and had diversified into subtypes by 1960 (11). The subtypes, and the most common circulating recombinant forms (CRFs) between the subtypes, took different routes for global spread, establishing strong associations with geography (12), ethnicity, and mode of transmission. Differences in virulence between subtypes and CRFs have been reported, though it is challenging to disentangle genotypic effects on virulence from confounding effects while retaining large sample sizes, given the strong associations between viral, host, and epidemiological factors (13). The co-receptor used for cell entry has long been understood to affect virulence (14, 15), and this has been proposed as a mechanism that underlies differences in virulence between subtypes and CRFs (13),

as well as one reported difference within a CRF (16).

HIV-1 virulence is most commonly measured by viral loads (the concentration of viral particles in blood plasma) and CD4 counts (the concentration of CD4⁺ T cells in peripheral blood, which tracks immune system damage by the virus). Successful treatment with anti-retroviral drugs suppresses viral load and interrupts the decline in CD4 counts that would otherwise lead to AIDS. Both viral load and rate of CD4 cell decline are heritable properties—that is, these properties are causally affected by viral genetics, leading to correlation between an individual and whomever they infect (17–21). It has therefore been expected that viral load and CD4 cell decline could change with the emergence of a new viral variant. We substantiate that expectation with empirical evidence by reporting a subtype-B variant of HIV-1 with exceptionally high virulence that has been circulating within the Netherlands during the past two decades.

Discovery of the highly virulent variant

Within an ongoing study (the BEEHIVE project; www.beehive.ox.ac.uk), we identified a group of 17 individuals with a distinct subtype-B viral variant, whose viral loads in the set-point window of infection (6 to 24 months after a positive test obtained early in the course of infection) were highly elevated (Table 1, middle column). BEEHIVE is a study of individuals enrolled in eight cohorts across Europe and Uganda, who were selected because they have well-characterized dates of infection and samples available from early infection, for whom whole viral genomes were sequenced. The 17 individuals with the distinct viral variant comprised 15 participants in the ATHENA study in the Netherlands, 1 from Switzerland, and 1 from Belgium. See materials and methods for details on the initial discovery.

Replication of the discovery in Dutch ATHENA data

To replicate the finding and to investigate this viral variant in more detail, we then analyzed data from 6706 participants in ATHENA with

¹Big Data Institute, Li Ka Shing Centre for Health Information and Discovery, Nuffield Department of Medicine, University of Oxford, Oxford, UK. ²Stichting HIV Monitoring, Amsterdam, Netherlands. ³Centre for Interdisciplinary Research in Biology (CIRB), Collège de France, CNRS, INSERM, PSL Research University, Paris, France. ⁴IAE, UMR 1137, INSERM, Université de Paris, Paris, France. ⁵European Molecular Biology Laboratory, European Bioinformatics Institute, Wellcome Genome Campus, Hinxton, Cambridge, UK. ⁶Laboratory of Experimental Virology, Department of Medical Microbiology and Infection Prevention, Amsterdam University Medical Centers, University of Amsterdam, Amsterdam, Netherlands. ⁷Wellcome Sanger Institute, Wellcome Genome Campus, Cambridge, UK. ⁸Wellcome Centre for Human Genetics, Nuffield Department of Medicine, University of Oxford, Oxford, UK. ⁹Department of Microbiology, Tumor and Cell Biology, Karolinska Institutet, Stockholm, Sweden. ¹⁰Department of Clinical Microbiology, Karolinska University Hospital, Stockholm, Sweden. ¹¹Division for HIV and Other Retroviruses, Department of Infectious Diseases, Robert Koch Institute, Berlin, Germany. ¹²School of Life Sciences, Ecole Polytechnique Fédérale de Lausanne, Lausanne, Switzerland. ¹³Swiss Institute of Bioinformatics, Lausanne, Switzerland. ¹⁴Precision Medicine Unit, Lausanne University Hospital and University of Lausanne, Lausanne, Switzerland. ¹⁵Department of Pathology, Johns Hopkins University, Baltimore, MD, USA. ¹⁶Department of Infectious Disease Epidemiology, Robert Koch Institute, Berlin, Germany. ¹⁷Division of Infectious Diseases and Hospital Epidemiology, University Hospital Zurich, Zurich, Switzerland. ¹⁸Institute of Medical Virology, University of Zurich, Zurich, Switzerland. ¹⁹Department of Infectious Diseases, Helsinki University Hospital, Helsinki, Finland. ²⁰Division of Intramural Research, NIAID, NIH, Baltimore, MD, USA. ²¹INSERM CESP U1018, Université Paris Saclay, APHP, Service de Santé Publique, Hôpital de Bicêtre, Le Kremlin-Bicêtre, France. ²²Institute for Global Health, University College London, London, UK. ²³Kymab Ltd., Cambridge, UK. ²⁴Department of Infectious Diseases, Faculty of Medicine, Imperial College London, London, UK. ²⁵Molecular Diagnostic Unit, Department of Medical Microbiology and Infection Prevention, Amsterdam University Medical Centers, University of Amsterdam, Amsterdam, Netherlands. ²⁶Department of Global Health, Amsterdam University Medical Centers, University of Amsterdam and Amsterdam Institute for Global Health and Development, Amsterdam, Netherlands. *Corresponding author. Email: chris.wymant@bdi.ox.ac.uk (C.W.); christophe.fraser@bdi.ox.ac.uk (C.F.) †Contributors and affiliations are listed in the supplementary materials.

subtype-B infections (expanding on the subset of 521 participants in ATHENA who were eligible for inclusion in BEEHIVE). We found 92 additional individuals infected with the viral variant, bringing the total to 109 such individuals in either dataset. When replicating the BEEHIVE test with the ATHENA data (Table 1, right column), we again observed a large rise in viral load in individuals with this viral variant: an increase of 0.54 \log_{10} viral copies/ml (i.e., a ~3.5-fold increase). The effect size was the same in a linear model including age at diagnosis and sex as covariates, and persisted in newly diagnosed individuals over time (Fig. 1A). Henceforth, for brevity, we refer to this viral variant as the “VB variant” (for virulent subtype B), to individuals infected with this variant as “VB individuals,” and to individuals infected with a different strain of HIV as “non-VB individuals.”

Search for closely related viruses

To test whether the variant was more widely disseminated, we searched publicly available databases for similar HIV viral genotypes. All results had <95% sequence similarity to a representative viral sequence for the variant. Of the 17 VB individuals originally found in BEEHIVE, one was from the Swiss HIV Cohort Study (22) (SHCS). By examining previously published data (23), we found that three other individuals from the SHCS were closely related (a phylogenetic distance below 2.5%). The high coverage of the Swiss HIV Cohort [including 89% of reported new infections from 2009 through 2018, with ~65% of the cohort sequenced (24)] makes it unlikely that

many more VB individuals in Switzerland were undetected. Data to assess viral load or CD4 cell decline for these three individuals were not available, owing to early initiation of treatment.

More-rapid CD4 cell decline

At the time of diagnosis, CD4 counts for VB individuals were already lower than for non-VB individuals by 73 cells/mm³ [95% confidence interval (CI): 12 to 134]. These counts subsequently declined faster, by a further 49 cells/mm³ per year (CI: 20 to 79), in addition to the decline for comparable non-VB individuals [49 cells/mm³ per year (CI: 46 to 51) for men diagnosed at the age of 30 to 39 years]. The VB variant is therefore associated with a doubling in the rate of CD4 cell decline. These values are averages estimated by using a linear mixed model adjusted for sex and age at diagnosis. Figure 1B illustrates the CD4 count decline that would be expected if disease progression were to continue linearly in the absence of treatment. Initiating treatment at a CD4 count of 350 cells/mm³, instead of immediately, was previously shown to substantially increase the subsequent hazard for serious adverse events (25). As seen in Fig. 1B, this stage of CD4 cell decline is expected to be reached in 9 months (CI: 2 to 17) from the time of diagnosis for VB individuals, as opposed to 36 months (CI: 33 to 39) for non-VB individuals, in males diagnosed at the age of 30 to 39 years. It is reached even more quickly in older age groups, for which we found progressively lower CD4 counts at time of diagnosis (table S1). At a CD4 count of 200 cells/

mm³, there is a high risk of immediate AIDS-related complications; without treatment this stage of decline would be reached, on average, between 2 and 3 years after diagnosis for VB individuals and between 6 and 7 years after diagnosis for comparable non-VB individuals [the latter being similar to previous reports in Europe (26)].

The effect of the VB variant on CD4 cell decline remained after we adjusted for the effect of higher viral load. With this adjustment, VB individuals have a CD4 count at diagnosis as would be expected given their high viral loads, but their subsequent decline in CD4 counts is again twice as fast as for as comparable non-VB individuals with high viral loads—their rate of decline is accelerated by 44 cells/mm³ per year (CI: 16 to 72). Comparison of this additional decline with that expected from a +1 increase in \log_{10} viral load, 15 cells/mm³ per year (CI: 11 to 18), shows that the variant's effect on CD4 count decline is equivalent to that expected from a +3.0 increase in \log_{10} viral load. The same analysis of measurements of CD4 percentages (the percentage of all T cells that express CD4) showed that these also declined twice as fast for VB individuals, and again this doubling in speed of decline remained when we adjusted for the higher viral load of the variant (table S2 and fig. S1).

No difference in CD4 cells after treatment, or in mortality

Measurements of treatment success include CD4 cell recovery and mortality. CD4 counts and percentages after treatment initiation were

Table 1. Comparison of viral loads between individuals infected with the VB viral variant and other individuals. When analyzing the viral loads of individuals in the ATHENA study, we first excluded individuals who were in BEEHIVE, so that the test would be independent of the initial finding within the BEEHIVE study. After our statistical tests of viral load, we did not exclude BEEHIVE individuals from the ATHENA data for subsequent analyses. *N*, number of individuals after those without viral load measurements before treatment were excluded; IQR, interquartile range.

Test	Discovery [BEEHIVE dataset (Europe)]	Replication [ATHENA dataset (Netherlands), excluding overlap with BEEHIVE]
Viral load measurements compared	Set-point viral loads for <i>N</i> = 15 VB individuals and <i>N</i> = 2446 individuals with any other HIV-1 strain	Mean pretreatment viral loads for <i>N</i> = 91 VB individuals and <i>N</i> = 5272 individuals with any other subtype-B HIV-1 strain
Mean and IQR of viral load in non-VB individuals, in \log_{10} copies per milliliter	5.10 (IQR: 4.69 to 5.58)	4.79 (IQR: 4.34 to 5.27)
Mean and IQR of viral load in VB individuals, in \log_{10} copies per milliliter	5.84 (IQR: 5.57 to 6.09)	5.33 (IQR: 4.94 to 5.75)
Viral load increase in VB individuals	0.74 \log_{10} viral copies/ml 5×10^{-6}	0.54 \log_{10} viral copies/ml
<i>P</i> value for increase	(two-tailed <i>t</i> test, significant at a level of 5×10^{-5} when Bonferroni-corrected for performing 50 such tests)	1×10^{-12} (one-tailed <i>t</i> test)

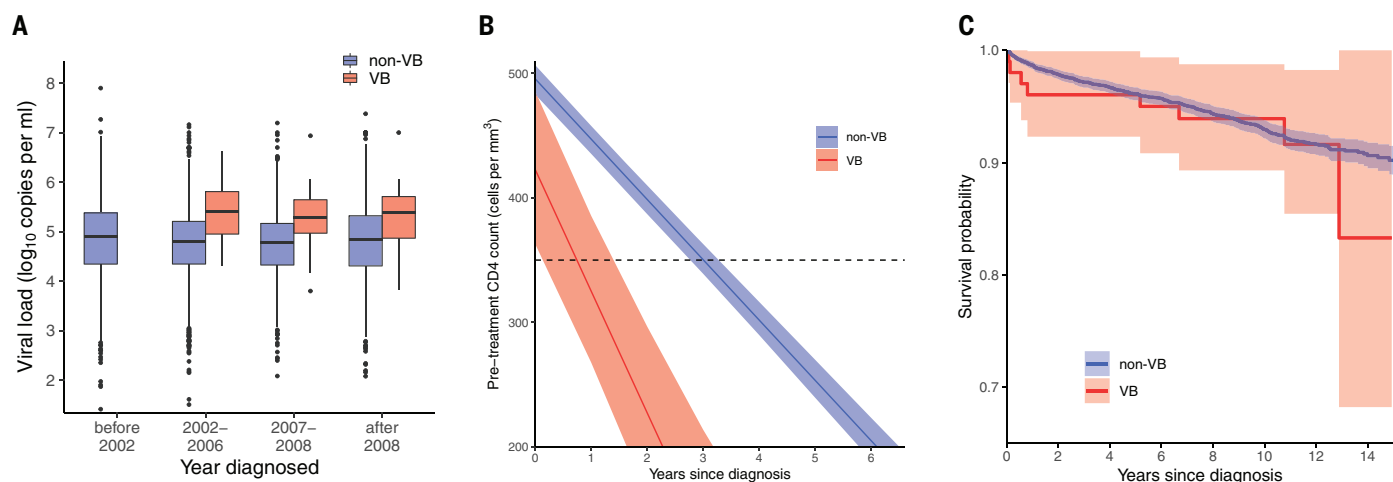


Fig. 1. Clinical characteristics of VB individuals. Those infected with the highly virulent variant (VB individuals) are represented in red; those infected with any other subtype-B virus (non-VB individuals) are shown in blue. **(A)** Box-and-whisker plots of viral load, by year of diagnosis. Diagnosis dates were grouped to produce boundaries that coincide with years and roughly equal numbers of VB individuals (39 in 2002–2006, 35 in 2007–2008, and 27 after 2008; the pattern is robust to other groupings). **(B)** Expected decline in CD4 count in the

absence of treatment. The model was adjusted for sex and age at diagnosis; values shown are for males diagnosed at the age of 30 to 39 years. Shaded regions indicate 95% CIs in the model's prediction of mean values, given the uncertainty in estimation of parameter values (it does not reflect the variability between individuals in each of the two groups, which is much greater). The dashed black line denotes a CD4 count of 350 cells/mm³ (see text for details). **(C)** Probability of still being alive at a given time after diagnosis.

similar for VB and non-VB individuals, as measured with both linear mixed modeling of the CD4 dynamics (tables S3 and S4 and fig. S2) and an individual-matching procedure. The hazard for death (from any cause) was also similar: VB individuals had a relative hazard of 1.4 (CI: 0.7 to 2.8, $P = 0.35$, Cox proportional hazards model). Our study had statistical power to detect only very large differences in mortality, as reflected in the wide CI for relative hazard for death and shown in Fig. 1C. VB individuals had similar CD4 counts and mortality after treatment despite a faster CD4 cell decline before treatment; this could be explained by their tendency to start treatment sooner after diagnosis (fig. S3). For example, although the probability of having started treatment was estimated to be similar 6 months after diagnosis [42% (CI: 41 to 44%) for non-VB individuals compared with 46% (CI: 35 to 54%) for VB individuals], it was different 2 years after diagnosis [65% (CI: 64 to 67%) for non-VB individuals and 93% (CI: 85 to 96%) for VB individuals]. Had VB individuals not started treatment earlier than others, lower CD4 counts at treatment initiation would have been expected, potentially causing increased morbidity and mortality (25). This information could be relevant if VB or variants like it are found in settings with less widespread availability of HIV care.

Characteristics of individuals infected with the VB variant

VB individuals were mostly (82%) men who have sex with men, similar to non-VB individ-

uals (76%). Age at diagnosis was also similar for VB and non-VB individuals (fig. S4). Neither ethnicity nor host genotype data were available, but the place of birth was mostly recorded as Western Europe for both groups (71% for non-VB individuals, 86% for VB individuals). VB individuals were present in all regions of the Netherlands, but with a different distribution relative to that of non-VB individuals ($N = 102$ versus 6604 individuals, $P < 10^{-7}$, simulated Fisher's exact test): VB individuals were more common in the south (25% of VB individuals versus 6% of non-VB individuals) and less common in Amsterdam (20% versus 51%), as shown in table S5. Table S6 lists the hospitals included in each region. The average time from infection to diagnosis, for men who have sex with men in this cohort diagnosed in the late 2000s, was previously estimated to be 3.6 years (CI: 3.3 to 4.0) (27).

Genotype of the VB variant

Sequence data from the BEEHIVE project are whole-genome data, providing the 17 whole genomes available for the variant; sequence data from ATHENA are partial *pol* gene data only, available for the additional 92 VB individuals. We subtyped the 17 whole genomes for the variant as pure subtype B [with 100% support from two concordant methods (28, 29)], like most HIV-1 in the Netherlands. We predicted co-receptor usage from the 17 whole genomes using two concordant methods (30, 31): one was likely CXCR4-tropic; the other 16 were likely CCR5-tropic. Only one drug-resistance mutation was common for the VB

variant: Met⁴¹→Leu (M41L), present in 91 of 109 partial *pol* gene sequences. Without other linked resistance mutations, M41L causes only low-level resistance to zidovudine (32, 33). Two of the whole genomes were found to be recombinants between the VB variant and another subtype-B cluster in ATHENA (containing a small amount of sequence from the latter) and were excluded from subsequent sequence analysis. Among whole genomes in BEEHIVE and all whole genomes in the Los Alamos National Laboratory HIV Database (www.hiv.lanl.gov), none appeared to be a candidate for a “recombination parent” of the VB variant—i.e., the many mutations that distinguish the VB variant from any other known virus appear to have arisen de novo, not through recombination.

We compared the consensus sequence for the VB variant with the consensus of all Dutch subtype-B sequences in BEEHIVE, at both the amino acid and the nucleotide level: There were 250 amino acid changes and 509 nucleotide changes, as well as insertions and deletions. These alignments are included as data S1, and the amino acid alignment is illustrated in fig. S5. The distribution of nucleotide changes over the genome is in line with expectations (for example, fewer in the conserved *pol* gene region and more in the variable *env* gene region; see fig. S6). The VB-variant genotype is thus characterized by many mutations spread through the genome, meaning that a single genetic cause for the enhanced virulence cannot be determined from the current data.

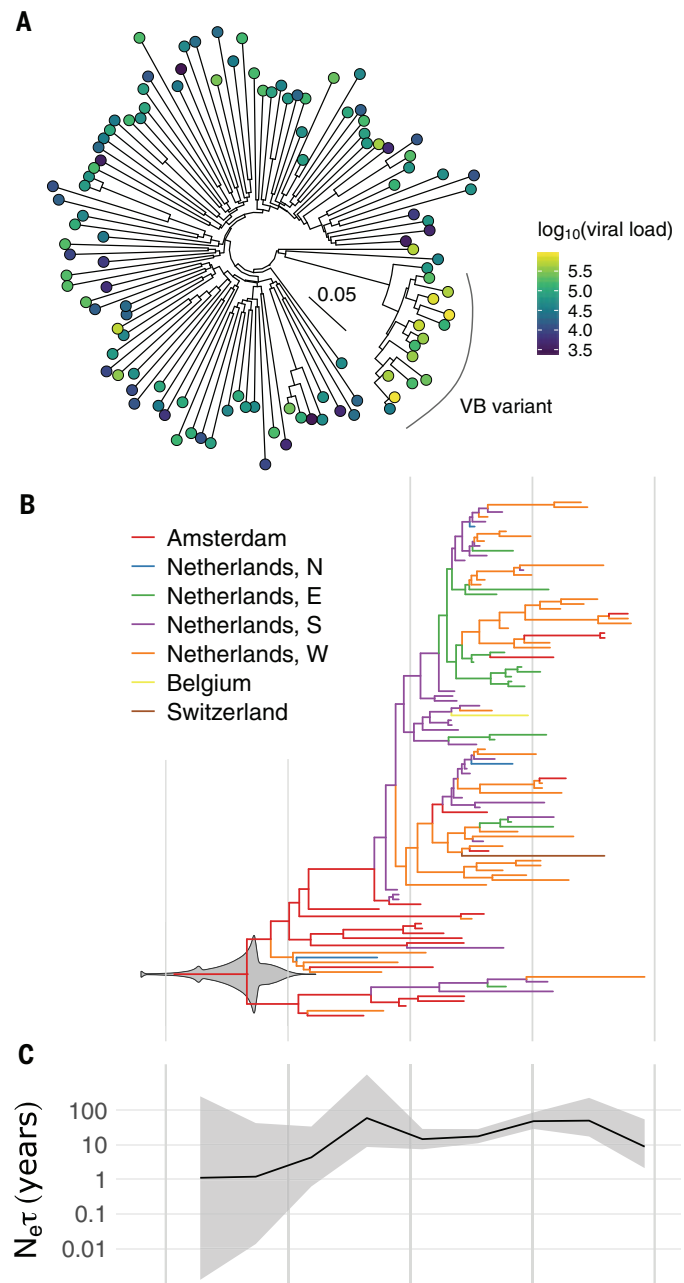
We conducted descriptive analyses of the mutations that distinguish the VB variant from the Dutch subtype-B consensus. All of the amino acid-level changes are listed in data S2 with annotations. Of the observed amino acid substitutions, 30 were previously shown to be positively associated with escape from cytotoxic T lymphocyte (CTL) response for at least one human leukocyte antigen type, and 13 were shown to be negatively associated (34). To provide context for these numbers, within Dutch subtype-B data in BEEHIVE we defined 16 other clades that are similar to the lineage in size (see materials and methods). For each clade, we calculated the amino acid consensus sequence, compared this to the Dutch subtype-B overall consensus, and determined CTL escape mutations. This showed that the number of such mutations for the VB variant is typical when normalized by its overall level of divergence (fig. S11). We also calculated the ratio of rates of nonsynonymous and synonymous changes (d_n/d_s) for each gene, for the VB variant and the other 16 Dutch subtype-B clades used for comparison. The VB variant had lower d_n/d_s values than all of the other clades for *env*, *pol*, and *tat*, though its values were not extreme; for the other genes, its d_n/d_s value was in the range spanned by the other clades (fig. S12). Finally, at codon position 77 of the protein Vpr, the consensus of all Dutch subtype-B sequences in BEEHIVE is glutamine, whereas the VB consensus is arginine. Glutamine was previously found to be more common in long-term nonprogressors, and mutation to arginine increased T cell apoptosis in vitro and strongly increased T cell decline in mouse models (35). However, both alleles have been commonly observed in subtype B to date (of 2178 subtype-B Vpr protein sequences in the Los Alamos National Laboratory HIV Database, 52% have glutamine and 36% have arginine), making it implausible that this mutation alone is the dominant mechanism for the virulence effect we observed.

Evolution of the VB variant

The maximum-likelihood phylogeny in Fig. 2A shows the VB variant in the context of background sequences, demonstrating that it is a distinct genetic cluster characterized by high viral loads. The phylogeny was inferred from 15 whole-genome VB-variant sequences and 100 randomly chosen whole-genome subtype-B background sequences from BEEHIVE. Figure 2B shows a dated phylogeny for VB-variant sequences only, estimated by using *BEAST* (36) and partial *pol* sequences. This phylogeny is colored by region, inferred with an ancestral state reconstruction by parsimony (minimizing changes of region). Amsterdam was assigned to the most recent common ancestor in 97% of trees in the posterior, showing that this reconstruction was robust to the uncertainty in

Fig. 2. Phylogenetic and phylodynamic analysis of the VB variant. (A) Whole-genome maximum-likelihood phylogeny of 15 VB-variant sequences and 100 background subtype-B sequences.

The color of each circle indicates the individual's viral load in \log_{10} copies per milliliter. The inset scale bar shows the branch length scale in units of substitutions per site. (B) Dated maximum-clade-credibility tree for 107 partial *pol* gene sequences from the VB variant. Colors indicate geographical regions (N, E, S, and W: north, east, south, and west), which are known for the tips of the tree but are otherwise inferred by ancestral state reconstruction. The gray violin plot superimposed on the root node shows the posterior density for its date (i.e., the TMRCA); 1994 contains overflow to earlier dates for clarity. (C) Effective population size (N_e) (scaled by the coalescent generation time τ) over time with 95% credibility intervals, with the same time axis as in (B).



the phylogeny. All VB-variant sequences date from 2003 onward; the time of their most recent common ancestor (TMRCA) was estimated as 1998.0 (95% credibility interval: 1995.7 to 2000.1). Trees were visualized by using *ggtree* (37).

Phylodynamics of the VB variant

The effective population size (N_e) of a pathogen is indicative of the number of infectious people. For the VB variant, N_e was estimated by using a skygrid demographic model (38) in *BEAST* and is shown in Fig. 2C (scaled by the coalescent generation time τ). N_e increased until roughly 2010; after this, there is more uncertainty but a possible downward trend

[which may be an artefact of N_e inference methods in the recent past (39)]. The proportion of VB-variant cases among all new subtype-B cases increased until a peak in 2008 and subsequently decreased, though again with appreciable uncertainty [absolute numbers of both VB and non-VB diagnoses in our dataset have been decreasing since roughly 2008, and the data are right-censored by several years (fig. S7)]. In a recent analysis of an updated version of the ATHENA dataset (40), 33 additional VB individuals were found, which suggests that VB diagnoses were stable until roughly 2013 and have since been declining, still with appreciable uncertainty.

We calculated the local branching index (LBI), which is a measure of fitness (41). For HIV in a context in which most individuals start treatment without long delays, the LBI is closely related to transmissibility (see supplementary text). Compared with that of other transmission clusters, the LBI was higher for the VB variant both in BEEHIVE ($P = 2 \times 10^{-7}$) and ATHENA ($P < 2 \times 10^{-16}$; fig. S8). High pretreatment transmissibility may explain why the VB variant grew to be the 10th largest of 1783 clusters in the full ATHENA tree.

Tree imbalance and evolution within the VB-variant clade

We found nothing unusual in the extent to which the VB variant's phylogeny is imbalanced, nor did we detect any indication of further evolution of viral load within the variant's clade (supplementary text and fig. S9).

The first sampled VB individual

We retrieved and sequenced two additional samples from the VB individual who was diagnosed in 1992, 10 years before subsequent diagnoses of other VB individuals. Phylogenetic analysis suggested that this individual was infected with a virus that had evolved most of the way, but not entirely, toward VB-variant viruses typical of later dates (supplementary text and fig. S10). This individual was diagnosed in Amsterdam, consistent with the aforementioned ancestral reconstruction of region. In the 10 years before this first VB diagnosis, the proportion of individuals diagnosed in the Netherlands for whom a viral sequence was available was roughly one-third. The proportion of those diagnosed or undiagnosed would be smaller still. This means that the infector of the 1992 individual was most likely not sampled, and indeed two or three steps in the transmission chain could have been unsampled. The long phylogenetic branch leading to the 1992 individual could therefore represent between-host evolution, not necessarily within-host evolution in a single individual.

Discussion

Previous studies of the heritability of viral load and CD4 cell decline led us to expect that these properties could change with the emergence of a new variant of HIV-1. We provided strong evidence for this, discovering a virulent subtype-B variant (the VB variant) that has been circulating in the Netherlands since the late 1990s. We characterized the variant's genotype and evolutionary history, as well as its association with high viral loads, rapid decline of CD4 cells, and increased transmissibility. We found 109 individuals with the variant (VB individuals) whose age, sex, suspected mode of transmission, and region of birth are all typical for people living with HIV in the Netherlands. This suggests that the ob-

served association is causal: The increased virulence is a property of the virus rather than a confounding property of individuals in this transmission cluster. An absence of viral load evolution inside the clade of VB variants suggests that the increased virulence is a property of the whole clade and not a subset of it—i.e., that the virulence evolution occurred on the long phylogenetic branch that connects this clade to other known viruses.

Deferring the initiation of treatment until the measurement of a CD4 count's decline to ≤ 350 cells/mm³ or the onset of AIDS, instead of immediate treatment initiation upon diagnosis, was previously shown to increase the subsequent hazard of serious AIDS-related events by a factor of 3.6 (CI: 2.0 to 6.7) and of any serious event (including death) by a factor of 2.4 (CI: 1.6 to 3.3) (25). This long-lasting immunological damage justifies WHO's classification of 350 CD4 cells/mm³ as "advanced HIV" (www.who.int/hiv/pub/guidelines/HIVstaging150307.pdf). Without treatment, advanced HIV is expected to be reached in only 9 months (CI: 2 to 17) from the time of diagnosis for VB individuals, compared with 36 months (CI: 33 to 39) for non-VB individuals, in males diagnosed at the age of 30 to 39 years. Advanced HIV is reached even more quickly in older age groups, and there is considerable variation between individuals around these expected values. Many individuals could therefore progress to advanced HIV by the time they are diagnosed, with a poorer prognosis expected thereafter in spite of treatment. In practice, there is still substantial variation in the delay from becoming infected to starting treatment, making the VB variant a concern even in the high-awareness and highly monitored context of the Dutch HIV-1 epidemic. In contexts with less awareness and monitoring, in which diagnosis often occurs later in infection, the probability of reaching advanced HIV before diagnosis would be even greater.

Future *in vitro* investigations could more firmly establish the role of the viral genotype, and reveal an as-yet-unknown virulence mechanism at the molecular or cellular level. A higher replicative capacity of the virus might be observed, given the increased viral loads seen here. However, it is likely that there will be more to the virulence mechanism: The VB variant doubles the rate of CD4 cell decline, measured with both counts and T cell percentages, even after adjusting for its higher viral load. This rate is equivalent to the acceleration of CD4 degradation that would be expected from a 3.0 log₁₀ increase in viral load, though we observed a 0.54 to 0.74 log₁₀ increase. This means that the virulence normalized by the amount of virus—the "per-parasite pathogenicity" (42, 43), which for HIV is heritable (19)—is much higher for the VB variant. Using two aforementioned methods, we predicted

that, of the 17 whole genomes available, 16 use only the R5 co-receptor for cell entry, which is typical for subtype-B viruses in early infection (13). This finding suggests that the underlying virulence mechanism is distinct from the well-known effect of cell tropism (14, 15).

Previous studies have reported population-wide increases (44, 45) and decreases (46) in virulence over time. Mixed results between individual studies [see (47) for a meta-analysis] can be attributed to differences in epidemic context (such as the dominant subtypes), statistical power, and observational biases over time. Temporal virulence trends could also be due to changing confounders, such as a shift in which subpopulations are most affected, the stage of infection at time of diagnosis, or coinfections. We expand on these studies by resolving a change in virulence to an individual viral variant.

The basic theory of an infectiousness–virulence trade-off is that infectiousness and virulence are linked (for example, by how fast a pathogen replicates in its host) and that selection pressures favor intermediate values rather than extreme ones. If infectiousness is too low, the pathogen cannot be transmitted when its host contacts other hosts, but if virulence is too high, the host becomes too ill to have such contacts. In the case of HIV, the implication of this theory is that we would not expect highly virulent viruses to spread widely through a population in the absence of widespread treatment, because their hosts would progress to AIDS very quickly, limiting the opportunities for transmission (9). Most of the evolution that gave rise to the VB variant occurred before 1992, before effective combination treatment was available. However, our findings may stimulate further interest in whether widespread treatment shifts the balance of the infectious–virulence trade-off toward higher virulence, thus promoting the emergence and spread of new virulent variants. Previous modeling studies have investigated this idea for pathogens generally (48) and for HIV specifically (49, 50). We discuss subtleties of the argument in the supplementary text, but our conclusion is that widespread treatment is helpful to prevent new virulent variants, not harmful. The absolute fitness of viral variants must be considered in addition to their relative fitness, and treatment reduces the total onward transmission over the course of one infection, regardless of virulence. Put simply, "viruses cannot mutate if they cannot replicate" (anonymous), and "the best way to stop it changing is to stop it" [Marc Lipsitch (57)]. Early treatment also prevents CD4 cell decline from leading to later morbidity and mortality; thus clinical, epidemiological, and evolutionary considerations are aligned. Our discovery of a highly virulent and transmissible viral variant therefore emphasizes the importance of access

to frequent testing for at-risk individuals and of adherence to recommendations for immediate treatment initiation for every person living with HIV (www.who.int/hiv/pub/arv/).

REFERENCES AND NOTES

- J. L. Geoghegan, E. C. Holmes, *Nat. Rev. Genet.* **19**, 756–769 (2018).
- C. E. Cressler, D. V. McLeod, C. Rozins, J. van den Hoogen, T. Day, *Parasitology* **143**, 915–930 (2016).
- J. J. Bull, A. S. Luring, *PLOS Pathog.* **10**, e1004387 (2014).
- R. Challen *et al.*, *BMJ* **372**, n579 (2021).
- N. G. Davies *et al.*, *Nature* **593**, 270–274 (2021).
- D. J. Grint *et al.*, *Euro Surveill.* **26**, (2021).
- N. G. Davies *et al.*, *Science* **372**, eabg3055 (2021).
- E. Volz *et al.*, *Nature* **593**, 266–269 (2021).
- C. Fraser, T. D. Hollingsworth, R. Chapman, F. de Wolf, W. P. Hanage, *Proc. Natl. Acad. Sci. U.S.A.* **104**, 17441–17446 (2007).
- P. M. Sharp, B. H. Hahn, *Cold Spring Harb. Perspect. Med.* **1**, a006841 (2011).
- M. Worobey *et al.*, *Nature* **455**, 661–664 (2008).
- J. Hermelaar *et al.*, *Lancet Infect. Dis.* **19**, 143–155 (2019).
- B. S. Taylor, M. E. Sobieszczyk, F. E. McCutchan, S. M. Hammer, *N. Engl. J. Med.* **358**, 1590–1602 (2008).
- B. Asjö *et al.*, *Lancet* **2**, 660–662 (1986).
- M. Koot *et al.*, *Ann. Intern. Med.* **118**, 681–688 (1993).
- H. Song *et al.*, *Proc. Natl. Acad. Sci. U.S.A.* **116**, 239–244 (2019).
- C. Fraser *et al.*, *Science* **343**, 1243727 (2014).
- F. Blanquart *et al.*, *PLOS Biol.* **15**, e2001855 (2017).
- F. Bertels *et al.*, *Mol. Biol. Evol.* **35**, 27–37 (2018).
- C. Fraser, T. D. Hollingsworth, *AIDS* **24**, 2596–2597 (2010).
- V. Mitov, T. Stadler, *Mol. Biol. Evol.* **35**, 756–772 (2018).
- F. Schoeni-Affolter *et al.*, *Int. J. Epidemiol.* **39**, 1179–1189 (2010).
- K. Kusejko *et al.*, *J. Infect. Dis.* **220**, 244–253 (2019).
- A. U. Scherrer *et al.*, *Int. J. Epidemiol.* **10**, 1093/ije/dyab141 (2021).
- J. D. Lundgren *et al.*, *N. Engl. J. Med.* **373**, 795–807 (2015).
- S. Lodi *et al.*, *Clin. Infect. Dis.* **53**, 817–825 (2011).
- A. van Sighem *et al.*, *Epidemiology* **26**, 653–660 (2015).
- A.-C. Pineda-Peña *et al.*, *Infect. Genet. Evol.* **19**, 337–348 (2013).
- D. Struck, G. Lawyer, A.-M. Ternes, J.-C. Schmit, D. P. Bercoff, *Nucleic Acids Res.* **42**, e144 (2014).
- M. A. Jensen *et al.*, *J. Virol.* **77**, 13376–13388 (2003).
- M. C. Prosperi *et al.*, *AIDS Res. Hum. Retroviruses* **25**, 305–314 (2009).
- P. Kellam, C. A. Boucher, B. A. Larder, *Proc. Natl. Acad. Sci. U.S.A.* **89**, 1934–1938 (1992).
- S.-Y. Rhee *et al.*, *Nucleic Acids Res.* **31**, 298–303 (2003).
- J. M. Carlson *et al.*, *J. Virol.* **86**, 13202–13216 (2012).
- J. J. Lum *et al.*, *J. Clin. Invest.* **111**, 1547–1554 (2003).
- M. A. Suchard *et al.*, *Virus Evol.* **4**, vey016 (2018).
- G. Yu, D. K. Smith, H. Zhu, Y. Guan, T. T.-Y. Lam, *Methods Ecol. Evol.* **8**, 28–36 (2017).
- M. S. Gill *et al.*, *Mol. Biol. Evol.* **30**, 713–724 (2013).
- E. de Silva, N. M. Ferguson, C. Fraser, *J. R. Soc. Interface* **9**, 1797–1808 (2012).
- D. Bezemer *et al.*, *AIDS* **36**, 83–94 (2022).
- R. A. Neher, C. A. Russell, B. I. Shraiman, *eLife* **3**, e03568 (2014).
- L. Råberg, M. Stjernman, in *Ecoimmunology*, G. Demas, R. Nelson, Eds. (Oxford Univ. Press, 2011), pp. 548–578.
- L. Råberg, *PLOS Biol.* **12**, e1001989 (2014).
- N. Pantazis *et al.*, *Lancet HIV* **1**, e119–e126 (2014).
- J. O. Wertheim *et al.*, *Nat. Commun.* **10**, 5788 (2019).
- F. Blanquart *et al.*, *eLife* **5**, e20492 (2016).
- J. T. Herbeck *et al.*, *AIDS* **26**, 193–205 (2012).
- T. C. Porco, J. O. Lloyd-Smith, K. L. Gross, A. P. Galvani, *J. Theor. Biol.* **233**, 91–102 (2005).
- J. T. Herbeck *et al.*, *Virus Evol.* **2**, vew028 (2016).
- H. E. Roberts, P. J. R. Goulder, A. R. McLean, *J. R. Soc. Interface* **12**, 20150888 (2015).
- Marc Lipsitch (@mlipsitch), Twitter, 15 February 2020, <https://twitter.com/mlipsitch/status/1228734360716791815>.
- C. Wymant, C. Fraser, F. Blanquart, Analysis code for “A highly virulent variant of HIV-1 circulating in the Netherlands”, Zenodo, version 1 (2021); <https://doi.org/10.5281/zenodo.5761935>.

ACKNOWLEDGMENTS

We thank K. Fransen and G. Vanham for help with the Belgian data, O. Ratmann for help in identifying the Dutch clusters, K. Kusejko for testing for additional VB individuals in the SHCS, B. Foley for help with genome sharing, B. Dearlove and L. Thomson for help with software, and J. Herbeck and three other reviewers for helpful suggestions. **Funding:** This study was funded by ERC Advanced Grant PBDR-339251 and a Li Ka Shing Foundation grant, both

awarded to C.F. The ATHENA Cohort is managed by Stichting HIV Monitoring and supported by a grant from the Dutch Ministry of Health, Welfare and Sport through the Centre for Infectious Disease Control of the National Institute for Public Health and the Environment. **Author contributions:** Funding acquisition: C.F. Conceptualization: C.W. and C.F. Data generation and management: all authors. Investigation: C.W., F.B., D.B., L.F., P.R., and C.F. Writing, original draft: C.W. and C.F. Writing, review and editing: all authors. **Competing interests:** P.K. is an employee of Kymab, a Sanofi company. H.F.G. reports grants from the Swiss National Science Foundation, National Institutes of Health (NIH), and the Swiss HIV Cohort Study; unrestricted research grants from Gilead Sciences, Roche, and the Yvonne Jacob Foundation; and personal fees from consulting or advisory boards or data safety monitoring boards for Merck, Gilead Sciences, Viiv Healthcare, Mepha, and Sandoz. H.F.G.’s institution received money for participation in the following clinical COVID-19 studies: 540-7773/5774 (Gilead), TICO (ACTIV-3, INSIGHT/NIH), and the Morningsky study (Roche). **Data and materials availability:** Code illustrating the analysis of the source clinical data, and of the genomic distribution and annotation of VB-variant mutations, is openly available at GitHub (https://github.com/ChrisHIV/hiv_vb_variant); a version has also been deposited at Zenodo (52). The 17 VB-variant whole genomes are publicly available at GenBank with accession numbers MT458931 to MT458935 and MW689459 to MW689470; the two putative recombinants have accession numbers MW689465 and MW689466. Data on viral loads, pretreatment CD4 counts, and mortality are provided as data S3. Requests for further data access can be made by submission of a concept sheet to the corresponding authors; these will be reviewed on a case-by-case basis, given that the data underlying this study contain sensitive and potentially identifying information. Once submitted, the proposed research and/or analysis will undergo review by the BEEHIVE Data Access Committee, which includes representatives of the ATHENA Cohort, for evaluation of scientific value, relevance to the study, design and feasibility,

statistical power, and overlap with existing projects. If the proposed analysis is for verification and/or replication, data will then be made available. If the proposed research is for novel science, upon completion of the review, feedback will be provided to the proposer(s). In some circumstances, a revision of the concept may be requested. If the concept is approved for implementation, a writing group will be established that will consist of the proposers (up to three persons that were centrally involved in the development of the concept) and members of the BEEHIVE Collaboration and ATHENA Cohort (or other appointed cohort representatives). All persons involved in the process of reviewing these research concepts are bound by confidentiality. **Ethics statement:** At initiation, the ATHENA Cohort was approved by the institutional review board of all participating institutions. People beginning HIV care receive written material about participation in the ATHENA study and are informed by their treating physician of the purpose of data collection, after which they can consent verbally or opt out. Data are pseudonymized before being provided to investigators and may be used for scientific purposes. A designated quality management coordinator safeguards compliance with the European General Data Protection Regulation. Additional written informed consent was obtained for ATHENA participants enrolled in BEEHIVE for whole-genome sequencing.

SUPPLEMENTARY MATERIALS

science.org/doi/10.1126/science.abk1688

Materials and Methods

Supplementary Text

Figs. S1 to S12

Tables S1 to S7

References (53–85)

MDAR Reproducibility Checklist

Data S1 to S4

25 June 2021; accepted 4 January 2022

10.1126/science.abk1688

REPORTS

ORGANIC CHEMISTRY

Diversification of aliphatic C–H bonds in small molecules and polyolefins through radical chain transfer

Timothy J. Fazekas, Jill W. Alty, Eliza K. Neidhart, Austin S. Miller, Frank A. Leibfarth*, Erik J. Alexanian*

The ability to selectively introduce diverse functionality onto hydrocarbons is of substantial value in the synthesis of both small molecules and polymers. Herein, we report an approach to aliphatic carbon–hydrogen bond diversification using radical chain transfer featuring an easily prepared O-alkenylhydroxamate reagent, which upon mild heating facilitates a range of challenging or previously undeveloped aliphatic carbon–hydrogen bond functionalizations of small molecules and polyolefins. This broad reaction platform enabled the functionalization of postconsumer polyolefins in infrastructure used to process plastic waste. Furthermore, the chemoselective placement of ionic functionality onto a branched polyolefin using carbon–hydrogen bond functionalization upcycled the material from a thermoplastic into a tough elastomer with the tensile properties of high-value polyolefin ionomers.

The direct transformation of unreactive aliphatic C–H bonds to useful functionality is a streamlined and sustainable approach to accessing complex molecules and materials with enhanced properties from readily available compounds

(1–4). Late-stage diversification of drug-like molecules, in which complex substrates are modified selectively to alter their function, has emerged as a powerful strategy to access new lead compounds for medicinal chemistry and structure–activity relationship studies without resorting to de novo synthesis (5). Despite substantial progress, there remains a pressing need for new aliphatic C–H diversification platforms that facilitate the site-selective

Department of Chemistry, University of North Carolina–Chapel Hill, Chapel Hill, NC 27599, USA.

*Corresponding author. Email: frankl@email.unc.edu (F.A.L.); ejalex@email.unc.edu (E.J.A.)

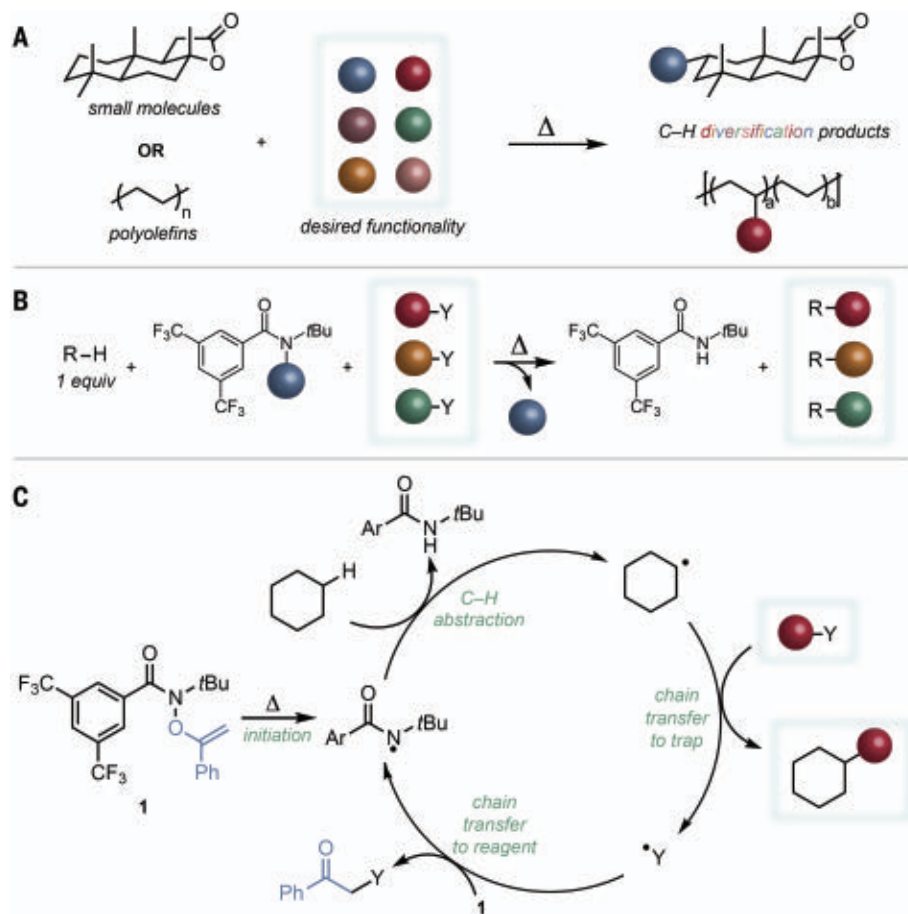


Fig. 1. Aliphatic C-H diversification using N-functionalized amides. (A) A universal approach to C-H diversification would enable the introduction of a range of desired functionality onto small molecules and commodity polyolefins. (B) An N-functionalized amide and a diverse set of chain transfer agents constitute a general platform for C-H diversification. (C) The mechanistic hypothesis for C-H diversification using O-alkenylhydroxamates separates the HAT reagent from the chain transfer agent. Ar, 3,5-bis(trifluoromethyl)phenyl.

introduction of a range of desirable functionality to small-molecule substrates with substrate as the limiting reagent.

An estimated 95% of the economic value of plastics is lost after a single use (6). Specifically, branched polyolefins represent >35% of polymers produced worldwide but undergo deleterious chain scission events during mechanical reprocessing or polymer functionalization, which degrades their thermomechanical properties and contributes to their poor recycling rate (<5% in the United States) (7, 8). Developing synthetic methods to place desired functionality on postconsumer branched polyolefins would lead to performance-advantaged thermoplastics derived from single-stream or mixed plastic waste (9, 10). The new materials realized from such platform methods could serve as sustainable substitutes to current high-value materials that are derived from petrochemical resources, thus representing an example of polymer upcycling (11).

Currently, a number of transformations of aliphatic C-H bonds exist and are used for the late-stage diversification of drug-like molecules and commodity polymers, but most of these use either nearby directing groups to control reaction site selectivity or involve promiscuous reactive intermediates that limit the scope of these approaches (12, 13). A notable exception that uses substrate as the limiting reagent is the use of high-valent transition metal-oxo complexes in aliphatic C-H functionalization, but this approach is limited by the scope of accessible transformations because of the use of highly oxidizing intermediates (14, 15). Intermolecular alkylation or borylation of C-H bonds using rhodium catalysis is also well developed, but the requirement for donor-acceptor diazo reagents for alkylation limits overall scope, and the use of a precious metal limits high-volume applications in polymer science (16, 17). Singlet carbenes generated from the photochemical or thermal

decomposition of diazirines represent an efficient C-H functionalization strategy for polymer cross-linking and biopolymer photo-affinity labeling, but the required substitution pattern of the diazirine and limited functional group tolerance hinders broad applicability (18, 19). Furthermore, several valuable C-H transformations, such as aliphatic C-H iodination and C-H methylation, remain limited regardless of approach. A universal strategy for aliphatic C-H functionalization, in which a wide array of functionality can be placed site selectively in an intermolecular transformation on both complex organic substrates and commodity polymers, remains a grand challenge (Fig. 1A) (20).

Recent studies have demonstrated the utility of heteroatom-centered radicals to facilitate site-selective, intermolecular functionalizations of unactivated aliphatic C-H bonds on a variety of small molecules and materials, constituting a complementary strategy to metal-catalyzed methods (21–26). These reactions principally harness the capacity of a tuned, nitrogen-centered radical to achieve facile hydrogen atom transfer (HAT) from strong, unactivated aliphatic C-H sites. A critical drawback to these previous studies is the requirement for direct group transfer of the functionality appended to nitrogen, which greatly restricts the diversity of products accessible through the HAT platform. With this in mind, we hypothesized that decoupling the formation of the nitrogen-centered radical responsible for HAT from the chain transfer step would unlock a universal C-H diversification manifold applicable to a vast range of transformations (Fig. 1B). We identified an O-alkenylhydroxamate (**1**) as an ideal reagent capable of forming reactive nitrogen-centered radicals while also manifesting slow enough chain transfer kinetics for external radical traps to outcompete it in substrate functionalization (Fig. 1C). We hypothesized that such a versatile C-H diversification strategy would encompass many important transformations, including ones inaccessible with current synthetic technology, and extend to areas ranging from the late-stage C-H diversification of complex molecules to applications in the transformation of postconsumer plastic waste to functional polyolefins.

Our initial studies demonstrated the versatility of easily accessed, shelf-stable O-alkenylhydroxamate **1** for the intermolecular, aliphatic C-H diversification of a range of small molecules (Fig. 2). The C-H functionalizations promoted by reagent **1** proceeded simply upon mild heating (70°C) or visible light irradiation without the need for an exogenous initiator, which is an enabling aspect of the approach. The C-H diversification of cyclooctane with substrate as limiting reagent was successful using 10 diverse trapping agents in good to

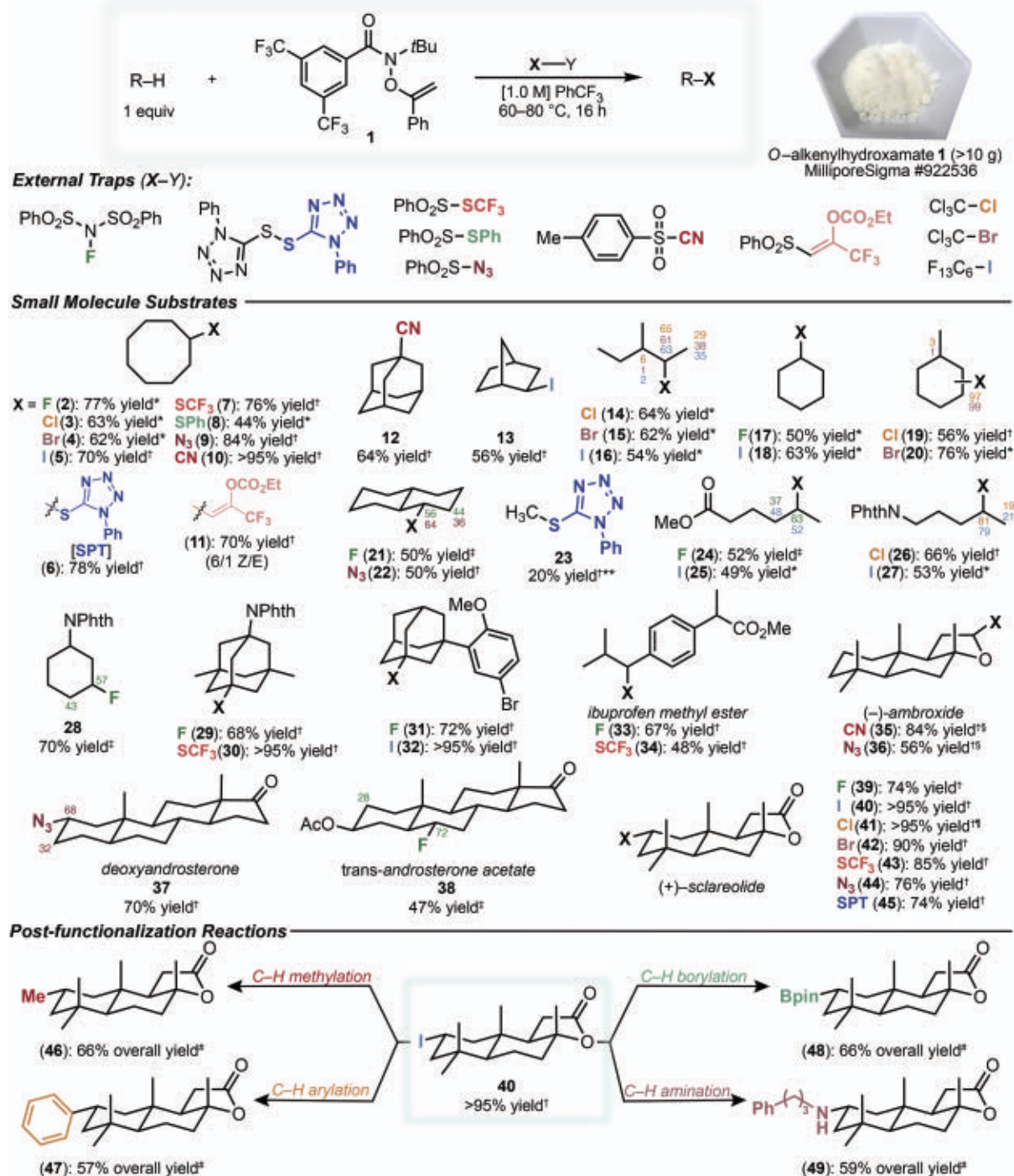


Fig. 2. C–H diversification of small molecules using reagent 1. Yields refer to combined isolated products or were determined by gas chromatography (GC), ^1H -NMR, or ^{19}F -NMR with the addition of internal standard. Percent functionalizations are provided in examples involving minor regioisomers; see

the supplementary materials for reaction details. *GC yield. † ^1H -NMR yield using internal standard. ‡ ^{19}F -NMR yield using internal standard. §Mixture of diastereomers, see the supplementary materials. ¶Irradiated with blue light. #Isolated yield. **Reaction performed under 50 atm methane.

excellent yield, establishing the broad scope of the platform (**2** to **11**). Practical intermolecular, aliphatic C–H iodination sets the stage for a range of challenging C–H transformations (vide infra) (**27**). Whereas there are extant methods

available for a subset of these reactions, examples using substrate as the limiting reagent remain quite rare; commonly, the alkane is used in large excess (>5 equivalents) and often as a reaction solvent. Furthermore, there are

no platforms for aliphatic C–H functionalization that rival the synthetic scope demonstrated herein with respect to both the diversity of accessible transformations and the viable substrates ranging from small molecules to

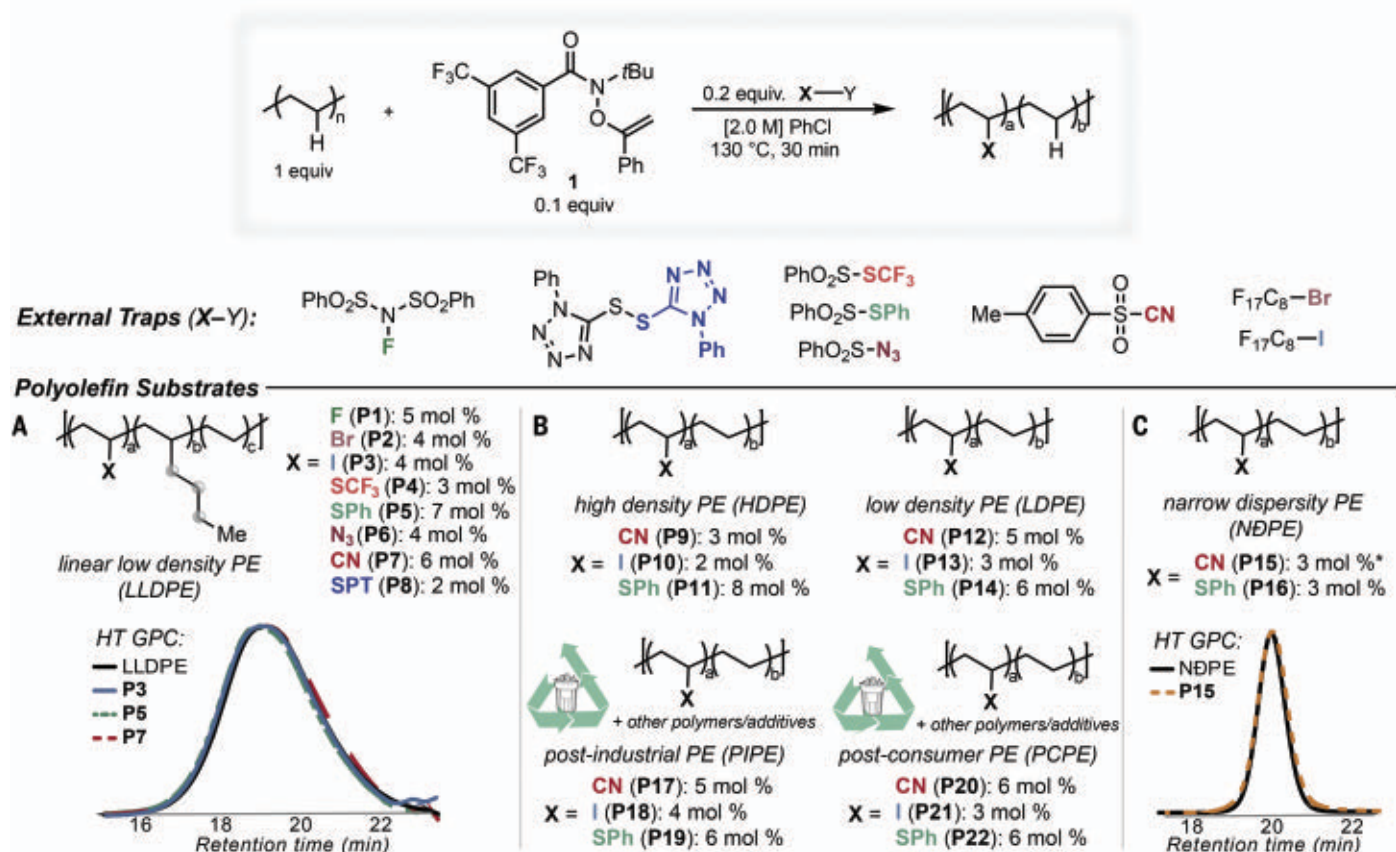


Fig. 3. C–H diversification of polyolefins using reagent 1. Polymer functionalization is indicated as mol % compared with repeat unit and were determined by ^1H -NMR on the isolated product. Gray spheres indicate minor regioisomers; see the supplementary materials for reaction details. High-temperature gel-permeation chromatography (HT-GPC) was conducted at 140°C in trichlorobenzene. *Reaction time was 10 min.

postconsumer waste. Although we targeted many synthetically valuable C–H transformations, additional processes are easily envisioned using alternative radical traps.

We next applied the C–H diversification to several representative small-molecule substrates. Diverse cyclic and linear hydrocarbons react efficiently using substrate as limiting reagent (**12** to **22**). The sterically dictated site selectivities controlled by the bulky *N*-*t*Bu amidyl radical favor accessible secondary C–H sites over weaker, tertiary C–H bonds, which are commonly the most reactive in C–H functionalizations (**14** to **16**, **19** to **22**). For comparison, prior efforts toward C–H diversification through HAT using photoredox catalysis strongly favored tertiary functionalization; such tertiary-selective functionalization is also characteristic of reactions involving HAT with sulfate radicals (28, 29). The transformation of the unreactive C–H bond of gaseous methane remains a considerable challenge for any C–H functionalization. The strong N–H bond (110.7 kcal/mol) of the parent amide of **1** suggested that methane HAT (C–H bond ~105 kcal/mol) could be viable (30). As a demonstration of the notable reactivity of

the amidyl radical in HAT, we successfully performed the (phenyltetrazole)thiolation of methane under our standard conditions to deliver **23** in 20% yield with respect to **1**. Functionalized substrates containing electron-withdrawing groups (**24** to **28**) exhibit strong polar effects in discriminating between methylene sites, with sites distal to the electron-withdrawing group preferred (31). With respect to the mechanism of reactions involving **1**, a C–H iodination competition experiment between cyclohexane and *d*₁₂-cyclohexane proceeded with a *k*_H/*k*_D of 6.4, consistent with an irreversible aliphatic C–H HAT. Additionally, the C–H (phenyltetrazole)thiolation reaction produces the α -SPT acetophenone byproduct, consistent with the chain transfer mechanism outlined in Fig. 1C. The notable sterically and electronically dictated site selectivities characteristic of this platform, when combined with the breadth of accessible C–H transformations, enable a wealth of valuable late-stage diversifications of complex molecules as described below.

We next examined the C–H functionalization of several representative natural products and drug derivatives to highlight the scope

of our approach. The reactions of adamantyl substrates were highly efficient (**29** to **32**). The benzylic functionalization of ibuprofen methyl ester provided fluorination and trifluoromethylthiolation products **33** and **34**, respectively, as single regioisomers in contrast to previous C–H functionalizations of this substrate (28). Functionalization of terpenoid and steroid natural products—complex molecules with a multitude of aliphatic C–H sites—favors the activated C–H site α to the ether oxygen atom of (–)-ambroxide (**35** and **36**), whereas reaction of deoxyandrosterone favored functionalization of the C2 position of the A ring (**37**) and reaction of *trans*-androsterone acetate favored a single diastereomer of a B-ring fluoride (**38**). For comparison, a previous C–H fluorination of this substrate with Selectfluor yielded greater than seven alkyl fluorides, with none formed in greater than 6% yield (32). Last, we performed several C–H functionalizations of the terpenoid natural product (+)-sclareolide, favoring the most reactive A-ring methylene site (**39** to **45**; for reaction optimization studies, see table S1). In each case, a single regioisomer was obtained in good to excellent yield with high (>10:1)

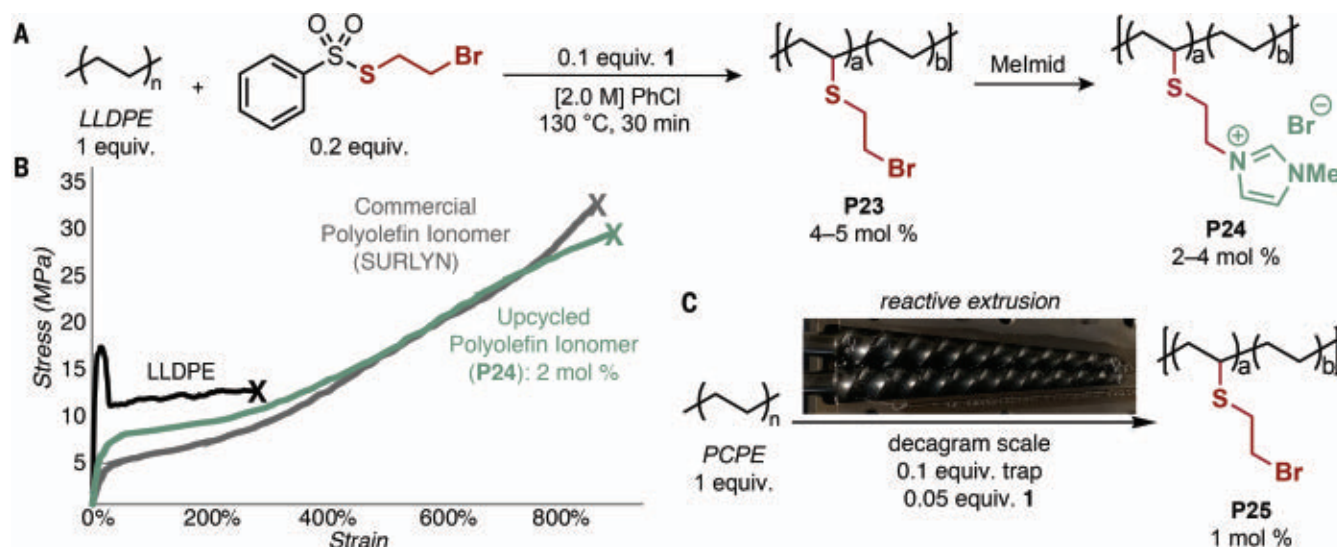


Fig. 4. Access to polyolefin ionomers through C-H functionalization. (A) Polyolefin C-H functionalization enabled the production of ionomers from commercial plastics in a two-step approach. (B) Tensile tests demonstrate the change in polymer properties upon functionalization and how they compare with a commercial sample of Dow SURLYN. Strain rate = 1.0 mm/s. (C) Reactive extrusion was performed on PCPE at a decagram scale.

diastereoselectivity, including the C-H iodination which delivers iodide **40** in virtually quantitative yield. The present platform thus offers a powerful tool for the late-stage introduction of fluorinated groups at unactivated aliphatic sites in complex molecules for modulating the absorption, distribution, metabolism, and excretion properties of drug-like compounds.

With respect to late-stage diversification, the versatility of our approach enables more valuable, yet rare, C-H transformations from now easily accessible, functionalized compounds. As a second step after the highly efficient iodination of sclareolide (>95% yield), reaction with Me_2CuLi delivers the formal C-H methylation product **46** in good yield as a single diastereomer, furnishing a two-step protocol to investigate “magic methyl” effects through late-stage, intermolecular methylation of unactivated aliphatic C-H bonds (33, 34). Alternatively, iron-catalyzed cross-coupling of **40** with PhMgBr leads to the C-H arylation product **47**; previous C-H arylation of this substrate required the use of superstoichiometric amounts of (+)-sclareolide (35). Facile borylation of **40** using B_2cat_2 followed by transesterification yielded **48** as a single product, another transformation with very limited precedent using substrate as the limiting reagent (36–38). Finally, the copper-catalyzed cross-coupling of **40** with a primary alkyl amine delivered the C-H amination product **49**, constituting a formal dehydrogenative alkane-amine coupling (39). Other attractive C-H transformations are also easily envisioned capitalizing on the versatility of the phenyltetrazole sulfone group, which can be easily accessed from product **45** (40).

We envisioned that this versatile C-H diversification strategy could unlock numerous transformations on branched polyolefins. Commercial approaches to polyolefin functionalization proceed through high-energy radical processes that selectively abstract tertiary C-H bonds in branched polymers, resulting in β -scission processes that deteriorate thermomechanical properties. We hypothesized that the high regioselectivity of HAT involving reagent **1** favoring methylene sites would prevent polymer chain scission by eliminating the formation of tertiary radicals during reactive processing, and the generality of this method would enable access to a range of branched polyolefins with polar functionality. Such polar polyolefins, which are inaccessible using traditional Ziegler-Natta or metallocene catalysis, enhance interfacial adhesion and provide sites for controlled polymer deconstruction (41). Linear low-density polyethylene (LLDPE; Dow DNDA-1081) was chosen as a model branched polyolefin to exemplify this method (melting temperature of 122°C; 36 branches per 1000 carbons). As a representative transformation to introduce polar functionality incompatible with early transition metal catalysts, cyanation of LLDPE with **1** under homogeneous conditions (130°C in chlorobenzene) proceeded efficiently with selectivity for methylene sites and involved no discernable chain scission, as confirmed by size-exclusion chromatography (SEC) and a variety of one- and two-dimensional nuclear magnetic resonance (NMR) techniques (Fig. 3A and figs. S1 and S12 to S15). More precise analysis of selectivity was obtained using a narrow-dispersity PE (NDPE), made through the reduction of poly(1,4-butadiene).

The SEC chromatogram was virtually identical before and after functionalization, demonstrating the lack of chain scission or long-chain branching accompanying polymer functionalization (Fig. 3C). By contrast, an analogous cyanation using dicumyl peroxide as a radical initiator in place of **1** yielded no functionalization and a decrease in polymer molecular weight. All polymer functionalizations target a maximum of 10 mol % repeat-unit modification to add functionality while maintaining the beneficial semicrystalline nature of the material.

In addition to polyolefin cyanation, the installations of fluoride, bromide, iodide, trifluoromethylthiol, thiophenyl, azido, and (phenyltetrazole)thiol groups onto LLDPE exemplified the versatility of this approach. Several of these polyolefin C-H transformations deliver products inaccessible by other means (24, 25, 42, 43). To further extend the scope, C-H cyanation, thiophenylation, and iodination were successful on complementary substrates, including highly crystalline high-density PE (HDPE), branched LDPE (41 branches per 1000 carbons), postindustrial waste PE (PIPE) remnants from packaging forms, and postconsumer waste PE (PCPE) obtained from PE foam packaging (Fig. 3B). Furthermore, thiophenylation of isotactic polypropylene (500 branches per 1000 carbons) proceeded successfully without discernable chain scission (fig. S9), demonstrating the value of this method for these tough and highly branched thermoplastics. It is notable that functionalization proceeded efficiently even with an undefined mixture of oxidation by-products and/or additives in PCPE evident by infrared and ^1H -NMR spectroscopy, indicating the tolerance

of this method to common impurities in plastic waste.

The ability to place diverse functionality onto polyolefins through this universal approach provides an opportunity to substitute current high-value plastics, and create new ones, using postconsumer waste as a starting material. Polyolefin ionomers such as SURLYN are a high-value class of thermoplastics toughened by ionic cross-links, with applications ranging from structural adhesives to ion-conducting membranes (44). However, SURLYN is synthesized through radical copolymerization of acrylic acid and ethylene, which limits polymer architecture to a highly branched microstructure, precludes use of α -olefins as comonomers, and limits functional group identity to a carboxylate. These limitations compromise the potential strength, toughness, and transport properties of the materials. There are currently limited strategies to prepare polyolefin ionomers on materials made through Ziegler-Natta or related catalytic approaches (i.e., LLDPE or HDPE). Given the structural fidelity and lack of long-chain branching of our polyolefin functionalization approach, we envisioned creating ionomers from polyolefins through late-stage functionalization. The generality of the C–H functionalization mediated by **1** enabled the development of a 2-bromoethyl thiosulfonate radical trapping reagent that installed a primary bromide onto the polyolefin (**P23**; Fig. 4A). Displacement of the bromide by methyl imidazole yielded imidazolium-functionalized LLDPE (**P24**), which represents a formal copolymerization of α -olefins with an ion-containing vinyl monomer. The ionomers had distinct properties from the parent LLDPE, including solubility in polar aprotic solvents, a decreased melting temperature, and enhanced clarity (fig. S25). Introduction of the imidazolium to only 2 mol % of the repeat units substantially changed the material from a thermoplastic to a tough elastomer (Fig. 4B). Although yield stress and the Young's modulus (E) of **P24** decreased compared with the parent LLDPE, the strain at break (ϵ_B) quadrupled and the stress at break (σ_B) more than doubled, leading to an increase in the tensile toughness (U_T) of >550%. These tensile properties compare favorably to a commercial sample of Dow SURLYN, demonstrating the marked effect that a small amount of targeted functionalization can have on material properties.

Collectively, the ability to produce an ionomer from a postconsumer waste stream with functional equivalence to the thermomechanical properties of a high-value commercial material make this upcycled material a potentially environmentally sustainable substitute for polyolefin ionomers (45). The translational potential of this method was further

demonstrated through C–H functionalization of PCPE in a twin-screw extruder, which is the infrastructure used for processing plastic waste. Reacting reagent **1** with a 5 mol % 2-bromoethyl thiosulfonate radical trapping reagent, we procured 7 g of 1 mol % bromoethylthiolated PCPE (**P25**; Fig. 4C). Reaction of the extruded material with methyl imidazole afforded a large-scale synthesis of the polyolefin ionomer. Although further reagent development is required to make this material an economically sustainable substitute, this C–H functionalization platform enables access to a library of polyolefin ionomers, among other materials, from plastic waste. These ionomers can be systematically studied to assess the impact of ion identity, ion content, and polymer branching on polyolefin properties and circularity, and could ultimately contribute to a more sustainable plastics economy.

REFERENCES AND NOTES

- J. F. Hartwig, *J. Am. Chem. Soc.* **138**, 2–24 (2016).
- H. M. L. Davies, *J. Org. Chem.* **84**, 12722–12745 (2019).
- M. C. White, *Science* **335**, 807–809 (2012).
- B. Hong, T. Luo, X. Lei, *ACS Cent. Sci.* **6**, 622–635 (2020).
- T. Cernak, K. D. Dykstra, S. Tyagarajan, P. Vachal, S. W. Krska, *Chem. Soc. Rev.* **45**, 546–576 (2016).
- D. E. MacArthur, D. Waughray, M. R. Stuchty, "The new plastics economy: Rethinking the future of plastics" (World Economic Forum, 2016); https://www3.weforum.org/docs/WEF_The_New_Plastics_Economy.pdf.
- A. Rahimi, J. M. Garcia, *Nat. Rev. Chem.* **1**, 0046 (2017).
- A. E. Hamielec, P. E. Gloor, S. Zhu, *Can. J. Chem. Eng.* **69**, 611–618 (1991).
- J. B. Williamson, S. E. Lewis, R. R. Johnson 3rd, I. M. Manning, F. A. Leibfarth, *Angew. Chem. Int. Ed.* **58**, 8654–8668 (2019).
- F. P. Britt *et al.*, "Report of the Basic Energy Sciences Roundtable on Chemical Upcycling of Polymers" (Office of Science and Technical Information, US Department of Energy, 2019); <https://www.osti.gov/biblio/1616517>.
- L. T. J. Korley, T. H. Epps 3rd, B. A. Helms, A. J. Ryan, *Science* **373**, 66–69 (2021).
- Q. An *et al.*, *J. Am. Chem. Soc.* **142**, 6216–6226 (2020).
- N. K. Boan, M. A. Hillmyer, *Chem. Soc. Rev.* **34**, 267–275 (2005).
- D. Ravelli, M. Fagnoni, T. Fukuyama, T. Nishikawa, I. Ryu, *ACS Catal.* **8**, 701–713 (2018).
- M. C. White, J. Zhao, *J. Am. Chem. Soc.* **140**, 13988–14009 (2018).
- K. Liao *et al.*, *Nat. Chem.* **10**, 1048–1055 (2018).
- Y. Kondo *et al.*, *J. Am. Chem. Soc.* **124**, 1164–1165 (2002).
- M. L. Lepage *et al.*, *Science* **366**, 875–878 (2019).
- S.-S. Ge *et al.*, *RSC Advances* **8**, 29428–29454 (2018).
- D. C. Blakemore *et al.*, *Nat. Chem.* **10**, 383–394 (2018).
- V. A. Schmidt, R. K. Quinn, A. T. Brusoe, E. J. Alexanian, *J. Am. Chem. Soc.* **136**, 14389–14392 (2014).
- R. K. Quinn *et al.*, *J. Am. Chem. Soc.* **138**, 696–702 (2016).
- W. L. Czaplyski, C. G. Na, E. J. Alexanian, *J. Am. Chem. Soc.* **138**, 13854–13857 (2016).
- C. M. Plummer *et al.*, *Polym. Chem.* **9**, 1309–1317 (2018).
- J. B. Williamson, W. L. Czaplyski, E. J. Alexanian, F. A. Leibfarth, *Angew. Chem. Int. Ed.* **57**, 6261–6265 (2018).
- J. B. Williamson *et al.*, *J. Am. Chem. Soc.* **141**, 12815–12823 (2019).
- A. Artaryan *et al.*, *J. Org. Chem.* **82**, 7093–7100 (2017).
- K. A. Margrey, W. L. Czaplyski, D. A. Nicewicz, E. J. Alexanian, *J. Am. Chem. Soc.* **140**, 4213–4217 (2018).
- H. Wu *et al.*, *Angew. Chem. Int. Ed.* **54**, 4070–4074 (2015).
- M. M. Tierney, S. Crespi, D. Ravelli, E. J. Alexanian, *J. Org. Chem.* **84**, 12983–12991 (2019).
- C. R. Pitts *et al.*, *J. Am. Chem. Soc.* **136**, 9780–9791 (2014).
- R. D. Chambers *et al.*, *J. Fluor. Chem.* **129**, 811–816 (2008).
- H. Schönherr, T. Cernak, *Angew. Chem. Int. Ed.* **52**, 12256–12267 (2013).
- K. Feng *et al.*, *Nature* **580**, 621–627 (2020).
- I. B. Perry *et al.*, *Nature* **560**, 70–75 (2018).
- R. Oeschger *et al.*, *Science* **368**, 736–741 (2020).
- C. Shu, A. Noble, V. K. Aggarwal, *Nature* **586**, 714–719 (2020).
- Y. Cheng, C. Mück-Lichtenfeld, A. Studer, *Angew. Chem. Int. Ed.* **57**, 16832–16836 (2018).
- C. D. Matier, J. Schwaben, J. C. Peters, G. C. Fu, *J. Am. Chem. Soc.* **139**, 17707–17710 (2017).
- R. R. Merchant *et al.*, *Science* **360**, 75–80 (2018).
- M. Häubler, M. Eck, D. Rothauer, S. Mecking, *Nature* **590**, 423–427 (2021).
- D. Liu, C. W. Bielawski, *Polym. Int.* **66**, 70–76 (2017).
- C. M. Plummer, L. Li, Y. Chen, *Polym. Chem.* **11**, 6862–6872 (2020).
- B. P. Grady, *Polym. Eng. Sci.* **48**, 1029–1051 (2008).
- C. Vadenbo, S. Hellweg, T. F. Astrup, *J. Ind. Ecol.* **21**, 1078–1089 (2017).

ACKNOWLEDGMENTS

Funding: This work was supported by the National Institute of General Medical Sciences (award no. R35 GM131708 to E.J.A.) and the Air Force Office of Scientific Research (award no. 17RT0487 under the Young Investigator Program to F.A.L.). J.W.A. thanks the Henry G. Luce Foundation and the University of North Carolina–Chapel Hill (UNC) for a Clare Boothe Luce Graduate Student Fellowship and the UNC Chemistry Department for the Venable Award. The UNC Department of Chemistry's Mass Spectrometry Core Laboratory provided expertise and instrumentation that enabled this study with support from the National Science Foundation (grant no. CHE-1726291) and the National Institute of General Medical Sciences of the National Institutes of Health (grant no. R35GM118055). The UNC Department of Chemistry's NMR Core Laboratory provided expertise and instrumentation that enabled this study with support from National Science Foundation (grant nos. CHE-1828183 and CHE-0922858). We thank the Dow Chemical Company for supplying samples of SURLYN ionomers and HighCube or providing samples of postindustrial and postconsumer plastic waste. **Author contributions:** E.J.A. and F.A.L. conceived of the work. All authors designed the experiments. T.J.F., J.W.A., E.K.N., and A.S.M. performed and analyzed the experiments. E.J.A., F.A.L., T.J.F., and J.W.A. prepared the manuscript. **Competing interests:** E.J.A. and F.A.L. are inventors on US provisional patent application 63/188,215 covering the diversification of C–H bonds in small molecules and polyolefins, including the upcycling of polymers, filed by UNC. **Data and materials availability:** Experimental and characterization data are available in the supplementary materials.

SUPPLEMENTARY MATERIALS

science.org/doi/10.1126/science.abh4308
Materials and Methods
Figs. S1 to S18
Tables S1 to S3
References (46–77)

8 March 2021; resubmitted 10 August 2021
Accepted 20 December 2021
10.1126/science.abh4308

MATERIALS SCIENCE

Multiscale engineered artificial tooth enamel

Hewei Zhao^{1†}, Shaojia Liu^{1†}, Yan Wei^{2†}, Yonghai Yue^{1†}, Mingrui Gao¹, Yangbei Li¹, Xiaolong Zeng¹, Xuliang Deng^{2*}, Nicholas A. Kotov^{3,4*}, Lin Guo^{1*}, Lei Jiang^{1,5}

Tooth enamel, renowned for its high stiffness, hardness, and viscoelasticity, is an ideal model for designing biomimetic materials, but accurate replication of complex hierarchical organization of high-performance biomaterials in scalable abiological composites is challenging. We engineered an enamel analog with the essential hierarchical structure at multiple scales through assembly of amorphous intergranular phase (AIP)-coated hydroxyapatite nanowires intertwined with polyvinyl alcohol. The nanocomposite simultaneously exhibited high stiffness, hardness, strength, viscoelasticity, and toughness, exceeding the properties of enamel and previously manufactured bulk enamel-inspired materials. The presence of AIP, polymer confinement, and strong interfacial adhesion are all needed for high mechanical performance. This multiscale design is suitable for scalable production of high-performance materials.

Effective combination of diverse mechanical properties is highly desirable for engineering applications but is difficult to realize (1), especially for properties that require contradictory material design elements such as high stiffness, hardness, viscoelasticity, strength, and toughness (2–4). Tooth enamel—the outer shell of teeth with a thickness of several millimeters (Fig. 1A)—is the hardest tissue in the human body and exhibits excellent resistance to deformational and vibrational damage (5, 6). This unusual combination of properties originates from enamel's hierarchical architecture, which is made up of 96 wt % hydroxyapatite (HA) nanowires interconnected by confined biomolecules (7). Most crystalline segments in HA nanowires in natural enamel are interconnected by amorphous intergranular phase (AIP, Mg-substituted amorphous calcium phosphate) (8), which considerably influences the mechanical performance of enamel (9, 10). Efforts have been made to mimic the parallel arrangement of nanowires in enamel to improve the stiffness, hardness, or viscoelasticity (2, 11–14) of nanocomposites, but physical forms are usually limited to coatings with submillimeter thicknesses. It has proven difficult to assemble analogs of enamel that retain full structural complexity of the biological prototype with several essential structural elements responsible for their mechanical and biological functions (i.e., nanowire alignment, presence of AIP, and the confined organic matrix) as bulk machinable materials.

The hierarchical structure of tooth enamel provides a biomimetic blueprint. Self-assembled HA nanowires with 30- to 50-nm diameters align with each other, forming nanocolumns

(Fig. 1B) that represent the key structural motif of enamel. The AIP layer closely connects to the HA nanowires and has a thickness of 3 to 10 nm (Fig. 1, C and D, and figs. S1 and S2). This interface characterization implies that there are strong chemical bonds between the AIP layer and HA nanowires, which enhance the interface connectivity and contribute to mechanical improvement (Fig. 1E and fig. S3).

Our materials are made from aligned HA nanowires coated with amorphous ZrO₂ serving as the AIP. First, HA nanowires with length ~10 μm and diameter ~30 nm [Fig. 1F (left) and fig. S4] were synthesized by the solvothermal method (15). The HA nanowires grew along the [001] direction with no obvious defects (fig. S5) and were then coated with a ~3-nm amorphous layer of ZrO₂ (A-ZrO₂) through in situ hydrolysis of Zr precursors, followed by subsequent annealing to form the interfaces between the ceramics in the crystalline and amorphous phases [Fig. 1F (middle)]. The geometry and morphology of the HA nanowires were retained, and the amorphous layer was tightly connected to the crystalline core of HA [Fig. 1F (right)]. The amorphous state and constituents of the coated layer were demonstrated by high-resolution transmission electron microscopy [Fig. 1F (right)], energy dispersive x-ray spectroscopy (EDS) mapping (fig. S6), and x-ray diffraction patterns (fig. S7). The abundance of surface groups –OH and PO₄^{3–} on HA absorbed Zr⁴⁺, contributing to the formation of the thin, amorphous ZrO₂ layer (Fig. 1F). To verify the role of the AIP in mechanical performance enhancement, in situ tensile tests were performed on HA and A-ZrO₂-coated HA (HA@A-ZrO₂) nanowires with a push-to-

pull (fig. S8) platform and a Picoindenter 85 nanoindenter in an environmental scanning electron microscope (ESEM). The fracture strength and strain of HA@A-ZrO₂ nanowires are ~1.6 GPa and ~6.2%, respectively (Fig. 1G), which are 2.5 and 1.6 times as high as those of HA nanowires (~0.65 GPa and ~4%, respectively), surpassing the mechanical properties of bulk HA (16). Detailed observation of the tensile process of the HA@A-ZrO₂ nanowire reveals that the nanowires can endure tensile deformation as large as ~5.2% before fracture (fig. S9), whereas the value of HA is ~2.5%. The fracture surface of the HA@A-ZrO₂ surface forms a crack deflection (fig. S10) instead of the brittle failure usually seen in brittle ceramics, which contributed to fracture strain improvement due to the presence of the amorphous layer.

Dual-directional freezing of HA@A-ZrO₂ nanowire dispersions in the presence of polyvinyl alcohol (PVA) was used to self-assemble macroscale composites with parallel arrangement of the nanowires (Fig. 1H). The polydimethylsiloxane (PDMS) wedge produced a bidirectional temperature gradient, driving the ice crystal growth in perpendicular and parallel directions (Fig. 1H). The perpendicular growth of the ice crystals forced the HA@A-ZrO₂ nanowires and PVA to occupy the gaps between ice lamellae, and the parallel growth forced them to acquire a parallel orientation (fig. S11). After freeze-drying (fig. S12) and mechanical compression, dense artificial tooth enamel (ATE) was produced (Fig. 1H and fig. S13).

ATE is machinable and can be formed into tooth-like macroscopic shapes (Fig. 1I) with densely packed parallel columns with microscale alignment (Fig. 1J). X-ray nanotomography of ATE reveals that the nanowires exhibit an overall architecture of parallel columns for the bulk composite (fig. S14). The AIP layers between the HA nanowires are nearly identical to those in enamel (Fig. 1C), as they have a thickness of ~5 nm (Fig. 1K). Higher-magnification observation shows the AIP and verifies that the HA and AIP are closely connected (Fig. 1L). EDS mapping and line scanning (fig. S15) of the crystal-amorphous-crystal interface further demonstrate that amorphous ZrO₂ fills the gaps between HA nanowires. Spectroscopic characterizations (figs. S16 and S17) including Raman, Fourier transform infrared spectroscopy (FTIR), and x-ray photoelectron spectroscopy implied strong chemical adhesion (Fig. 1M) as a result of coordination between Zr⁴⁺ and O of PO₄^{3–} and –OH. This is in contrast to simple physical

¹School of Chemistry, Beijing Advanced Innovation Center for Biomedical Engineering, Beihang University, Beijing 100191, China. ²Department of Geriatric Dentistry, NMPA Key Laboratory for Dental Materials, National Engineering Laboratory for Digital and Material Technology of Stomatology, Beijing Laboratory of Biomedical Materials, Peking University School and Hospital of Stomatology, Beijing 100081, China. ³Department of Chemical Engineering, Department of Materials Science, Biointerface Institute, University of Michigan, Ann Arbor, MI 48109, USA. ⁴Michigan Institute of Translational Nanotechnology (MITRAN), Ypsilanti, MI 48198, USA. ⁵CAS Key Laboratory of Bio-Inspired Materials and Interfacial Science, CAS Center for Excellence in Nanoscience, Technical Institute of Physics and Chemistry, Chinese Academy of Sciences, Beijing 100190, China.

*Corresponding author. Email: guolin@buaa.edu.cn (L.G.); kotov@umich.edu (N.A.K.); kqdengxuliang@bjmu.edu.cn (X.D.)

†These authors contributed equally to this work.

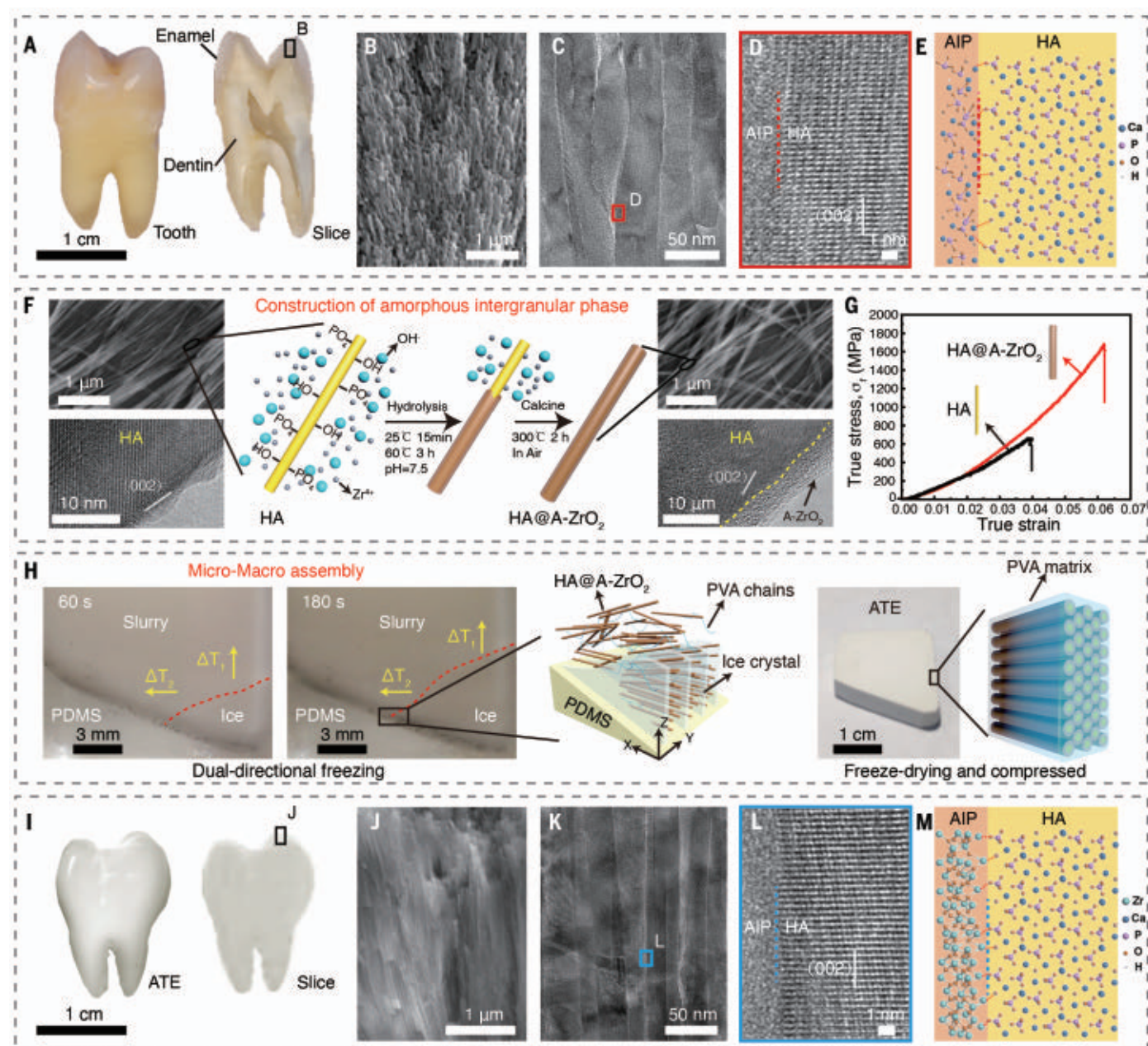


Fig. 1. Tooth enamel and synthesis of artificial tooth enamel (ATE).

(A) Optical photographs of tooth enamel, including a closeup view and a sectional slice perpendicular to the midcoronal cervical plane. (B) Scanning electron microscope (SEM) image of tooth enamel. (C) Transmission electron microscopy (TEM) image of tooth enamel. (D) Enlarged TEM image taken from the red zone in (C). (E) Molecular structure of HA with amorphous intergranular phase (AIP). (F) Schematic illustration of construction of the mimicked tooth enamel process; the corresponding SEM and TEM images of HA and HA@A-ZrO₂ are displayed on the left and right side, respectively. The exposed -OH on HA

and the balance between nucleation and growth of ZrO₂ precursor is the key to formation of the amorphous thin layer. (G) The tensile mechanical performance of HA with and without AIP, showing that the AIP indeed makes the nanowire stronger and tougher. (H) Schematic illustration of micro- and macro-assembly of the HA@A-ZrO₂ nanowires coupled with PVA. (I) Optical photographs of ATE, including a closeup view and a sectional slice perpendicular to the midcoronal cervical plane. (J) SEM image of ATE. (K) TEM image of ATE. (L) Enlarged TEM image taken from the blue zone in (K). (M) Molecular structure of HA and amorphous ZrO₂ (A-ZrO₂).

absorption (17), which may contribute to improved mechanical properties.

We evaluated the mechanical performance of ATE by both nanoindentation (for stiffness, hardness, and viscoelasticity, with load direction parallel to the nanowires) and the three-

point bending test (for strength and toughness, with load direction perpendicular to the nanowires). To explore the role of each structural element, we also produced two benchmark HA-based composites, namely ATE from nanowires with no AIP (ATE-NAIP) (fig. S18) and

a composite with an HA@A-ZrO₂ nanowire loading similar to ATE but with no ordered microstructure (ATE-NOM) (fig. S19). We evaluated Young's modulus (E), hardness (H), storage modulus (E'), damping coefficient ($\tan \delta$), strength (σ), and toughness (K_{IC}) of these

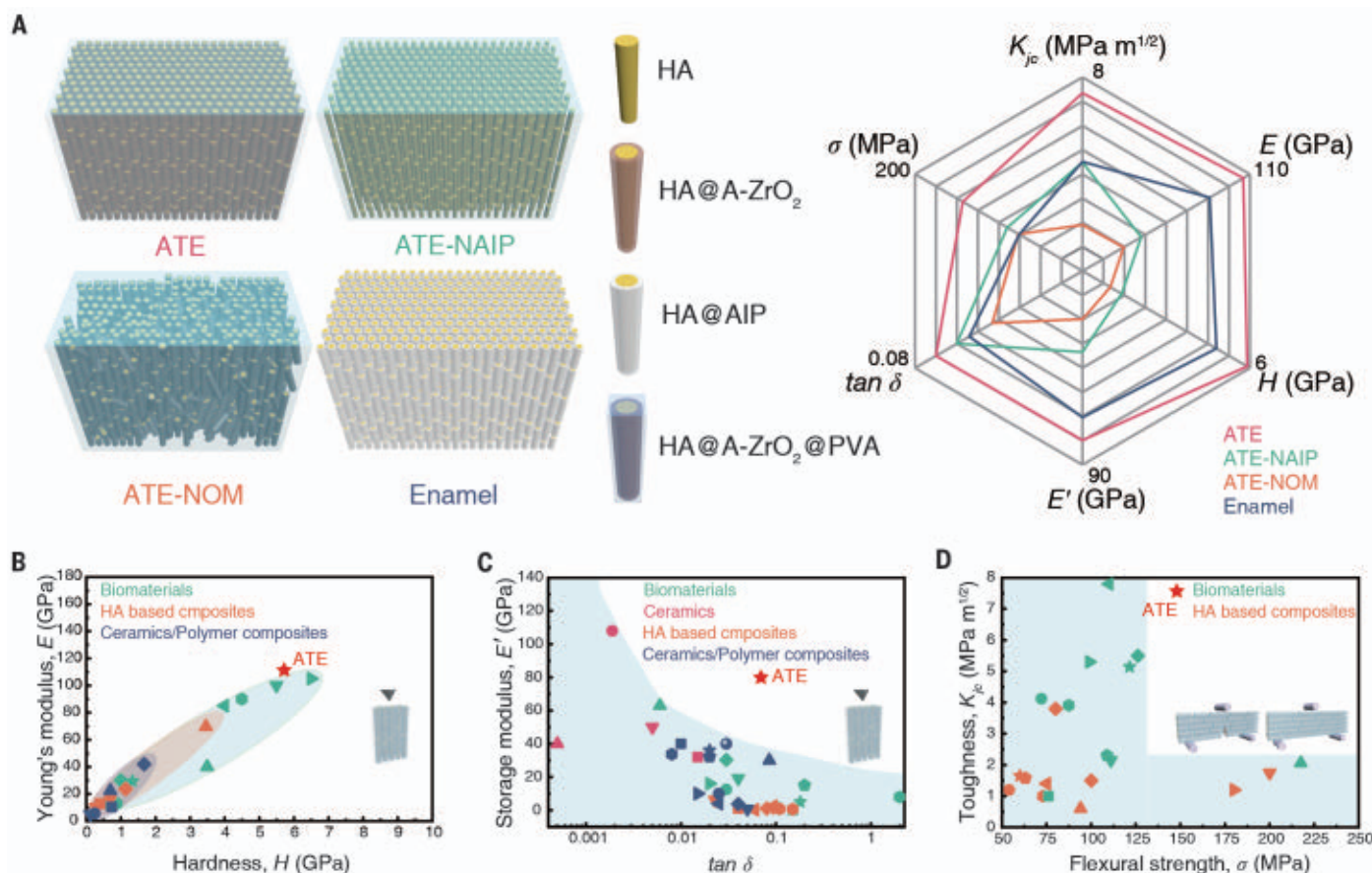


Fig. 2. Mechanical properties of ATE. (A) Left, schematic illustration of ATE, ATE-NAIP, ATE-NOM, and enamel; right, mechanical performance of different enamel-like composites with Young's modulus (E), hardness (H), storage modulus (E'), damping coefficient ($\tan \delta$), flexural strength (σ), and toughness (K_{jc}), for ATE, ATE-NAIP, ATE-NOM, and enamel plotted as a radar map. (B) Young's modulus and hardness of ATE and referenced

engineering materials including biomaterials and HA/other ceramic-based composites. The performance of ATE is outstanding. (C) Storage modulus and damping coefficient of ATE compared with biomaterials, HA-based composites, ceramics, and ceramic-based composites. (D) Flexural strength and toughness of ATE compared with biomaterials and HA-based composites.

materials, comparing them with each other and with natural tooth enamel (Fig. 2A and fig. S20). The average E and H of ATE, calculated from the quasistatic nanoindentation, reach 105.6 ± 12.1 GPa and 5.9 ± 0.6 GPa, respectively. These values are higher than those of natural enamel (Fig. 2A), whereas the inorganic content of ATE (78.06 wt %, fig. S21) is far less than that of enamel (>96 wt %) (18). The presence of high-modulus ZrO_2 is one reason that the modulus of ATE surpasses that of enamel. The twofold increase in stiffness and hardness compared with ATE-NAIP and ATE-NOM indicates the necessity of the nanoscale crystal-amorphous interface and parallel organization of columns at the microscale to reach the high values of macroscale stiffness and hardness seen in ATE. This conclusion can be confirmed by comparing the stiffness and hardness of ATE to those of stiff natural biomaterials (e.g., teeth, nacre, bones of many animals), previously reported HA-based composites, and ceramic-polymer composites (19) (Fig. 2B and table S1).

ATE exhibits high viscoelasticity without sacrificing its stiffness and hardness (20), (Fig. 2C and table S2). The average storage modulus of ATE can be up to 78.6 ± 9.8 GPa with a frequency of 10 Hz, whereas the average damping coefficient ($\tan \delta$) of ATE reaches ~ 0.07 (Fig. 2A and fig. S20, C and D), which exceeds the limits of traditional engineering materials with similar storage modulus such as ceramics and metals (20) (usually 0.001 to 0.01). The viscoelastic figure of merit (VFOM, defined as the product of E' and $\tan \delta$) is as high as 5.5 GPa, nine times as high as the limitation of traditional engineering materials (~ 0.6 GPa) and six times as high as in the ZnO-based enamel-like composites (2). The data for ATE-NAIP and ATE-NOM composites (Fig. 2A) point to the importance of the AIP and hierarchical organization with microscale alignment. Considering that clinically relevant loadings for natural tooth enamel occur at a typical frequency of 1 Hz (21), we have also tested the viscoelastic performance of ATE at a frequency of 1 Hz. The E' and $\tan \delta$ of ATEs

are 73.5 ± 10.1 GPa and ~ 0.075 , respectively (fig. S22), comparable to the values for 10 Hz.

ATE achieved a flexural strength of ~ 142.9 MPa and fracture strain of 0.018, which are superior to those of enamel (Fig. 2A and fig. S20E). The flexural strength and fracture strain of ATE are, respectively, ~ 2 and ~ 10 times as high as those of HA ceramic (22) (fig. S23). The nearly two-fold reduction of flexural strength in ATE-NAIP and ATE-NOM (Fig. 2A) compared with ATE further supports the necessity of multiscale engineering of organic-inorganic composites.

Single-edge notched beam (SENB) tests were carried out (23) and their mechanical behavior were observed through in situ bending with an ESEM. The typical stress-strain curves from SENB tests were plotted in fig. S24. The initial fracture toughness (K_{Ic}) of ATE (2.0 ± 0.5 $\text{MPa m}^{1/2}$) is higher than both ATE-NAIP (1.0 ± 0.1 $\text{MPa m}^{1/2}$) and ATE-NOM (1.2 ± 0.1 $\text{MPa m}^{1/2}$) (fig. S25), meaning that ATE shows more resistance to the initial crack during deformation. Increased toughness during crack propagation can be

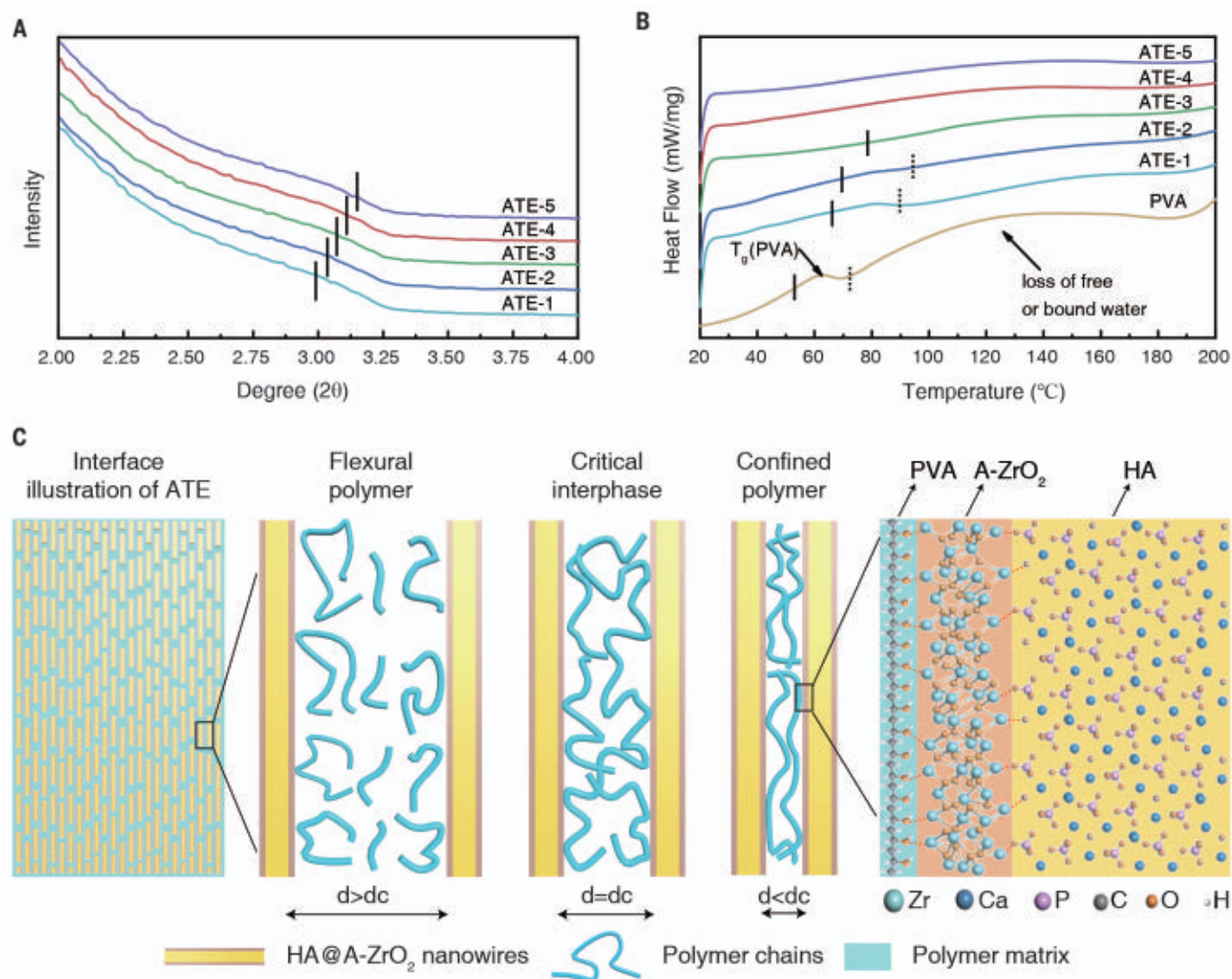


Fig. 3. Polymer confinement in ATE. (A) Small-angle x-ray diffraction (SAXD) of ATEs with different HA@A-ZrO₂ nanowires contents. (B) Differential scanning calorimetry (DSC) analysis of ATEs with different inorganic content and PVA. (C) Schematic illustration of polymer confinement and chemical bonding at the A-ZrO₂/PVA interfaces in ATE.

evaluated by the so called R-curve effect (23), enabling us to calculate K_{Jc} . This type of toughness for ATE was $K_{Jc} = 7.4 \pm 0.4 \text{ MPa m}^{1/2}$, a 3.7-fold increase compared with $K_{Jc} = 2.0 \pm 0.5 \text{ MPa m}^{1/2}$ (Fig. 2A and fig. S20F) and also higher than the fracture toughness of ATE-NAIP (1.6-fold increase), ATE-NOM (3.8-fold increase), enamel (1.6-fold increase), and referenced HA ceramics (12.3-fold increase) (22) (Fig. 2A). When compared with biomaterials and HA-based composites (24) (Fig. 2D and table S3), ATE shows an excellent combination of high strength and high toughness. High toughness of ATE can also be observed with bending tests for angles unusually high for ceramic materials (fig. S26). Additionally, the strength and toughness of ATE tested in the direction parallel to the nanowires are also analyzed (fig. S27). Because of the anisotropic

structure of ATE, the strength and toughness of ATE parallel to the nanowires are lower than those perpendicular to the nanowires but are still higher than those of enamel with the same direction (fig. S27).

The excellent combination of mechanical properties can be attributed to ATE's hierarchical enamel-mimetic structure and the design of inorganic and organic constituents. To understand the functional mechanism between the inorganic and organic constituents, we synthesized five types of ATEs with varying content of inorganic nanofillers (HA@A-ZrO₂ and PVA ratios range from 1:1 to 5:1 and are defined as ATE-1 to ATE-5; the corresponding inorganic nanofillers content increased from 41.28 to 78.06%, fig. S21), and tested their mechanical properties (fig. S28). We found that stiffness (E), hardness (H), and viscoelasticity (VFOM)

increased with increasing percentage of inorganic nanofillers reaching the highest value for ATE-5; strength and toughness increased with the content of inorganic phase reaching a plateau for ATE-3 (fig. S28). A greater concentration of inorganic nanofillers equates to a denser composite and smaller distance between inorganic nanowires, which can be demonstrated by the shift of peaks to higher degrees (Fig. 3A), as seen in the small-angle x-ray diffraction (25) spectrum. The distances between inorganic nanofillers affect the mobility of the polymeric chains, which can be evaluated by differential scanning calorimetry (26). The glass transition temperature (T_g) of PVA strongly shifted toward the higher values with the concentration of inorganic components increasing, and even disappeared for ATE when there are more inorganic components (Fig. 3B), which is

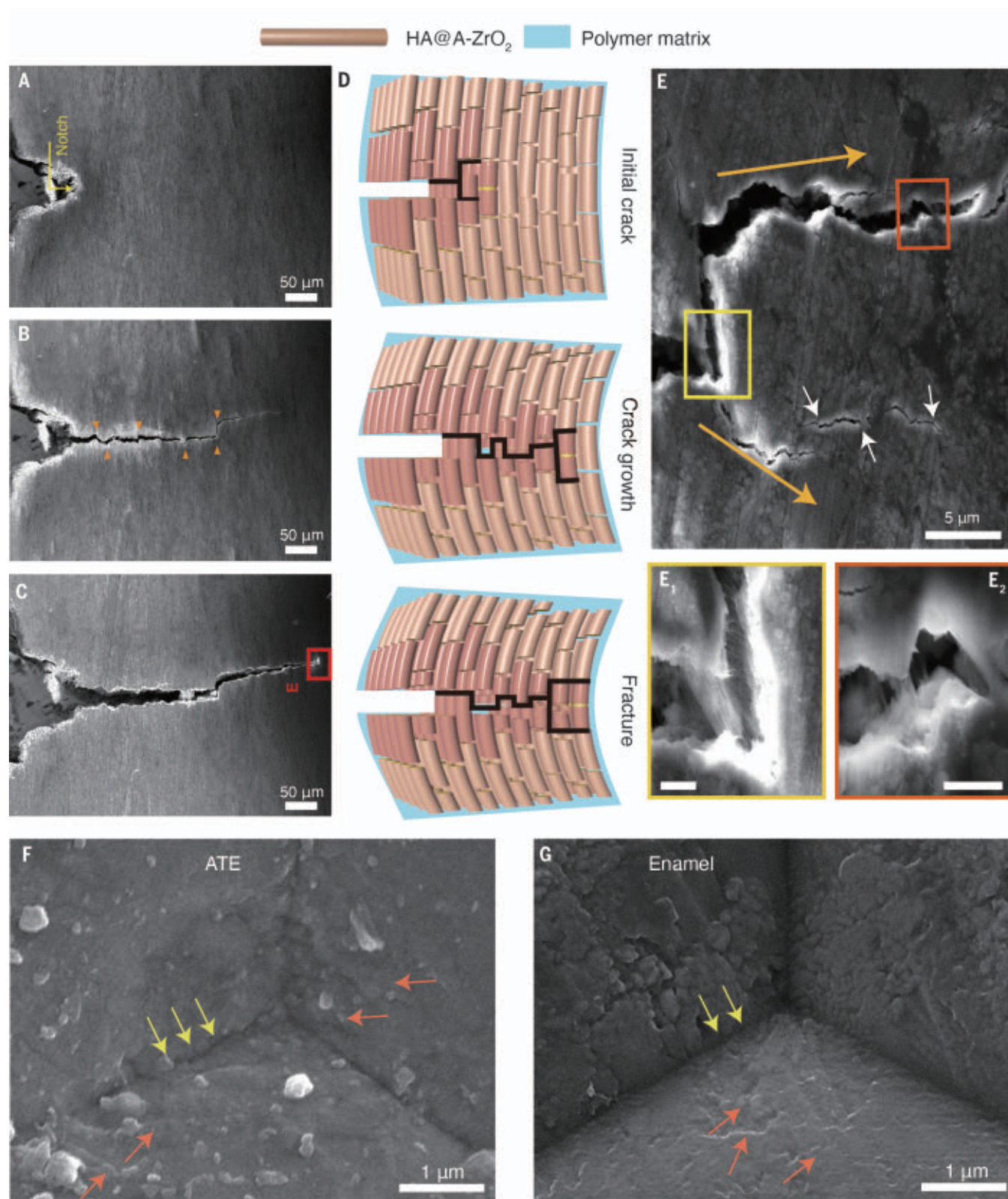


Fig. 4. Deformation and failure modes in ATE. (A to C) SEM images taken from in situ three-point bending tests. (D) Schematic illustration of the crack deflection of ATE during the three-point bending test. (E) Enlarged image taken from the red boxed area in (B). (E₁ and E₂) Enlarged SEM images taken from the yellow boxed area and the orange boxed area in (E),

respectively, showing crack bridging and nanowires pulling up. Scale bar, E₁ and E₂ 1 μm. (F and G) SEM images of the permanent deformation zone of ATE and enamel after nanoindentation, where the yellow arrows refer to the crack deflection route and the orange arrows refer to the interface delamination.

attributed to suppression of the thermal motion of the polymer chains in the presence of more inorganic nanowires (27); this is schematically depicted in Fig. 3C. When the inorganic phase content is small, the distance (d) between nanowires is larger than the critical distance, $d_c = 2.88$ nm (table S4), and the polymer chains become flexible, thus decreasing stiffness, hardness, and strength. With an increase in the inorganic phase, the mobility of the polymer is partially confined by the suitable distance ($d = d_c$), providing sufficient support and a strong interface connection which leads to a simultaneous increase in stiffness, hardness, and strength. As the concentration of nanowires increases, the distance between them becomes smaller than the critical distance ($d < d_c$), which creates a strong confinement for the polymer chains (the thermal mobility of the polymer chains almost disappears) and provides strong support for the composite (28). As a result, the stiffness and hardness of ATE-5 are the highest, and higher than those of tooth enamel. However, this partially sacrifices the polymer's mobility and its ability to adapt to changing interfaces between the organic and inorganic phases, leading to a slight decrease in strength and toughness of ATE-5, which can also be observed in cellulose composites (29). Regardless, the comprehensive mechanical performance of ATE-5 is still outstanding for overall stiffness, hardness, strength, viscoelasticity, and toughness. FTIR analysis (fig. S29) of A-ZrO₂/PVA interfaces imply that there also exists chemical bonding between Zr⁴⁺ and -OH of PVA, and these strong chemical bonds strengthen the interface connection. Furthermore, considering that both the HA nanowires and the PVA matrix are closely connected to the AIP through chemical bonding as illustrated in Fig. 3C, right, the AIP provides a buffer layer which can not only facilitate the stress transfer but also enhance the inorganic-organic interface connection, which efficiently contributes to the outstanding mechanical performance of ATE.

The improved mechanical properties observed during bending tests can be attributed to fracture-resistant deformation and crack deflection (Fig. 4, A to D). Specifically, when an external load was applied to the sample, the nanowires initially slid, dissipating a considerable amount of energy as a result of tight binding between the organic phase and the inorganic amorphous layer. Similar to other biomaterials and composites, the confinement of the organic phase in the gap between the nanowires maximized the contribution of interfaces but also restricted their motion, thus improving crack deflection (Fig. 4E). Pull-out of the nanowires (Fig. 4, E₁ and E₂) and fracturing of the sample with large-range crack deflection (Fig. 4C) dissipated

a large amount of energy. Moreover, the pull out nanowires can connect to each other to restrict the further failure of the sample. Crack splitting, bridging, and bunching (Fig. 4E) also occurred during crack propagation, which can further dissipate energy and result in ATE's excellent flexural toughness without sacrificing strength (30). In comparison, ATE-NAIP exhibited a relatively small crack deflection owing to the lack of amorphous restriction. Additionally, ATE-NOM exhibited almost brittle fracture (fig. S30).

To investigate the role of the enamel-like hierarchical architecture on increased stiffness, hardness, and viscoelasticity, we observed the permanent deformation zone obtained by a maximum load of 200 mN from the top view. We attributed their outstanding mechanical performance to sliding nanowires and crystal-amorphous phase-facilitated energy dissipation. Upon closer observation of the nanoindentation zone undergoing permanent deformation, we found jagged nanoscale cracks growing along the indenter (Fig. 4F, yellow arrows) and interface delamination (Fig. 4F, orange arrows) generated by the sliding, bending, and fracture of the nanowires. This can dissipate energy by transferring it from one nanowire to the organic layer and the adjacent nanowire, thus avoiding collapse of the structure and enhancing the stiffness, hardness, and viscoelasticity of ATEs simultaneously (31). Similar mechanical behavior is also detected in enamel (18) (Fig. 4G), which means that the complex structure of ATE with the three identified structural elements engenders enamel's mechanical performance.

In summary, we have engineered a multiscale assembly pathway to macroscale analogs of tooth enamel, revealing atomic, nanoscale, and microscale organization of inorganic nanostructures similar to the original biomaterial. The designed biomimetic composite retaining the structural complexity of the biological prototype combines high stiffness, hardness, strength, viscoelasticity, and toughness.

REFERENCES AND NOTES

1. X. Liao *et al.*, *Science* **366**, 1376–1379 (2019).
2. B. Yeom *et al.*, *Nature* **543**, 95–98 (2017).
3. Y. Yue *et al.*, *Nature* **582**, 370–374 (2020).
4. L. Liu *et al.*, *Science* **368**, 1347–1352 (2020).
5. E. Beniash, R. A. Metzler, R. S. Lam, P. U. Gilbert, *J. Struct. Biol.* **166**, 133–143 (2009).
6. Y. Wei *et al.*, *Adv. Mater.* **32**, e1907067 (2020).
7. L. C. Palmer, C. J. Newcomb, S. R. Kaltz, E. D. Spörke, S. I. Stupp, *Chem. Rev.* **108**, 4754–4783 (2008).
8. A. La Fontaine *et al.*, *Sci. Adv.* **2**, e1601145 (2016).
9. L. M. Gordon *et al.*, *Science* **347**, 746–750 (2015).
10. K. A. DeRocher *et al.*, *Nature* **583**, 66–71 (2020).

11. J. Wei *et al.*, *Adv. Funct. Mater.* **30**, 1904880 (2020).
12. Z. Chen *et al.*, *J. Mater. Chem. B Mater. Biol. Med.* **7**, 5237–5244 (2019).
13. Y. Wang, K. Lin, C. Wu, X. Liu, J. Chang, *J. Mater. Chem. B Mater. Biol. Med.* **3**, 65–71 (2015).
14. H. Yu, Y. Zhu, Z. Xiong, B. Lu, *Chem. Eng. J.* **399**, 125666 (2020).
15. R. L. Yang, Y. J. Zhu, F. F. Chen, D. D. Qin, Z. C. Xiong, *ACS Nano* **12**, 12284–12295 (2018).
16. M. Y. Shareef, P. F. Messer, R. van Noort, *Biomaterials* **14**, 69–75 (1993).
17. Y. Deng *et al.*, *Adv. Mater.* **31**, 1902432 (2019).
18. L. H. He, M. V. Swain, *J. Mech. Behav. Biomed. Mater.* **1**, 18–29 (2008).
19. This diagram is plotted according to results summarized in table S1.
20. This diagram is plotted according to results summarized in table S2.
21. R. V. Mesquita, D. Axmann, J. Geis-Gerstorf, *Dent. Mater.* **22**, 258–267 (2006).
22. Z. Shen *et al.*, *Adv. Mater.* **13**, 214–216 (2001).
23. F. Bouville *et al.*, *Nat. Mater.* **13**, 508–514 (2014).
24. This diagram is plotted according to results summarized in table S3.
25. H. S. Mansur, R. L. Oréfice, A. A. Mansur, *Polymer* **45**, 7193–7202 (2004).
26. E. P. Giannelis, *Adv. Mater.* **8**, 29–35 (1996).
27. H. Hu, J. H. Xin, H. Hu, A. Chan, L. He, *Carbohydr. Polym.* **91**, 305–313 (2013).
28. C. Zhao *et al.*, *Nature* **580**, 210–215 (2020).
29. P. Podsiadlo, Z. Tang, B. S. Shim, N. A. Kotov, *Nano Lett.* **7**, 1224–1231 (2007).
30. E. Munch *et al.*, *Science* **322**, 1516–1520 (2008).
31. J. Meaud *et al.*, *ACS Nano* **8**, 3468–3475 (2014).

ACKNOWLEDGMENTS

We thank M. Liu for help with analyzing and discussing these results. **Funding:** This work was supported by the National Key R&D Program of China (2020YFA0710403 to L.G., 2020YFA0710401 to Y.W.), the National Natural Science Foundation of China (51532001 and 51772011 to L.G.; 51802010 and 52073008 to H.Z.; 51922017 and 51972009 to Y.Y.), AFOSR FA9550-20-1-0265 and Graph Theory Description of Network Material and NSF 1463474 to N.K. **Author contributions:** L.G., H.Z., L.J., and N.K. conceived this project. H.Z., S.L., M.G., Y.L., and X.Z. prepared the artificial tooth enamel. L.G., H.Z., and S.L. performed the morphology and spectroscopy characterization. H.Z. and S.L. carried out the mechanical tests, including nanoindentation, bending test and in situ tensile test. H.Z., Y.Y., and S.L. performed the FIB cutting slice and TEM observation. Y.W. and X.D. provided the natural tooth enamel and performed the atom probe tomography. L.G., N.K., L.J., H.Z., S.L., Y.W., and X.D. analyzed the data and wrote this paper. All authors participated in the discussions of the research. H.Z., S.L., Y.W., and Y.Y. contributed equally to this work. **Competing interests:** The authors declare no competing interests. **Data and materials availability:** All data are available in the main text or the supplementary materials.

SUPPLEMENTARY MATERIALS

science.org/doi/10.1126/science.abj3343
Materials and Methods
Figs. S1 to S30
Tables S1 to S4
References (32–92)

6 May 2021; accepted 7 December 2021
10.1126/science.abj3343

GREENHOUSE GASES

Global assessment of oil and gas methane ultra-emitters

T. Lauvaux^{1*}, C. Giron², M. Mazzolini², A. d'Aspremont^{2,3}, R. Duren^{4,5}, D. Cusworth⁶, D. Shindell^{7,8,9}, P. Ciais^{1,10}

Methane emissions from oil and gas (O&G) production and transmission represent a considerable contribution to climate change. These emissions comprise sporadic releases of large amounts of methane during maintenance operations or equipment failures not accounted for in current inventory estimates. We collected and analyzed hundreds of very large releases from atmospheric methane images sampled by the Tropospheric Monitoring Instrument (TROPOMI) between 2019 and 2020. Ultra-emitters are primarily detected over the largest O&G basins throughout the world. With a total contribution equivalent to 8 to 12% (~8 million metric tons of methane per year) of the global O&G production methane emissions, mitigation of ultra-emitters is largely achievable at low costs and would lead to robust net benefits in billions of US dollars for the six major O&G-producing countries when considering societal costs of methane.

As the second most important contributor to global warming, methane (CH₄) has continued to accumulate in the atmosphere at a rate of ~50 million metric tons (Mt) per year over the past two decades, primarily because of increases in agricultural activities, waste management, coal, and oil and gas (O&G) production (1, 2). Large discrepancies between atmospheric inversions, bottom-up inventories, and biogeochemical models remain largely unexplained (1, 3–5). This complicates attribution of the recent global rise in atmospheric methane to an anthropogenic or biogenic source, a possible decline in the atmospheric OH radical sink (6, 7), or changes in biogenic or anthropogenic sources (8). Evidence of a large underestimation of fossil sources was suggested by a recent analysis of ¹⁴CH₄ isotopic ratios (9). Representing a quarter of anthropogenic emissions alone, emissions from O&G production activities have increased from 65 to 80 Mt per year over the past 20 years (10). This rapid increase imperils the success of the Paris Agreement (11). Anthropogenic emissions trends are partly explained by the increase in shale gas production in the US, which will soon be followed by the develop-

ment of large, currently underexploited shale reserves in China, Africa, and South America (12). Although O&G emissions from national inventories have been widely underestimated by conventional reporting (13), airborne imagery surveys have confirmed the omnipresence of intermittent emissions, distributed according to a power law (14–16) with a righthand tail resulting from very large O&G emissions, often referred to as super-emitters (17) (top 1% of emitters or >25 kg/hour) (18).

Until recently, observation-based CH₄ emission quantification efforts were restricted regionally to short-duration aircraft surveys (lasting a few weeks) (19) or the deployment of in situ sensor networks (20, 21). Global efforts were limited by sparse sampling of coarse-resolution CH₄ column retrievals, such as the GOSAT mission (22). More routine and higher spatially resolved emission quantification was made possible by the European Space Agency Sentinel 5-P satellite mission, which carried the Tropospheric Monitoring Instrument (TROPOMI; launched 2018) (23). TROPOMI samples daily CH₄ column mole fractions over the whole globe at moderate resolutions (5.5 km by 7 km²) and has revealed multiple individual cases of unintended very large leaks (24) and regional basin-wide anomalies (25, 26). We systematically examine this dataset over multiple locations worldwide, which allows us to statistically characterize visible ultra-emitters (>25 tons/hour) of CH₄ from O&G activities across various basins. By nature, reducing these ultra-emitters by enforcing leak detection and repair strategies or by reducing venting during routine maintenance and repairs provides an actionable and cost-efficient solution for emission abatement (27).

Detection of atmospheric column CH₄ enhancements from single point sources is limited by TROPOMI instrument sensitivity [5 to 10

parts per billion (ppb)] (28), by the overlap of multiple plumes from closely located natural gas facilities (e.g., in the Permian basin), and by complex spatial gradients from remote sources that affect background conditions (supplementary materials). Rapidly varying meteorological conditions require sufficiently robust approaches, especially with curved CH₄ plume structures for which common mass balance methods are too simplistic (29). We addressed this problem by applying an automated plume detection algorithm and quantified the associated emissions using the Lagrangian particle model HYSPLIT (30) driven by meteorological reanalysis products for each detected plume enhancement (>25 ppb averaged over several pixels; supplementary materials) over the whole globe. The detection threshold was adjusted to exclusively capture statistically significant enhancements against highly variable backgrounds (supplementary materials). Finally, we estimated the potential reductions along with abatement costs for various countries, to determine effective gains at national levels.

The number of detections of large total column CH₄ mole fraction enhancements around the world, each associated with an ultra-emitter, totals >1800 single observed anomalies over 2 years (2019–2020); a large fraction of them are located over Russia, Turkmenistan, the US (excluding the Permian basin where regional enhancements comprise many small to medium emitters), the Middle East, and Algeria (Fig. 1). Detections vary in magnitude and number (between 50 and 150 per month), most of them corresponding to O&G production or transmission facilities (about two-thirds of detections, or ~1200), whereas ultra-emitters from coal, agriculture, and waste management represent only a relatively small fraction (33%) of total detections (supplementary materials). Ultra-emitters attributed to O&G infrastructure appear along major transmission pipelines and over most of the largest O&G basins, representing more than 50% of total onshore natural gas production worldwide (10). Offshore emissions remain invisible to TROPOMI, and cloud cover almost entirely blocks O&G basins in tropical areas; hence, these are excluded from our analysis (supplementary materials).

Estimated emissions from O&G ultra-emitters rank highest for Turkmenistan with 1.3 Mt of CH₄ per year, followed by Russia, the US (excluding the Permian basin), Iran, Kazakhstan, and Algeria (Fig. 2A). Because leak duration varies and S5-P provides only snapshots, each leak duration was determined either on the basis of an observed duration deduced from the plume length (advection time) or setting a 24-hour duration when consecutive images can confirm the presence of the same anomaly over multiple days (Fig. 2A). Leaks lasting several days

¹Laboratoire des Sciences du Climat et de l'Environnement, IPSL, Univ. de Saclay, Saclay, France. ²Kayros, 33 rue Lafayette, 75009 Paris, France. ³CNRS & DI, Ecole Normale Supérieure, Paris, France. ⁴Office of Research, Innovation and Impact, University of Arizona, Tucson, AZ, USA. ⁵Carbon Mapper, 12 S. Raymond St., Suite B, Pasadena, CA 91105, USA. ⁶Jet Propulsion Laboratory, California Institute of Technology, Pasadena, CA, USA. ⁷Earth & Climate Sciences Division, Nicholas School of the Environment, Duke University, Durham, NC, USA. ⁸Porter School of the Environment and Earth Sciences, Tel Aviv University, Tel Aviv, Israel. ⁹Climate and Clean Air Coalition, 1 Rue Miollis, Building VII, F-75015 Paris, France. ¹⁰Climate and Atmosphere Research Centre, the Cyprus Institute (Cyt), Nicosia, 2121, Cyprus.

*Corresponding author. Email: thomas.lauvaux@lscse.ipsl.fr

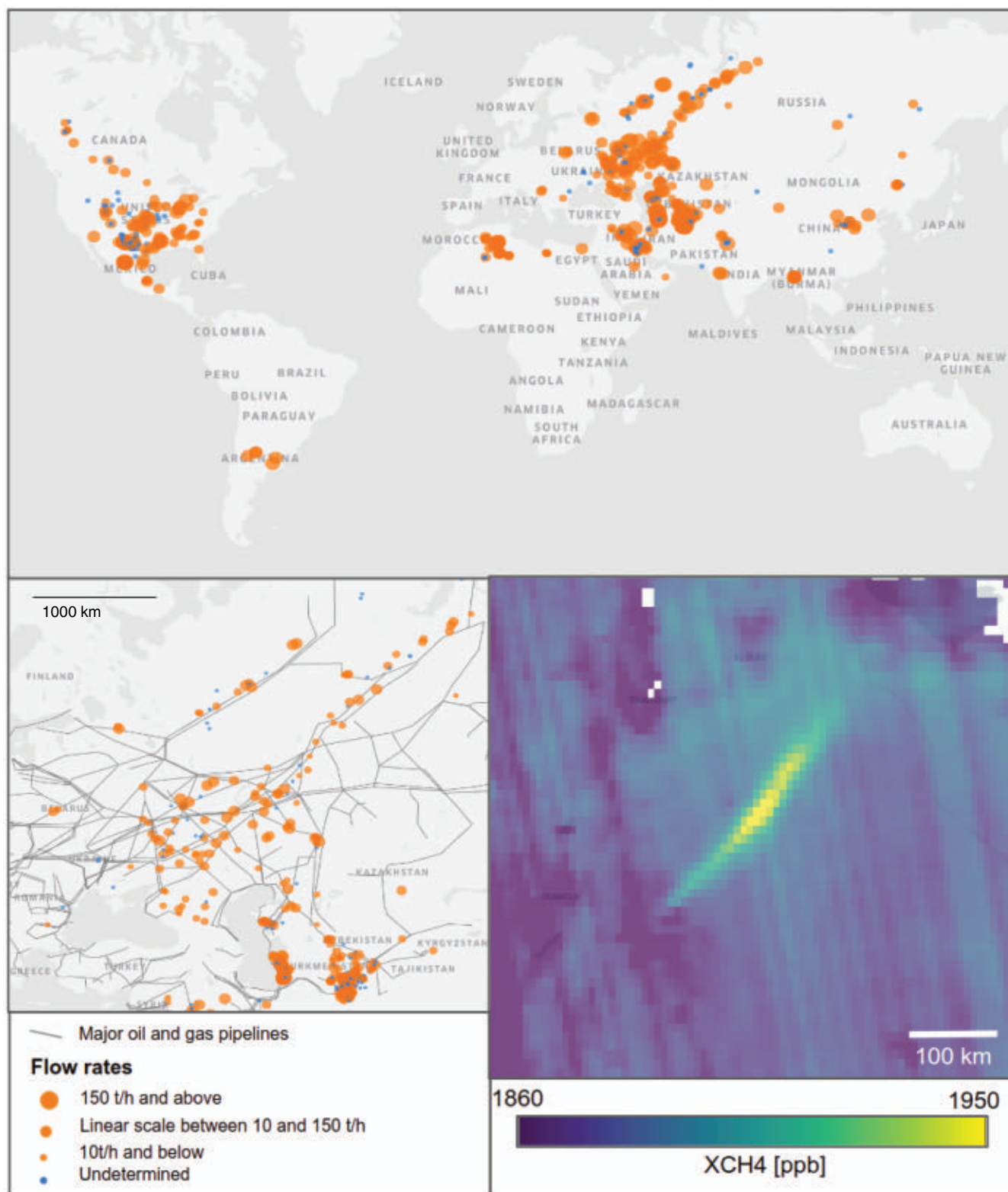


Fig. 1. Global map of ~1200 O&G detections from TROPOMI between 2019 and 2020 (**upper panel**), zoomed in over Russia and Central Asia (**lower left panel**), including the main gas pipeline (dark gray) and an example of a detected plume over northern Africa (Hassi Messaoud; **lower right panel**). Circles are scaled according to the magnitude of the ultra-emitters. Undetermined sources are indicated in blue. [Map: MapBox]

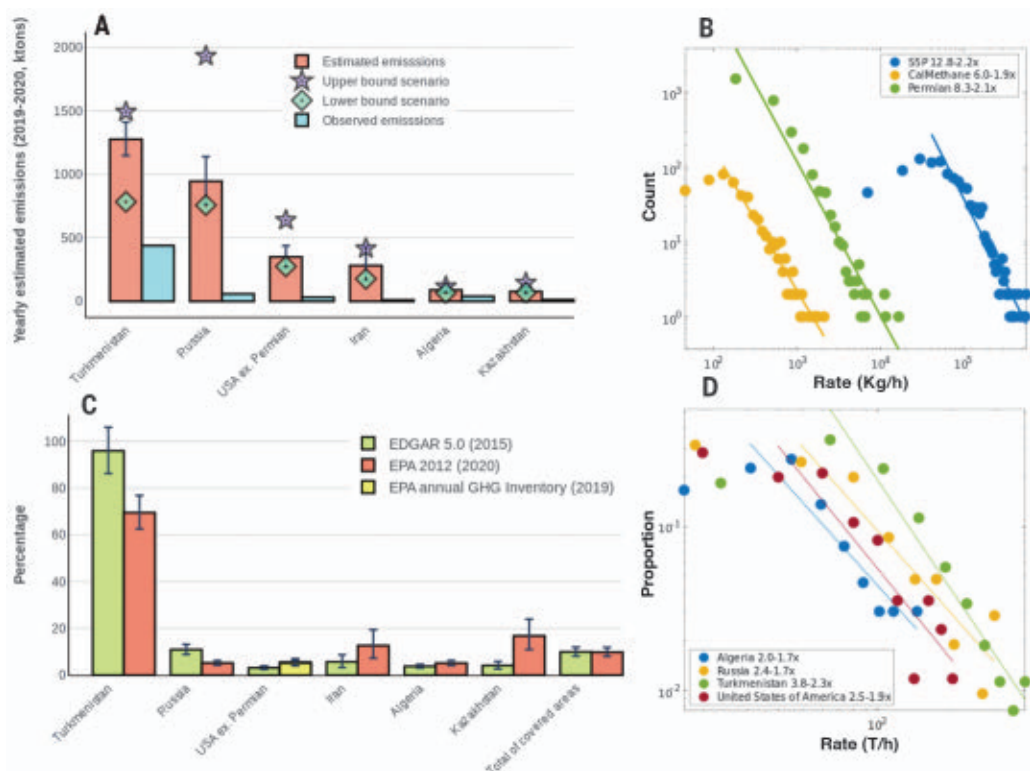
were adjusted according to lack of coverage and hence quantized to 24 hours (supplementary materials). Two additional scenarios—based on (i) a systematic 24-hour duration and (ii) based on the length of the observed plumes—were constructed to define the upper and lower bounds of durations (supplementary materials). The lack of coverage due to clouds, albedo, or aerosols was quantified by adjusting for the number of observed days compared with the full period length (supplementary materials). Uncertainties were quantified by a negative binomial probability function (31) (supplementary materials). We illustrate this adjustment in Fig. 2A, which is large for some countries (e.g., Russia), by subsampling the coverage over Turkmenistan (originally 118 detected ultra-emitters) with the lowest coverage observed over Iran (22). After adjustment, estimated emissions fall within 2% of the original estimate, and estimated uncertainty (1.26 MtCH₄) matches the full statistical test on the interval 0.96 to 1.6 MtCH₄ (fig. S10). On the basis of adjusted emissions, O&G ultra-emitter estimates represent 8 to 12% of global O&G CH₄ emissions (according to national inventories; Fig. 2C), a contribution not included in most current inventories (13).

As one of the largest natural gas reserves in the world [~20 trillion m³, ranking fourth in the world according to the International Energy Agency (IEA) (10)], Turkmenistan is likely to

see its O&G CH₄ emissions double from inventories estimates based on mean emissions, as its ultra-emitters are not accounted for by current inventory calculation methods (Fig. 2C). Ultra-emitters are also relatively common and particularly large in Russia, Iran, and Kazakhstan, representing between 10 and 20% of annual reported emissions. The US was found to have fewer ultra-emitters (5% of annual inventory emissions), but we excluded the Permian basin (~10% of US natural gas production) as a result of the large, basin-wide XCH₄ enhancement which obscures single detections (32). A recent study estimated the O&G CH₄ emissions from the Permian basin at 2.7 Mt per year using TROPOMI (33), which represents 35% of US O&G production emissions from the top-down estimate for the entire US (13). Because of the higher density of flaring equipment in the Permian basin, we assume that the proportion of ultra-emitters over the US (excluding the Permian basin) represents a lower bound at the country scale. Middle Eastern countries such as Iraq or Kuwait have even fewer detections (31 detected ultra-emitters) possibly because of fewer accidental releases and/or more stringent maintenance operations. The detection limit of ultra-emitters is around 25 tons of CH₄ per hour, whereas the largest events reach several hundred tons per hour with associated plumes spanning hundreds of kilometers. Countries such as Kuwait, Iraq, and Saudi Arabia—all major gas producers—have

few ultra-emitters despite clear sky conditions and homogeneous albedo. However, ultra-emitters from oil and gas basins throughout the world unequivocally follow a power-law distribution (Fig. 2B), which implies that if the power-law coefficients are well defined, ultra-emitters should scale directly with smaller emitters. To establish this relationship over a broader range of emissions, the power-law of smaller emitters (from 0.1 to 10 tons of CH₄ per hour) observed in high-resolution airborne imaging spectrometer surveys of California (15) and the Permian basin (16) was combined with the S5-P-derived power-law for ultra-emitters alone, revealing similar regression parameters (slope 1.9 to 2.3; Fig. 2B). The actual number of ultra-emitters varies by country (Fig. 2D) but the relationship between the number of events and their magnitudes remains similar, in the range of 0.1 to 300 tons of CH₄ per hour over two gas basins in the US. Very small leaks (<100 kg of CH₄ per hour)—mostly caused by nominal operations (i.e., pneumatic devices)—might fall within a different relationship (34), whereas larger leaks are mostly accidental or related to specific maintenance operations (35). Overall, the total fraction of CH₄ emissions from ultra-emitters remains difficult to quantify accurately owing to the lack of observations of smaller emitters, but their relative contribution compared with known sources is nonnegligible and thus offers a cost-efficient and actionable opportunity to

Fig. 2. Country-level emissions from O&G ultra-emitters between 2019 and 2020 observed and estimated (adjusted for leak duration and lack of coverage), together with two extreme leak duration scenarios: **(A)** relative size of the estimated ultra-emitters to two national scale methane inventories, EDGAR 5.0 and EPA; **(C)** distribution of super-emitters and ultra-emitters from airborne visible-infrared imaging spectrometer campaigns over 2 years in California, over 2 months in Texas (15, 41), and from 2-year Sentinel 5-P data (log-log scale; **(B)** same for S5-P but over four different countries; **(D)** EPA emissions (C) corresponding to the latest 2012 global inventory extrapolated to 2020, except for the US (most recent EPA annual greenhouse gas inventory for 2019) (44). Permian basin and offshore emissions were removed from inventory estimates (~1 Mt per year) (33).



reduce CH₄ emissions, whereas natural gas production increases steadily by ~3% per year (10).

We evaluate the industry spending required to eliminate ultra-emitter-based methane emissions based on analyses of mitigation costs recently produced by several groups: the IEA (10), the US Environmental Protection Agency (US EPA) (36), and the International Institute for Applied Systems Analysis (IIASA) (37). All costs are evaluated in 2018 US dollars per ton of methane. Briefly, we first analyze marginal abatement cost curves developed by these groups at the national level (regional level for IIASA), excluding valuation of environmental impacts. Because large emissions are expected to be related to upstream operations or long-distance transport of fuels, we exclude local distribution networks from the IIASA analysis as it separates those sources. The IEA analysis provides separate cost estimates for high emission sources, whereas the EPA and IEA do not. However, methane emissions from ultra-emitters are expected to be more cost-effective to mitigate than average sources, and IEA estimates for our six countries of interest show costs of ~\$110 to \$300 per ton less than the average cost of mitigation in the O&G sector in those countries. We therefore evaluate average mitigation costs within the O&G sector for EPA and IIASA analyses, screening for the subset of measures costing <\$600 per ton. This same threshold was recently used to define “low-cost” controls (38) and would correspond to ~\$20 per ton of carbon dioxide equivalent if converted using the Intergovernmental Panel on Climate Change Sixth Assessment Report’s GWP100 value of 29.8 for fossil methane. Averaged across these mitigation analyses, spending is net positive in Iran (~\$60 per ton) but is net negative in all other high-emission countries with net savings ~\$100 to \$150 per ton in Russia, Kazakhstan, and Turkmenistan, ~\$250 per ton in the US, and \$400 per ton in Algeria, though values vary greatly across available analyses (Fig. 3A).

Examining the total spending required to eliminate the high-emission sources in each country, there is a large spread across the available analyses: Iran has the largest average expenditure (\$16 million), but values range from \$30 million to \$95 million throughout the analyses. Results for the US are more robust in that all show net savings, but the values still vary markedly ranging from \$19 million to \$217 million. The IIASA values are the most favorable (lowest) in five of the six countries but the least favorable in Iran (though IIASA provides averages across the Middle East, which may affect that result). IEA values are typically the least favorable, with the US EPA values in the middle, except for Russia and Kazakhstan where the EPA values are the highest. Aver-

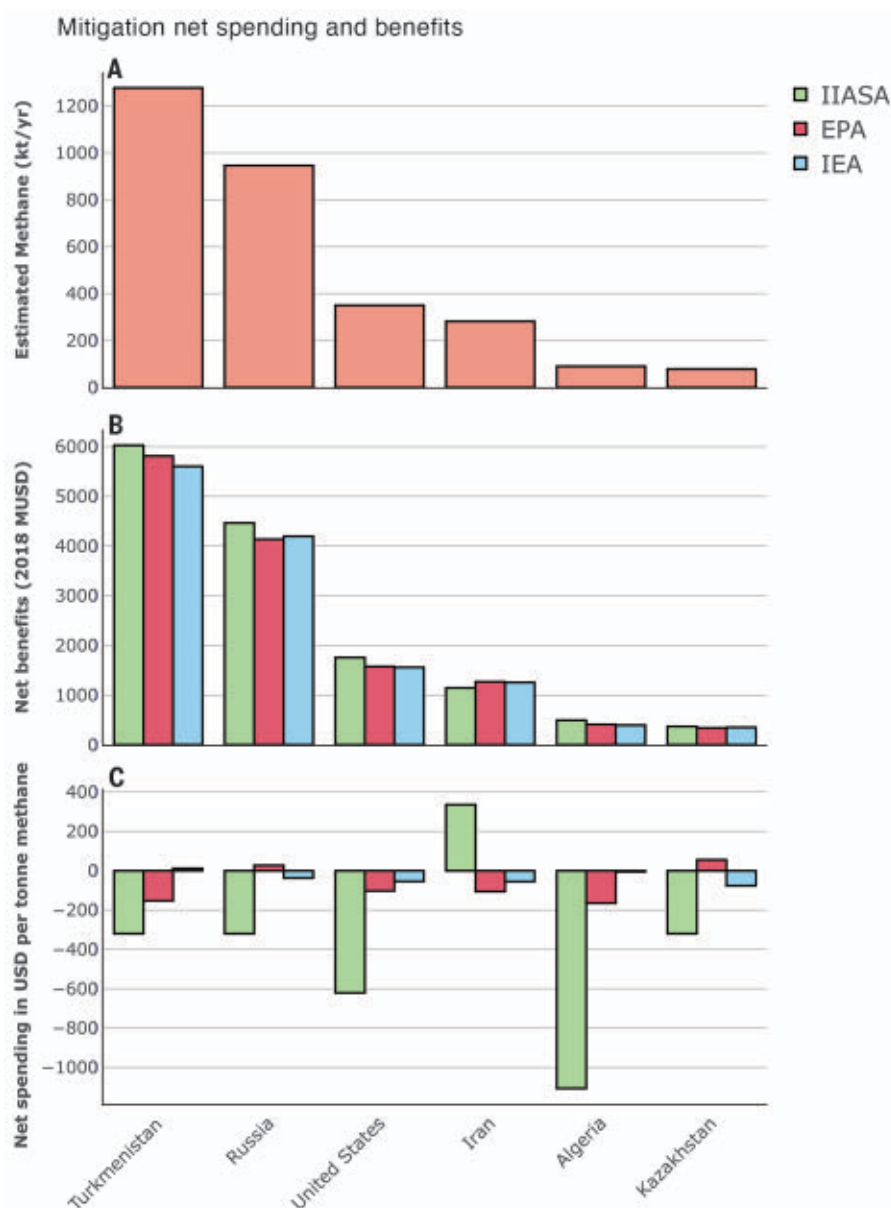


Fig. 3. (A) Estimated methane emissions from ultra-emitters in the oil and gas sector in kilotonnes per year; (B) net societal benefits of mitigation of ultra-emitters, including monetized environmental impacts; and (C) net mitigation costs per ton for ultra-emitters without environmental benefits. MUSD, millions of US dollars.

aged across the three analyses, the largest total benefits (a function of costs and emissions magnitude) appear to lie in Turkmenistan, with net savings of ~\$200 million, followed by Russia and the US, with net savings of ~\$100 million each.

We also evaluate societal costs when accounting for monetized environmental impacts. We incorporate the recently described valuation from the Global Methane Assessment (38), which assigns a value of \$4400 per ton of methane, accounting for the manifold impacts

of methane on climate and surface ozone, both of which affect human health (mortality and morbidity), labor productivity, crop yields, and other climate-related impacts. In addition to these effects, controlling high emitters in the six highlighted countries leads to robust net benefits of ~\$6 billion for mitigation for Turkmenistan, ~\$4 billion for Russia, ~\$1.6 billion for the US, ~\$1.2 billion for Iran, and ~\$400 million each for mitigation in Kazakhstan and Algeria. The range across the three mitigation cost analyses is small in this case— ~10%

(Fig. 3B). Our valuation of societal costs is much larger than current European Union emissions prices using GWP100 (~\$1130 per ton) because we include effects related to air pollution and ~50% larger than values using GWP20 (~\$2770 per ton).

In terms of net climate benefits, eliminating methane emissions from ultra-emitters would lead to $0.005^\circ \pm 0.002^\circ\text{C}$ of avoided warming over the next one to three decades on the basis of linearized estimates from prior modeling (38). Though small, this value is approximately equal to the total influence from all emissions since 2005 from Australia or the Netherlands (39), or removal of 20 million vehicles from the road for 1 year. The avoided warming would prevent $\sim 1600 \pm 800$ premature deaths annually due to heat exposure and $\sim 1.3 \pm 0.9$ billion hours of labor productivity lost annually due to exposure to heat and humidity, with the latter valued at ~\$200 million per year.

On the basis of the power-law distribution of emitters, we derived a detection threshold of 25 tons of CH₄ per hour, in agreement with previous estimates (40) using a cross-sectional flux approach to estimate the leakage rates of a major leak in Turkmenistan. For lower emission rates, the number of emitters invisible to TROPOMI far surpasses visible ultra-emitters, as suggested by airborne surveys over oil and gas production basins in California, the Four Corners region, and the Permian basin (14, 15, 41). High-resolution satellite imagery from Sentinel-2 (42) or from PRISMA and GHGSat (41) depict turbulent XCH₄ plume structures enabling facility attribution and quantification of leaks above 5 tons of CH₄ per hour. These imagers offer limited coverage (tasking mode or along-track scanning over small regions), which suggests that combined use with TROPOMI is necessary to achieve monitoring needs. Additional satellite instruments are planned to be launched in the near future (e.g., EnMAP, Carbon Mapper, SBG, CHIME, EMIT) offering high-resolution images (30 to 60 m resolution) or MethaneSAT (43) (130 by 400 m resolution) over selected high-priority areas, precursors to full constellations of imagers covering the globe daily. Until then, and given the robust power-law distribution of CH₄ ultra-emitters, the link between intermittent high-resolution imagery and regular low-resolution images from TROPOMI can help fill gaps in coverage. ImproLaved attribution of methane to specific facilities or operations remains critical to support the development of robust national emissions inventory as defined by the United Nations Framework Convention on Climate Change to inform oil and gas operators of accidental releases and to help regulators assess progress toward CH₄ emission targets.

REFERENCES AND NOTES

- M. Saunio et al., *Earth Syst. Sci. Data* **12**, 1561–1623 (2020).
- R. B. Jackson et al., *Environ. Res. Lett.* **15**, 071002 (2020).
- S. Kirschke et al., *Nat. Geosci.* **6**, 813–823 (2013).
- E. G. Nisbet, E. J. Dlugokencky, P. Bousquet, *Science* **343**, 493–495 (2014).
- M. Saunio et al., *Earth Syst. Sci. Data* **8**, 697–751 (2016).
- M. Rigby et al., *Proc. Natl. Acad. Sci. U.S.A.* **114**, 5373–5377 (2017).
- Y. Zhao et al., *Atmos. Chem. Phys.* **20**, 9525–9546 (2020).
- E. G. Nisbet et al., *Global Biogeochem. Cycles* **33**, 318–342 (2019).
- B. Hmiel et al., *Nature* **578**, 409–412 (2020).
- IEA, “Methane Tracker 2021” (IEA, 2021); www.iea.org/reports/methane-tracker-2021.
- E. G. Nisbet et al., *Rev. of Geophys.* **58**, e2019RG000675 (2020).
- V. A. Kuuskraa et al., EIA, “Technically Recoverable Shale Oil and Shale Gas Resources: An Assessment of 137 Shale Formations in 41 Countries Outside the United States” (EIA report, United States Energy Information Administration 2013); www.eia.gov/analysis/studies/worldshalegas/pdf/overview.pdf.
- R. A. Alvarez et al., *Science* **361**, 186–188 (2018).
- C. Frankenberg et al., *Proc. Natl. Acad. Sci. U.S.A.* **113**, 9734–9739 (2016).
- R. M. Duren et al., *Nature* **575**, 180–184 (2019).
- D. H. Cusworth et al., *Environ. Sci. Technol. Lett.* **8**, 567–573 (2021).
- D. Zavala-Araiza et al., *Proc. Natl. Acad. Sci. U.S.A.* **112**, 15597–15602 (2015).
- D. Zavala-Araiza et al., *Nat. Commun.* **8**, 14012 (2017).
- A. Karion et al., *Environ. Sci. Technol.* **49**, 8124–8131 (2015).
- D. R. Lyon et al., *Atmos. Chem. Phys.* **21**, 6605–6626 (2021).
- E. Chan et al., *Environ. Sci. Technol.* **54**, 14899–14909 (2020).
- J. D. Maasakkers et al., *Atmos. Chem. Phys.* **19**, 7859–7881 (2019).
- J. Veeffkind et al., *Remote Sens. Environ.* **120**, 70–83 (2012).
- S. Pandey et al., *Proc. Natl. Acad. Sci. U.S.A.* **116**, 26376–26381 (2019).
- O. Schneising et al., *Atmos. Chem. Phys.* **20**, 9169–9182 (2020).
- J. Barré et al., *Atmos. Chem. Phys.* **21**, 5117–5136 (2021).
- E. N. Mayfield, A. L. Robinson, J. L. Cohon, *Environ. Sci. Technol.* **51**, 4772–4780 (2017).
- H. Hu, J. Landgraf, R. Detmers, T. Borsdorff, *Geophys. Res. Lett.* **45**, 3682–3689 (2018).
- D. J. Varon et al., *Atmos. Meas. Tech.* **11**, 5673–5686 (2018).
- A. Stein et al., *Bull. Am. Meteorol. Soc.* **96**, 2059–2077 (2015).
- Biometrika* **5**, 351–360 (1907).
- J. A. de Gouw et al., *Sci. Rep.* **10**, 1379 (2020).
- Y. Zhang et al., *Sci. Adv.* **6**, eaaz5120 (2020).
- M. Omara et al., *Environ. Sci. Technol.* **50**, 2099–2107 (2016).
- S. Conley et al., *Science* **351**, 1317–1320 (2016).
- E. P. A. Global, “Non-CO₂ Greenhouse Gas Emission Projections & Mitigation Potential: 2015–2050” (United States Environmental Protection Agency, 2019).
- L. Höglund-Isaksson, A. Gómez-Sanabria, Z. Klimont, P. Rafaj, W. Schöpp, *Environ. Res. Commun.* **2**, 025004 (2020).
- UNEP/CCAC, “Global Methane Assessment: Benefits and Costs of Mitigating Methane Emissions” (United Nations Environment Programme and Climate and Clean Air Coalition, 2021).
- H. D. Matthews et al., *Environ. Res. Lett.* **9**, 014010 (2014).
- D. Varon et al., *Geophys. Res. Lett.* **46**, 13507–13516 (2019).
- D. H. Cusworth et al., *Geophys. Res. Lett.* **48**, e2020GL090864 (2021).
- D. J. Varon et al., *Atmos. Meas. Tech.* **14**, 2771–2785 (2021).
- A. M. Propp, J. S. Benmergui, A. J. Turner, S. C. Wofsy, “MethaneSat: Detecting Methane Emissions in the Barnett Shale Region” in *AGU Fall Meeting Abstracts* vol. 2017 A32D-06 (2017).

ACKNOWLEDGMENTS

The authors thank A. Rostand, J. Bastin, C. Lelong, O. Dhobb, and S. B. Arous from Kayrros Inc. for fruitful discussions. **Funding:** This research was supported by CNRS Make Our Planet Great Again French program CIUDAD project (to T.L. and P.C.); NASA GISS grant 80NSSC19M0138 (to D.S.); ANR *Investissements d’avenir* program grant PRAIRIE: ANR-19-P3IA-0001 (to A.A.); European Space Agency ESTEC contract (4000134070/21/NL/MM/gm) (to A.A. and T.L.); NASA Carbon Monitoring System (CMS) program (to R.D. and D.C.); and the High Tide Foundation and NASA Jet Propulsion Laboratory (to R.D.). **Author contributions:** Conceptualization: T.L., C.G., M.M., A.A., D.S., and P.C. Methodology: T.L., C.G., M.M., A.A., R.D., D.C., D.S., and P.C. Visualization: C.G. and M.M. Writing: T.L., C.G., M.M., A.A., R.D., D.C., D.S., and P.C. **Competing interests:** T.L. and P.C. have consulting fees and stock options from Kayrros. D.S. is also affiliated with the Porter School of the Environment and Earth Sciences (Tel Aviv, Israel) and the Climate and Clean Air Coalition (Paris, France). The other authors declare that they have no competing interests. **Data and materials availability:** The HYSPLIT model (v4.2.0; 2019) was developed by the Air Resources Laboratory at NOAA and is available from www.arl.noaa.gov/hysplit/. TROPOMI data (SSP L2 CH₄ OFFLINE) are available every day from the Copernicus Open Access Hub (<https://scihub.copernicus.eu/>). The meteorological reanalysis data used for the simulation of the plumes in HYSPLIT are available from the Copernicus Climate Change Service (C3S) (2017): ERA5: Fifth generation of ECMWF atmospheric reanalyses of the global climate. Copernicus Climate Change Service Climate Data Store (CDS). <https://cds.climate.copernicus.eu/cdsapp#!/home>, from the Global Forecast System (GFS), Environmental Modeling Center, National Centers for Environmental Prediction (National Weather Service, NOAA, U.S. Department of Commerce, NCEI DSI 6182, gov.noaa.ncdc:C00634); and from the Global Data Assimilation System (GDAS), Environmental Modeling Center, National Centers for Environmental Prediction (National Weather Service, NOAA, U.S. Department of Commerce, NCEI DSI 6172, gov.noaa.ncdc:C00379). Data related to mapping and infrastructures are available from the GDAL/OGG contributors (2021), GDAL/OGG Geospatial Data Abstraction software Library (Open Source Geospatial Foundation, <https://gdal.org>), from ESRI. “World Imagery” [basemap]. Scale ~1:591M to ~1:72K. “World Imagery Map” (April 2021), the Oil and Gas Infrastructure (<http://www12.oilandgasinfrastructure.com/>), and the Global Energy Monitor for coal mine activity and location data (<https://globalenergymonitor.org/projects/global-coal-mine-tracker/tracker-map/>). The locations, magnitudes, and dates of the ultra-emitters from oil and gas activities over the period 2019 to 2020 are publicly available at www.kayrros.com/methane-watch/.

SUPPLEMENTARY MATERIALS

science.org/doi/10.1126/science.abj4351
Supplementary Text
Figs. S1 to S18
References (44–52)

17 May 2021; accepted 17 December 2021
10.1126/science.abj4351

ATMOSPHERIC CHEMISTRY

Nocturnal survival of isoprene linked to formation of upper tropospheric organic aerosol

Paul I. Palmer^{1,2,*}†, Margaret R. Marvin^{1,2}†, Richard Siddans^{3,4}, Brian J. Kerridge^{3,4}, David P. Moore^{5,6}

Isoprene is emitted mainly by terrestrial vegetation and is the dominant volatile organic compound (VOC) in Earth's atmosphere. It plays key roles in determining the oxidizing capacity of the troposphere and the formation of organic aerosol. Daytime infrared satellite observations of isoprene reported here broadly agree with emission inventories, but we found substantial differences in the locations and magnitudes of isoprene hotspots, consistent with a recent study. The corresponding nighttime infrared observations reveal unexpected hotspots over tropical South America, the Congo basin, and Southeast Asia. We used an atmospheric chemistry model to link these nighttime isoprene measurements to low- NO_x regions with high biogenic VOC emissions; at sunrise the remaining isoprene can lead to the production of epoxydiols and subsequently to the widespread seasonal production of organic aerosol in the tropical upper troposphere.

The main source of atmospheric isoprene [$\text{CH}_2=\text{C}(\text{CH}_3)-\text{CH}=\text{CH}_2$] is terrestrial plants, including some mosses, ferns, gymnosperms, and angiosperms (1). Isoprene is emitted from leaves, with the emission rate dependent mostly on temperature and photosynthetically active radiation (PAR). Only at chronic levels of water stress and temperature do isoprene emissions cease; even after this stress is alleviated, the emissions resume, sometimes at rates higher than before the stress began (2). The main loss of atmospheric isoprene is oxidation by the hydroxyl radical (OH), resulting in a typical lifetime of 1 hour, which varies according to the photochemical environment. The impor-

tance of isoprene emissions lies in the resulting atmospheric chemistry. Inventories estimate the global annual mean flux of isoprene to be $\sim 500 \text{ Tg C (3)}$ but with a large uncertainty that reflects individual model assumptions (4) and the sparsity of measurements that underpin inventories. Tropical ecosystems represent $\sim 80\%$ of this global total (3), although estimates inferred from satellite observations suggest that this fraction might be overestimated by 30% (5). The fate of isoprene oxidation products depends on the relative abundances of nitrogen oxides ($\text{NO}_x = \text{NO} + \text{NO}_2$) and hydroperoxy (and organic peroxy) radicals. Broadly, at comparatively high NO_x levels, the chemistry results in the rapid production

of formaldehyde (HCHO) that is now routinely observed by Earth-observing satellites and can be used to infer the emissions of the parent hydrocarbons, predominantly isoprene (6–8). At comparatively low levels of NO_x , isoprene peroxy radicals react with hydroperoxy radicals to form an organic peroxide, and to a lesser extent they can undergo unimolecular isomerization reactions. The peroxides can then be further oxidized by OH (lifetime of ~ 3 to 5 hours) to form isoprene epoxydiols (IEPOX) (9). The atmospheric lifetime of IEPOX against oxidation by OH is ~ 20 to 30 hours, during which time it can partition into the particle phase, either by condensation or reactive uptake by preexisting particles, to form IEPOX secondary organic aerosol (SOA) (10–13).

Recent studies have reported isoprene retrievals from highly spectrally resolved infrared (IR) data from the Cross-track Infrared Sounder (CrIS) aboard the NASA/NOAA Suomi-NPP satellite (14); these data have been used to revise isoprene emission inventories (15). The satellite was launched in 2011 into a Sun-synchronous orbit with equator-crossing local times of 0130 and 1330. CrIS measures IR radiation in three bands that span 650 to

¹National Centre for Earth Observation, University of Edinburgh, Edinburgh, UK. ²School of GeoSciences, University of Edinburgh, Edinburgh, UK. ³National Centre for Earth Observation, STFC Rutherford Appleton Laboratory, Chilton, UK. ⁴Remote Sensing Group, STFC Rutherford Appleton Laboratory, Chilton, UK. ⁵National Centre for Earth Observation, University of Leicester, Leicester, UK. ⁶School of Physics and Astronomy, University of Leicester, Leicester, UK. *Corresponding author. Email: paul.palmer@ed.ac.uk †These authors contributed equally to this work.

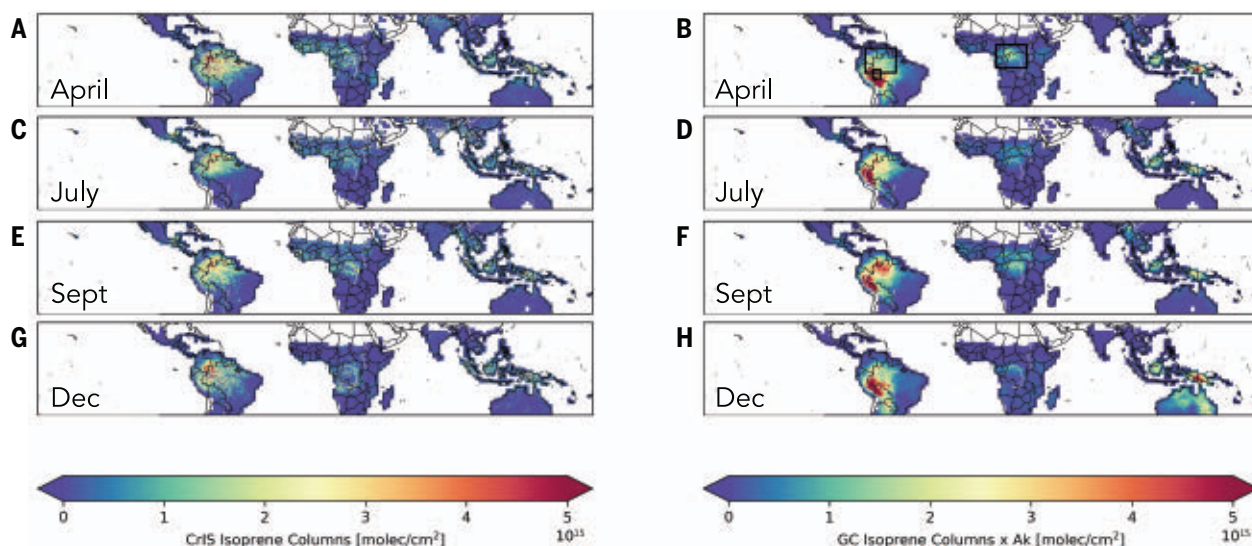


Fig. 1. Monthly CrIS and GEOS-Chem model distributions of nighttime (local equatorial overpass time 0130) effective isoprene columns. (A and B) April 2018. (C and D) July 2018. (E and F) September 2018. (G and H) December 2018. The magnitudes of these effective columns depend on how the isoprene vertical profile is represented in the retrieval and on scene-dependent averaging kernels (16). The GEOS-Chem model is sampled at

the time and location of each CrIS measurement and is convolved with the scene-dependent averaging kernel. Satellite data and model output are filtered to exclude scenes where co-retrieved aerosol optical thickness (AOT) > 0.05 and effective cloud fraction (= cloud fraction \times cloud top height) $> 4 \text{ km}$. Black squares over tropical South America and tropical Africa denote regions used in Figs. 2 and 3 and the corresponding plots over tropical Africa (16).

2550 cm^{-1} at a spectral resolution of 1.25 cm^{-1} (16). Here, we report the results from an independent, physically based CrIS isoprene retrieval scheme (17) that uses an optimal estimation approach (16), which naturally

provides a full error characterization of the a posteriori solution. We retrieve isoprene columns from spectral features in the range 890 to 908 cm^{-1} sampling 21 CrIS channels. The retrieval scheme assumes the isoprene volume

mixing ratio to be height-invariant, so that the geographical distribution of retrieved columns is exclusively due to measurement information, in contrast to (14). The vertical sensitivity needed for quantitative interpretation

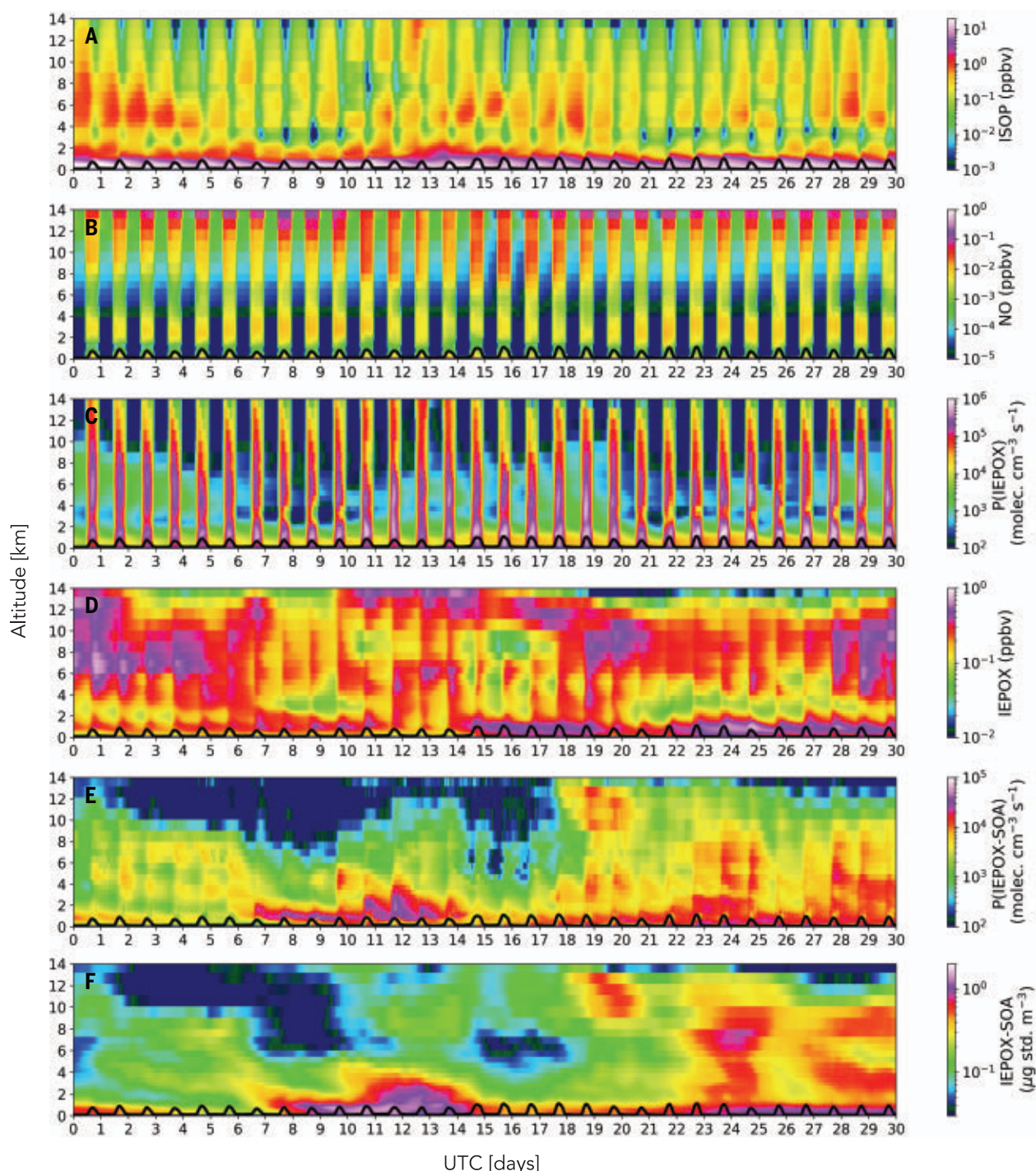


Fig. 2. GEOS-Chem model altitude-time cross sections of isoprene, NO, and some isoprene gas-phase and organic aerosol oxidation products over tropical South America during April 2018. The region is defined as 6° to 12°S and 65° to 70°W and is denoted by the smaller rectangle in Fig. 1. (A) isoprene (ppbv). (B) NO (ppbv). (C) Production rate of IEPOX ($\text{molec. cm}^{-3}\text{ s}^{-1}$). (D) IEPOX (ppbv). (E) Production rate of IEPOX SOA ($\text{molec. cm}^{-3}\text{ s}^{-1}$). (F) IEPOX-SOA ($\mu\text{g std. m}^{-3}$ at standard conditions of 273 K and 1013 hPa unless otherwise stated). Time is expressed in days at Coordinated Universal Time (UTC). The solid black lines denote the GEOS 3-hourly boundary layer height.

of “effective” columns is provided in the form of scene-dependent averaging kernels (16). We describe daytime and nighttime measurements during 2018, taking advantage of the nature of IR measurements that do not require sunlight, and focus on nighttime measurements that have not previously been reported. Our daytime measurements are broadly consistent with recent studies (14–16). We also use HCHO and nitrogen dioxide (NO_2) column data from the Tropospheric Monitoring Instrument (TROPOMI) aboard the Copernicus Sentinel-5 Precursor, in orbit with the same equator-crossing time as CrIS, to help interpret the CrIS daytime isoprene column data (16). To interpret these column data, we use the GEOS-Chem global 3D model of atmospheric chemistry that includes a detailed description of gas- and particle-phase chemistry associated with isoprene (16, 18). To compare against CrIS, the model is sampled at the time and location of each measurement and convolved with scene-dependent averaging kernels to account for the vertical sensitivity of the retrieval (16). We evaluate our model results using measurements of total OA from the Atmospheric Tomography Mission (ATom, <https://espoarchive.nasa.gov/archive/browse/atom/id14/DC8>) collected downwind of our study region (16, 19), representing the total amount of relevant aircraft data available during our study period.

Figure 1 shows monthly distributions of CrIS and GEOS-Chem nighttime isoprene data (local equatorial overpass time of 0130) during April, July, September, and December 2018. We apply inverse variances from the gridded isoprene columns to calculate these weighted monthly means, which helps to reduce noise in the aggregated CrIS measurements. Elevated values are consistently found over northern tropical South America (the northern half of Brazil, Colombia, Venezuela), central Africa (Congo basin, Angola), and Southeast Asia (northern Sumatra, the island of Borneo, Papua New Guinea). We find broad agreement between CrIS and GEOS-Chem in the location and magnitude of the elevated isoprene during nighttime, when it is determined primarily by atmospheric transport that helps to mix the atmospheric signals from low- and high-emitting daytime regions. Consequently, isoprene observed by CrIS at 0130 represents more of a homogeneous distribution than we find during the daytime, when columns are also strongly influenced by photochemistry (16). Our analysis of nighttime columns provides confidence in the model to interpret the data, although there remain differences that mainly reflect errors in emission inventories (16). Here, we focus on the origin and evolution of nighttime isoprene over tropical South America, with complementary analysis over tropical Africa, particularly over the Congo

Basin (16). The coarse model spatial resolution ($2^\circ \times 2.5^\circ$) precludes any meaningful comparison over maritime Southeast Asia associated with sub-grid-scale features.

Figure 2 shows GEOS-Chem model time-altitude plots for a region over tropical South America during April 2018 where nighttime isoprene is elevated (Fig. 2A). Isoprene emis-

sions (not shown) have a strong diurnal pattern with values peaking in early afternoon, coinciding with peak values of PAR and leaf temperatures, and absent during the night when PAR is zero. Loss of atmospheric isoprene also peaks during the day, reflecting peak production rates of OH that are correlated with sun elevation angle. Current knowledge

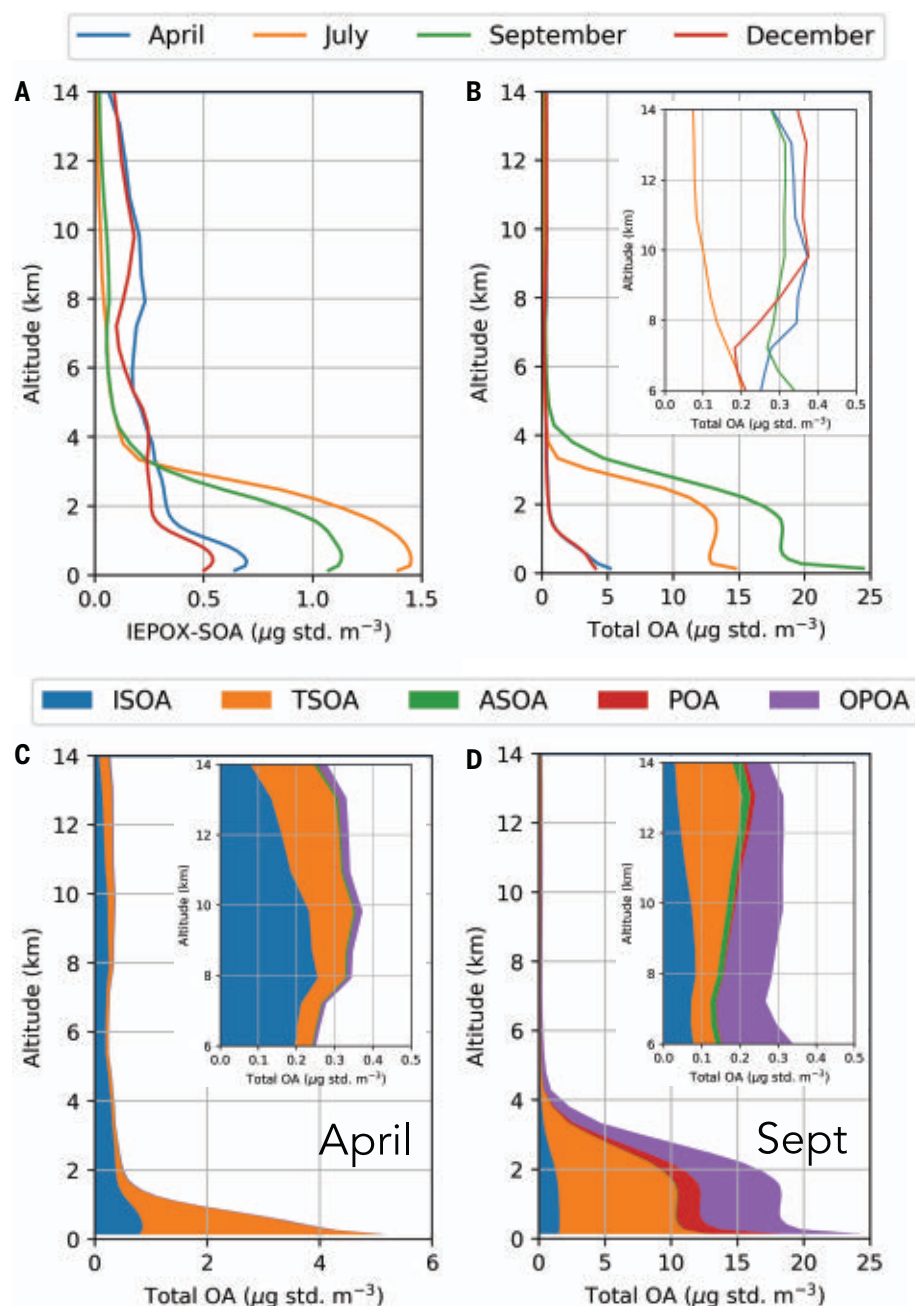


Fig. 3. Monthly GEOS-Chem model vertical profiles of organic aerosol over tropical South America.

The region is defined as 6° to 12°S and 65° to 70°W and is denoted by the smaller rectangle in Fig. 1. (A and B) IEPOX-SOA ($\mu\text{g std. m}^{-3}$) (A) and total OA ($\mu\text{g std. m}^{-3}$) (B) during April, July, September, and December 2018. (C and D) Constituents of total OA during April 2018 (C) and September 2018 (D). ISOA, TSOA, and ASOA denote SOA from isoprene, higher terpenes, and aromatic VOCs, respectively; POA and OPOA denote primary OA and oxidized POA. Inset plots zoom in on total OA at altitudes between 6 and 14 km.

suggests that atmospheric isoprene is quickly consumed by OH (with a lifetime of ~ 1 hour). In pristine environments, where nitrogen oxide levels are low, the photo-oxidation of isoprene can lead to the suppression of OH (20). We find in the model that there remains substantial atmospheric isoprene during nighttime [>1 ppbv (parts per billion by volume); Fig. 2A], not just in the shallow boundary layer (21) but also in the mid- to upper free troposphere. Temporal and spatial variations in nighttime free tropospheric isoprene are correlated with conditions at sunset of the previous day when convective mass fluxes remain elevated and OH levels are beginning to decline (16). The lifetime of isoprene during nighttime, determined primarily by ozone and nitrate oxidation, is much longer than during the daytime when it is determined primarily by OH oxidation. Over South America, the resulting free tropospheric production of IEPOX precursors and IEPOX begins at sunrise of the next day. Periods of elevated NO found in the upper troposphere (Fig. 2B) suppress the production of IEPOX (Fig. 2C), as expected. In the model, we find that this NO is mostly due to lightning (16). As we show later, this helps to explain why the origin of IEPOX SOA does not

necessarily coincide with the highest emissions of isoprene. Free tropospheric levels of gas-phase (Fig. 2D) and particle-phase IEPOX (Fig. 2F) closely follow their production rates (Fig. 2, C and E).

Figure 3A shows the GEOS-Chem model mean vertical distributions of IEPOX-SOA over tropical South America (Fig. 3B, 6° to 12° S, 65° to 70° W) during April, July, September, and December 2018. Values are generally higher near the surface during July and September, reflecting higher isoprene emissions (16). Upper free tropospheric IEPOX-SOA levels are higher in April and December as a result of larger convective fluxes. Lumped SOA from IEPOX and other low-volatility isoprene oxidation products represents 8 to 34% of mean total OA below 6 km, and 22 to 62% above 6 km, during April and December (Fig. 3B). During April, most of the OA in the lowest 6 km is due to SOA from terpene oxidation (Fig. 3C)—an expected result based on the parameterization we use to describe this source of SOA (16) with a small contribution from oxygenated primary OA (OPOA). In the upper troposphere, total OA is dominated by isoprene but with a 32% contribution from higher-order terpenes. In contrast, during September (Fig. 3D) when there is substantial biomass burn-

ing, OPOA and anthropogenic SOA play a larger fractional and absolute role in OA throughout the tropospheric profile.

Figure 4 shows a comparison between mean aircraft profile measurements of total OA (Fig. 4A) from ATom-4 (16) and GEOS-Chem model values (Fig. 4B) off the coast of tropical South America during May 2018. [See (16) for model evaluation using other campaign data.] For ATom-4, we find that the mean model profile agrees within one standard deviation of the mean measured profile, except at altitudes of >12 km (representing only nine 1-min data points), where the model underestimates the measurements by $0.29 \mu\text{g std m}^{-3}$ (62%). The best agreement is achieved at 10 to 12 km (two altitude bins each containing ~ 50 data points), where mean model OA matches the measurements within 15%. To understand the influence of nighttime isoprene on these measurements, in a sensitivity run, we set nighttime values (determined by Sun elevation angle) to zero so that they cannot be lofted to the free troposphere and subsequently influence the chemistry of organic aerosol. We find that nighttime isoprene plays only a small role ($<0.035 \mu\text{g std m}^{-3}$) in the lower-troposphere measurements but rises to as much as $0.098 \mu\text{g std m}^{-3}$ (63%) in the mid- and upper troposphere,

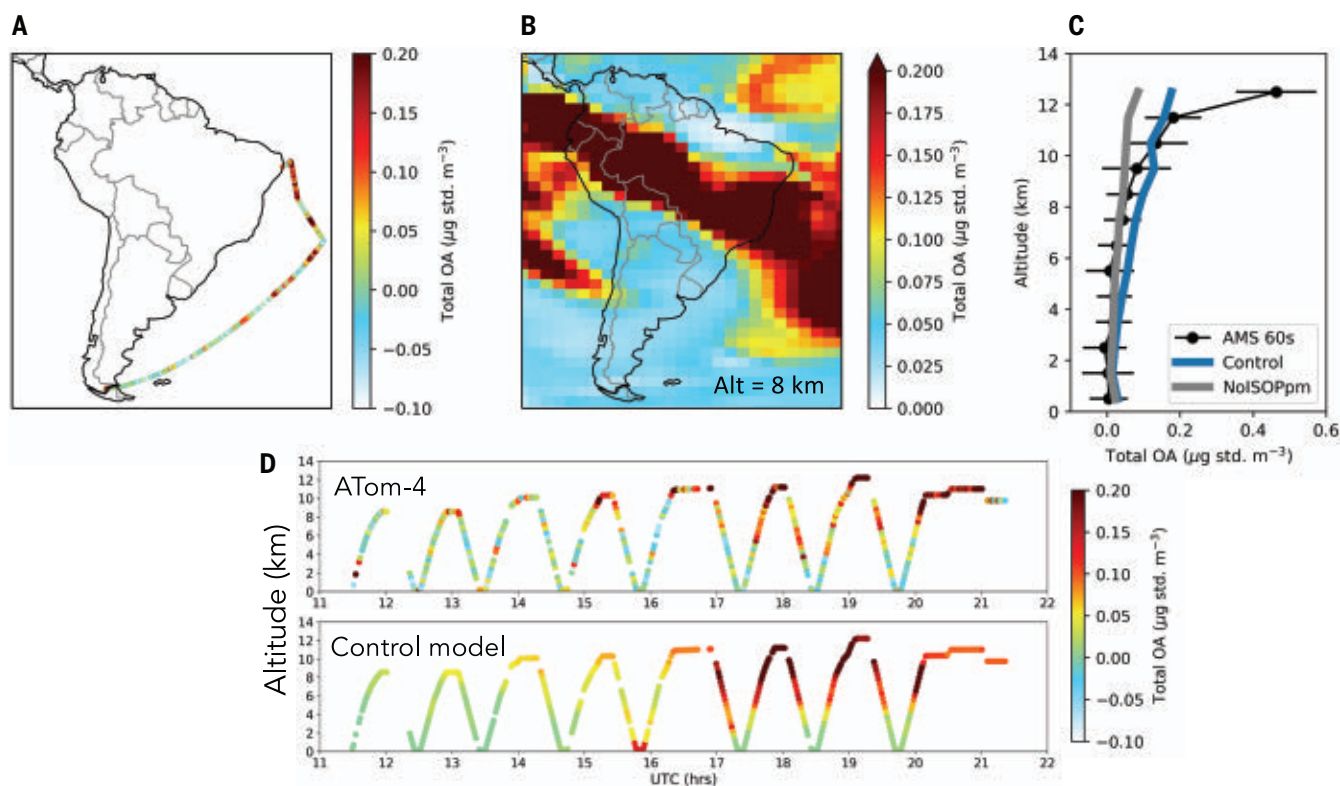


Fig. 4. Spatial and temporal distribution of observed and model total organic aerosol. (A and B) ATom-4 aircraft 60-s measurements (A) and corresponding GEOS-Chem model values of total OA ($\mu\text{g std m}^{-3}$) on 12 May 2018 (B). (C and D) Mean observed vertical distribution of OA and the GEOS-Chem model with and without nighttime isoprene (NoISOPm) (C) along a cross section of the ATom-4 flight track (D). Horizontal lines in (C) denote SD.

as also indicated by the profiles along this flight track (Fig. 4D). Using the GEOS-Chem model as an intermediary, we find that the nighttime detection of isoprene by CrIS over tropical South America is consistent with downwind levels of OA observed by aircraft.

Previous studies based on ensemble analyses of aircraft observations have noted that chemistry models are missing a substantial source of free tropospheric OA (22, 23). Increasing the anthropogenic component of OA helps to explain the measurement-model gap near source regions (24) but fails to reconcile measurements in the remote atmosphere (23). Similarly, improved knowledge of atmospheric chemistry only partly addresses the model bias (25). Our analysis suggests that over the tropics more attention should be given to the magnitude and distribution of isoprene and the chemical and physical processes that determine its transport to the free troposphere at sunset, in addition to studying the atmospheric fate of isoprene oxidation products. By virtue of its atmospheric lifetime, IEPOX-SOA can be transported across the tropical upper troposphere, where it represents about one-third of total OA (16), eventually subsiding to provide a large seasonal supply of cloud condensation nuclei in the lower troposphere (26–29).

REFERENCES AND NOTES

1. T. D. Sharkey, A. E. Wiberley, A. R. Donohue, *Ann. Bot.* **101**, 5–18 (2008).
2. E. Pegoraro, A. Rey, L. Abrell, J. Van Haren, G. Lin, *Glob. Change Biol.* **12**, 456–469 (2006).
3. A. Guenther et al., *Atmos. Chem. Phys.* **6**, 3181–3210 (2006).
4. A. Arneth et al., *Atmos. Chem. Phys.* **11**, 8037–8052 (2011).
5. T. Stavroukou et al., *Atmos. Chem. Phys.* **14**, 4587–4605 (2014).
6. P. I. Palmer et al., *J. Geophys. Res.* **108**, 4180, (2003).
7. P. I. Palmer et al., *J. Geophys. Res.* **111**, D12315 (2006).
8. D. B. Millet et al., *J. Geophys. Res.* **113**, D02307 (2008).
9. F. Paulot et al., *Science* **325**, 730–733 (2009).
10. J. D. Surratt et al., *Proc. Natl. Acad. Sci. U.S.A.* **107**, 6640–6645 (2010).
11. C. J. Gaston et al., *Environ. Sci. Technol.* **48**, 11178–11186 (2014).
12. Y. Zhang et al., *Environ. Sci. Technol. Lett.* **5**, 167–174 (2018).
13. E. L. D'Ambro et al., *Atmos. Chem. Phys.* **19**, 11253–11265 (2019).
14. D. Fu et al., *Nat. Commun.* **10**, 3811 (2019).
15. K. C. Wells et al., *Nature* **585**, 225–233 (2020).
16. See supplementary materials.
17. R. Siddans, L. Ventress, D. Knappett, B. Kerridge, RAL extended Infrared Microwave Sounder (IMS) retrievals of atmospheric and surface properties: Subset of four selected months in 2018 from Suomi-NPP (2021).
18. E. A. Marais et al., *Atmos. Chem. Phys.* **16**, 1603–1618 (2016).
19. S. Wofsy et al., ATom: Merged atmospheric chemistry, trace gases, and aerosols (Oak Ridge National Laboratory, 2018).
20. K. H. Bates, D. J. Jacob, *Atmos. Chem. Phys.* **19**, 9613–9640 (2019).
21. M. P. Barkley et al., *J. Geophys. Res.* **113**, D20304 (2008).
22. C. L. Heald et al., *Geophys. Res. Lett.* **32**, n/a (2005).
23. C. L. Heald et al., *Atmos. Chem. Phys.* **11**, 12673–12696 (2011).
24. V. Spracklen et al., *Atmos. Chem. Phys.* **11**, 12109–12136 (2011).
25. S. J. Pai et al., *Atmos. Chem. Phys.* **20**, 2637–2665 (2020).
26. M. O. Andreae et al., *Atmos. Chem. Phys.* **18**, 921–961 (2018).
27. C. Schulz et al., *Atmos. Chem. Phys.* **18**, 14979–15001 (2018).
28. C. J. Williamson et al., *Nature* **574**, 399–403 (2019).
29. Y. Liu et al., *Sci. Adv.* **4**, eaar2547 (2018).

ACKNOWLEDGMENTS

We thank the ATom team for collecting and distributing the data, particularly P. Campuzano-Jost and J.-L. Jimenez (U. Colorado,

Boulder) for sharing their AMS-60s data; the ACRIDICON-CHUVA team, including C. Schulz and J. Schneider (MPI, Mainz), for advice regarding their aerosol measurements; D. Jo (U. Colorado, Boulder) for useful discussions on modeling IEPOX-SOA; the GEOS-Chem community, particularly the team at Harvard who help maintain the GEOS-Chem model; and the NASA Global Modeling and Assimilation Office (GMAO) who provide the meteorological reanalysis data products.

Funding: All authors acknowledge support from the UK National Centre for Earth Observation funded by the National Environment Research Council (NE/R016518/1 and NE/R000115/1). **Author contributions:** P.I.P. and M.R.M. originated the ideas, with contributions from B.J.K., designed the experiments, and led the data analysis; M.R.M. led the model calculations; R.S. and B.J.K. developed the Infrared Microwave Sounder (IMS) isoprene data product and provided technical information that supported the data analysis; D.P.M. provided information about non-isoprene absorbers in the fitting window; P.I.P. led the writing of the paper, with contributions from coauthors

M.R.M., R.S., B.J.K., and D.P.M. **Competing interests:** The authors declare no competing interests. **Data and materials availability:** All the data and materials used in this study are freely available. The IMS isoprene data are available from (17). Data from the NASA ATom campaign are available from (19). TROPOMI tropospheric NO₂ and HCHO data are freely available from <https://scihub.copernicus.eu/>. The GEOS-Chem model code is available at www.geos-chem.org.

SUPPLEMENTARY MATERIALS

science.org/doi/10.1126/science.abg4506

Materials and Methods

Supplementary Text

Figs. S1 to S23

Tables S1 and S2

References (30–76)

7 January 2021; accepted 28 December 2021

10.1126/science.abg4506

GENE REGULATION

Genome organization controls transcriptional dynamics during development

Philippe J. Batut*, Xin Yang Bing, Zachary Sisco, João Raimundo, Michal Levo, Michael S. Levine*

Past studies offer contradictory claims for the role of genome organization in the regulation of gene activity. Here, we show through high-resolution chromosome conformation analysis that the *Drosophila* genome is organized by two independent classes of regulatory sequences, tethering elements and insulators. Quantitative live imaging and targeted genome editing demonstrate that this two-tiered organization is critical for the precise temporal dynamics of Hox gene transcription during development. Tethering elements mediate long-range enhancer-promoter interactions and foster fast activation kinetics. Conversely, the boundaries of topologically associating domains (TADs) prevent spurious interactions with enhancers and silencers located in neighboring TADs. These two levels of genome organization operate independently of one another to ensure precision of transcriptional dynamics and the reliability of complex patterning processes.

Genome organization is emerging as a potentially important facet of gene regulation (1–5). Because transcriptional enhancers often reside far from their target promoters, chromatin folding may guide the timely and specific establishment of regulatory interactions (1, 3, 4, 6–10). Although long-range enhancer-promoter contacts are prevalent, it remains unclear whether they actually determine transcriptional activity (9, 11). Boundary elements partition chromosomes into topologically associating domains (TADs) (7, 12), whose importance for gene regulation remains controversial (8, 13–16). There is also an unresolved dichotomy between elements that promote and prevent enhancer-promoter interactions, because CTCF binding sites have been implicated in both (7, 9, 17). We show here that distinct classes of regulatory elements mediate these opposing functions genome-wide: Dedicated tethering elements foster appropriate enhancer-promoter inter-

actions and are key to fast activation kinetics, whereas insulators prevent spurious interactions and regulatory interference between neighboring TADs.

We characterized genome organization at single-nucleosome resolution in developing *Drosophila* embryos using Micro-C (18). We focused on the critical ~60-min period preceding gastrulation, when the fate map of the embryo is established by localized transcription of a cascade of patterning genes, culminating with the Hox genes that specify segment identity. Analysis of the *Antennapedia* gene complex (ANT-C), one of two Hox gene clusters and an archetype of regulatory precision, reveals an intricate hierarchical organization. Insulators partition the locus into a series of TADs, whereas tethering elements mediate specific intra-TAD focal contacts between promoters of *Scr* and *Antp* and their distal regulatory regions (Fig. 1A and fig. S1).

The entire genome is similarly organized by 2034 insulators and 620 tethering elements. Insulators and tethers display notably little physical overlap (Fig. 1B) and have sharply contrasting chromatin signatures (Fig. 1C;

Lewis-Sigler Institute for Integrative Genomics, Princeton University, Princeton, NJ, USA.

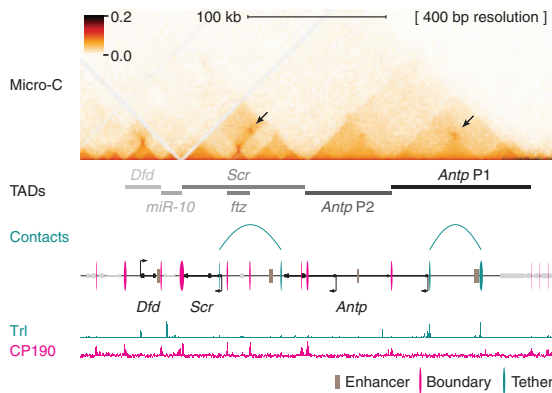
*Corresponding author. Email: msl2@princeton.edu (M.S.L.); pbatut@princeton.edu (P.J.B.)

fig. S2, A to C; and table S1). Insulators are characterized by H3 lysine 4 trimethylation (H3K4me3) and the binding of canonical insulator proteins (CTCF, CP190), whereas tethers are distinguished by H3K4 monomethylation (H3K4me1) and the binding of pioneer factors Trithorax-like (Trl), grainyhead

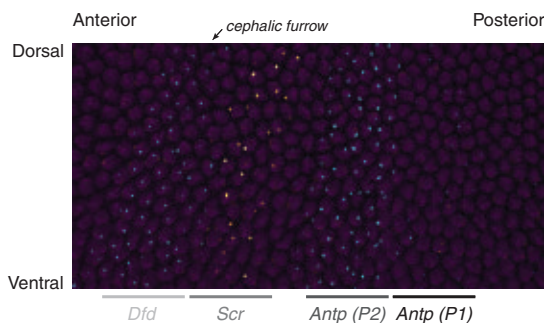
(grh), and zelda (zld; fig. S2, A and B). There are 103 focal contacts (33%) that connect promoters of protein-coding genes to “orphan” intergenic sequences, which we term distal tethering elements (DTEs; Fig. 1D); others connect different genes together. These contacts typically span tens of kilobases (mean

43.5 kb; Fig. 1D and table S2) and are observed at many critical developmental loci, including *vestigial* and *cut* (fig. S3). Because DTEs generally display no enhancer activity in the early embryo (Fig. 1E and fig. S2D), we hypothesized that they might be organizational elements dedicated to fostering long-range

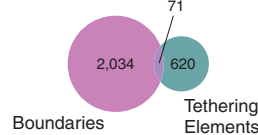
A ANT-C Organization: Boundaries & Tethering Elements



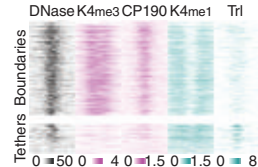
F Live imaging of transcription



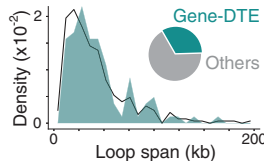
B Distinct regulatory classes



C Chromatin profiles



D Focal contacts (N=313)



E Enhancer activity

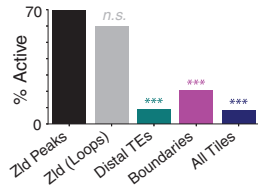
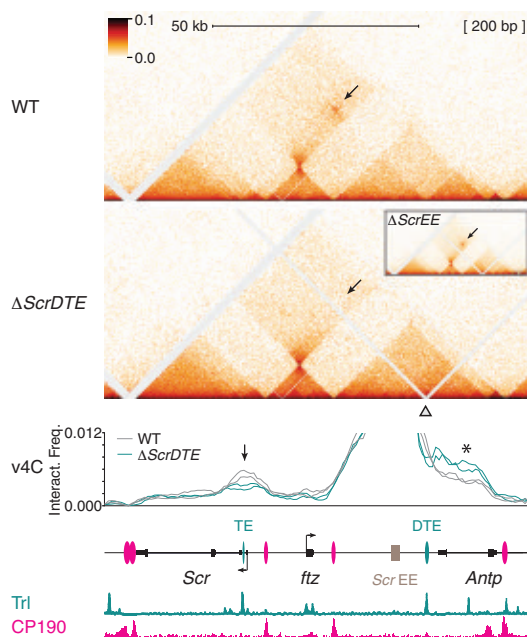


Fig. 1. Hierarchical genome organization: Boundaries and focal contacts. (A) ANT-C organization (*Dfd-Antp* interval). The following are shown from top to bottom: Micro-C contact map showing TADs and focal contacts (arrows); Hox genes (black); other genes (gray); regulatory elements; and chromatin immunoprecipitation (ChIP) data for Trl and CP190. (B) Tethers and boundaries are physically distinct. (C) Epigenetic signatures of tethers and boundaries. DNase, deoxyribonuclease I. (D) Fraction of contacts connecting gene promoters to “orphan” DTEs and a histogram of loop spans (black, all loops). (E) Enhancer activity, by functional class (***) $p < 10^{-7}$ versus Zld peaks, Bonferroni-corrected chi-square test; n.s., not significant). (F) Image of a live embryo showing transcription of *Dfd*, *Antp* (cyan), and *Scr* (yellow, image enhanced), with nuclei in purple.

A Spatial organization of the Scr TAD



B Live transcription measurements

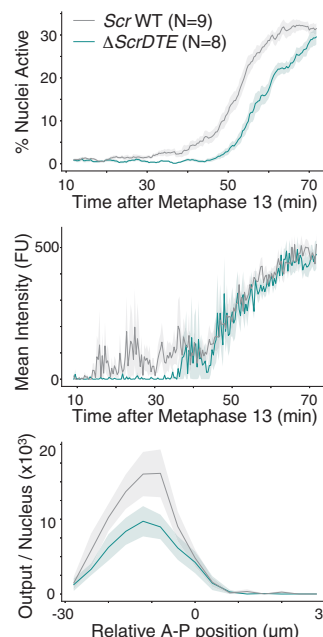


Fig. 2. Tethering elements foster enhancer-promoter interactions and control activation kinetics. (A) Micro-C for *Scr* DTE mutant embryos. (The triangle indicates the location of the deletion.) Virtual 4C (v4C) shows decreased interactions of the EE enhancer with the promoter upon DTE deletion (arrow) and increased interactions with regions beyond the DTE (asterisk). The focal contact persists in Δ ScrEE embryos (inset). (B) Live measurements of endogenous *Scr* transcription show delayed activation in Δ ScrDTE embryos. A-P, anterior-posterior; FU, fluorescence units; N, number of embryos; shading, \pm SEM).

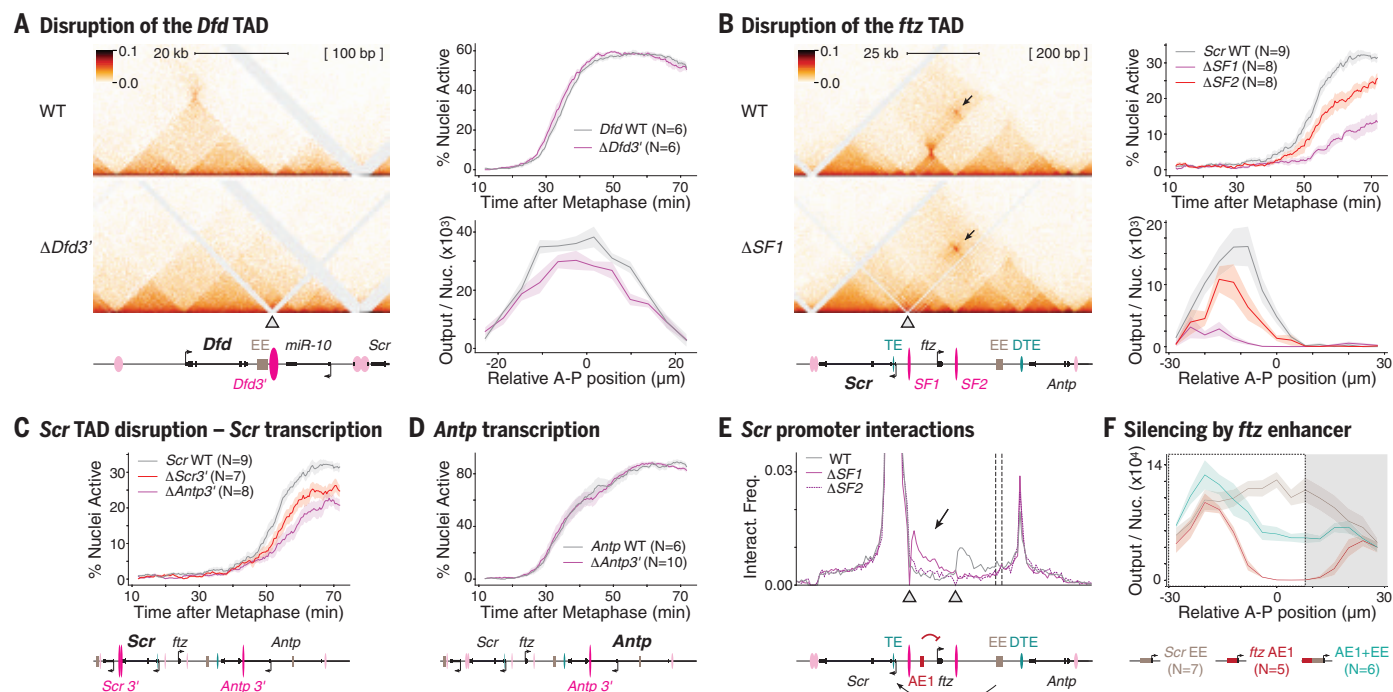


Fig. 3. Insulators prevent regulatory interference and promote transcriptional precision. (A) Micro-C and *Dfd* transcription measurements for $\Delta Dfd3'$ insulator mutant embryos. The triangle indicates the location of the deletion. (B) Micro-C and *Scr* transcription measurements for $\Delta SF1$ (and $\Delta SF2$) embryos. The focal contact persists (arrows). (C) *Scr* transcription

in $\Delta Scr3'$ and $\Delta Antp3'$ embryos. (D) *Antp* transcription in $\Delta Antp3'$ embryos. (E) Interaction landscape of the *Scr* promoter upon disruption of the *ftz* TAD (see Micro-C above). (F) Reporter assay showing silencing by the AE1 enhancer within the *Scr* expression domain (dashed box). In all panels, shading indicates \pm SEM.

enhancer-promoter interactions. In contrast to enhancers, DTEs retain an “open” chromatin conformation throughout embryogenesis (fig. S2E), consistent with evidence that focal contacts are stable across cell types (19) and developmental stages (11). To explore their potential roles in transcriptional regulation, we systematically disrupted tethers and insulators throughout the ANT-C (tables S3 and S4) and leveraged quantitative live-imaging methods to measure changes in the transcriptional dynamics of Hox genes in developing embryos (Fig. 1F).

The *Sex combs reduced* (*Scr*) gene, contained within a 90-kb TAD, is regulated by an early embryonic enhancer (*Scr* EE) located 35 kb upstream of the promoter [figs. S4 and S5; (20)]. This enhancer bypasses an intervening TAD that contains *ftz*—a highly expressed pair-rule gene—to selectively regulate *Scr* transcription. A DTE situated 6 kb upstream of the enhancer anchors a focal contact with a promoter-proximal tether (Fig. 2A). These tethering elements correspond to sequences previously shown by reporter assays to modulate enhancer-promoter selectivity (21, 22). The DTE lacks any intrinsic enhancer activity (fig. S4), suggesting a specific role in fostering long-range enhancer-promoter interactions.

A targeted deletion of the DTE completely abolishes this focal contact and diminishes

interactions between the EE enhancer and the *Scr* promoter (Fig. 2A and figs. S6 and S7). Single-cell transcription measurements in living embryos reveal a marked delay in the dynamics of *Scr* activation across the cells of the prospective stripe (Fig. 2B). Transcription levels in nuclei that become active appear unaffected, and the mutant allele ultimately reaches a regime of activity indistinguishable from that of the wild type. Overall, the mutant allele is active in the appropriate spatial domain, but its transcriptional output is substantially reduced owing to the delayed onset of expression (Fig. 2B and fig. S6A). Deletion of the EE enhancer reduces *Scr* transcription but does not disrupt the focal contact—it may even be somewhat strengthened (Fig. 2A and fig. S8). These observations suggest that promoter-DTE focal contacts are autonomous features of the regulatory genome. Disruptions of focal contacts have strictly gene-specific effects: Deletion of the *Scr* DTE has no impact on the structure or transcription of the neighboring *Dfd* locus (fig. S6, C to E).

Similarly, the *Antennapedia* (*Antp*) P1 early enhancer is associated with a DTE directly adjacent to it, which forms a focal interaction with a tethering element near the P1 promoter, 38 kb away. Upon deletion of the DTE, the focal interaction is lost, and enhancer-promoter interactions are disrupted (figs. S6 and S7).

Antp activation is substantially delayed but transcription levels in active nuclei are normal, and transcription appears to fully recover after this initial lag (fig. S9).

These observations show that DTEs specifically determine the dynamics of transcriptional activation in development. This temporal precision may be critical for the programming of cellular identities within stringent developmental windows. We propose that tethering elements foster physical interactions between promoters and remote enhancers to prime genes for rapid activation; they may also modulate other aspects of enhancer-promoter communication through interactions with core transcription complexes.

In addition to fostering preferential associations with target promoters, DTEs also suppress “backward” interactions of associated enhancers with distal regions of their TADs (Fig. 2A and fig. S7). Both effects probably synergize to increase the specificity of enhancer-promoter communication. Although DTE deletions have a strong impact on local genome organization, they have little effect on the overall structure of TADs (Fig. 2A and fig. S7), suggesting that insulators and tethering elements operate largely independently of one another. To better understand the relationship between long-range enhancer-promoter interactions and TAD structures, we systematically disrupted each of

the TAD boundaries across the *Dfd-Scr-Antp* interval (tables S3 and S4).

Deletion of the *Dfd* 3' insulator causes a wholesale fusion of the *Dfd* TAD with the adjacent *miR-10* TAD and reduces transcription of the *Dfd* gene (Fig. 3A and figs. S10 to S12). Notably, it does not appear to weaken interactions between the *Dfd* promoter and enhancer, suggesting that TAD boundaries play no role in fostering appropriate regulatory interactions. Rather, the 3' insulator specifically prevents inappropriate contacts with the *miR-10* regulatory region.

Similarly, individual deletions of the boundaries of the *ftz* TAD, which is nested within the *Scr* locus, cause fusions with either side of the *Scr* TAD. The remaining insulator continues to enforce a robust boundary (Fig. 3B and figs. S10 to S12). *Scr* transcription is markedly reduced in both cases, though the deletion of *SF1* has a substantially more severe impact than *SF2* (Fig. 3B and fig. S10). Neither deletion disrupts the promoter-DTE interaction (fig. S11), suggesting that TAD boundaries are not required for the establishment or maintenance of long-range focal contacts. This supports the view that tethers and boundaries constitute independent levels of organization, as suggested by our genome-wide analysis.

The disruption of *Scr* TAD boundaries is also consistent with this model. Deletion of the *Scr* 3' insulator is recessive lethal, probably because of the loss of essential 7SL genes, and could not be analyzed by Micro-C. But a targeted deletion of the *Antp* 3' intronic insulator is viable and causes a partial fusion of the *Scr* and *Antp* P2 TADs (figs. S10 to S12). The persistence of a residual boundary can be explained by the presence of a secondary insulator located ~4 kb away. Deletion of either *Scr* TAD boundary severely reduces *Scr* transcription (Fig. 3C and figs. S10 and S11). Notably, disruption of the *Scr*-*Antp* boundary does not weaken the interaction of the DTE with the *Scr* promoter (fig. S11), suggesting that reduced *Scr* expression is not due to diminished enhancer-promoter interactions. This partial fusion of the *Scr* and *Antp* P2 TADs has, at most, only a marginal impact on *Antp* transcription (Fig. 3D and figs. S10 and S11), revealing that boundary deletions can have sharply asymmetric regulatory effects on flanking TADs.

Because TAD boundary deletions do not alter appropriate enhancer-promoter interactions, we sought an alternative explanation for reduced *Scr* transcription arising from disruptions of the *ftz* TAD. *SF1* removal exposes the *Scr* promoter to interactions with the *ftz* regulatory region (Fig. 3E and fig. S11), which may thus directly interfere with *Scr* transcription. By contrast, *SF2* removal allows *ftz* regulatory sequences to interact with the EE enhancer (fig. S11), but not directly with the *Scr* promoter (Fig. 3E and fig. S11), which

may explain its more subtle transcriptional impact. In the absence of *SFI*, the severely narrowed *Scr* domain and distinctive ectopic stripes suggest both activation and silencing by *ftz* enhancers (fig. S13). A prime suspect for this altered expression pattern is the AE1 enhancer, which binds both activators and the Hairy repressor (fig. S13). Indeed, the AE1 element functions as a potent silencer within the *Scr* expression domain (Fig. 3F and fig. S10), and *Scr* transcription faithfully mirrors AE1 activity upon *SFI* removal (fig. S13). We conclude that the primary function of insulators is to prevent regulatory interference between TADs, and this can explain even surprising quantitative differences in the transcriptional effects of boundary deletions.

To assess the functional importance of tethering elements and insulators, we analyzed the number of teeth on the sex combs of adult males, a quantitative phenotype under sexual selection governed by *Scr* expression. All relevant deletions reduce the average number of teeth, and the magnitude of the transcriptional defects is highly predictive of the severity of the morphological phenotypes (Fig. 4, A and B, and fig. S14). These observations demonstrate the importance of genome structure for the control of transcriptional dynamics and the precision of developmental patterning.

Taken together, our observations support a general model in which genome organization canalizes regulatory interactions through two classes of organizing elements with diametrically opposing functions. A dedicated class

of tethering elements, often physically distinct from enhancers, foster enhancer-promoter interactions and are key to fast transcriptional activation kinetics during development (Fig. 4C). We anticipate that similar mechanisms will prove to be an important property of vertebrate genomes, where large distances often separate genes from their regulatory sequences (9, 23, 24). By contrast, TAD boundaries have a pervasive role in enforcing regulatory specificity by preventing interference between neighboring TADs (Fig. 4C).

Although prior studies have emphasized the spatial regulation of gene expression, temporal dynamics have proven far more elusive. Quantitative measurements in live embryos revealed clear delays in the onset of transcription upon deletion of tethering elements. The Trl protein, which binds most of these sequences, has been proposed to act as a DNA looping factor (25, 26). We suggest that tethering elements “jump-start” expression by establishing enhancer-promoter loops before activation, though it is likely that they also serve a broader function. Indeed, it is intriguing that the *Scr* DTE coincides with a classical Polycomb response element (27). This is consistent with a possible role for Polycomb repressive complex 1 (PRC1) components in the establishment of enhancer-promoter loops (28) and suggests that focal contacts constitute a versatile topological infrastructure used by a variety of regulatory mechanisms. Our study shows that genome organization shapes transcription dynamics through two complementary mechanisms:

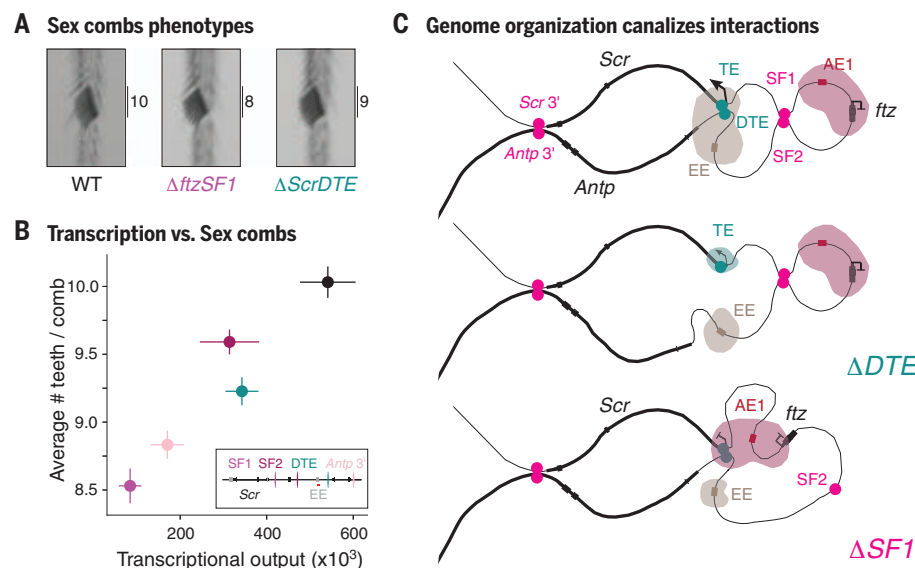


Fig. 4. Genome organization controls transcriptional dynamics and developmental patterning. (A) Representative images of sex combs from adult males. (Numbers indicate tooth counts.) (B) Correlation of transcriptional output and tooth count (inset, locus map; red bar, sex comb enhancer; error bars, \pm SEM). (C) Organization of the *Scr* locus: Tethers foster specific enhancer-promoter interactions, whereas boundaries prevent regulatory interference between TADs.

Tethering elements foster appropriate enhancer-promoter interactions, whereas TAD boundaries prevent inappropriate associations.

REFERENCES AND NOTES

1. J. Dekker, L. Mirny, *Cell* **164**, 1110–1121 (2016).
2. H. K. Long, S. L. Prescott, J. Wysocka, *Cell* **167**, 1170–1187 (2016).
3. E. E. M. Furlong, M. Levine, *Science* **361**, 1341–1345 (2018).
4. M. I. Robson, A. R. Ringel, S. Mundlos, *Mol. Cell* **74**, 1110–1122 (2019).
5. H. Chen et al., *Nat. Genet.* **50**, 1296–1303 (2018).
6. G. Andrey et al., *Science* **340**, 1234167 (2013).
7. V. Narendra et al., *Science* **347**, 1017–1021 (2015).
8. B. K. Kragesteen et al., *Nat. Genet.* **50**, 1463–1473 (2018).
9. C. Paliou et al., *Proc. Natl. Acad. Sci. U.S.A.* **116**, 12390–12399 (2019).
10. E. Rodríguez-Carballo et al., *Proc. Natl. Acad. Sci. U.S.A.* **117**, 31231–31241 (2020).
11. Y. Ghavi-Helm et al., *Nature* **512**, 96–100 (2014).
12. J. R. Dixon et al., *Nature* **485**, 376–380 (2012).
13. D. G. Lupiáñez et al., *Cell* **161**, 1012–1025 (2015).
14. S. S. P. Rao et al., *Cell* **171**, 305–320.e24 (2017).
15. Y. Ghavi-Helm et al., *Nat. Genet.* **51**, 1272–1282 (2019).
16. A. Despang et al., *Nat. Genet.* **51**, 1263–1271 (2019).
17. N. Kubo et al., *Nat. Struct. Mol. Biol.* **28**, 152–161 (2021).
18. T. S. Hsieh et al., *Mol. Cell* **78**, 539–553.e8 (2020).
19. E. Ing-Simmons et al., *Nat. Genet.* **53**, 487–499 (2021).
20. J. G. Gindhart Jr., A. N. King, T. C. Kaufman, *Genetics* **139**, 781–795 (1995).
21. V. C. Calhoun, A. Stathopoulos, M. Levine, *Proc. Natl. Acad. Sci. U.S.A.* **99**, 9243–9247 (2002).
22. V. C. Calhoun, M. Levine, *Proc. Natl. Acad. Sci. U.S.A.* **100**, 9878–9883 (2003).
23. Q. Zhou et al., *Nat. Commun.* **12**, 43 (2021).
24. T. Pachano et al., *Nat. Genet.* **53**, 1036–1049 (2021).
25. M. L. Espinás et al., *J. Biol. Chem.* **274**, 16461–16469 (1999).
26. T. Mahmoudi, K. R. Katsani, C. P. Verrijzer, *EMBO J.* **21**, 1775–1781 (2002).
27. J. G. Gindhart Jr., T. C. Kaufman, *Genetics* **139**, 797–814 (1995).
28. V. Loubiere, G. L. Papadopoulos, Q. Szabo, A. M. Martinez, G. Cavalli, *Sci. Adv.* **6**, eaax4001 (2020).
29. P. Batut, phil-batut/transcription_imaging: transcription_imaging (Batut et al., 2021). Zenodo (2021); <http://doi.org/10.5281/zenodo.5730297>.

ACKNOWLEDGMENTS

We thank J. Rowley for his help in using Significant Interaction Peak-caller (SIP) and optimizing parameters; N. Treen, X. Li, L. Lemaire, C. Cao, A. Mariotti, P. Paul, and J. Batut for helpful comments and suggestions; and S. Blythe and E. Gatzogiannis for technical advice. **Funding:** National Institutes of Health grant R35 GM118147. **Author contributions:** Conceptualization: P.J.B., M.S.L.; Methodology: P.J.B., M.L., J.R.; Investigation: P.J.B., X.Y.B., Z.S.; Software: P.J.B.; Formal analysis: P.J.B., X.Y.B.; Visualization: P.J.B., X.Y.B.; Funding acquisition: M.S.L.; Project administration: M.S.L.; Supervision: M.S.L.; Writing – original draft: P.J.B.; Writing – review and editing: P.J.B., M.S.L., X.Y.B. **Competing interests:** The authors declare that they have no competing interests. **Data and materials availability:** All Micro-C sequencing data are available through GEO accession number GSE171396. All imaging data are freely available upon request. All materials used in the analysis are available upon request, and custom data analysis code is available through GitHub (https://github.com/phil-batut/transcription_imaging.git) and Zenodo (29).

SUPPLEMENTARY MATERIALS

science.org/doi/10.1126/science.abi7178
Materials and Methods
Figs. S1 to S14
Tables S1 to S4
References (30–57)
MDAR Reproducibility Checklist

25 March 2021; resubmitted 16 October 2021
Accepted 6 December 2021
10.1126/science.abi7178

NEUROSCIENCE

Probing subthreshold dynamics of hippocampal neurons by pulsed optogenetics

Manuel Valero^{1*}, Ipsita Zutshi¹, Euisik Yoon^{2,3}, György Buzsáki^{1,4,5*}

Understanding how excitatory (E) and inhibitory (I) inputs are integrated by neurons requires monitoring their subthreshold behavior. We probed the subthreshold dynamics using optogenetic depolarizing pulses in hippocampal neuronal assemblies in freely moving mice. Excitability decreased during sharp-wave ripples coupled with increased I. In contrast to this “negative gain,” optogenetic probing showed increased within-field excitability in place cells by weakening I and unmasked stable place fields in initially non-place cells. Neuronal assemblies active during sharp-wave ripples in the home cage predicted spatial overlap and sequences of place fields of both place cells and unmasked preexisting place fields of non-place cells during track running. Thus, indirect probing of subthreshold dynamics in neuronal populations permits the disclosing of preexisting assemblies and modes of neuronal operations.

Understanding how neurons integrate excitatory (E) and inhibitory (I) inputs requires access to the neuron’s subthreshold dynamics (1–4). Because intracellular monitoring of cell assemblies in behaving animals is currently unrealistic, different single-cell modes of operations (or “models”) have been proposed to explain firing characteristics in various circumstances (Fig. 1, A and B, and fig. S1) (I). In the “tuned excitation” (“blanket” inhibition) (I, 5) and “balanced network” models (I activity tracks E changes) (6–8), both membrane polarization (V_m) and firing rate response decrease at more depolarized V_m (Fig. 1, A and B) (9–11). By contrast, in the “reciprocal network” model, reduction of I is coupled to V_m depolarization and increased firing rate (Fig. 1, A and B) (12–14). Thus, by varying V_m experimentally and observing the changes in firing rates, one can gain access to the subthreshold behavior of neurons (fig. S1). Adding active conductances to the model neuron affected its quantitative features but did not change these predictions qualitatively (figs. S2 and S3).

We probed V_m with short optogenetic pulses. Using micro-light-emitting diode (μ LED) probes (four shanks with three μ LEDs on each shank) (15), we recorded and probed large numbers of CA1 pyramidal neurons simultaneously in freely moving calcium/calmodulin-dependent protein kinase II α (CamKII α) -Cre::Ai32 mice (Fig. 1, C and D, and fig. S4; $n = 822$

pyramidal neurons in four mice; 43.3 ± 8.37 pyramidal neurons per session). μ LEDs were activated (0.02 to 0.1 μ W, 20 ms duration) with randomly variable (20 to 40 ms) offsets so that stimulation of each site recurred at ~ 0.3 - to 0.6-s intervals (Fig. 1C and fig. S5). Random intervals (20 ms) between the light pulses served as control epochs for comparison (materials and methods). Of 822 neurons, 611 responded unequally to the three neighboring μ LEDs, owing to their different distances from the recorded neurons (Fig. 1, D and E, and figs. S4 and S5), and these responses were used as a proxy for estimating relative changes of V_m and E/I dynamics. The evoked spike responses varied as a function of brains state (fig. S6) but did not perturb the firing features of the neurons (fig. S7). No changes were observed in nonresponsive neurons, safeguarding against local network-induced effects (fig. S8).

During sharp-wave ripples (SPW-Rs), excitatory neurons increased their firing rates more than inhibitory neurons (fig. S9) (6). In contrast to this population gain of excitation, light-induced spike responses in individual pyramidal cells decreased during SPW-Rs (Δ Rate; Fig. 1, F to I). Increasing V_m depolarization decreased the light-induced response during SPW-Rs (Fig. 1J), resembling the balanced mode of operation (Fig. 1A). This conclusion was further supported by the negative correlation between firing-rate change during SPW-R and baseline firing rates of neurons ($\rho = -0.19$, $P < 10^{-7}$; fig. S10) and more directly by intracellular experiments, in which V_m was systematically varied (Fig. 1, K to M), reproducing the effect seen with optogenetic V_m depolarization (Fig. 1I) and favoring the balanced E/I model.

Next, we examined the subthreshold E/I dynamics of place cells. During track running, three blocks of 10 baseline runs on a linear track were interleaved with two blocks of 40 to 50 stimulation runs (fig. S7D). We observed a

¹Neuroscience Institute, Langone Medical Center, New York University, New York, NY 10016, USA. ²Department of Electrical Engineering and Computer Science, University of Michigan, Ann Arbor, MI 48109, USA. ³Center for Nanomedicine, Institute for Basic Science (IBS) and Graduate Program of Nano Biomedical Engineering (Nano BME), Yonsei University, Seoul 03722, South Korea. ⁴Neuroscience Institute and Department of Neurology, Langone Medical Center, New York, NY 10016, USA. ⁵Center for Neural Science, New York University, New York, NY 10003, USA.
*Corresponding author. Email: valegarman@gmail.com (M.V.); gyorgy.buzsaki@nyumc.org (G.B.)

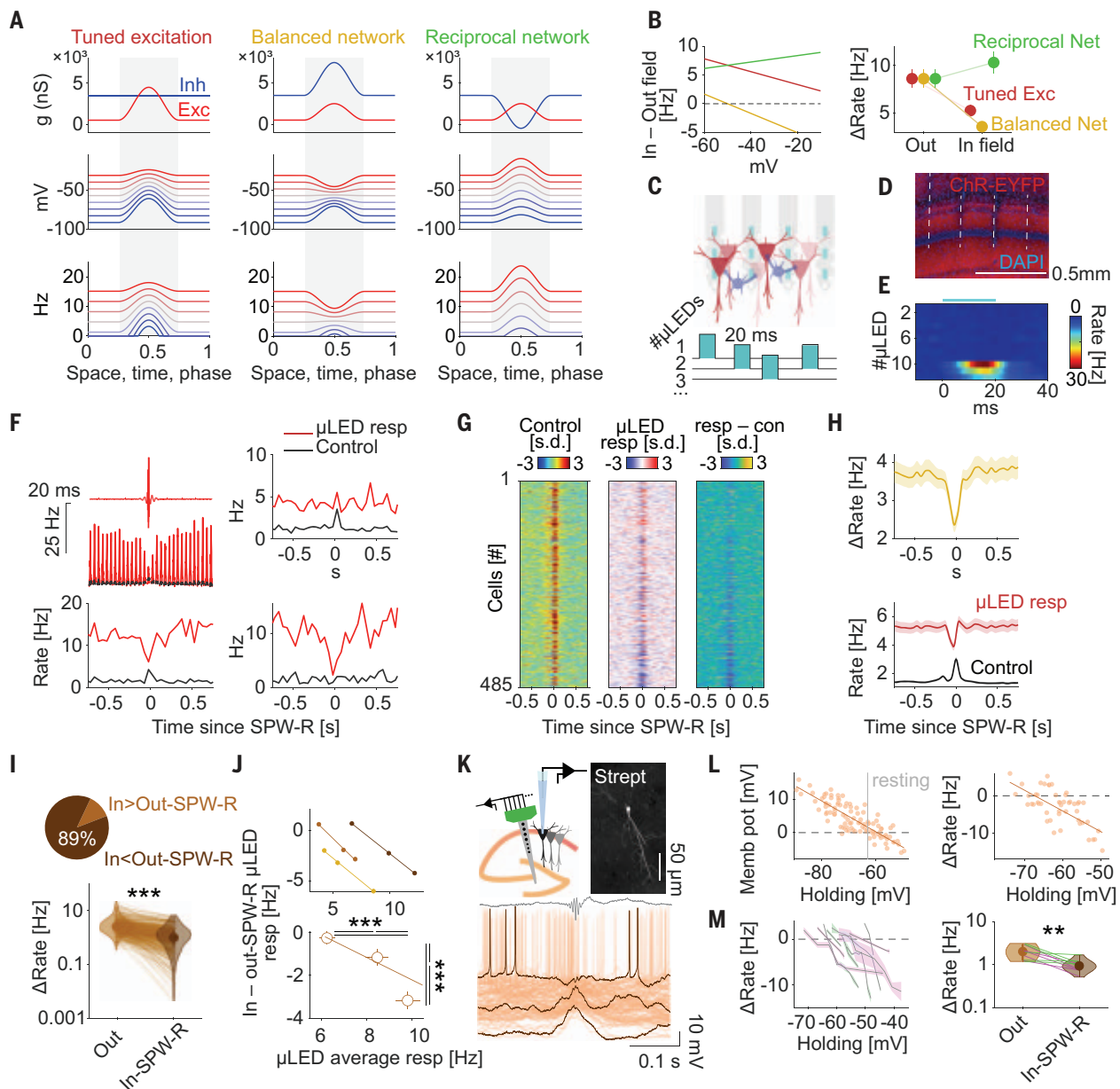


Fig. 1. Decreased single-neuron excitability during SPW-Rs. (A) Different relationships of the excitatory and inhibitory conductances (top row) lead to specific membrane potential (middle row) and firing rate (bottom row). (B) Rate predictions as a function of the holding V_m . (C) CA1 neurons in CamKII α -Cre::Ai32 mice respond to 20-ms random pulses. (D) Probe shank locations. (E) Peristimulus time histogram (PSTH) from a pyramidal cell responding to three μ LEDs on the same shank but not one to nine μ LEDs on different shanks. (F) (Top left) Histograms showing responses to light pulses (red) and control rate (black dashed line) during SPW-Rs (30 bins of 50 ms). (Bottom) Response displayed for the same single neuron. (Right) Two other example cells. (G) Z-scored control rate (left), optogenetic responses (center), and rate change (Δ Rate = μ LED responses – control; right) during SPW-Rs for all light-responding cells ranked by light-response amplitude. (H) Group control firing rate (black), light response rate (red

[mean \pm confidence interval at 95% (CI95), bottom], and rate difference (gold; mean \pm CI95). (I) Optogenetic responses decreased during SPW-Rs (Δ Rate; $n = 485$ neurons; $P < 10^{-55}$, Wilcoxon paired signed-rank test) (J) (Top) Difference between in-SPW-R versus outside SPW-R firing rates as a function of three light intensities in three neurons. (Bottom) Population average (mean \pm CI95 $\rho = -0.55$, $P < 10^{-57}$; $P < 10^{-9}$ for all comparisons, Friedman test). (K) Pyramidal neuron filled with biocytin from a head-fixed waking mouse experiment. (Bottom) Responses of the filled neuron at different V_m (three traces are highlighted in black) during SPW-Rs (top gray line, average ripple). (L) Relationship between the holding V_m and V_m change (left) and firing-rate change (right) for all SPW-R in (K). (M) Group results for five cells from five anesthetized rats (green) and five cells from four head-fixed mice (pink). (Right) Decreased gain during SPW-Rs ($P = 0.002$; Wilcoxon paired signed-rank test). ** $P < 0.01$ and *** $P < 0.001$.

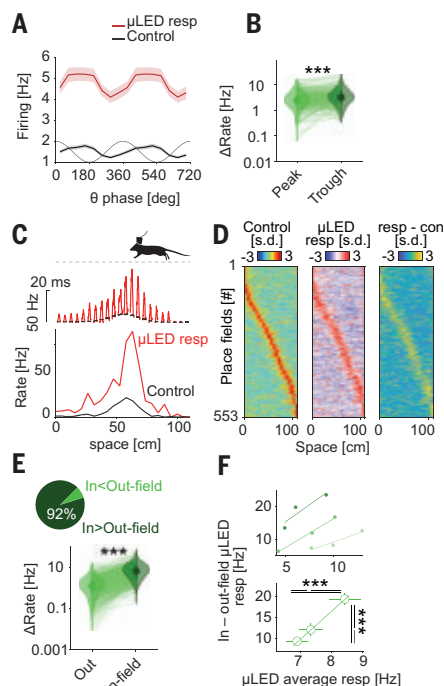
gain at the trough of the theta cycle, the phase corresponding to the strongest synchrony of pyramidal neurons (Fig. 2A) (16). We then compared neuronal excitability within and outside the place fields of place cells (17).

With a standard definition of “place field” (materials and methods) (18), more than half of the pyramidal neurons were classified as place cells [73% and 71% of light-responsive and nonresponsive neurons, respectively; $P =$

0.90, χ^2 test; (17–19); fig. S11]. The induced spike responses varied within and outside the place field (Fig. 2, C and D). The induced rate increase was higher within than outside the place field (Fig. 2E and fig. S12). Increasing

Fig. 2. Increased excitability during theta oscillations and within place fields.

(A) Thin line, theta phase. Red and black lines, phase histograms of spikes during optostimulation and control pulses, respectively (mean \pm CI95). (B) Rate gain at the trough of the theta cycle ($P < 10^{-6}$, Wilcoxon test). (C) (Top) Light-induced spike histograms (red line) and control rate (black line). (Bottom) for the same single neuron. (D) Control, light responses and difference (resp-con) for all light-responsive neurons, ranked by the control rate peak position. (E) Responses were larger inside than outside the place field ($n = 553$ place fields; $P < 10^{-115}$, Wilcoxon test). (F) (Top) Difference between in-field and out-of-field firing rates (gain), as a function of three light intensities in three neurons (top) and group average (bottom; $p = 0.24$, $P < 10^{-6}$, $P < 10^{-8}$, Friedman test). *** $P < 0.001$.

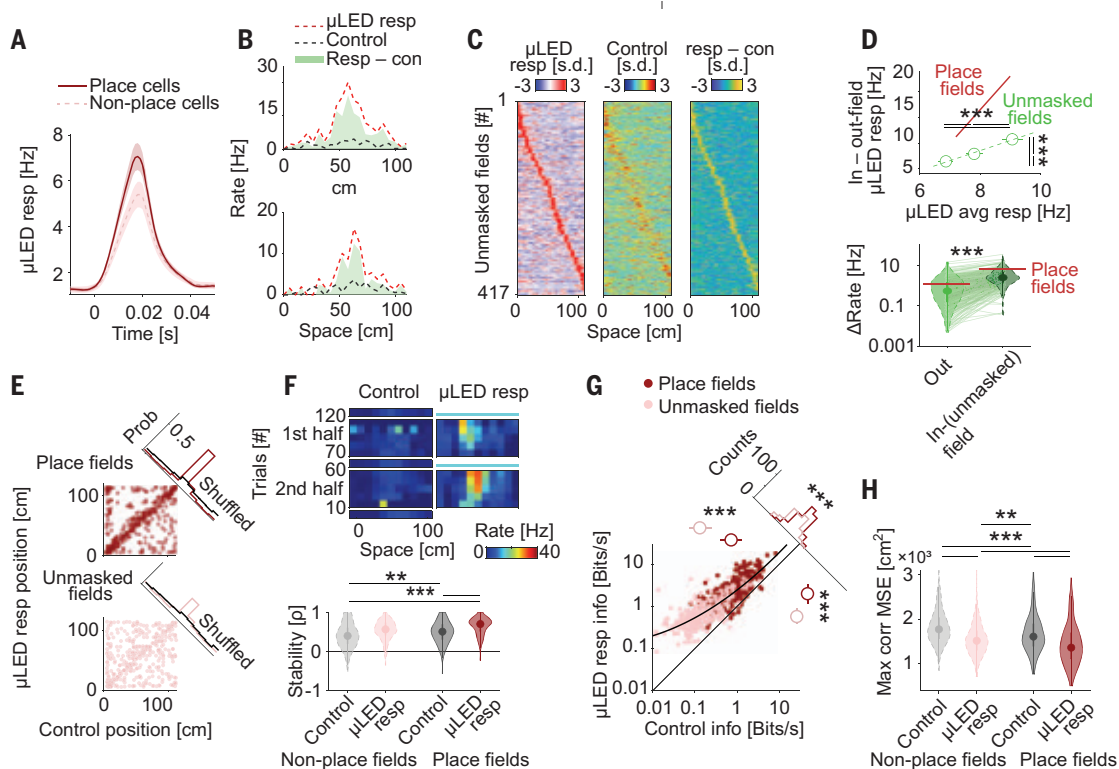


depolarization of V_m by stronger light intensity increased the in-field gain several-fold (Fig. 2F). This in-field gain was positively correlated with both the out-of-field firing rate and the home-cage firing rate of the neuron ($p = 0.17$, $P < 10^{-5}$ and $p = 0.25$, $P < 10^{-7}$, respectively; fig S12). No rate changes were observed in nonresponsive pyramidal neurons (fig. S8). These results support the reciprocal mode of operation.

Light responses in place cells, tested in the home cage before the track, were significantly stronger than in non-place cells, and these results cannot be explained by differences in firing rate (Fig. 3A and fig. S13), suggesting that neurons with higher excitability more likely express place fields. In support of this hypothesis, optogenetic depolarization revealed place fields in the majority of non-place cells (Fig. 3, B and C; 69.3%, 289 of 417; materials and methods), although the in-field gain was less for the induced place fields than for real place fields (Fig. 3D and fig. S13). We found a robust correlation between the spatial location of induced place field spikes

Fig. 3. Unmasking sub-threshold place fields.

(A) Evoked responses in home cage sessions in place cells and non-place cells [$P < 10^{-4}$, Kruskal-Wallis (KW) test]. (B) Light responses (red) and control (black) spikes for two example non-place neurons. (C) Light-induced place fields, control spike rate, and rate gain during light stimulation for all light-responding non-place cells ranked by the light responses. (D) Difference between in-field and out-of-field firing rates at three light intensities ($P < 10^{-56}$, Wilcoxon paired test; $p = 0.38$, $P < 10^{-5}$ for all comparisons, Friedman test). For comparison, the slope from place cells (Fig. 2F) is superimposed. (E) Correlation between peak location in control epochs and light responses for place fields of place cells (top; $P < 10^{-40}$, χ^2 test against 500 shuffles) and unmasked place fields of non-place cells (bottom; $P < 10^{-10}$, χ^2 test). (F) Spike activity for an example non-place cell during baseline (no stimulation) runs (1 to 10, 61 to 70, 121 to 130) and stimulation runs. Spike activity during light stimulation (20-ms pulses; right panel) and between stimulation (control) epochs (left panel). Correlation between first and second halves (trials 11 to 60 and 71 to 120) of the session was used to compute place field stability. (Bottom) Place fields during light stimulation were more stable for both true place fields and unmasked place fields ($P < 10^{-9}$ and $P < 10^{-19}$, respectively; two-ways analysis of variance (ANOVA)) than during control epochs. (G) Correlation of spatial information (Bits/spike) between control and light-stimulated epochs ($P < 10^{-62}$ and $P < 10^{-58}$, respectively; KW test). Black line shows an exponential fit. Light-boosted effect was stronger for unmasked place fields of non-place cells than for place cell place fields ($P < 10^{-15}$, KW test). (H) Spatial decoding accuracy of the mouse's position on the track increased during light-stimulation epochs of both non-place cells and place cells ($P < 10^{-8}$ and $P < 10^{-27}$ for control and light epochs, respectively; two-way ANOVA). Note lower mean squared error (MSE) during light stimulation of non-place cells compared to control spiking of place cells ($P = 0.001$, Tukey test). ** $P < 0.01$ and *** $P < 0.001$.



and the sparse spikes of non-place cells in the absence of stimulation (Fig. 3, C and E; “ghost fields”).

Features of the optogenetically unmasked place fields were similar to those of real place fields (Fig. 3, F and G, and fig. S12). To anchor neuronal firing to behavior, we examined the precision by which the animal's position on the track can be predicted by active neurons (19). The root mean squared error of the decoded position was highest for the sparse non-place cell spikes and lowest for light-boosted spikes of place cells. The induced spikes of non-place cells more accurately predicted the mouse's position on the track than those of “bona fide” place cells (Fig. 3H and fig. S11).

We found a reliable correlation between spatial correlations of place cell pairs on the track and firing rate correlations of the same pairs during SPW-Rs in the home cage (Fig. 4, A to C). (20). No such relationship was present

for non-place cell pairs (Fig. 4C). However, during optogenetic stimulation, the relationship between cofiring during SPW-Rs and spatial overlap was revealed for unmasked place fields of non-place field pairs (Fig. 4C). To study the population consequence of the pairwise effects, we performed independent component analysis (ICA) on the Z-scored spike matrix of pyramidal neurons (21) to extract patterns of higher-order cofiring in the home cage (Fig. 4D). Assembly members of place cells, but not of mixtures of place and non-place cells, showed higher spatial correlation than chance (Fig. 4E). However, when spikes of unmasked place fields were considered, they expressed spatial correlation at the level of real place cells (Fig. 4F and fig. S14). Sequential firing of place cells was correlated with spike sequences during SPW-Rs (Fig. 4G) (22, 23). The fraction of SPW-R events with significant virtual track trajectories increased when unmasked place fields were also included

for the construction of the place field sequence template (Fig. 4H).

Optogenetic depolarization of neurons increased the within-field firing rate gain in hippocampal place cells and unmasked place fields in non-place cells (1, 24–26), implying that almost any pyramidal cell can express a place field and that the entire CA1 population contributes to forming specific attractors or trajectories in any given situation (1, 24, 26, 27). In these preconfigured attractors (23, 28, 29), neurons with the highest excitability form a scaffold map and emit high-enough spike rates to be classified as place cells (17). Place cells are not continuously “driven” by outside cues (30, 31) but emerge by transient disinhibition, perhaps coupled with excitation, as predicted by the reciprocal mode of operation and further supported by the position-dependent firing rates of inhibitory interneurons as well as the decreased inhibition of place cells within their fields (fig. S15). Our results challenge

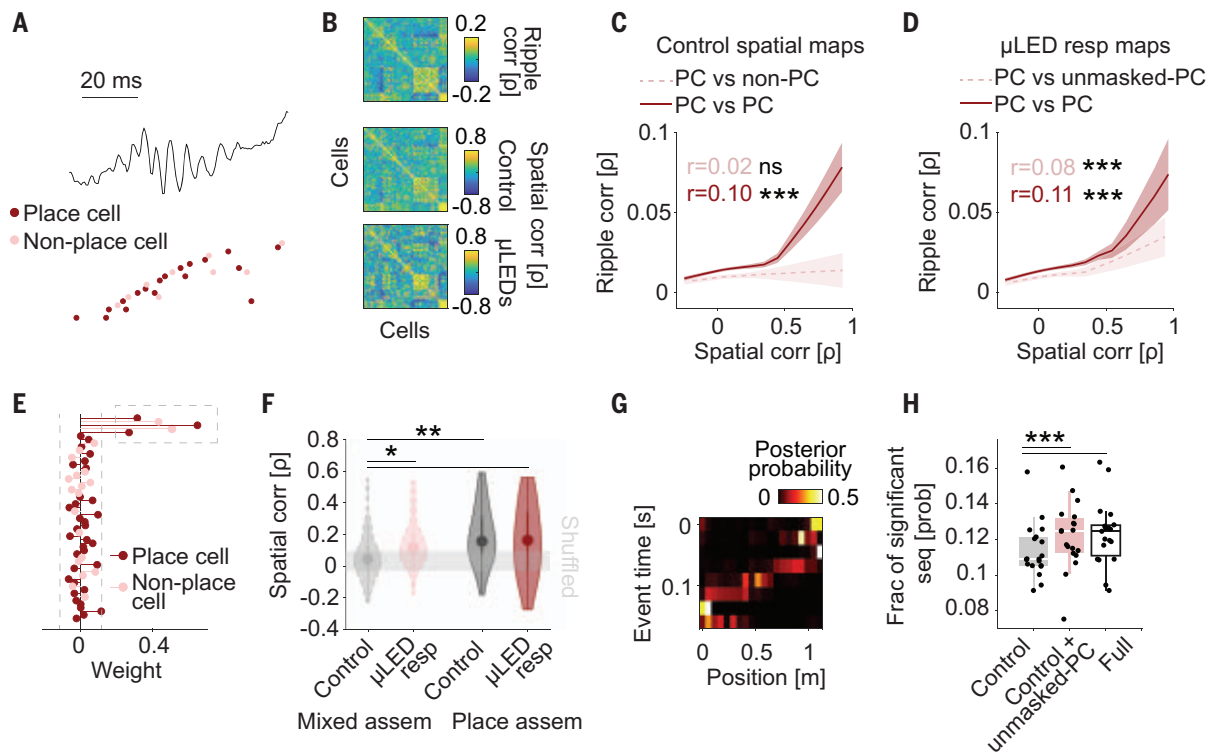


Fig. 4. Uncovering spatial overlap of preexisting cell ensembles. (A) Neural sequence of place cells and non-place cells during a SPW-R. (B) Similarity matrices show cofiring of 47 pyramidal neurons in an example session during SPW-R in the home cage and spatial correlations of the same pairs (Spearman's ρ) during control and light-stimulation epochs on the track. (C) SPW-R cofiring was positively correlated with spatial overlap in place cell pairs ($P < 10^{-27}$, Spearman correlation) but not in pairs with place and non-place cell (non-PC) partners ($P = 0.11$). (D) Same as (C), but for light-induced responses ($P < 10^{-5}$, Spearman correlation; $P < 10^{-29}$ for place cell pairs; $P = 0.002$ between control and light stimulation after correcting by the spatial cofiring; repeated-measures ANOVA). (E) Cell assemblies (21) in home cage recordings. Relative weights of neuron in an

example assembly. Neurons with > 2 SDs (dashed gray line) of the weight distribution were classified as members of the assembly. (F) Spatial overlap on the track (ρ) was higher among assemblies consisting of only-place cells than for assemblies of mixed place cells and non-place cells ($P = 0.006$, $P = 0.31$, and $P = 0.02$ for assemblies, light stimulation, and their interaction, respectively; two-way ANOVA). (G) Forward replay sequence during home cage recording. Bayesian decoding (22). (H) The fraction of SPW-R events with significant trajectories (against 500 shuffles) increased ($P < 10^{-4}$, Friedman test) when unmasked place fields of non-place cells ($P < 10^{-4}$, Tukey test) and when spikes from both stimulated place fields and unmasked place fields ($P < 10^{-3}$) were included for the construction of the place field sequence template. * $P < 0.05$, ** $P < 0.01$ and *** $P < 0.001$.

the current notion of spatially uniform inhibition underlying place cell properties and reconcile several models of place field emergence (1, 25, 26, 29, 32).

Optogenetic perturbation during the theta cycles and SPW-Rs revealed opposite excitability rules, and the SPW-R data were best fitted by a balanced network model (33–35). Even though SPW-R represents the highest excitability state of the CA1 network, the contributing individual neurons decrease their excitability. This negative gain enables larger rate changes of slow firing, compared to fast firing, neurons during SPW-R. By contrast, the reciprocal mode of operation during exploration allows for larger in-field gain for faster-firing, compared to slow-firing, neurons. Brain state-dependent shifts between the reciprocal and balanced E/I modes of operations may be brought about by the altered temporal relationship between interneuron and pyramidal cell spiking and the consequent V_m (36), perhaps set by subcortical neuromodulators. SPW-R is a natural V_m changer (37) during which more neurons fire than can be accounted for by place cells active during waking experience (37–39). These spikes are emitted by those neurons whose sparse spiking activity also contributes to the same hippocampal map.

REFERENCES AND NOTES

- Grienberger, A. D. Milstein, K. C. Bittner, S. Romani, J. C. Magee, *Nat. Neurosci.* **20**, 417–426 (2017).
- C. C. H. Petersen, *Neuron* **95**, 1266–1281 (2017).
- M. A. Long, A. K. Lee, *Curr. Opin. Neurobiol.* **22**, 34–44 (2012).
- M. Valero, D. F. English, *J. Neurosci. Methods* **326**, 108397 (2019).
- M. M. Karnani, M. Agetsuma, R. Yuste, *Curr. Opin. Neurobiol.* **26**, 96–102 (2014).
- J. Csicsvari, H. Hirase, A. Czúrkó, A. Mamiya, G. Buzsáki, *J. Neurosci.* **19**, 274–287 (1999).
- B. V. Atallah, M. Scanziani, *Neuron* **62**, 566–577 (2009).
- L. J. Borg-Graham, C. Monier, Y. Frégnac, *Nature* **393**, 369–373 (1998).
- J. Mariño et al., *Nat. Neurosci.* **8**, 194–201 (2005).
- M. Wehr, A. M. Zador, *Nature* **426**, 442–446 (2003).
- A. Bhatia, S. Moza, U. S. Bhalla, *eLife* **8**, e43415 (2019).
- J. S. Anderson, M. Carandini, D. Ferster, *J. Neurophysiol.* **84**, 909–926 (2000).
- R. I. Wilson, R. A. Nicoll, *Nature* **410**, 588–592 (2001).
- H. C. Barron, T. P. Vogels, T. E. Behrens, M. Ramaswami, *Proc. Natl. Acad. Sci. U.S.A.* **114**, 6666–6674 (2017).
- F. Wu et al., *Neuron* **88**, 1136–1148 (2015).
- G. Buzsáki, L. W. Leung, C. H. Vanderwolf, *Brain Res.* **6**, 139–171 (1983).
- John. O'Keefe, L. Nadel, *The Hippocampus as a Cognitive Map* (Clarendon, 1978).
- K. Mizuseki, K. Diba, E. Pastalkova, G. Buzsáki, *Nat. Neurosci.* **14**, 1174–1181 (2011).
- M. A. Wilson, B. L. McNaughton, *Science* **261**, 1055–1058 (1993).
- M. A. Wilson, B. L. McNaughton, *Science* **265**, 676–679 (1994).
- V. Lopes-dos-Santos, S. Ribeiro, A. B. L. Tort, *J. Neurosci. Methods* **220**, 149–166 (2013).
- B. E. Pfeiffer, D. J. Foster, *Nature* **497**, 74–79 (2013).
- A. D. Groszmark, G. Buzsáki, *Science* **351**, 1440–1443 (2016).
- K. C. Bittner et al., *Nat. Neurosci.* **18**, 1133–1142 (2015).
- G. Dragoi, K. D. Harris, G. Buzsáki, *Neuron* **39**, 843–853 (2003).
- D. Lee, B.-J. Lin, A. K. Lee, *Science* **337**, 849–853 (2012).
- A. Samsonovich, B. L. McNaughton, *J. Neurosci.* **17**, 5900–5920 (1997).
- G. Dragoi, S. Tonegawa, *Nature* **469**, 397–401 (2011).
- S. McKenzie et al., *Neuron* **109**, 1040–1054.e7 (2021).
- J. O'Keefe, N. Burgess, *Nature* **381**, 425–428 (1996).
- J. O'Keefe, J. Krupic, *Physiol. Rev.* **101**, 1427–1456 (2021).
- J. D. Cohen, M. Bolstad, A. K. Lee, *eLife* **6**, e23040 (2017).
- D. F. English et al., *J. Neurosci.* **34**, 16509–16517 (2014).
- M. Valero et al., *Nat. Neurosci.* **18**, 1281–1290 (2015).
- M. Valero et al., *Neuron* **94**, 1234–1247.e7 (2017).
- B. K. Hulse, E. V. Lubenov, A. G. Siapas, *Cell Rep.* **18**, 136–147 (2017).
- G. Buzsáki, *Hippocampus* **25**, 1073–1188 (2015).
- H. R. Joo, L. M. Frank, *Nat. Rev. Neurosci.* **19**, 744–757 (2018).
- D. J. Foster, *Annu. Rev. Neurosci.* **40**, 581–602 (2017).

ACKNOWLEDGMENTS

We thank L. Menéndez de la Prida, A. Fernandez-Ruiz, A. Navas-Olivé, R. Huszar, E. Barrio-Alonso, and members of our laboratory for helpful comments on the project. **Funding:** This work was supported by the European Molecular Biology Organization (EMBO) postdoctoral fellowship (EMBO ALTF 1161-2017) and Human Frontiers Science Program (HFSP) postdoctoral fellowship (LT0000717/2018) to M.V.; a Leon Levy Neuroscience Fellowship to I.Z.; and NIH MH107396, NS 090583, NSF PIRE grant (1545858), U19 NS107616, U19 NS104590, and NSF NeuroNex MINT grant 1707316. **Author contributions:**

M.V. and G.B. designed the experiments. M.V. performed and analyzed the experiments with I.Z. G.B. and M.V. wrote the paper with contributions from other authors. **Competing interests:** E.Y. is a cofounder of NeuroLight Technologies, a for-profit manufacturer of neurotechnology. The other authors declare no competing interests. **Data and material availability:** E.Y. is inventor on patents applications US Patent 9,247,889 (2016) and US Patent 9,642,545 (2017) held by the University of Michigan that covers the neural probes with optical stimulation capability. All data needed to evaluate the conclusions are present in the paper and/or the supplementary materials and are publicly available in the Buzsaki Lab Databank: <https://buzsakilab.com/wp/public-data/>. Custom MATLAB scripts can be downloaded from <https://github.com/buzsakilab/buzcode>.

SUPPLEMENTARY MATERIALS

science.org/doi/10.1126/science.abm1891
Material and Methods
Figs. S1 to S15
References (40–54)
MDAR Reproducibility Checklist

31 August 2021; accepted 23 December 2021
10.1126/science.abm1891

DEVELOPMENT

Establishment of mouse stem cells that can recapitulate the developmental potential of primitive endoderm

Yasuhide Ohinata^{1,2*}, Takaho A. Endo³, Hiroki Sugishita², Takashi Watanabe³, Yusuke Iizuka², Yurie Kawamoto², Atsunori Saraya¹, Mami Kumon², Yoko Koseki², Takashi Kondo², Osamu Ohara^{3,4}, Haruhiko Koseki^{1,2}

The mammalian blastocyst consists of three distinct cell types: epiblast, trophoblast (TB), and primitive endoderm (PrE). Although embryonic stem cells (ESCs) and trophoblast stem cells (TSCs) retain the functional properties of epiblast and TB, respectively, stem cells that fully recapitulate the developmental potential of PrE have not been established. Here, we report derivation of primitive endoderm stem cells (PrESCs) in mice. PrESCs recapitulate properties of embryonic day 4.5 founder PrE, are efficiently incorporated into PrE upon blastocyst injection, generate functionally competent PrE-derived tissues, and support fetal development of PrE-depleted blastocysts in chimeras. Furthermore, PrESCs can establish interactions with ESCs and TSCs and generate descendants with yolk sac-like structures in utero. Establishment of PrESCs will enable the elucidation of the mechanisms for PrE specification and subsequent pre- and postimplantation development.

Epiblast, trophoblast (TB), and primitive endoderm (PrE) are differentiated from the zygote by the late blastocyst stage of mouse preimplantation development and contribute to generate the major parts of the embryo, placenta, and yolk sac, respectively, during postimplantation development.

Our understanding of the functional properties of epiblast and TB has been enhanced by the use of embryonic stem cells (ESCs) and trophoblast stem cells (TSCs), which retain functional properties of epiblast and TB, respectively, and have provided experimental platforms to dissect their functions (1, 2). By contrast, although extraembryonic endoderm cells (XENCs) have been derived from PrE, they do not fully recapitulate the developmental potential of the PrE (3).

The PrE lineage is vital for normal embryonic development and is the origin of the visceral endoderm (VE) of the visceral yolk sac, the parietal endoderm (PE) of the parietal yolk sac, and the marginal zone endoderm (MZE) lining the boundary between the placenta and

¹Department of Cellular and Molecular Medicine, Graduate School of Medicine, Chiba University, 1-8-1 Inohana, Chuo ward, Chiba 260-8670, Japan. ²Laboratory for Developmental Genetics, RIKEN Center for Medical Sciences (IMS), 1-7-22 Suehiro-cho, Tsurumi, Yokohama 230-0045, Japan.

³Laboratory for Integrative Genomics, RIKEN Center for Medical Sciences (IMS), 1-7-22 Suehiro-cho, Tsurumi, Yokohama 230-0045, Japan. ⁴Facility for Clinical Omics Analysis, Kazusa DNA Research Institute, 2-6-7 Kazusakamatori, Kisarazu, Chiba 292-0818, Japan.

*Corresponding author. Email: yasuhideohinata@chiba-u.jp

Fig. 1. Long-term culture of PrE-derived cells. (A) Culture conditions tested in this study. (B) Derivation of cells in the indicated culture conditions from blastocysts. Derived cells at passage 2 (P2) are shown. Serum+L and Serum+C3 conditions induced XEN-like colonies, whereas +C3PD03 induced ESC colonies. +C3 induced distinct dome-shaped colonies. Scale bar, 100 μ m. (C) Colony morphology of CHIR99021-induced cells maintained under the indicated conditions for at least five passages. Scale bar, 100 μ m.

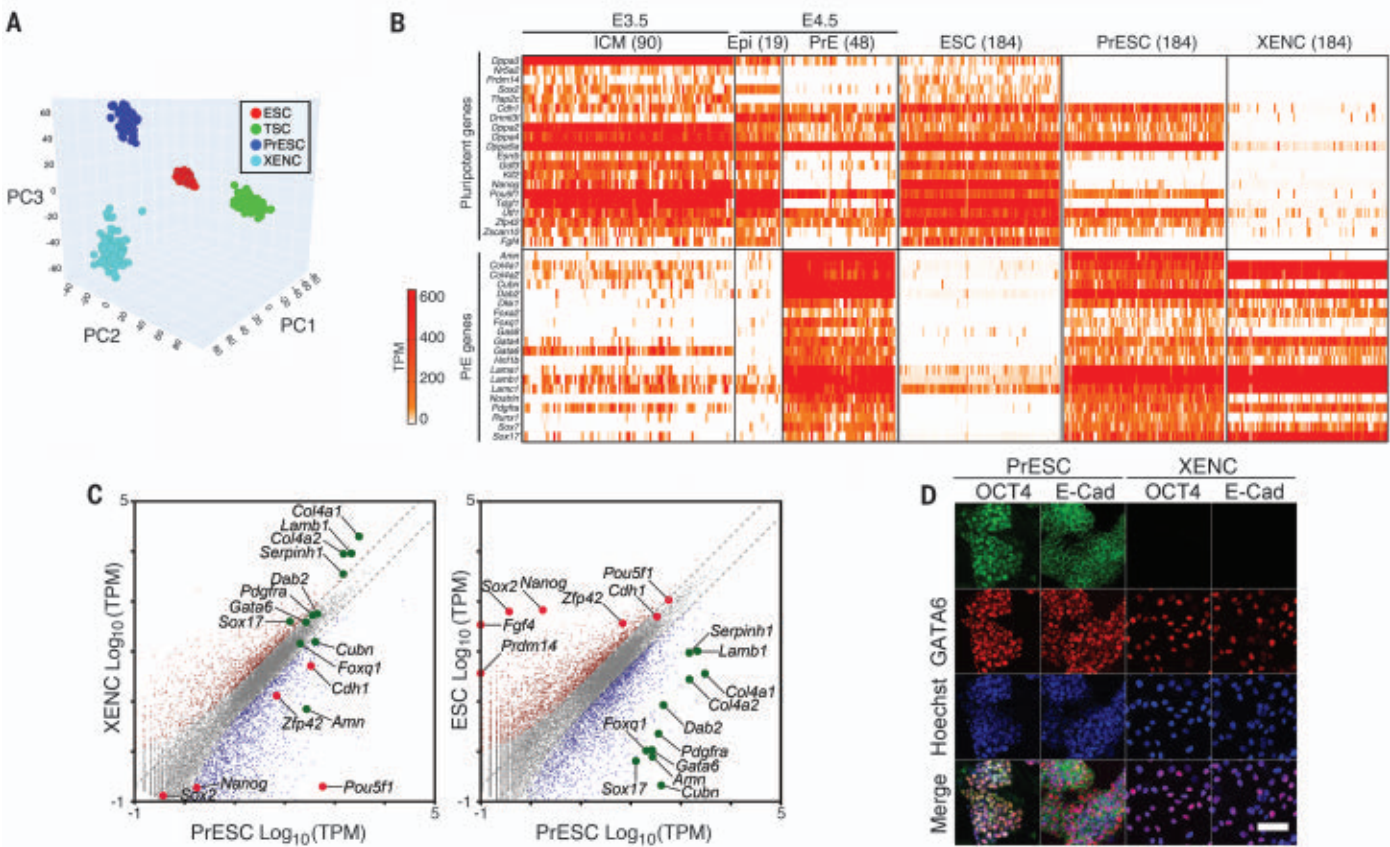
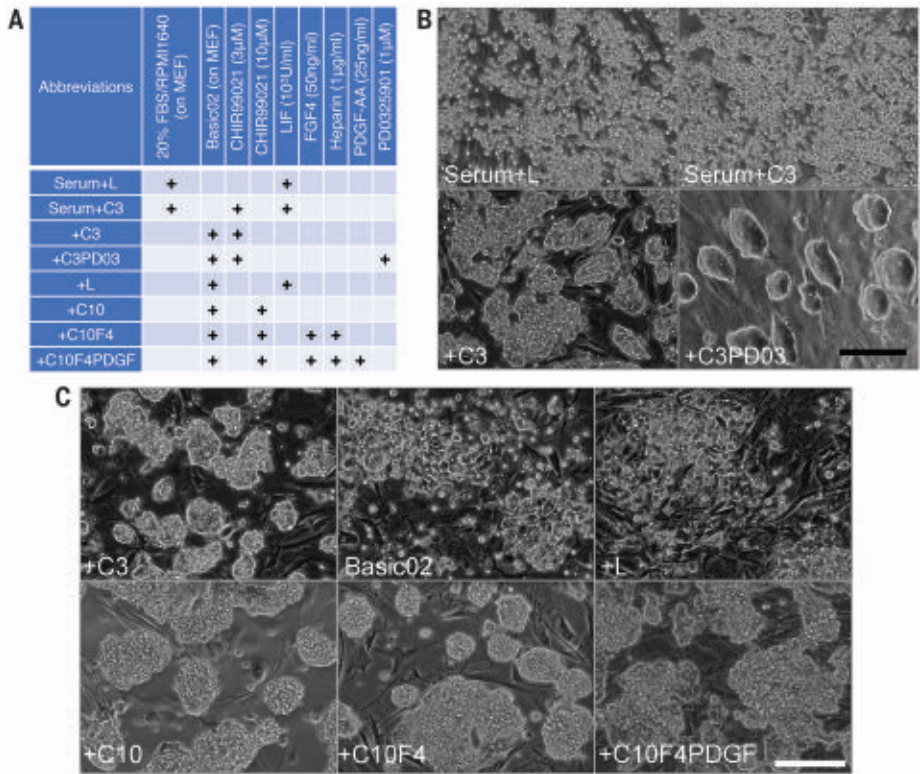


Fig. 2. PrESCs retain properties of PrE. (A) PCA comparison of gene expression profiles among ESCs, TSCs, PrESCs, and XENCs. (B) Comparison of pluripotent and PrE marker gene expression among E3.5 ICM, E4.5 ICM, ESCs, PrESCs, and XENCs. (C) Comparison of gene expression profiles of PrESCs with those of XENCs and ESCs. Red and green dots indicate pluripotency and PrE marker genes, respectively. (D) The expression of OCT4, E-cadherin, and GATA6 in PrESCs and XENCs. Scale bar, 50 μ m.

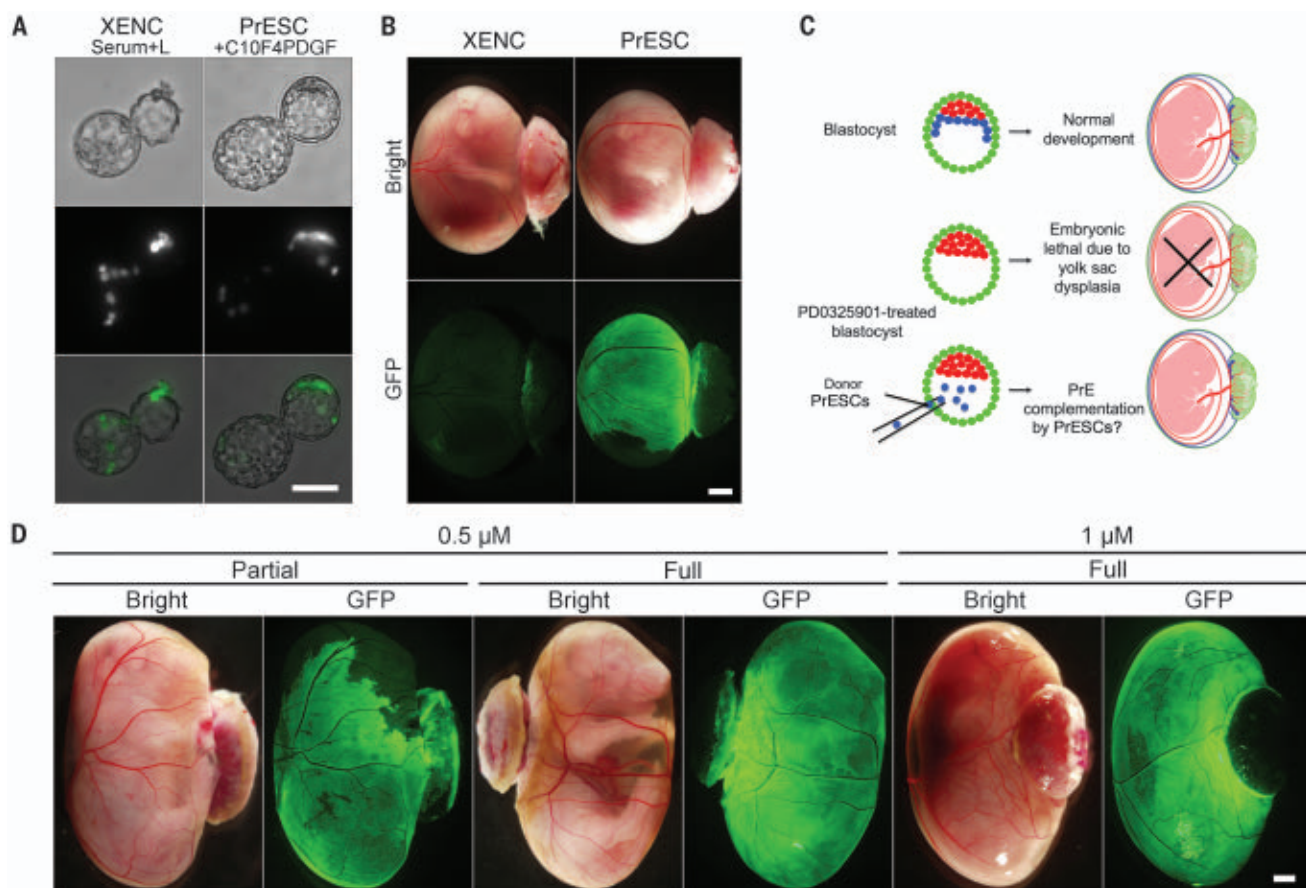


Fig. 3. Developmental potential of PrESCs. (A) Distribution of GFP-labeled XENCs and PrESCs 18 hours after blastocyst injection. Scale bar, 50 μ m. (B) Distribution of GFP-labeled XENCs and PrESCs in E14.5 chimeric conceptuses. Scale bar, 1 mm. (C) Schematic representation of the PrESC

complementation assay. (D) Complementation of PrE-depleted blastocysts by GFP-labeled PrESCs generated through 0.5 or 1 μ M PD0325901 treatment. E18.5 chimeric conceptuses revealed either partial or full reconstitution of extra-embryonic endoderm derivatives by PrESCs. Scale bar, 1 mm.

chorionic plate of the placental disk (4). These extraembryonic endoderm tissues play crucial roles in nourishing the embryo through nutrient provision at the maternal-fetal interface (5), especially before the establishment of placental circulation [approximately embryonic day 10.5 (E10.5) in mice], in anterior-posterior patterning of the epiblast during gastrulation (6), and in yolk sac hematopoiesis (7). VE cells derived from the PrE are further suggested to contribute to formation of the fetal gut (8).

To gain further insight into how the PrE functions during pre- and early postimplantation development, it would be useful to establish stem cell lines that fully retain PrE developmental potential beyond that possessed by XENCs, which can only contribute to the distal region of the PrE (3). We tested for culture conditions that enabled robust growth of PrE-derived cells from blastocysts (Fig. 1A and table S1) and examined the impact of serum, which provides undefined differentiation signals. As reported (3), serum-containing culture allowed efficient derivation of XENCs from the inner cell mass (ICM). Derivation efficiency of XENCs from the ICM was further

facilitated by addition of 3 μ M CHIR99021, a GSK3 inhibitor, but was suppressed by the mitogen-activated protein kinase (MAPK) kinase (MEK) inhibitor PD0325901 (Fig. 1B and fig. S1A). By contrast, serum-free medium could not support colony formation from the ICM by itself, but addition of 3 μ M CHIR99021 promoted characteristic outgrowths and subsequent generation of dome-shaped colonies (Fig. 1B and fig. S1A). This effect of CHIR99021 was inhibited by PD0325901, leading to the induction of ESCs. These results suggested that the CHIR99021-induced cells exhibited a competitive period for fate decision with ESCs and originated from PrE rather than epiblasts.

We next investigated whether CHIR99021-induced cells retained the functional properties of PrE by maintaining them under various serum-free culture conditions (Fig. 1C). The maintenance of these cells was dependent on CHIR99021. Leukemia inhibitory factor (LIF) did not replace CHIR99021 to maintain proliferation, suggesting that these cells are different from ESCs. However, increasing the concentration of CHIR99021 to 10 μ M accel-

erated their proliferation and resulted in a more compacted colony morphology. The impact of fibroblast growth factor 4 (FGF4) and/or platelet-derived growth factor-AA (PDGF-AA), which are known to expand the PrE in blastocysts (9, 10), was also tested and found to accelerate the growth rate of the CHIR99021-induced cells even further, without any additional morphological changes. The CHIR99021-induced cells transformed into XENC-like cells in serum+C3 medium but were not maintained in ESC medium (fig. S1, B and C). Therefore, CHIR99021-induced cells appear to be PrE derivatives captured at an earlier stage than were XENCs. Together with their self-renewing property in culture, we tentatively refer to CHIR99021-induced cells derived and maintained in +C10F4PDGF medium as primitive endoderm stem cells (PrESCs).

Next, we explored the developmental origin of PrESCs by comparing the gene expression profiles revealed through single-cell RNA-sequencing (scRNA-seq) data from the ICM of E3.5 and E4.5 blastocysts. To enable a direct comparison, scRNA-seq analysis for PrESCs was performed in parallel with ESCs, TSCs,

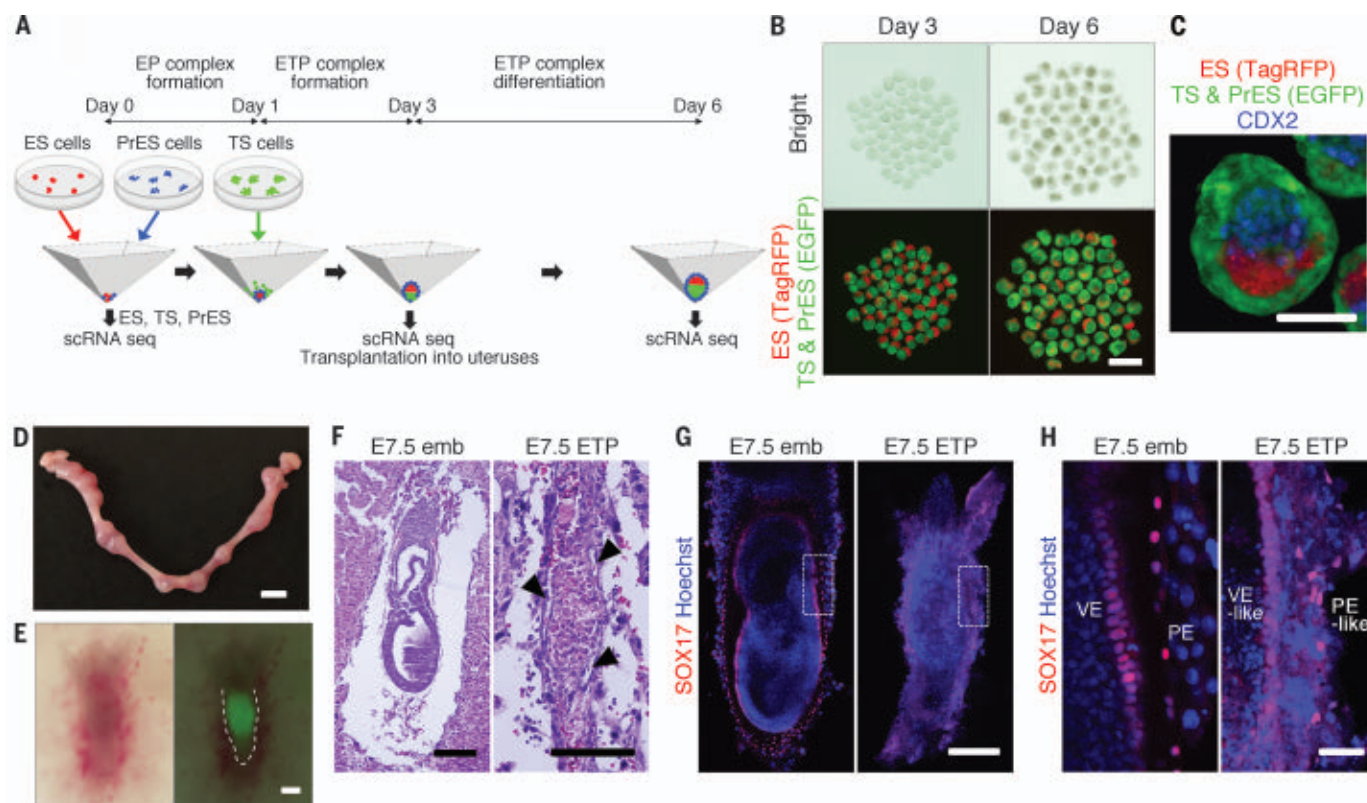


Fig. 4. Differentiation potential of PrESCs in ETPs. (A) Schematic representation of ETP generation. (B) ETP morphology at day 3 and day 6. Scale bar, 200 μ m. (C) Higher magnification view of a day 3 ETP. TSC-derivatives are demarcated by CDX2 expression. Scale bar, 100 μ m. (D) Decidual reaction induced by ETPs on prospective E7.5. (E) The ETP descendant on prospective E7.5. (Left) Vasculature is surrounding the ETP descendant. (Right) Merged view of PrESC-derivatives (green) in

the ETP-descendant. The outline of ETP descendant is indicated by the dashed line. Scale bar, 500 μ m. (F) Histological comparison between (left) the E7.5 embryo and (right) the ETP descendant on prospective E7.5. The yolk sac cavity-like structures are indicated with arrowheads. Scale bar, 500 μ m. (G and H) Confocal images of (left) the E7.5 embryo and (right) the ETP descendant. The boxed areas in (G) are enlarged in (H). Scale bars, (G) 500 μ m; (H) 100 μ m.

and XENCs. The homogeneity of PrESCs and their similarity to other cell lines were examined through principal components analysis (PCA). PrESCs were found to represent a homogeneous population that is distinct from ESCs, TSCs, and XENCs (Fig. 2A and table S2). Gene expression profiles of ESCs, PrESCs, and XENCs were further compared with those of individual cells in the ICM of E3.5 and E4.5 blastocysts (11) by means of agglomerative clustering analysis (fig. S2A). Sixteen clusters were identified; the E4.5 ICM could be segregated into putative epiblasts and PrE through differential expression of genes from clusters 1 to 5, which were barely expressed in the E3.5 ICM. Previously known PrE marker genes, such as *Gata4* and *Gata6*, were enriched in cluster 1, which began to express these genes from E4.5. By contrast, pluripotent marker genes were enriched in clusters 6 and 10, which were expressed as early as E3.5. In cell lines, cluster 1 genes were expressed by PrESCs and XENCs but not by ESCs. Reciprocally, Cluster 6 genes were more abundantly expressed in ESCs than in PrESCs and XENCs. Taken together, global clustering analysis revealed

that PrESCs were closely related to putative PrE in the E4.5 ICM and to XENCs. To further investigate their similarity, we examined the expression of representative PrE marker genes, selected mainly from cluster 1, and pluripotent marker genes from clusters 6 and 10 (Fig. 2B). The putative PrE expressed not only PrE markers but also some pluripotent markers such as *Pou5f1* [encoding octamer-binding transcription factor 4 (OCT4)] and *Cdh1* (encoding E-cadherin). Whereas PrESCs expressed both PrE markers and certain pluripotent markers expressed in the putative PrE, XENCs failed to express these pluripotent markers (table S3). The differences between PrESCs and XENCs were confirmed with conventional RNA-seq analysis (Fig. 2C and table S4). Coexpression of the PrE marker (GATA6) and pluripotent markers (OCT4 and E-cadherin) in PrESCs was further validated with immunofluorescence analysis (Fig. 2D). Therefore, PrESCs retain the molecular properties of founder PrE, which appear around E4.5. Imprinted X-chromosome inactivation was consistently established in PrESCs as well as in XENCs (fig. S2, B and C, and table S4) (3, 12). We further examined

the PrE origin of PrESCs by investigating derivation efficacy of PrESCs from ICM depleted of PrE by PD0325901, which dropped to 50% of the untreated ICM (fig. S2, D and E). GATA6⁺OCT4⁺ monolayer cells that were spread out from the ICM explants after 7 days culture in +C10F4HPDGF were also reduced upon PrE depletion (fig. S2F). These observations also support the PrE origin of PrESCs.

Next, we investigated the differentiation capability of PrESCs by injecting 15 green fluorescent protein (GFP)-labeled PrESCs or XENCs into blastocysts and examining their distribution after 18 hours. PrESCs were efficiently integrated into the PrE layer, whereas XENCs were randomly localized in the blastocoel (Fig. 3A and fig. S3A). In chimeric conceptuses at later stages, PrESCs contributed to both VE and PE, whereas XENCs were in only a small portion of the PE (Fig. 3B and fig. S3, B to F). To confirm the potential of PrESCs to contribute to both VE and PE, individual PrESCs were isolated and propagated. Each clone retained both VE and PE potentials (fig. S3, G and H). Next, we used a blastocyst complementation assay to examine whether PrESCs

can fully replace the endogenous PrE (Fig. 3C). The PrE was depleted in blastocysts by treating them with PD0325901 for 48 hours (fig. S4A) (13). Injected PrESCs efficiently reconstituted the PrE layer in PD0325901-treated blastocysts and improved the frequency of implantation of PrE-depleted blastocysts (fig. S4B and table S5). Moreover, nine neonates were recovered from reconstituted blastocysts treated with 0.5 or 1 μ M PD0325901. In these chimeras, PrESCs efficiently contributed to extraembryonic endoderm tissues and, in four cases, fully reconstituted these tissues (Fig. 3D, fig. S4F, and table S5). Full complementation of VE and PE by PrESCs was further confirmed in E6.5 embryos (fig. S4E); however, no contribution of PrESCs to fetal tissues, including the gut, was observed ($n = 9$, all obtained complementation chimeras at E18.5) (Fig. 3D and fig. S4F). PrESCs therefore can functionally replace the endogenous PrE and thus can be annotated as PrE stem cells for the extraembryonic endoderm lineage.

We further investigated the differentiation capability of PrESCs by using a modified blastoid self-organization method (14), in which ESCs, TSCs, and PrESCs were sequentially assembled to form ETP (ESC/TSC/PrESC) complexes (ETPs hereafter) (Fig. 4, A and B). In this condition, respective stem cells established uniform contacts in ETPs by day 3 (Fig. 4C). The differentiation status of the respective stem cells was assessed by means of scRNA-seq analysis of the respective stem cells and day 3 and day 6 ETPs (fig. S5A). Ten clusters were identified by means of PCA, and

clusters from different stem cells were juxtaposed but temporally separated, suggesting differentiation of respective stem cells in ETPs. The derivatives of ESCs and TSCs appropriately expressed differentiation-related genes in day 6 ETPs (fig. S5B). Through PCA for PrESC derivatives, PrESC descendants were found to exist in four distinct states (fig. S5C). A variety of PE-related or VE-related genes were expressed in cluster 1 or cluster 8, respectively (fig. S5D). PrESC can differentiate into PE- and VE-like cells and, reciprocally, facilitate differentiation of ESCs and TSCs in ETPs. To evaluate to what extent these ETPs represent normal development, day 3 ETPs were transferred into pseudopregnant uterus, and efficient implantation was observed, as revealed by decidual development, on prospective E7.5 embryos (23.3%, 28 of 120) (Fig. 4D). Implanted ETPs were elongated and associated with yolk sac-like structures on their surface (Fig. 4, E and F). PrESC-derived SOX17⁺ cells formed VE-like and PE-like sheets (Fig. 4, G and H). Therefore, PrESCs can establish interactions with ESCs and TSCs and generate descendants with yolk sac-like structures in utero. ETPs, however, failed to form normal embryos (Fig. 4G).

This study presents a robust protocol for the efficient generation of PrE stem cell lines, which can be used to elucidate the mechanisms that underpin PrE specification in vitro and to reconstitute embryos with ESCs and TSCs in vivo.

REFERENCES AND NOTES

1. M. J. Evans, M. H. Kaufman, *Nature* **292**, 154–156 (1981).

2. S. Tanaka, T. Kunath, A. K. Hadjantonakis, A. Nagy, J. Rossant, *Science* **282**, 2072–2075 (1998).
3. T. Kunath *et al.*, *Development* **132**, 1649–1661 (2005).
4. H. Igarashi *et al.*, *Biol. Reprod.* **99**, 578–589 (2018).
5. W. P. Jollie, *Teratology* **41**, 361–381 (1990).
6. J. Brennan *et al.*, *Nature* **411**, 965–969 (2001).
7. H. Ueno, I. L. Weissman, *Int. J. Dev. Biol.* **54**, 1019–1031 (2010).
8. G. S. Kwon, M. Viotti, A. K. Hadjantonakis, *Dev. Cell* **15**, 509–520 (2008).
9. N. Schrodde, N. Saiz, S. Di Talia, A. K. Hadjantonakis, *Dev. Cell* **29**, 454–467 (2014).
10. J. Artus, J. J. Panthier, A. K. Hadjantonakis, *Development* **137**, 3361–3372 (2010).
11. H. Mohammed *et al.*, *Cell Rep.* **20**, 1215–1228 (2017).
12. P. P. Tam, E. A. Williams, S. S. Tan, *Dev. Genet.* **15**, 491–503 (1994).
13. J. Nichols, J. Silva, M. Roode, A. Smith, *Development* **136**, 3215–3222 (2009).
14. B. Sozen *et al.*, *Dev. Cell* **51**, 698–712.e8 (2019).

ACKNOWLEDGMENTS

Funding: This work was supported by JSPS KAKENHI under grants 18H05366 and 19H05757 and by AMED under grant 19bk0104093h0001 to Y.O. **Author contributions:** Y.O. and H.K. designed the study and wrote the manuscript. Y.O. and T.A.E. analyzed next-generation sequencing (NGS) data. Y.O., Y.I., Y.Ka., A.S., T.K., M.K., Y.Ko., H.S., T.W., and O.O. performed experiments. **Competing interests:** RIKEN has a patent pending (JP2019-118733) on the method for derivation and maintenance of PrES cells. Y.O. and H.K. are the inventors of the patent. There is no conflict of interest relevant to this study. **Data and materials availability:** RNA-seq data are available at the Gene Expression Omnibus (GEO) website (www.ncbi.nlm.nih.gov/geo) under accession no. GSE185461.

SUPPLEMENTARY MATERIALS

science.org/doi/10.1126/science.aay3325
Materials and Methods
Figs. S1 to S5
Tables S1 to S5
MDAR Reproducibility Checklist

9 June 2019; resubmitted 16 October 2020
Accepted 21 December 2021
[10.1126/science.aay3325](https://doi.org/10.1126/science.aay3325)



AAV9 Titer Kit

Gyros Protein Technologies has released the Gyrolab AAV9 Titer Kit for rapid determination of physical titer in adeno-associated virus serotype 9 (AAV9) vector-based cell and gene therapy manufacturing. The kit enables researchers to improve productivity and is based on a highly selective

AAV9 affinity ligand developed with Thermo Fisher Scientific's CaptureSelect technology. These ligands are also the basis of POROS CaptureSelect AAV9 Affinity Resin, which is frequently used to purify AAV9 viral vectors. The AAV9 serotype is attractive as a gene-delivery vector, as it crosses the blood-brain barrier and targets the central nervous system with high efficiency. The AAV9 Titer Kit provides fast results, enabling 96 data points to be generated in 80 min, an improved assay working range compared to ELISA methods, and can handle small sample volumes (10X less than an ELISA), shortening development timelines of novel biotherapeutics, including cell and gene therapies.

Gyros Protein Technologies

For info: +1-877-433-9400
www.gyrosproteintechnologies.com

RNA Prestain Loading Dye

Biotium announces the release of EMBER500 RNA Prestain Loading Dye. This novel prestain loading dye is much more sensitive than conventional prestaining with ethidium bromide (EtBr), and is also compatible with blue LED gel imagers, unlike EtBr. Staining for RNA is commonly done with EtBr on a denaturing gel after electrophoresis. However, denaturing gels can be complicated to prepare and involve handling hazardous reagents. RNA prestaining with EtBr can be performed with nondenaturing agarose gels, but requires large amounts of the dye and still limits sensitivity severely. For maximum convenience, the prestain also includes formamide as well as electrophoresis tracking dyes, allowing sample denaturing, loading, tracking, and staining in a single step. In addition, EMBER500 stains both RNA and DNA, allowing detection of contaminating genomic DNA in purified RNA samples. Detection of EMBER500 is flexible, with compatibility for UV transilluminators and blue LED gel imagers, which eliminate UV exposure hazards.

Biotium

For info: +1-800-304-5357
www.biotium.com

Basic Lyophilized Isothermal Amplification Microbeads

PrimeAmp Basic Lyophilized Isothermal Amplification Microbeads contain reaction buffer, Mg^{2+} , deoxynucleoside triphosphate, and *Bst* DNA/RNA polymerase, in the lyophilized form. Only primers and templates are needed to be added for isothermal amplification. The microbeads do not contain any dyes and can be flexibly used for various isothermal amplification applications. They can also be stored at room temperature (25°C) for a year, which is also very convenient for transportation.

Beijing SBS Genetech

For info: +86-(0)-10-62969345
www.sbsgenetech.com

Microplate for Nucleic Acid Purification

The Porvair Sciences 96 deep well plate, 96-well elution plate, and 96-well magnetic tip combs are fully compatible with Thermo Fisher Scientific's KingFisher range of purification systems. These consumables are made from medical-grade polypropylene to ensure low affinity binding of biomolecules and low leachables and extractables throughout the extraction and purification workflow. This maximizes the yield and quality of isolated proteins and nucleic acids from samples and improves assay performance when used in conjunction with KingFisher Flex, Duo Prime, and Presto instruments. Each v-shaped bottom well supports the specialized magnetic tips of all KingFisher instruments with a perfect fit and maximizes liquid-sample collection, mixing, and uptake during purification. From sample collection and mixing to purification, the Porvair Sciences 96 deep well plate ensures reproducible purification of cells, proteins, and nucleic acids from a wide range of samples.

Porvair Sciences

For info: +1-800-552-3696
www.microplates.com/kingfisher-compatible-96-well-microplate

Evaporator

The Smart Evaporator uses the Vacuum Vortex Concentration (VVC) method, the world's first concentration method enabling users to remove dimethyl sulfoxide (DMSO) and dimethyl formamide, which are difficult and time-consuming to concentrate. The novel Spiral Plug technology generates a helical flow of air or inert gas over the surface of your solvent, increasing the surface area. Since the vial isn't under high vacuum, there is no risk of bumping or splashing. The spiral plugs come in various sizes for compatibility with many different sample tubes, flasks, and vials. The Smart Evaporator has been used in a wide range of fields and applications, including chemical biology, complex chemistry, material science, food analysis, analytical chemistry, bioimaging, and sample recovery when DMSO is used in nuclear magnetic resonance spectroscopy.

BioChromato

For info: +81-(0)-466-23-8382
biochromato.com/smart-evaporator

Target Enrichment Panels

Combine the performance of hybrid-capture NGS target enrichment and the convenience and turnaround time of amplicon-based methods with KAPA HyperPETE target enrichment panels. KAPA HyperPETE (Primer Extension Target Enrichment) is a novel hybridization capture technology that uses primer extension reactions to specifically capture and release target library molecules for sequencing. These panels detect all major somatic variants in cell-free DNA, FFPE, and RNA samples, including single-nucleotide variants, short indels, copy number variants, microsatellite instability, and fusion transcripts (known and novel). This technology preserves the performance of conventional hybridization while enabling a more efficient workflow. Interrogate difficult regions by leveraging Roche's expertise in panel content and design. Save time and resources with single-day, automatable workflow. Increase analysis efficiency with focused, high-uniformity panel design with no need for primer trimming. Preserve precious samples and improve sensitivity by avoiding the need to split panels.

Roche Sequencing and Life Science

For info: +1-800-262-4911
sequencing.roche.com/en-us

Electronically submit your new product description or product literature information! Go to www.science.org/about/new-products-section for more information.

Newly offered instrumentation, apparatus, and laboratory materials of interest to researchers in all disciplines in academic, industrial, and governmental organizations are featured in this space. Emphasis is given to purpose, chief characteristics, and availability of products and materials. Endorsement by *Science* or AAAS of any products or materials mentioned is not implied. Additional information may be obtained from the manufacturer or supplier.



TENURE TRACK FACULTY POSITION IN REGENERATIVE MEDICINE AND CELL BIOLOGY

Medical University of South Carolina, Department of Regenerative Medicine and Cell Biology

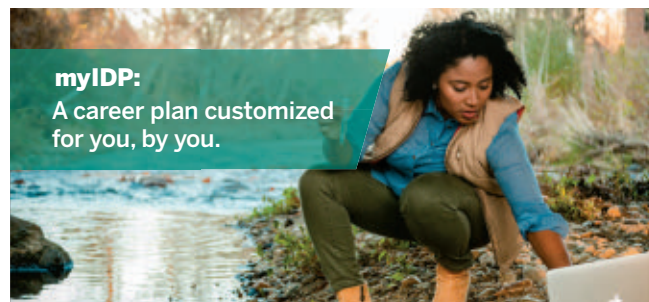
A tenure track faculty position at the **Assistant, Associate, or Professor** level is available for a researcher that focuses on a topic broadly related to the digestive system. Candidates at the senior levels are expected to bring a vigorous research program with significant extramural funding. Candidates whose research complements existing strengths, which include tissue engineering, pluripotent stem cell differentiation, cellular basis of disease, and molecular biology of cell function, are particularly encouraged to apply. Competitive salary, laboratory space and start-up funds are available. Research at MUSC is supported by excellent core facilities specializing in advanced imaging, genetically modified mice and rats, drug discovery, proteomics, and stem cell and organoid models of disease. Information about the Department can be found at <https://medicine.musc.edu/departments/regenerative-medicine>.

Applicants should provide a research plan and a curriculum vitae including the names of three references through the MUSC employment portal: <https://careers.pageuppeople.com/756/cw/en-us/job/541082/univ-regenerative-medicine-open-rank>. Review of applications will begin in February and continue until the position is filled.

The Medical University of South Carolina in Charleston was established in 1824 and is the 10th oldest continuously operating medical school in the United States. It has approximately 2,200 graduate and professional students that are supported by 1300 faculty members. Total annual research funding exceeds \$250 million. This includes funding that supports the NCI-designated Hollings Cancer Center, a Clinical and Translational Science Award, a Center for Biomedical Research Excellence in Digestive and Liver Disease, and Digestive Disease Research Core Center (<https://medicine.musc.edu/departments/dom/divisions/gastroenterology/research/labs-and-centers/ddrcc>) along with multiple institutional training grants that support graduate student stipends.

Charleston is a unique coastal city of half a million residents that is consistently ranked as a top international destination. It has a rich history, food culture, and offers extensive outdoor recreation opportunities. The city hosts the internationally renowned Spoleto Festival USA, which offers the finest in theater, opera, dance, music and art. Information can be found at <http://www.charlestoncvb.com/>.

MUSC is an Affirmative Action/Equal Opportunity Employer.



myIDP:
A career plan customized for you, by you.

For your career in science, there's only one **Science**

Features in myIDP include:

- Exercises to help you examine your skills, interests, and values.
- A list of 20 scientific career paths with a prediction of which ones best fit your skills and interests.



Visit the website and start planning today!
myIDP.sciencecareers.org

Science Careers



In partnership with:



Who's the top employer for 2021?

Science Careers' annual survey reveals the top companies in biotech & pharma voted on by Science readers.

Read the article and employer profiles at
sciencecareers.org/topemployers





**Shenzhen Institute of
Advanced Technology**
Chinese Academy of Sciences



Established in partnership between the Chinese Academy of Sciences and the Shenzhen Municipal Government, the Shenzhen Institute of Advanced Technology (SIAT) is a newly-created university with an objective to become the world's preeminent institute for emerging science and engineering programs. SIAT is equipped with state-of-art teaching and research facilities and is dedicated to cultivating international, visionary, and interdisciplinary talents while delivering research support to pursue innovation-driven development.

SIAT is located in Shenzhen, also known as the "Silicon Valley of China," a modern, clean, and green city, well-known for its stunning architecture, vibrant economy, and its status as a leading global technology hub. SIAT is seeking applications for faculty positions of all ranks in the following academic programs: Computer Science and Engineering, Bioinformatics, Robotics, Life Sciences, Material Science and Engineering, Bio-medical Engineering, Pharmaceutical Sciences, Synthetic Biology, Neurosciences, etc. SIAT seeks individuals with a strong record of scholarship who possess the ability to develop and lead high-quality teaching and research programs. SIAT offers a comprehensive benefits package and is committed to faculty success throughout the academic career trajectory, providing support for ambitious and world-class research projects and innovative, interactive teaching methods.

Further information:

<http://english.siat.cas.cn/DP/Va/>



ICYS Research Fellow at ICYS, NIMS, Japan

The International Center for Young Scientists (ICYS) of the National Institute for Materials Science (NIMS) invites applications for ICYS Research Fellow positions. ICYS will offer you the freedom to conduct independent and self-directed research in various areas of materials science with full access to NIMS advanced research facilities.

The common language at ICYS is English. Clerical and technical support in English will be given by the ICYS staff. An annual salary of approximately 5.35 million yen is guaranteed, which may be increased to a maximum of ~5.88 million yen depending on the performance of the Research Fellow*. In addition, a research grant of 2 million yen per year will be provided to each Research Fellow. The initial contract term is two years, which may be extended for another year depending on one's performance. Also, advantage is given when applying to NIMS permanent researcher position (about 50% of the applicants are accepted).

All applicants must have obtained a PhD degree within the last ten years. Applicants should submit an **application form** including a research proposal during the ICYS term, CV, a **list of DOI of journal publications**, **PDF files of three significant publications**, and **PhD Certificate** to the ICYS Recruitment Desk by **March 31, 2022 JST**. The format for the application documents can be downloaded from our website. The selection will be made on the basis of originality and quality of the research proposal as well as the research achievements. Please visit our website for more details.

* Approximately 23% of annual salary will be deducted as social insurance premium, residence tax and income tax.

ICYS Recruitment Desk
National Institute for Materials Science
www.nims.go.jp/icys/recruitment/



香港城市大學
City University of Hong Kong

#53

World
University

#4

World's top 50
Universities
under age 50

#1

World's Most
International Universities



Global Scholar Recruitment Campaign

City University of Hong Kong (CityU) is one of the world's leading universities, known for innovation, creativity and research. We are now seeking exceptional scholars to join us as Assistant Professors/Associate Professors/Professors/Chair Professors (on substantiation-track) in all academic fields with special focuses on **One Health, Digital Society, Smart City, Matter, Brain**, and related interdisciplinary areas. Research fields of particular interest include, but not limited to:



- biomedical science and engineering
- veterinary science
- computer science and data science
- neuroscience and neural engineering
- bio-statistics and AI-healthcare
- smart/semi-conductor manufacturing
- AI/robotics/autonomous systems
- aerospace and microelectronics engineering
- energy generation and storage
- digital business and innovation management
- fintech and business analytics
- computational social sciences
- digital humanities
- digital and new media
- law and technology
- private law
- healthy, smart and sustainable cities

Successful candidates should have a demonstrated ability to build a world-class research programme related to CityU's strategic research areas, plus a commitment to education and student mentorship. Candidates must possess a doctorate in their respective field by the time of appointment.

Outstanding faculty joining the University will be considered for nomination of the **Global STEM Professorship Scheme** sponsored by the Government of the Hong Kong Special Administrative Region, and may be provided with subsidy for their research teams and for setting up laboratories.

Please visit Colleges, Schools and Departments in CityU at
<https://www.cityu.edu.hk/academic/colleges-schools-and-departments>



City University of Hong Kong is an equal opportunity employer. We are committed to the principle of diversity. Personal data provided by applicants will be used for recruitment and other employment-related purposes.

Worldwide recognition ranking #53 (QS 2022), and #4 among top 50 universities under age 50 (QS 2021); #1 in the World's Most International Universities (THE 2020); #1 in Automation & Control/Electrical & Electronic Engineering/Materials Science & Engineering/Metallurgical Engineering/Nanoscience & Nanotechnology/Telecommunication Engineering in Hong Kong (GRAS 2021); and #39 Business School in the World and #4 in Asia (UT Dallas 2016 to 2020)

By Gabriela Lopez

More than an exam

My Ph.D. adviser had encouraged me to take a vacation. So I was sitting at an airport restaurant, sipping a margarita, when I received the email. It informed me I had failed my qualifying exam on my third attempt, which meant dismissal from the program. I knew things hadn't gone perfectly. A day earlier my committee had told me it needed more time to decide whether I passed. But I was still dumbfounded. How was it possible that one exam—1 hour of my life—could erase all my other successes and define me as unfit to be a scientist?

I wasn't sure what to expect when I started my Ph.D. program. As an Afro-Latinx first-generation college graduate, I didn't have family members who could tell me what it was like. I had worked in a lab as an undergrad student and I assumed I was prepared for what was to come. But I struggled with my classes during my first year, spending countless hours receiving tutoring and studying in the library. Often, I had to interrupt my reading to look up the definition of scientific words and concepts.

I ended that year with increased confidence, eager to put my newfound knowledge into action as I dove deeper into my research. But my confidence took another plunge shortly thereafter, when I made my first attempt at the qualifying exam. I had never taken an oral exam before, so the experience was terrifying. I stood in front of my exam committee while they asked me about my research project and then peppered me with questions about concepts and methods, some not directly relevant to my research.

I had switched research projects 5 months earlier, after my first adviser left the university, so I wasn't as confident going into the exam as I might have been otherwise. I struggled to remember terminology and come up with thorough answers on the spot, especially when I was asked questions I hadn't previously thought about.

Once it was over, my committee told me I'd conditionally passed, which meant I had to take more time to study and prepare to talk about a subset of topics. I was shaken but still hopeful. But when I retook the exam, I failed again. That's when I was told I'd have one more chance.

For the next 2 months, I did everything in my power to prepare. I sat down with my committee chairs and asked them for guidance. I practiced answering oral questions with my adviser and lab. I even stopped doing lab work to focus on my exam preparations. I was all in.

When the exam was over, I left the room feeling a mix of



"I still have a little voice in the back of my head fretting I'm not good enough. But I try to quiet it."

fear and relief. But those feelings changed to frustration the next day, after I learned I'd failed. I reflected on how different my experience going into the exam was from my peers'. Many had college-educated family members they could speak with about their work. My family members, in contrast, are less familiar with science. We also speak Spanish at home, and I have difficulty translating even the simplest scientific concepts into Spanish. These struggles and many others hampered my ability to comfortably speak the expected "language of science."

My adviser believed in me and persuaded the department to allow me to complete a master's degree. So I carried on with my research, resigned to my situation. But with the onset of the COVID-19 pandemic

and the Black Lives Matter protests, things started to change. I watched as movements such as #BlackInTheIvory took hold, initiating discussions about the lack of support for first-generation, underrepresented students in academia. And I was heartened to see my program reassess its own approach.

After a series of meetings and open forums—during which I submitted anonymous feedback—faculty members voted to do away with the qualifying exam structure I'd struggled with. From then on, students would be asked questions, so that faculty could gauge their knowledge and skills and provide constructive feedback. But they wouldn't face expulsion from the program.


My adviser petitioned to reinstate me to the Ph.D. program, and I'm now back to working on my doctorate. I still have a little voice in the back of my head fretting I'm not good enough. But I try to quiet it by surrounding myself with mentors who support me and by staying focused on developing into the great scientist I know I can be. In the end, I am much more than that 1 hour exam. ■

Gabriela Lopez is a Ph.D. candidate at Northwestern University.

PUT YOUR RESEARCH OUT IN FRONT

Submit your research:
cts.ScienceMag.org

ScienceSignaling


 Twitter: @SciSignal

 Facebook: @ScienceSignaling



You heard the message.

We've told you before that NEB® offers a broad portfolio of reagents for purification, quantitation, detection, synthesis and manipulation of RNA. But did you know that these products are available from bench-scale to commercial-scale to enable both academic and industrial needs? Further, we provide these products at quality levels that support vaccine and diagnostic manufacturing. Experience improved performance and increased yields, enabled by our expertise in enzymology.



RNA purification: Extract up to 100 µg of high quality, total RNA from a variety of sample types with the Monarch® Total RNA Miniprep Kit. Monarch RNA Cleanup Kits can quickly and easily clean up and concentrate RNA in just minutes, with no carryover contamination.



RNA detection: Optimize your RT-qPCR across a variety of sample types with Luna®. High-concentration mixes and kits optimized for multiplexing enable sensitive detection of SARS-CoV-2. Simple, one-step solutions for LAMP and RT-LAMP are also available.



RNA-seq: NEBNext® kits are available for RNA library preparation, rRNA depletion and poly(A) mRNA isolation. Save time with streamlined workflows, reduced hands-on time and automation compatibility.



RNA synthesis: Synthesize high-quality RNA with reagents designed to simplify your workflow, including HiScribe™ IVT kits and capping reagents. GMP-grade* reagents are available for mRNA synthesis of therapeutics and vaccines.

Find more details on products available, request samples, and access helpful RNA-related resources at www.neb.com/RNA2021.

**GMP-grade* is a branding term NEB uses to describe reagents manufactured at our Rowley, MA facility, where we utilize procedures and process controls to manufacture reagents in compliance with ISO 9001 and ISO 13485 quality management system standards. NEB does not manufacture or sell products known as Active Pharmaceutical Ingredients (APIs), nor do we manufacture products in compliance with all of the Current Good Manufacturing Practice regulations.

One or more of these products are covered by patents, trademarks and/or copyrights owned or controlled by New England Biolabs, Inc. For more information, please email us at gbd@neb.com. The use of these products may require you to obtain additional third party intellectual property rights for certain applications.

© Copyright 2021, New England Biolabs, Inc.; all rights reserved.



be INSPIRED
drive DISCOVERY
stay GENUINE